





#### Dissertation

# CO<sub>2</sub> Utilization by Biomass Gasification:

# Experimental Investigations, Measurement Innovation, and Process Design for Carbon Recycling in Ironmaking

Carried out for the purpose of obtaining the degree of Doctor technicae (Dr. techn.), submitted at Technische Universität Wien, Faculty of Mechanical and Industrial Engineering by

# Florian J. MÜLLER

Mat. No.: 01228914

under the supervision of Univ.Prof. Dipl.-Ing. Dr.techn. Franz Winter and the co-supervision of Ing. Dipl.-Ing. Dr.techn. Stefan Müller Dipl.-Ing. Dr.techn. Josef Fuchs

at the

Institute of Chemical, Environmental, and Bioscience Engineering in Vienna, June 2025.

#### Reviewed by

Prof. Dr. David Pallarès Chalmers University of Technology Department of Space, Earth, Environment Hörsalsvägen 7B, level 4 SE-412 96 Gothenburg, Sweden

Ao. Univ. Prof. Dipl.-Ing. Dr. techn. Andreas Werner Technische Universität Wien Institute of Energy Systems and Thermodynamics Getreidemarkt 9, E302 1060 Vienna, Austria



# **Imprint**

© Florian J. Müller, 2025

#### florian.johann.mueller@tuwien.ac.at

Institute of Chemical, Environmental and Bioscience Engineering

TU Wien

Getreidemarkt 9/166

1060 Vienna

Austria

CO2 Utilization by Biomass Gasification: Experimental Investigations, Measurement Innovation, and Process Design for Carbon Recycling in Ironmaking

Reproduction requires color print.



# **Examination committee**

Supervisor: Univ.Prof. Dipl.-Ing. Dr.techn. Franz Winter

Co-supervisors: Ing. Dipl.-Ing. Dr.techn. Stefan Müller

Dipl.-Ing. Dr.techn. Josef Fuchs

Reviewer 1: Prof. Dr. David Pallarès

Reviewer 2: Ao. Univ. Prof. Dipl.-Ing. Dr. techn. Andreas Werner Chair: Dipl.-Ing.in Dr.in techn. Bettina Mihalyi-Schneider

I confirm that the printing of this thesis requires the approval of the examination board.

# Acknowledgment of funding

This work was carried out within the doctoral school CO<sub>2</sub>Refinery at TU Wien. Further funding was provided by ArcelorMittal Innovación Investigación e Inversión (CO<sub>2</sub> Reduction for Ironmaking by Utilization of Process Gases, Part 1 and 2) and by the Austrian Science Fund FWF (10.55776/I5404).

## **Affidavit**

I declare in lieu of oath that I wrote this thesis and carried out the associated research myself, using only the literature cited in this volume. If text passages from sources are used literally, they are marked as such.

I confirm that this work is original and has not been submitted for examination elsewhere, nor is it currently under consideration for a thesis elsewhere.

I acknowledge that the submitted work will be checked electronically using suitable and state-of-the-art means (plagiarism detection software). On the one hand, this ensures that the submitted work was prepared according to the high-quality standards within the applicable rules to ensure good scientific practice "Code of Conduct" at the TU Wien. On the other hand, a comparison with other student theses avoids violations of my personal copyright.

# **Danksagung**

Ich möchte diese Danksagung nutzen, um mich bei einigen der zahlreichen Leute zu bedanken, ohne deren Unterstützung, Motivation und Inspiration diese Dissertation nicht in dieser Form hätte entstehen können.

Für die wissenschaftliche Betreuung dieser Dissertation möchte ich meinen Betreuern Franz Winter, Stefan Müller und Josef Fuchs sowie dem Leiter der CO<sub>2</sub>Refinery Michael Harasek ausdrücklich danken. Danke für die Möglichkeit, meine Arbeit in diesem interessanten, abwechslungsreichen und zukunftsträchtigen Themenfeld verfassen zu können. Ich bin froh, dass ich durch eure unterschiedlichen Zugänge eine durchweg kompetente, aber auch vielfältige Leitung und Orientierung erfahren habe, die mir die Möglichkeit gegeben hat, mich fachlich und persönlich weiterzuentwickeln.

Ich bin sehr dankbar für die emotionale Unterstützung die ich durch Partnerschaft, Freunde und Familie erfahren habe - insbesondere durch die Schaffung von Rückzugsorten und Freuden abseits der Arbeit. Besonders hervorstreichen möchte ich hier meine Partnerin Stephanie, die mich seit mehr als einem Jahrzehnt unterstützt und aushält. Danke für alles - du warst vom Bachelor bis zur Dissertation meine wichtigste Stütze und ohne dich würde es diese Arbeit so nicht geben. Auch meinen langjährigen besten Freund Michael möchte ich ausdrücklich hervorheben – neben der privaten Unterstützung war es eine riesige Freude mit dir an unserer gemeinsamen Publikation zu arbeiten.

Für die konstante Bestärkung von früher Kindheit möchte ich mich bei meiner Mutter Maria und ihren Eltern Franz und Hermine als wichtigste familiäre Bezugspersonen bedanken. Von euch habe ich gelernt, neugierig, weltverbesserisch und unnachgiebig zu sein - Eigenschaften die sich glücklicherweise hervorragend auf ein Doktorat anwenden lassen. Auch mein Vater Peter und dessen Eltern Peter und Rosina haben mich stets bestärkt. Durch meinen Vater Peter habe ich zur Verfahrenstechnik gefunden deine Empfehlung war es, die mich entscheidend in diese Forschungsdisziplin gelenkt hat. Von euch allen habe ich den nötigen Stolz auf Wissen gezeigt bekommen, der meinen Lebensweg prägt und ermöglicht - dafür und für jegliche Unterstützung danke ich euch von ganzem Herzen. Auch meinen Geschwistern, Tanten sowie meiner und Steffis restlicher Familie danke ich für alles.

Ich habe beim Schreiben dieser Danksagung zunächst vergeblich versucht, zwischen Freund\*innen und Kolleg\*innen zu unterscheiden und freue mich, dass mir das nicht gelungen ist. Die Brettspiele-SELFhilfegruppe mit meinem Büro-Brudi Simon, Eugen und Lena bleibt hoffentlich noch lange über das Doktorat hinaus bestehen. Auch den vielen anderen tollen Leuten aus der CO<sub>2</sub>Refinery sowie dem FB3 und FB7 der Verfahrenstechnik möchte ich für berufliche Hilfe und private Freuden herzlich danken.

Abschließend möchte ich Professor David Pallarès und Professor Andreas Werner für ihren Aufwand und ihre Unterstützung im Rahmen der Begutachtung dieser Dissertation danken.



# **Abstract**

**Keywords**: CO<sub>2</sub> conversion, CCU, Biomass Gasification, Fluidized bed, Ironmaking

Biomass CO<sub>2</sub> gasification offers a promising thermochemical route to convert biomass and CO<sub>2</sub> into a CO-rich product gas, providing renewable carbon and energy. However, key challenges must be addressed for this process to be considered a robust CO<sub>2</sub> utilization strategy: process optimization, validating CO<sub>2</sub> conversion, and industrial integration. This thesis tackles these three central questions through targeted experiments, novel measurement methods, and process simulations:

First, the thesis explores how CO<sub>2</sub> conversion can be increased in fluidized bed biomass gasifiers. Hightemperature operation (≥850 °C) is identified as a key driver, enhancing both the CO concentration in equilibrium and the kinetics of the Boudouard reaction (C +  $CO_2 \rightleftharpoons 2CO$ ). Experiments reveal that  $CO_2$ conversion can also be limited by solid carbon availability and gas-solid contact time. A CO2 conversion of 93 % is achieved when gasifying wood char under optimized conditions in a lab-scale fluidized bed gasifier.

Second, this thesis validates the conversion of feedstock CO<sub>2</sub> by introducing a novel assessment strategy based on carbon isotope analysis. Previous investigations used estimation methods for CO<sub>2</sub> conversion that could not differentiate carbonaceous product gas components by the origin of their carbon: biomass or CO<sub>2</sub>. This method allows for accurate calculation of how much externally supplied CO<sub>2</sub> is converted during the process by leveraging the distinct  $\delta^{13}$ C signatures of biomass and external CO<sub>2</sub> sources. These findings validate CO<sub>2</sub> gasification as a technology for CO<sub>2</sub> conversion and help process understanding.

Third, the thesis evaluates the integration of biomass CO<sub>2</sub> gasification into an ironmaking process by process simulations. A plant design is proposed where the gasifier supplies reducing gas for ironmaking while utilizing process-emitted CO<sub>2</sub>, forming a compact CCU-loop. Techno-economic and life cycle assessments show this approach to be both cost-effective and environmentally superior to natural gasbased alternatives, achieving net-negative emissions of -83 kg<sub>CO2e</sub>/t<sub>CDRI</sub> at a levelized cost of 350 €/t<sub>CDRI</sub> – compared to 892 kg<sub>CO2e</sub>/t<sub>CDRI</sub> and 416 €/t<sub>CDRI</sub> for a conventional MIDREX process.

Two supporting research avenues further advance the biomass gasification field. First, a two-step process of biomass pretreatment by torrefaction followed by biomass CO<sub>2</sub> gasification is used to produce biochar with up to 800 m<sup>2</sup>/g surface area at similar temperatures as those for high CO<sub>2</sub> conversion. Second, a spectroscopy-based method using a 2.3 THz quantum cascade laser is introduced for online H<sub>2</sub>O quantification in the hot, tar-laden product gas, addressing key measurement challenges.

In summary, this thesis enhances the scientific and technical foundations of CO<sub>2</sub>-assisted biomass gasification. It provides new tools for measurement, strategies for performance improvement, and evidence of real-world viability, positioning the technology as a credible pathway for renewable carbon production and industrial carbon utilization.

# Kurzfassung

Schlüsselwörter: CO<sub>2</sub>-Umwandlung, CCU, Biomassevergasung, Wirbelschicht, Eisenherstellung

Biomassevergasung mit CO<sub>2</sub> bietet einen vielversprechenden Pfad, um aus Biomasse und CO<sub>2</sub> ein COreiches Produktgas mit erneuerbarem Kohlenstoff und Energie bereitzustellen. Damit dies als tragfähige CO<sub>2</sub>-Nutzungsstrategie gelten kann, müssen zentrale Herausforderungen bewältigt werden: Prozessoptimierung, Validierung der CO2-Umwandlung und industrielle Integration. Diese Arbeit adressiert diese drei Fragen durch gezielte Experimente, neue Messmethoden und Prozesssimulationen.

Erstens untersucht die Arbeit, wie die CO2-Umwandlung in Wirbelschicht-Biomassevergasern erhöht werden kann. Hohe Betriebstemperatur (≥850 °C) wird als entscheidender Faktor identifiziert, da sowohl die Gleichgewichtskonzentration von CO als auch die Kinetik der Boudouard-Reaktion (C + CO<sub>2</sub> ≠ 2CO) begünstigt werden. Für hohe CO<sub>2</sub>-Umwandlung müssen ausreichende Verfügbarkeit von Festkohlenstoff und Gas-Feststoff-Kontaktzeiten sichergestellt werden. Unter optimierten Bedingungen wird eine CO<sub>2</sub>-Umwandlung von 93 % bei der Vergasung von Holzkohle erreicht.

Zweitens validiert die Arbeit die Umwandlung von zugeführtem CO<sub>2</sub> im Reaktor durch eine neue Messmethode auf Basis von Kohlenstoffisotopen. Vorhergehende Untersuchungen schätzten die CO<sub>2</sub> Umwandlung ohne zwischen Kohlenstoff aus Biomasse und CO2 zu differenzieren. Die neue Methode ermöglicht es durch Analyse der unterschiedlichen δ<sup>13</sup>C-Signaturen von Biomasse und zugeführtem CO<sub>2</sub> nachzuverfolgen, welcher Anteil des zugeführten CO2 im Prozess umgesetzt wird. Dies validiert Biomassevergasung mit CO<sub>2</sub> als CO<sub>2</sub>-Nutzungsstrategie und fördert Prozessverständnis.

Drittens bewertet die Arbeit durch Prozesssimulation die Integration der CO<sub>2</sub>-Biomassevergasung in einen Eisenherstellungsprozess. Der Vergaser stellt Reduktionsgas für die Eisenherstellung bereit und recyclet dabei prozessbedingt emittiertes CO<sub>2</sub> – ein kompaktes CCU-System. Techno-ökonomische und Lebenszyklusbewertungen zeigen hierbei Vorteile gegenüber erdgasbasierten Verfahren: Netto-negative Emission von -83 kg<sub>CO2e</sub>/t<sub>CDRI</sub> bei levelisierten Kosten von 350 €/t<sub>CDRI</sub> stehen Emissionen von 892 kg<sub>CO2e</sub>/t<sub>CDRI</sub> und Kosten von 416 €/t<sub>CDRI</sub> im konventionellen MIDREX-Prozess gegenüber.

Zwei ergänzende Themen erweitern das Forschungsfeld. Erstens wird ein zweistufiger Prozess aus Torrefizierung und CO<sub>2</sub>-Vergasung zur Herstellung hochporöser Biokohle mit spezifischer Oberfläche bis zu 800 m<sup>2</sup>/g untersucht. Zweitens wird ein 2.3 THz Quantenkaskadenlaser zur spektroskopischen Quantifizierung von H<sub>2</sub>O in heißem, teerhaltigen Produktgas vorgestellt, was zur Überwindung bestehender Messtechnikhürden beiträgt.

Zusammenfassend stärkt diese Arbeit die wissenschaftlich-technische Basis Biomassevergasung. Sie liefert neue Messwerkzeuge, Strategien zur Leistungssteigerung und Belege für die industrielle Anwendbarkeit. Dies positioniert die Technologie als glaubwürdigen Pfad zur Bereitstellung erneuerbaren Kohlenstoffs und zur industriellen CO<sub>2</sub>-Nutzung.



# **Table of Contents**

Overview of scientific work	i
Nomenclature	iv
1. Introduction	1
1.1. Motivation	1
1.2. Aim of this thesis	6
1.3. Thesis outline	7
2. State of the art on biomass CO <sub>2</sub> gasification	9
2.1. Fundamentals of biomass gasification	9
2.2. Reactor types used for biomass gasification	11
2.3. Characteristics of CO <sub>2</sub> gasification by comparison to steam gasification	14
2.4. CO <sub>2</sub> utilization in fluidized bed biomass gasifiers	17
3. Methodology	21
3.1. Reactors	21
3.2. Measurements	24
3.3. Simulations and modeling	27
3.4. Calculation of key parameters	32
4. Results and discussion	38
4.1. Increasing CO <sub>2</sub> conversion by varying operating conditions	38
4.2. Validating CO <sub>2</sub> conversion by stable carbon isotope analysis	44
4.3. Implementing CO <sub>2</sub> conversion for ironmaking	48
4.4. Additional research on biomass CO <sub>2</sub> gasification	54
5. Summary and conclusions	61
5.1. Findings on individual research questions	61
5.2. Synthesis and implications of core results	63
6. Outlook	66
References	68
Appended articles	93
Journal article I (JA I): CO <sub>2</sub> conversion to CO by fluidized bed biomass gasificati	ion: Analysis of

operational parameters

Journal article II (JA II): CO2 conversion to CO by fluidized bed biomass gasification: Measuring CO<sub>2</sub> utilization via stable carbon isotope ratios

Journal article III (JA III): Water vapor quantification in raw product gas by THz quantum cascade laser

Journal article IV (JA IV): Eco-friendly ironmaking by biomass CO<sub>2</sub> gasification: Process simulations for ecological and economic evaluation of CO<sub>2</sub> recycling in direct reduction ironmaking

Conference article I (CA I): Surface adjustment of biochar by CO<sub>2</sub> gasification under fixed and fluidized bed conditions



# Overview of scientific work

# List of appended publications

This thesis is based on the following articles, which are referred to as Journal/Conference articles (JA/CA) and their Roman numeral in the text, which was given chronologically by publication date.

Journal article	JA I.	F. J. Müller, J. Fuchs, M. Fanjul Cuesta, A, Oblanca Gutiérrez, S. Pratschner, S. Müller, F. Winter, "CO2 conversion to CO by fluidized bed biomass gasification: Analysis of operational parameters," <i>Journal of CO2 Utilization</i> , vol. 81, no. March 2024, 2024, doi: 10.1016/j.jcou.2024.102706.
Journal article	JA II.	F. J. Müller, J. Fuchs, S. Müller, and F. Winter, "CO2 conversion to CO by fluidized bed biomass gasification: Measuring CO2 utilization via stable carbon isotope ratios," <i>Journal of CO2 Utilization</i> , vol. 83, May 2024, doi: 10.1016/j.jcou.2024.102792.
Journal article	JA III.	F. J. Müller, M. Jaidl, D. Theiner, J. Zeitlhofer, F. Benedikt, L. Steiner, A. Bartik, M.C. Ertl, A.M. Andrews, G. Strasser, S. Müller, F. Winter, K. Unterrainer, "Water vapor quantification in raw product gas by THz quantum cascade laser," <i>Energy Conversion and Management: X</i> , p. 100906, Feb. 2025, doi: 10.1016/J.ECMX.2025.100906.
Journal article*	JA IV.	F. J. Müller, S. Jankovic, J. Fuchs, D. Dimande, S. Müller, and F. Winter, "Eco-friendly ironmaking by biomass CO2 gasification: Process simulations for ecological and economic evaluation of CO2 recycling in direct reduction ironmaking," <i>Energy Conversion and Managment</i> , under review at the time of thesis submission.
Conference article**	CA I.	F. J. Müller, C. Rodríguez M., E. Schöfbänker, and F. Winter, "Surface adjustment of biochar by CO2 gasification under fixed and fluidized bed conditions," in <i>Proceedings of the 14th International Conference on Fluidized Bed Technology</i> , G. Yue, H. Yang, T. Zhou, and S. Ma, Eds., Taiyuan, China, 2024. doi: 10.34726/9639.

<sup>\*</sup>This Journal article is under review at the time of thesis submission.



<sup>\*\*</sup>This conference article did not receive a formal peer review but was recognized with the "Best Paper Award" by the conference's organizing committee.

# Author's contributions to appended publications

Florian J. Müller's contribution to the listed articles organized by CRediT roles was as follows:

	Conceptualization	Data curation	Formal analysis	Funding acquisition	Investigation	Methodology	Project administration	Software	Resources	Supervision	Validation	Visualization	Writing – original draft	Writing – review & editing	Corresponding author
JA I.	X	X	X		X	X		X			X	X	X	X	X
JA II.	X	X	X		X	X		X			X	X	X	X	X
JA III.	X	X	X		X	X	X	X				X	X	X	X
JA IV.	X	X	X		X	X	X	X		X	X	X	X	X	
CA I.	X	X	X			X				X		X	X	X	X

# Further publications

Journal article as co-author	S. Pratschner, M. Hammerschmid, F. J. Müller, S. Müller, and F. Winter, "Simulation of a Pilot Scale Power-to-Liquid Plant Producing Synthetic Fuel and Wax by Combining Fischer—Tropsch Synthesis and SOEC," <i>Energies (Basel)</i> , vol. 15, no. 11, p. 4134, 2022, doi: 10.3390/en15114134.
Oral and poster presentation	Thermochemische CO <sub>2</sub> -Umwandlung mittels Biomasse zu Syngas. CO <sub>2</sub> Refinery Industry Day 2022, Vienna, Austria. 22.09.2022
Oral presentation	Thermochemische CO <sub>2</sub> -Umwandlung zu CO bei der Biomasse-Gaserzeugung. CO <sub>2</sub> Refinery Winter Symposium, Vienna, Austria. 25.02.2025
Conference article as co-author	A. Pitkäoja, F.J. Müller, F. Winter, "Investigation of biomass CO <sub>2</sub> -H <sub>2</sub> O-O <sub>2</sub> circulating fluidized bed biomass gasification for methanol production," in <i>Proceedings of the 25<sup>th</sup> International Conference on Fluidized Bed Conversion</i> , Nanjing, China, 2025.
Conference article as co-author*	A. Pitkäoja, F.J. Müller, F. Winter, "Model-based estimation of fuel mixing in a lab-scale bubbling fluidized bed biomass CO <sub>2</sub> gasifier," in <i>Proceedings of the 25<sup>th</sup> International Conference on Fluidized Bed Conversion</i> , Nanjing, China, 2025.

<sup>\*</sup>This conference article was recognized with the "Best Paper Award" by the conference's organizing committee.

# Thesis co-supervision

Master thesis	Camila Rodrìguez M. Surface adjustment of biochar via gasification. TU Wien 2022
Master thesis	Jesse Ziegler. Experimental design for the evaluation of advanced CO <sub>2</sub> gasification feedstocks. TU Wien 2024
Bachelor thesis	Jakob Reich. Vorbereitung von Versuchen zur Untersuchung des Kohlenstoffumsatzes während der Vergasung mittels 14C-Isotopenmarkierung. TU Wien 2021
Bachelor thesis	Benjamin Lang. CO <sub>2</sub> -Quellen in Österreich und deren Nutzbarkeit für Carbon Capture and Utilization. TU Wien 2021
Bachelor thesis	Ana Lapiedra. Application of Innovative Plants for Carbon dioxide utilization. Design and Implementation. TU Wien 2022
Bachelor thesis	Amir Muzaferovic. Technical comparison of biomass pretreatment methods for CO <sub>2</sub> gasification. TU Wien 2023



# Nomenclature

# Terminology

Abbreviation	Full term
BCCS	Biogenic/bioenergy carbon capture and storage
BCG	Biomass CO <sub>2</sub> gasification
BET	Brunauer-Emmett-Teller
CA	Conference article
CAPEX	Capital expenditure
CCS	Carbon capture and storage
CCU	Carbon capture and utilization
CDRI	Cold direct reduced iron
DFB	Dual fluidized bed
DRI	Direct reduction ironmaking or direct reduced iron
EU-ETS	European Union Emission Trading Scheme
FRU	Formation Rate Unit
GC	Gas chromatography
IPCC	Intergovernmental Panel on Climate Change
JA	Journal article
LC	Low conversion
MC	Medium conversion
MEA	Monoethanolamine
MS	Mass spectrometry
NGR	Natural gas reforming
pp	Percentage points
QCL	Quantum cascade laser
RME	Rapeseed methyl ester
TEG	Triethylene glycol
TGA	Thermogravimetric analysis
VPDB	Vienna Peedee Belemnite (carbon isotope standard)

# Math

Repeating indices	Meaning
A	Variable representing multiple chemical species
BCCS	Value determined with hypothetical economic incentive for biogenic carbon
	capture and storage
BM	Biomass
С	Carbon
CDRI	Cold direct reduced iron
CO <sub>2</sub> e	CO <sub>2</sub> -equivalents for global warming potential over a 100 years (GWP100)
fuel	Biomass for gasification
in	Inlet/feed side
iron	The ferrous phase for balancing; the ironmaking process for energy efficiency
LCA	Value as determined by a simplified life cycle assessment
out	Outlet/drain side
PG	Product gas
RG	Reducing gas

Parameter	Meaning	Unit (if unspecified)
α	Fitting parameter	-
β	Fitting parameter	-
γ	Fitting parameter	-
$\delta^{I3}C$	Carbon isotope ( <sup>13</sup> C) abundance difference compared to Vienna Peedee Belemnite standard	% VPDB
3	Bed void fraction	$m^3/m^3$
$\varepsilon_{CO}$	Isotope enrichment factor for CO	% VPDB
€CO2	Isotope enrichment factor for CO <sub>2</sub>	% VPDB
$arepsilon_{H2O}$	Molar extinction coefficient of water vapor	m²/mol
η	Energy efficiency	%
λ	Equivalence ratio	mol <sub>O2</sub> /mol <sub>O2,stoichiometric</sub>
$ au_{FGC}$	Fuel-gas contact time	S
[]	Flow of []	[]/s
$a_{BET}$	BET surface area	$m^2/g$
В	Initial bed-to-fuel ratio	$m^3/m^3$
b	Burn-off	kg/kg
С	Molar concentration	mol/mol
$C_{eq}$	Subsystem equipment costs	€
CDF	Cumulative discount factor	-
CEPCI	Chemical engineering plant cost index	-
CF	Carbon footprint per unit of cold direct reduced iron	$kg_{CO2(e)}/t_{CDRI}$
d	Optical path length	m
E	Expenses	€
$E_a$	Activation energy	J/mol
EABEP	Emission allowance break-even price	€/t <sub>CO2</sub>
F	Initial fuel loading	m
fcoze G I I	CO <sub>2</sub> -equivalent emission factor	kg <sub>CO2e</sub> /kg <sub>reference unit</sub>
G	Feed gas flow rate	$Nm^3/s$
I	Context=laser: Signal intensity at lock-in amplifier	V
I	Context=techo-economy: Investment costs	€
i	Interest rate	-



$k_0$	Pre-exponential factor	$m^{\gamma-1}/s$ (in simplified model 1/s)
LCOP	Levelized cost of product	€/t <sub>product</sub>
LHV	Lower heating value	J/kg
m	Mass	kg
M	Fitting parameter for bed material type	-
n	Amount of substance	mol
p	Pressure	Pa
$p_{EA,0}$	Price of emission allowance	€/t <sub>CO2</sub>
r	Scale factor	-
R	Context=thermodynamics: Ideal gas constant	J/mol/K
R	Context=techno-economy: Revenues from secondary products	€
RP	Reduction Potential	mol/mol
S	Context=experiments: Fitting parameter for fuel size	-
S S	Context=techno-economy: Size of equipment	Varies per equipment
T	Context=techno-economy: Size of equipment Temperature	Varies per equipment K
$\frac{S}{T}$ $T_0$		
$\frac{T}{T_0}$	Temperature	K
$T \over T_0$	Temperature Standard temperature (273.15 K)	K K
$T \ T_0 \ V \ X_{CO2}$	Temperature Standard temperature (273.15 K) Volume	K K m³
$\frac{T}{T_0}$	Temperature Standard temperature (273.15 K) Volume CO <sub>2</sub> conversion as measured or in general	K K m³
$T$ $T_0$ $V$ $X_{CO2}$ $X_{CO2,balance}$	Temperature Standard temperature (273.15 K) Volume CO <sub>2</sub> conversion as measured or in general CO <sub>2</sub> conversion estimation by <i>Eq. 24</i>	K K m³ % %
$T$ $T_0$ $V$ $X_{CO2}$ $X_{CO2,balance}$ $X_{CO2,stoichiometric}$ $Y$	Temperature Standard temperature (273.15 K) Volume CO <sub>2</sub> conversion as measured or in general CO <sub>2</sub> conversion estimation by <i>Eq. 24</i> CO <sub>2</sub> conversion estimation by <i>Eq. 30</i> Surface yield Share of product gas species x from parental carbon	K K m³ % % % % % m²/gfeedstock
$T$ $T_0$ $V$ $X_{CO2}$ $X_{CO2,balance}$	Temperature Standard temperature (273.15 K) Volume CO <sub>2</sub> conversion as measured or in general CO <sub>2</sub> conversion estimation by <i>Eq. 24</i> CO <sub>2</sub> conversion estimation by <i>Eq. 30</i> Surface yield	K K m³ % %

## 1. Introduction

The introductory chapter starts by explaining the motivation to work on biomass CO<sub>2</sub> gasification before presenting the aim and outline of this thesis.

## 1.1. Motivation

## 1.1.1. The urgency of climate change mitigation

The Intergovernmental Panel on Climate Change (IPCC) states the scientific consensus on climate change research every few years in their assessment reports, which are the most comprehensive and scientifically sound source of information on global warming. The latest sixth reporting cycle was concluded in 2023 by the Climate Change 2023 Synthesis Report [1], which united the results by thousands of scientists and dozens of editors involved in working group I on the physical science base of climate change [2], working group II on the impacts, adaptation and vulnerability [3], and working group III on the mitigation of climate change [4]. This quote from the synthesis report's foreword summarizes the urgency of climate change mitigation:

[This report] confirms that unsustainable and unequal energy and land use as well as more than a century of burning fossil fuels have unequivocally caused global warming, with global surface temperature reaching 1.1°C above 1850–1900 in 2011–2020. This has led to widespread adverse impacts and related losses and damages to nature and people. The nationally determined contributions (NDCs) committed by 2030 show the temperature will increase by 1.5°C in the first half of the 2030s, and will make it very difficult to control temperature increase by 2.0°C towards the end of 21st century. Every increment of global warming will intensify multiple and concurrent hazards in all regions of the world.

The report points out that limiting human-caused global warming requires net zero CO<sub>2</sub> emissions. Deep, rapid, and sustained mitigation and accelerated implementation of adaptation actions in this decade would reduce projected losses and damages for humans and ecosystems and deliver many cobenefits, especially for air quality and health. Delayed mitigation and adaptation action would lock-in high-emissions infrastructure, raise risks of stranded assets and cost-escalation, reduce feasibility, and increase losses and damages. Near-term actions involve high up-front investments and potentially disruptive changes that can be lessened by a range of enabling policies.

IPCC, 2023 [1]

Just one year after this report was published, 2024 was already the first year with more than 1.5 °C global warming over the pre-industrial level [5]. 2024 also included the day with the highest global average temperature ever measured [5]. This drastic speed of global warming emphasizes the need to reach net-zero CO<sub>2</sub> emissions as quickly as possible.

# 1.1.2. The potential of carbon capture and utilization processes for emission reductions

Reaching net-zero CO<sub>2</sub> emissions requires radical change to abolish emissions from fossil feedstock in many fields. Fossil feedstocks are widely used for energy and as chemical ingredients, e.g., for producing transport fuels, plastics, or steel [4]. However, many of these products shape our daily lives, and some will never be entirely replaced by carbon-free alternatives, as carbon is an integral part of their characteristics [6]. Uniting the goal of net-zero CO<sub>2</sub> emissions with continued use of limited-lifetime carbonaceous goods demands alternative carbon life cycles that do not pump carbon from the geosphere into the atmosphere [7]. Instead, this circular carbon economy needs to ensure that the same amount of CO<sub>2</sub> is removed from the atmosphere as it is emitted.

Figure 1 shows two ways to close carbon life cycles and achieve net-neutral CO<sub>2</sub> emissions: If carbon originates from the geosphere, it must be transferred back to the geosphere by carbon capture and storage (CCS). However, if carbon originates from CO<sub>2</sub> in the atmosphere and is then processed into carbonaceous products by carbon capture and utilization (CCU), it can also be emitted as CO2 to the atmosphere while retaining net-zero CO<sub>2</sub> emissions [8]. Both ways of closing the carbon loops are theoretically acceptable; however, CCU is critical for use cases like aviation, where carbon capture is impractical [9] and it avoids the risk of emissions from carbon leakages during transport or storage [10], [11].

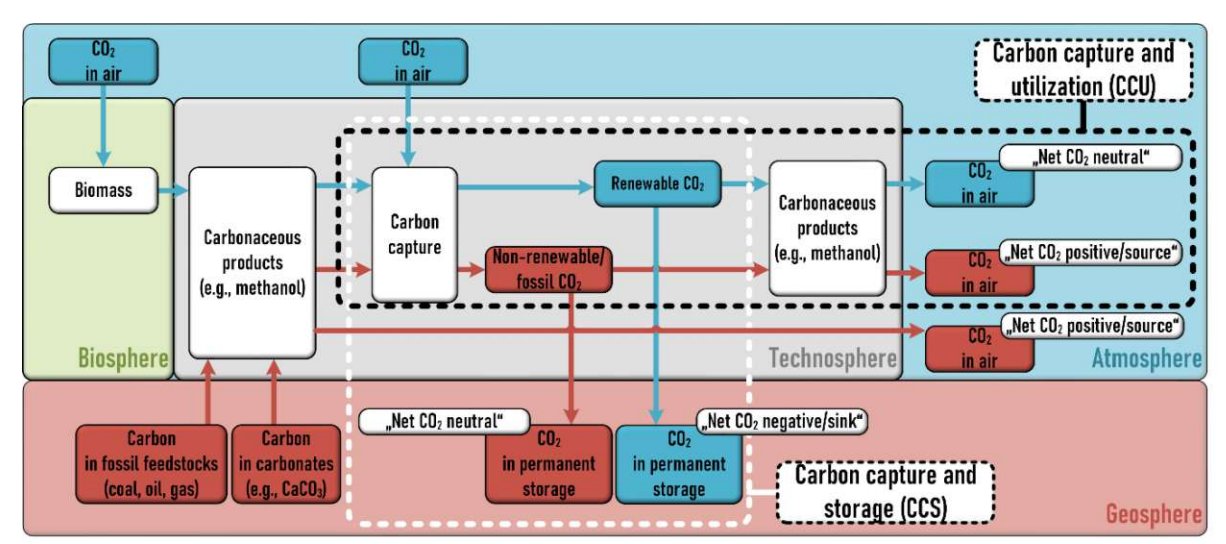


Figure 1: Closing carbon life cycles by carbon capture and utilization (CCU) and carbon capture and storage (CCS). The figure was adapted from [12].

The IPCC quote stated that much damage from global warming could be avoided by achieving netneutrality. The German Environment Agency recently calculated the climate damage costs at 300 €2024/t<sub>CO2e</sub> when placing a higher weight on the welfare of current generations over future

#### CO<sub>2</sub> Conversion to CO by Fluidized Bed Biomass Gasification Chapter 1: Introduction

generations and an astonishing 880 €2024/t<sub>CO2e</sub> when no such premium for current generations is considered [13]. The main drivers for these costs are damages in the agricultural sector (59%) and increased mortality (32 %) [13]. If these costs were appropriately internalized into the unmitigated use of fossil carbon, most CCU technologies would already be economically favorable, as many studies already report renewable carbon technologies as competitive at much lower carbon prices [14], [15], [16], [17]. In reality, increasing carbon emission prices will likely internalize some of these costs, but technological advancements to reduce capital costs and increase efficiency for CCU technologies are also needed to achieve cost parity and incentivize industrialization [14], [18].

Once adequately developed and rolled out, CCU technologies using renewable CO2 would offer an advantage over fossil carbon use combined with CCS technologies, which is especially relevant for Europe: Increased security of supply in times of geopolitical turbulence. The distribution of fossil resources is much more uneven globally than that of renewable energy sources and CO<sub>2</sub> [19], [20]. Europe is notably poor in fossil resources compared to its economic significance and relies on extensive imports of fossil feedstocks. The International Energy Agency (IEA) reports that Europe imported 46.1% of used coal [21], 60.6 % of natural gas [22], and 76.6 % of crude oil [23] in 2022. This reliance on imports brings economic and security risks as supply can be impacted by external circumstances or, on purpose, diminished to apply pressure. The price shocks and supply scares of the 2022 gas crisis in Europe resemble the turmoil caused by the oil embargo and price shocks of the 1970s [24], [25]. Relying on domestically available energy and carbon resources such as biomass and CO<sub>2</sub> can help to lower these risks and enable more countries to become independent of imports [20].

Von der Assen et al. [8] identified pitfalls to avoid when assessing the climate impact of CCU processes. One clear pitfall is the misclassification of CCU processes as "negative emission technologies" regardless of CO<sub>2</sub> source, even though producing limited-lifetime products by CCU can only delay instead of avoid emissions from fossil CO<sub>2</sub> sources (Figure 1). Unfortunately, this pitfall is not widely avoided, as CCU is often seen as an "end-of-pipe CO<sub>2</sub> waste management"-technology, e.g., [26]. It is important to avoid this pitfall and further carbon lock-in effects that could lead to overshooting climate targets [4] by recognizing that renewable CO2 sources are necessary for a net-zero emissions future relying on CCU. However, there are challenges with the availability and cost of renewable CO2 for CCU until direct air capture matures as a technology [27] (Figure 2). Consequently, CO<sub>2</sub> needs to be utilized efficiently, which demands technical development and motivates this thesis.

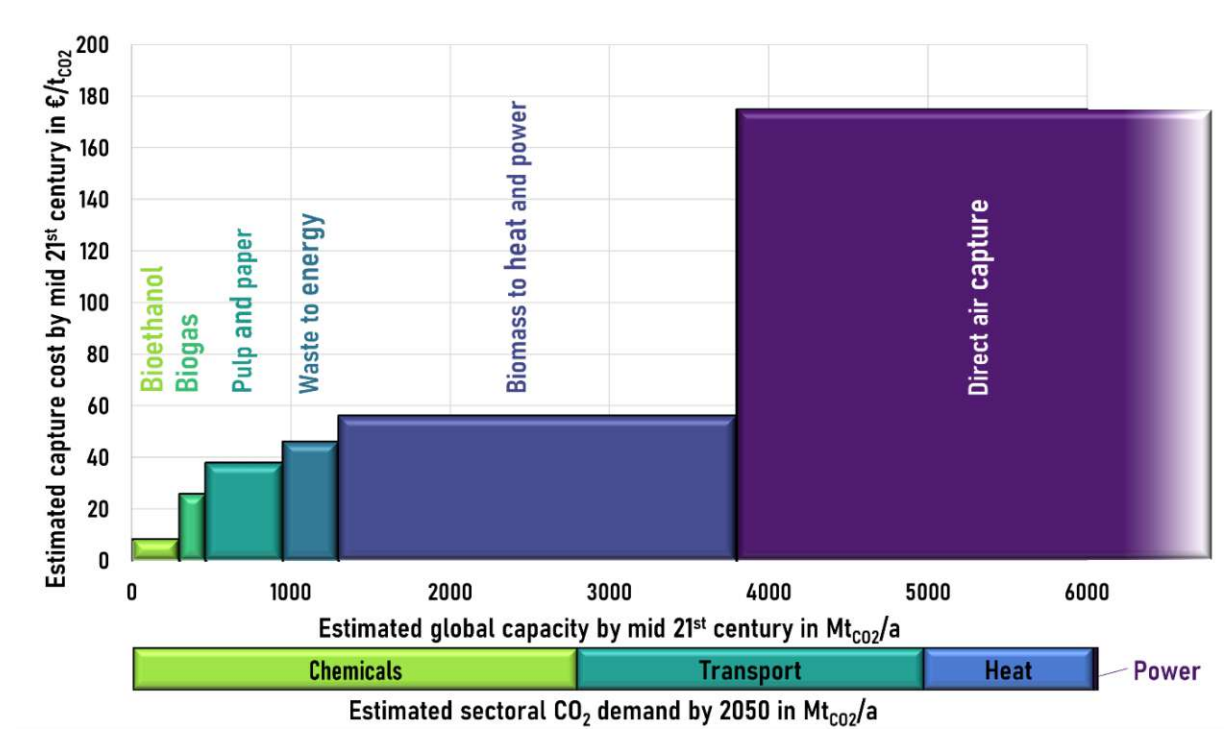


Figure 2: Estimated renewable CO<sub>2</sub> capture cost vs. global capacity and demand by the middle of the 21st century. Figure was produced using data from [12], [28] for capture cost and capacity and [27] for sectoral demand.

# 1.1.3. The initial case for CO<sub>2</sub> utilization by biomass gasification

CO is an important platform chemical with a variety of uses. It is industrially highly relevant as a carbon source to produce chemicals [29] and as a reduction agent in metallurgical applications [30]. For example, CO is used in carbonylation reactions to produce various aldehydes, carboxylic acids, and esters [31]. CO can also be used to produce energy carriers such as methanol or methane by hydrogenation [32], and various products by Fischer-Tropsch synthesis [33], [34]. The water-gas shift reaction is often used to produce hydrogen by converting CO to CO<sub>2</sub>, which is critical in today's ammonia production via the Haber-Bosch process and refineries for hydrocracking [35]. In metallurgy, CO is used as a reduction agent and takes up oxygen from ore to produce elemental metals, e.g., iron [36] or platinum [37].

Carbon monoxide is usually produced and consumed in integrated processes, as CO's toxicity brings challenges to transport and storage [31]. Industrially, CO is often produced as part of synthesis gas (syngas), which also contains hydrogen (H<sub>2</sub>) [38]. Syngas can be produced by reforming natural gas [38] or other hydrocarbons, among which coal and biomass are the most significant [39]. Another route for producing CO that has attracted research attention in recent years is CO<sub>2</sub> capture and utilization (CCU), which describes a large group of technologies aiming to upcycle CO2 into value-added carbon products [40]. These technologies include various electrochemical [41], [42], solar-driven [43], non-thermal plasma [44], catalytic [45], and thermochemical [46] processes.

#### CO<sub>2</sub> Conversion to CO by Fluidized Bed Biomass Gasification Chapter 1: Introduction

Biomass CO<sub>2</sub> gasification is a thermochemical process that generates a product gas from biomass [47]. This product gas is rich in CO and contains H<sub>2</sub>, CO<sub>2</sub>, H<sub>2</sub>O, and various hydrocarbons [46], [48]. The thermochemical conversion process includes the energy-demanding Boudouard reaction, during which the feedstock CO<sub>2</sub> reacts with the solid carbon from biomass [46]. This reaction is the main pathway that allows biomass CO<sub>2</sub> gasification to function as a thermochemical CCU process, converting CO<sub>2</sub> to CO [47]. In general, biomass CO<sub>2</sub> gasification has strong potential for defossilization as it offers several key strengths as a CCU technology:

- Utilizing CO<sub>2</sub> and biomass in the same process allows for more renewable carbon products than utilizing either resource alone. This additional renewable carbon source is especially relevant if renewable CO<sub>2</sub> availability at competitive prices is limited.
- CO<sub>2</sub> conversion to CO demands much energy, as CO<sub>2</sub> is a thermodynamically stable molecule [48], [49]. Biomass CO<sub>2</sub> gasification inherently covers some of that energy from biomass and does not need as much additional clean energy input as many other CCU processes.
- Gasification processes are fuel-flexible and can convert various biomass types, residues, and waste [50]. This flexibility creates opportunities for dual-purpose applications uniting waste management and industrial production.
- Biomass CO<sub>2</sub> gasification is flexible when it comes to CO<sub>2</sub> quality. While many other CCU processes have high demands for CO<sub>2</sub> purity or pressure [51], biomass CO<sub>2</sub> gasification works at atmospheric conditions [46], [48] and when CO<sub>2</sub> is mixed with other gases [52], [53].
  - Mixing CO<sub>2</sub> with H<sub>2</sub>O is no problem and can lead to synergistic effects [53], [54], [55], [56], [57]. This finding is relevant for industrial applications, where CO<sub>2</sub> is often wet from carbon capture, e.g., after chemical absorption [58] or oxy-fuel combustion [59]. Avoiding a drying step can make processes more efficient.
  - Biomass CO<sub>2</sub> gasification is a thermochemical conversion process that can work without a catalyst with various fuel types. This characteristic avoids challenges from catalyst poisoning that trouble other CCU processes [60], [61], [62].
- Many downstream syntheses using CO or CO<sub>2</sub> also demand H<sub>2</sub>, e.g., methanol [63] or synthetic natural gas [64] production. The syngas from biomass CO<sub>2</sub> gasification is CO-rich but also contains H<sub>2</sub> that can be used for further processing [47]. The ratio of CO to H<sub>2</sub> in syngas can be adjusted by changing the ratio of H<sub>2</sub>O and CO<sub>2</sub> used as a gasifying agent [65].
- Biomass gasification with steam as a gasifying agent has been demonstrated at up to 32 MW<sub>th</sub> biomass input power [66]. The biomass CO<sub>2</sub> gasification process is similar enough to assume that it can also be scaled to higher technical readiness levels in a reasonable timeframe. This scalability is critical since time is of the essence in the fight to curb global warming.

# 1.2. Aim of this thesis

The motivation chapters explained how biomass CO<sub>2</sub> gasification as a technology for CO<sub>2</sub> utilization fits into the fight against global warming. This thesis aims to strengthen biomass CO2 gasification as a technology for CO<sub>2</sub> conversion by answering the following three core questions.

#### 1. How can CO<sub>2</sub> conversion be increased in a fluidized bed biomass gasifier?

Various authors have reported on the conversion of CO<sub>2</sub> during biomass CO<sub>2</sub> gasification in general, but the number of publications that also consider the operational aspects of fluidized bed gasifiers is small (Section 2.3). Additionally, the differences in CO2 conversion reporting make it hard to compare the relative influence of identified factors across publications. For this reason, a comprehensive investigation of CO<sub>2</sub> conversion in a fluidized bed gasifier under various operating conditions is needed to help gasification processes achieve high CO<sub>2</sub> utilization.

#### *2*. How can $CO_2$ conversion be validated in a biomass gasifier?

The literature has varying definitions and estimation strategies for CO<sub>2</sub> conversion, while no direct measurement has been reported (Section 2.3). It is difficult to differentiate between carbon from biomass or CO<sub>2</sub>, which is troublesome for data comparison and questions to what degree biomass CO<sub>2</sub> gasification can be used for CO<sub>2</sub> utilization. Improving measurement procedures to track the conversion of CO<sub>2</sub> is necessary for deepening process understanding and validating biomass CO<sub>2</sub> gasification as a CCU process.

#### 3. How does implementing biomass CO<sub>2</sub> gasification for CO<sub>2</sub> recycling affect the economic viability and CO<sub>2</sub> emissions of direct reduction ironmaking?

Direct reduction ironmaking seems like a good fit for implementing biomass CO2 gasification for multiple reasons, as explained in Section 3.3.2. However, the question remains whether biomass CO2 gasification could bring tangible benefits over an established ironmaking technology like MIDREX, which uses natural gas reforming to produce the needed reducing gas. Furthermore, whether a correlation exists between overall plant performance, such as economic or ecological indicators, and CO<sub>2</sub> utilization in the gasifier remains to be clarified.

These three core research questions are supported by two additional research questions, which closely relate to biomass CO<sub>2</sub> gasification but do not directly investigate CO<sub>2</sub> utilization.

#### i. Is there a potential synergy between the operating conditions needed for CO<sub>2</sub> utilization and producing high-surface-area biochar by CO<sub>2</sub> gasification?

Biochar is a valuable product and has many uses as a bioresource [67]. If the production conditions are similar, biochar could be extracted as a valuable side-product from a biomass CO<sub>2</sub> gasification process aiming at high-quality product gas.

#### CO<sub>2</sub> Conversion to CO by Fluidized Bed Biomass Gasification Chapter 1: Introduction

#### ii. How can water vapor concentration be measured in hot and raw product gas?

Reliable data collection is essential for process operation, assessment, and design. H<sub>2</sub>O is one of the most important components in hot product gas. H<sub>2</sub>O is challenging to measure online in product gas due to condensation issues with tar, spectral band overlap with hydrocarbons, and other issues [68], [69]. Developing a robust online measurement for  $H_2O$ quantification is helpful for biomass CO<sub>2</sub> gasification and many other processes.

### 1.3. Thesis outline

The core topic of this thesis is strengthening biomass CO<sub>2</sub> gasification as a carbon capture and utilization process. This thesis chases this goal by including experimental work, measurement innovation, and process simulations to increase, validate, and implement CO<sub>2</sub> utilization by biomass gasification into an industrial application (Figure 3).

The first research question concerns the enhancement of CO<sub>2</sub> conversion during the biomass CO<sub>2</sub> gasification process. Journal article I (JA I) tackled this research question through experimental campaigns in a lab-scale biomass CO<sub>2</sub> gasifier. These experiments were conducted with biochar as fuel. Batch-feeding of fuel was used to be more flexible with operating conditions and increase the number of experiments per time. The results were used to identify the operating conditions conducive to a high conversion of feedstock CO<sub>2</sub>. A semi-empirical model based on reaction kinetics was proposed for CO<sub>2</sub> conversion in this setup. JA II followed these findings by switching to continuous fuel feeding in the same reactor and investigated additional operational changes, e.g., softwood instead of char as fuel.

The second research question concerns the validation of CO<sub>2</sub> conversion. The importance of this question became apparent during the work on JAI, which used an estimation method to describe CO<sub>2</sub> conversion. JA II tackled the research question by introducing stable carbon isotope measurements. The <sup>13</sup>C natural abundance differences between bottled CO<sub>2</sub> and biomass were investigated for both carbon sources. These isotopic fingerprints were used to trace carbon streams and measure the conversion of feedstock CO2. This method was successfully demonstrated for continuously-fed biomass CO2 gasification, confirmed some observations from JA I, and validated biomass CO<sub>2</sub> gasification as a technology for CO<sub>2</sub> utilization.

The third research question concerns the implementation of the CO-rich product gas from biomass CO<sub>2</sub> gasification into an industrial process. JA IV investigated the direct reduction of iron ore as an important large-scale application where the low H<sub>2</sub>:CO ratios from biomass CO<sub>2</sub> gasification are not an issue and higher CO content offers some benefits. Process simulations were conducted, which described how the product gas could be used to reduce iron ore and how part of the CO<sub>2</sub> produced during ironmaking could be recycled into the gasifier as new feedstock. JA IV included detailed mass and energy balancing for new biomass CO<sub>2</sub> gasification-direct reduction ironmaking process concepts, which were the basis for techno-economic and CO<sub>2</sub> emissions assessments. Experimental data for these simulations were derived

#### CO<sub>2</sub> Conversion to CO by Fluidized Bed Biomass Gasification Chapter 1: Introduction

from the literature and JA II. These concepts were compared to a reference case process, which used natural gas reforming to produce the reducing gas for iron reduction.

Two additional research articles in this thesis concern biomass gasification in general but are not directly related to CO<sub>2</sub> utilization. Conference article I (CAI) shifted the focus from the gaseous to the solid byproducts of biomass CO2 gasification. This work investigated the surface development of biomass pellets during CO<sub>2</sub> gasification. Experiments were performed in a lab-scale gasifier under fixed and fluidized bed conditions. High-surface area biochar could be a valuable by-product of biomass CO<sub>2</sub> gasification if extracted before complete conversion.

JA III described the development of a novel spectroscopic setup for H<sub>2</sub>O measurement in product gas. A quantum cascade laser was used to measure the water vapor content in hot and raw product gas from steam gasification of waste wood in a dual fluidized bed pilot plant. Finding a reliable H<sub>2</sub>O measurement in the presence of uncondensed tar in the product gas had been an unresolved issue at TU Wien. While this new method was demonstrated during steam gasification, it is also suitable and important for biomass CO<sub>2</sub> gasification.

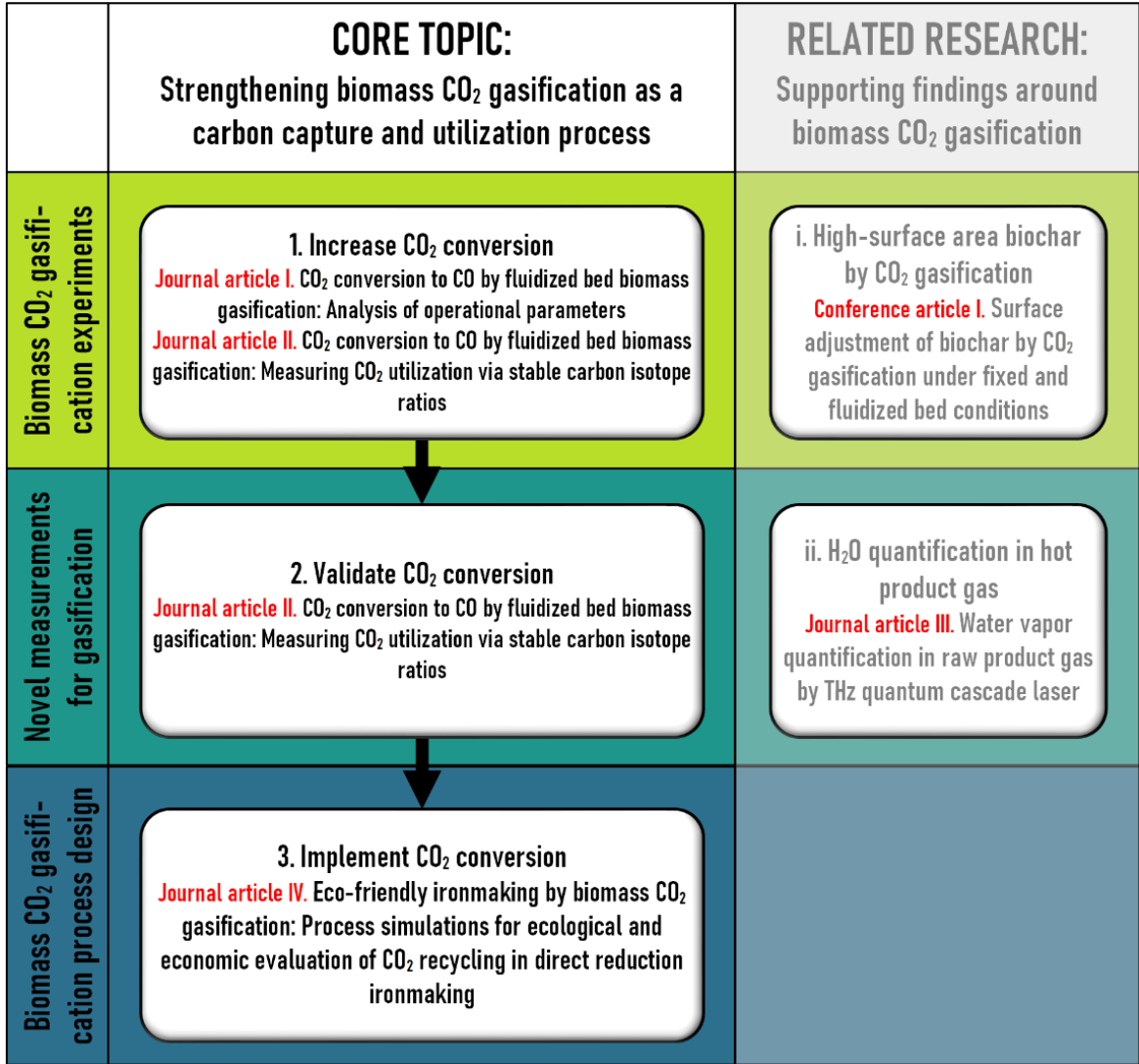


Figure 3: Thesis outline - core and related research on biomass CO2 gasification grouped by scope and method

# 2. State of the art on biomass CO<sub>2</sub> gasification

This chapter aims to provide an introduction to the topic of biomass CO<sub>2</sub> gasification based on available literature by other authors. Sections 2.1 and 2.2 introduce the topic of biomass gasification technology by discussing the fundamentals of thermochemical biomass conversion and reactor design. Section 2.3 sharpens the technology profile of biomass CO2 gasification by comparing it to biomass steam gasification to identify strengths and weaknesses for industrial application. Section 2.4 discusses the state of the art on CO<sub>2</sub> utilization during biomass CO<sub>2</sub> gasification and contextualizes the knowledge gaps that research questions 1 and 2 address.

# 2.1. Fundamentals of biomass gasification

The term gasification describes the thermochemical conversion of carbonaceous feedstocks to a socalled producer or product gas, which can be used as fuel gas or to produce chemicals [70]. Suitable feedstocks include fossil coal and a wide range of more sustainable feedstocks, e.g., agricultural residues and waste [50], [70]. The gasification process is conducted in an oxidizing atmosphere, which is needed to maximize chemical energy transfer from the solid into the gaseous phase [71]. This oxidizing atmosphere is created by introducing a so-called gasification agent or moderator gas that can transfer oxygen to the solid carbon in the feedstock, forming CO [71]. The most common gasification agents are air, O<sub>2</sub>, H<sub>2</sub>O, and CO<sub>2</sub> [70], [71]. Biomass CO<sub>2</sub> gasification refers to those gasification processes that use biomass as carbonaceous feedstock and CO<sub>2</sub> as the gasification agent.

The overall thermochemical conversion of feedstocks can be divided into several sub-processes. Fuel particles entering the process are subjected to these phases depending on the temperature and oxygen availability (expressed as equivalence ratio  $\lambda$ ). In a reactor with continuous biomass feeding, these phases overlap as discrete biomass particles can be at different conversion stages. Gasification processes demand  $\lambda$  between 0 and 1, with ideal  $\lambda$  typically between 0.2 and 0.45 for maximizing product gas output [72]. The overall gasification process is endothermic at low  $\lambda$  values, and additional energy is needed for operation. The following sub-processes are typically distinguished (Figure 4) [70], [71], [73]:

- Heating and drying: Biomass particles enter the reactor at storage temperature. H<sub>2</sub>O leaves the particles as they are heated to process temperature. This phase is globally endotherm.
- Pyrolytic decomposition: The fuel's large organic molecules start breaking into smaller, gaseous molecule fragments. The gaseous products (volatiles) are released, and a carbon-rich solid fraction (char or coke) remains. The volatiles contain a range of permanent (e.g., H<sub>2</sub>, CO, CH<sub>4</sub>, CO<sub>2</sub>, ...) and condensable gases (H<sub>2</sub>O, high-molecular-weight hydrocarbons often referred to as tar). Fuel composition, decomposition temperature, and heating rates strongly influence the composition of this pyrolysis gas. This phase is globally endotherm.

- Gasification: Char remaining after pyrolytic decomposition reacts with gaseous O<sub>2</sub>, oxygen in the fuel itself, H<sub>2</sub>O, or CO<sub>2</sub> to form CO or CO<sub>2</sub> as gaseous products. Char can also be converted by reaction with hydrogen to CH<sub>4</sub>. Heterogeneous (gas-gas) reactions take place, further decreasing the molecule size of volatiles and shifting the gas composition. This phase includes endotherm and exotherm reactions.
- Oxidation: Carbonaceous and hydrogenous molecules are further oxidized to CO<sub>2</sub> and H<sub>2</sub>O. Gasification processes aiming to provide a gaseous product are operated with a low enough amount of oxygen to avoid complete oxidation. This phase is globally exotherm.

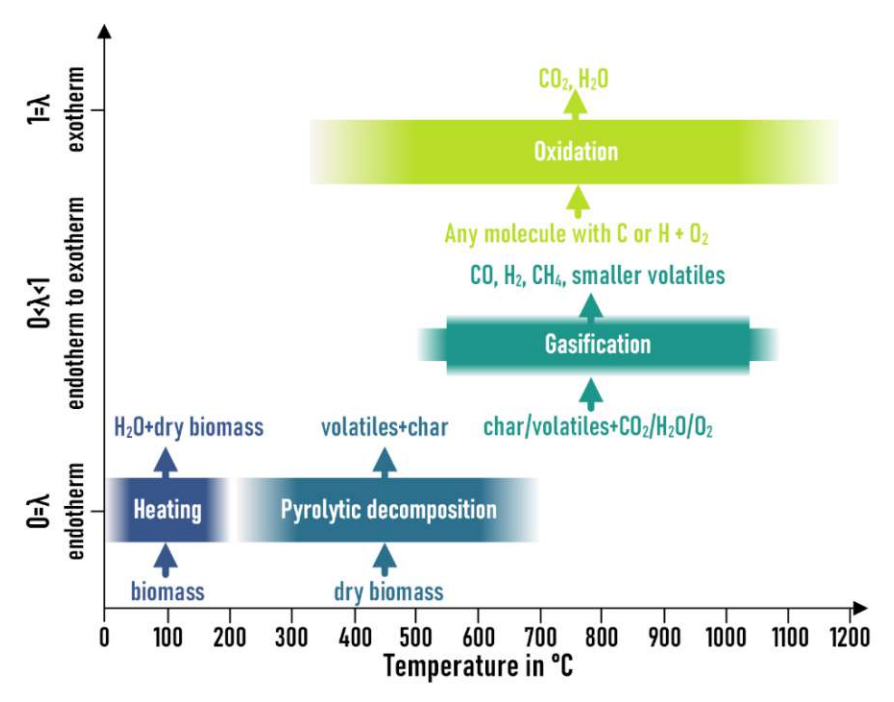


Figure 4: Phases of thermochemical fuel conversion organized by temperature and equivalence ratio  $\lambda$ . Redrawn following [71] with additional information from [47], [48], [70], [73], [74]

The pyrolysis phase can be further differentiated by the degree and conditions of decomposition. A standard classification distinguishes torrefaction, slow pyrolysis, and fast pyrolysis [71]. Torrefaction and slow pyrolysis can be used to prepare advanced solid feedstocks that can be beneficial for gasification [54], [75]. In contrast, fast pyrolysis is usually applied to maximize the liquid products in the form of bio-crude oil [71]. Kaltschmitt [71] states the typical technical parameters of these three subprocesses of pyrolysis:

- Torrefaction: Equivalence ratio  $\lambda$  is 0, operating temperature is 200 320 °C, heating gradients are below 1 K/s, and solids residence times are 30 - 90 min. These conditions lead to only partial destruction of the organic macromolecules.
- Slow pyrolysis: Equivalence ratio λ is 0, the operating temperature can reach around 600 °C, heating gradients are between 0.01 - 2 K/s, solids residence times are long enough to reach (near) complete decomposition of macromolecules and yield only carbon as a solid product.

Fast pyrolysis: Equivalence ratio  $\lambda$  is 0, the operating temperature can be about 400 - 500 °C, heating gradients are much higher and might reach up to 1,000 – 10,000 K/s, solids residence times are only 1-2 s. The phase of pyrolytic decomposition is nearly fully realized, but the short residence times prevent the breakdown of large into small molecules.

Gas-gas reactions further influence the overall composition of the product gas from thermochemical conversion, which can also contain unconverted gasification agents. A summary of reactions in biomass gasification is given in Table 1. For biomass CO<sub>2</sub> gasification, one of the most important reactions is the endothermic Boudouard reaction, as it is the primary reaction for CO<sub>2</sub> conversion [46].

Table 1: Thermochemical biomass conversion reactions [47], [48], [71], [74]. The reaction enthalpies at 850 °C were calculated using HSC Chemistry 6.

Reaction	ΔH <sub>r</sub> (850 °C) in kJ/mol	Reaction name	
Pyrolytic decomposition of large organic mo	lecules		
$C_xH_yO_z \rightarrow Tar + Gas(CO, H_2, C_aH_b, CO_2)$ + Char(C)	Endothermic	Pyrolysis (biomass)	Eq. 1
$C_x H_y \leftrightarrow \frac{y}{4} CH_4 + (x - \frac{y}{4})C$	Endothermic	Pyrolysis (low O-content feedstocks)	Eq. 2
$C_x H_y \leftrightarrow C_{x-a} H_{y-z} + C_a H_b + \frac{z-b}{2} H_2$	Endothermic	Pyrolysis (low O-content feedstocks)	Eq. 3
Carbon gasification reactions			
$C + CO_2 \leftrightarrow 2CO$	+169	Boudouard	Eq. 4
${\rm C} + {\rm H_2O} \leftrightarrow {\rm CO} + {\rm H_2}$	+136	Steam-carbon (also water-gas)	Eq. 5
$C + 2H_2 \leftrightarrow CH_4$	-90	Methanation	Eq. 6
$C + \frac{1}{2}O_2 \rightarrow CO$	-225	Partial carbon oxidation	Eq. 7
$C + O_2 \rightarrow CO_2$	-395	Complete carbon oxidation	Eq. 8
Other important gasification reactions			
$CO + H_2O \leftrightarrow CO_2 + H_2$	-34	Water-gas shift	Eq. 9
$CO_2 + H_2 \leftrightarrow CO + H_2O$	+34	Reverse water-gas shift	Eq. 10
$C_x H_y O_z + \left(x + \frac{y}{4} - \frac{z}{2}\right) O_2 \to nCO_2 + \frac{m}{2} H_2 O$	Exothermic	General oxidation	Eq. 11
$C_x H_y + xCO_2 \rightarrow 2xCO + \frac{y}{2}H_2$	Endothermic	Dry reforming	Eq. 12
$C_x H_y + x H_2 O \rightarrow x CO + (\frac{y}{2} + x) H_2$	Endothermic	Steam reforming	Eq. 13
$C_x H_y + (2x - \frac{y}{2})H_2 \rightarrow xCH_4$	Exothermic	Hydrocracking	Eq. 14
$C_x H_y + CO_2 \rightarrow C_{x-1} H_{y-2} + 2CO + H_2$	Endothermic	Dry dealkylation	Eq. 15
$C_x H_v + H_2 O \rightarrow C_{x-1} H_{v-2} + CO + 2H_2$	Endothermic	Steam dealkylation	Eq. 16
$C_x H_y + H_2 \rightarrow C_{x-1} H_{y-2} + CH_4$	Exothermic	Hydrodealkylation	Eq. 17

# 2.2. Reactor types used for biomass gasification

Many reactor concepts have been developed and used for biomass gasification. Typically, the design of a gasifier is selected based on the target scale, downstream process requirements, and fuel type [70]. Gasifier design differences can be grouped by various characteristics, among which the most common distinctions concern the choice of gasification agent, heat supply, and gas-solid contact mechanism



(Figure 5) [47], [73]. Furthermore, operating conditions like pressure, temperature, equivalence ratio, residence time, and material properties can vary significantly [57]. Operating conditions can also lead to significant design differences, e.g., when ash is removed as a dry solid or melts and is removed as slag [73]. This thesis contains research in allothermal, fluidized bed reactors with CO<sub>2</sub> as a gasification agent. This section contextualizes these characteristics by discussing them among competing reactor design choices. Section 2.3 gives more insights into the differences between CO2 and steam gasification for biomass conversion.

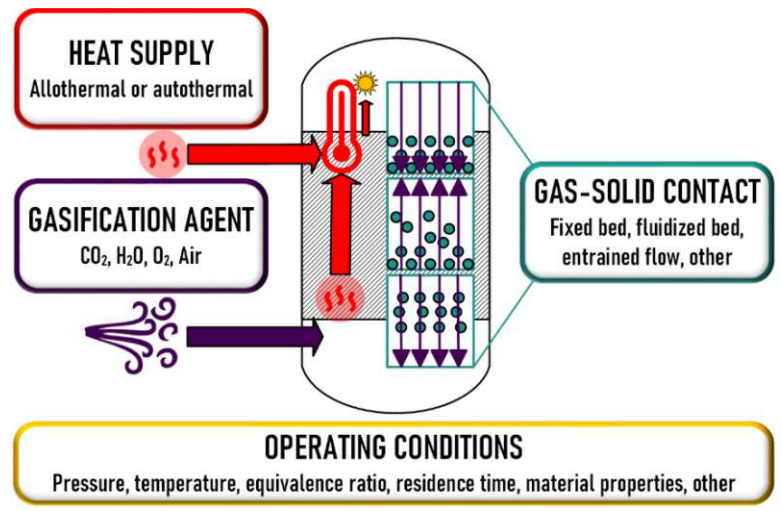


Figure 5: Areas of significant design differences between biomass gasifiers [47], [73]

The choice of gasification agent impacts the process' heat demand and is, therefore, connected to the choice of heat supply. Table 1 shows that thermochemical biomass conversion is a mix of both exothermic and endothermic reactions. The carbon gasification reactions split into exothermic (Eq. 7-Eq. 8) reactions for air- and O<sub>2</sub>-blown gasification and endothermic reactions when the char is gasified with H<sub>2</sub>O and CO<sub>2</sub> (Eq. 4-Eq. 5). This leads to two fundamentally different approaches of heat supply.

- Autothermal or direct heating gasifiers provide the heat for endothermic sub-processes by utilizing the exothermic carbon oxidation reactions with oxygen. Air or  $O_2$  is fed pure [76], [77] or mixed with steam or CO<sub>2</sub> [78], [79], [80] into the reactor, where part of the carbon is burned. The advantages of autothermal gasifiers are the simple and mature designs and low operational costs of using air [57]. These advantages also make autothermal gasifiers suitable for large-scale and continuous operation [81]. Downsides of autothermal gasifiers include the demand to produce pure oxygen and the dilution of syngas with N<sub>2</sub> if air is used instead [57]. Since part of the syngas is also combusted, the energetic content of the syngas and the gasifiers' efficiency are lower than for allothermal gasifiers [57], [82].
- Allothermal or indirect gasifiers supply the heat for gasification from external sources. The energy for process heating can be provided by electricity [83], combustion outside the main reactor [84], or solar collectors [85]. One reactor design that supplies heat by combustion in a second reactor is the dual fluidized bed (DFB) concept, which was used for biomass CO2

gasification at TU Wien before this thesis by Mauerhofer [47]. The two reactors used in the DFB concept (gasifier and combustor) are connected by loop seals, allowing for solid exchange without mixing the gaseous atmospheres. Olivine, limestone, or other solid materials are circulated between both reactors and transport the heat generated in the combustor to the gasifier [86]. Advantages of allothermal gasification include higher product gas quality and better control over reaction conditions [82], [87]. Disadvantages are the more complex design needed for heat transfer [87] and, depending on the efficiency and costs of external heat supply, potentially lower process efficiencies or high costs [70].

The main categories for gas-solid contact mechanisms in gasifiers are fixed bed, fluidized bed, and entrained flow [70], [73]. Less widespread types, like plasma gasifiers and rotary kiln gasifiers [70], [88], are not explicitly discussed here.

- The feedstock stays in place in fixed bed gasifiers while the gasification agent passes through or along the bed [70], [73]. The most common configurations supply the gasification agent at the reactor's bottom (updraft) or top (downdraft). Advantages include the simple design, low pressure drop, and low dust content in syngas [88], [89]. Downsides include poor mixing and heat transfer [73], which limits fixed bed gasifiers to autothermal operation [47], reduces scalability [70], and increases tar content in the syngas for updraft gasifiers [89]. The heat transfer challenges can also lead to agglomeration for certain feedstocks, which is why fixed bed gasifiers can be problematic for biomass conversion [73].
- Fluidized bed reactors suspend the biomass feedstock in a bed of granular solids that is fluidized by the drag force of an upward-flowing gasification agent [70], [71], [73]. These gasifiers can be grouped into two sub-groups based on the fluidization conditions: Bubbling bed gasifiers, where the solids largely stay in place while the gasification agent rises through them in bubbles, and circulating fluidized bed, where the drag force is enough to entrain the solids before they are recirculated. The main strengths of these gasifiers are good mixing and heat transfer, which lead to a nearly uniform heat distribution [70]. This excellent heat distribution reduces the risk of fuel agglomeration, which is particularly advantageous for biomass gasification [73]. Reaction rates are faster than in fixed bed gasifiers due to the intensified gas-solid contact from turbulent flow [70]. Scale-up for fluidized bed biomass gasifiers has been demonstrated up to 140 MW<sub>th</sub> thermal input for autothermal [81] and 32 MW<sub>th</sub> for allothermal designs [66]. Disadvantages of fluidized bed gasifiers are the more complex design compared to fixed bed gasifiers and the limitation of using operating temperatures below the fuel's ash melting point to avoid agglomeration [70].
- Entrained flow reactors feed fine fuel particles in co-current flow with the gasification agent into a reactor with a hot gas atmosphere generally exceeding 1000 °C [73], [90], [91]. The high temperatures allow for a very high conversion of solid carbon to gas and effective reforming of

[92].

# **TU Sibliothek**, Die approbierte gedruckte Originalversion dieser Dissertation ist an der TU Wien Bibliothek verfügbar. The approved original version of this doctoral thesis is available in print at TU Wien Bibliothek.

tar and hydrocarbons [73]. Entrained flow reactors are generally built autothermally, and high temperatures are achieved by co-feeding oxygen [90], [91]. Ash is removed as slag since the operating temperatures usually exceed the ash melting temperatures [73]. Entrained flow gasifiers have been successfully commercialized at a large scale for converting fossil feedstocks like coal and petroleum coke [70], [73], but their application for biomass conversion also has some issues. The short residence time in the gasifier requires fine particles for complete conversion, which increases fuel preparation complexity and expenses for heterogeneous biomass feedstocks, especially if they are fibrous and hard to grind [70], [73]. Additional problems arise with ash melting. The ash melting point of biomass can vary greatly, which needs to be accounted for when designing this type of gasifier [73], [92]. Also, some biomass fuels

produce highly corrosive slag, which reduces the lifetime of the refractory linings [70], [73],

CO<sub>2</sub> Conversion to CO by Fluidized Bed Biomass Gasification Chapter 2: State of the art on biomass CO2 gasification

In summary, allothermal fluidized bed reactors offer several characteristics that position them well as reactor design choices for biomass conversion. These advantages include high-quality product gas, mixing, and heat transfer.

# 2.3. Characteristics of CO<sub>2</sub> gasification by comparison to steam gasification

While gasification topics have attracted significant research interest in recent years, the more specific sub-topic of biomass CO<sub>2</sub> gasification remains a niche within the gasification community. Less than 5 % of original research articles on gasification consider both the topics of "biomass" and include "CO2" in the title (*Figure 6*). This underrepresentation is reflected in most biomass gasification textbooks, which consider air, oxygen, and steam as the primary choices of gasification agents [70], [73], [93]. Like CO<sub>2</sub> gasification, steam generally leads to endothermic reactions, and external heat input is necessary. For this reason, this section compares the unique characteristics of biomass CO<sub>2</sub> gasification to biomass H<sub>2</sub>O gasification. The comparison is centered on application-centric aspects; the interested reader is referred to relevant review papers [26], [46], [48], [94], [95] for more mechanisms-focused descriptions of kinetic models or catalytic effects in CO<sub>2</sub> gasification.

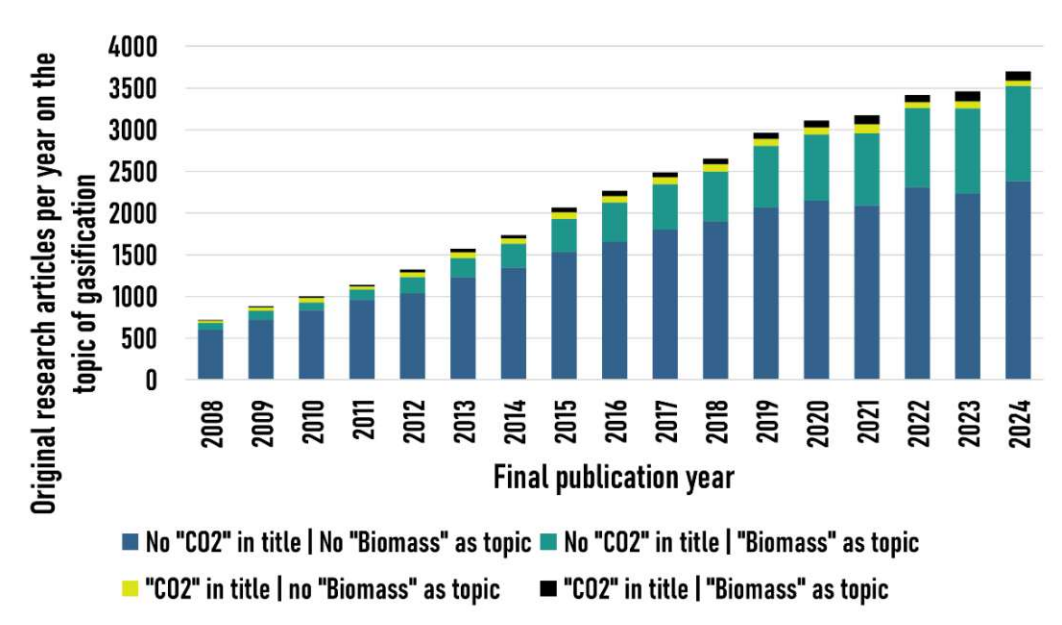


Figure 6: Original research articles on biomass CO2 gasification. The Web of Science Topic function searches title, abstract, keyword plus, and author keywords. Certain data included herein are derived from Clarivate  $^{TM}$  (Web of Science  $^{TM}$ ) [96].  $^{C}$ Clarivate 2025. All rights reserved.

Both biomass gasification processes have unique strengths that should be considered when choosing a process design for biomass conversion. The following aspects are generally reported in favor of biomass CO<sub>2</sub> gasification:

- Higher output of renewable carbon products: Utilizing CO<sub>2</sub> and biomass in the same process allows for more renewable carbon products than utilizing either resource alone.
- Higher carbon efficiency: The carbon efficiency (how much feedstock carbon is converted to products) of allothermal biomass steam gasification systems can be markedly improved if CO2 can be recycled [52], [97]. Doing so typically requires external H<sub>2</sub> input for the production of chemicals.
- Lower energy demand for preheating the gasification agent: CO<sub>2</sub> gasification needs less energy than steam gasification to heat the gasification agent. Water has a large heat of vaporization (40.7 kJ/mol), which needs to be overcome to generate steam [98]. As a result, the energy needed to heat 1 mol of CO<sub>2</sub> from 25 °C to a typical gasification temperature of 850 °C is nearly 50 % lower than for 1 mol of  $H_2O$  (40.2 kJ/mol vs 75.2 kJ/mol at 1 bar).
- Higher exergetic efficiency: Shahbeig et al. [57] reviewed all major gasification agent choices and reported on their mean exergetic efficiencies. They reported that the average exergetic efficiency for biomass CO<sub>2</sub> gasification was markedly higher than for steam gasification (76.9 % vs 53.7 %). Shahbeig et al. attributed these findings to H<sub>2</sub>O and CO<sub>2</sub> promoting different reactions, with the Boudouard and reforming reactions enhancing the exergy efficiency of gasification in the presence of CO<sub>2</sub>. Another explanation for the higher average exergy efficiency of CO<sub>2</sub> gasification, which was not listed by Shahbeig et al., could be the lower heat demand for preheating CO2 as the gasification agent. The higher heat demand of preheating/vaporizing H<sub>2</sub>O could increase losses if gasification agents are removed from the

system without complete conversion. In Shahbeigs et al.'s study, pure CO<sub>2</sub> gasification was only surpassed in mean exergetic efficiency by mixtures of CO<sub>2</sub> and H<sub>2</sub>O (82.2 %), suggesting a synergistic effect.

- Inert gas synergy: Since CO<sub>2</sub> is a permanent gas, it can be used as an inert gas for fuel-feeding systems and measurement instruments [47], [99]. Doing so can avoid product gas dilution with nitrogen, which would otherwise often be used as an inert gas.
- Lower corrosiveness: CO<sub>2</sub> is conducive to a less corrosive gasification environment than H<sub>2</sub>O, potentially reducing reactor maintenance [98].
- Smaller pores: CO<sub>2</sub> gasification creates micro- and macropores in char, while H<sub>2</sub>O gasification mainly creates macropores [98], [100]. This difference can be of interest if the char is extracted from the process and designated for further use, e.g., for increasing the material strength after reaction for metallurgical applications [101].

In contrast, the following parameters are generally disadvantageous for CO<sub>2</sub> gasification compared to steam gasification for biomass conversion:

- Lower H<sub>2</sub>:CO ratio: Steam gasification yields a product gas with higher hydrogen content and H<sub>2</sub>:CO ratios [52]. Many common downstream processes need H<sub>2</sub>:CO ratios of 2 or above [97], e.g., methanol [102], Fischer-Tropsch [33], or synthetic natural gas [64] processes. Steam gasification can achieve and exceed these ratios, especially if CO2 is selectively removed by an active bed material like limestone [103]. In comparison, the CO-rich product gas from CO<sub>2</sub> gasification requires either additional hydrogen input or a composition shift by the water-gas shift reaction and further carbon capture to reach ideal compositions for downstream chemical synthesis [48].
- Higher energy demand for sourcing the gasification agent: Sourcing water as feedstock for steam gasification is possible without excessive energy input in many world regions. CO<sub>2</sub> is available everywhere but typically needs to be captured in energy-intensive processes to be a suitable feed medium for gasification [48], [104].
- Lower technological readiness level: The steam biomass gasification process has been successfully upscaled to 32 MWth of thermal input power and demonstrated in the nowdecommissioned GoBiGas plant in Gothenburg, Sweden [66], [97], [105]. Biomass CO<sub>2</sub> gasification is usually operated at a laboratory scale, with only a few pilot-scale demonstrations, e.g., [47], [106].
- Lower reactivity: At typical gasification temperatures of 1,073 1,273 K, the rate constant of biochar gasification is 3-10 times higher with  $H_2O$  than with  $CO_2$  [107]. This fact can introduce challenges for reaching high conversion of CO<sub>2</sub> and biochar if residence times are limited.

Steam and CO<sub>2</sub> can also be mixed as gasification agents, for which several authors have reported synergistic advantages. Compared to using pure H<sub>2</sub>O or pure CO<sub>2</sub> as a gasification agent, mixed



atmospheres allow higher exergetic efficiencies [57] and char reactivity [108]. In other aspects, gasification with CO<sub>2</sub>/H<sub>2</sub>O mixtures results fall between pure steam gasification and pure CO<sub>2</sub> gasification. For example, varying the mixing ratio of CO<sub>2</sub>/H<sub>2</sub>O as the gasification agent allows for adjusting the product gas composition towards H<sub>2</sub>-rich or CO-rich gas [47]. However, the H<sub>2</sub>:CO ratios stay between the pure H<sub>2</sub>O and CO<sub>2</sub> gasification ratios.

The most significant argument for steam gasification is that H<sub>2</sub>:CO ratios are more suitable for most downstream synthesis processes, since CO<sub>2</sub> gasification cannot overcome this inherent chemical difference through technological advancements. CO2 gasification offers various advantages for processes where lower H<sub>2</sub>:CO ratios suffice, e.g., acetic acid and oxo-synthesis, which only require an H<sub>2</sub>:CO ratio of 1:1 [109]. However, as Thunmann et al. discussed in their "lessons-learned-from-GoBiGas"-publication, the value of renewable carbon is rising, and additional green hydrogen can be added by electrolysis [97]. With the increasing availability and economic competitiveness of green hydrogen [110], [111], this trend might make biomass CO<sub>2</sub> gasification promising for various applications, as it offers direct advantages for inserting more renewable carbon and, consequently, achieving deeper defossilization in various industries. An application where the CO-rich product gas from biomass CO<sub>2</sub> gasification could be applied independent of hydrogen rollout is the ironmaking sector, where both H<sub>2</sub> and CO provide reduction equivalents [112]. In this sector, high H<sub>2</sub> content can challenge heat distribution through endothermic reactions, and a carbonaceous reducing agent enables carburization, which can bring various advantages, such as protecting the product against re-oxidation [17], [113].

## 2.4. CO<sub>2</sub> utilization in fluidized bed biomass gasifiers

This thesis uses the terms CO<sub>2</sub> conversion or CO<sub>2</sub> utilization to describe the percentage of externally fed CO<sub>2</sub> converted to other carbonaceous gas molecules during gasification. The literature on CO<sub>2</sub> gasification is clear that one of the key advantages of this technology is the possibility of converting CO<sub>2</sub> into valuable products. Furthermore, unconverted CO<sub>2</sub> in the product gas lowers the heating value and can induce significant energy penalties for additional carbon capture processes. Nevertheless, none of the review papers on biomass CO<sub>2</sub> gasification [26], [46], [48], [94], [95] reported CO<sub>2</sub> conversions in fluidized bed gasifiers. These missing descriptions are likely caused by two problems with the literature on CO<sub>2</sub> conversion in fluidized bed biomass gasifiers:

The first issue is data availability. A bibliographical screening in the Web of Science<sup>TM</sup> by Clarivate<sup>TM</sup> [96] was conducted to clarify how many studies reported CO<sub>2</sub> conversion in fluidized bed gasifers. This search combined the topics "gasification" & "biomass" with either "CO2 conver..." or "CO2 utili..." and aimed to strike a balance between finding false positives and including all relevant work (Figure 7). This search in March 2025 yielded 159 original research articles outside this thesis, with the first publication appearing in 2010. A closer examination of these studies revealed that only 75 described the

CO<sub>2</sub>-assisted conversion of solid feedstocks, while the rest described adjacent topics like methanation or water-gas shift reactors. Of these 75 studies, 54 contained experimental research, and only 36 quantified experimental CO<sub>2</sub> conversion. Based on the aforementioned screening criteria, the sample contained only seven works that quantified CO<sub>2</sub> conversion in biomass gasification experiments in fluidized bed gasifiers [65], [106], [114], [115], [116], [117], [118]. This low count of articles suggests that additional research on CO<sub>2</sub> conversion in fluidized bed reactors is still needed.

The most recent review paper on CO<sub>2</sub> gasification that mentioned fluidized bed gasifiers was authored by Chan et al. in 2021 [48] and reported a similar lack of data. It states: "As most of the current commercial gasifiers are designed to be operated in steam, air and/or O2, the influence of the gasifiers' configuration (fluidized bed, fixed bed, entrained flow and bed materials) on the performance and efficiency of gasification [...] is still unknown. Most of the CO<sub>2</sub> gasification studies reported in the literature are using lab-scale or TGA [(thermogravimetric analysis)], hence the optimized results/parameters of a commercial gasifier using CO<sub>2</sub> as the feed gas have yet to be established."

The second issue with reporting is that articles that consider and discuss CO<sub>2</sub> conversion have not agreed on a unified way to determine this value. The simultaneous conversion of feedstock CO2 and the formation of new CO<sub>2</sub> from biomass devolatilization make it challenging to pin down the conversion of feedstock CO<sub>2</sub>. Authors have dealt with this issue using different assumptions or simplifications, which makes the reported CO<sub>2</sub> conversion results inconsistent. For example, Mauerhofer et al. have proposed comparisons with steam gasification and pyrolysis data to ascertain the amount of CO<sub>2</sub> produced from biomass [52]. Both assumptions seem plausible. However, they disagreed significantly: The difference in the assumed comparison process resulted in CO<sub>2</sub> conversion estimations of 26 % or 45 % for the same experiment [52]. Applying the mass balance method, which compares the net change of CO<sub>2</sub> in the feed to the drain stream and is the most common estimation method for CO<sub>2</sub> conversion (see **Section 3.4.1**), to Mauerhofer's data yields only 15 % conversion. These discrepancies from varying estimation methods are a serious problem with reporting. Establishing a direct measurement of CO<sub>2</sub> conversion would clarify the standing of biomass CO<sub>2</sub> gasification as a CCU process and potentially help technical development.

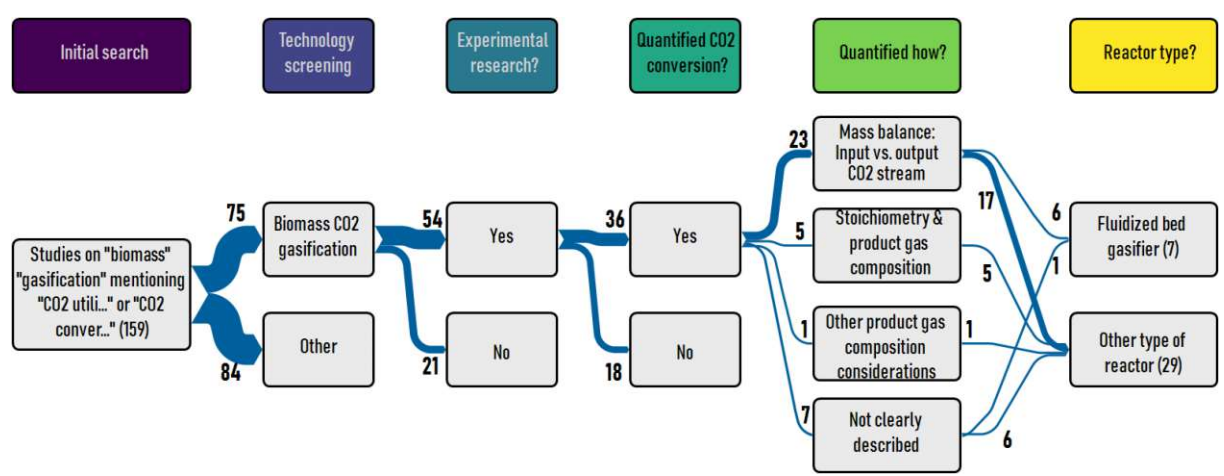


Figure 7: CO<sub>2</sub> utilization reporting in literature as of March 2025: Original research articles outside this thesis sampled by searching for the topics of "biomass" & "gasification" & ("CO2 conver..." OR "CO2 utili...). Certain data included herein are derived from Clarivate™ (Web of Science™) [96]. © Clarivate 2025. All rights reserved.

These limits of available literature are why the following list refrains from reporting absolute numbers and why the results of various authors are not directly compared. Still, these factors can be identified to increase CO<sub>2</sub> conversion in fluidized bed biomass gasifiers based on the authors reporting or further analysis of their results:

- High temperatures are consistently reported as a critical factor for CO<sub>2</sub> conversion because the entropic term that lowers the free energy for the Boudouard reaction becomes dominant at higher temperatures, leading to high CO production at temperatures above ~800 °C [52], [106], [116], [119], [120] (see *Figure 8*).
- Zhang et al. reported CO<sub>2</sub> conversion in autothermal circulating fluidized bed reactors [117], [118]. Their study found that the highest CO<sub>2</sub> conversion was reached using CO<sub>2</sub>/O<sub>2</sub> feed mixtures with around 30 vol.-% O<sub>2</sub>, which balanced high CO<sub>2</sub> availability and temperatures [117].
- Mauerhofer et al. reported that high carbon content in the feedstock leads to enhanced CO formation, likely by increasing CO<sub>2</sub> utilization through the Boudouard reaction [65].
- Couto et al. reported higher CO<sub>2</sub> conversion in their pilot scale plant fed with air-CO<sub>2</sub> mixtures and municipal solid waste for low equivalence ratios and high CO2-to-MSW (municipal solid waste) ratios [106].
- Chai et al. did not perform experiments themselves [115], but provided thermodynamic analysis based on the experimental data reported by Arregi et al. [121]. Based on their analysis, Chai et al. suggested reaching high CO<sub>2</sub> conversion by a) adding solid carbon (e.g., biochar) to the reactor and b) using low steam-to-feed ratios if CO<sub>2</sub> is mixed with H<sub>2</sub>O as a gasification agent.
- He et al. reported that char reactivity and CO<sub>2</sub> conversion are closely related to char properties, such as the alkali metal content [116]. This finding is consistent with other reports emphasizing the effect of catalysts or impregnation on char reactivity. E.g., Medvedev et al. published

multiple papers on this topic and described the catalytic effects of various nickel, iron, and potassium compounds [122], [123], [124], [125].

Kibret et al. did not report on CO<sub>2</sub> conversion. However, their experimental data from gasification in a fluidized bed reactor suggested higher CO<sub>2</sub> conversion at lower CO<sub>2</sub>: fuel ratios since CO<sub>2</sub> concentration in the product gas increased at higher CO<sub>2</sub>:fuel ratios [126].

Authors who have reported on non-fluidized bed reactors have found high CO2 conversion numbers when using novel allothermal heat sources like a plasmatron [114] or microwave radiation [49], [127], [128], [129]. Hunt et al. found that this could be explained by a sharp decrease in apparent activation energy for the Boudouard reaction under microwave radiation [120]. They hypothesized that this decrease arises from the interaction of CO<sub>2</sub> with the electron-hole pairs at the carbon surface from the space-charge mechanism that heats carbon by microwaves.

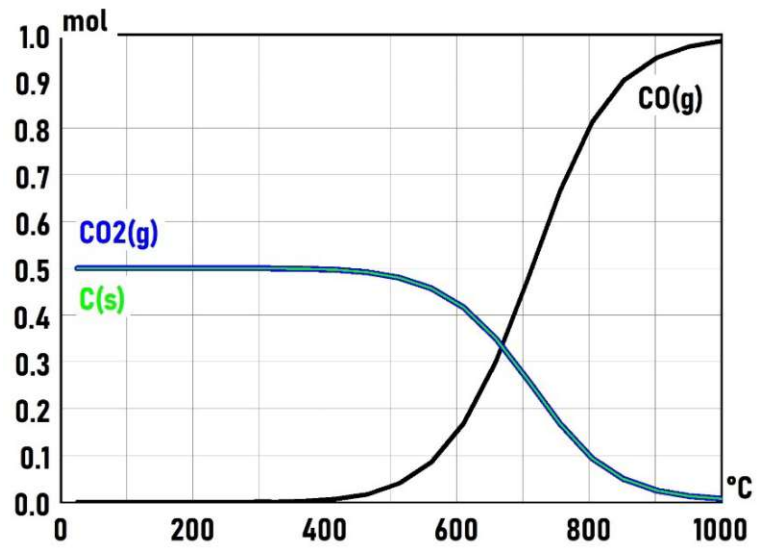


Figure 8: Mol CO (black line) formed from C (green line) and CO2 (blue line) by the Boudouard reaction as a function of temperature. The gas composition was calculated by Gibbs energy minimization in HSC Chemistry 6 at 1 bara.

Zhang et al. reported that feed gas flow rates should not be too high in their fixed-bed reactor, and CO<sub>2</sub> conversion increased at longer experimental durations [130]. The thermodynamic analysis by Renganathan et al. suggested that maximum CO<sub>2</sub> conversion can be achieved at the carbon boundary point, which is the point with the highest solid carbon feed that can still be gasified at given operating conditions [131]. The reason for this global maximum is that if more CO2 is fed, then the understoichiometric availability of solid carbon is limiting CO<sub>2</sub> conversion. If, however, less CO<sub>2</sub> is fed and the solid carbon feed is available in excess, then the oxygen in the biomass has a higher relative contribution to solid carbon conversion. The result is a lower net CO2 conversion if the mass balance estimation (explained in *Section 3.4.1*) is used to calculate CO<sub>2</sub> conversion.

# 3. Methodology

This chapter summarizes the methods used to derive the findings of this thesis. Section 3.1 provides an overview of used reactors. Section 3.2 explains how two novel measurements complement the established biomass and gasification analysis suite. Section 3.3 describes the applied simulations and modeling principles for analyzing thermodynamic and process characteristics. Section 3.4 concludes the methodology chapter by introducing formulae and calculations used for performance assessment.

## 3.1. Reactors

The description of experimental setups includes a short description of the used reactors and established measurements. More detailed information, including analysis of the used materials, is available in the research articles. The gasification experiments reported in this work were conducted in three different plants. The main characteristics of these plants are summarized below.

## 3.1.1. Single-bed fluidized bed gasifier #1 (NERO)

Most of this thesis' experimental work on CO<sub>2</sub> biomass gasification was conducted in a single-bed bubbling fluidized bed gasifier called NERO (Table 2, Figure 9). NERO was used to conduct experiments for JA I-II, and some of the experimental results included in JA II are the basis of process simulations in JA IV.

Table 2: Key information about the single-bed fluidized bed gasifier #1 (Nero).

Parameter	Reactor information
Thermal fuel power to gasifier	2-3 kW <sub>th</sub>
Heat supply design	Electrical heating shells
Typical fuel-gas contact mode	Bubbling fluidized bed or fixed bed
Maximum operating temperature	1000 °C
Design pressure	Atmospheric
Available feed gases	CO <sub>2</sub> , Air, N <sub>2</sub> , H <sub>2</sub> O
Apparatus was used for	JA I-II and CA I. Data was re-used in JA IV

The biomass CO<sub>2</sub> gasification experiments in JA I-II used continuous gas feeding. However, biomass feeding differed as it was fed in batches for JA I and continuously by a screw feeder JA II. The reactor was also used for fuel pre-processing by torrefaction in CA I. JA I-II used wood char derived from Eucalyptus globulus as biomass feedstock. JA II also used commercial softwood pellets. CA I used Pinus sylvestris pellets produced from a mixture of needles and branches. NERO was operated with olivine or limestone as bed material in fluidized bed mode for JA I-II and fixed bed mode without bed material for torrefaction in CA I.

Temperatures were measured by thermocouples (mostly type K) in all reactors. The pressure sensors in NERO and the advanced DFB pilot plant were used for process control but were not central for data analysis. The dry product gas components CO<sub>2</sub>, CO, H<sub>2</sub>, CH<sub>4</sub>, and O<sub>2</sub> from NERO and the DFB gasifier were analyzed using Emerson Rosemount NGA 2000 continuous gas analyzers. An EL3020 gas analyzer by ABB was used to screen O2, CO, SO2, CO2, and NO from FRU.

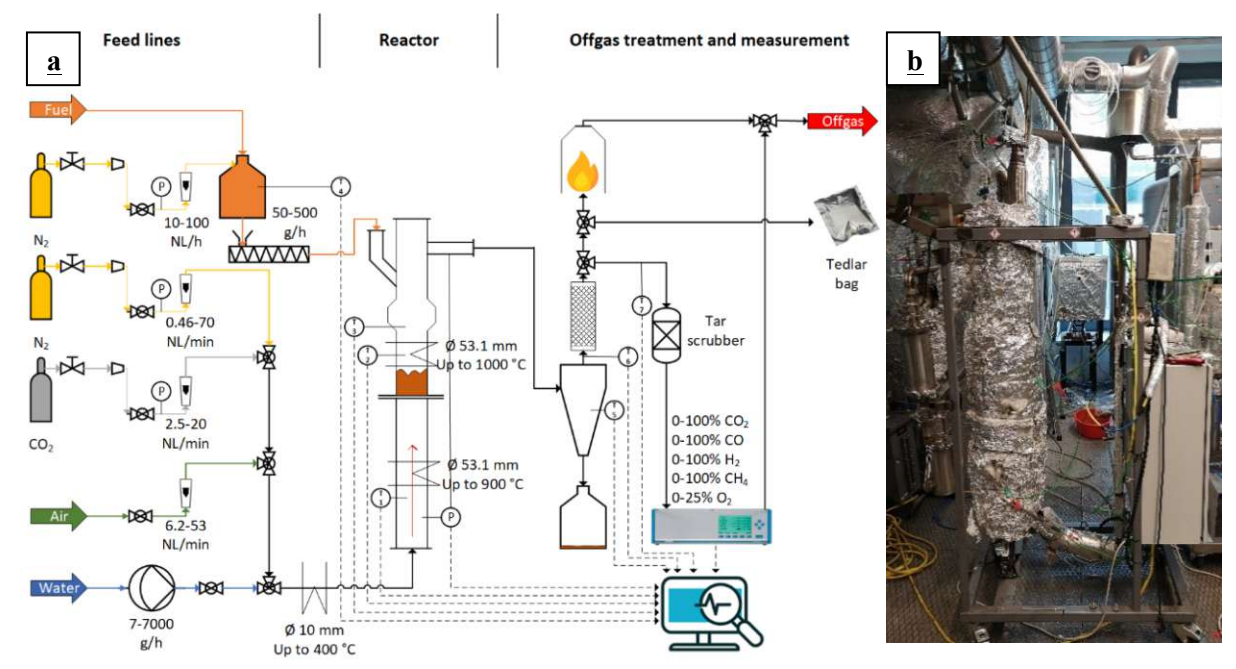


Figure 9: a) Schematic and b) photograph of the gasifier unit "Nero". a) is reprinted from [JA II].

## 3.1.2. Single-bed fluidized bed gasifier #2 (FRU)

Experimental work for CAI was conducted in a smaller reactor called FRU, which is short for Formation Rate Unit (Table 3, Figure 10). Most of the experimental investigations were conducted by Camila Rodríguez-M., whose closely supervised master thesis [132] provided data for CA I.

Table 3: Key information about the single-bed fluidized bed gasifier #2 (FRU).

Parameter	Reactor information
Thermal fuel power to gasifier	~1-100 g batch feed
Heat supply design	Electrical heating shells
Typical fuel-gas contact mode	Bubbling fluidized bed or fixed bed
Maximum operating temperature	1000 °C
Design pressure	Atmospheric
Available feed gases	$CO_2$ , Air, $N_2$
Apparatus was used for	CAI

Compared to NERO, FRU was smaller and did not offer continuous fuel or H<sub>2</sub>O feeding capabilities. The advantage of this unit was the option to quickly batch-feed and extract solid fuel in a sampling cage through an airlock. This option was used for *CAI* to adjust the biochar surface and extract the produced biochar. The CO<sub>2</sub> gasification experiments in this unit were performed in fixed bed mode and fluidized bed mode with silica sand and partially converted the previously torrefied *Pinus sylvestris* pellets.



#### CO<sub>2</sub> Conversion to CO by Fluidized Bed Biomass Gasification Chapter 3: Methodology

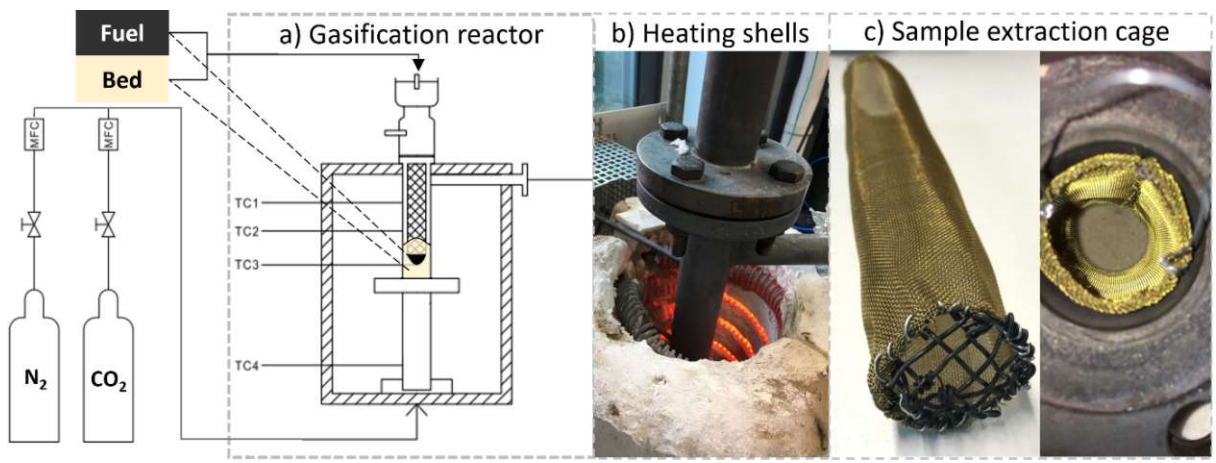


Figure 10: Schematic and photograph of the gasifier "FRU" with sample extraction cage. The figure is reprinted from [CA I].

## 3.1.3. Advanced 100 kWth dual fluidized bed pilot plant

The product gas for JAIII was produced by steam gasification in a dual fluidized bed (DFB) pilot plant (Table 4, Figure 11). The DFB gasifier was not operated with CO<sub>2</sub> as the gasification agent within this thesis but has been used for biomass CO<sub>2</sub> gasification by Mauerhofer et al. [47], [52], [65].

*Table 4: Key information about the advanced 100 kW*<sub>th</sub> dual fluidized bed pilot plant.

Parameter	Reactor information
Thermal fuel power to gasifier	100 kW <sub>th</sub>
Heat supply design	Dual fluidized bed with gasification and combustion columns
Typical fuel-gas contact mode	Bubbling fluidized bed in lower part of the gasification column
Maximum operating temperature	~850 °C in bubbling bed, ~950 °C above bubbling bed
Design pressure	Atmospheric
Available feed gases	CO <sub>2</sub> , H <sub>2</sub> O for gasification column
Apparatus was used for	JA III. Data from Mauerhofer et al. [52] obtained in this apparatus were used in JA IV.

The gasification experiments in this apparatus with steam as the gasification agent and waste wood as feedstock in JA III were only relevant for this thesis to generate a realistic product gas to test the novel H<sub>2</sub>O measurement. Experiments were conducted in this pilot plant to achieve similar measurement conditions as in larger-scale applications, as the DFB concept has been scaled to larger sizes and the apparatus contained some product gas conditioning steps. Data obtained by Mauerhofer et al. [52] in this plant have been used for the process simulation studies in JA IV.



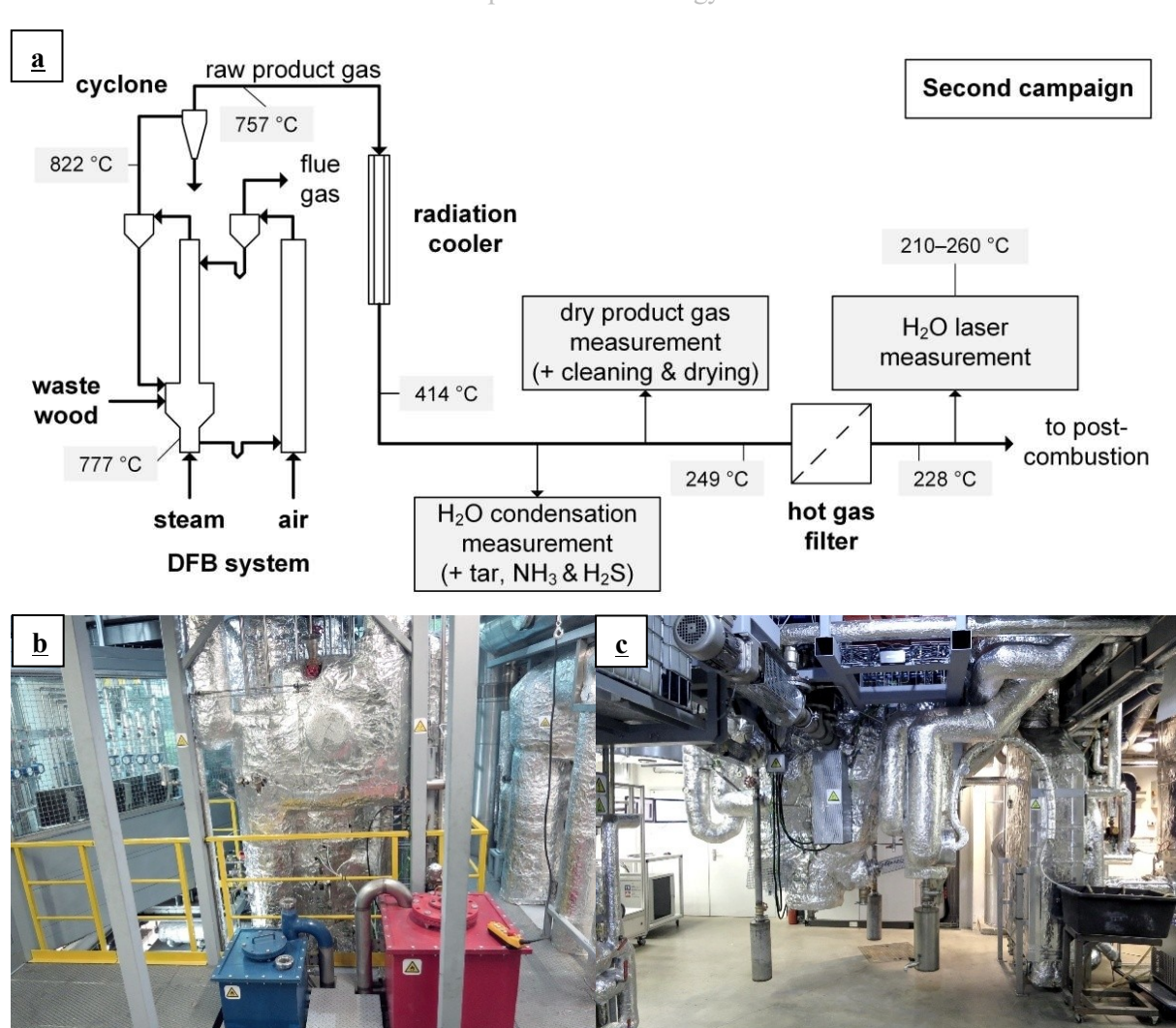


Figure 11: Schematic and photographs of the dual fluidized bed gasifier. a) Product gas pathway (reprinted from [JA III]), b) upper reactor part, c) lower reactor part.

### 3.2. Measurements

This section explains how conventional biomass and gasification analyses were complemented by novel measurements to determine the CO<sub>2</sub> conversion and H<sub>2</sub>O content in product gas.

### 3.2.1. Conventional biomass and gasification analysis

Temperatures were measured by thermocouples (mostly type K) in all reactors. The pressure sensors in NERO and the advanced DFB pilot plant were used for process control but were not central for data analysis in this thesis. The dry product gas components CO<sub>2</sub>, CO, H<sub>2</sub>, CH<sub>4</sub>, and O<sub>2</sub> from NERO and the DFB gasifier were analyzed using Emerson Rosemount NGA 2000 continuous gas analyzers. An EL3020 gas analyzer by ABB was used to screen O2, CO, SO2, CO2, and NO from FRU.

The Testing Laboratory for Combustion Systems at Technische Universität Wien supported the reported experiment in the DFB gasifier and provided standardized fuel analysis. The additional measurements for the DFB gasifier included discontinuous water vapor measurements by condensation, discontinuous

tar analysis by gravimetry and gas chromatography-mass spectrometry (GC-MS), discontinuous NH<sub>3</sub> analysis by ion chromatography, and discontinuous H<sub>2</sub>S analysis by titration. The ultimate analysis of biomass fuels was conducted in an Elementar Analyzer EA 1108 CHNS-O by Carlo Erba. Fuel moisture content was measured following DIN 51718:2002-06 Method A, and volatile content following EN ISO 18123:2015-11. The ash content was analyzed using an Axios advanced XRF device by Panalytical Analysis according to EN ISO 18122:2015-11.

Biomass surface analysis for CA I was conducted using nitrogen adsorption in a Belsorp Max G by Microtrac Retsch. After degassing in a Belprep Vac degassing station, the isotherm data were used to calculate the Brunauer-Emmett-Teller (BET) surface area [133] following DIN ISO 9277:2014-01 and the guidelines proposed by Rouquerol et al. [134] for microporous materials.

### 3.2.2. CO<sub>2</sub> conversion by carbon isotope analysis

**JAII** introduced a novel method of measuring the CO<sub>2</sub> conversion  $X_{CO2}$ . This method was developed to fill the identified knowledge gap around the inconsistent determination of CO<sub>2</sub> conversion and serves as a tool for validating biomass CO2 gasification as a CCU process. The method determines the share of CO and CO<sub>2</sub> in the product gas that contains carbon from feedstock CO<sub>2</sub> (Y<sub>CO from CO2</sub>, Y<sub>CO2 from CO2</sub>) by analyzing the abundance of stable carbon isotopes <sup>13</sup>C in feed streams and products.

Product gas samples were collected with Tedlar bags during stationary gasifier operation in the "NERO" gasifier. The Tedlar bags were filled with gas, which took 1-3 min. The gas was transferred with gastight syringes into gas chromatography vials. The filled syringes were left in the Tedlar bag for 2 min to allow gas homogenization between the bag and the syringe. The process was repeated three times for each sample. These gas samples were sent with a sample of the bottled CO2 feed gas and the used biomass feedstocks to Imprint Analytics GmbH, where the samples were analyzed for the abundance of the stable carbon isotope  $^{13}$ C, expressed as  $\delta^{I3}$ C.  $\delta^{I3}$ C expressed the samples' relative deviation in \% from the Vienna Peedee Belemnite (VPDB) standard that has a <sup>13</sup>C abundance of 0.011180 [135], [136].

At Imprint Analytics GmbH, the samples were separated by gas chromatography, combusted, and sent for isotope analysis to a NU Horizon 1 isotope-ratio mass spectrometer with a measurement precision of  $\pm 0.5$  % for gas samples and  $\pm 0.3$  % for solid samples. If a hypothetical sampling error were included, the accredited measurement precision would drop to  $\pm 1.1$  % and  $\pm 0.63$  %; however, this sampling error was deemed unlikely due to good agreement of the triplicate analysis for all samples.

The resulting  $\delta^{I3}C$  values for each sample were then combined with mass flow data from the plant to calculate CO<sub>2</sub> conversion. The central calculations needed to assign CO<sub>2</sub> and CO in product gas to the parental carbon materials biomass and CO<sub>2</sub> are given in Eq. 18-Eq. 21. The isotopic enrichment factors  $(\varepsilon_{CO2})$  and  $\varepsilon_{CO}$  are needed to consider the differences in reaction characteristics between isotopes resulting from different bond strengths [137]. Literature values for the isotopic enrichment in this

process were still rare; therefore, assumptions were needed to calculate  $\varepsilon_{CO2}$  and  $\varepsilon_{CO}$ . JA II proposed the following two assumptions to determine  $\varepsilon_{CO2}$  and  $\varepsilon_{CO}$  before calculating  $X_{CO2}$ :

- $\varepsilon_{CO2}$  is zero: This simplification is based on the data by Flude et al. [137], who reasoned that concurrent isotopic fractionation effects for CO<sub>2</sub> are likely to average out.
- $\varepsilon_{CO}$  can be determined from carbon balances by assuming all carbon from feedstock CO<sub>2</sub> leaves the reactor as CO or CO<sub>2</sub>. This assumption seems reasonable based on the important gasification reactions summarized in Table 1.

$$Y_{\text{CO from CO}_2} = \frac{(\delta^{13}C_{\text{CO,out}} + \epsilon_{\text{CO}}) - \delta^{13}C_{\text{fuel}}}{\delta^{13}C_{\text{CO2,in}} - \delta^{13}C_{\text{fuel}}}$$
 Eq. 18

$$Y_{CO_2 \text{ from } CO_2} = \frac{(\delta^{13}C_{CO_2,\text{out}} + \varepsilon_{CO_2}) - \delta^{13}C_{\text{fuel}}}{\delta^{13}C_{CO_2,\text{in}} - \delta^{13}C_{\text{fuel}}}$$
 Eq. 19

$$X_{CO2 \text{ unconverted}} = \frac{\dot{m}_{CO2,\text{out}}}{\dot{m}_{CO2 \text{ in}}} \cdot Y_{CO2 \text{ from } CO2}$$
 Eq. 20

$$X_{CO2} = 1 - X_{CO2 \text{ unconverted}}$$
 Eq. 21

The feed CO<sub>2</sub> mass flow  $(\dot{m}_{CO2,in})$  was controlled, and the drain CO<sub>2</sub> mass flow  $(\dot{m}_{CO2,out})$  calculated from measurements of the dry product gas composition and mass balances. The resulting  $X_{CO2}$  value expresses the conversion of feedstock CO<sub>2</sub>, differentiating it from previous estimation methods that can only provide net-conversion values that include biomass devolatilization effects (see **Section 3.4.1**).

# 3.2.3. Online water vapor quantification by THz quantum cascade laser

Accurate online quantification of raw product gas components is essential for controlling and optimizing thermochemical biomass conversion. Water vapor is usually among the most prominent species in raw product gas [52], [138]. However, existing methods for water vapor quantification often struggle with the harsh conditions of hot, uncleaned gas streams containing tar, particulates, and a variable gas matrix [139], [140]. Common issues for online methods include fouling, signal interference, and limited sensitivity [68], [69], [141]. Offline methods lack real-time capability, while soft sensors require extensive calibration and prior data [142]. This lack of a robust, standardized solution for continuous water vapor measurement in raw product gas necessitated the development of a new method, presented in JA III.

A measurement setup consisting of a heated gas cell, a quantum cascade laser (QCL), and a pyroelectric detector was created and tested in cooperation with the Photonics Institute and the Institute of Solid State Electronics at TU Wien (Figure 12).



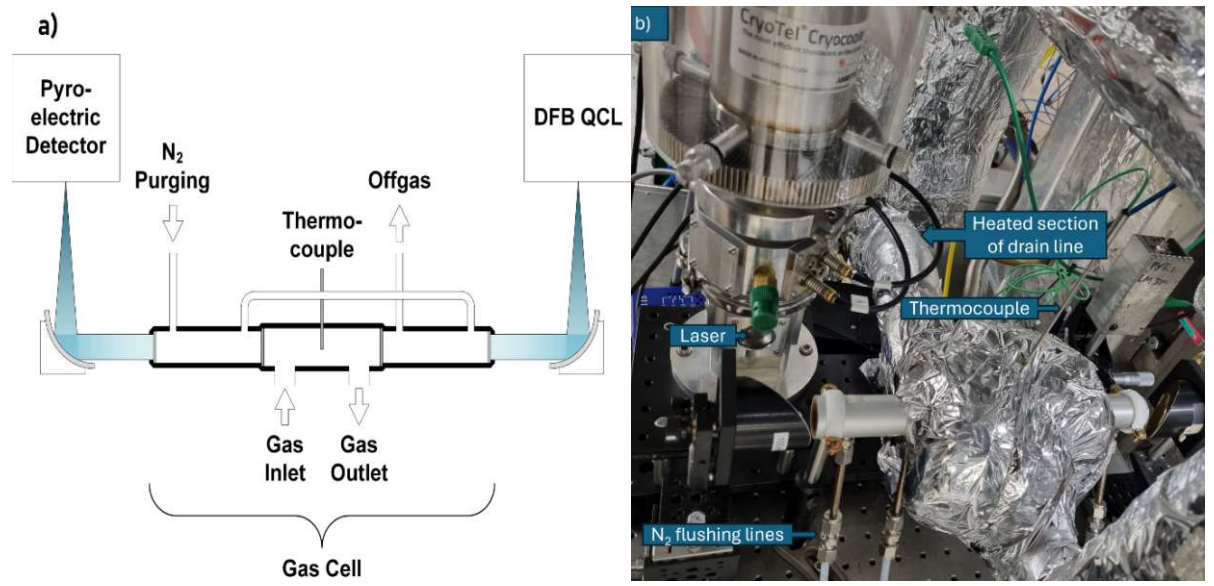


Figure 12: Schematic and photograph of the developed laser setup for quantifying H<sub>2</sub>O in hot and raw product gas. Both subfigures are reprinted from [JA III].

A suitable laser frequency was selected using the Spectral Calculator [143], which uses HITRAN2020 [144] as a line list to calculate the Voigt profile. A primary design target was to avoid significant band overlap with common product gas species from biomass steam gasification [138] and biomass CO<sub>2</sub> gasification [52]. The QCL used a material combination of GaAs/AlGaAs for its active region and a 1storder distributed feedback grating to ensure single-mode operation at the desired H<sub>2</sub>O absorption line  $(2.294 \text{ THz} = 130.69 \,\mu\text{m} = 76.52 \text{ cm}^{-1})$ . The aluminum-made gas cell had an optical path length (d) through the product gas of 8.6 cm and was heated up to around 260 °C by a heating coil. H<sub>2</sub>O concentration data (c<sub>Laser</sub>) was calculated based on the direct absorption principle, with Beer-Lambert's law correlating the measured signal intensity (I) to the signal intensity measured in an inert gas  $(I_0)$ . Further values used in the calculation were the pressure (p), temperature (T), ideal gas constant (R), and molar extinction coefficient of water vapor ( $\varepsilon_{H2O}$ ). A numerical solver was developed to account for the  $H_2O$  concentration dependence of  $\varepsilon_{H_2O}$  and the influence of cross-absorption by CO. The rearranged form of Lambert-Beer's law as it was applied is given in Eq. 22.

$$c_{Laser} = \frac{R \cdot T \cdot log_{10} \left(\frac{I_0}{I}\right)}{\varepsilon_{H2O} \cdot d \cdot p}$$
 Eq. 22

## 3.3. Simulations and modeling

This chapter describes the applied simulation tools and the primary considerations leading to the proposed process design for direct reduction ironmaking.

### 3.3.1. Simulation tools

Various process data were analyzed in Microsoft Excel and MATLAB. In addition, two dedicated simulation tools were used for thermodynamic equilibrium and process flowsheet modeling.



### 3.3.1.1. FactSage

The experimental investigations in **JA I-II** were supported by thermodynamic equilibrium modeling. The equilibrium module integrated in FactSage [145] was used to calculate equilibrium compositions by minimizing the free Gibbs energy. Thermodynamic equilibrium modeling was used for:

- Experimental design by investigating the influence of temperature and feed ratios on the expected product gas composition,
- comparison with the experimental results to uncover kinetic limitations if the product gas composition was significantly different from the equilibrium composition,
- verification of the experimental findings.

The complex chemical composition of biomass feedstocks made it necessary to use simplifications. Biomass was simulated in FactSage as a mixture of liquid H<sub>2</sub>O (measured by proximate analysis) and elemental C, H<sub>2</sub>, and O<sub>2</sub> (measured by ultimate analysis).

### 3.3.1.2. IPSEpro

Mass and energy balancing by process modeling in IPSEpro [146], [147], [148] was one of the main methods used in this thesis. IPSEpro is an equation-based flowsheet simulation environment that simultaneously solves stationary mass- and energy balances [146]. JA IV used extensive process flowsheet modeling for the process concept study that described how biomass CO<sub>2</sub> gasification could be industrially used for direct reduction ironmaking. JA II used mass balances in a flowsheet model to calculate the product gas mass flows, which were not directly available as measurements. JA II-III also used IPSEpro to estimate the water vapor concentration in the product gas.

The software package IPSEpro consists of multiple program modules [147]. The Model Development Kit allows the user to design and mathematically describe models. Three types of models are differentiated: connection, global, and unit. Units represent equipment or unit operations, e.g., a heat exchanger or pump. Connections do as their name implies: They connect different units and transfer information from one to another, e.g., the mass flow or temperature of a gas stream. Globals can be used to describe streams by separate, reusable functions. These globals are used in biomass gasification simulations for composition data, e.g., to retain the same chemical gas composition for a gas stream from feed to the drain side of a heat exchanger. Models can also call on external property libraries to derive material parameters such as the heat of formation. The model compiler can compile a collection of individual models into model libraries.

Extensive model libraries suited for gasification modeling have been created in IPSEpro at TU Wien over the last decades, e.g., [148], [149]. These libraries have been extended by creating several new models for JA IV. The most significant new units were:

- An iron reduction unit was added that considers the thermodynamic stability of iron phases in gas mixture atmospheres where iron reduction happens with CO and/or H<sub>2</sub>.
- Separate scrubber and stripper units for CO<sub>2</sub> capture in aqueous amines, e.g., monoethanolamine (MEA), were added. The new units include options for heat integration. They can calculate the specific energy demand for carbon capture based on a mix of operating conditions and material data like the heat of absorption.

The extended model libraries were used to draft flowsheet models in the Process Simulation Environment. The Process Simulation Environment offers a graphical interface to arrange models from the selected model library. Variables established within the Model Development Kit can be defined by entering process data into the flowsheet. The model can be solved once the number of independent process data points entered equals the number of independent variables. The solver first checks in the analysis phase if the flowsheet model is correctly specified and determines the optimum solution method. Second, the solver applies numerical methods defined during the analysis phase to solve the flowsheet model and calculate all dependent variables. The results are presented directly in the flowsheet model and can, for example, be exported to Microsoft Excel using the PSXLink extension module.

### 3.3.2. Modeling the direct reduction ironmaking process

JA IV aimed to contextualize the experimental results by a concept study to describe how biomass CO<sub>2</sub> gasification can be applied as a CCU process at an industrial scale. The direct reduction ironmaking (DRI) process was selected as it has some characteristics that make it particularly suited for combining biomass CO<sub>2</sub> gasification.

- Importance of the steelmaking sector: The average carbon intensity of steelmaking was 2.3 t<sub>CO2</sub>/t<sub>steel</sub> [4] in 2020, and steel demand reached around 1.81 Gt in 2023 [150]. At a total of 4.1 Gt<sub>CO2-eq.</sub> in 2020, the steelmaking sector was responsible for around 6.9 % of all global emissions contributing to global warming [4]. Developing low-emission technologies for direct reduction ironmaking is a promising approach for decarbonization in this sector. The DRI product can be used as feedstock for electric arc furnaces (EAF) [151]. Various DRI-EAF process configurations have been proposed to achieve significant emission reductions compared to steelmaking via the blast furnace-basic oxygen furnace route [17], [152], [153], [154], [155].
- H<sub>2</sub>:CO ratio: The DRI process does not need a specific H<sub>2</sub>:CO ratio as both CO and H<sub>2</sub> can independently take up oxygen and act as reducing agents [112]. A high CO content, as observed in the product gas from CO2 gasification, can even be beneficial for ironmaking. Iron ore reduction with H<sub>2</sub> is endothermic, which can bring heat distribution challenges in the reactor [113], [156]. Iron reduction with CO is exothermic [156], which potentially helps with heat distribution. Furthermore, the formation of Fe<sub>3</sub>C is a desired side effect in the DRI process [17], and is increased at H<sub>2</sub>:CO ratios of 1 or lower [157].

- Carbon recycling potential: Since the gas is used as a reducing agent in DRI, the CO is converted back to CO<sub>2</sub>, which is available at the site and can be recirculated back to the CO<sub>2</sub> gasifier with minimal delay. Furthermore, if the only external carbon source is biomass, this CO<sub>2</sub> is renewable, and excess CO<sub>2</sub> can be carbon-neutrally emitted or stored to reach net-negative CO<sub>2</sub> emissions. This small integration loop is advantageous, as it gives economic control over a significant feedstock, enables heat integration for carbon capture, saves on transport costs, provides renewable carbon from a point source, and allows for adjusting the capture conditions to the process needs.
- Impurity tolerance: Bürgler and Di Donato reported on biomass gasification for DRI production within the Ultra Low Carbon Dioxide Steelmaking (ULCOS) program [158]. One aspect that they described was product gas purification for DRI. They concluded that typical product gas impurities like dust, tar, and sulfur were either unproblematic for the DRI process or easy to remove with established gas cleaning steps.

After selecting ironmaking as the target application, further process development aimed to project own experimental results into a high-efficiency process design that included thorough mass and energy balances for the primary unit operations. It was decided to measure the quality of the developed design regarding emission intensity and production costs by comparison with a simplified MIDREX process, which uses natural gas to produce reducing gas for DRI [159]. Economic and ecological calculations are described in Section 3.4. These primary units of the selected design are briefly characterized here; the interested reader is referred to JA IV for in-depth information on process design and data. An overview of the simulated process routes is given in *Figure 13*.

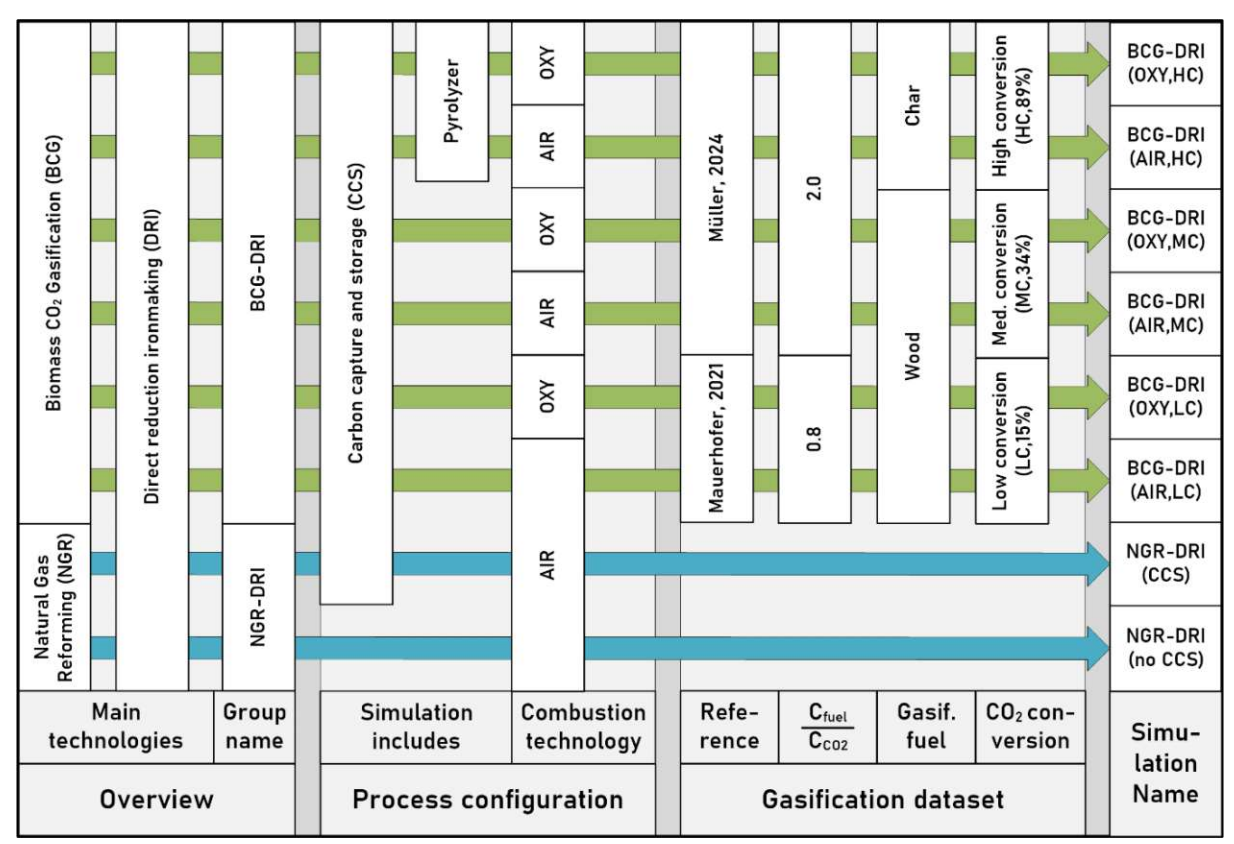


Figure 13: Overview of simulated process routes in JA IV. References for gasification datasets are as follows: "Mauerhofer, 2021"=[52], "Müller, 2024"=[JA II]. The figure is adjusted from [JA IV].

A dual fluidized bed reactor design was assumed for biomass CO<sub>2</sub> gasification (BCG). Mauerhofer et al. have demonstrated BCG in such a gasifier and provided various data that were also used in this study, e.g., for simulation of the combustion reactor and the abundance of tar, dust, and fly char in the product gas [47], [52], [160]. Data from experiment #5 by Mauerhofer et al. [52] were also used as one of three datasets for the product gas composition to prove the feasibility of a dual fluidized bed reactor in this process. Two other datasets were taken from the work in JA II. Experiments #4 and #7 were selected because they used different biomass feedstocks (#4: softwood, #7: wood char), had relatively high CO<sub>2</sub> conversion and some moisture in the feed gas. These three datasets were ranked by their CO<sub>2</sub> conversion as low conversion ("LC", #5 in [52]), medium conversion ("MC", #4 in JA II), and high conversion ("HC", #7 in JA II). Each dataset was simulated once with air ("AIR") and once with oxygen-enriched flue gas ("OXY) for combustion.

Following published plant data by Shams and Moazeni [161] and Parisi and Laborde [162], a shaft furnace was assumed for iron reduction and carburization. The reducing gas' (=gas fed to shaft furnace) and top gas' (=gas drained from shaft furnace) compositions were characterized by the reduction potential (RP). Iron reduction was assumed to occur by reactions with both H<sub>2</sub> and CO. Carburization was assumed to occur only by reactions with CO.

$$RP = \frac{n_{H_2} + n_{CO}}{n_{H_2O} + n_{CO_2}}$$
 Eq. 23



A carbon capture unit using aqueous monoethanolamine as a solvent in two columns, one for absorbing and one for stripping, was assumed to capture CO<sub>2</sub> from top gas based on a book by Madeddu et al. [58]. Part of the captured CO<sub>2</sub> was fed to the gasifier as the gasification agent. Any excess CO<sub>2</sub> underwent compression and purification, and left the flowsheet at 100 bar with designation for transport and geological storage. The "OXY"-simulations merged the excess CO2 with flue gas from oxy-fuel combustion before purification and transport.

Cryogenic air separation and CO<sub>2</sub> purification units were not simulated in detail, but electrical energy demand and gas purities were assumed following Habib et al. [59] and Xu et al. [163]. A biomass dryer was included in all simulations [164]. A screw pyrolyzer was included in "HC"-simulations for wood char production based on data by Solar et al. [165]. The gaseous pyrolysis products were assumed to merge with the product gas from gasification. Cyclones and a tar scrubber using rapeseed methyl ester as solvent were assumed for cleaning the (merged) product gas [16]. Counter-current heat exchangers were assumed for heat integration. The natural gas reformer data for the comparison process were mainly derived from Shams and Moazeni [161] and Farhadi et al. [166].

### 3.4. Calculation of key parameters

### 3.4.1. CO<sub>2</sub> conversion estimations

 $CO_2$  conversion ( $X_{CO2}$ ) in this thesis is defined as the percentage of feedstock  $CO_2$  converted to other carbonaceous products during biomass CO<sub>2</sub> gasification. Section 2.4 explained that reporting in the literature is limited to estimation methods and can significantly vary based on selected estimation methods and assumptions. Two of the most common estimation methods were applied to work in this thesis and are explained below. JA I used  $X_{CO2,stoichiometric}$  for CO<sub>2</sub> conversion assessment under various operating conditions, and JAII compared  $X_{CO2,balance}$  and  $X_{CO2,stoichiometric}$  to the novel measurement based on stable carbon isotope analysis that was introduced in Section 3.2.2. Results from the isotopic measurement method are referred to simply as  $X_{CO2}$ .

One method for  $CO_2$  conversion calculation is to determine  $X_{CO2,balance}$  by relating the difference between ingoing  $(\dot{m}_{CO2,in})$  and outgoing  $(\dot{m}_{CO2,out})$  CO<sub>2</sub> stream to the ingoing CO<sub>2</sub> stream (Eq. 24) [167]. This method needs gas flow rate and CO2 composition data for the reactor's inlet and outlet. If CO2 is formed in the reactor, e.g., by devolatilization, the term  $\dot{m}_{CO2,out}$  contains new CO<sub>2</sub> in addition to the unconverted feedstock CO<sub>2</sub>. Consequently, X<sub>CO2,balance</sub> tends to underestimate the conversion of feedstock CO<sub>2</sub>. Some authors have tried to account for this effect by estimating how much CO<sub>2</sub> is newly produced in the reactor and subtracting this amount of CO<sub>2</sub> from the outlet side, e.g., Mauerhofer et al. compared CO<sub>2</sub> streams with data from pyrolysis and steam gasification [52]. However, they found significant divergence in the results based on these different assumptions, as comparison with pyrolysis and steam gasification yielded either 26 % or 45 % of CO<sub>2</sub> conversion.

$$X_{CO2,balance} = \frac{\dot{m}_{CO2,in} - \dot{m}_{CO2,out}}{\dot{m}_{CO2,in}}$$
 Eq. 24

Some authors used a different method, which calculates the  $CO_2$  conversion  $X_{CO2,stoichiometric}$  based on stoichiometric considerations and the product gas composition [119]. This method assumes that CO and  $H_2$  in the product gas are formed from the Boudouard (Eq. 4) and steam-carbon (Eq. 5) reactions. XCO2, stoichiometric also assumes that any CO2 in the product gas is leftover unconverted feed CO2. Although it seems possible to apply similar estimation strategies as Mauerhofer et al. showed for  $X_{CO2,balance}$  to account for other reactions in  $X_{CO2,stoichiometric}$ , no one has yet done so to the author's best knowledge. The advantage of this method is that it only needs dry product gas composition data, which is typically measured and reported. This relatively low hurdle of application also allows for calculating X<sub>CO2,stoichiometric</sub> from literature sources, which did not explicitly report on CO<sub>2</sub> conversion but provided product gas compositions. Another advantage is that the concentrations can be used as relative numbers, allowing for quick evaluation of semi-batch experiments before gas composition is stabilized. One disadvantage of this method is that it does not accurately reflect all reactions in a gasifier. Similar to X<sub>CO2,balance</sub>, this can introduce a significant error if biomass devolatilization contributes much to the product gas. The derivation of  $X_{CO2,stoichiometric}$  is provided in **Eq. 25-Eq. 30**. The amount of each substance A is expressed as  $n_A$  and its molar concentration as  $c_A$ . The indices in and out refer to the reactor's inlet and outlet.

$$\Delta n_A = n_{A,in} - n_{A,out} \qquad Eq. 25$$

$$n_{CO,in} = 0 \rightarrow \Delta n_{CO} = -n_{CO,out}$$
 Eq. 26

$$n_{H2,in}=0$$
  $\rightarrow$   $\Delta n_{H2}=-n_{H2,out}$  Eq. 27

$$(C + CO_2 \to 2CO) \&$$
 $(C + H_2O \to CO + H_2) \to$ 
 $-\frac{1}{2}(\Delta n_{CO} - \Delta n_{H2}) = \Delta n_{CO2}$ 
Eq. 28

$$n_A = n \cdot c_A$$
 Eq. 29

$$X_{CO2,stoichiometric} = \frac{\Delta n_{CO2}}{n_{CO2,in}} = \frac{c_{CO,out} - c_{H2,out}}{c_{CO,out} - c_{H2,out} + 2 \cdot c_{CO2,out}}$$
 Eq. 30

Both  $X_{CO2,balance}$  and  $X_{CO2,stoichiometric}$  suffer from inaccuracies if the activity of reactions other than the Boudouard and steam-carbon reactions increases. The simplification that all product gas is a product of these reactions is likely more accurate if the fixed carbon content of the biomass feedstock is higher, as the error induced by devolatilization is lower in this case. For this reason, both methods are most applicable to CO<sub>2</sub> gasification processes that use char or coal with high fixed carbon content as fuel.

### 3.4.2. Energy efficiency

Energy efficiency was calculated in JA IV for the designed ironmaking process routes. All chemical energy in used materials plus heat and electricity demands are considered energy expenses. This

evaluation's electrical and chemical input power includes the demands of various sub-tasks like gasification, carbon capture, and air separation. Chemical energy in feedstock and raw product gas is considered by the lower heating value (LHV) and mass flow  $(\dot{m})$ . The chemical energy stored in cold direct reduced iron (CDRI) is classified as the desired energy output. The energy contained in the CDRI can be calculated as the difference in enthalpy  $(\Delta H)$  between the iron ore and CDRI. As an additional representation of energy efficiency, the total energy expenses were referred to the mass flow of CDRI to calculate the specific energy demand per unit of CDRI ( $e_{IRON}$ : Eq. 32)

$$\eta_{IRON} = \frac{\Delta \dot{H}_{IRON}}{P_{EL} + \sum LHV \cdot \dot{m}}$$
 Eq. 31

$$e_{IRON} = \frac{P_{EL} + \sum LHV \cdot \dot{m}}{\dot{m}_{CDRI}}$$
 Eq. 32

### 3.4.3. Carbon footprint calculation

The process simulations in **JA IV** included three carbon footprint (CF) calculations: two for economic evaluations and one for ecological assessment.

The first calculation ( $CF_{EU\text{-}ETS}$ : Eq. 33) follows the European Union Emission Trading Scheme (EU-ETS) rules and was used to calculate the necessary CO<sub>2</sub> allowances for techno-economic calculations. The calculation followed the mass balance methodology described in the amended Commission Implementing Regulation 2018/2066 [168] and considers the sustainability and greenhouse gas emission saving criteria given in Directive (EU) 2018/2001 [169]. Relevant ingoing carbon streams ( $\dot{m}_C$ ) for this method include the carbon in natural gas (NG), triethylene glycol (TEG), monoethanolamine (MEA), and rapeseed methyl ester (RME). Within the framework of the current EU-ETS rules given in Regulation 2018/2066 [168], it is currently not possible to generate CO<sub>2</sub> allowances through netnegative emissions resulting from bioenergy with carbon capture and storage (BCCS) [170], [171], [172]. Therefore, outgoing carbon streams into cold direct reduced iron (CDRI) and geological storage are only assumed to reduce  $CF_{EU-ETS}$  for the fossil comparison process with natural gas.

The second calculation ( $CF_{EU\text{-}ETS,BCCS}$ : **Eq. 34**) includes a hypothetical change to the EU-ETS framework that would allow for generating CO<sub>2</sub> removal credits from BCCS activities. In this hypothetical case, the outgoing carbon streams into CDRI and geological storage are subtracted for all cases.

The third calculation ( $CF_{LCA}$ : Eq. 35) uses a cradle-to-gate system boundary to account for the indirect emissions of material and energy streams entering the proposed process. This method uses mass balance data and  $CO_2$ -equivalent ( $CO_2$ e) emission factors ( $f_{CO2e}$ ), e.g., as described by the Federal Environmental Agency of Austria (Umweltbundesamt) [173], [174]. It represents a simplified life cycle assessment with the global warming potential over 100 years as a sole impact category.



$$CF_{EU-ETS} = \frac{\sum_{NG,TEG,MEA,RME} (\dot{m}_C \cdot 3.664) - \dot{m}_{C \ in \ CDRI,fossil} \cdot 3.664 - \dot{m}_{CO2,CCS,fossil}}{\dot{m}_{CDRI}} \qquad \textit{Eq. 33}$$

$$CF_{EU-ETS,BCCS} = \frac{\sum_{NG,TEG,MEA,RME} (\dot{m}_C \cdot 3.664) - \dot{m}_{C \ in \ CDRI} \cdot 3.664 - \dot{m}_{CO2,CCS}}{\dot{m}_{CDRI}}$$
 Eq. 34

$$CF_{LCA} = \frac{\sum_{all\ streams} (reference\ unit\ flow \cdot f_{CO2e})}{\dot{m}_{CDRI}}$$
 Eq. 35

The applied  $f_{CO2e}$  values (*Table 5*) combine mass balance data for direct emissions and indirect emission data from the ecoinvent database (version 3.10.1) [175].

*Table 5: CO<sub>2</sub>e emission factors used for CF<sub>LCA</sub> carbon footprint calculation.* 

Stream	Unit	fc02e	Direct CO <sub>2</sub> emissions by mass balance	Indirect CO <sub>2</sub> e emissions (upstream)	Source
Iron ore pellets	kg <sub>CO2e</sub> /kg <sub>iron ore</sub>	0.103		0.1033	[176]
Triethylene glycol	$kg_{CO2e}/kg_{TEG}$	3.968	1.758	2.21	[177]
Monoethanolamine	kg <sub>CO2e</sub> /kg <sub>MEA</sub>	5.827	1.847	3.98	[178]
Rapeseed methyl ester	kg <sub>CO2e</sub> /kg <sub>RME</sub>	5.340	2.840	2.5*	[179]
Olivine	kg <sub>CO2e</sub> /kg <sub>olivine</sub>	0.043		0.0432**	[180]
Biomass (LC/MC)-	kg <sub>CO2e</sub> /kg <sub>dry</sub> wood	1.906	1.861	0.045	[181]
simulations	(LC/MC)				
Biomass (HC)-	kg <sub>CO2e</sub> /kg <sub>dry</sub> wood	1.793	1.748	0.045	[181]
simulations	(HC)				
Electricity	kg <sub>CO2e</sub> /kWh <sub>grid elect.</sub>	0.260		0.26	[182]
Natural gas	kg <sub>CO2e</sub> /m <sup>3</sup> natural gas	2.646	2.046	0.6	[183]
CO <sub>2</sub> to storage	kg <sub>CO2e</sub> /kg <sub>CO2 to CCS</sub>	-1.000	-1.000		
Carburization	kg <sub>CO2e</sub> /kg <sub>CDRI</sub>	-0.073	-0.073		
Plant growth	kg <sub>CO2e</sub> /kg <sub>dry</sub> wood	-1.861		-1.861	Mass
(LC/MC)-simulations	(LC/MC)				balance
Plant growth (HC)-	kg <sub>CO2e</sub> /kg <sub>dry</sub> wood	-1.748		-1.748	Mass
simulations	(HC)				balance

<sup>\*</sup>Data for fatty acid methyl ester.

### 3.4.4. Techno-economic assessment

The techno-economic assessment in JA IV applied the net present value method to determine the levelized cost of CDRI production (LCOP, Eq. 36), representing the cost per unit in a new plant [184], [185], [186]. This approach has been widely used for biomass-fed gasifier systems [16], [155], [187]. The LCOP method incorporates a cumulative discount factor (CDF, Eq. 37) to discount future cash flows.

A production scale of 1 Mt<sub>CDRI</sub>/a was assumed to align with a similar work by Pissot et al. [17]. LCOP accounts for investment costs  $(I_{\theta})$ , expenses (E), and revenues from secondary products (R). An estimate for the investment costs ( $I_0$ : Eq. 38), or capital expenditure (CAPEX) was derived as the sum of subsystem equipment cost estimates. Subsystem equipment costs at design capacity ( $C_{eq,design}$ : Eq. 39) were estimated from literature values [105], [163], [164], [188], [189], [190], [191], [192], [193], [194], [195], [196], [197], [198] using the capacity method, which typically has an accuracy of -30 % to +50 %

<sup>\*\*</sup>Data for silica sand.

at this stage [185]. The variables S, r, and Z express the equipment size, scale, and overall installation factors. The chemical engineering plant cost index (CEPCI) is used to account for price development over time.

Expenses (E), or operational expenditures (OPEX), are categorized into fixed and variable costs. Fixed OPEX depend on equipment size, while variable OPEX arise from input and output streams per CDRI unit. Energy prices were based on Austria and Germany (Nov 2023 – Oct 2024) [199], [200], [201]. Other cost factors [155], [164], [202], [203], [204], [205], [206], [207], [208] were preferably taken from previous techno-economic biomass gasification investigations in these regions and adjusted for Austrian inflation via the consumer price index [209].

Additionally, the emission allowance break-even price (EABEP: Eq. 40) served as a comparative economic indicator, representing the emission allowance price required for cost parity with a natural gas-based comparison process without carbon capture and storage (NG-DRI). If a nonzero emission allowance price  $(p_{EA,0})$  is assumed in *LCOP*, it must be included in the *EABEP* calculation.

Both  $LCOP_{BCCS}$  and  $EABEP_{BCCS}$  are calculation variants that replace  $CF_{EU-ETS}$  with  $CF_{EU-ETS,BCCS}$  for calculating emission costs to account for potential CO2 removal credit revenues within the EU-ETS in the hypothetical policy-change scenario.

$$LCOP = \frac{I_0 + (E - R) \cdot CDF}{m_{CDRI} \cdot CDF}$$
 Eq. 36

$$CDF = \frac{(1+i)^n - 1}{i \cdot (1+i)^n}$$
 Eq. 37

$$I_0 = \sum_{i} C_{eq,design,i}$$
 Eq. 38

$$C_{eq,design} = C_{eq,base} \cdot \left(\frac{S_{design}}{S_{base}}\right)^{r} \cdot Z \cdot \frac{CEPCI_{2024}}{CEPCI_{base\ year}}$$
Eq. 39

$$EABEP = \frac{LCOP_{process} - LCOP_{NG-DRI}}{CF_{EU-ETS,NG-DRI} - CF_{EU-ETS,process}} + p_{EA,0}$$

$$Eq. 40$$

The assumed economic parameters are summarized in *Table 6*.



CO<sub>2</sub> Conversion to CO by Fluidized Bed Biomass Gasification Chapter 3: Methodology

Table 6: Economic parameters assumed for techno-economic calculations

Net present value calculation	Unit		Value	Source			
Nameplate capacity	Mt <sub>CDRI</sub> /a		1000	Assumption based on [17]			
Plant lifetime	a		20	[204]			
Interest rate	%		6	[205]			
Fixed OPEX calculation	Unit		Value	Source			
Maintenance cost per year	%	of	2.00	[206]			
	CAPEX/a						
Insurance, administration, and tax per	%	of	1.50	[155]			
year	CAPEX/a						
Cost of one employee per year	€/a		88000	[155] i.a.*			
Operating hours	h/a		8000	[155]			
Number of employees	-		25	Assumption based on [155],			
				[204]			
Variable OPEX calculation:	Unit		Cost in	Source			
expenses			€/unit				
Wood (35 wt% H <sub>2</sub> O)	$MWh_{LHV}$		28.8**	[199] 1 year average			
Natural gas	$MWh_{LHV}$		56.5	[200] 1 year average			
Electricity	MWh		74.8	[201] 1 year average			
Iron ore pellets	t		104	[207] 1 year average			
Rapeseed Methyl Ester			[204] i.a.*				
Process water	t		2.4	[206] i.a.*			
Olivine			260	[164] i.a.*			
Triethylene glycol	t		1000	Online markets			
Monoethanolamine	t		850	Online markets			
Cooling water	t		0.06	[208] 1 year average			
Ash/olivine landfilling			[164] i.a.*				
Wastewater disposal	t 4 [204] i.a.*						
CO <sub>2</sub> transport and storage	t		60	[202]			
CO <sub>2</sub> emission price (fossil)	t		146	[203] 2030 forecast			
Side revenues	Unit		Cost in	Source			
			€/unit				
CO <sub>2</sub> removal credit	t		146	[203] 2030 forecast			
District heating	MWh		15	[204] i.a.*			

<sup>\*</sup>i.a.=inflation-adjusted (and rounded) from year of cost data to October 2024 based on Austria's consumer price index

<sup>\*\*</sup>Recalculated from a net price of 89.6 €/t using a calculated lower heating value (LHV) of 3.17 MWh/t

## 4. Results and discussion

This section summarizes and discusses the most important findings from JA I-IV and CA I. The first three subsections each address one of the three core research questions, while the fourth section summarizes the findings for the additional related research questions:

- Section 4.1: How can CO<sub>2</sub> conversion be increased in a fluidized bed biomass gasifier?
- **Section 4.2**: How can CO<sub>2</sub> conversion be validated in a biomass gasifier?
- Section 4.3: How does implementing biomass CO<sub>2</sub> gasification for CO<sub>2</sub> recycling affect the economic viability and CO<sub>2</sub> emissions of direct reduction ironmaking?
- Section 4.4: What additional results relevant to biomass CO<sub>2</sub> gasification were found regarding surface adjustment of biochar and H<sub>2</sub>O quantification in hot gas?

Each of these chapters includes a discussion section and a key findings box. The discussion sections synthesize the results from different articles (if applicable) and contextualize them. The key findings boxes provide the basis for answering the research questions in the thesis conclusions.

# 4.1. Increasing $CO_2$ conversion by varying operating conditions

The focus of this chapter is to describe how CO<sub>2</sub> conversion can be increased in biomass CO<sub>2</sub> gasification. All investigations described in this chapter have been experimentally conducted in the single-bed fluidized bed gasifier #1 "NERO" (see Section 3.1.1).

### 4.1.1. Results: Increasing CO<sub>2</sub> conversion

Different strategies were used in JA I and JA II to address the research question of how to increase CO<sub>2</sub> conversion. JA I used semi-continuous experiments to screen a wide range of operating conditions. JA II aimed to validate and demonstrate the process with continuous feeding experiments, which take more time but are practically more relevant.

### 4.1.1.1. Semi-continuous investigation of operating conditions

CO<sub>2</sub> conversion was investigated in JA I in a fluidized bed gasifier under semi-continuous feeding conditions. Eucalyptus globulus wood char was used as fuel, which had high fixed carbon content. This fuel was batch-fed to the reactor under nitrogen flow. CO2 replaced nitrogen as the gas feed to start the experiments. The  $CO_2$  conversion was estimated using Eq. 30  $(X_{CO2,stoichiometric})$  because these experiments happened before the new isotopic CO<sub>2</sub> conversion measurement was developed, and mass flow rates from the reactor were unavailable. Two of the investigated parameters, temperature and fuel height in the reactor, decreased after the experimental start because of endothermic gasification

reactions. CO<sub>2</sub> conversion was evaluated close to the experimental start to avoid a significant deviation of these parameters from the initially controlled conditions. *Table 7* lists the investigated operational parameters in JA I.

Table 7: Experimental parameters investigated in 53 experiments in JA I.

Variable	Investigated factor	Analyzed parameters (target values)	Variations
T	Temperature	800 − 1000 °C	5
F	Initial fuel loading (height)	5 - 15  cm	4
S	Fuel size	0.8 - 8  mm	4
G	Feed gas flow rate	$0.30 - 0.43 \text{ Nm}^3/\text{h}$	2
M	Bed material type	Silica sand limestone olivine	3
В	Initial bed-to-fuel ratio	$0.66 - 4 \text{ m}^3/\text{m}^3$	6

The article tried to overcome the limitations of unclear comparability between experiments by proposing a semi-empirical CO<sub>2</sub> conversion model that could replicate CO<sub>2</sub> conversion in the reactor based on all six investigated factors. Comparisons of the experimental results with thermodynamic equilibrium calculations in FactSage suggested that the system behavior was controlled by reaction rate. First-order reaction kinetic considerations in a perfectly stirred reactor [210] were used as a simplified modeling basis based on the typically good mixing in fluidized bed reactors. Various considerations regarding the influence of the investigated parameters on the hydrodynamic residence time, pre-exponential factor, and activation energy led to the unified CO<sub>2</sub> conversion model. Before simplification (Eq. 41), this model contained defined variables for each operational parameter (T, F, S, G, M, B), exponential fitting parameters  $(\alpha, \beta, \gamma)$ , and variables for the pre-exponential factor  $(k_0)$ , standard temperature  $(T_0)$ , activation energy  $(E_a)$ , and bed void fraction  $(\varepsilon)$ .

$$X_{CO2,stoichiometric} = \frac{k_0 \cdot S \cdot \exp\left(\frac{-E_a \cdot M}{R \cdot T}\right) \cdot \frac{A \cdot F^{\gamma} \cdot (1 + B^{\alpha}) \cdot \varepsilon}{(G \cdot T/T_0)^{\beta}}}{1 + k_0 \cdot S \cdot \exp\left(\frac{-E_a \cdot M}{R \cdot T}\right) \cdot \frac{A \cdot F^{\gamma} \cdot (1 + B^{\alpha}) \cdot \varepsilon}{(G \cdot T/T_0)^{\beta}}}$$
Eq. 41

The model was then numerically fit to the experimental data by varying the fitting parameters and activation energy. Operational parameters with limited influence on the model fit were eliminated. A new parameter termed fuel-gas contact time ( $\tau_{FGC}$ ) was defined that resembled the hydrodynamic residence time but only considered the time that CO<sub>2</sub> is in contact with the biomass feedstock. The simplified version of the CO<sub>2</sub> conversion model (Eq. 42) used only  $\tau_{FGC}$ , T, and M as variables. Increasing the temperature and fuel-gas contact time were the governing factors leading to increased CO<sub>2</sub> conversion. The fuel-gas contact time was experimentally increased at higher fuel loading in the reactor and lower CO<sub>2</sub> feed gas flow rates. It was also found that using olivine as a bed material likely led to higher CO<sub>2</sub> conversion than silica sand because it reduced the activation energy.

$$X_{CO2,stoichiometric} = \frac{k_0 \cdot \exp\left(\frac{-E_a \cdot M}{R \cdot T}\right) \cdot \tau_{FGC}}{1 + k_0 \cdot \exp\left(\frac{-E_a \cdot M}{R \cdot T}\right) \cdot \tau_{FGC}}$$
 Eq. 42



The simplified model replicated CO<sub>2</sub> conversion for all experiments with a root mean square error of 4 percentage points. Figure 14 shows how the semi-empirical model prediction compared to experimental and thermodynamic equilibrium data.

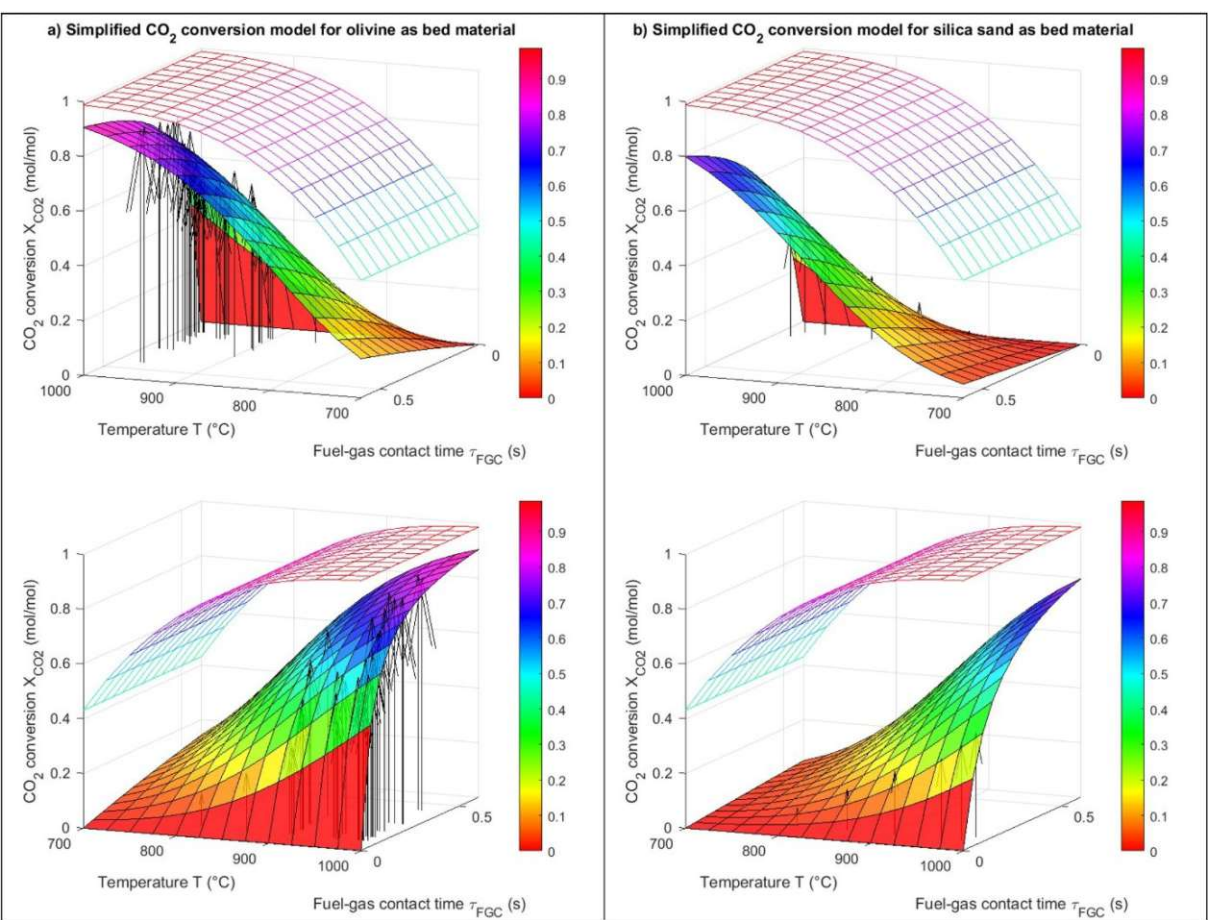


Figure 14: Simplified semi-empirical CO2 conversion model (filled lattice), thermodynamic equilibrium (empty lattice), and experimentally observed values (arrow tips) for CO2 conversion. The figure is reprinted from [JA I].

### 4.1.1.2. Demonstration in continuously fed gasifier

JA II used the new isotopic measurement (Section 4.2) to investigate CO2 conversion in seven experiments with continuous biomass fuel and CO<sub>2</sub> feed. The experimental data from these investigations are summarized in Table 8. All presented results are average values over one hour of gasification after reaching stable gas compositions. Experiments with CO2-steam mixtures as the gasifying agent were included to a) investigate the influence of co-feeding H<sub>2</sub>O and b) generate data that could represent using a moist CO<sub>2</sub> stream from capture in a MEA absorber for gasification. The wood char used in this investigation was the same type as in JAI, and standard commercial softwood pellets were added to see if the type of biomass influenced the CO<sub>2</sub> conversion under comparable conditions. The highest possible heating temperature in the gasifier, olivine as bed material, and a low CO<sub>2</sub> feed rate were adopted to achieve high  $CO_2$  conversion based on the findings from JAI. The fuel height in the reactor could not be measured and controlled for these continuous-feed experiments; therefore, different fuel feeding rates were used to see if these had a similar effect. Molar biomass-to-CO<sub>2</sub> carbon feed ratios of at least 1:1 were used to avoid stoichiometric limitations for the Boudouard reaction.

CO<sub>2</sub> Conversion to CO by Fluidized Bed Biomass Gasification Chapter 4: Results and discussion

Table 8: Summary of experimental data in JA II.

Parameter	Unit	Data source	Exp #1	Exp #2	Exp #3	Exp #4	Exp #5	Exp #6	Exp #7
Selected param									
Bed material	-	Setting				Olivine			
CO <sub>2</sub> feed	NL/min	Setting				2.8			
Temperature	°C	Setting				1000			
Fuel type	-	Setting	SW	SW	SW	SW	Char	Char	Char
Carbon feed	-	Setting	1.35	1.35	2	2	1	2	2
ratio C <sub>fuel</sub> :C <sub>CO2</sub>									
Fuel feed	g/min	Setting	4.2	4.2	6.4	6.4	1.9	3.7	3.7
H <sub>2</sub> O feed	NL/min	Setting	0	0.23	0	0.23	0	0	0.36
Measured and	calculated	results							
Temperature	°C	Measurement	903	856	821	825	877	864	856
Unconverted	%	Mass balance	2	12	13	14	23	46	42
fuel carbon									
$X_{CO2}$	%	Measurement	48	49	56	55	71	91	93
$\dot{V}_{total,out}$	NL/min	Mass balance	8.6	8.5	10.6	10.7	5.4	6.3	7.0
$\dot{V}_{CO,out}$	NL/min	Mass balance	4.2	3.9	5.0	5.0	3.9	5.3	5.6
$\dot{V}_{CO2,out}$	NL/min	Mass balance	1.8	1.8	1.9	1.8	1.0	0.4	0.3
$\dot{V}_{H2,out}$	NL/min	Mass balance	1.7	1.5	2.2	2.1	0.4	0.6	0.7
$\dot{V}_{CH4,out}$	NL/min	Mass balance	0.4	0.3	0.6	0.6	0.0	0.1	0.1
$\dot{V}_{H2O,out}$	NL/min	Mass balance	0.5	1.1	0.9	1.2	0.1	0.0	0.3
H <sub>2</sub> /CO ratio	-	Measurement	0.4	0.4	0.4	0.4	0.1	0.1	0.1
RP*	-	Mass balance	2.5	1.8	2.7	2.3	3.9	14.1	10.2
RP*	-	Gibbs energy	4.4	7.1	8.8	7.5	11.6	23.2	21.3
equilibrium		minimization							
LHV	$MJ/Nm^3$	Mass balance	9.8	8.8	10.3	10.0	10.0	11.8	11.5

<sup>\*</sup>RP stands for "Reduction Potential" and is calculated as the ratio of (H2+CO)/(H2O+CO2) in the product gas. This value is commonly used in ironmaking applications to characterize the gas' ability to reduce iron ore (thermodynamic equilibrium).

The product gas composition was also compared to the predictions for thermodynamical equilibrium given by FactSage, see Figure 15.

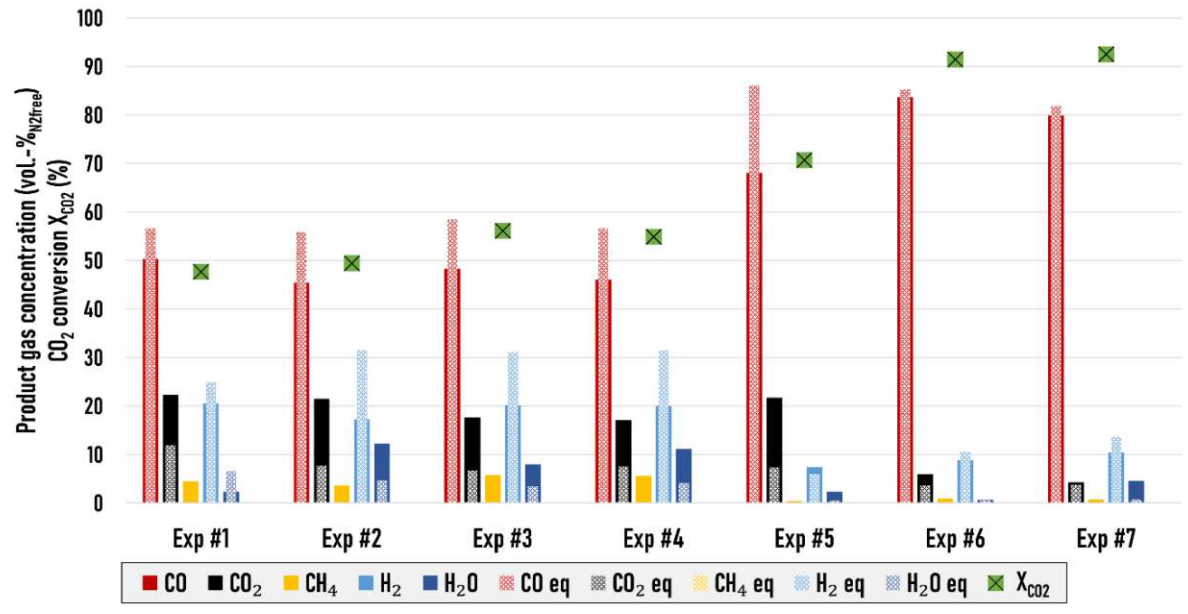


Figure 15: Product gas composition: Measured concentrations (full bars) vs. thermodynamic equilibrium concentrations calculated in FactSage (checkered bars). H2O concentrations result from mass balancing. The figure is adjusted from [JA II].



### 4.1.2. Discussion: *Increasing CO<sub>2</sub> conversion*

The 53 experiments described in JA I were conducted in four experimental campaigns. This step-bystep approach allowed for incorporating the learnings of previous experiments into the next one and increase  $X_{CO2,stoichiometric}$  from 6 % in the first campaign up to 86 % in the last campaign. The semiempirical CO<sub>2</sub> conversion model was created after conducting all experiments to provide general directions for how operating conditions should be selected in fluidized bed biomass CO<sub>2</sub> gasification for maximum CO<sub>2</sub> conversion. Its most important findings for increasing CO<sub>2</sub> conversion are:

- Higher operating temperatures of 850 °C and above favor CO<sub>2</sub> conversion.
- Longer contact times between CO<sub>2</sub> and solid biomass feedstock lead to higher CO<sub>2</sub> conversion.
- Olivine is favorable as a bed material compared to silica sand, as it lowers the activation energy.

Olivine is a well-known bed material in biomass gasification that various authors have used and favorably described [86], [139], [211], [212]. The finding about higher temperatures is consistent with the general literature on CO<sub>2</sub> gasification, which suggests that higher temperatures lead to more CO<sub>2</sub> conversion by the Boudouard reaction [46], [52], [106], [116], [119]. The difficulty of practically achieving higher temperatures in the reactor depends on the reactor type. For example, the electric heating powering the NERO gasifier had trouble reaching the desired temperatures in the reactor core for experiments with high fuel feed rates, as shown in JA II. In such a case, it might be necessary to balance high biomass feed rates and high temperatures in line with reactor characteristics.

The correlation between longer fuel-gas contact times and CO<sub>2</sub> conversion results from not reaching equilibrium due to reaction kinetic limitations. Figure 15 shows that the product gas composition had significantly higher CO<sub>2</sub> content for Exp.#1-5 compared to equilibrium. Fluidized bed gasifiers are somewhat constrained regarding the increase of fuel-gas contact time by lowering the feed gas flow rate because the minimal gas flow rate for fluidization needs to be surpassed. The other option for increasing the fuel-gas contact time is to increase solid carbon availability along the reactor's gas path. JA II demonstrated that the CO2 conversion could be increased by increasing the ratio of biomass to CO2 feed rate. The practical challenges of increasing this ratio again depend on the type of gasifier. If increasing the heat input from an allothermal heating system is unproblematic, then higher biomass input seems like a good option. For biomass feedstocks with low oxygen content, doing so would also decrease  $\lambda$ and increase the heating value of the produced gas if the biomass is gasified to the same degree. For more complex reactor types, such as a dual fluidized bed gasifier, that needs carefully balanced operation for transferring the desired energy from the combustor to the gasifier, further investigations are necessary to determine if higher biomass to CO<sub>2</sub> feed ratios are feasible. For example, a challenge could be that increased heat demand in the gasifier would need increased combustion temperatures that could surpass material ratings.

The influence of molar carbon feeding ratios can also be discussed by comparison with the data from other authors. JA IV used data from JA II and Mauerhofer et al., who investigated biomass CO2 gasification in a dual fluidized bed gasifier [52]. The used datasets (Mauerhofer vs. JA II) had the same softwood feedstock, similar temperatures in the bubbling bed (837 °C vs. 825 °C), and olivine as bed material. However, the molar carbon feeding ratio C<sub>fuel</sub>:C<sub>CO2</sub> was very different (0.8 vs. 2.0). Using the mass balance estimation as a comparison, which can be easily calculated for both datasets, Mauerhofer reached much lower values for  $X_{CO2,balance}$  (15% vs. 34%). Even before considering devolatilization, the feeding ratio C<sub>fuel</sub>:C<sub>CO2</sub> of 0.8 in Mauerhofer's work means that too little biomass carbon was available for CO<sub>2</sub> conversion through the Bouardourd reaction. Since the temperature in Mauerhofer's work was slightly higher, this is a strong indicator that carbon feeding ratios are highly relevant for CO<sub>2</sub> conversion. Higher C<sub>fuel</sub>:C<sub>CO2</sub> ratios leading to higher CO<sub>2</sub> conversion is also consistent with the thermodynamic investigations by Chai et al. [115] and the experimental data by Kibret et al. [126], even though Kibret et al. did not report on the CO<sub>2</sub> conversion themselves.

In general, the option to increase contact times by having more fuel in the reactor was also suggested by Chai et al. [115], who proposed adding additional solid carbon as biochar. Biochar addition seems like a smart solution, as the CO<sub>2</sub> conversion with wood char as feedstock was significantly higher than with softwood. It was reasoned in JA II that this could be a consequence of the lower fixed carbon content in softwood. Too little solid carbon was likely available for very high CO2 conversion in the experiments with softwood since it was converted to gas by decomposition reactions. The ~50 %:50 % split between carbon from biomass and carbon from CO<sub>2</sub> found in CO formed during the gasification of wood char (Exp. #5-7 in Figure 17) is a strong indicator that the Boudouard reaction stoichiometrically converted CO<sub>2</sub>. This finding suggests that solid carbon should be stoichiometrically available in the reactor after devolatilization to convert CO<sub>2</sub>. Consequently, the semi-empirical CO<sub>2</sub> conversion model could be extended by a parameter considering fuel carbon content and/or fixed carbon content. This adjustment would also agree with Mauerhofer et al., who reported that CO formation increased for fuels with higher carbon content [65].

The introduction (Section 2.4) described that data on CO<sub>2</sub> conversion in fluidized bed biomass gasifiers is relatively sparse. To the author's best knowledge, no other authors have reported more than 50 % of CO<sub>2</sub> conversion in a fluidized bed biomass gasifier, with most reports significantly undercutting this value [52], [65], [106], [114], [115], [116]. Section 4.2 shows that insufficiencies in the established estimation methods might have led to other authors underestimating their actual CO<sub>2</sub> conversion results. Additionally, the literature search criteria might have excluded some relevant literature. Nevertheless, the up to 93 % CO<sub>2</sub> conversion demonstrated in continuous-feed experiments in **JA II** is a significant step forward for biomass CO2 gasification in fluidized bed reactors as a CCU process. The CO concentration of 80 vol.-% and more in the product gas confirms that this technology needs to be supported by additional hydrogen input or applied to a downstream process that can work with very low H<sub>2</sub>:CO ratios.

### 4.1.3. Key findings: *Increasing CO<sub>2</sub> conversion*

Journal articles I-II described and demonstrated under which operating conditions a high CO2 conversion can be achieved in a fluidized bed biomass gasifier. Key findings 1 summarizes the most important results.

Key findings 1: Chapter "Increasing CO<sub>2</sub> conversion by varying operating conditions".

- High (850 °C+) temperatures and longer contact times between CO<sub>2</sub> and solid carbon increase CO<sub>2</sub> conversion.
- The carbon monoxide from CO<sub>2</sub> gasification of wood char contained a ~50 %:50 % split of carbon from biomass and carbon from CO2. This split suggests that the Boudouard reaction is critical for CO<sub>2</sub> conversion.
- Higher CO<sub>2</sub> conversion was observed in experiments with wood char compared to softwood, likely due to insufficient fixed carbon in softwood for CO2 conversion via the Boudouard reaction.
- Up to 93 % of CO<sub>2</sub> conversion was demonstrated in continuous-feed experiments.

# 4.2. Validating CO<sub>2</sub> conversion by stable carbon isotope analysis

This chapter describes the development of a new measurement for determining the conversion of feedstock CO<sub>2</sub> during biomass gasification. Measurement data are presented to support arguments, but this chapter focuses on establishing the new technique and not discussing the gasification results. Further discussion on the value of CO<sub>2</sub> conversion under varying operating conditions can be found in Section **4.1**.

### 4.2.1. Results: Validating CO<sub>2</sub> conversion

JA II introduced a novel way of measuring CO<sub>2</sub> conversion in biomass CO<sub>2</sub> gasification. This new method aimed to establish a way to differentiate unconverted feedstock CO2 and CO2 that is formed anew in the reactor. This goal was achieved by measuring the stable carbon isotope ratios in the two parental carbon sources, CO<sub>2</sub> and biomass. These carbon isotope ratio fingerprints of CO<sub>2</sub> and biomass were then used to assign shares of CO<sub>2</sub> and CO in the product gas to both parental carbon sources. Figure 16 depicts the main carbon flows in this biomass CO<sub>2</sub> gasification process and illustrates how the isotopic fingerprints (colors) of carbon in CO<sub>2</sub> and biomass carry over to the product gas. A detailed explanation of this method to determine  $X_{CO2}$  is available in **Section 3.2.2**.

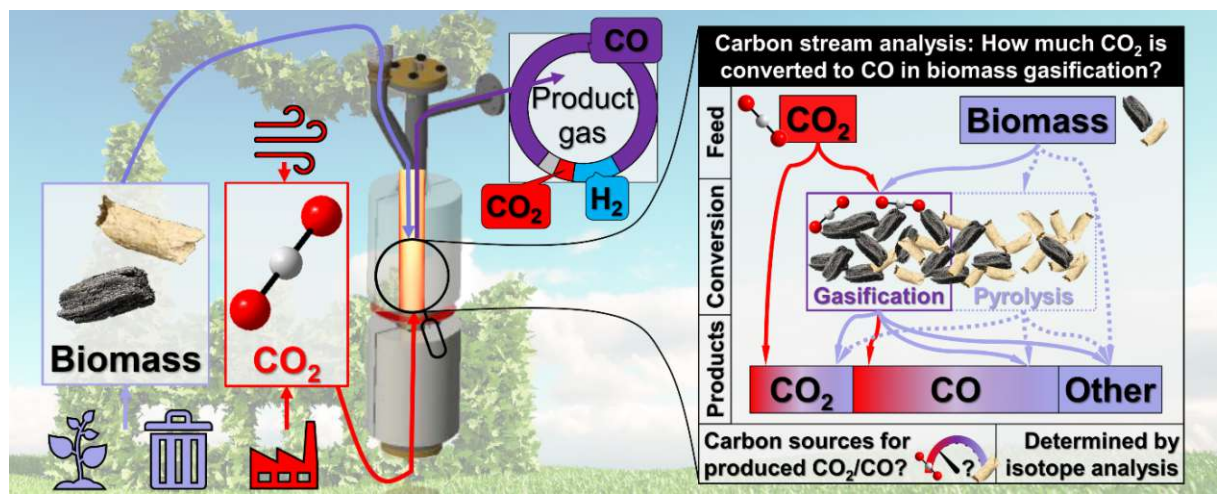


Figure 16: Graphical abstract showing how carbon enters the reactor via CO2 and biomass, where various thermochemical conversion processes convert it to product gas. The figure is reprinted from [JA II].

This novel method was applied for biomass CO<sub>2</sub> gasification experiments with softwood (Exp. #1-4) and wood char (Exp. #5-7) as biomass feedstock. CO2 and CO in the product gas could be attributed to their parental carbon sources (*Figure 17*).

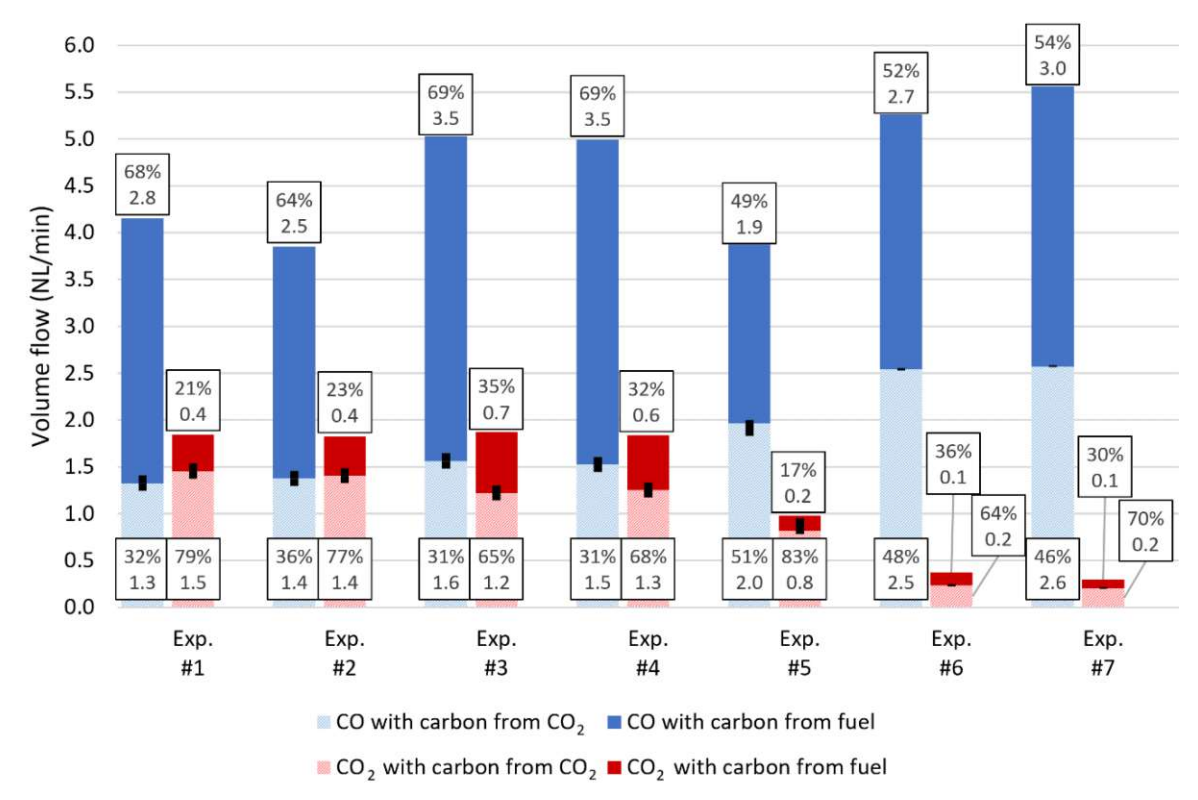


Figure 17: Parental carbon sources of CO and CO2 in the product gas. The figure is reprinted from [JA II].

The attribution of CO<sub>2</sub> in product gas to biomass or CO<sub>2</sub> as carbon feedstock allowed for calculating feedstock CO<sub>2</sub> conversion irrespective of new-formed CO<sub>2</sub> from biomass. The results of this novel measurement method were compared to the two established CO2 conversion estimation schemes that were introduced in Section 3.4.1 (Figure 18).



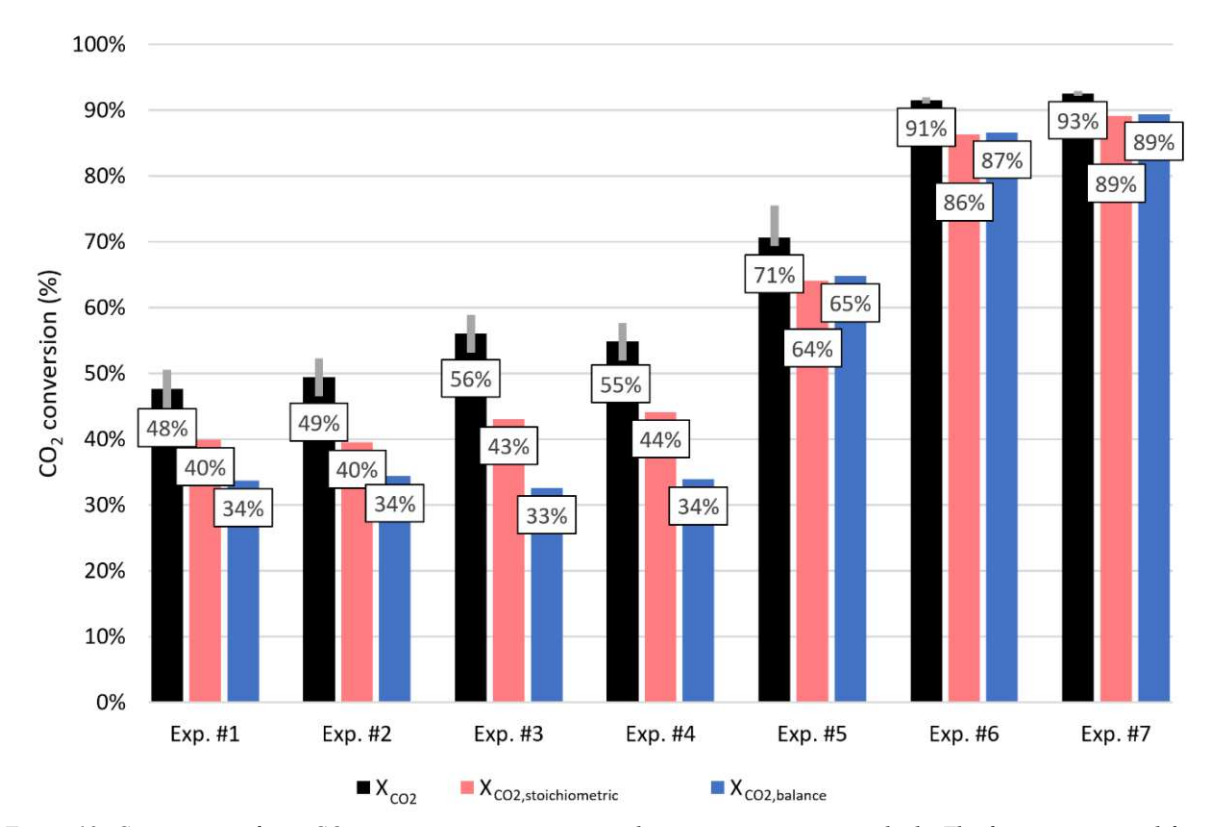


Figure 18: Comparison of new CO<sub>2</sub> conversion measurement with previous estimation methods. The figure is reprinted from [JA II].

### 4.2.2. Discussion: Validating CO<sub>2</sub> conversion

The comparison of CO<sub>2</sub> conversion data from the new measurement method versus previous estimation methods in Figure 18 shows apparent differences. Measurement uncertainties were below ±5 pp (percentage points) despite relatively small differences in the natural abundance of parental carbon sources. In contrast, the established estimation methods yielded results that differed by 10 pp from each other and up to 23 pp from the new measurement. The deviation from the new measurement was higher for experiments with softwood as feedstock (Exp.#1-4), as this fuel has a higher volatile content. For experiments with wood char, the deviation also seemed to decrease when the CO2 conversion approached 100 %, as all methods would correctly show 100 % conversion if no CO<sub>2</sub> were present in the product gas. The isotopic measurement accuracy could be further improved by doping one of the carbon streams with an increase of <sup>13</sup>C or <sup>12</sup>C. However, these isotopically pure compounds are expensive, and it is a significant advantage that the new method could provide these results without any doping.

One of the main shortcomings shared between both presented estimation methods is their inability to differentiate unconverted CO2 and CO2 from biomass (see Section 3.4.1). The new measurement could distinguish between those two carbon sources using natural stable carbon isotope abundance differences as a label. Understanding carbon flows in the reactor in more detail can help with process design and optimization. The meaning of this ability to distinguish is best explained using an example:

Exp.-#1-4 shown in Figure 17 and Figure 18 used identical CO2 feed flow rates and softwood as biomass feedstock. The softwood feed rate was around 50 % higher for Exp.-#3-4 than Exp.-#1-2. This increased biomass feed increased total product gas volume flow because more gas was formed from biomass decomposition reactions. Curiously, the flow rate of CO<sub>2</sub> in product gas remained nearly constant even though the total flow rate increased. Consequently, the mass balance estimation, which is the most common method in the literature, showed more or less the same CO<sub>2</sub> conversion for all Exp.-#1-4, because it only considers the absolute CO<sub>2</sub> feed and drain streams. However, the new measurement detected that a larger share of the CO<sub>2</sub> in product gas was produced from the increased softwood feed (Exp. #3-4 in Figure 17). Therefore, the new measurement recognized that more feedstock CO<sub>2</sub> was converted, and the product gas now contained more CO<sub>2</sub> formed from biomass decomposition. This additional knowledge can be used for more targeted process design. For example, the point of CO<sub>2</sub> release in the reactor could be adjusted to increase the conversion of CO<sub>2</sub> released from biomass, e.g., by switching from on-bed feeding to in-bed feeding. Another option would be to use a second reactor to further reduce the CO<sub>2</sub> content of product gas by reactions with a different biomass feedstock with lower volatile content.

### 4.2.3. Key findings: Validating CO2 conversion

The isotopic measurement of CO<sub>2</sub> conversion is key for firmly establishing biomass CO<sub>2</sub> gasification as a process for CO<sub>2</sub> utilization. The uncertainties in previous measurements have led to doubts about the conversion of external CO<sub>2</sub> during the process. A reviewer for JA I, which came before the new measurement was demonstrated, stated: "[...] the authors emphasize the conversion of  $CO_2$  to CO and pretend that this is related to CO<sub>2</sub> utilization." JA II proved that this is - indeed - related to CO<sub>2</sub> utilization as the technology can convert most of the externally fed CO<sub>2</sub>. The central results of this chapter are summarized in Key findings 2.

Key findings 2: Chapter "Validating CO<sub>2</sub> conversion by stable carbon isotope analysis".

- Stable carbon isotope abundance differences in biomass and CO2 can be used to attribute carbonaceous product gas components to their parental carbon sources. This attribution allows for a CO<sub>2</sub> conversion assessment limited to feedstock CO<sub>2</sub>.
- If there are natural differences in isotopic abundance between both carbon sources, this analysis is possible without adding an isotopic tracer.
- Both CO and CO<sub>2</sub> in product gas contain carbon from biomass and CO<sub>2</sub>.
- Further product gas optimization strategies that aim to decrease CO<sub>2</sub> content in the product gas can use this new measurement to identify where CO<sub>2</sub> originates to apply targeted solutions.

## 4.3. Implementing CO<sub>2</sub> conversion for ironmaking

Section 3.3.2 reasoned why the direct reduction ironmaking process was chosen as the application in JA IV. That section also explained the main design choices and investigated process routes. The main findings on how CO<sub>2</sub> conversion by biomass CO<sub>2</sub> gasification can be industrially applied for ironmaking are given in the following section.

### 4.3.1. Results: *Implementing CO<sub>2</sub> conversion*

Three different gasification datasets, two from JA II and one by Mauerhofer et al. [52], were used to investigate the influence of CO<sub>2</sub> conversion in the gasifier on overall process performance. They were labeled by their reported CO<sub>2</sub> conversion as low-conversion (LC), medium-conversion (MC), and highconversion (HC). The (HC) dataset used wood char as gasification fuel, which demanded the inclusion of a pyrolyzer, while process configuration was the same for (LC) and (MC), which used softwood. Each gasification dataset was used for two simulations: air as a combustion agent and oxy-fuel combustion. The six process configurations resulting from biomass CO<sub>2</sub> gasification (BCG) were compared to two simulations describing a standard process where natural gas reforming (NGR) was used to produce reducing gas.

In JA IV, the mass and energy balancing results for all routes formed the basis of carbon footprint and techno-economic calculations. Sankey diagrams depicting the main mass and energy flows were chosen to visualize the results for all six BCG-DRI routes. The main mass and energy stream results for two process routes, BCG-DRI(AIR,LC) and BCG-DRI(AIR,MC), are given in Figure 19 and Figure 20. These two routes were selected for presentation to facilitate the discussion on the influence of CO<sub>2</sub> conversion for this application since they used the same process configuration. All differences result from the difference in gasification data, which influences the mass and energy balances of the whole process.



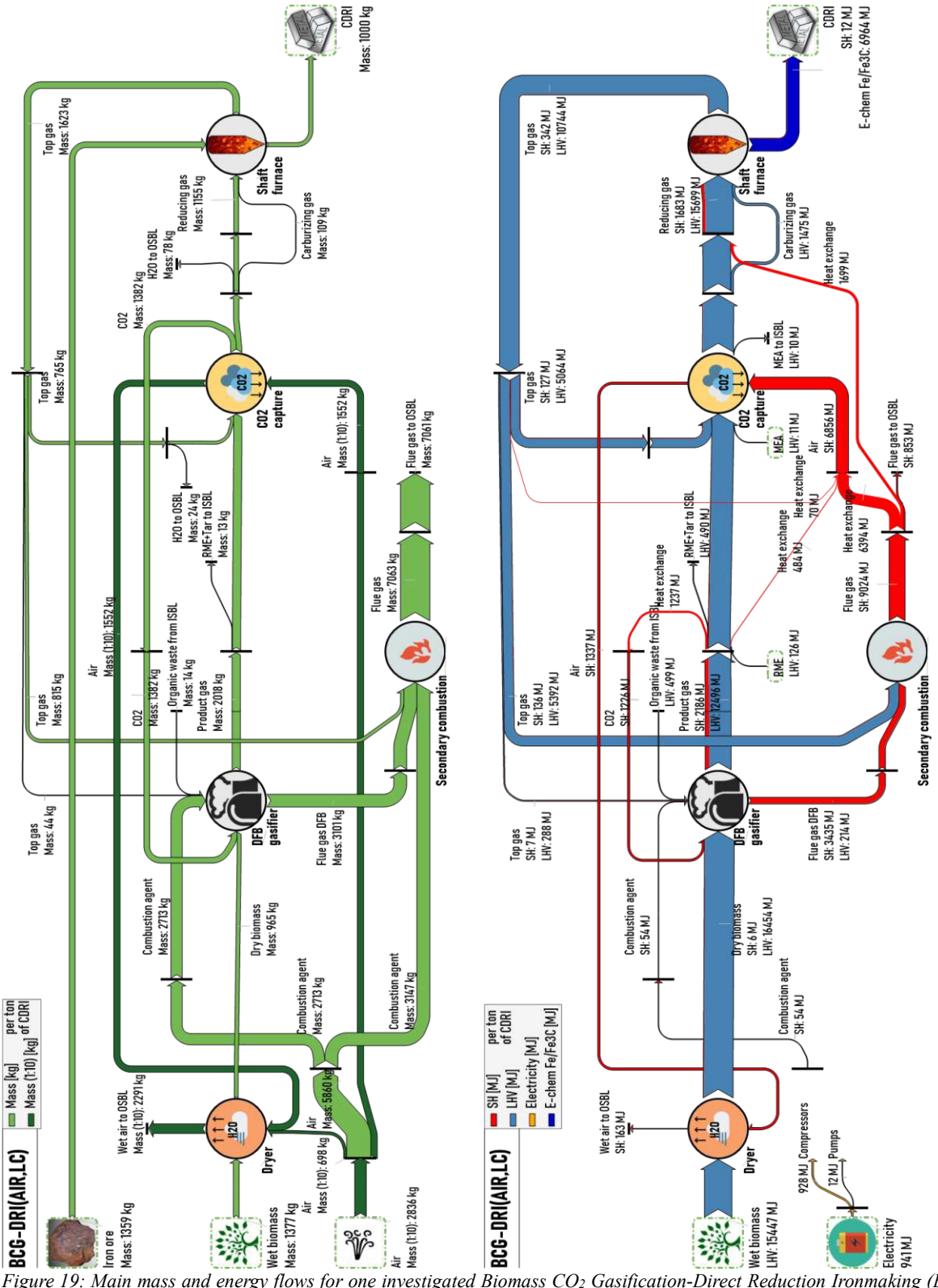


Figure 19: Main mass and energy flows for one investigated Biomass CO2 Gasification-Direct Reduction Ironmaking (BCG-DRI) route. The process uses air (AIR) for combustion. (LC) stands for Low Conversion of CO2 during gasification. SH=Sensible Heat, LHV=Lower Heating Value, ISBL/OSBL=Inside/Outside Battery Limit. The figure is reprinted from [JA IV].

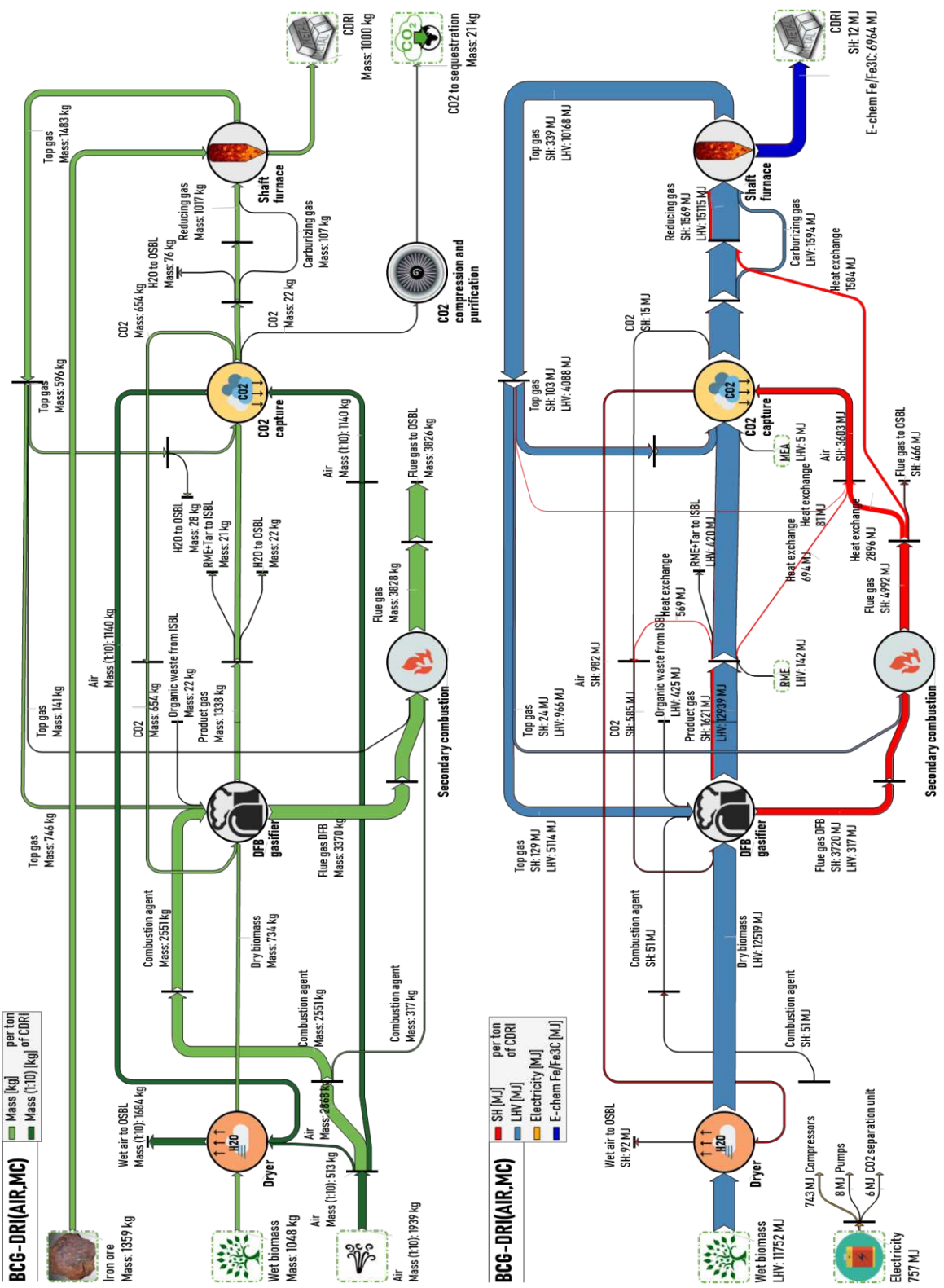


Figure 20: Main mass and energy flows for one investigated Biomass CO2 Gasification-Direct Reduction Ironmaking (BCG-DRI) route. The process uses air (AIR) for combustion. (MC) stands for Medium Conversion of CO2 during gasification. SH=Sensible Heat, LHV=Lower Heating Value, ISBL/OSBL=Inside/Outside Battery Limit. The figure is reprinted from [JA IV].

Key results from mass and energy balancing, carbon footprint calculations, and techno-economic assessments are summarized in **Table 9** for all simulated process routes.  $(H_2:CO)_{RG}$  and  $RP_{RG}$ characterize the reducing gas composition and are relevant for ironmaking.  $\eta_{IRON}$  and  $e_{IRON}$  describe process energy efficiency.  $CF_{LCA}$  and LCOP are the cradle-to-gate carbon footprint and levelized cost of

producing cold direct reduced iron (CDRI). The LCOP values presented in Table 9 used an EU-ETS CO₂ emission allowance price of 146 €/t<sub>CO₂</sub>, which is the value predicted for 2030 based on a forecast by BloombergNEF analysts published in 2024 [203]. The emission allowance break-even price (EABEP) was included in the techno-economic assessment to clarify which emission allowance prices would be necessary to achieve cost parity with the fossil NGR-DRI process without carbon capture and storage. LCOP<sub>BCCS</sub> and EABEP<sub>BCCS</sub> use a hypothetical policy change scenario where it is possible to generate and sell carbon removal credits from net-negative emission processes.

Table 9: Key performance indicators for each simulated process route in JA IV.

Key performance indicators for each		NGR- DRI	NGR- DRI	BCG- DRI	BCG- DRI	BCG- DRI	BCG- DRI	BCG- DRI	BCG- DRI
simulated process route		(no CCS)	(CCS)	(AIR, LC)	(OXY, LC)	(AIR, MC)	(OXY, MC)	(AIR, HC)	(OXY, HC)
$(H_2:CO)_{RG}$	mol/mol	1.75	1.75	0.46	0.46	0.55	0.56	0.67	0.68
$RP_{RG}$	mol/mol	8.74	8.74	13.47	13.47	25.76	25.49	28.80	28.53
$\eta_{IRON}$	%	63.5	62.6	42.3	38.7	55.2	50.9	56.3	52.1
$e_{IRON}$	$MJ/kg_{CDRI}$	11.0	11.1	16.5	18.0	12.6	13.7	12.4	13.4
$CF_{LCA}$	kg <sub>CO2e</sub> /t <sub>CDRI</sub>	892	441	166	-1,227	124	-935	-83	-910
LCOP	€/t <sub>CDRI</sub>	416	403	396	554	354	478	350	457
$LCOP_{BCCS}$	€/t <sub>CDRI</sub>	416	403	386	320	341	297	305	279
EABEP	€/t <sub>CO2</sub>	-	118	105	424	21	271	14	227
$EABEP_{BCCS}$	€/t <sub>CO2</sub>	-	118	92	100	18	77	9	66

The main techno-economic and emission-intensity key performance indicators were analyzed for trends observed depending on the CO<sub>2</sub> conversion in the process (Figure 21). The mass balance estimation method for calculating CO<sub>2</sub> conversion (Eq. 24) was applied to all three gasification datasets to establish comparability because CO<sub>2</sub> conversion was calculated differently by Mauerhofer et al. [52] and in JA II.



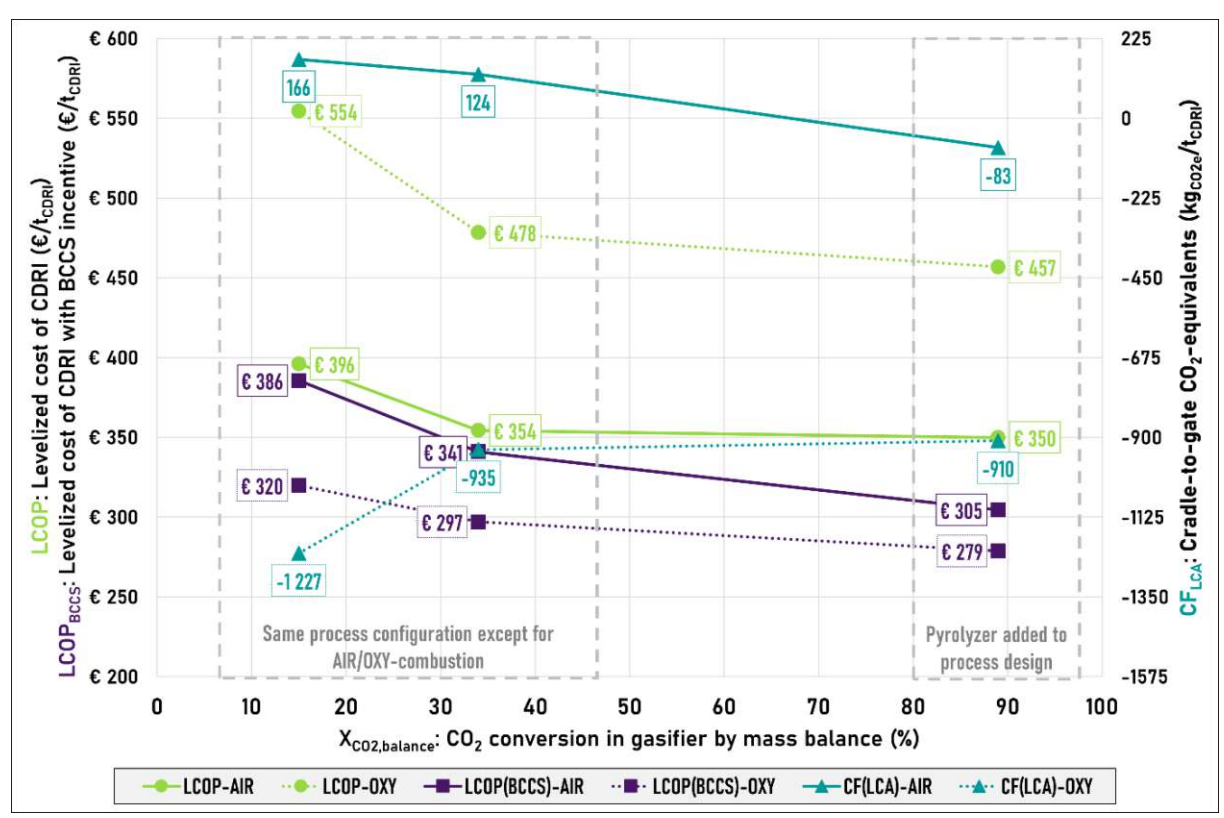


Figure 21: Levelized cost and cradle-to-gate CO<sub>2</sub>-equivalent emissions of producing cold direct reducing iron. The figure is reprinted from [JA IV].

### 4.3.2. Discussion: Implementing CO<sub>2</sub> conversion

The reducing gas' reduction potential  $RP_{RG}$  for all BCG-DRI routes is well above the value of around 9, which can be calculated from plant data reported on the Gilmore and Siderca NGR-DRI MIDREX installations [213]. The H<sub>2</sub>:CO ratios around 0.5 fall into the range reported as ideal for carburization [157]. Those H<sub>2</sub>:CO ratios are lower than the values found for the NGR-DRI process and reported by other authors investigating steam gasification [17], [154]. These findings suggest that biomass CO<sub>2</sub> gasification is technically well-positioned to produce reducing gas for the DRI process, which might also bring unique advantages to carburization and heat management in the shaft furnace due to the exothermic reactions with CO.

Five out of six key performance indicators plotted in Figure 21 showed clear improvement at higher CO<sub>2</sub> conversion. While the process configuration for the (HC) simulations is slightly different, these improvements can be explained straightforwardly for the (LC) and (MC) simulations that use the same gasification feedstock and process configuration. Figure 19 and Figure 20 compared the mass and energy flows for (LC) and (MC) with air as a combustion agent. The higher rate of unconverted CO<sub>2</sub> combined with the increased CO<sub>2</sub> feed per biomass used by Mauerhofer et al. meant that CO<sub>2</sub> concentration in the (LC) product gas was much higher than in the (MC) product gas (41 vol.-% [52] vs. 19 vol.-% [JA II]). The increased CO<sub>2</sub> concentration induced a higher load on the carbon capture system in the simulations (1,382 kg<sub>CO2</sub>/t<sub>CDRI</sub> vs. 676 kg<sub>CO2</sub>/t<sub>CDRI</sub>). In this process design, the increased sensible heat demand for solvent regeneration (6,886 MJ/t<sub>CDRI</sub> vs. 3,603 MJ/t<sub>CDRI</sub>) was ultimately

covered by additional biomass input in the (LC) simulation. This additional biomass input induces additional costs and lowers the energy efficiency of the (LC) process. Another consequence is that no excess CO<sub>2</sub> is available in the (AIR,LC) simulation case, as all captured CO<sub>2</sub> is recycled to the gasifier. The additional biomass input for the (LC) simulations also explains the inverse trend of  $CF_{LCA}$  for (OXY) simulations because the additional renewable CO<sub>2</sub> created by additional biomass combustion is sent to sequestration. This analysis shows that looking at only the gasifier to understand the significance of increasing CO<sub>2</sub> conversion is insufficient, as significant benefits can be achieved in downstream processes.

Including a pyrolyzer for wood char production to further increase CO<sub>2</sub> conversion in the (HC) simulations brings several drawbacks. First, including additional unit operations induced additional points of energy loss. Second, the share of unconverted carbon in the gasifier was much higher in experiments with wood char as gasification feedstock in JAII, which meant that the DFB combustor in JA IV had to burn a sizeable amount of high-quality feedstock. Third, the char combustion in the DFB system meant that the best option for dealing with CO<sub>2</sub> in pyrolysis and top gas mostly still was carbon capture. If more fixed carbon were gasified or extracted from the gasifier, the need for carbon capture could likely be further lowered by burning more top gas or pyrolysis gas instead of residual fixed carbon. Another option could be to recycle the unconverted carbon and reduce the feeding rate, but this would need engineering work and testing if the char would still be reactive under these conditions. Despite these drawbacks, the overall techno-economic and emission indicators show that the higher CO<sub>2</sub> conversion still outweighs the drawbacks, making including a pyrolyzer a worthy trade-off. This finding further strengthens the suggestion by Chai et al. [115], who proposed adding additional solid carbon in the form of biochar to the gasifier to increase CO<sub>2</sub> conversion.

The results show that the developed BCG-DRI processes can produce CDRI at lower unit costs than the natural gas reforming process, even assuming no carbon removal credits. The two main advantages of BCG-DRI are avoiding high CO<sub>2</sub> emission allowance and natural gas costs. The 146 €/t<sub>CO2</sub> [203] assumed in JA IV are much higher than the current cost of emission allowances in the EU-ETS, which was only around 67 €/t<sub>CO2</sub> on average between 11/2023 and 10/2024 [214]. Forecasts on this price for 2030 vary: For example, analysts by Enerdata predicted a much slower increase to around 70 − 75 €/t<sub>CO2</sub> [215], while a study by Zeyen et al. also suggested around 140 €/t<sub>CO2</sub> while noting that this should increase to 290 €/t<sub>CO2</sub> to achieve decarbonization targets [216]. However, this uncertainty is less important to the economic comparison than the natural gas/biomass price. EABEP calculations showed that the BCG-DRI process is already favorable at emission allowance costs of 10-20 €/t<sub>CO2</sub> if other cost factors stayed the same. Energy price forecasts are uncertain, as prices can be very volatile because of geopolitical turmoil, such as Russia's 2022 invasion of Ukraine or the oil price shocks of the 1970s [24], [25]. There is no guarantee that biomass will continue to be cheaper per energy unit compared to

natural gas; however, the decentralization of energy supply offered by domestic biomass helps to lower the risk of price increases and enables more countries to become independent of imports [20].

Using biomass, which has low indirect emissions [167] and offsets its direct emissions by carbon capture during the growth phase, leads to much lower emissions for all BCG-DRI processes than the natural gas process. Several process configurations result in net-negative emissions, particularly those with oxyfuel combustion and the (HC) simulation with air combustion. These findings agree with other authors, who reported that steam gasification of biomass can lead to net-negative emissions for iron- and steelmaking [17], [154], [155]. However, emphasizing large-scale net-negative emissions by oxy-fuel combustion would need to be economically incentivized, e.g., by carbon removal credits [170], [171]. If net-negative emissions are not rewarded, further options to profit from the captured biogenic CO<sub>2</sub> should be investigated. Depending on market conditions, directly selling biogenic CO<sub>2</sub> to the chemical sector could become an option. Another option would be to aim for converting all CO<sub>2</sub> in the process and use the excess CO-rich product gas for other applications.

### 4.3.3. Key findings: Implementing CO<sub>2</sub> conversion

JA IV investigated if and how biomass CO2 gasification could produce the reducing gas for direct reduction ironmaking. The process simulations included three gasification datasets to investigate the consequences of increasing CO<sub>2</sub> conversion in the gasifier on the overall process. The investigations included techno-economic and emission evaluations and were compared to a reference case using natural gas reforming. The most important results are given in *Key findings 3*.

Key findings 3: Chapter "Implementing CO2 conversion for ironmaking".

- Biomass CO<sub>2</sub> gasification can produce reducing gas with high reduction potential and low H<sub>2</sub>:CO ratio for direct reduction ironmaking.
- Higher CO<sub>2</sub> conversion in the gasifier leads to advantages for the overall process regarding techno-economics and CO<sub>2</sub>-equivalent emissions.
- The developed biomass CO<sub>2</sub> gasification process showed lower production costs and lower emissions per unit of cold direct reduced iron than a reference process using natural gas reforming.
- Net-negative cradle-to-gate emissions are possible with the biomass CO<sub>2</sub> gasificationdirect reduction ironmaking process.
- Additional incentives are necessary to make the process routes with the most significant net-negative emissions the most economical options.

### 4.4. Additional research on biomass CO<sub>2</sub> gasification

The findings in this chapter branch out from the main topic of CO<sub>2</sub> conversion to investigate two other important topics in and around biomass CO<sub>2</sub> gasification.

### 4.4.1. Results: Surface adjustment of biochar

CA I changed the focus from the gaseous products of biomass CO<sub>2</sub> gasification to the solid products by investigating the surface adjustment of biochar. This work described a two-step torrefaction and biomass CO<sub>2</sub> gasification process to create biochar with a high surface area from wood pellets (*Figure 22*).

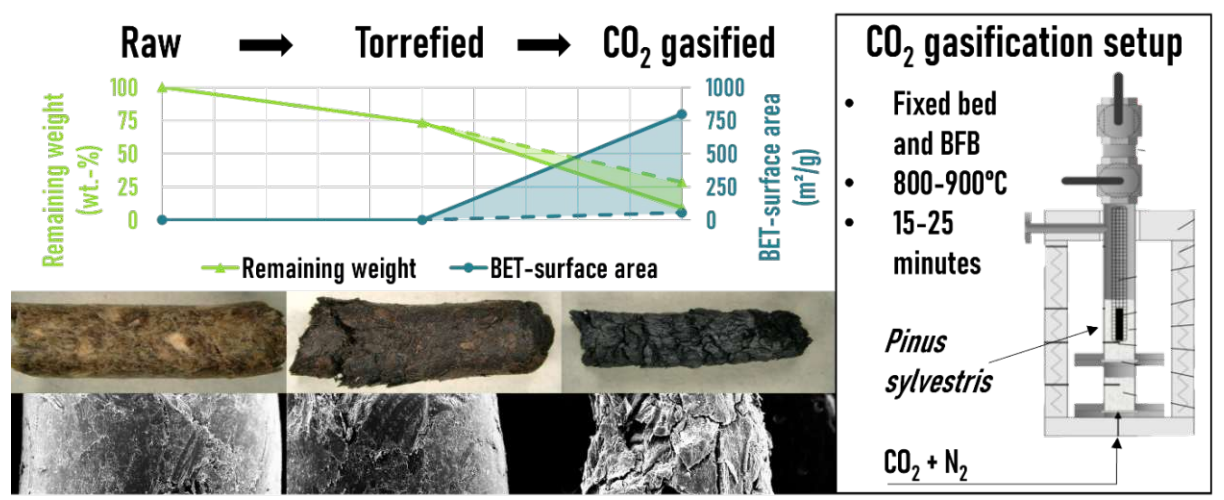


Figure 22: Summary of two-step surface adjustment procedure including torrefaction and CO2 gasification of Pinus sylvestris wood pellets. The figure was adjusted from [CA I].

The pellets were torrefied under an N<sub>2</sub> atmosphere and fixed bed conditions at 300 °C for 45 minutes in a single batch. The resulting pellets had lost some mass but still had a surface area below 1 m<sup>2</sup>/g. The torrefied pellets were then subjected to CO<sub>2</sub> gasification in an 80/20 vol.-% mixture of N<sub>2</sub> and CO<sub>2</sub> under various conditions (*Table 10*). Torrefied pellets were inserted into the reactor in a sample extraction cage (see Figure 10 and Figure 22). Half of the experiments were performed under fluidized bed conditions, which meant that the samples were submerged in silica sand, which formed a bubbling fluidized bed.

Table 10: Investigated CO<sub>2</sub> gasification conditions

Name	Fluidization		Temper	ature	Activation time		
	Fluidized bed	Fixed bed	800°C	850°C	900°C	15 min	25 min
E1		X	X			X	
E2		X		X		X	
E3		X			X	X	
E4		X	X				X
E5		X		X			X
E6		X			X		X
E7	X		X			X	
E8	X			X		X	
E9	X				X	X	
E10	X		X				X
E11	X			X			X
E12	X				X		X

The biochar samples were analyzed for their weight loss and BET surface area. The surface yield y was defined as an efficiency indicator that relates the BET surface area ( $a_{BET}$ ) in the final product to the mass of raw biomass feedstock by considering the burn-off (b) during each conversion step (Eq. 43). While



 $a_{BET}$  is an indicator that describes the final product quality, y instead is an efficiency indicator for the whole process.

$$y = a_{BET} \cdot (1 - b_{torrefaction}) \cdot (1 - b_{gasification})$$
 Eq. 43

The results obtained from these experiments are summarized in *Figure 23*.

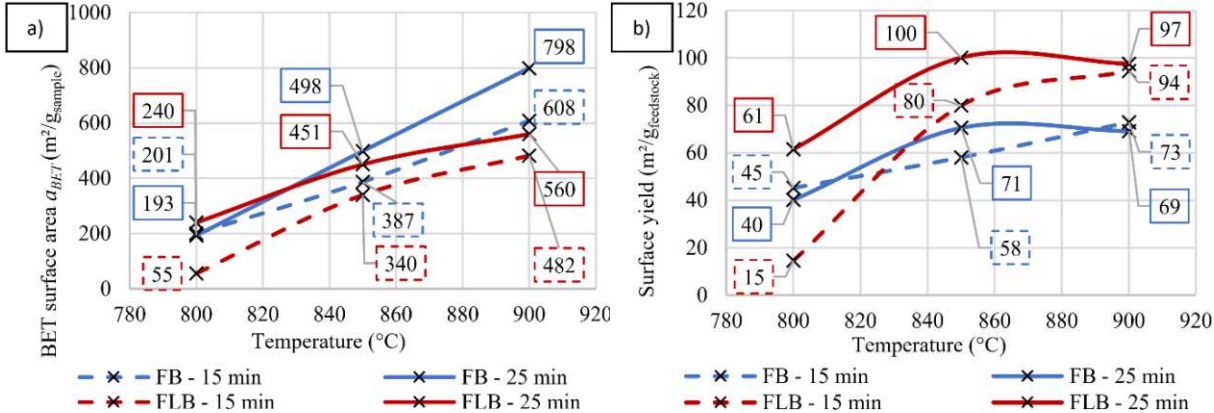


Figure 23: a) BET surface area of biochar, b) Surface yield from raw biomass to biochar. The figure is reprinted from [CA I].

### 4.4.2. Discussion: Surface adjustment of wood char

CA I showed that CO<sub>2</sub> gasification could produce high-surface-area biochar. The optimal conditions leading to high surface areas were higher temperatures, longer residence time, and, at higher temperatures, fixed bed conditions. Surface yield analysis found that 850 - 900 °C, longer residence times, and fluidized bed conditions tended to yield the most surface area per mass of original feedstock. In summary, there are trade-offs for fixed and fluidized bed conditions. However, the temperature and residence time findings agree that around 850 - 900 °C and 25 minutes of solids residence time are suitable for producing high-surface area biochar.

The findings on temperature and residence time are consistent with the literature. Ngernyen also found that burn-off and BET surface area increased with increasing activation time [217]. Various authors, e.g., Chang et al. [218] and Pallarés et al. [219], reported that the surface area found in biochar produced by CO<sub>2</sub> gasification after a given residence time increases in total surface area at higher temperatures due to the increase in Boudouard reaction rate. The literature also matches the order of magnitude for the BET surface area values. Premchand et al. reviewed biochar production under CO<sub>2</sub> atmosphere up to 700 °C [95]. The highest surface area in their table 2 was around 560 m<sup>2</sup>/g after 240 minutes of residence time at 700 °C [220]. Surface areas up to 789 m<sup>2</sup>/g were reported at 800 °C by Pallarés et al. [219]. However, some authors have also reported much more, e.g., Chang et al. reported 1705 m<sup>2</sup>/g at 900 °C [218].

There are challenges and chances for combining these results on high-surface-area biochar production with a biomass CO<sub>2</sub> gasification process that aims at high CO<sub>2</sub> conversion and good product gas compositions. One challenge is that data on the gaseous products and the CO<sub>2</sub> conversion during these

experiments is unavailable. Also, these experiments used mixtures of CO2 and N2, which would not be done in experiments aiming to form high-quality gas products. The torrefaction step was included in CA I for reasons beyond this thesis. It was not investigated whether the BET surface area of the produced biochars would be as high without this pretreatment step. On the positive side, temperatures in this investigation were similar to those measured in the gasifier during JA II, where up to 93 % of CO<sub>2</sub> conversion was measured in experiments with biochar. Additionally, JA II found that up to 46 % of carbon remained unconverted in the high biochar feeding rate experiments. The discussion in Section 4.3.2 on JAIV identified this high rate of unconverted carbon as an opportunity for improvement, which could be taken by extracting the biochar instead of burning it. Consequently, it should be tested if it is possible to create a high CO<sub>2</sub> conversion process with biochar as feedstock, where excess char is extracted. This extracted char, if it had a high-surface area such as found in CAI, could be used for more valuable applications than as combustion fuel, e.g., for soil carbon sequestration [95], as soil amendment [221] or to restore degraded sites [222]. Extracting high-surface-area biochar could open an additional revenue stream for the industrial application of biomass CO<sub>2</sub> gasification.

### 4.4.3. Results: $H_2O$ in raw product gas by quantum cascade laser

A novel measurement for quantifying water vapor in hot and raw product gas was presented in JA III. The setup is described in **Section 3.2.3**. It was successfully used to quantify H<sub>2</sub>O content in raw product gas from steam gasification of waste wood in the 100 kWth gasifier. Hot and tar-laden product gas was sampled at around 230 °C following the hot gas filter and kept hot and uncondensed until the measurement by a heating coil (Figure 24).

Sample Gas

#### CO<sub>2</sub> Conversion to CO by Fluidized Bed Biomass Gasification Chapter 4: Results and discussion

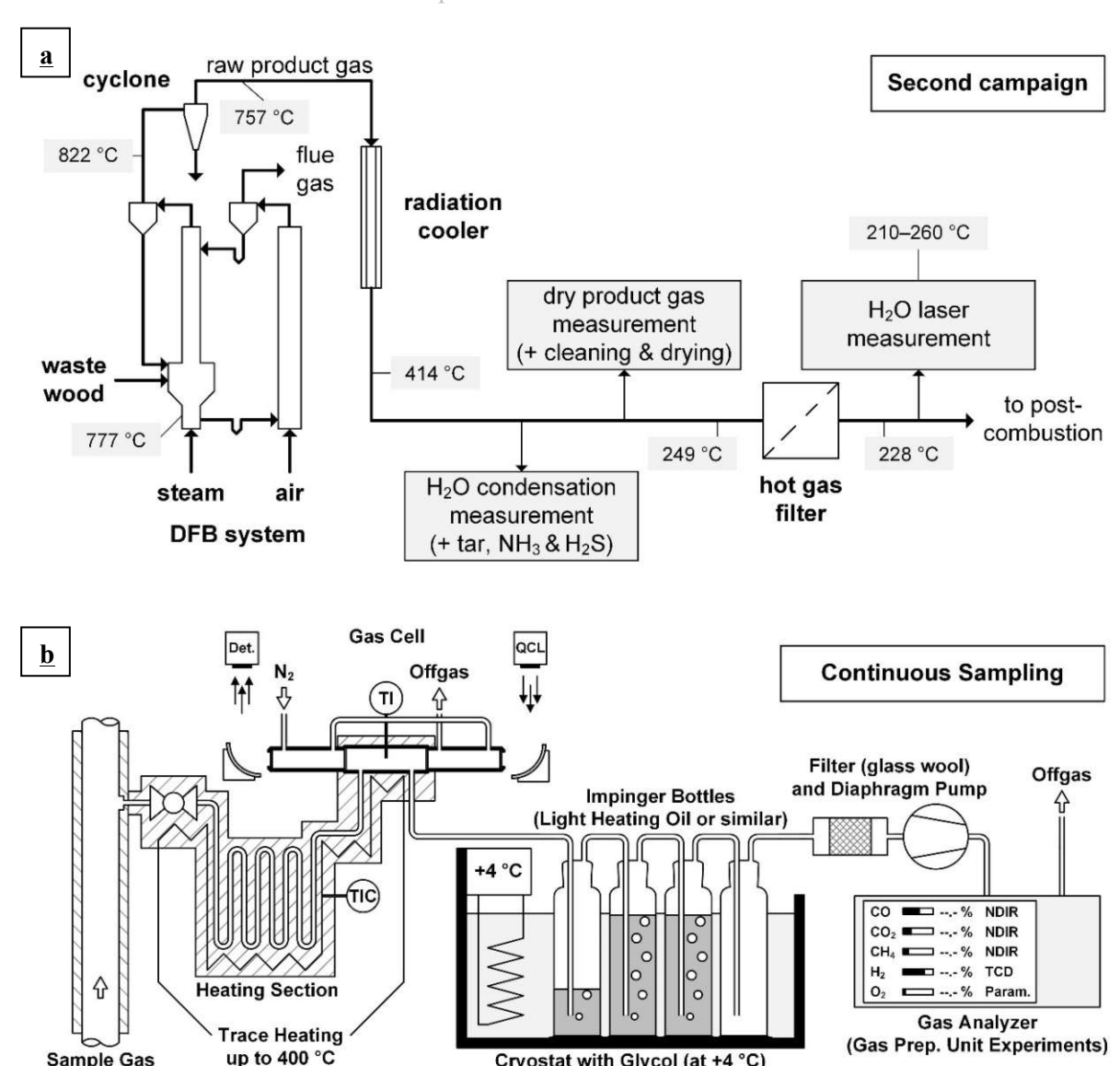


Figure 24: a) gas sampling point and b) sampling line used to test the novel THz quantum cascade laser during experiments with the advanced 100 kWth dual fluidized bed pilot gasifier. Both sub-figures are reprinted from [JA III].

Cryostat with Glycol (at +4 °C)

The novel QCL-based measurement was validated by comparison with H<sub>2</sub>O condensation measurements. A prototype agreed with the condensation measurements for several stationary gas mixtures prepared in a gas mixing setup (Figure 25a). An advanced setup was tested for online measurement of product gas, which contained various dry product gas species and tar compounds in addition to H<sub>2</sub>O (Figure 25b). The measurements in this second campaign agreed very well with a condensation measurement and an estimation by mass balancing over the compared duration:

- New QCL-measurement: 45.1 46.9 vol.-%; data were available online with a resolution of less than 5 seconds
- Condensation measurement: 46.7 vol.-%; 1 data point was available hours to days later, representing an average value over the investigated duration
- Mass balance estimation: 44.6 45.3 vol.-%; data were available online for this plant with a resolution of 1 minute, but model convergence sometimes failed

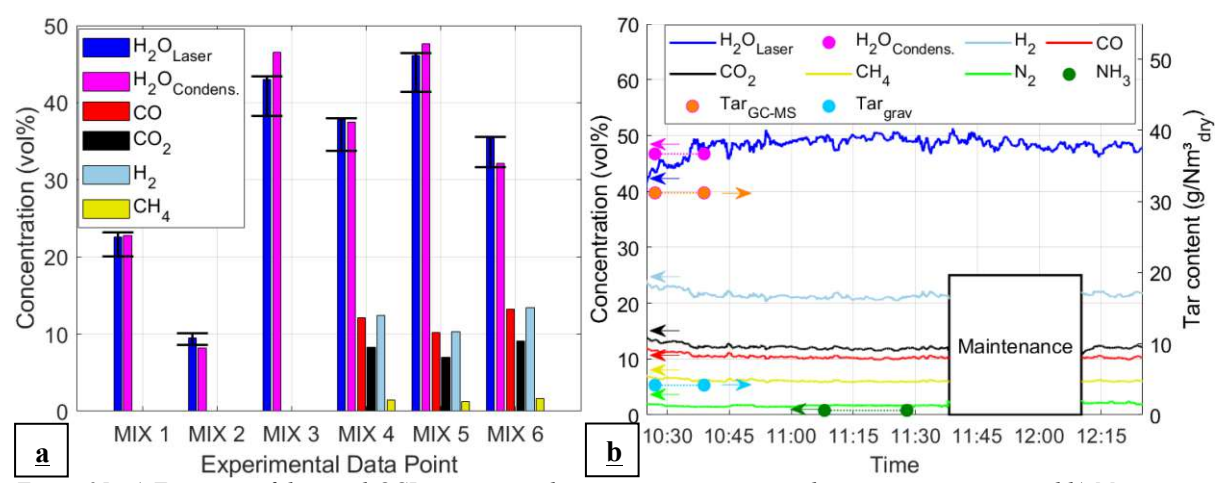


Figure 25: a) First tests of the novel QCL setup in synthetic gas mixtures prepared in gas mixing setup, and b) Measurement in raw product gas with significant tar loading from waste wood gasification. Both sub-figures are reprinted from [JA III].

### 4.4.4. Discussion: $H_2O$ in raw product gas by quantum cascade laser

The new H<sub>2</sub>O measurement in raw product gas introduced in JA III is a significant step forward in gasification data collection. H<sub>2</sub>O can constitute 50 vol.-% or more of the raw product gas from steam biomass gasification [164], [223], [224]. Mauerhofer et al. also found that the water content in product gas was around 8-30 vol.-% for biomass gasification with CO<sub>2</sub> or mixtures of CO<sub>2</sub> and H<sub>2</sub>O as gasification agents [52]. Mass balances in JA II also suggested up to 8 vol.-% H<sub>2</sub>O in the product gas from gasification with only CO<sub>2</sub> as the gasification agent. Since H<sub>2</sub>O is such a big part of product gas, it is critical to have a good measurement for this value. The measurements by Mauerhofer et al. (and in other gasification work by TU Wien) were conducted as offline analysis, which has significant drawbacks like delays, low resolution, and the need for manual procedures. To the author's best knowledge, most - if not all - other methods that could be used for fast online H<sub>2</sub>O quantification in raw product gas have some shortcomings:

- Analysis via chromatography faces co-absorption and maintenance challenges [68], [69].
- Hygrometers, acoustic measurements, and most spectroscopic measurements in the near- or mid-infrared region are affected by dust, tar deposits, and band overlapping [68], [69].
- High-quality Raman spectra are challenging to obtain due to the low density and cross-section of gases [225], and the H<sub>2</sub>O quantification by Raman spectroscopy can suffer under high gas flows or tar loading from biomass gasification [141]
- Far-infrared spectroscopy without QCL light sources, as demonstrated by other authors, had to use gas cells with 1 m or more of optical path length, which lead to temperature control problems and is generally less practical [226], [227].
- Tuneable diode laser absorption spectroscopy emitting in the mid-infrared range has been demonstrated for this application. However, its uncertainty of  $\pm 10$ -15 % is higher than in our new setup [228], [229].



## CO<sub>2</sub> Conversion to CO by Fluidized Bed Biomass Gasification Chapter 4: Results and discussion

This first demonstration of the new QCL setup in JA III seems to have overcome these issues as measurements agreed very well with comparison methods, even in the presence of around 30 g/Nm³ tar (measured by GC-MS). However, although successful, this work was only the first proof of principle, and this new measurement should receive significant further development.

The setup needs to be tested more often and under varying conditions. For example, the experimental work in this article used a hot gas filter to remove most dust particles before entering the cell. Future works could also try measurement under dusty conditions, as an inherent advantage of far-infrared spectroscopy with longer wavelengths should be their increased resistance to Mie scattering [230], [231]. Measuring under dusty conditions with this new far-infrared setup will likely succeed because Sepman et al. already demonstrated measurement in reactor cores with their mid-infrared setup [229], [232], [233]. In addition to further testing, the setup should be further developed to improve usability, reduce noise, and potentially measure other gas components.

## 4.4.5. Key findings: Additional research on biomass CO2 gasification

The research in this chapter did not investigate CO<sub>2</sub> conversion but instead described how better measurements and high-value side products could support biomass CO<sub>2</sub> gasification. The QCL-based H<sub>2</sub>O quantification method is also broadly applicable to other types of thermochemical biomass conversion or other processes where quantifying water vapor is desired. The key findings of this chapter are summarized in Key findings 4.

Key findings 4: Chapter "Additional research on biomass CO2 gasification".

- A two-step torrefaction and CO<sub>2</sub> gasification process produced biochar with BET surface areas up to around 800 m<sup>2</sup>/g.
- The temperatures used for high-surface-area biochar production resembled those used for high CO<sub>2</sub> utilization.
- Spectroscopy in the far-infrared domain with a quantum cascade laser as a light source can quantify H<sub>2</sub>O in raw product gas from biomass gasification accurately, swiftly, and online.

# 5. Summary and conclusions

The research in this thesis contained experimental investigations of biomass CO<sub>2</sub> gasification, the development of new measurements, and process simulations. First, this section addresses how the results in this thesis answer the given research questions. Second, it ties together the core findings to identify overall implications for the field of research.

## 5.1. Findings on individual research questions

The following answers to the stated research questions are given based on the results and scope of this thesis:

### 1. How can CO<sub>2</sub> conversion be increased in a fluidized bed biomass gasifier?

The conversion of CO<sub>2</sub> is enhanced at high temperatures. A temperature of 850 °C and higher led to the highest CO<sub>2</sub> conversions in semi-batch and continuous-feeding experiments in this thesis. These high temperatures are necessary for CO2 conversion via the Boudouard reaction. High temperatures lead to a higher CO<sub>2</sub> conversion under equilibrium conditions and increase the reaction rate. The importance of the Boudouard reaction, combined with its reaction stoichiometry, suggests that a molar ratio of at least 1:1 between solid carbon from biomass and carbon from CO2 should be targeted for maximum CO2 conversion. Furthermore, semi-batch experiments in a fluidized bed gasifier in this thesis found that the reaction rate can severely limit the conversion of CO<sub>2</sub>. Therefore, the increase in reaction rate at high temperatures is significant for fluidized bed gasifiers, where the residence time of CO<sub>2</sub> in the gasifier is limited. Another finding of these investigations was that only the residence time in the reactor when CO<sub>2</sub> is in contact with solid carbon should be considered for CO<sub>2</sub> conversion via the Boudouard reaction. The more fixed carbon is in the reactor, the longer the fuel-gas contact times and, therefore, the higher the CO<sub>2</sub> conversion is. Another important factor to consider is that the availability of fixed carbon for the Boudouard reaction is reduced by biomass devolatilization, suggesting that biomass with low volatile content is better suited for CO2 conversion at similar molar carbon feeding ratios. The highest experimentally obtained CO2 conversion over one hour of continuous feeding to a lab-scale fluidized bed gasifier was 93 %. This experiment used wood char as biomass feedstock at a measured temperature of 856 °C, atmospheric pressure, a carbon feed ratio (Cfuel: CCO2) of 2, and a gasification agent mixture with a volumetric ratio of around 9:1 for CO<sub>2</sub>:H<sub>2</sub>O.

### 2. How can CO<sub>2</sub> conversion be validated in a biomass gasifier?

The conversion of feedstock CO<sub>2</sub> in biomass gasification is challenging to determine because new CO<sub>2</sub> is formed from biomass devolatilization in the reactor. Isotopic analysis of carbon streams can be used to isolate carbon streams and determine the conversion of feedstock CO2 under these conditions, validating the biomass CO<sub>2</sub> gasification process for CO<sub>2</sub> utilization. If there are natural abundance

differences in <sup>13</sup>C between the CO<sub>2</sub> and biomass feedstocks, this is possible without adding any tracer substance. The isotopic carbon fingerprints of the carbonaceous feedstocks, biomass and CO<sub>2</sub>, and the carbonaceous gasification products, e.g., CO<sub>2</sub> and CO, can be analyzed in an isotope-ratio mass spectrometer. These measurements allow for the attribution of carbonaceous products to their parental carbon materials. The conversion of feedstock CO<sub>2</sub> in the gasifier can be determined by comparing the initial feedstock CO<sub>2</sub> to the remaining feedstock CO<sub>2</sub> in the product gas.

## 3. How does implementing biomass CO<sub>2</sub> gasification for CO<sub>2</sub> recycling affect the economic viability and CO<sub>2</sub> emissions of direct reduction ironmaking?

Economic and ecological comparisons favor the biomass CO<sub>2</sub> gasification process against the established MIDREX plant concept using natural gas reforming. Calculations show that a carbon emission allowance price of around 10 -20 €/t<sub>CO2</sub> could suffice for reaching lower costs of production at a much lower carbon footprint per unit of cold direct reduced iron for the new process. Including biogenic carbon capture and storage makes it possible to achieve net-negative cradle-to-gate emissions for ironmaking. The highest net-negative emissions could be achieved if oxy-fuel combustion were used as additional carbon capture technology; however, this would need some economic incentives in the form of carbon removal credits to be economically feasible. Without these credits, the lowest levelized costs of iron reduction via a biomass CO<sub>2</sub> gasification process are 350 €/t<sub>CDRI</sub>. This configuration also shows net-negative CO<sub>2</sub>-equivalent emissions of -83 kg<sub>CO2e</sub>/t<sub>CDRI</sub>. The natural gas reforming comparison process costs 416 €/t<sub>CDRI</sub> and emits 892 kg<sub>CO2e</sub>/t<sub>CDRI</sub>, which could be lowered to 403 €/t<sub>CDRI</sub> and 441 kg<sub>CO2e</sub>/t<sub>CDRI</sub> by including carbon capture and storage.

## i. Is there a potential synergy between the operating conditions needed for CO<sub>2</sub> utilization and producing high-surface-area biochar by CO<sub>2</sub> gasification?

A two-step process of wood pellet torrefaction and CO<sub>2</sub> gasification can obtain biochar with specific surface areas of up to 800 m<sup>2</sup>/g<sub>biochar</sub>. The surface area of biochar was increased at higher temperatures (up to 900 °C tested), longer solids residence time in the reactor (up to 25 min tested), and under fixed bed conditions. The surface yield was also determined as a process efficiency indicator, which relates the total produced biochar surface area to the initial wood pellet feedstock mass prior to torrefaction. The surface yield was up to 100 m<sup>2</sup>/g<sub>feedstock</sub>. This value was also maximized at the same temperatures and residence times but was higher when the biomass was submerged in a fluidized bed with silica sand as bed material. The CO<sub>2</sub> gasification temperatures leading to the highest BET surface areas in biochar agree with those used for reaching more than 90 % CO<sub>2</sub> conversion in this thesis. The long residence times of biochar in the reactor (25 minutes) would need a reactor concept where biochar is not quickly fully converted. Further development is necessary to clarify if the goals of high CO2 conversion to produce high-quality product gas and high-surface-area biochar production are compatible.

### ii. How can water vapor concentration be measured in hot and raw product gas?

Water vapor can be quantified in hot and raw product gas by spectroscopy in the far-infrared domain. A quantum cascade laser combining GaAs/AlGaAs as materials can produce light at around 2.3 THz. This light is selectively absorbed by water vapor, which enables quantification. Condensation of water and tars can be prevented, and measurement is achieved by directing a gas flow through a heated gas cell with an optical path length of 8.6 cm. A pyroelectric detector can be used for signal recording. Based on molar absorption coefficients, a numerical solver can correlate the signal to water content. These molar absorption coefficients can be calculated from the Voigt line shapes obtained from the line list in the HITRAN2020 database.

# 5.2. Synthesis and implications of core results

This thesis aims to underpin biomass CO<sub>2</sub> gasification as a technology for CO<sub>2</sub> utilization. The literature reviewed in Section 2 suggests that some key challenges for recognizing CO<sub>2</sub>-assisted biomass gasification as a promising technology for CO<sub>2</sub> conversion are the uncertainty of CO<sub>2</sub> conversion and a lack of available data for plants that exceed TGA or lab-scale [48], [52]. Additionally, the H<sub>2</sub>:CO ratio in the gas produced by CO<sub>2</sub>-assisted gasification is too low for many applications, which is an important reason why steam gasification is often the preferred gasification technology [97]. This thesis addressed these challenges with its three core research questions, which inform the following integrative synthesis.

The experiments presented in this work showed that an allothermally heated bubbling fluidized bed gasifiers can convert more than 90 % of feedstock CO<sub>2</sub> in a single pass-through, which brought CO<sub>2</sub> concentrations in the product gas below 10 vol.-% [JA II]. This high conversion should suffice for most applications, as the remaining  $CO_2$  could remain in the gas for some applications like ironmaking [JA IV and methanol production [234] or be separated at a comparatively low energy cost. Introducing the novel carbon isotope method to measure CO<sub>2</sub> conversion while demonstrating high CO<sub>2</sub> conversion in continuous bench scale experiments further validated carbon conversion technology [JA II]. While these experiments proved the process' viability beyond batch-fed TGA experiments, there are also challenges for scaling up the single-bed reactor concept with electrical heating shells used in JA II and JA II. First, heat input was already constrained at this reactor size, as evidenced by the significant difference between heating shell temperature (1000 °C) and reactor core temperature (approximately 820 - 900 °C) in continuous feeding mode [JA II]. Second, the price difference between electricity and biomass per unit of energy is currently vastly in favor of biomass, at least in the year 2024 in Austria [199], [201]. For these reasons, the results from this thesis imply that an allothermal reactor concept using biomass or a partial recycling stream for combustion could balance CO<sub>2</sub> conversion, scalability, and economical operation.

In principle, such a biomass CO<sub>2</sub> gasification process was already demonstrated by Mauerhofer in a dual fluidized bed (DFB) system, although with much lower CO<sub>2</sub> conversion [47]. Mauerhofer applied CO<sub>2</sub>assisted gasification in the advanced 100 kWth advanced dual fluidized bed pilot plant at TU Wien. DFB

gasifiers based on TU Wien designs were also successfully operated at MWth scale for steam gasification [235]. Observed temperatures in the bubbling bed of Mauerhofer's experiments [52] resembled the investigations in this thesis [JA III], and the tested bed material (olivine) and biomass feedstock (softwood) had the same composition. Additionally, both the electrically heated and DFB gasification reactors supply the energy needed for the endothermic gasification reactions allothermally. These agreements suggest that achieving higher CO<sub>2</sub> conversion in a DFB gasifier could also be possible, making efficient CO<sub>2</sub> utilization an option in a more easily scalable reactor concept. Based on the observations in this thesis, one key area to investigate in the DFB gasifier would be to increase the availability of solid carbon in the gasifier and its contact time with CO<sub>2</sub>.

JA IV used the agreements listed above to hypothesize that the experiments from JA II would be transferable to a direct reduction ironmaking plant, where a dual fluidized bed gasifier is used for CO<sub>2</sub> conversion. The ironmaking sector's high CO<sub>2</sub> emissions make it an impactful selection for defossilization efforts [4]. Direct reduction ironmaking has several characteristics that make it wellsuited for implementing biomass CO<sub>2</sub> gasification, e.g., its tolerance to low H<sub>2</sub>:CO ratios and gas impurities [112], [158]. The on-site conversion of CO to CO<sub>2</sub> in the use phase offers an interesting option for on-site carbon recycling [JA IV]. The CO-rich product gas from biomass CO<sub>2</sub> gasification can be integrated into the direct reduction ironmaking process. CO and H<sub>2</sub> can act as reducing agents that take oxygen from the iron ore to produce elemental iron that can be further processed to steel via the electric arc furnace route. JA IV showed economic and ecological advantages for this process compared to current ironmaking with natural gas as feedstock. While the base scenario calculations in JA IV used a prediction of 146 €/t<sub>CO2</sub> for the EU-ETS CO<sub>2</sub> allowance price in 2030 [203], calculations showed that biomass CO<sub>2</sub> gasification already has cheaper costs of production at 67 €/t<sub>CO2</sub>, which was the average between 11/2023 and 10/2024 [214]. This finding implies that technology development should aim to validate further and scale up the process, as the economic process can already be made and speed is essential in the fight to curb global warming.

Direct reduction ironmaking by hydrogen is currently at the forefront of strategic discussions about reducing CO<sub>2</sub> emissions from ironmaking [151], [236], [237]. Although JA IV did not explicitly compare biomass CO<sub>2</sub> gasification to this process, it is possible to make an economic comparison by comparing both to the natural gas reforming process. While JA IV found the gasification process lower than natural gas reforming in levelized production costs, the literature reports that ironmaking by reduction with hydrogen is economically disadvantaged against ironmaking using natural gas reforming [113], [238]. While blue hydrogen was reported at "only" 18 % higher costs, Benavides et al. estimated the costs of an ironmaking process using green hydrogen at a 79 % cost increase compared to natural gas reforming [238]. Furthermore, JA IV found that several process configurations with biomass CO<sub>2</sub> gasification offer the chance to achieve net-negative CO2 emissions. In contrast, ironmaking by hydrogen usage provides no option to generate such net-negative emissions since it generally does not

include carbon capture from the atmosphere. Additional technical considerations, such as the easier heat distribution in the shaft reactor and the option for carburization with CO in the reducing gas, could be key strengths of a biomass CO<sub>2</sub> gasification implementation in ironmaking [113] [JA IV]. These points imply that biomass gasification's appeal for ironmaking goes beyond the option to reduce emissions from current fossil technology, as it is also a potentially attractive option compared to other low-emission technologies.

This thesis ties together the findings on gasifier optimization with the process design for ironmaking by finding that increasing the CO<sub>2</sub> conversion in the gasifier directly increases the efficiency and economic performance of the overall ironmaking process [JA IV]. Three gasification datasets with varying CO<sub>2</sub> conversions in the gasifier were used in JA IV to investigate the effect of CO<sub>2</sub> conversion on the overall plant performance of the proposed ironmaking process. The dataset with the lowest CO<sub>2</sub> conversion was from prior work by Mauerhofer et al. [52], while the other datasets were taken from JA II and used optimized process parameters. The gasification dataset with the highest conversion used wood char as gasification feedstock, while the others used softwood. The results show that plant efficiency increases and levelized costs for producing cold direct reduced iron decrease at higher CO<sub>2</sub> conversions. These trends remain even if it is necessary to integrate a pyrolyzer into the plant concept to produce wood char as gasification feedstock. Increasing the CO<sub>2</sub> conversion in the gasifier also decreases the CO<sub>2</sub> footprint per unit of cold direct reduced iron if air is used as a combustion agent. The carbon footprint with oxyfuel combustion increased, but this comes directly from increased biomass demand, and even the oxyfuel scenario with the highest emissions still has significant net-negative emissions. Going forward, the identified correlation between CO<sub>2</sub> conversion in the gasifier and overall plant performance indicators should be considered in plant concepts. Recurring reasons for optimizing the CO<sub>2</sub> conversion might be the reduced need for downstream carbon capture and a decrease in demand for externally sourced renewable CO<sub>2</sub>, which is likely limited and expensive until direct air capture matures as a technology [27].

In summary, the findings of this thesis are strongly relevant to the development of biomass CO<sub>2</sub> gasification as a technology for CO<sub>2</sub> utilization and the ironmaking sector. Biomass CO<sub>2</sub> gasification offers a credible pathway for reducing global emissions in a strategically relevant and economically competitive environment such as ironmaking. These results should help to raise awareness of biomass CO<sub>2</sub> gasification's potential for CO<sub>2</sub> utilization and inspire further development to see this process brought to the industrial scale.

# 6. Outlook

This thesis tried to strengthen biomass CO<sub>2</sub> gasification as a carbon capture and utilization process by a) increasing, b) validating, and c) implementing CO<sub>2</sub> utilization to a relevant industrial process. One route for continued development should be applying the developed measurement to additional experiments and gasification conditions to gain further insights. There are many options for such investigations, for example:

- Future experimental investigations should focus on a more diverse range of feedstocks. Feedstock availability, sustainability, and cost of biomass should guide the selection of tested materials. The influence of feedstock pretreatment could be investigated, e.g., pyrolysis, hydrothermal carbonization, or impregnation with catalytically active substances.
- Similarly, further attention should be given to screening for a bed material with heightened catalytic behavior to support CO<sub>2</sub> conversion and tar destruction.
- The developed semi-empirical CO<sub>2</sub> conversion model should be transferred to continuous operation. An effort should be made to make it applicable to various fuel types, e.g., by considering their volatile content and catalytic ash components.
- The findings about CO<sub>2</sub> conversion for feedstock CO<sub>2</sub> should also be applied to improve the conversion of CO<sub>2</sub> formed by devolatilization in the reactor. For example, this could be done by adjusting the point of biomass feeding to in-bed instead of on-bed, adding additional solid carbon to the reactor, or feeding the product gas to a secondary reactor with solid carbon.
- Investigations should be extended to experiments in larger-scale reactors with reactor concepts that could be feasible for industrialization, such as dual fluidized or autothermal circulating bed reactors.
- Similar considerations regarding rate-controlled behavior and stoichiometric feeding ratios should be applied for efficient steam conversion in co-gasification with CO<sub>2</sub>.

The continued development of the proposed biomass CO<sub>2</sub> gasification for ironmaking demands experimental testing of the iron reduction process with the calculated reducing gas compositions. Suppose this is successful; as many combined unit operations as possible should be tested to ensure no practical problems arise from the proposed process configuration. The following considerations are important for the industrialization of this or any other process that uses biomass CO2 gasification for CO<sub>2</sub> utilization.

- It is important to prioritize renewable CO<sub>2</sub> sources to avoid carbon lock-in effects that could lead to overshooting climate targets or stranded assets.
- The limits of biomass availability, sustainability, and competing demand from other applications must be investigated for each region and project.

## CO<sub>2</sub> Conversion to CO by Fluidized Bed Biomass Gasification Chapter 6: Outlook

- Political frameworks should be adjusted to attract desired behavior, e.g., by creating incentives for biogenic carbon capture and storage and raising carbon emission prices to such levels that the externalized costs of fossil emissions are appropriately internalized.
- The roll-out of renewable electricity and green hydrogen production needs to have high priority, as additional hydrogen is needed for most carbon capture and utilization processes.
- It is important to focus on processes where CO<sub>2</sub> utilization is the most effective strategy for defossilization. Electrification and green hydrogen usage should be investigated and preferred if more effective over carbon capture and utilization for energy-centric applications.

# References

- [1] IPCC, Climate Change 2023: Synthesis Report. Contribution of Working Groups I, II and III to the Sixth Assessment Report of the Intergovernmental Panel on Climate Change. Geneva: Cambridge University Press, 2023. doi: 10.59327/IPCC/AR6-9789291691647.
- IPCC, Climate Change 2021: The Physical Science Basis. Contribution of Working Group I to [2] the Sixth Assessment Report on the Intergovernmental Panel on Climate Change, no. 6. Cambridge: Cambridge University Press, 2021. doi: 10.1017/9781009157896.
- [3] IPCC, Climate Change 2022: Impacts, Adaptation, and Vulnerability. Contribution of Working Group II to the Sixth Assessment Report of the Intergovernmental Panel on Climate Change. Cambridge, UK and New York, USA: Cambridge University Press, 2022. doi: 10.1017/9781009325844.
- [4] IPCC, Climate Change 2022: Mitigation of Climate Change. Contribution of Working Group III to the Sixth Assessment Report of the Intergovernmental Panel on Climate Change, no. 6. Cambridge: Cambridge University Press, 2022. doi: 10.1017/9781009157926.
- Copernicus, "Global Climate Highlights 2024." Accessed: Apr. 07, 2025. [Online]. Available: [5] https://climate.copernicus.eu/global-climate-highlights-2024
- [6] T. Rajabloo, W. De Ceuninck, L. Van Wortswinkel, M. Rezakazemi, and T. Aminabhavi, "Environmental management of industrial decarbonization with focus on chemical sectors: A review," Jan. 15, 2022, Academic Press. doi: 10.1016/j.jenvman.2021.114055.
- J. Zhang, C. D. Sewell, H. Huang, and Z. Lin, "Closing the Anthropogenic Chemical Carbon [7] Cycle toward a Sustainable Future via CO2 Valorization," Dec. 01, 2021, John Wiley and Sons Inc. doi: 10.1002/aenm.202102767.
- N. Von Der Assen, J. Jung, and A. Bardow, "Life-cycle assessment of carbon dioxide capture and [8] utilization: Avoiding the pitfalls," Energy Environ Sci, vol. 6, no. 9, pp. 2721–2734, Sep. 2013, doi: 10.1039/c3ee41151f.
- [9] E. Cabrera and J. M. Melo de Sousa, "Use of Sustainable Fuels in Aviation—A Review," Apr. 01, 2022, MDPI. doi: 10.3390/en15072440.
- [10] R. Gholami, A. Raza, and S. Iglauer, "Leakage risk assessment of a CO2 storage site: A review," Earth Sci Rev, vol. 223, Dec. 2021, doi: 10.1016/j.earscirev.2021.103849.
- J. H. García and A. Torvanger, "Carbon leakage from geological storage sites: Implications for [11] trading," carbon Energy Policy, vol. 127, 320–329, Apr. 2019, pp. doi: 10.1016/j.enpol.2018.11.015.

- IRENA and Methanol Institute, "Innovation Outlook: Renewable Methanol," Abu Dhabi, 2021. [12]
- A. Matthey, B. Bünger, and N. Eser, "Methodological Convention 3.2 for the Assessment of [13] Environmental Costs Value Factors," Dessau-Roßlau, Oct. 2024. Accessed: Feb. 20, 2025. [Online]. Available: https://www.umweltbundesamt.de/sites/default/files/medien/479/publikationen/methodological convention 3 2 value factors bf.pdf
- S. U. R. Memon et al., "A Comprehensive Review of Carbon Capture, Utilization, and Storage [14] (CCUS): Technological Advances, Environmental Impact, and Economic Feasibility," Scholars Acad J Biosci, vol. 12, no. 07, pp. 184–204, Aug. 2024, doi: 10.36347/sajb.2024.v12i07.003.
- C. Dong, Z. Sun, J. Jiang, and Y. Yang, "Using agent-based modelling to simulate the emission [15] reduction potential of CCUS technologies in China under alternative policy packages," Environmental Research Letters, vol. 20, no. 1, Jan. 2025, doi: 10.1088/1748-9326/ad9c9b.
- M. Hammerschmid et al., "Economic and Ecological Impacts on the Integration of Biomass-[16] Based SNG and FT Diesel in the Austrian Energy System," Energies (Basel), vol. 16, no. 16, 2023, doi: 10.3390/en16166097.
- [17] S. Pissot, H. Thunman, P. Samuelsson, and M. Seemann, "Production of negative-emissions steel using a reducing gas derived from dfb gasification," Energies (Basel), vol. 14, no. 16, 2021, doi: 10.3390/en14164835.
- [18] S. G. Gizer, O. Polat, M. K. Ram, and N. Sahiner, "Recent developments in CO2 capture, utilization, related materials, and challenges," Oct. 10, 2022, John Wiley and Sons Ltd. doi: 10.1002/er.8347.
- F. Johnsson, J. Kjärstad, and J. Rootzén, "The threat to climate change mitigation posed by the [19] abundance of fossil fuels," Climate Policy, vol. 19, no. 2, pp. 258-274, Feb. 2019, doi: 10.1080/14693062.2018.1483885.
- [20] I. Overland, J. Juraev, and R. Vakulchuk, "Are renewable energy resources more evenly distributed than fossil fuels?," Renew Energy, vol. 200, pp. 379-386, Nov. 2022, doi: 10.1016/j.renene.2022.09.046.
- International Energy Agency, "Europe Coal supply." Accessed: Feb. 20, 2025. [Online]. [21] Available: https://www.iea.org/regions/europe/coal
- [22] International Energy Agency, "Europe – Natural gas supply." Accessed: Feb. 20, 2025. [Online]. Available: https://www.iea.org/regions/europe/natural-gas
- [23] International Energy Agency, "Europe – Oil supply." Accessed: Feb. 20, 2025. [Online]. Available: https://www.iea.org/regions/europe/oil

- I. Tache, "OPEC and the 1970s Oil Crises: Lessons for the 2021 Global Energy Crisis," in [24] Conflicts and Challenges in the Middle East: Religious, Political and Economic Perspectives, H.-D. Yan, O. Bajo-Rubio, D. S. Kwan, and F.-L. T. Yu, Eds., Cham: Springer Nature Switzerland, 2024, pp. 61–77. doi: 10.1007/978-3-031-62739-2 5.
- L. Schramm, "Some differences, many similarities: comparing Europe's responses to the 1973 [25] oil crisis and the 2022 gas crisis," European Political Science Review, Feb. 2023, doi: 10.1017/S1755773923000255.
- A. M. Parvez, M. T. Afzal, T. G. Victor Hebb, and M. Schmid, "Utilization of CO2 in [26] thermochemical conversion of biomass for enhanced product properties: A review," Journal of CO2 Utilization, vol. 40, Sep. 2020, doi: 10.1016/j.jcou.2020.101217.
- T. Galimova et al., "Global demand analysis for carbon dioxide as raw material from key [27] industrial sources and direct air capture to produce renewable electricity-based fuels and chemicals," J Clean Prod, vol. 373, Nov. 2022, doi: 10.1016/j.jclepro.2022.133920.
- [28] C. Hepburn et al., "The technological and economic prospects for CO2 utilization and removal," Nov. 07, 2019, Nature Publishing Group. doi: 10.1038/s41586-019-1681-6.
- [29] European Commission, "Reference Document on Best Available Techniques for the Manufacture of Large Volume Inorganic Chemicals - Ammonia, Acids, Fertilisers," Aug. 2007.
- [30] R. Remus, M. A. Aguado-Monsonet, S. Roudier, and Luis. Delgado Sancho, "Best available techniques (BAT) reference document for iron and steel production," Publications Office, 2013.
- [31] L. Wu, Q. Liu, R. Jackstell, and M. Beller, "Carbonylations of alkenes with CO surrogates," Angewandte Chemie - International Edition, vol. 53, no. 25, pp. 6310-6320, Jun. 2014, doi: 10.1002/anie.201400793.
- C. Du, P. Lu, and N. Tsubaki, "Efficient and New Production Methods of Chemicals and Liquid [32] Fuels by Carbon Monoxide Hydrogenation," ACS Omega, vol. 5, no. 1, pp. 49–56, Jan. 2020, doi: 10.1021/acsomega.9b03577.
- [33] H. Gruber et al., "Fischer-Tropsch products from biomass-derived syngas and renewable hydrogen," Biomass Convers Biorefin, vol. 11, no. 6, pp. 2281–2292, 2021, doi: 10.1007/s13399-019-00459-5.
- A. P. Steynberg, "Chapter 1 Introduction to Fischer-Tropsch Technology," in Fischer-Tropsch [34] Technology, vol. 152, A. Steynberg and M. Dry, Eds., in Studies in Surface Science and Catalysis, vol. 152., Elsevier, 2004, pp. 1–63. doi: https://doi.org/10.1016/S0167-2991(04)80458-0.

- A. Ambrosi and S. E. Denmark, "Harnessing the Power of the Water-Gas Shift Reaction for [35] Organic Synthesis," Angewandte Chemie International Edition, vol. 55, no. 40, pp. 12164-12189, Sep. 2016, doi: https://doi.org/10.1002/anie.201601803.
- [36] D. Xiao, J. An, Y. He, and M. Wu, "The chaotic characteristic of the carbon-monoxide utilization blast furnace," ISA Trans, vol. 68, pp. 109–115, 2017, ratio in the https://doi.org/10.1016/j.isatra.2017.03.004.
- J. Wu, A. Gross, and H. Yang, "Shape and Composition-Controlled Platinum Alloy Nanocrystals [37] Using Carbon Monoxide as Reducing Agent," Nano Lett, vol. 11, no. 2, pp. 798–802, Feb. 2011, doi: 10.1021/nl104094p.
- [38] J. D. Medrano-García, R. Ruiz-Femenia, and J. A. Caballero, "Optimal carbon dioxide and hydrogen utilization in carbon monoxide production," Journal of CO2 Utilization, vol. 34, pp. 215–230, Dec. 2019, doi: 10.1016/j.jcou.2019.05.005.
- Magnus. Rydén, "Hydrogen production from fossil fuels with carbon dioxide capture, using [39] chemical-looping technologies," Dissertation, Chalmers University of Technology, Göteborg, 2008.
- [40] L. Fu et al., "Research progress on CO2 capture and utilization technology," Dec. 01, 2022, Elsevier Ltd. doi: 10.1016/j.jcou.2022.102260.
- R. Küngas, "Review-Electrochemical CO 2 Reduction for CO Production: Comparison of [41] Low- and High-Temperature Electrolysis Technologies," J Electrochem Soc, vol. 167, no. 4, p. 044508, Jan. 2020, doi: 10.1149/1945-7111/ab7099.
- K. C. Poon, W. Y. Wan, H. Su, and H. Sato, "A review on recent advances in the electrochemical [42] reduction of CO2 to CO with nano-electrocatalysts," Aug. 15, 2022, Royal Society of Chemistry. doi: 10.1039/d2ra03341k.
- [43] J. He and C. Janáky, "Recent Advances in Solar-Driven Carbon Dioxide Conversion: Expectations versus Reality," Jun. 12, 2020, American Chemical Society. 10.1021/acsenergylett.0c00645.
- A. George et al., "A Review of Non-Thermal Plasma Technology: A novel solution for CO2 [44] conversion and utilization," Jan. 01, 2021, Elsevier Ltd. doi: 10.1016/j.rser.2020.109702.
- F. Ren and W. Liu, "Review of CO2 Adsorption Materials and Utilization Technology," Aug. 01, [45] 2023, Multidisciplinary Digital Publishing Institute (MDPI). doi: 10.3390/catal13081176.
- P. Lahijani, Z. A. Zainal, M. Mohammadi, and A. R. Mohamed, "Conversion of the greenhouse [46] gas CO2 to the fuel gas CO via the Boudouard reaction: A review," Renewable and Sustainable Energy Reviews, vol. 41, pp. 615–632, 2015, doi: 10.1016/j.rser.2014.08.034.

- A. M. Mauerhofer, "Carbon Utilization by Application of CO2 Gasification," Dissertation, [47] 2020. Technische Universität Wien, [Online]. Available: http://hdl.handle.net/20.500.12708/79844
- [48] Y. H. Chan, S. N. F. Syed Abdul Rahman, H. M. Lahuri, and A. Khalid, "Recent progress on COrich syngas production via CO2 gasification of various wastes: A critical review on efficiency, challenges and outlook," Environmental Pollution, vol. 278, pp. 1-16, 2021, doi: 10.1016/j.envpol.2021.116843.
- [49] P. Lahijani, Z. A. Zainal, A. R. Mohamed, and M. Mohammadi, "Microwave-enhanced CO2 gasification of oil palm shell char," Bioresour Technol, vol. 158, pp. 193-200, 2014, doi: 10.1016/j.biortech.2014.02.015.
- F. Benedikt, "Fuel flexible advanced dual fluidized bed steam gasification," Dissertation, [50] Technische Universität Wien, 2020. doi: 10.34726/hss.2020.39988.
- H. J. Ho, A. Iizuka, and E. Shibata, "Carbon Capture and Utilization Technology without Carbon [51] Dioxide Purification and Pressurization: A Review on Its Necessity and Available Technologies," Ind Eng Chem Res, vol. 58, no. 21, pp. 8941–8954, May 2019, doi: 10.1021/acs.iecr.9b01213.
- [52] A. M. Mauerhofer et al., "Conversion of CO2 during the DFB biomass gasification process," Biomass Convers Biorefin, vol. 11, no. 1, pp. 15–27, 2021, doi: 10.1007/s13399-020-00822-x.
- N. A. Ahmad, K. A. Al-attab, Z. A. Zainal, and P. Lahijani, "Microwave assisted steam CO2 [53] char gasification of oil palm shell," Bioresour Technol Rep, vol. 15, Sep. 2021, doi: 10.1016/j.biteb.2021.100785.
- [54] A. Lampropoulos et al., "Effect of Olive Kernel thermal treatment (torrefaction vs. slow pyrolysis) on the physicochemical characteristics and the CO2 or H2O gasification performance of as-prepared biochars," 2021. doi: 10.1016/j.ijhydene.2020.11.230.
- [55] S. Tong, L. Li, L. Duan, C. Zhao, and E. J. Anthony, "A kinetic study on lignite char gasification with CO2 and H2O in a fluidized bed reactor," Appl Therm Eng, vol. 147, no. June 2018, pp. 602–609, 2019, doi: 10.1016/j.applthermaleng.2018.10.113.
- M. Jeremiáš et al., "Gasification of biomass with CO2 and H2O mixtures in a catalytic fluidised [56] bed," Fuel, vol. 210, no. September, pp. 605–610, 2017, doi: 10.1016/j.fuel.2017.09.006.
- H. Shahbeig, A. Shafizadeh, M. A. Rosen, and B. F. Sels, "Exergy sustainability analysis of [57] biomass gasification: a critical review," Biofuel Research Journal, vol. 9, no. 1, pp. 1592–1607, Mar. 2022, doi: 10.18331/BRJ2022.9.1.5.

- C. Madeddu, M. Errico, and R. Baratti, CO2 Capture by Reactive Absorption-Stripping. [58] Modeling, Analysis and Design, 1st ed. Cham: SpringerBriefs in Energy, 2019. doi: 10.1007/978-3-030-04579-1 2.
- [59] M. A. Habib, M. Nemitallah, and R. Ben-Mansour, "Recent development in oxy-combustion technology and its applications to gas turbine combustors and ITM reactors," Energy and Fuels, vol. 27, no. 1, pp. 2–19, 2013, doi: 10.1021/ef301266j.
- J. Ahn, W. Chung, and S. Chang, "Deactivation and regeneration method for ni catalysts by h2s [60] poisoning in co2 methanation reaction," Catalysts, vol. 11, no. 11, Nov. 2021, doi: 10.3390/catal111111292.
- S. Xu et al., "CO Poisoning of Ru Catalysts in CO2Hydrogenation under Thermal and Plasma [61] Conditions: A Combined Kinetic and Diffuse Reflectance Infrared Fourier Transform Spectroscopy-Mass Spectrometry Study," ACS Catal, vol. 10, no. 21, pp. 12828–12840, Nov. 2020, doi: 10.1021/acscatal.0c03620.
- [62] N. H. M. Dostagir et al., "Mitigating the Poisoning Effect of Formate during CO2 Hydrogenation to Methanol over Co-Containing Dual-Atom Oxide Catalysts," JACS Au, vol. 4, no. 3, pp. 1048– 1058, Mar. 2024, doi: 10.1021/jacsau.3c00789.
- [63] S. Pratschner, F. Radosits, A. Ajanovic, and F. Winter, "Techno-economic assessment of a powerto-green methanol plant," Journal of CO2 Utilization, vol. 75, Sep. 2023, doi: 10.1016/j.jcou.2023.102563.
- A. Bartik, F. Benedikt, J. Fuchs, H. Hofbauer, and S. Müller, "Experimental investigation of [64] hydrogen-intensified synthetic natural gas production via biomass gasification: a technical comparison of different production pathways," Biomass Convers Biorefin, 2023, doi: 10.1007/s13399-023-04341-3.
- A. M. Mauerhofer, S. Müller, F. Benedikt, J. Fuchs, A. Bartik, and H. Hofbauer, "CO2 [65] gasification of biogenic fuels in a dual fluidized bed reactor system," Biomass Convers Biorefin, vol. 11, no. 4, pp. 1101–1116, 2021, doi: 10.1007/s13399-019-00493-3.
- [66] H. Thunman and M. Seemann, "The gobigas plant," in Substitute Natural Gas from Waste: Technical Assessment and Industrial Applications of Biochemical and Thermochemical Processes, Elsevier, 2019, pp. 455–474. doi: 10.1016/B978-0-12-815554-7.00017-9.
- S. Nanda, A. K. Dalai, F. Berruti, and J. A. Kozinski, "Biochar as an Exceptional Bioresource for [67] Energy, Agronomy, Carbon Sequestration, Activated Carbon and Specialty Materials," Apr. 01, 2016, Springer Netherlands. doi: 10.1007/s12649-015-9459-z.

- IEA Bioenergy, Gas analysis in gasification of biomass and waste Guideline Report Document [68] 1. 2018.
- IEA, Gas analysis in gasification of biomass and waste Guideline Report Document 2 -Factsheets on gas analysis techniques. 2018.
- [70] S. De, A. K. Agarwal, V. S. Moholkar, and B. Thallada, Coal and Biomass Gasification, 1st ed., no. January. Springer Singapore, 2018. doi: 10.1007/978-981-10-7335-9.
- M. Kaltschmitt, S. Science, and S. Edition, Energy from Organic Materials (Biomass), vol. i. [71] 2019. doi: 10.1007/978-1-4939-7813-7.
- S. Osowski, J. Neumann, and H. Fahlenkamp, "Gasification of biogenic solid fuels," Chem Eng [72] Technol, vol. 28, no. 5, pp. 596–604, May 2005, doi: 10.1002/ceat.200407097.
- [73] P. Basu and P. Kaushal, Biomass Gasification, Pyrolysis, and Torrefaction: Practical Design, Theory, and Climate Change Mitigation, Fourth Edition, 4th ed. London, San Diego, Cambridge, Kidlington: Elsevier, 2024. doi: 10.1016/C2022-0-02464-8.
- M. Pohořelý, M. Jeremiáš, K. Svoboda, P. Kameníková, S. Skoblia, and Z. Beňo, "CO2 as [74] moderator for biomass gasification," Fuel, vol. 117, pp. 198-205, 2014, doi: 10.1016/j.fuel.2013.09.068.
- Q. Chen, J. S. Zhou, B. J. Liu, Q. F. Mei, and Z. Y. Luo, "Influence of torrefaction pretreatment [75] on biomass gasification technology," Chinese Science Bulletin, vol. 56, no. 14, pp. 1449–1456, May 2011, doi: 10.1007/s11434-010-4292-z.
- C. L. Hsi et al., "Characteristics of an air-blown fixed-bed downdraft biomass gasifier," Energy [76] and Fuels, vol. 22, no. 6, pp. 4196–4205, Nov. 2008, doi: 10.1021/ef800026x.
- [77] M. Kremling, L. Briesemeister, M. Gaderer, S. Fendt, and H. Spliethoff, "Oxygen-Blown Entrained Flow Gasification of Biomass: Impact of Fuel Parameters and Oxygen Stoichiometric Energy and Fuels, vol. 31, no. 4, pp. 3949–3959, Apr. 2017, doi: 10.1021/acs.energyfuels.6b02949.
- H. C. Yoon, T. Cooper, and A. Steinfeld, "Non-catalytic autothermal gasification of woody [78] biomass," Int J Hydrogen Energy, vol. 36, no. 13, pp. 7852-7860, Jul. 2011, doi: 10.1016/j.ijhydene.2011.01.138.
- S. Sharma and P. N. Sheth, "Air-steam biomass gasification: Experiments, modeling and [79] simulation," Energy Convers Manag, vol. 110, pp. 307-318, Feb. 2016, doi: 10.1016/j.enconman.2015.12.030.

- [80] B. Pandey, P. N. Sheth, and Y. K. Prajapati, "Air-CO2 and oxygen-enriched air-CO2 biomass gasification in an autothermal downdraft gasifier: Experimental studies," Energy Convers Manag, vol. 270, Oct. 2022, doi: 10.1016/j.enconman.2022.116216.
- [81] J. Isoksson, "Commercial scale gasification to replace fossil fuel in power generation-Vaskiluodon Voima140 MW CFB Gasification Project," Berlin, Oct. 2015. Accessed: Feb. 28, 2025. [Online]. Available: https://task33.ieabioenergy.com/wpcontent/uploads/sites/33/2022/07/Isaksson.pdf
- A. Gómez-Barea and B. Leckner, "Modeling of biomass gasification in fluidized bed," Prog [82] Energy Combust Sci, vol. 36, no. 4, pp. 444–509, 2010, doi: 10.1016/j.pecs.2009.12.002.
- [83] M. Dossow, D. Klüh, K. Umeki, M. Gaderer, H. Spliethoff, and S. Fendt, "Electrification of gasification-based biomass-to-X processes - a critical review and in-depth assessment," Dec. 21, 2023, Royal Society of Chemistry. doi: 10.1039/d3ee02876c.
- N. Hanchate, S. Ramani, C. S. Mathpati, and V. H. Dalvi, "Biomass gasification using dual [84] fluidized bed gasification systems: A review," Jan. 20, 2021, Elsevier Ltd. doi: 10.1016/j.jclepro.2020.123148.
- [85] D. Xu, X. Gu, and Y. Dai, "Concentrating solar assisted biomass-to-fuel conversion through gasification: A review," Jan. 17, 2023, Frontiers Media S.A. doi: 10.3389/fenrg.2022.1029477.
- A. M. Mauerhofer, F. Benedikt, J. C. Schmid, J. Fuchs, S. Müller, and H. Hofbauer, "Influence [86] of different bed material mixtures on dual fluidized bed steam gasification," *Energy*, vol. 157, pp. 957–968, 2018, doi: 10.1016/j.energy.2018.05.158.
- [87] A. Leclerc and F. Larachi, "Allothermal fluidized bed reactor for steam gasification of biomass," Sci Technol, vol. 43, 4, 390-428, Jul. 2015, doi: Instrum no. pp. 10.1080/10739149.2015.1010090.
- [88] G. Maitlo et al., "Thermochemical Conversion of Biomass for Syngas Production: Current Status and Future Trends," Sustainability (Switzerland), vol. 14, no. 5, Mar. 2022, doi: 10.3390/su14052596.
- S. Chopra and A. Jain, "A review of fixed bed gasification systems for biomass," Agricultural [89] Engineering International: the CIGR Ejournal. Invited Overview No. 5., vol. 9, Apr. 2007.
- J. Billaud, S. Valin, M. Peyrot, and S. Salvador, "Influence of H2O, CO2 and O2 addition on [90] biomass gasification in entrained flow reactor conditions: Experiments and modelling," Fuel, vol. 166, pp. 166–178, Feb. 2016, doi: 10.1016/j.fuel.2015.10.046.

- [91] X. Ku, T. Li, and T. Løvås, "Eulerian-lagrangian simulation of biomass gasification behavior in a high-temperature entrained-flow reactor," Energy and Fuels, vol. 28, no. 8, pp. 5184-5196, Aug. 2014, doi: 10.1021/ef5010557.
- [92] E. Henrich and F. Weirich, "Pressurized entrained flow gasifiers for biomass," *Environ Eng Sci*, vol. 21, no. 1, pp. 53–64, 2004, doi: 10.1089/109287504322746758.
- [93] M. Kaltschmitt, H. Hofbauer, and V. Lenz, Energie aus Biomasse, 4th editio. in Energie aus Biomasse. Wiesbaden: Springer Fachmedien Wiesbaden, 2024. doi: 10.1007/978-3-658-41216-6.
- [94] Y. Yang et al., "Recent advances in organic waste pyrolysis and gasification in a CO2 environment to value-added products," J Environ Manage, vol. 356, Apr. 2024, doi: 10.1016/j.jenvman.2024.120666.
- P. Premchand, F. Demichelis, D. Chiaramonti, S. Bensaid, and D. Fino, "Biochar production [95] from slow pyrolysis of biomass under CO2 atmosphere: A review on the effect of CO2 medium on biochar production, characterisation, and environmental applications," J Environ Chem Eng, vol. 11, no. 3, Jun. 2023, doi: 10.1016/j.jece.2023.110009.
- [96] Clarivate, "Document Search - Web of Science Core Collection," Web of Science. Accessed: Feb. 27, 2025. [Online]. Available: https://www.webofscience.com/wos/woscc/basic-search
- [97] H. Thunman et al., "Advanced biofuel production via gasification – lessons learned from 200 man-years of research activity with Chalmers' research gasifier and the GoBiGas demonstration plant," Energy Sci Eng, vol. 6, no. 1, pp. 6–34, 2018, doi: 10.1002/ese3.188.
- [98] H. C. Butterman and M. J. Castaldi, "CO2 as a carbon neutral fuel source via enhanced biomass gasification," Environ Sci Technol, vol. 43, no. 23, pp. 9030-9037, 2009, doi: 10.1021/es901509n.
- [99] S. Valin, L. Bedel, J. Guillaudeau, S. Thiery, and S. Ravel, "CO2 as a substitute of steam or inert transport gas in a fluidised bed for biomass gasification," Fuel, vol. 177, pp. 288–295, 2016, doi: 10.1016/j.fuel.2016.03.020.
- [100] G. Chang, J. Xie, Y. Huang, H. Liu, X. Yin, and C. Wu, "Gasification Reactivity and Pore Structure Development: Effect of Intermittent Addition of Steam on Increasing Reactivity of PKS Biochar with CO2," Energy and Fuels, vol. 31, no. 3, pp. 2887–2895, Mar. 2017, doi: 10.1021/acs.energyfuels.6b02859.
- [101] R. Xu, B. Dai, W. Wang, J. Schenk, A. Bhattacharyya, and Z. Xue, "Gasification Reactivity and Structure Evolution of Metallurgical Coke under H2O/CO2 Atmosphere," *Energy and Fuels*, vol. 32, no. 2, pp. 1188–1195, Feb. 2018, doi: 10.1021/acs.energyfuels.7b03023.

- [102] G. A. Olah, A. Goeppert, M. Czaun, T. Mathew, R. B. May, and G. K. S. Prakash, "Single Step Bi-reforming and Oxidative Bi-reforming of Methane (Natural Gas) with Steam and Carbon Dioxide to Metgas (CO-2H2) for Methanol Synthesis: Self-Sufficient Effective and Exclusive Oxygenation of Methane to Methanol with Oxygen," J Am Chem Soc, vol. 137, no. 27, pp. 8720– 8729, Jul. 2015, doi: 10.1021/jacs.5b02029.
- [103] J. Fuchs, J. C. Schmid, S. Müller, and H. Hofbauer, "Dual fluidized bed gasification of biomass with selective carbon dioxide removal and limestone as bed material: A review," Renewable and Sustainable Energy Reviews, vol. 107, no. June 2019, pp. 212-231, 2019, doi: 10.1016/j.rser.2019.03.013.
- [104] M. Mirparizi, F. Shakeriaski, F. Salehi, and C. Zhang, "Available challenges and recent progress in carbon dioxide capture, and reusing methods toward renewable energy," Aug. 01, 2023, Elsevier Ltd. doi: 10.1016/j.seta.2023.103365.
- [105] H. Thunman, C. Gustavsson, A. Larsson, I. Gunnarsson, and F. Tengberg, "Economic assessment of advanced biofuel production via gasification using cost data from the GoBiGas plant," Energy Sci Eng, vol. 7, no. 1, pp. 217–229, 2019, doi: 10.1002/ese3.271.
- [106] N. Couto, V. Silva, and A. Rouboa, "Municipal solid waste gasification in semi-industrial conditions using air-CO2 mixtures," Energy, vol. 104, pp. 42-52, Jun. 2016, doi: 10.1016/j.energy.2016.03.088.
- [107] Y. Okumura, "Detailed gasification process of woody biomass-derived char with H2O and CO2 gasifying agents," Journal of Thermal Science and Technology, vol. 15, no. 3, pp. 1–9, 2020, doi: 10.1299/jtst.2020jtst0035.
- [108] C. Guizani, "Effects of CO2 on the biomass pyro-gasification in High Heating Rate and Low Heating Rate conditions," Doctoral thesis, Ecole des Mines d'albi-Carmaux, 2014. [Online]. Available: https://theses.hal.science/tel-01146829v1
- [109] S. A. Salaudeen, B. Acharya, M. Heidari, P. Arku, and A. Dutta, "Numerical investigation of CO2 valorization via the steam gasification of biomass for producing syngas with flexible H2 to CO ratio," Journal of CO2 Utilization, vol. 27, pp. 32-41,Oct. 2018, doi: 10.1016/j.jcou.2018.07.003.
- [110] E. Curcio, "Techno-economic analysis of hydrogen production: Costs, policies, and scalability in the transition to net-zero," May 15, 2025, Elsevier Ltd. doi: 10.1016/j.ijhydene.2025.04.013.
- [111] F. Frieden and J. Leker, "Future costs of hydrogen: a quantitative review," Mar. 25, 2024, Royal Society of Chemistry. doi: 10.1039/d4se00137k.



- [112] M. Skorianz, "Classification of iron ores regarding their reduction behaviour in fluidized bed Dissertation, Montanuniversität Leoben, 2012. technologies," [Online]. Available: https://pure.unileoben.ac.at/en/publications/classification-of-iron-ores-regarding-theirreduction-behavior-in
- [113] M. Shahabuddin, G. Brooks, and M. A. Rhamdhani, "Decarbonisation and hydrogen integration of steel industries: Recent development, challenges and technoeconomic analysis," J Clean Prod, vol. 395, no. February, p. 136391, 2023, doi: 10.1016/j.jclepro.2023.136391.
- [114] H. Zhang et al., "Boosting the Conversion of CO2 with Biochar to Clean CO in an Atmospheric Plasmatron: A Synergy of Plasma Chemistry and Thermochemistry," ACS Sustain Chem Eng, vol. 10, no. 23, pp. 7712–7725, Jun. 2022, doi: 10.1021/acssuschemeng.2c01778.
- [115] Y. Chai, N. Packham, and M. Wang, "Process improvement analysis of pyrolysis/gasification of biomass and waste plastics with carbon capture and utilisation through process simulation," Fuel, vol. 324, Sep. 2022, doi: 10.1016/j.fuel.2022.124571.
- [116] P. He, Y. Xiao, Y. Tang, J. Zhang, and H. Song, "Simultaneous Low-Cost Carbon Sources and CO2 Valorizations through Catalytic Gasification," Energy and Fuels, vol. 29, no. 11, pp. 7497– 7507, Nov. 2015, doi: 10.1021/acs.energyfuels.5b01712.
- [117] S. Zhang, C. Liang, X. Wang, and Z. Zhu, "Experimental study and equilibrium analysis on thermal reduction of CO2 by CFB gasification," Journal of the Energy Institute, vol. 115, Aug. 2024, doi: 10.1016/j.joei.2024.101623.
- [118] S. Zhang, C. Liang, Z. Zhu, and R. Cui, "Experimental Study on the Thermal Reduction of CO2 by Activated Solid Carbon-Based Fuels," Energies (Basel), vol. 17, no. 9, May 2024, doi: 10.3390/en17092164.
- [119] R. Liu, R. Tsiava, S. Xu, and D. Chen, "Experimental study of char gasification characteristics with high temperature flue gas," Journal of the Energy Institute, vol. 97, no. April, pp. 187–193, 2021, doi: 10.1016/j.joei.2021.04.015.
- [120] J. Hunt, A. Ferrari, A. Lita, M. Crosswhite, B. Ashley, and A. E. Stiegman, "Microwave-specific enhancement of the carbon-carbon dioxide (boudouard) reaction," Journal of Physical Chemistry C, vol. 117, no. 51, pp. 26871–26880, Dec. 2013, doi: 10.1021/jp4076965.
- [121] A. Arregi et al., "Hydrogen-rich gas production by continuous pyrolysis and in-line catalytic reforming of pine wood waste and HDPE mixtures," Energy Convers Manag, vol. 136, pp. 192– 201, 2017, doi: 10.1016/j.enconman.2017.01.008.

- [122] A. A. Medvedev et al., "Influence of the Method of Fe Deposition on the Surface of Hydrolytic Lignin on the Activity in the Process of Its Conversion in the Presence of CO2," Int J Mol Sci, vol. 24, no. 2, Jan. 2023, doi: 10.3390/ijms24021279.
- [123] A. A. Medvedev et al., "Carbon Dioxide Assisted Conversion of Hydrolysis Lignin Catalyzed by Nickel Compounds," *Energies (Basel)*, vol. 15, no. 18, Sep. 2022, doi: 10.3390/en15186774.
- [124] A. A. Medvedev et al., "A Synergistic Effect of Potassium and Transition Metal Compounds on the Catalytic Behaviour of Hydrolysis Lignin in CO2-Assisted Gasification," Energies (Basel), vol. 16, no. 11, Jun. 2023, doi: 10.3390/en16114335.
- [125] A. A. Medvedev et al., "Carbon Dioxide-Assisted Gasification of Fresh and Pyrolysis Residues of Macadamia F.Muell Nutshells: The Catalytic Properties of Na, K, and Co," Catalysts, vol. 15, no. 1, Jan. 2025, doi: 10.3390/catal15010062.
- [126] H. A. Kibret, Y. L. Kuo, T. Y. Ke, and Y. H. Tseng, "Gasification of spent coffee grounds in a semi-fluidized bed reactor using steam and CO2 gasification medium," J Taiwan Inst Chem Eng, vol. 119, pp. 115–127, 2021, doi: 10.1016/j.jtice.2021.01.029.
- [127] P. Lahijani, M. Mohammadi, Z. A. Zainal, and A. R. Mohamed, "Improvement of biomass char-CO2 gasification reactivity using microwave irradiation and natural catalyst," Thermochim Acta, vol. 604, pp. 61–66, Mar. 2015, doi: 10.1016/j.tca.2015.01.016.
- [128] Y. Wu, S. Z. Li, Y. L. Niu, H. J. Yan, D. Yang, and J. Zhang, "Experimental investigation of CO2 conversion in Boudouard reaction driven by an atmospheric-pressure microwave plasma torch," J Phys D Appl Phys, vol. 56, no. 6, Feb. 2023, doi: 10.1088/1361-6463/acaeda.
- [129] Y. N. Chun and J. An, "Microwave Converter for High-Quality Fuel Production Applying Biochar-Combustion Gas," J Mater Cycles Waste Manag, vol. 25, no. 6, pp. 3395–3403, Nov. 2023, doi: 10.1007/s10163-023-01764-y.
- [130] J. Zhang et al., "Syngas production by integrating CO2 partial gasification of pine sawdust and methane pyrolysis over the gasification residue," Int J Hydrogen Energy, vol. 44, no. 36, pp. 19742–19754, Jul. 2019, doi: 10.1016/j.ijhydene.2019.06.014.
- [131] T. Renganathan, M. V. Yadav, S. Pushpavanam, R. K. Voolapalli, and Y. S. Cho, "CO2 utilization for gasification of carbonaceous feedstocks: A thermodynamic analysis," Chem Eng Sci, vol. 83, pp. 159–170, Dec. 2012, doi: 10.1016/j.ces.2012.04.024.
- [132] C. Rodríguez-M., "Surface adjustment of biochar via gasification," Master thesis, Technische Universität Wien, Wien, 2022. doi: 10.34726/hss.2022.102636.
- [133] S. Brunauer, P. H. Emmett, and E. Teller, "Adsorption of Gases in Multimolecular Layers," 1938, Accessed: Mar. 14, 2024. [Online]. Available: https://pubs.acs.org/sharingguidelines

- [134] J. Rouquerol, P. Llewellyn, and F. Rouquerol, "Is the bet equation applicable to microporous adsorbents?," Stud Surf Sci Catal, vol. 160, pp. 49-56, Jan. 2007, doi: 10.1016/S0167-2991(07)80008-5.
- [135] W. A. Brand, T. B. Coplen, J. Vogl, M. Rosner, and T. Prohaska, "Assessment of international reference materials for isotope-ratio analysis (IUPAC technical report)," Pure and Applied Chemistry, vol. 86, no. 3, pp. 425–467, 2014, doi: 10.1515/pac-2013-1023.
- [136] IUPAC Commission on Atomic Weights and Isotopic Abundances, "Atomic weights of the elements 1991," J. Phys. Chem. Ref. Data, vol. 22, pp. 1571–1584, 1993, doi: 10.1063/1.555933.
- [137] S. Flude, G. Johnson, S. M. V. Gilfillan, and R. S. Haszeldine, "Inherent Tracers for Carbon Capture and Storage in Sedimentary Formations: Composition and Applications," Environ Sci Technol, vol. 50, no. 15, pp. 7939–7955, 2016, doi: 10.1021/acs.est.6b01548.
- [138] J. Karl and T. Pröll, "Steam gasification of biomass in dual fluidized bed gasifiers: A review," Renewable and Sustainable Energy Reviews, vol. 98, no. August, pp. 64-78, 2018, doi: 10.1016/j.rser.2018.09.010.
- [139] F. Benedikt, M. Kuba, J. C. Schmid, S. Müller, and H. Hofbauer, "Assessment of correlations between tar and product gas composition in dual fluidized bed steam gasification for online tar prediction," 2019, Elsevier. doi: 10.1016/j.apenergy.2019.01.181.
- [140] H. Hofbauer and R. Rauch, "Stoichiometric Water Consumption of Steam Gasification by the FICFB-Gasification Process," in Progress in Thermochemical Biomass Conversion (Vol.1), Blackwell Science Ltd, 2001, pp. 199–208.
- [141] S. Karellas and J. Karl, "Analysis of the product gas from biomass gasification by means of laser spectroscopy," Opt Lasers Eng, vol. 45, 9, 935–946, 2007. doi: no. pp. 10.1016/j.optlaseng.2007.03.006.
- [142] J. Vogler, L. Stanger, A. Bartik, A. Schirrer, and M. Kozek, "Soft Sensor Design for Product Gas Composition Monitoring Including Fault Isolation in a Dual Fluidized Bed Biomass Gasifier," in 2024 International Conference on Control, Automation and Diagnosis (ICCAD), IEEE, 2024, pp. 1-6. doi: 10.1109/ICCAD60883.2024.10553785.
- [143] GATS, "Calculation of molecular spectra with the Spectral Calculator," 1994. [Online]. Available: http://www.spectralcalc.com/info/CalculatingSpectra.pdf
- [144] I. E. Gordon et al., "The HITRAN2020 molecular spectroscopic database," J Quant Spectrosc Radiat Transf, vol. 277, p. 107949, 2022, doi: 10.1016/j.jqsrt.2021.107949.
- [145] C. W. Bale et al., "FactSage thermochemical software and databases, 2010-2016," CALPHAD, vol. 54, pp. 35-53, Sep. 2016, doi: 10.1016/j.calphad.2016.05.002.

- [146] E. Perz, "A computer method for thermal power cycle calculation," Proceedings of the ASME Turbo Expo, vol. 4, no. April, 1990, doi: 10.1115/90-GT-351.
- [147] SimTech GmbH, "The Process Simulation Environment IPSEpro." Accessed: Mar. 24, 2025. [Online]. Available: https://simtechnology.com/ipsepro/process-simulation-and-heat-balancesoftware
- [148] T. Pröll and H. Hofbauer, "Development and application of a simulation tool for biomass gasification based processes," International Journal of Chemical Reactor Engineering, vol. 6, no. January 2008, 2008, doi: 10.2202/1542-6580.1769.
- [149] T. Pröll, C. Aichernig, R. Rauch, and H. Hofbauer, "Fluidized bed steam gasification of solid biomass - Performance characteristics of an 8 MWth combined heat and power plant," International Journal of Chemical Reactor Engineering, vol. 5, no. January, 2007, doi: 10.2202/1542-6580.1398.
- [150] World Steel Association (worldsteel), "worldsteel Short Range Outlook October 2023," 2023. 2024. [Online]. Available: https://worldsteel.org/media/pressreleases/2023/worldsteel-short-range-outlook-october-2023
- [151] M. Nakamizu, "Latest developments in steelmaking capacity and outlook until 2026," Jun. 2024. [Online]. Available: http://www.oecd.org/termsandconditions.
- [152] A. Trinca, D. Patrizi, N. Verdone, C. Bassano, and G. Vilardi, "Toward green steel: Modeling and environmental economic analysis of iron direct reduction with different reducing gases," J Clean Prod, vol. 427, Nov. 2023, doi: 10.1016/j.jclepro.2023.139081.
- [153] A. Nurdiawati, I. N. Zaini, W. Wei, R. Gyllenram, W. Yang, and P. Samuelsson, "Towards fossilfree steel: Life cycle assessment of biosyngas-based direct reduced iron (DRI) production process," J Clean Prod, vol. 393. 136262, 2023, no. January, p. 10.1016/j.jclepro.2023.136262.
- [154] I. N. Zaini et al., "Decarbonising the iron and steel industries: Production of carbon-negative direct reduced iron by using biosyngas," Energy Convers Manag, vol. 281, no. February, p. 116806, 2023, doi: 10.1016/j.enconman.2023.116806.
- [155] M. Hammerschmid, S. Müller, J. Fuchs, and H. Hofbauer, "Evaluation of biomass-based production of below zero emission reducing gas for the iron and steel industry," Biomass Convers Biorefin, vol. 11, no. 1, pp. 169–187, 2021, doi: 10.1007/s13399-020-00939-z.
- [156] F. Patisson, O. Mirgaux, and J. P. Birat, "Hydrogen steelmaking. Part 1: Physical chemistry and process metallurgy," Materiaux et Techniques, vol. 109, no. 3-4, pp. 1-10, 2021, doi: 10.1051/mattech/2021025.

- [157] M. L. Ali, Q. Fradet, and U. Riedel, "Kinetic Mechanism Development for the Direct Reduction of Single Hematite Pellets in H2/CO Atmospheres," Steel Res Int, vol. 93, no. 12, 2022, doi: 10.1002/srin.202200043.
- [158] T. Bürgler and A. Di Donato, "Biomass gasification for DRI production," La Revue de Métallurgie, 2009, doi: 10.1051/metal/2009075.
- [159] Inc. Midrex Technologies, "MIDREX® Process Midrex Technologies, Inc." Accessed: Oct. 15, 2024. [Online]. Available: https://www.midrex.com/technology/midrex-process/
- [160] A. M. Mauerhofer, J. Fuchs, S. Müller, F. Benedikt, J. C. Schmid, and H. Hofbauer, "CO2 gasification in a dual fluidized bed reactor system: Impact on the product gas composition," 2019. doi: 10.1016/j.fuel.2019.04.168.
- [161] A. Shams and F. Moazeni, "Modeling and Simulation of the MIDREX Shaft Furnace: Reduction, Transition and Cooling Zones," Jom, vol. 67, no. 11, pp. 2681–2689, 2015, doi: 10.1007/s11837-015-1588-0.
- [162] D. R. Parisi and M. A. Laborde, "Modeling of counter current moving bed gas-solid reactor used in direct reduction of iron ore," Chemical Engineering Journal, vol. 104, no. 1–3, pp. 35–43, 2004, doi: 10.1016/j.cej.2004.08.001.
- [163] G. Xu, F. Liang, Y. Yang, Y. Hu, K. Zhang, and W. Liu, "An improved CO2 separation and purification system based on cryogenic separation and distillation theory," *Energies (Basel)*, vol. 7, no. 5, pp. 3484–3502, 2014, doi: 10.3390/en7053484.
- [164] S. Müller, "Hydrogen from biomass for industry industrial application of hydrogen production based on dual fluid gasification," Dissertation, Technische Universität Wien, 2013. [Online]. Available: https://resolver.obvsg.at/urn:nbn:at:at-ubtuw:1-96540
- [165] J. Solar et al., "Influence of temperature and residence time in the pyrolysis of woody biomass waste in a continuous screw reactor," Biomass Bioenergy, vol. 95, pp. 416-423, 2016, doi: 10.1016/j.biombioe.2016.07.004.
- [166] F. Farhadi, M. Y. Motamed Hashemi, and M. Bahrami Babaheidari, "Modelling and simulation of syngas unit in large scale direct reduction plant," Ironmaking and Steelmaking, vol. 30, no. 1, pp. 18–24, 2003, doi: 10.1179/030192303225009515.
- [167] Y. Cheng, Z. Thow, and C. H. Wang, "Biomass gasification with CO2 in a fluidized bed," *Powder* Technol, vol. 296, pp. 87–101, 2016, doi: 10.1016/j.powtec.2014.12.041.
- [168] European Commission, "COMMISSION IMPLEMENTING REGULATION (EU) 2018/2066 of 19 December 2018 on the monitoring and reporting of greenhouse gas emissions pursuant to

- Directive 2003/87/EC of the European Parliament and of the Council and amending Commission Regulation (EU) No 601/2012 (Text with EEA relevance)," Jul. 2024.
- [169] European Commission, "DIRECTIVE (EU) 2018/2001 OF THE EUROPEAN PARLIAMENT AND OF THE COUNCIL of 11 December 2018 on the promotion of the use of energy from renewable sources (recast) (Text with EEA relevance)," Jul. 2024.
- [170] W. Rickels, A. Proelß, O. Geden, J. Burhenne, and M. Fridahl, "Integrating Carbon Dioxide Removal Into European Emissions Trading," Frontiers in Climate, vol. 3, no. June, pp. 1–10, 2021, doi: 10.3389/fclim.2021.690023.
- [171] L. Schuett, "Permanence and Liability: Legal Considerations on the Integration of Carbon Dioxide Removal into the EU Emissions Trading System," Transnational Environmental Law, vol. 13, no. 1, pp. 87–110, 2024, doi: 10.1017/S2047102524000013.
- [172] Directorate-General for Climate Action, "Carbon Removals and Carbon Farming European Commission." Accessed: Dec. 04, 2024. [Online]. Available: https://climate.ec.europa.eu/euaction/carbon-removals-and-carbon-farming en
- [173] D. Fritz, M. Gössl, E. Hatzl, S. Poupa, W. Pölz, and H. Schreiber, "Harmonisierte österreichische direkte ud indirekte THG-Emissionsfaktoren für relevante Energieträger & Technologien," Wien, 2023. Accessed: Nov. 26, 2024. [Online]. Available: https://www.umweltbundesamt.at/fileadmin/site/publikationen/rep0888.pdf
- [174] Federal Environmental Agency Austria (Umweltbundesamt), "Berechnung von Treibhausgas (THG)-Emissionen verschiedener Energieträger," HARMONISIERTE ÖSTERREICHISCHE UND INDIREKTE THG-EMISSIONSFAKTOREN FÜR ENERGIETRÄGER & TECHNOLOGIEN. Accessed: Nov. 26, 2024. [Online]. Available: https://secure.umweltbundesamt.at/co2mon/co2mon.html
- [175] G. Wernet, C. Bauer, B. Steubing, J. Reinhard, E. Moreno-Ruiz, and B. Weidema, "The ecoinvent database version 3 (part I): overview and methodology," International Journal of Life Cycle Assessment, vol. 21, no. 9, pp. 1218–1230, Sep. 2016, doi: 10.1007/s11367-016-1087-8.
- [176] [dataset] system/ecoinvent, "Market for iron pellet, GLO, Allocation, APOS, ecoinvent 3.10.1," Dec. 31, 2023.
- [177] [dataset] D. FitzGerald/ecoinvent, "Market for triethylene glycol, RER, Allocation, APOS, ecoinvent 3.10.1," Dec. 31, 2023.
- [178] [dataset] system/ecoinvent, "Market for monoethanolamine, GLO, Allocation, APOS, ecoinvent 3.10.1.," Dec. 31, 2023.

- [179] [dataset] system/ecoinvent, "Market for fatty acid methyl ester, RoW, Allocation, APOS, ecoinvent 3.10.1," Dec. 31, 2023.
- [180] [dataset] system/ecoinvent, "Market for silica sand, GLO, Allocation, APOS, ecoinvent 3.10.1," Dec. 31, 2023.
- [181] [dataset] F. Werner/ecoinvent, "Market for wood chips, wet, measured as dry mass, Europe without Switzerland, Allocation, APOS, econvent database version 3.10.1.," Dec. 31, 2023.
- [182] [dataset] K. Treyer/ecoinvent, "Market for electricity high voltage, AT, Allocation, APOS, ecoinvent database version 3.10.1.," Dec. 31, 2023.
- [183] [dataset] M. Faist Emmenegger/ecoinvent, "Market for natural gas, high pressure, AT, Allocation, APOS, ecoinvent database version 3.10.1.," Dec. 31, 2023.
- [184] R. Sinnott and G. Towler, Chemical Engineering Design, 6th ed. Oxford: Butterworth-Heinemann (Coulson & Richardson's chemical engineering series), 2019.
- [185] D. W. Green and M. Z. Southard, Perry's Chemical Engineers' Handbook. McGraw-Hill 2019. Education, Accessed: Oct. 06, 2023. [Online]. Available: https://www.accessengineeringlibrary.com/content/book/9780071834087
- [186] D. O. Kunysz, Kostenschätzung im chemischen Anlagenbau. Leverkusen: Springer Fachmedien Wiesbaden GmbH, 2020. doi: 10.1007/978-3-658-29251-5.
- [187] V. Gubin et al., "Hydrogen production from woody biomass gasification: a techno-economic analysis," Biofuels, Bioproducts and Biorefining, vol. 18, no. 4, pp. 818-836, 2024, doi: 10.1002/bbb.2647.
- [188] K. Sahoo, A. Upadhyay, T. Runge, R. Bergman, M. Puettmann, and E. Bilek, "Life-cycle assessment and techno-economic analysis of biochar produced from forest residues using portable systems," International Journal of Life Cycle Assessment, vol. 26, no. 1, pp. 189–213, 2021, doi: 10.1007/s11367-020-01830-9.
- [189] T. Zimmer, A. Rudi, S. Glöser-Chahoud, and F. Schultmann, "Techno-Economic Analysis of Intermediate Pyrolysis with Solar Drying: A Chilean Case Study," *Energies (Basel)*, vol. 15, no. 6, 2022, doi: 10.3390/en15062272.
- [190] T. Toan Vu, J. Seo, E. Kim, S. G. Ryoo, B. C. Park, and D. Song, "Techno-economic analysis of integrated MIDREX process with CO2 capture and storage: Evaluating sustainability and viability for iron production," Process Safety and Environmental Protection, vol. 189, no. May, pp. 1314–1322, 2024, doi: 10.1016/j.psep.2024.07.005.

- [191] M. Arvidsson, M. Morandin, and S. Harvey, "Biomass gasification-based syngas production for a conventional oxo synthesis plant - Greenhouse gas emission balances and economic evaluation," J Clean Prod, vol. 99, pp. 192–205, 2015, doi: 10.1016/j.jclepro.2015.03.005.
- [192] S. Heyne and S. Harvey, "Impact of choice of CO2 separation technology on thermo-economic performance of Bio-SNG production processes," Int J Energy Res, vol. 38, no. 3, pp. 299–318, Mar. 2014, doi: 10.1002/ER.3038.
- [193] K. Li, W. Leigh, P. Feron, H. Yu, and M. Tade, "Systematic study of aqueous monoethanolamine (MEA)-based CO2 capture process: Techno-economic assessment of the MEA process and its improvements," *Appl Energy*, vol. 165, pp. 648–659, 2016, doi: 10.1016/j.apenergy.2015.12.109.
- [194] B. Batidzirai, A. P. R. Mignot, W. B. Schakel, H. M. Junginger, and A. P. C. Faaij, "Biomass torrefaction technology: Techno-economic status and future prospects," *Energy*, vol. 62, pp. 196– 214, 2013, doi: 10.1016/j.energy.2013.09.035.
- [195] M. Veress, "Optimization of a process concept for the industrial production of Bio-SNG from low-grade fuels," Master thesis, Technische Universität Wien, 2020. doi: 10.34726/hss.2020.63703.
- [196] T. Poudel, S. Bhandari, Y. Thapa, and S. Nepal, "Design of Major Components of Green Urea Production Plant," International Journal on Engineering Technology, vol. 1, no. 2, pp. 132–148, Jun. 2024, doi: 10.3126/injet.v1i2.66724.
- [197] F. Rosner et al., "Green steel: design and cost analysis of hydrogen-based direct iron reduction," Energy Environ Sci, vol. 16, no. 10, pp. 4121–4134, 2023, doi: 10.1039/d3ee01077e.
- [198] C. Zhou, K. Shah, and B. Moghtaderi, "Techno-economic assessment of integrated chemical looping air separation for oxy-fuel combustion: An Australian case study," Energy and Fuels, vol. 29, no. 4, pp. 2074–2088, Apr. 2015, doi: 10.1021/ef5022076.
- [199] "Marktpreise Hackschnitzel C.A.R.M.E.N. e.V." Accessed: Oct. 29, 2024. [Online]. Available: https://www.carmen-ev.de/service/marktueberblick/marktpreise-energieholz/marktpreisehackschnitzel/
- [200] "Österreich Gaspreis Industrie 2024 | Statista." Accessed: Nov. 12, 2024. [Online]. Available: https://de.statista.com/statistik/daten/studie/323647/umfrage/gaspreise-fuer-industriekunden-inoesterreich/
- [201] "Austria: monthly electricity prices 2024 | Statista." Accessed: Nov. 12, 2024. [Online]. https://www.statista.com/statistics/1271527/austria-monthly-wholesale-electricity-Available: price/

- [202] V. Moen, "The Economics of Carbon Capture and Storage," Master thesis, University of Stavanger, 2023. Accessed: Nov. 12, 2024. [Online]. Available: https://uis.brage.unit.no/uisxmlui/bitstream/handle/11250/3087156/no.uis%3Ainspera%3A152006185%3A94025276.pdf? sequence=1&isAllowed=y
- [203] BloombergNEF, "Forecast European Union Emissions Trading System (EU-ETS) average carbon allowance prices from 2024 to 2035 (in euros per metric ton of CO2 equivalent)." Accessed: Nov. 12, 2024. [Online]. Available: https://www.statista.com/statistics/1401657/forecast-average-carbon-price-eu-emissionstrading-system/
- [204] DBFZ Deutsches Biomasseforschungszentrum gemeinnützige GmbH/Helmholtz-Zentrum für GmbH - UFZ/Universität Leipzig et al., Methodenhandbuch Stoffstromorientierte Bilanzierung der Klimagaseffekte - Methoden zur Bestimmung von Technologiekennwerten, Gestehungskosten und Klimagaseffekten von Vorhaben im Rahmen der energetischen Biomassenutzung, 5th ed. DBFZ Deutsches Biomasseforschungszentrum gemeinnützige GmbH, 2021. doi: 10.48480/ddpt-ys74.
- [205] H. Hofbauer, A. M. Mauerhofer, F. Benedikt, H. Martin, A. Bartik, and M. Veress, "Reallabor zur Herstellung von Holzdiesel und Holzgas aus Biomasse und biogenen Reststoffen für die Land- und Forstwirtschaft," p. 218, 2020, Accessed: Apr. 25, 2025. [Online]. Available: http://hdl.handle.net/20.500.12708/40216
- [206] H. Hofbauer, M. Bolhar-Nordenkampf, M. Kaltschmitt, and A. Vogel, *Analyse und Evaluierung* der thermo-chemischen Vergasung von Biomasse - in Schriftenreihe "Nachwachsende Rohstoffe" Band 29. Landwirtschaftsverlag GmbH, 2006. Accessed: Nov. 12, 2024. [Online]. Available: http://hdl.handle.net/20.500.12708/22263
- [207] "Iron Ore PRICE Today | Iron Ore Spot Price Chart | Live Price of Iron Ore per Ounce | Markets Insider." Accessed: Nov. 12, 2024. [Online]. Available: https://markets.businessinsider.com/commodities/iron-ore-price
- [208] "Cooling Water Costs | Current and Forecast | Intratec.us." Accessed: Oct. 06, 2023. [Online]. Available: https://www.intratec.us/products/water-utility-costs/commodity/cooling-water-cost
- [209] "Consumer price index (CPI/HICP) STATISTICS AUSTRIA The Information Manager." Accessed: Nov. 12, 2024. [Online]. Available: https://www.statistik.at/en/statistics/nationaleconomy-and-public-finance/prices-and-price-indices/consumer-price-index-cpi/-hicp
- [210] M. Baerns et al., Technische Chemie, 1. Edition. Weinheim: WILEY-VCH, 2006.

- [211] F. Kirnbauer and H. Hofbauer, "The mechanism of bed material coating in dual fluidized bed biomass steam gasification plants and its impact on plant optimization," Powder Technol, vol. 245, no. 2013, pp. 94–104, 2013, doi: 10.1016/j.powtec.2013.04.022.
- [212] S. Koppatz, C. Pfeifer, and H. Hofbauer, "Comparison of the performance behaviour of silica sand and olivine in a dual fluidised bed reactor system for steam gasification of biomass at pilot plant scale," Chemical Engineering Journal, vol. 175, no. 1, pp. 468-483, 2011, doi: 10.1016/j.cej.2011.09.071.
- [213] R. Béchara, H. Hamadeh, O. Mirgaux, and F. Patisson, "Optimization of the iron ore direct reduction process through multiscale process modeling," *Materials*, vol. 11, no. 7, pp. 1–18, 2018, doi: 10.3390/ma11071094.
- [214] "EU-ETS price 2022-2024 | Statista." Accessed: Nov. 12, 2024. [Online]. Available: https://www.statista.com/statistics/1322214/carbon-prices-european-union-emission-tradingscheme/
- [215] G. Mantulet, A. Peffen, and S. Cail, "Carbon price forecast under the EU ETS," Nov. 2023. Accessed: Apr. 01, 2025. [Online]. Available: https://www.enerdata.net/publications/executivebriefing/carbon-price-forecast-under-eu-ets.pdf
- [216] E. Zeyen, S. Kalweit, M. Victoria, and T. Brown, "Shifting burdens: How delayed decarbonisation of road transport affects other sectoral emission reductions," Environmental Research Letters, Mar. 2025, doi: 10.1088/1748-9326/adc290.
- [217] Y. Ngernyen, C. Tangsathitkulchai, and M. Tangsathitkulchai, "Porous properties of activated carbon produced from Eucalyptus and Wattle wood by carbon dioxide activation," Korean Journal of Chemical Engineering, vol. 23, no. 6, pp. 1046-1054, Nov. 2006, doi: 10.1007/S11814-006-0028-9/METRICS.
- [218] C. F. Chang, C. Y. Chang, and W. T. Tsai, "Effects of burn-off and activation temperature on preparation of activated carbon from corn cob agrowaste by CO2 and steam," J Colloid Interface Sci, vol. 232, no. 1, pp. 45–49, Dec. 2000, doi: 10.1006/jcis.2000.7171.
- [219] J. Pallarés, A. González-Cencerrado, and I. Arauzo, "Production and characterization of activated carbon from barley straw by physical activation with carbon dioxide and steam," Biomass Bioenergy, vol. 115, pp. 64–73, Aug. 2018, doi: 10.1016/j.biombioe.2018.04.015.
- [220] H. Bin Kim, J. G. Kim, T. Kim, D. S. Alessi, and K. Baek, "Interaction of biochar stability and abiotic aging: Influences of pyrolysis reaction medium and temperature," Chemical Engineering Journal, vol. 411, May 2021, doi: 10.1016/j.cej.2021.128441.

- [221] B. M. Ohsowski, K. Dunfield, J. N. Klironomos, and M. M. Hart, "Plant response to biochar, compost, and mycorrhizal fungal amendments in post-mine sandpits," Restor Ecol, vol. 26, no. 1, pp. 63–72, Jan. 2018, doi: 10.1111/rec.12528.
- [222] M. Ahmad, S. S. Lee, S. E. Lee, M. I. Al-Wabel, D. C. W. Tsang, and Y. S. Ok, "Biochar-induced changes in soil properties affected immobilization/mobilization of metals/metalloids in contaminated soils," J Soils Sediments, vol. 17, no. 3, pp. 717-730, Mar. 2017, doi: 10.1007/s11368-015-1339-4.
- [223] S. Koppatz, C. Pfeifer, R. Rauch, H. Hofbauer, T. Marquard-Moellenstedt, and M. Specht, "H2 rich product gas by steam gasification of biomass with in situ CO2 absorption in a dual fluidized bed system of 8 MW fuel input," Fuel Processing Technology, vol. 90, no. 7–8, pp. 914–921, Jul. 2009, doi: 10.1016/j.fuproc.2009.03.016.
- [224] S. Lin, M. Harada, Y. Suzuki, and H. Hatano, "Continuous experiment regarding hydrogen production by coal/CaO reaction with steam (I) gas products," Fuel, vol. 83, no. 7–8, pp. 869– 874, May 2004, doi: 10.1016/j.fuel.2003.10.030.
- [225] J. Xu et al., "Raman spectroscopy as a versatile tool for investigating thermochemical processing of coal, biomass, and wastes: Recent advances and future perspectives," Energy and Fuels, vol. 35, no. 4, pp. 2870–2913, 2021, doi: 10.1021/acs.energyfuels.0c03298.
- [226] H. Bidgoli, S. Cherednichenko, J. Nordmark, H. Thunman, and M. Seemann, "Terahertz Spectroscopy for Real-Time Monitoring of Water Vapor and CO Levels in the Producer Gas From an Industrial Biomass Gasifier," *IEEE Trans Terahertz Sci Technol*, vol. 4, no. 6, pp. 722– 733, 2014, doi: 10.1109/TTHZ.2014.2357344.
- [227] Y. Song, Z. Wang, J. Loh, and M. J. Thomson, "High-Temperature H2O Vapor Measurement Using Terahertz Spectroscopy for Industrial Furnace Applications," IEEE Trans Terahertz Sci Technol, vol. 6, no. 1, pp. 26–31, 2016, doi: 10.1109/TTHZ.2015.2503702.
- [228] A. Sepman, C. Fredriksson, Y. Ögren, and H. Wiinikka, "Laser-based, optical, and traditional diagnostics of no and temperature in 400 kw pilot-scale furnace," Applied Sciences (Switzerland), vol. 11, no. 15, 2021, doi: 10.3390/app11157048.
- [229] A. Sepman, J. Wennebro, J. Fernberg, and H. Wiinikka, "Following fuel conversion during biomass gasification using tunable diode laser absorption spectroscopy diagnostics," Fuel, vol. 374, no. July, p. 132374, 2024, doi: 10.1016/j.fuel.2024.132374.
- [230] I. W. Sudiarta and P. Chýlek, "Mie scattering by a spherical particle in an absorbing medium," Appl Opt, vol. 41, no. 18, p. 3545, 2002, doi: 10.1364/ao.41.003545.

- [231] Y. Wang, P. Zhao, W. Gao, and X. Chen, "Optimization of forward-scattered light energy and decoherence of Mie scattering for speckle suppression," Opt Quantum Electron, vol. 47, no. 2, pp. 235–246, 2015, doi: 10.1007/s11082-014-9907-1.
- [232] A. Sepman, Y. Ögren, M. Gullberg, and H. Wiinikka, "Development of TDLAS sensor for diagnostics of CO, H2O and soot concentrations in reactor core of pilot-scale gasifier," Appl Phys B, vol. 122, no. 2, pp. 1–12, 2016, doi: 10.1007/s00340-016-6319-x.
- [233] A. Sepman, Y. Ögren, Z. Qu, H. Wiinikka, and F. M. Schmidt, "Real-time in situ multi-parameter TDLAS sensing in the reactor core of an entrained-flow biomass gasifier," Proceedings of the Combustion Institute, vol. 36, no. 3, pp. 4541–4548, 2017, doi: 10.1016/j.proci.2016.07.011.
- [234] M. Behrens, "Chemical hydrogen storage by methanol: Challenges for the catalytic methanol synthesis from CO2," Recyclable Catalysis, vol. 2, no. 1, Mar. 2016, doi: 10.1515/recat-2015-0009.
- [235] S. Kraft, F. Kirnbauer, and H. Hofbauer, "CPFD simulations of an industrial-sized dual fluidized bed steam gasification system of biomass with 8 MW fuel input," Appl Energy, vol. 190, pp. 408–420, 2017, doi: 10.1016/j.apenergy.2016.12.113.
- [236] IEA, IRENA, and UN Climate Change High-Level Champions, "Breakthrough Agenda Report 2023," Paris, 2023. Accessed: Oct. 15, 2024. [Online]. Available: https://www.iea.org/reports/breakthrough-agenda-report-2023
- [237] "Iron & steel IEA." Accessed: Oct. 16, 2024. [Online]. Available: https://www.iea.org/energysystem/industry/steel#tracking
- [238] K. Benavides et al., "Mitigating emissions in the global steel industry: Representing CCS and hydrogen technologies in integrated assessment modeling," International Journal of Greenhouse Gas Control, vol. 131, Jan. 2024, doi: 10.1016/j.ijggc.2023.103963.

# **List of Figures**

Figure 1: Closing carbon life cycles by carbon capture and utilization (CCU) and carbon capture and
storage (CCS). The figure was adapted from [12]
Figure 2: Estimated renewable $CO_2$ capture cost vs. global capacity and demand by the middle of the
21st century. Figure was produced using data from [12], [28] for capture cost and capacity and [27] for
sectoral demand
Figure 3: Thesis outline – core and related research on biomass $\mathrm{CO}_2$ gasification grouped by scope and
method
Figure 4: Phases of thermochemical fuel conversion organized by temperature and equivalence ratio $\lambda$ .
$Redrawn\ following\ [71]\ with\ additional\ information\ from\ [47],\ [48],\ [70],\ [73],\ [74]10$
Figure 5: Areas of significant design differences between biomass gasifiers [47], [73]
Figure 6: Original research articles on biomass CO2 gasification. The Web of Science Topic function
searches title, abstract, keyword plus, and author keywords. Certain data included herein are derived
from Clarivate <sup>TM</sup> (Web of Science <sup>TM</sup> ) [96]. © Clarivate 2025. All rights reserved
Figure 7: CO <sub>2</sub> utilization reporting in literature as of March 2025: Original research articles outside this
thesis sampled by searching for the topics of "biomass" & "gasification" & (" $CO_2$ conver" OR " $CO_2$
utili). Certain data included herein are derived from Clarivate $^{TM}$ (Web of Science $^{TM}$ ) [96]. © Clarivate
2025. All rights reserved
Figure 8: Mol CO (black line) formed from C (green line) and $CO_2$ (blue line) by the Boudouard reaction
as a function of temperature. The gas composition was calculated by Gibbs energy minimization in HSC
Chemistry 6 at 1 bar <sub>a</sub>
Figure 9: a) Schematic and b) photograph of the gasifier unit "Nero". a) is reprinted from [JA II] 22
Figure 10: Schematic and photograph of the gasifier "FRU" with sample extraction cage. The figure is
reprinted from [CA I]
Figure 11: Schematic and photographs of the dual fluidized bed gasifier. a) Product gas pathway
(reprinted from [JA III]), b) upper reactor part, c) lower reactor part
Figure 12: Schematic and photograph of the developed laser setup for quantifying $H_2O$ in hot and raw
product gas. Both sub-figures are reprinted from [JA III]
Figure 13: Overview of simulated process routes in JA IV. References for gasification datasets are as
follows: "Mauerhofer, 2021"=[52], "Müller, 2024"=[JA II]. The figure is adjusted from [JA IV] 31 $$
$Figure\ 14: Simplified\ semi-empirical\ CO_{2}\ conversion\ model\ (filled\ lattice),\ thermodynamic\ equilibrium$
(empty lattice), and experimentally observed values (arrow tips) for CO2 conversion. The figure is
reprinted from [JA I]
Figure 15: Product gas composition: Measured concentrations (full bars) vs. thermodynamic equilibrium
concentrations calculated in FactSage (checkered bars). $H_2O$ concentrations result from mass balancing.
The figure is adjusted from [JA II].

Figure 16: Graphical abstract showing how carbon enters the reactor via CO <sub>2</sub> and biomass, where
various thermochemical conversion processes convert it to product gas. The figure is reprinted from [JA
II]45
Figure 17: Parental carbon sources of CO and CO2 in the product gas. The figure is reprinted from [JA
II]45
Figure 18: Comparison of new CO <sub>2</sub> conversion measurement with previous estimation methods. The
figure is reprinted from [JA II]
Figure 19: Main mass and energy flows for one investigated Biomass CO <sub>2</sub> Gasification-Direct Reduction
Ironmaking (BCG-DRI) route. The process uses air (AIR) for combustion. (LC) stands for Low
Conversion of CO <sub>2</sub> during gasification. SH=Sensible Heat, LHV=Lower Heating Value,
ISBL/OSBL=Inside/Outside Battery Limit. The figure is reprinted from [JA IV]
Figure 20: Main mass and energy flows for one investigated Biomass CO <sub>2</sub> Gasification-Direct Reduction
Ironmaking (BCG-DRI) route. The process uses air (AIR) for combustion. (MC) stands for Medium
Conversion of CO <sub>2</sub> during gasification. SH=Sensible Heat, LHV=Lower Heating Value,
ISBL/OSBL=Inside/Outside Battery Limit. The figure is reprinted from [JA IV]
Figure 21: Levelized cost and cradle-to-gate CO <sub>2</sub> -equivalent emissions of producing cold direct reducing
iron. The figure is reprinted from [JA IV]
Figure 22: Summary of two-step surface adjustment procedure including torrefaction and CO <sub>2</sub>
gasification of Pinus sylvestris wood pellets. The figure was adjusted from [CA I]55
Figure 23: a) BET surface area of biochar, b) Surface yield from raw biomass to biochar. The figure is
reprinted from [CA I]
Figure 24: a) gas sampling point and b) sampling line used to test the novel THz quantum cascade laser
during experiments with the advanced 100 kWth dual fluidized bed pilot gasifier. Both sub-figures are
reprinted from [JA III]
Figure 25: a) First tests of the novel QCL setup in synthetic gas mixtures prepared in gas mixing setup,
and b) Measurement in raw product gas with significant tar loading from waste wood gasification. Both
sub-figures are reprinted from [JA III]

# **List of Tables**

Table 1: Thermochemical biomass conversion reactions [47], [48], [71], [74]. The reaction er	thalpies at
850 °C were calculated using HSC Chemistry 6	11
Table 2: Key information about the single-bed fluidized bed gasifier #1 (Nero)	21
Table 3: Key information about the single-bed fluidized bed gasifier #2 (FRU)	22
Table 4: Key information about the advanced 100 kWth dual fluidized bed pilot plant	23
Table 5: CO <sub>2</sub> e emission factors used for CF <sub>LCA</sub> carbon footprint calculation	35
Table 6: Economic parameters assumed for techno-economic calculations	37
Table 7: Experimental parameters investigated in 53 experiments in JA I	39
Table 8: Summary of experimental data in JA II	41
Table 9: Key performance indicators for each simulated process route in JA IV	51
Table 10: Investigated CO <sub>2</sub> gasification conditions	55

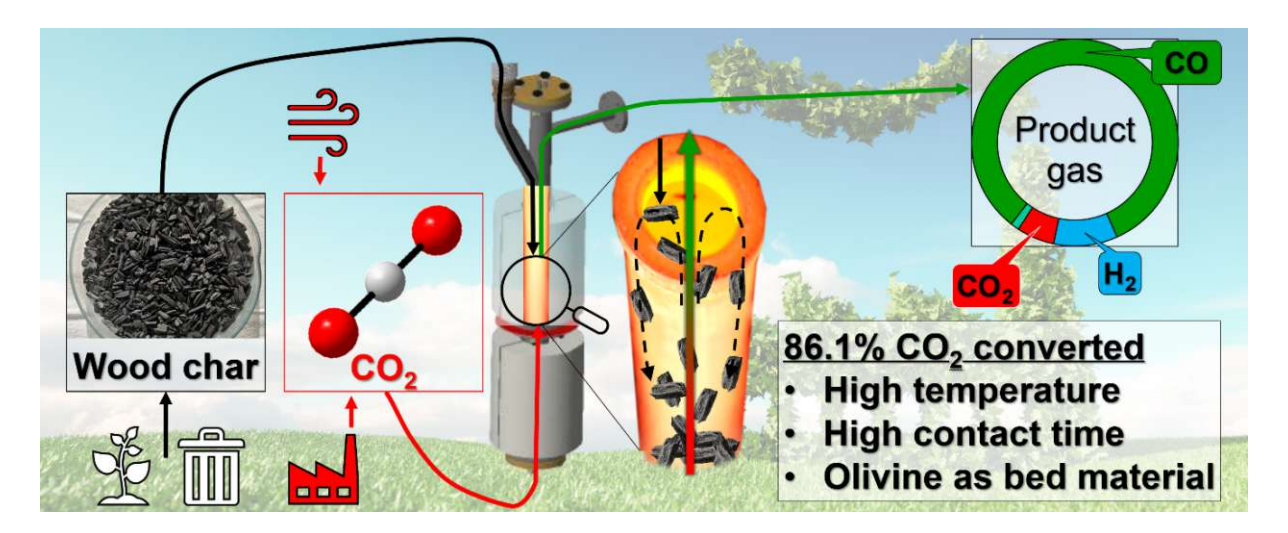
# **Appended articles**

# Journal article I (JA I): CO<sub>2</sub> conversion to CO by fluidized bed biomass gasification: Analysis of operational parameters

## Bibliographical reference

F. J. Müller, J. Fuchs, M. Fanjul Cuesta, A, Oblanca Gutiérrez, S. Pratschner, S. Müller, F. Winter, "CO2 conversion to CO by fluidized bed biomass gasification: Analysis of operational parameters," Journal of CO2 Utilization, vol. 81, no. March 2024, 2024, doi: 10.1016/j.jcou.2024.102706.

## Graphical abstract



## Highlights

- CO<sub>2</sub> gasification is demonstrated to convert 86 % of CO<sub>2</sub> in a fluidized bed reactor.
- Temperature and contact time of CO<sub>2</sub> and biomass strongly influence conversion.
- This paper includes 53 experiments and a semi-empirical model for CO<sub>2</sub> conversion.
- CO<sub>2</sub> conversion is investigated at low biomass conversions (differential reactor).

Contents lists available at ScienceDirect

## Journal of CO2 Utilization

journal homepage: www.elsevier.com/locate/jcou



## CO<sub>2</sub> conversion to CO by fluidized bed biomass gasification: Analysis of operational parameters

Florian J. Müller <sup>a,\*</sup>, Josef Fuchs <sup>a,2</sup>, Miguel Fanjul Cuesta <sup>b,3</sup>, Ana Oblanca Gutiérrez <sup>b,4</sup>, Simon Pratschner <sup>a,5</sup>, Stefan Müller <sup>a,6</sup>, Franz Winter <sup>a,7</sup>

a Technische Universität Wien, Faculty of Technical Chemistry, Institute of Chemical, Environmental and Bioscience Engineering, Getreidemarkt 9/166, Vienna 1060,

ArcelorMittal Global R&D Spain, Avenida de Marqués de Suances s/n, P.O. Box 90, 33400, Avilés, Asturias, Spain

## SARTICLE INFO

### Keywords: ਰ CO₂ Conversion Carbon Capture and Utilization \_\_\_ Gasification Fluidized Bed **Biomass**

### ABSTRACT

Thermochemical conversion of CO<sub>2</sub> with biomass to CO in fluidized bed gasifiers is promising for a sustainable carbon economy. Knowledge about this process is expanded by investigating experimental parameters influencing CO<sub>2</sub> conversion in such a system and combining them to demonstrate effective conversion. Wood char and CO2 are fed to a lab-scale gasifier in 53 semi-continuous experiments. Six experimental parameters are varied: temperature, bed material type, initial bed-to-fuel ratio, initial fuel loading in the reactor, feed CO2 flow rate, and fuel particle size. The results are compiled in a semi-empirical model based on reaction kinetics. High temperatures and high fuel-gas contact times are favorable for increasing CO2 conversion, with the latter achieved through high initial fuel loadings in the reactor and low feed gas flow rates. Choosing olivine instead of silica sand as a bed material also results in higher CO2 conversions. The highest CO2 conversion demonstrated in this paper is 86.1%. This experiment produces a gas with 82.75% CO, 10.01% H<sub>2</sub> and 5.90% CO<sub>2</sub> (nitrogen-free and dry).

### 1. Introduction

## 1.1. Carbon capture and utilization by biomass CO<sub>2</sub> gasification

The chemical industry accounts for 6.3% of global direct and indirect greenhouse gas emissions (2019) [1]. Two of the most effective strategies to decrease the industry's net emissions by 2030 are defossilizing feedstocks and increasing energy and material efficiency [1]. A limited number of molecules serve as synthesis starting points in this sector. One of these molecules is carbon monoxide, which is used as feedstock for producing various bulk chemicals, e.g., methanol, aldehydes, and alcohols [2]. In 2021, less than 1% of global methanol production was bio-methanol or e-methanol, meaning that most carbon monoxide for methanol production was derived from natural gas or coal [2,3]. The production and use of methanol accounts for about 0.3 Gt CO<sub>2</sub> emissions per year, about 10% of the total chemical sector emissions [3]. Therefore, defossilizing the production of CO holds vast potential for reducing global greenhouse gas emissions from the chemical industry sector, especially when combined with low-emission hydrogen. This study experimentally investigates how biomass gasification with CO2 as a gasification agent can be used as carbon capture and utilization (CCU) technology for producing a CO-rich gas from renewable resources.

While gasification in a CO2 atmosphere has been investigated extensively [4], many studies on CO2 gasification have neglected the efficient utilization of CO<sub>2</sub> as a feedstock and only considered the conversion of solid materials as a design goal, e.g., [5] or [6]. This work aims to increase the material efficiency of this process by optimizing the

https://doi.org/10.1016/j.jcou.2024.102706

Received 22 May 2023; Received in revised form 13 February 2024; Accepted 13 February 2024 Available online 21 February 2024

<sup>\*</sup> Corresponding author.

E-mail address: florian.johann.mueller@tuwien.ac.at (F.J. Müller).

https://orcid.org/0000-0002-8041-2317

<sup>&</sup>lt;sup>2</sup> https://orcid.org/0000-0002-4627-4475

<sup>&</sup>lt;sup>3</sup> https://orcid.org/0009-0008-8256-1106

https://orcid.org/0009-0007-9493-4478

<sup>&</sup>lt;sup>5</sup> https://orcid.org/0000-0001-6167-586X

<sup>6</sup> https://orcid.org/0000-0001-8878-429X

<sup>&</sup>lt;sup>7</sup> https://orcid.org/0000-0001-9854-3836

Nomeno	clature	$\dot{V}_{mf}$	Minimum fluidization flow rate, m <sup>3</sup> /s.
		$vol\%_{db}$	Volume percentage, dry-based, m <sup>3</sup> /m <sup>3</sup> .
$\%_{XCO2}$	Percentage points CO <sub>2</sub> conversion, mol/mol.	$vol\%_{db,N}$	72-free Volume percentage, dry-based, Nitrogen is excluded
$\boldsymbol{A}$	Cross-section of the reactor, m <sup>2</sup> .		and other gases are scaled to 100%, m <sup>3</sup> /m <sup>3</sup> .
Ar	Archimedes number, -	$w_n$	Mass fraction of total sample mass retained on the n <sup>th</sup> sieve
B	Initial bed-to-fuel ratio, m <sup>3</sup> /m <sup>3</sup> .		after sieving analysis, kg/kg.
$c_A$	Dry-based volumetric concentration of the species A, m <sup>3</sup> /	$X_{CO2}$	CO <sub>2</sub> conversion, mol/mol.
	$\mathrm{m}^3$ .	$\Delta p$	Pressure drop in the reactor, mbar.
$d_P$	Particle size (weighted average by sieving), m.	$\alpha$	Fitting parameter for B, -
$d_{P,n,avera}$	ge Average of mesh sizes on the n <sup>th</sup> and (n-1) <sup>th</sup> sieve, m.	β	Fitting parameter for <i>G</i> , -
$d_{SV}$	Sauter diameter, m.	γ	Fitting parameter for F, -
$E_a$	Activation energy, J/mol.	$\varepsilon$	Assumed bed void fraction of bubbling bed mixture
F	Initial fuel loading, m.		$(0.5 \text{ m}^3/\text{m}^3), \text{ m}^3/\text{m}^3.$
$f_{umf}$	Factor from $\dot{V}_{mf}$ to $G$ , -	$\mu$	Dynamic viscosity (fluid), N*s/m <sup>2</sup> .
g	Gravity of Earth (9.81 m/s $^2$ ), m/s $^2$ .	$ ho_F$	Density (fluid), kg/m <sup>3</sup> .
G	Feed gas flow rate, Nm <sup>3</sup> /s.	$\rho_P$	Density (particle), kg/m³.
k	Reaction rate constant, 1/s.	Φ	Particle sphericity, -
$k_0$	Preexponential factor, $m^{\gamma-1}/s$ (final model 1/s).	τ	Hydrodynamic residence time, s.
M	Fitting parameter for bed material type, -	$ au_{FGC}$	Fuel-gas contact time, s.
$m_0$	Total mass of sample in the sieving analysis, kg.	A hhami	stion Town
$m_n$	Mass retained on the n <sup>th</sup> sieve after sieving analysis, kg.		ntion, Term
S	Fitting parameter for fuel size, -	BECCS BET	Bioenergy with Carbon Capture, and Storage.
t	Reaction time, s.		Brunauer-Emmett-Teller (absorption).
T	Temperature, K.	CCU	Carbon Capture and Utilization.
$T_{O}$	Standard temperature (273.15 K), K.	DAC	Direct Air Capture.
$u_{mf}$	Minimum fluidization velocity, m/s.	NDIR	Non-Disperse InfraRed.
V	Reactive volume, m <sup>3</sup> .	PSR	Perfectly Stirred Reactor.
$\dot{V}$	Volume flow rate, m <sup>3</sup> /s.	RMSE	Root Mean Square Error.

utilization of CO<sub>2</sub> as a carbon source. Efficient conversion of CO<sub>2</sub> directly lowers carbon dioxide emissions from the process and can save energy by reducing the need for recirculation loops or gas upgrading steps to meet feedstock specifications of downstream units. CO<sub>2</sub> is proposed to come from renewable carbon sources like bioenergy carbon capture and storage (BECCS) or direct air capture (DAC). As the current availability of CO<sub>2</sub> from BECCS is limited, and the cost of CO<sub>2</sub> from DAC is reported at 300–600 \$/ton [3], more efficiently using CO<sub>2</sub> can bring economic benefits. Furthermore, sustainable biomass price and availability are common limitations when scaling up biomass processes to an industrial level [7]. Higher utilization of CO<sub>2</sub> as a carbon source allows more CO to be produced from the same biomass resources, increasing blow much conventional fossil production can be replaced.

Among various design options, fluidized bed reactors show key advantages in uniformity of temperature distribution, fuel flexibility, mass and energy transfer rates, and scalability [8]. The design of gasifiers is highly empiric, with a distinct lack of fundamental data on selecting the best process parameters, leading to less than optimal energy and material efficiencies [8]. The current study aims to solve these issues by systematically investigating design parameters and their importance in fluidized bed gasifiers to convert CO<sub>2</sub> to CO. These design parameters are then combined experimentally and in a semi-empirical model to describe and demonstrate the effective utilization of CO<sub>2</sub> as a feedstock.

#### 1.2. State of the art on CO<sub>2</sub> conversion efficiency in gasification

This chapter is used to list how efficiently previous works by other authors have converted  $CO_2$  in all othermal fluidized bed reactors. Experimental parameters are identified from the literature that can help utilize  $CO_2$  as a feedstock more efficiently.

Gasification processes are chemically complex and have the solid

Table 1
Basic heterogenous and homogenous reactions in CO<sub>2</sub> gasification; adjusted from [15].

Reaction	$\Delta H_r^0$ (25 °C) in kJ/mol	Reaction name	
Basic gas-solid (heterogene	ous) reactions		
$C + CO_2 = 2CO$	+173	Boudouard	(1)
$C + H_2O = CO + H_2$	+131	Steam-carbon (also water-gas)	(2)
$C+2H_2=CH_4$	-75	Methanation	(3)
$C + (1/2)O_2 = CO$	-111	Partial oxidation of char	(4)
Basic gas-gas (homogeneou	s) reactions		
$CO + H_2O = CO_2 + H_2$	-41	Water-gas shift	(5)
$CO_2 + H_2 = CO + H_2O$	+41	Reverse water-gas shift	(6)
$CO  +  (1/2)O_2  = CO_2$	-283	Oxidation of CO	(7)
$H_2+(1/2)O_2=H_2O$	-242	Oxidation of H <sub>2</sub>	(8)
Decomposition reactions of	organic components		
$C_x H_y + xCO_2 = 2xCO + (y/2)H_2$	Endothermic	Dry reforming	(9)
$C_xH_y + xH_2O = xCO + (y/2 + x)H_2$	Endothermic	Steam reforming	(10)
$C_x H_y + (2x - y/2)H_2 = xCH_4$	Exothermic	Hydrocracking	(11)
$C_x H_y + CO_2 = C_{x-1} H_{y-2} + 2CO + H_2$	Endothermic	Dry dealkylation	(12)
$\begin{array}{c} C_x H_y  + H_2 O  = C_{x-1} H_{y-2}  + \\ CO  +  2 H_2 \end{array}$	Endothermic	Steam dealkylation	(13)
$\begin{array}{c} C_x H_y  + H_2  = C_{x-1} H_{y-2}  + \\ C H_4 \end{array}$	Exothermic	Hydrodealkylation	(14)

carbonaceous feedstock undergoing multiple conversion steps. Many publications provide an overview of gasification in general and CO2 gasification more precisely [8-10]. The most important reactions for CO2 gasification are given below in Table 1. The reactions directly converting CO<sub>2</sub> are the Boudouard (Eq. 1), reverse water-gas shift (Eq. 6), dry reforming (Eq. 9), and dry dealkylation (Eq. 12) reactions. Many publications identify the Boudouard reaction as the dominant reaction in the presence of  $CO_2$  as gasification agent, e.g., [11–14].

The  $CO_2$  conversion  $X_{CO2}$  states how much  $CO_2$  fed to the reactor is converted to other carbonaceous molecules. This value is inconsistently described in the literature, usually due to one of two reasons. First, many studies focus on the conversion of solid feedstock in a CO2 atmosphere and do not describe the conversion of CO<sub>2</sub> in detail [16-19]. Second, inconsistent assumptions and calculation methods are used to evaluate the  $CO_2$  conversion  $X_{CO2}$ , negatively impacting comparability. One example of these differences is the consideration of CO2 released from biomass during gasification. Some authors consider CO2 released from biomass pyrolysis in comparable experiments under an N2 atmosphere to be a separate CO<sub>2</sub> stream entering the reactor [20]. Others only compare ingoing and outgoing CO<sub>2</sub> streams without this pyrolysis credit [21]. This difference in calculation can lead to vastly different results when assessing the same data. Another example of varying calculation methods producing different results is given by [22], which investigates the CO<sub>2</sub> conversion for the same experiment using two methods. In this case, the difference is not if credit for CO2 from biomass is given, but which: The CO<sub>2</sub> conversion is estimated at 26% using pyrolysis data or 45% using steam gasification data as a reference for the CO<sub>2</sub> produced from biomass.

Both identified problems of a) lacking investigation of the CO<sub>2</sub> conversion  $X_{CO2}$  and b) inconsistent calculation in the literature are solved by reproducing  $X_{CO2}$  from literature instead of directly giving the described values. This reproduction is done by applying a standardized calculation method to available data in the literature. The calculation is based only on the measured product gas composition and does not give credit for CO2 from pyrolysis. It is described in more detail in the methodology Section 2.3 and used for assessing experiments conducted as part of this paper. Therefore, the CO<sub>2</sub> conversions presented in the results section of this paper can also be directly compared to previous results from other authors given in Table 2. To further ensure comparability, the summary of literature results lists only experimental research on allothermal CO2 gasification in a fluidized bed. The table lists important parameters describing the process and identifies which correlations with  $X_{CO2}$  were found. The experiment with the highest  $X_{CO2}$  is shown if multiple experiments are described.

converted CO<sub>2</sub> [24]. This ratio can be lowered either by lowering the amount of CO2 fed to the reactor or by increasing the amount of fuel in the reactor. The highest value for  $X_{CO2}$  in all othermal fluidized bed reactors given in Table 2 is 35%. To the authors' best knowledge, no higher CO2 conversions have been demonstrated in allothermal fluidized bed reactors.

A comprehensive overview of parameters generally influencing CO<sub>2</sub> gasification processes is available in review papers [9,10]. Although these reviews lack CO2 conversion data availability and comparability, two more aspects are selected for experimental consideration in this current work. First, the type of bed material is an essential factor in such a system because it can act as a catalyst to promote several reactions. Practical experience shows that for a given bed material, adjusting the ratio of fuel to bed material is also necessary for maintaining stable operation. Second, the size of fuel particles was also varied based on reported significance for mass and heat transfer limitations [10].

Based on the presented previous works, six parameters are selected for experimental investigation on increasing the CO2 conversion in an allothermal fluidized bed reactor. The six chosen parameters are

- Temperature T,
- initial fuel loading of the reactor F,
- fuel particle size S,
- feed CO<sub>2</sub> gas flow rate G,
- bed material type M, and
- initial bed-to-fuel volumetric ratio B.

#### 2. Materials and methods

#### 2.1. Materials

Air (dry, compressed), CO<sub>2</sub> (99.995%), and N<sub>2</sub> (99.999%) are supplied to the feeding line with rotameters. Wood char derived from Eucalyptus globulus and prepared by pyrolysis at 700 °C for 20 minutes is used as fuel. The char particles range in size between 0 – 15 mm. Three classes of particles were extracted from this mixture by sieving for experiments investigating the influence of fuel particle size. The range given for the size of the particles refers to the mesh size of sieves used in the separation process. The three classes of fuel size are large fuel (5 -8 mm), medium fuel (2.5-5 mm), and small fuel (0.8-2.5 mm). Fuel is fed to the reactor using a screw feeder. In the case of experiments with defined particle size, the screw feeder is bypassed to avoid changing the particle size by abrasion. Proximate analysis is done following these standards: DIN 51718:2002-06 Method A for water content, EN ISO 18122:2015-11 for ash content, and EN ISO 18123:2015-11 for volatile content. Ultimate analysis of this wood char is performed using an Elementar Analyzer EA 1108 CHNS-O by Carlo Erba. An Axios advanced XRF device by Panalytical Analysis gives information on the ash content. Morphological information on the char was gathered by BET (Brunauer-Emmett-Teller) adsorption measurements with N2 and CO2 using a

To tially increasing CO <sub>2</sub> constraints and constraints of the constrai	onversion during gasific ding H <sub>2</sub> O. Increasing te conversions of biomass a the ratio of CO <sub>2</sub> to solid	cation in a fluidiz emperature is com and CO <sub>2</sub> in such a carbonaceous mat	poten- 18122 ed bed conter nmonly Eleme system XRF de terial is Morph	2:2015–11 for a nt. Ultimate an entar Analyzer l evice by Panaly nological inform	nsh content, and nalysis of this EA 1108 CHNS- ytical Analysis s nation on the c	ethod A for water cord EN ISO 18123:2015—wood char is performed by Carlo Erba. An Actives information on the har was gathered by Blackments with N <sub>2</sub> and	11 for volatile ned using an xios advanced e ash content. ET (Brunauer-
$ \stackrel{\bigcirc}{\vdash} {\vdash} {\vdash} { } \text{Comparison of CO}_2 \text{ gasifice} $	cation in allothermal fluidi (described in methodolog	ized bed reactors in	the literature. CO <sub>2</sub> o	conversion X <sub>CO2</sub>	is reproduced (r	ep.) from literature data	on product gas
Fuel vol% CO <sub>2</sub>   Balance=N <sub>2</sub>	Gasification agent °C	<b>Bed material</b> bara	Temperature %	Pressure	X <sub>CO2</sub> rep.	X <sub>CO2</sub> increased by	Source
Wood sawdust	100	SiC	850	1.5	21	No trend observed	[23] Rep. Fig.6
Wood sawdust	9	Silica sand	934 (700–934)	atm.	17	†Temperature	[12] Rep. Fig.7
Spent coffee grounds	15 (15–30)	Not given	900	atm.	13	↓CO <sub>2</sub> :C H <sub>2</sub> O:CO <sub>2</sub> synergy	[24] Rep. Fig.8
Lignite	100	Silica sand	850 (850–950)	atm.	35	†Temperature	[25] Rep. Fig.4
Softwood	100	Olivine	837 (740–840)	atm.	24	†Temperature	[22] Rep. Fig.8



Table 3 Analysis of Eucalyptus globulus derived wood char used as fuel.

Eucalyptus globulus char			
Proxin	nate and ultim	ate analysis	
		On dry basis	As received
Water content	wt%	-	6.33
Ash content	wt%	6.28	5.88
Carbon content	wt%	85.42	80.01
Hydrogen content	wt%	1.98	1.86
Nitrogen content	wt%	0.24	0.23
Sulfur content	wt%	< 0.02	< 0.02
Chlorine content	wt%	0.03	0.03
Oxygen content (by balance)	wt%	6.03	5.64
Volatile matter content	wt%	15.06	14.11
Gross calorific value	kJ/kg	30956	28996
Net calorific value	kJ/kg	30521	28433
Morpholog	gical analysis l	by adsorption of	
$CO_2$	$N_2$		
Specific surface area (BET)	$m^2/g$	593	676
Total pore volume	cm <sup>3</sup> /g	0.24	0.34
Average pore diameter	nm	1.6	2.0
	Ash melting ar	nalysis	
Deformation temperature	°C	1340	
Hemisphere temperature	°C	>1500	
Flow temperature	°C	>1500	
	Ash composi	tion	
CaO	wt%	53.0	
K <sub>2</sub> O	wt%	14.0	
$SiO_2$	wt%	7.8	
MgO	wt%	7.1	
$Fe_2O_3$	wt%	3.8	
$P_2O_5$	wt%	3.7	
Al <sub>2</sub> O <sub>3</sub>	wt%	2.8	
Na <sub>2</sub> O	wt%	2.5	
MnO	wt%	1.7	
$SO_3$	wt%	1.6	
Rest	wt%	2.0	

BELSORP-max II by Microtrac. This information is given in (Table 3).

Limestone, silica sand, and olivine are investigated in this paper as bed materials to act as fluidization matrices and potential catalysts. Limestone is expected to undergo thermal composition to quicklime before experiments are started based on the reactor's temperature between experiments (900  $^{\circ}\text{C+})$  and atmosphere (air and  $\text{N}_2)$  [26]. These

bed materials are compared in sixteen experiments. Olivine, with a chemical composition of 48-50 wt% MgO, 39-42 wt% SiO2 and 8.0-10.5 wt% Fe<sub>2</sub>O<sub>3</sub>, is further used in the remaining 37 experiments investigating other parameters. Due to the small particle size, these bed materials are fluidized at lower gas flow rates. For this reason, they form the bubbling bed fluidization matrix in the reactor, where the fuel is suspended. More detailed explanations and calculations on the fluidization of used materials and the selection of feed gas flow rates are available in Appendix A. The materials used in this investigation are presented in Fig. 1.

#### 2.2. Experimental setup

An electrically heated fluidized bed reactor with a nominal fuel input power of 2 kW<sub>th</sub> is used in semi-continuous operation. Its general layout is presented in Fig. 2.

The reactor is made from stainless steel (X15CrNiSi25-21), has an inner diameter of 53.1 mm, and has two main zones connected by a flange. The supplied gas is nearly pure CO<sub>2</sub> with a small stream of N<sub>2</sub> (<1%), which is necessary for purging the pressure measurement. CO<sub>2</sub> enters the reactor's lowest point and flows towards the off-gas line. The first zone the gas enters is the preheating zone, which is heated by two half-shell heating shells. These half-shells are rated at a nominal power of 0.75 kWel and are 250 mm high. They are made from ceramic fiber and can heat up to 900 °C. The preheated gas then flows towards a sieve tray, where the flow is distributed. The reaction zone is also heated by two identical half-shell heating shells, which can heat up to 1000 °C. These temperature limitations refer to the highest possible set points for the heating shells on the reactor's outside. The temperatures observed inside the reactor are lower due to static heat losses. The off-gas stream from the reactor is a mixture of product gas, entrained particles, and minor impurities such as tar. This mixture is conditioned for measurement by a two-step particle separation and drying in Impinger bottles at -2 °C.

The dry gas stream is fed to an Emerson Rosemount NGA 2000 continuous gas measuring device. This device can measure CO<sub>2</sub>, CO, H<sub>2</sub>, and CH<sub>4</sub> between 0% and 100% and O<sub>2</sub> up to 25%. CO<sub>2</sub>, CO, H<sub>2</sub>, and CH<sub>4</sub> are measured by non-disperse infrared (NDIR), while O2 is measured paramagnetically. The accuracy is  $\pm 1\%$  of the calibrated maxima,

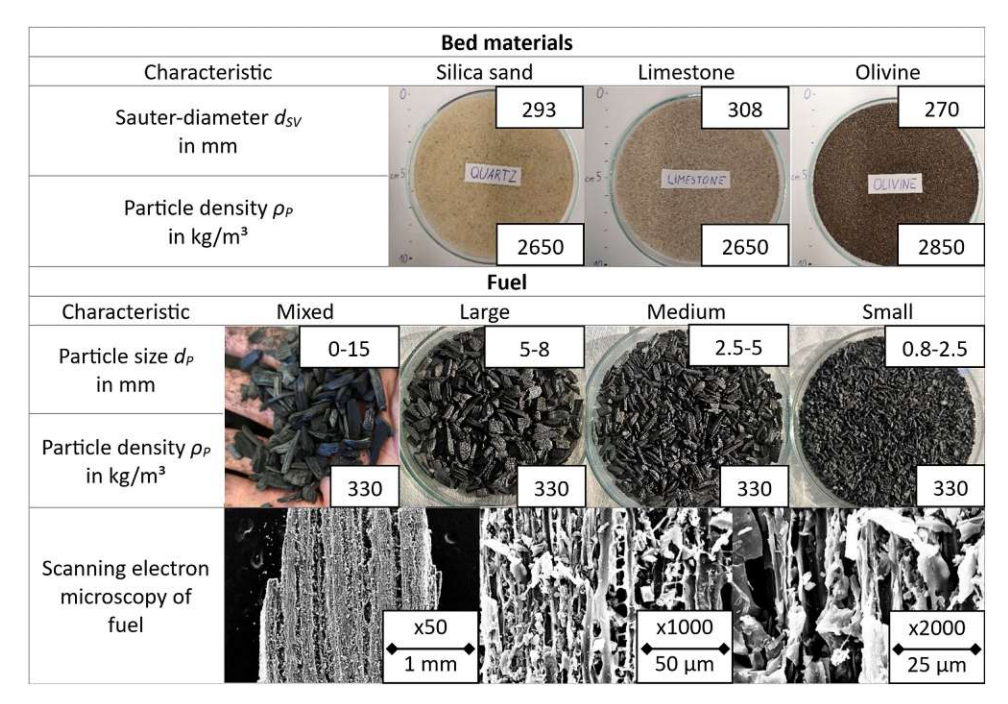


Fig. 1. Materials used in described experiments.

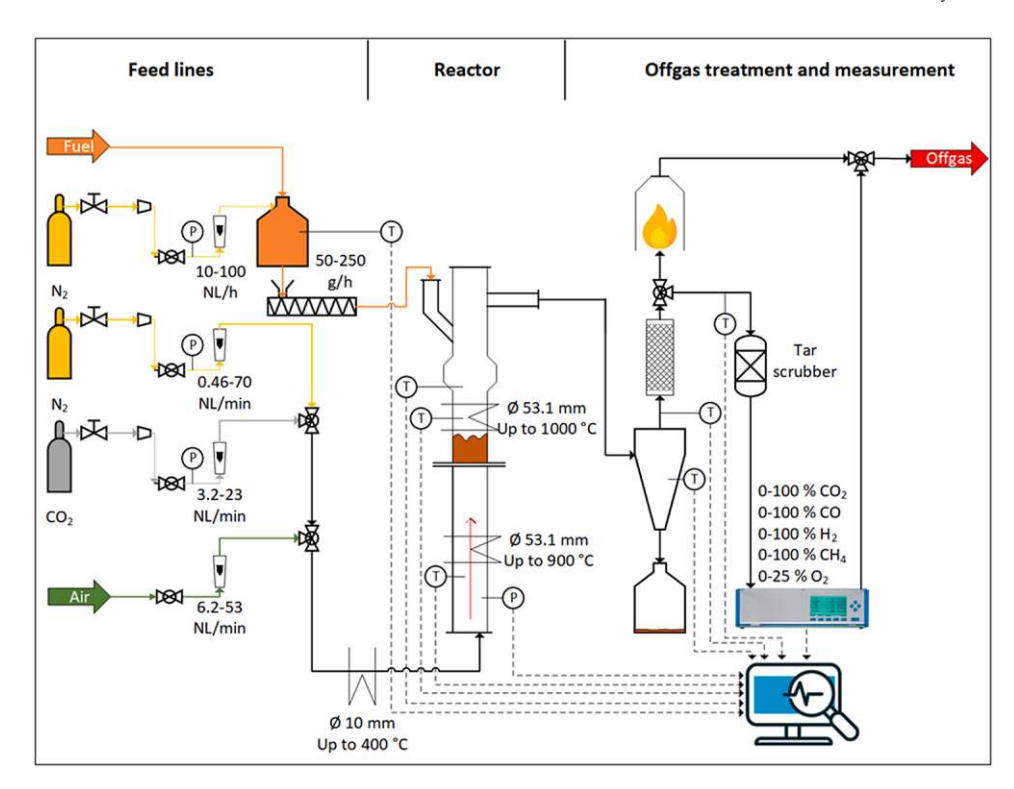


Fig. 2. Electrically heated fluidized bed reactor.

which are given in Appendix B. These accuracies were used to obtain the error ranges in Section 3.1. Further measurements include temperature measurements by thermocouples type K and a pressure measurement below the sieve tray. The temperature measurement used as the reference for this paper's investigations is centered in the reaction zone.

Semi-continuous experiments, as defined by Missen et al. [27], with a batch of initially inserted wood char and continuous feeding of CO2 and removal of product gas are used to determine the CO2 conversion within this paper. This type of experiment is favored over experiments using continuous fuel feed to increase the speed of the investigation and overcome reactor limitations from insufficient heating power. CO2 conversion is assessed close to the experiment's start when biomass conversion is still low, and wood char is available in excess (differential reactor). A more detailed explanation of the experimental procedure is given in Appendix B.

In total, 53 experiments are performed in this reactor (Fig. 2) to assess the influence of six parameters on CO<sub>2</sub> conversion. Parameters are  $\overline{\Sigma}$  varied in isolation and combined to determine their impact on  $X_{CO2}$ . A summary of investigated settings is given in Table 4. A complete list of experiments can be found in Appendix C.

Experimental parameters investigated within this work.

Abbreviation	Investigated factor	Operational parameters (target values)	Variations
T	Temperature	800 – 1000 °C	5
F	Initial fuel loading (height)	5 – 15 cm	4
S	Fuel size	0.8 – 8 mm	4
G	Feed gas flow rate	0.30 - 0.43 Nm <sup>3</sup> /h	2
М	Bed material type	Silica sand limestone  olivine	3
В	Initial bed-to-fuel ratio	$0.66 - 4 \text{ m}^3/\text{m}^3$	6

#### 2.3. Calculation of CO2 conversion

The CO<sub>2</sub> conversion is evaluated in this work by applying a calculation method using the dry-based volumetric concentrations of the product gas components CO, CO<sub>2</sub>, and H<sub>2</sub>, which are expressed as  $c_A$ , where A is the molecule species. Using this method,  $X_{CO2}$  can be calculated continuously with a matching resolution of one second as the gas measurement. The equation for this method is given by [28] and considers the Boudouard (Eq. 1) and steam-carbon (Eq. 2) reactions. It assesses how much educt CO<sub>2</sub> is converted to product CO by the Boudouard reaction. This calculation is corrected for any CO instead produced by the steam-carbon reaction, which also produces H<sub>2</sub>.

$$X_{CO2} = \frac{c_{CO} - c_{H2}}{c_{CO} - c_{H2} + 2 \cdot c_{CO2}}$$
 (15)

Eq. 15 describes the  $CO_2$  conversion  $X_{CO2}$ , which aims to describe the change in mass of CO<sub>2</sub> before and after the reactor. This equation is used to evaluate all experiments conducted in the scope of this paper. Reference [28] does not provide context for the applicability of this equation. The following assumptions are considered to apply:

- No CO or H<sub>2</sub> is present in the feed gas. This assumption is most valid for feedstocks like char and coal, which have relatively limited volatile content and do not contribute significantly to the gas composition via devolatilization. With increasing volatile content, the uncertainty of the calculation can increase.
- Solid carbon is only converted to gas via reactions in Eq. 1 to Eq. 3. This assumption also faces increasing uncertainty from increasing volatile content in biomass.

The fuel used in this study has low volatile and oxygen contents. Furthermore, fuel is fed into the hot reactor under a nitrogen atmosphere shortly before the gasification starts. Data show some gaseous pyrolysis products are released when fuel is fed into the hot nitrogen atmosphere, but minimal devolatilization products are measured at the gasification start (Appendix B). For these reasons, the assumptions described above are considered to apply, which lowers the uncertainty in calculating  $X_{CO2}$ .

The  $X_{CO2}$  data presented in the results section are the average value of a 10–14 second period near the start of gasification (Appendix B). This methodology is chosen because this period represents the maximum observed  $\mathrm{CO}_2$  conversion before the conversion drops due to temperature and fuel decreases. An average value over this short period is used instead of only the data point with maximum conversion to reduce noise from relying on a single data point. The error ranges of figures in Section 3.1 result from the uncertainty in gas concentration measurement.

#### 2.4. Semi-empirical CO2 conversion model development

Correlations between the six investigated parameters and the  $CO_2$  conversion are reported in the experimental Section 3.1. These empirical results are combined and conceptualized in the modeling part of this paper in a semi-empirical model based on simplified reaction kinetics. The proposed model replicates the  $CO_2$  conversion in the investigated bubbling bed reactor based only on the described parameters and excludes or generalizes phenomena for which data are unavailable, e.g., bed expansion and bubble formation. After simplification, this model can approximate the  $CO_2$  conversion in this allothermal fluidized bed reactor based on a small set of process characteristics.

The thermodynamic equilibrium of this chemical system in the investigated temperature range is calculated using FactSage. This calculation suggests high  $CO_2$  conversions of 78.7% at 800 °C to 98.3% at 1000 °C in equilibrium. The observed experimental  $CO_2$  conversions are generally significantly lower and suggest a rate-controlled system behavior, indicating  $X_{CO2}$  should be described as a function of the reaction time t. Fluidized bed reactors' essential advantage is their heat and material distribution uniformity. For this reason, the model is proposed using the hydrodynamic residence time distribution of a perfectly stirred reactor (PSR). For a first-order reaction in a PSR, the literature suggests Eq. 16 to describe the  $CO_2$  conversion [29].

$$X_{CO2} = \int_0^\infty \left[1 - \exp(-k \cdot t)\right] \cdot \frac{1}{\tau} \cdot \exp\left(-\frac{t}{\tau}\right) dt = \frac{k \cdot \tau}{1 + k \cdot \tau}$$
 (16)

The simplified form of this equation eliminates the reaction time tand describes the conversion of  $CO_2$  using the reaction rate constant kand the hydrodynamic residence time  $\tau$ . The hydrodynamic residence time  $\tau$  describes the average time of  $CO_2$  in the reactor as the ratio of reactive volume V and volume flow rate  $\dot{V}$  (Eq. 17). Since this investigation is heavily focused on solid-gas reactions, the reactive volume is assumed as the volume taken by the fuel-bed material mixture. For this reason, the feed gas flow rate (G), given at the standard temperature  $T_0$ , is corrected to reactor temperature T and combined with the crosssection of the reactor (A), initial fuel loading (F), initial bed materialto-fuel ratio (B), and bed void fraction of mixed bed ( $\varepsilon$ ) to calculate  $\tau$ . The bed void fraction and height during gasification are not available from this experimental setup. Bed void fractions between 0.4 and 0.6 are reported for binary bed material and biomass mixtures in bubbling fluidized beds, e.g., in [30-32]. In this work, an estimation of 0.5 for the mixed bed void fraction  $\varepsilon$  is used for all experiments. The height of the bed material-fuel mixture is described in two terms to assess two aspects individually: initial fuel loading (F) in an otherwise empty reactor and added bed material (1+B).

$$\tau = \frac{V}{\dot{V}} \to \tau = \frac{A \cdot F \cdot (1+B) \cdot \varepsilon}{G \cdot T/T_0}$$
 (17)

The reaction rate constant k describes the rate and direction of the reaction. k can be explained by the Arrhenius expression, which represents the temperature and activation energy  $E_a$  dependency of k (Eq. 18). The preexponential factor  $k_0$  summarizes various effects, e.g., the likelihood of reaction species collision, and is used as a fitting parameter.

The exponential term represents the fraction of collisions with enough energy to overcome the activation energy barrier. Initial fuel loading (F) and fuel size (S) in the reactor are proposed to be correlated with available reaction sites and, therefore, the preexponential factor. The potential catalytic activity of bed material is associated with changes in activation energy, which the variable M expresses.

$$k = k_0 \cdot \exp\left(\frac{-E_a}{R \cdot T}\right) \to$$

$$k = k_0 \cdot S \cdot F \cdot \exp\left(\frac{-E_a \cdot M}{R \cdot T}\right)$$
(18)

Initial bed-to-fuel ratio (B), feed gas flow rate (G), temperature (T), and initial fuel loading (F) are available as quantified values for each experiment and are plugged into the model in SI units. Exponential scaling factors  $\alpha$ ,  $\beta$  and  $\gamma$  are used to scale these values to investigate their relative influence while achieving the best fit. M and S are not available as representative quantified values and are therefore left as dimensionless variables to solve. Bed material influence is considered using the dimensionless variable M, which describes the scaling of activation energy as a function of bed material type. M has one value for all experiments with silica sand and another value for all experiments with olivine as a bed material. Limestone is not included in this model since its reactions with CO2 go beyond catalytic activity, so the calculated CO<sub>2</sub> conversion is not comparable within the same model. Fuel size is a complex parameter with a multifactorial influence. Morphological particle characteristics like specific surface area and pore size directly influence heat and mass transport. Particle size also affects  $X_{CO2}$  indirectly by stabilizing the bubbling bed fluidization regime at smaller particle sizes, leading to a more homogenous heat and material distribution. These varying correlations make values like the mean particle size an unsuitable scaling factor. A dimensionless variable S with four discrete values for the four size classes analogous to the procedure for bed material types is used as a way around this issue. The combined modeling expression is given by Eq. 19.

$$X_{CO2} = \frac{k_0 \cdot S \cdot \exp\left(\frac{-E_a \cdot M}{R \cdot T}\right) \cdot \frac{A \cdot F^T \cdot (1 + B^a) \cdot \varepsilon}{(G \cdot T / T_0)^{\beta}}}{1 + k_0 \cdot S \cdot \exp\left(\frac{-E_a \cdot M}{R \cdot T}\right) \cdot \frac{A \cdot F^T \cdot (1 + B^a) \cdot \varepsilon}{(G \cdot T / T_0)^{\beta}}}$$
(19)

#### 3. Results

Experimental data are presented in this chapter to describe the influence of individual parameters on  $\mathrm{CO}_2$  conversion. The data presented here aim to explain the trends in  $\mathrm{CO}_2$  conversion due to parameter variation. At the end of this chapter in Section 3.2, a semi-empirical model combining the individual investigations is proposed. This model describes which parameters can be selected to reach this fluidized bed reactor's highest  $\mathrm{CO}_2$  conversion.

#### 3.1. Influence of experimental parameters on the CO2 conversion

#### 3.1.1. Temperature

To assess the influence of temperature on the  $CO_2$  conversion, the reactor's electrical heating was operated at set points between 800 and 1000 °C. The measured temperature in the reaction zone during the evaluation period is used for all evaluations. The materials used for these experiments are 5 cm of wood char (16.9 g) and 10 cm of olivine.  $CO_2$  feed gas flow rate is 0.43 Nm³/h, around ten times the minimum fluidization velocity  $u_{mf}$  at 1200 K. Fig. 3a shows the evolution of  $X_{CO2}$  over the gasification duration, while Fig. 3b compares  $X_{CO2}$  at the time of evaluation.

Increasing the temperature strongly enhances the  $\rm CO_2$  conversion in the investigated interval.  $\it X_{\rm CO2}$  increases from 11.9% at 803.0 °C to 48.7% at 981.5 °C. Equilibrium conditions for this system were

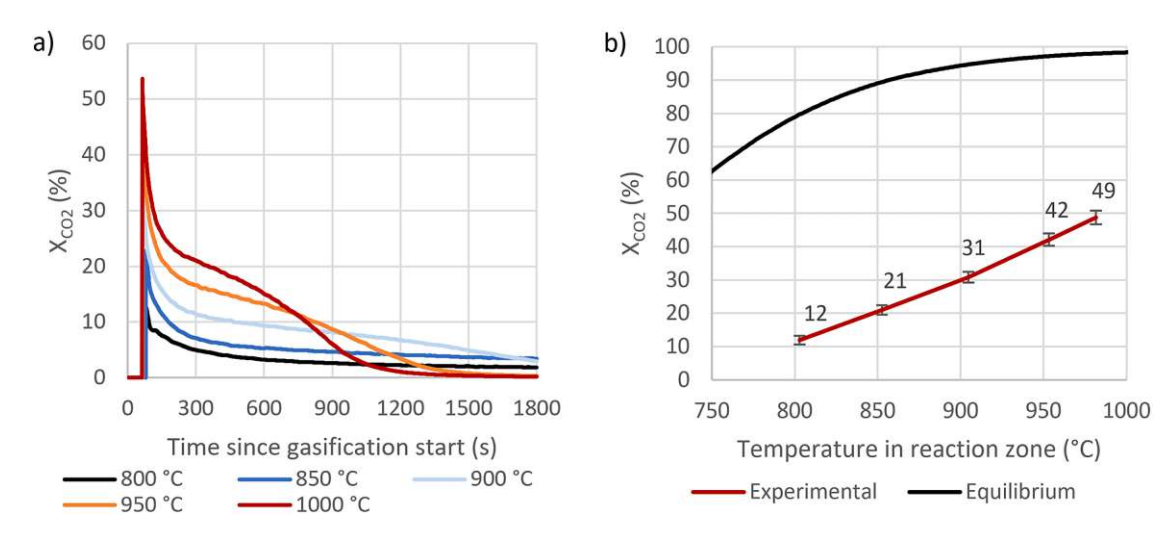


Fig. 3. a)  $X_{CO2}$  over the time of gasification (temperature given is the set point temperature; measured values differ). b) Influence of temperature on  $X_{CO2}$  at various temperatures (temperature measured). Thermodynamic equilibrium is calculated using FactSage.

calculated using FactSage and are dominated by the Boudouard reaction (Eq. 1). Thermodynamic equilibrium suggests a much smaller relative increase from about 80%  $X_{CO2}$  to 98% in the same temperature range. Therefore, the experimentally observed  $X_{CO2}$  is significantly closer to equilibrium at higher temperatures. These data align with literature finding CO2 char gasification to be the rate-limiting step of the global pyro-gasification reaction with a duration near 95% of the entire biomass conversion time [6]. Different rate-controlled regimes and increased reaction speeds at higher temperatures are reported [18]. In summary, this experimental data and FactSage calculation support that increasing the temperature is crucial for increasing CO production in thermodynamic equilibrium and lowering the reaction time necessary to reach equilibrium.

#### 3.1.2. Fuel loading in the reactor

Fig. 4 compares  $X_{CO2}$  for a range of initial fuel loadings in the reactor, given as the initial height at the experiment start. Experiments are performed at 1000 °C and 900 °C set point temperature with 10 cm of olivine as bed material in the reactor. The CO<sub>2</sub> feed gas flow rate is set to 0.30 or 0.43 Nm<sup>3</sup>/h, which equals seven or ten times the minimum gas flow rate for fluidization of the bed material particles.

The reactor's initial fuel amount significantly correlates with the CO<sub>2</sub>

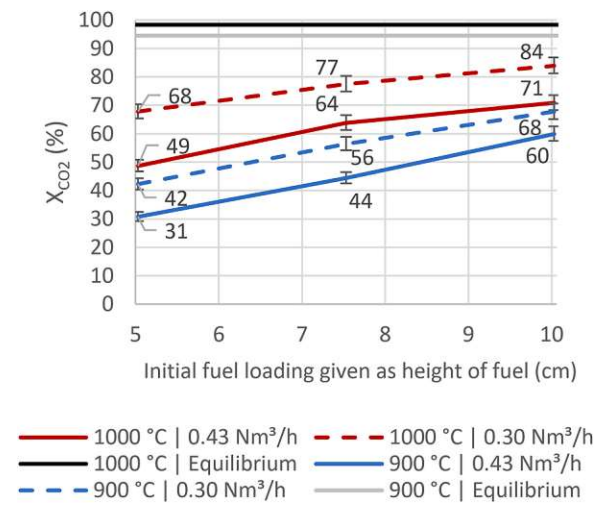


Fig. 4. Influence of initial fuel loading (given as initial height in the reactor at experiment start in cm) and feed gas flow rate (CO2 superficial flow rate) on CO<sub>2</sub> conversion X<sub>CO2</sub>. Thermodynamic equilibrium is calculated using FactSage.

conversion in these experiments. An increase from 67.8% to 83.9% for  $X_{CO2}$  is achieved by increasing initial fuel loading in the reactor from 5 cm (16.9 g) to 10 cm (33.9 g) at 1000  $^{\circ}$ C (set point). At the time of these evaluations, shortly after the experiments started, solid material was available in excess during all experiments, and only a negligible amount of fuel had been converted. Therefore, this increased CO2 conversion is a result of increasing the contact time of CO<sub>2</sub> with the fluidized bed. The contact time of feed CO<sub>2</sub> flowing with 0.3 Nm<sup>3</sup>/h in the mixture of olivine and wood char is increased from 0.42 s at 5 cm initial fuel loading to 0.56 s at 10 cm initial fuel loading for an assumed bed void fraction  $\varepsilon$  of 0.5 at 1000 °C. Calculating the gas-fuel contact time by disregarding the bed material and only considering the wood char in the reactor would result in a linear correlation between the contact time and the initial fuel loading in the reactor. For this assumption, doubling the fuel loading from 5 cm to 10 cm also doubles the gas-solid contact time from 0.14 s to 0.28 s.

The positive correlation between more fuel in the reactor and higher  $X_{CO2}$  values is also underpinned by the decline of  $X_{CO2}$  observed after the evaluated period. Fig. 3a shows a significant reduction of  $X_{CO2}$  over half an hour of gasification. Temperature set points, CO<sub>2</sub> feed gas flow rates, and bed material are constant, but the initially batch-fed fuel is used up and not replaced. While the sharp decline in  $X_{CO2}$  at the beginning is most likely due to endothermic reactions lowering the temperature in the reactive zone,  $X_{CO2}$  trends towards zero when the fuel amount in the reactor decreases. The CO<sub>2</sub> conversion approaches zero once the fuel is converted, which happens faster at higher temperatures with higher CO2 conversion and, therefore, fuel conversion via the Boudouard reaction. This trend supports the finding that  $X_{CO2}$  is higher with higher amounts of fuel in the reactor and higher fuel-gas contact time.

#### 3.1.3. Fuel particle size

Three classes of wood char size were extracted from the mixed-size fuel by sieving. The three classes of fuel size are large fuel (5 - 8 mm). medium fuel (2.5 - 5 mm), and small fuel (0.8 - 2.5 mm). Fig. 5 shows CO<sub>2</sub> conversions as measured for these three classes of particles and the mixed-size fuel at various initial fuel loading values. The set point temperature for all depicted experiments is 1000 °C. The feed gas flow rate is 0.30 Nm<sup>3</sup>/h, equivalent to seven times the minimum number necessary for fluidizing the bed material at 1200 K. Olivine is placed 10 cm high in the reactor as bed material for all experiments.

The CO<sub>2</sub> conversion efficiency increase observed with increasing initial fuel loading holds for all investigated fuel particle classes. At 5–10 cm fuel heights, there is little difference in performance between small, medium, and mixed-size wood char particles used as fuel. Large



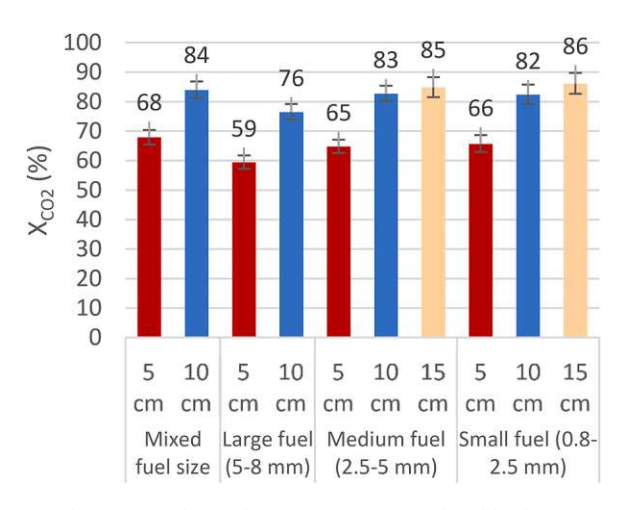


Fig. 5. Influence of fuel particle size at various initial fuel loadings (given as initial height in the reactor at experiment start in cm) on CO<sub>2</sub> conversion X<sub>CO2</sub>.

fuel particles (5–8 mm) show lower CO<sub>2</sub> conversions at 5 cm (59.4% vs. average 66.1%) and 10 cm initial fuel loading (76.5% vs. average 83.0%). A possible explanation is given by higher specific surface area and better heat and mass transfer in smaller particles [33,34]. In addition, an inhibition effect resulting from increased CO concentration in the particles' pores is reported to be more significant for larger particles [35]. These data suggest that this system might have a threshold fuel particle size, which sees larger fuel particles showing lower  $X_{CO2}$ .

Several authors report an increase in mixing quality when smaller biomass [36,37] or coal [38,39] particles are fluidized in smaller bed material particles. Fluidization calculations in Appendix A indicate that the lower  $X_{CO2}$  value observed for large fuel particles might be connected with the fluidization of fuel particles. The calculation shows that the applied feed gas flow rate leads to a superficial gas velocity that exceeds the minimum fluidization velocity  $u_{mf}$  of small wood char particles and is close to  $u_{mf}$  for medium-sized wood char. In contrast, the calculated minimal fluidization velocity for large wood char particles is not reached. Appendix D also shows differences observed for gasification experiments with small and medium fuel particles at high fuel loadings extended after the evaluation period.

#### 5 3.1.4. Feed gas flow rate

The CO<sub>2</sub> conversion as a function of the gas flow rate of CO<sub>2</sub> fed to the reactor is compared in Fig. 4 for various initial fuel loadings and temperatures.

Increased feed gas flow rates are correlated with lower  $X_{CO2}$  at all temperatures and initial fuel loadings. Decreasing the CO2 superficial flow rate from 0.43 Nm<sup>3</sup>/h to 0.30 Nm<sup>3</sup>/h increases the fuel-gas contact time by 41.1%. On average,  $X_{CO2}$  is increased by 26.1% due to this, again suggesting a strong correlation between fuel-CO<sub>2</sub> contact time and  $X_{CO2}$ . This observation is consistent with all investigated parameter combinations. It can be concluded that decreasing the feed gas flow rate increases  $X_{CO2}$  by increasing the fuel-gas contact time. At a flowrate of zero and infinite gas-solid contact time, the thermodynamic equilibrium limits this increase. For fluidized bed reactors, another practical limit is given by the minimal flow rate necessary for fluidization (Appendix A).

#### ₹ 3.1.5. Bed material type

Fig. 6 compares three bed materials described in Fig. 1 under identical conditions. The reactor's electrical heating is operated at set points between 800 and 1000 °C. The materials used for these experiments are  $\frac{1}{6}$  5 cm of wood char (16.9 g) and 10 cm of each bed material. CO<sub>2</sub> feed gas flow rate is 0.43 Nm<sup>3</sup>/h.

Comparing silica sand and olivine as bed material reveals a clear improvement in CO<sub>2</sub> conversion for using olivine over silica sand. At the

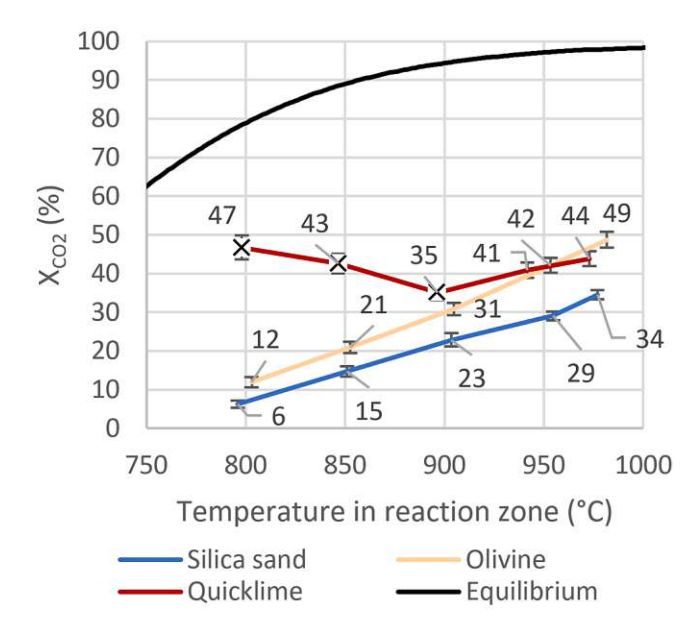


Fig. 6. Influence of bed material type on  $X_{\rm CO2}$  at various temperatures (temperature is measured). Thermodynamic equilibrium is calculated using FactSage. Data marked with X are an artifact resulting from quicklime binding CO2.

highest investigated set point temperature of 1000 °C, a reactor containing silica sand converts CO2 at 34.5%, while olivine exhibits a CO2 conversion of 48.7%.

Limestone is showing significantly higher CO2 conversions at temperatures below 950 °C. Carbon balancing around the reactor and comparing temperature changes at the beginning of gasification reveals this to be an artifact resulting from quicklime capturing CO2. Before every experiment, the reactor is conditioned by burning leftover fuel with air at 1000 °C and adjusting the set point temperature under a nitrogen atmosphere. These conditions favor the production of quicklime, which is the expected compound at the experiment start [26]. Up to 900 °C, the exothermic carbonation reaction of quicklime binding CO2 and forming limestone is expected. The overestimated CO2 conversions under these conditions result from removing unconverted CO<sub>2</sub> from the produced gas. This effect removes the comparability of the generated data from using limestone with other bed materials in this study, as indicated in Fig. 6. At higher temperatures, these data suggest conversion efficiency similar to olivine, but the trendline increases less steeply. Due to the carbonation reaction phasing out over increased temperature, these data are too inconclusive and restricted to estimate the effect of limestone as a bed material on CO<sub>2</sub> conversion with sufficient confidence.

#### 3.1.6. Bed-to-fuel ratio

Variations of the initial volumetric bed-to-fuel ratio are compared by keeping the same amount of wood char in the reactor and varying only the amount of olivine used as bed material. This variation is performed to see if the longer gas-solid contact time with the olivine-wood char mixture resulting from increased bed height would increase the CO<sub>2</sub> conversion. If olivine catalyzes the conversion of CO<sub>2</sub>, e.g., via the Boudouard reaction, another effect of increasing this ratio could be a more pronounced catalytic effect. Fig. 7 shows the results of this investigation, which was performed using 5 cm of wood char loaded into the reactor. Set point temperatures are varied between 900 and 1000 °C. The feed gas flow rate is  $0.30 \, \text{Nm}^3/\text{h}$ , equivalent to seven times the minimum number necessary for fluidizing the bed material at 1200 K.

Increasing the initial bed-to-fuel ratio B by 50% by adding more olivine increases  $X_{CO2}$  by only 0.8% on average. Doubling B lowers the observed  $X_{CO2}$  by 6.1% on average. The experimental error ranges obtained for these experiments are 3.6-5.4% in CO2 conversion. This

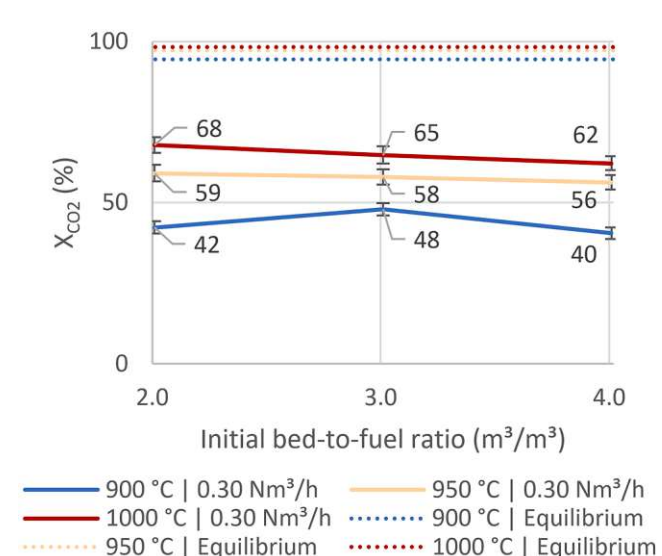


**Fig. 7.** Influence of initial volumetric bed-to-fuel ratio on  $X_{\rm CO2}$  at various parameters (temperature is set point) for olivine as bed material. Thermodynamic equilibrium is calculated using FactSage.

inconclusive trend, minor overall changes, and error ranges suggest the influence of B on  $CO_2$  conversion efficiency to be negligible.

The stability of the bubbling fluidized bed in continuous operation is an effect not consistently represented by the calculation method for  $CO_2$  conversions in this paper. Appendix D describes how differences in a fluidization could explain lower  $X_{CO2}$  values during prolonged investigation, using Figure D-1 as an example.

#### 3.2. CO2 conversion model

The 53 experimental results presented in Section 3.1 are plugged into the theoretical CO<sub>2</sub> conversion model (Eq. 19). First,  $X_{CO2}$  is calculated for each experiment using a placeholder value of 1 for  $\alpha$ ,  $\beta$ ,  $\gamma$ , M, S,  $k_0$ , and  $E_q$ . The root square error between the modeled and observed  $X_{CO2}$  is calculated for each experiment. The sum of errors is divided by 53 to calculate the root mean square error (RMSE), which describes the model's accuracy in estimating the measured CO2 conversions. Second, the variables  $\alpha$ ,  $\beta$ ,  $\gamma$ , M, S,  $k_0$ , and  $E_a$  are solved by Excel Solver, minimizing the root mean square error (RMSE). M for olivine and S for mixed-size fuel are kept at the initial value of 1 for comparability. Third, one by one, the scaling factors are excluded from the model to check if their exclusion significantly increases RMSE, lowering model quality. Excluding parameters from the model lowers its flexibility and increases RMSE to increase model simplicity and focus on the most important identified parameters. A parameter is deemed significant here if its exclusion from the model increases RMSE by more than 1%xco2. The remaining parameters and solved variables are proposed as a semiempirical model able to predict CO2 conversion in this gasification system (Table 5).

The proposed model simplifies the hydrodynamic residence time term  $\tau$  (Eq. 17) to a new time descriptor termed fuel-gas contact time  $\tau_{FGC}$ . This simplification results from the modeling suggesting no correlation between the amount of bed material and the conversion of  $CO_2$  in the reactor. The new term  $\tau_{FGC}$  describes a hypothetical reactor with the same initial fuel loading F and bed void fraction  $\varepsilon$  as the real fluidized bed reactor but without any bed material (Eq. 20).

$$\tau_{FGC} = \frac{A \cdot F \cdot \varepsilon}{G \cdot T / T_0} \tag{20}$$

Nearly no increase in RMSE is observed after eliminating the initial bed-to-fuel ratio B from the model by setting  $\alpha$  to 0 and only considering the gas flow rate G as a linear factor in calculating  $\tau_{FGC}$  by changing  $\beta$  to

the value 1. Eliminating the fuel size S as a parameter increases RMSE by around  $0.19\%_{\rm XCO2}$ . Further simplification of the model increases RMSE by  $0.63\%_{\rm XCO2}$  when the initial fuel loading F is also only considered as a linear factor in the calculation of  $\tau_{FGC}$  by changing  $\gamma$  to the value 1. Eliminating the bed material parameter M increases RMSE by more than  $1\%_{\rm XCO2}$  and is therefore not done. The simplified model uses only T, M, and  $\tau_{FGC}$  (formed using F and G) as parameters and approximates the experimental data at an RMSE value of  $4.06\%_{\rm XCO2}$ . This value lies within the error ranges obtained from experimental data due to the uncertainty in gas concentration data. The experimental data shows error ranges between 1.3% and  $7.1\%_{\rm XCO2}$ .

The temperature in the reactor has a strong influence on  $X_{CO2}$  in the final model. Higher temperatures decrease the time to approach equilibrium by increasing the reaction rate constant k according to the Arrhenius equation (Eq. 18). Higher temperatures also favor CO production via the Boudouard reaction (Eq. 1) in equilibrium. For a fuel-gas contact time of 0.25 seconds and olivine as bed material, the model predicts the CO<sub>2</sub> conversion to increase from 26% at 800 °C to 80% at 1000 °C.

The initial fuel loading in the reactor and the feed gas flow rate are combined to form the fuel-gas contact time (Eq. 20), significantly influencing the  $\mathrm{CO}_2$  conversion in the final model. A correlation between time and conversion is expected for all chemical systems which are not in thermodynamic equilibrium. This aspect of the model solution is confirmed by comparing the observed  $\mathrm{CO}_2$  conversions versus the higher conversions suggested by the thermodynamic equilibrium calculation using FactSage. For a temperature of  $1000~^\circ\mathrm{C}$  and olivine as bed material, the model predicts the  $\mathrm{CO}_2$  conversion to increase from 67% at 0.125 seconds to 80% at 0.25 seconds of fuel-gas contact time.

The activation energy  $E_a$  decreases by around 6% if the bed material is switched from silica sand to olivine. This decrease in activation energy increases  $X_{CO2}$  at all investigated temperatures, thus making olivine a better choice of bed material in CO2 gasification. Without a baseline for the investigated system given by experiments that use neither silica sand nor olivine, this study does not answer if either bed material catalyzes the conversion of CO2. The relative difference could be explained by olivine acting as a catalyst or silica sand as an inhibitor in this model. An alkali index reported in the literature, which evaluates the catalytic activity of ash in coal or char, supports both explanations [40]. Silicon, the main component in silica sand, is suggested to act as an inhibitor if it is part of the ash [40]. Magnesium and iron comprise around 60 wt% of olivine and are reported elsewhere to show moderate catalytic in the fuel matrix [10] or if mixed with the fuel as a powder. The low correlation between the bed-to-fuel ratio and  $X_{CO2}$  given by the model suggests that olivine might not be catalytically active.

The activation energy identified in this model is around 139 kJ/mol for olivine as a bed material. This value agrees with the literature, which identifies four reaction domains in CO2 gasification. For thermogravimetric analyzers, free-fall fixed-bed reactors, and drop-tube reactors, activation energies of 125-147 kJ/mol are reported in the temperature range of 900-1000 °C, and the system is characterized as particle or bed diffusion-controlled [18]. The same authors identify no diffusion limitation for a fluidized bed reactor but report a sharp decrease of activation energy at 1250 K from chemical-controlled 232 kJ/mol to a system-specific external mass transfer limitation. Other sources do not investigate different limitation regimes but agree with the broad range of activation energy (141-160 kJ/mol given by [41]) or find higher activation energies around ~250 kJ/mol, which is likely due to lower temperatures resulting in a chemically controlled system [18,42]. In summary, the activation energy found in this work generally agrees well with the literature data, giving credibility to the underlying model (Table 5).

The simplified model is depicted in Fig. 8, which uses olivine and silica sand as bed materials in two viewpoints each. The tips of the arrows represent experimentally found  $X_{CO2}$ . The colored lattice is the model approximation of these values, and the transparent lattice is the

Table 5 Modeling parameters for designing a semi-empirical  $CO_2$  conversion model in the described fluidized bed gasifier;  $1^*$ ...Set as 1 for comparability.

Parameter	Full model	Simplified model
Model equation	Eq. 19	$X_{CO2} = \frac{k_0 \cdot \exp\left(\frac{-E_a \cdot M}{R \cdot T}\right) \cdot \tau_{FGC}}{1 + k_0 \cdot \exp\left(\frac{-E_a \cdot M}{R \cdot T}\right) \cdot \tau_{FGC}}$
α	0.036	-
β	1.115	1
γ	1.377	1
Quartz	1.06	1.07
Olivine	1*	1*
Fuel mixed	1*	-
Small fuel	1.008	-
Medium fuel	1.121	-
Large fuel	0.878	-
$k_0$ in m <sup><math>\gamma-1</math></sup> /s	4.67E + 06	7.95E+06
$E_a$ in J/mol	138800	138800
RMSE in %XCO2	3.24	4.06

thermodynamic equilibrium for this system, as given by FactSage.

The gap between the thermodynamic equilibrium and the experimental  $\mathrm{CO}_2$  conversion decreases with higher temperatures and fuel-gas contact times. The system is closer to equilibrium for using olivine (left) instead of silica sand (right) as a bed material due to the lower observed activation energy using olivine. This model approximation matches the

highest experimentally observed  $X_{CO2}$ . Table 6 and Figure B-1 give information about the experiment using the highest investigated set point temperature and initial fuel loading, the lowest feed gas flow rate, and olivine as a bed material. With these settings, the described experiment operates close to the reactor's geometrical and durability limits to convert 86.1% of  $\rm CO_2$  compared to a model approximation of 83.4%. This conversion vastly exceeds the highest  $\rm CO_2$  conversion previously observed in a similar reactor, reproduced by the same calculation method at 35% (Table 2) [25]. The resulting gas is rich in  $\rm CO$  and has an  $\rm H_2$ -to- $\rm CO$  ratio of around 1:8. This ratio is too low for direct conversion of the gas to methanol or in Fischer-Tropsch-synthesis, which need an  $\rm H_2$ -to- $\rm CO$  ratio of around 2:1 [3,43]. For this reason, the gas needs to be enriched in  $\rm H_2$  to be used as a synthesis gas, e.g., by adding hydrogen from water electrolysis.

#### 4. Conclusion

The influence of experimental parameters on  $CO_2$  conversion in an allothermal fluidized bed reactor is described in this paper. Positive correlations are identified and combined to increase the conversion of  $CO_2$ . The investigated parameters are process characteristics, and the results can be used for highly efficient reactor design. The 53 semicontinuous experiments described in this work are performed in a fluidized bed reactor with a nominal power of 2 kW<sub>th</sub>. A parameter variation including the six parameters temperature (T), bed material type

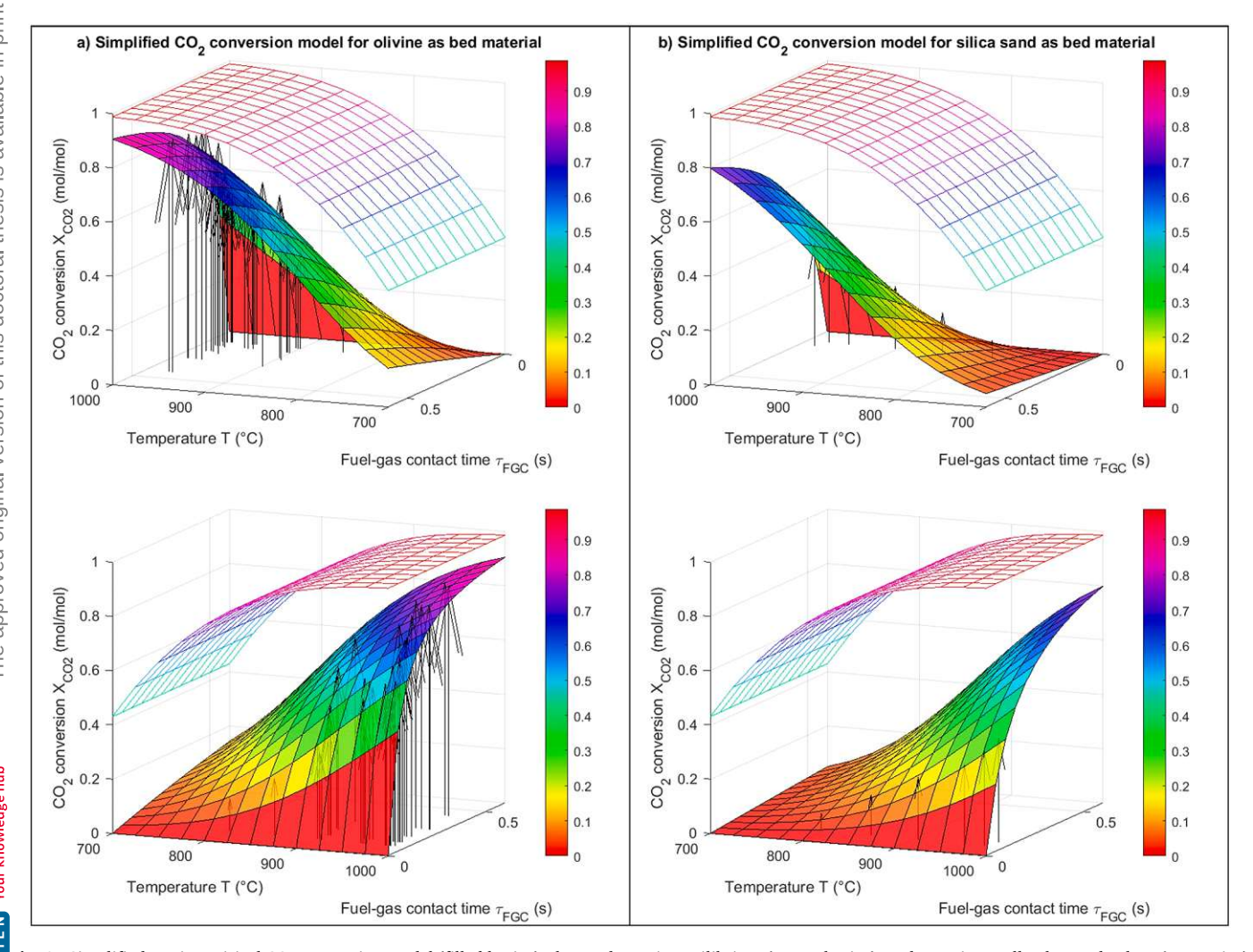


Fig. 8. Simplified semi-empirical CO<sub>2</sub> conversion model (filled lattice), thermodynamic equilibrium (empty lattice), and experimentally observed values (arrow tips) for CO<sub>2</sub> conversion. A) Olivine as bed material, and b) silica sand as bed material.

Table 6 Comparison of model approximation and experimental data on the experiment with the highest  $CO_2$  conversion  $X_{CO2}$  in this paper.

Experiment #53						
		Operatio	nal parameters			
Temperature (set point)	Temperature (measured)	Initial fuel loading	Feed gas flow rate	Bed material	Initial bed-to-fuel-ratio	Fuel size
°C	°C	cm	Nm <sup>3</sup> /h	-	$m^3/m^3$	mm
1000	970	15	0.30	Olivine	0.67	0.8 - 2.5
		Average data du	ring evaluation period			
CO	$CO_2$	$CH_4$	$H_2$	Rest	$X_{CO2}$ experimental	$X_{CO2}$ model
vol% <sub>db,N2-free</sub>	%	%				
82.75	5.90	0.05	10.01	1.30	86.1	83.4

(*M*), initial bed-to-fuel ratio (*B*), initial fuel loading in the reactor (*F*), feed gas flow rate (*G*), and particle size (*S*) is conducted. (Table 4) The main results of this study are:

- $CO_2$  gasification in a fluidized bed is demonstrated to convert  $CO_2$  to CO at very high rates. The highest conversion observed within this publication is 86.1%, producing gas with 82.75% CO, 10.01%  $H_2$ , and only 5.90%  $CO_2$ . (Table 6)
- This system's experimentally observed CO<sub>2</sub> conversion can be replicated in a semi-empirical model based on reaction kinetics with a root mean square error of 4.06%<sub>XCO2</sub>. The calculated activation energy of 139 kJ/mol matches well with the literature. (Table 5)
- The  $CO_2$  conversion in the investigated system can be effectively increased by using higher temperatures, higher initial fuel loading in the reactor, lower feed gas flow rates, and olivine instead of silica sand as a bed material. The fuel loading and feed gas flow rate can be combined as the newly defined fuel-gas contact time  $\tau_{FGC}$  (Eq. 20). No clear correlation was observed between  $X_{CO2}$  and a change in bed-to-fuel ratio or fuel particle size. (Fig. 8)
- Although fuel size and bed-to-fuel ratio are not observed to strongly influence  $X_{CO2}$  in the system, they are to be considered for the stability of the bubbling bed fluidization regime. Unstable fluidization from too low a bed-to-fuel ratio might also decrease  $X_{CO2}$ . This effect can be countered by lowering fuel particle size to promote their direct fluidization. (Figure D-1)

In summary, this work highlights the importance of multiple parameters for efficiently converting the greenhouse gas  $\mathrm{CO}_2$  with biomass to product gas with very high  $\mathrm{CO}$  content. While increasing temperature is the dominant parameter, this also likely comes with energy penalties in practical applications. Increasing fuel-gas contact time by optimizing reactor design promises a significant increase in  $X_{\mathrm{CO}2}$  without increasing the ongoing cost of operation. Larger commercial reactors operated under similar conditions would allow for higher gas-solid contact times, further increasing  $\mathrm{CO}_2$  conversion compared to the findings in this study.

Hydrodynamic aspects like bed expansion or bubble formation were not investigated in this work. Experiments were performed with a highly carbonaceous biomass with low volatile content. When using biomass with higher volatile content, the resulting gas could be mixed with a devolatilization products and potentially lowered in CO content.

This thermochemical carbon conversion pathway could provide COrich gas for multiple green production chains in the chemical industry. Additional hydrogen is necessary for chemical synthesis to meet the hydrogen-to-carbon monoxide ratio demands of common processes, such as methanol production or Fischer-Tropsch synthesis. This hydrogen should be produced by low-emission technologies, e.g., water electrolysis with renewable electricity, to achieve overall emission savings. For industrial applications, it has to be considered that utilizing CO<sub>2</sub> via the Boudouard reaction is highly energy-intensive due to its endothermic nature. Compared to other biomass gasification processes, the high conversion of CO<sub>2</sub> to CO demonstrated in this work means that less carbon monoxide needs to be produced from biomass. Furthermore, a lowered CO<sub>2</sub> content in the produced gas can bring energy savings

from reduced gas separation and recirculation demand. This process can substitute CO from coal or natural gas in synthesizing bulk chemicals like methanol, aldehydes, and alcohols. Therefore, biomass  $CO_2$  gasification as a carbon capture and utilization technology could lower the life cycle emissions from the chemical industry significantly, supposed  $CO_2$  and biomass are sustainably sourced and renewable.

The chemical interactions between fuel and bed materials should be investigated in future studies to improve the understanding of catalytic effects. A numeric simulation study looking into hydrodynamic aspects could provide further insights into the specifics of mass transfer and gasfuel contact times. Using a water-CO<sub>2</sub> mixture as the gasification agent or using different fuels should be investigated for their potential to increase the hydrogen-to-carbon monoxide ratio in the produced gas. The model proposed within this work should be compared to results obtained from continuous operation at a larger scale and with other fuel types. Special attention needs to be given to energy demands and losses, which are beyond the scope of this study. The technical results should be contextualized in future investigations with life cycle and technoeconomic assessments in various production chains.

#### CRediT authorship contribution statement

Florian J. Müller: Writing – review & editing, Writing – original draft, Visualization, Validation, Software, Methodology, Investigation, Formal analysis, Data curation, Conceptualizationa, Josef Fuchs: Writing – review & editing, Validation, Resources, Project administration, Methodology, Funding acquisition, Conceptualization, Miguel Fanjul Cuesta: Writing – review & editing, Validation, Resources, Ana Oblanca Gutiérrez: Writing – review & editing, Validation, Resources, Simon Pratschner: Writing – review & editing, Visualization, Stefan Müller: Writing – review & editing, Supervision, Resources, Project administration, Funding acquisition, Conceptualization, Project administration, Funding acquisition, Conceptualization.

#### **Declaration of Competing Interest**

The authors declare that they have no known competing financial interests or personal relationships that could have appeared to influence the work reported in this paper.

#### Data availability

Data will be made available on request.

#### Acknowledgments

This study was carried out within the doctoral college  $CO_2$ Refinery at TU Wien. This work is also part of the research project  $CO_2$  Reduction for Ironmaking by Utilization of Process Gases, Part 1, and received support from ArcelorMittal Innovación Investigación e Inversión, S.L. Furthermore, the authors would like to thank Microtrac MRB for the characterization of the fuel particle surface. In addition, the authors would like to thank TU Wien Bibliothek for covering article processing charges through its

Open Access Funding program.

#### Appendix A. Fluidization calculations

The fluidization state of particles is a function of particle and gas characteristics and operating conditions. The following section explains the calculations behind selecting gas flow rates for the bubbling fluidized bed used in this work.

Particle size is determined by sieving analysis. Bed materials were analyzed by a cascade of sieves with mesh sizes from 1 mm to 63 µm. The sieving analysis results and particle size  $d_P$  values are given in Table A-1.

Table A-1 Sieving analysis of bed materials. The data reflect the average result for each bed material. Three samples were analyzed per bed material. N.d...Not detected

Bed material	<b>m</b> 0 μm	<b>Sieve number n</b> μm	Mesh size	d <sub>P,n,average</sub>	<b>m</b> n μm	$w_n$	$d_p \pm \text{standard deviation}$
g	-	•	g	g/g	μιιι		266124
Silica sand	448.097	1	1000	700	160 000	0.270	$366{\pm}2.1$
		2 3	400 280	700 340	169.883 177.983	0.379 0.397	
		4	224	252	61.237	0.137	
		5	180	202	28.653	0.064	
		6	140	160	7.950	0.018	
		7	100	120	2.033	0.005	
		8	63	81.5	0.320	0.001	
		9	0	31.5	0.037	0.000	
Limestone	176.917	1	1000				385±3.5
		2	400	700	122.307	0.691	
		3	280	340	46.953	0.265	
		4	224	252	3.717	0.021	
		5	180	202	1.170	0.007	
		6	140	160	0.310	0.002	
		7	100	120	0.323	0.002	
		8	63	81.5	0.483	0.003	
		9	0	31.5	1.653	0.009	
Olivine	112.497	1	1000				$337 \pm 0.1$
		2	400	700	0.193	0.002	
		3	280	340	109.563	0.974	
		4	224	252	2.603	0.023	
		5	180	202	0.110	0.001	
		6	140	160	0.027	0.000	
		7	100	120	N.d.	N.d.	
		8	63	81.5	N.d.	N.d.	
1 was used to de	termine the par	9 a from three analyses, ticle size $d_P$ from $d_{P,\eta,q}$	and the standard of average, the average	31.5 deviations observe	N.d. ed in these analys	N.d. ses for the par	ticle size $d_P$ are noted. E $_1$ the corresponding we
was used to defraction $w_n$ , which	termine the par h relates the ma	a from three analyses, ticle size $d_P$ from $d_{P,\eta,\iota}$ ss retained on the n <sup>th</sup>	and the standard of average, the average	31.5 deviations observe	N.d. ed in these analys	N.d. ses for the par	ticle size $d_P$ are noted. Eq. 1 the corresponding we
1 was used to defraction $w_n$ , which $d_p = 1/\sum_{n=2}^9 \frac{m}{m_0 \cdot d_{P,p}}$	termine the par h relates the ma $\frac{dn}{dn} = 1/\sum_{n=2}^{9} \frac{1}{dn}$	a from three analyses, ticle size $d_P$ from $d_{P,n,t}$ is retained on the n <sup>th</sup> $\frac{w_n}{[P_{P,n,average}]}$	and the standard $c_{average}$ , the average sieve $m_n$ to the to	deviations observe e of mesh sizes on tal sample mass m	ed in these analys the n <sup>th</sup> and (n-	ses for the par 1) <sup>th</sup> sieve, and	the corresponding wei
1 was used to defraction $w_n$ , which $d_p = 1/\sum_{n=2}^9 \frac{m}{m_0 \cdot d_{P,x}}$ For the expericles of particle The remaining function the mesh size of sphericity $\Phi$ is use for ideal spheres. Suggesting a sphealso taken from the density change and the sphere of all hed	termine the part h relates the mathematical hardware the mathematical hardware end of the following	a from three analyses, ticle size $d_P$ from $d_{P,n,o}$ is retained on the n <sup>th</sup> of $\frac{w_n}{P_{P,n,average}}$ and the effect of fuel particle size $d_P$ to the Samit of 0 for increasingly average sand particle size $d_P$ to particle size of $d_P$ or $d_P$ of $d_P$ or $d_P$ of $d_P$ or $d_P$ of $d_$	and the standard of average, the average sieve $m_n$ to the total article size (see Sea sizes were used at $0.8 - 2.5 \text{ mm}$ (sming bed material at a uter-diameter $d_{SV}$ by non-spherical piss, which is used follows stochiometric lows stochiometric lower and the average $0.8 - 0.00$ lower	deviations observed of mesh sizes on tal sample mass materials of the sample materials of the sample of the sa	N.d.  ed in these analyst the n <sup>th</sup> and (n-to).  sieves were used limits, with larged mm (medium codes are given as defor fluidization code is not measured [44]. Particle spectone particles wased on the calculation code is said on the calculation.	N.d.  ses for the par 1) <sup>th</sup> sieve, and d to separate ger and smalle thar), and 5.0 lp in <i>Table</i> A-2 alculations, sed in this work ohericity of wo of this size at cination reacti	the fuel mixture into the particles being discardes and <i>Table</i> A-3. The particle Eq A-2. The sphericity but is taken from literate od char from wood chip 900 °C [46]. The resulting of CaCO <sub>3</sub> . The resulting the care and the care and the care and the care are also and the care and the care are also are also and the care are also and the care are also are also and the care are also are also and the care are also are also are also are also and the care are also
1 was used to defraction $w_n$ , which $d_p = 1/\sum_{n=2}^9 \frac{m}{m_0 \cdot d_{P,x}}$ For the expericles of particle The remaining function the mesh size of sphericity $\Phi$ is use for ideal spheres. Suggesting a sphealso taken from the density change and the sphere of all hed	termine the part h relates the mathematical hardware the mathematical hardware end of the following	a from three analyses, ticle size $d_P$ from $d_{P,n,o}$ is retained on the n <sup>th</sup> of $\frac{w_n}{P_{P,n,average}}$ and the effect of fuel particle size $d_P$ to the Samit of 0 for increasingly average sand particle size $d_P$ to particle size of $d_P$ or $d_P$ of $d_P$ or $d_P$ of $d_P$ or $d_P$ of $d_$	and the standard of average, the average sieve $m_n$ to the total article size (see Sea sizes were used at $0.8 - 2.5 \text{ mm}$ (sming bed material at a uter-diameter $d_{SV}$ by non-spherical piss, which is used follows stochiometric lows stochiometric lower and the average $0.8 - 0.00$ lower	deviations observed of mesh sizes on tal sample mass materials of the sample materials of the sample of the sa	N.d.  ed in these analyst the n <sup>th</sup> and (n-to).  sieves were used limits, with larged mm (medium codes are given as defor fluidization code is not measured [44]. Particle spectone particles wased on the calculation code is said on the calculation.	N.d.  ses for the par 1) <sup>th</sup> sieve, and d to separate ger and smalle thar), and 5.0 lp in <i>Table</i> A-2 alculations, sed in this work ohericity of wo of this size at cination reacti	the fuel mixture into the particles being discard—8.0 mm (large char) ba and <i>Table</i> A-3. The particle Eq A-2. The sphericity but is taken from literate od char from wood chip 900 °C [46]. Therefore,
1 was used to defraction $w_n$ , which $d_p = 1/\sum_{n=2}^9 \frac{m}{m_0 \cdot d_{P,x}}$ For the expericlasses of particle. The remaining fut on the mesh size of sphericity $\Phi$ is use for ideal spheres. Suggesting a sphealso taken from the density change from the density of all bed $d_{sv} = \Phi \cdot d_P$ The minimum force of the particular fluidizing the bed	termine the part h relates the mathematical hardware the mathematical hardware end of the following	a from three analyses, ticle size $d_P$ from $d_{P,n,o}$ is retained on the n <sup>th</sup> of $\frac{w_n}{P_{P,n,average}}$ and the effect of fuel particle size $d_P$ to the Samit of 0 for increasingly average sand particle size $d_P$ to particle size of $d_P$ or $d_P$ of $d_P$ or $d_P$ of $d_P$ or $d_P$ of $d_$	and the standard of average, the average sieve $m_n$ to the total article size (see Sea sizes were used at $0.8 - 2.5$ mm (sming bed material article-diameter $d_{SV}$ by non-spherical pies, which is used for nge is suggested follows stochiometrical clined lime, is talk that it is transition from a given in the litera	deviations observed of mesh sizes on tal sample mass materials and lower all char), 2.5 – 5.0 and fuel particle size, which is needed for tall bed materials or calcinating limits of considerations be ken from an earlied which the drag for fixed bed to a fluid ture [48,49]. Eq.A.	N.d.  and in these analyst the n <sup>th</sup> and (n-to).  sieves were used limits, with larged mm (medium of the color fluidization of the color fluidization of the color study at TU We color fluidized bed regiments.	N.d.  ses for the par 1) <sup>th</sup> sieve, and d to separate ger and smalle thar), and 5.0 dp in Table A-2 alculations, sed in this work of this size at cination reactifien, which using gas become the minimum.	the fuel mixture into the particles being discardand <i>Table</i> A-3. The particle Eq A-2. The sphericity but is taken from literator of CaCO <sub>3</sub> . The resulted the same materials [

$$\frac{1}{2}d_{p} = 1/\sum_{n=2}^{9} \frac{m_{n}}{m_{0} \cdot d_{p,n,average}} = 1/\sum_{n=2}^{9} \frac{w_{n}}{d_{p,n,average}}$$
(A-1)

$$d_{sv} = \Phi \cdot d_P \tag{A-2}$$

$$u_{mf} = \frac{\mu}{\rho_r \cdot d_{SV}} \cdot (\sqrt{33.7^2 + 0.0408 \cdot Ar} - 33.7)$$
(A-3)

$$Ar = \frac{\rho_F \cdot d_{sv}^3 \cdot (\rho_P - \rho_F) \cdot g}{\mu^2} \tag{A-4}$$

suitable t **Table A-2**Fluidization

The results of these calculations are summarized for all bed materials and distinct fuel size classes in *Table* A-2. Feed gas flow rates are selected as 0.30 and 0.43 Nm<sup>3</sup>/h to achieve five to ten times  $u_{mf}$  of the investigated bed material as superficial gas velocity, expressed as  $f_{umf}$ . These values result in a bubbling bed fluidization regime for all three bed materials. Quicklime exceeds this window due to its lower density, but the calculated  $f_{umf}$  is still suitable to form a bubbling fluidized bed.

**Table A-2** Fluidization properties of all used bed materials at 1200 K and atmospheric pressure.

Variable	Unit	Silica sand	Limestone	Quicklime	Olivine
$d_P$	m	3.66E-04	3.85E-04	3.85E-04	3.37E-04
$\Phi$	-	7.60E-01 [44]	7.60E-01 [44]	7.60E-01 [44]	7.60E-01 [44]
$d_{SV}$	m	2.79E-04	2.93E-04	2.93E-04	2.56E-04
$\rho_F$ (1200 K)	kg/m <sup>3</sup>	4.34E-01	4.34E-01	4.34E-01	4.34E-01
$ ho_P$	kg/m³	2.65E+03 [47]	2.65E+03 [47]	1.50E+03 [47]	2.85E+03 [47]
μ (1200 K)	$N*s/m^2$	4.68E-05 [50]	4.68E-05 [50]	4.68E-05 [50]	4.68E-05 [50]
g	m/s <sup>2</sup>	9.81E+00	9.81E+00	9.81E+00	9.81E+00
Ar	-	1.11E+02	1.29E+02	7.33E+01	9.32E+01
$u_{mf}$	m/s	2.61E-02	2.88E-02	1.63E-02	2.37E-02
A	$m^2$	2.21E-03	2.21E-03	2.21E-03	2.21E-03
$\dot{V}_{mf}$	Nm <sup>3</sup> /h	4.73E-02	5.23E-02	2.96E-02	4.31E-02
$f_{umf}$ (0.30 Nm <sup>3</sup> /h)	-	6.3	5.7	10.1	7.0
$f_{umf}$ (0.43 Nm <sup>3</sup> /h)	-	9.1	8.2	14.5	10.0

The selected flow rates of  $0.30 - 0.43 \text{ Nm}^3/\text{h}$  can also be used to calculate  $f_{umf}$  for the fuel particles (*Table* A-3). The particle density of wood char was determined by water displacement measurement. These calculations result in  $f_{umf}$  above 1 for small fuel particles, around 1 for medium-sized particles and below 1 for large particles. The effect of these differences is described and discussed in the main body of this work (see Section 3.1.3).

**Table A-3** Fluidization properties of char used as fuel at 1200 K and atmospheric pressure.

Variable	Unit	Small char	Medium char	Large char
$d_P$	m	1.65E-03	3.75E-03	6.50E-03
$\Phi$	-	6.60E-01 [45]	6.60E-01 [45]	6.60E-01 [45]
$d_{SV}$	m	1.09E-03	2.48E-03	4.29E-03
$\rho_F$ (12 <sub>00 K)</sub>	kg/m <sup>3</sup>	4.34E-01	4.34E-01	4.34E-01
$\rho_P$	kg/m <sup>3</sup>	3.30E+02	3.30E+02	3.30E+02
μ (1200 K)	$N*s/m^2$	4.68E-05 [50]	4.68E-05 [50]	4.68E-05 [50]
g	$m/s^2$	9.81E+00	9.81E+00	9.81E+00
Ar	-	8.28E+02	9.72E+03	5.06E+04
u <sub>mf</sub>	m/s	4.93E-02	2.37E-01	5.75E-01
A	m <sup>2</sup>	2.21E-03	2.21E-03	2.21E-03
$\dot{V}_{mf}$	Nm <sup>3</sup> /h	8.94E-02	4.30E-01	1.04E+00
$f_{umf}$ (0.30 Nm <sup>3</sup> /h)	-	3.4	0.7	0.3
$f_{umf}$ (0.43 Nm <sup>3</sup> /h)	-	4.8	1.0	0.4

#### Appendix B. Detailed description of the experimental procedure

Semi-continuous experiments with continuously fed CO<sub>2</sub> and initially inserted wood char are used to determine the CO<sub>2</sub> conversion within this paper. This type of experiment has trade-offs with continuous experiments.

Three advantages can be identified compared to evaluating stationary points in continuous experiments: A first reason, which is essential when assessing so many operational parameters, is the speed of investigation. Semi-continuous experiments are quicker to perform than investigating stable continuous operation points because there is no need to wait for the system to reach its steady state. For this reason, more parameters can be studied in the same amount of time. This advantage is present in many batch or semi-batch experiments.

The other reasons are system-specific and hail from reactor and measurement limitations with the used setup. Second, the conditions at the time of investigation are close to the initial conditions and can thus be relatively accurately known. The fuel amount and size of particles in the reactor change during the gasification process and are not measured in this system. Evaluating only close to the experimental start reduces unknown modifications to the selected parameters. Third, endothermic reactions (see Table 1) cool the reactor significantly and lower its temperature. Since this system's primary reaction converting  $CO_2$  is the endothermic Boudouard reaction, the cooling effect intensifies with increasing  $X_{CO2}$ . This effect reduces the maximum achievable temperature in the reactor. During comparable continuous experiments, the highest temperatures achieved in this reactor were around 100 °C lower. As a result, semi-continuous experiments can be used to correlate reactor temperature to  $CO_2$  conversion in fluidized bed reactors over a broader range.

Compared to continuous experiments, some disadvantages of this type of experiment are less accurately representing industrial production and

lacking the ability to conduct an energy balance properly. Mid- and long-term effects like catalyst deactivation or the risk of reactor blockage could be assessed better in continuous experiments. Additionally, ongoing fuel feeding would lead to overlapping fuel devolatilization and gasification reactions, which might produce different gas compositions than semi-continuous experiments. While these aspects are not the primary focus of this study, future follow-up works performed with continuous feeding are expected to expand the knowledge compared to the data presented in this paper.

During the experiments conducted in this work, gasification is preceded in the reactor by a short pyrolysis phase, as shown in Figure B-1. During pyrolysis (white background), the reactor is heated and flushed under a nitrogen atmosphere. Fuel is added under the N<sub>2</sub> atmosphere at experimental temperature, leading to small amounts of devolatilization. This phase of devolatilization reduces the influence of the pyrolysis gases on the measured gas composition during gasification, increasing the accuracy of the CO<sub>2</sub> conversion calculation.

In the gasification phase (green), CO2 replaces N2 as a fluidization agent. The physical distance between the reaction zone and NDIR measurement induces a delay of 30-60 seconds, which depends on the amounts of gases produced, temperature, and feed gas flow rate. Evaluating close to the starting conditions reduces the uncertainty of fuel loading and fuel size, and also ensures that wood char is available in excess and does not limit the conversion of CO2 stoichiometrically. To comparably start the evaluation period for all experiments at small fuel conversions, a standardized method to eliminate this delay is applied. The evaluation begins once the sum of carbonaceous components (CO, CO<sub>2</sub>, CH<sub>4</sub>) in the produced gas exceeds 10 vol %<sub>db</sub>. This cutoff number is selected because it coincides well with the first observed CO<sub>2</sub> conversion plateau before the conversion starts dropping due to the temperature and fuel decrease. The CO<sub>2</sub> conversion is averaged over 10 s for the higher and 14 s for the lower investigated feed gas flow rate to assess equal amounts of CO<sub>2</sub> fed to the reactor. Concentrations are measured every 1 s, and Eq. 15 is applied each second. Averaging over this short evaluation period means that changes to reactor conditions remain minor, while potential errors in assessing X<sub>CO2</sub> resulting from measurement noise are reduced (see Figure B-1). Some nitrogen is in the measured gas throughout the gasification experiment because N<sub>2</sub> is used as an inert gas to flush the fuel hopper and is added to the product gas after the reactor but before measurement.

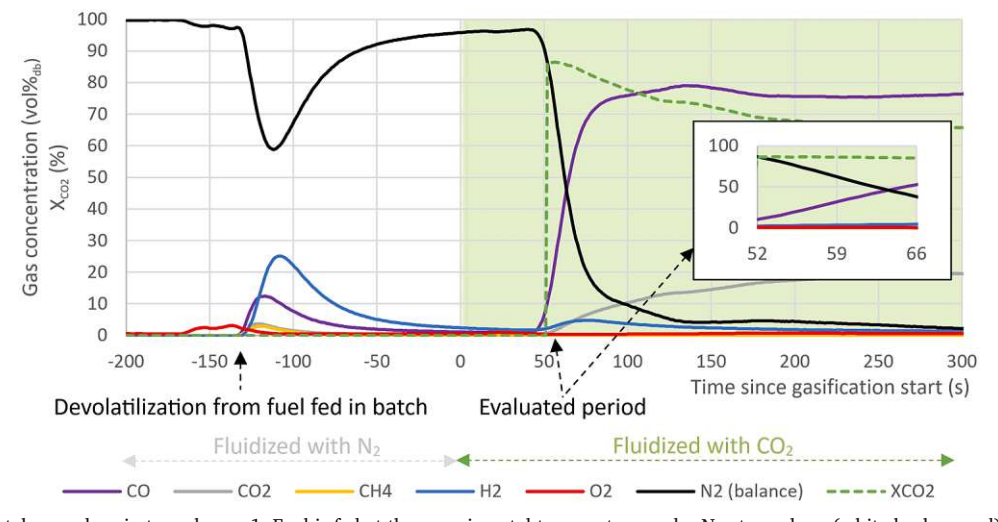


Figure B-1. Experimental procedure in two phases: 1. Fuel is fed at the experimental temperature under N<sub>2</sub> atmosphere (white background). 2. CO<sub>2</sub> replaces N<sub>2</sub> to start gasification (green background). Magnified: Evaluated period for the CO<sub>2</sub> conversion X<sub>CO2</sub>. More information on experimental parameters for this experiment is  $\textbf{Figure B-1.} \ \ \text{Experimental procedure in two phases: 1. Fuel is fed at the experimental temperature under $N_2$ atmosphere (white background). 2. $CO_2$ replaces $N_2$ to$ 

to the temperature and assess equal amounts of evaluation period measure reduced (see Figure the fuel hopper and is are Temperatures used in the evaluations are taken at the beginning of gasification since thermocouples do not suffer from the same 30 – 60 seconds delay in measurement. The measured temperatures in the reactor are lower than the heating shells' outside temperature set point due to static heat losses and rapidly cool with increasing CO<sub>2</sub> conversion due to the endothermic reactions. Evaluating the CO<sub>2</sub> conversion as described close to the experimental start minimizes the changes to the reactor temperature resulting from this cooling effect. CO<sub>2</sub> is replaced by air after 30 minutes of gasification to combust residual unconverted coke in the reactor, preparing it for the next experiment. During the combustion phase, the temperature is between 900 – 1000 °C, which is also expected to facilitate a complete decomposition of limestone to quick lime and CO<sub>2</sub>. However, with this setup, solid samples are not available during operation; therefore, experimental proof of this decomposition cannot be given.

The equipment used in this study has the following error tolerances:

- Dry gas composition measurement: 1 vol% of calibrated maximum. The calibrated maxima were

- Temperature measurement by thermocouple type K: 4‰ of measured temperature

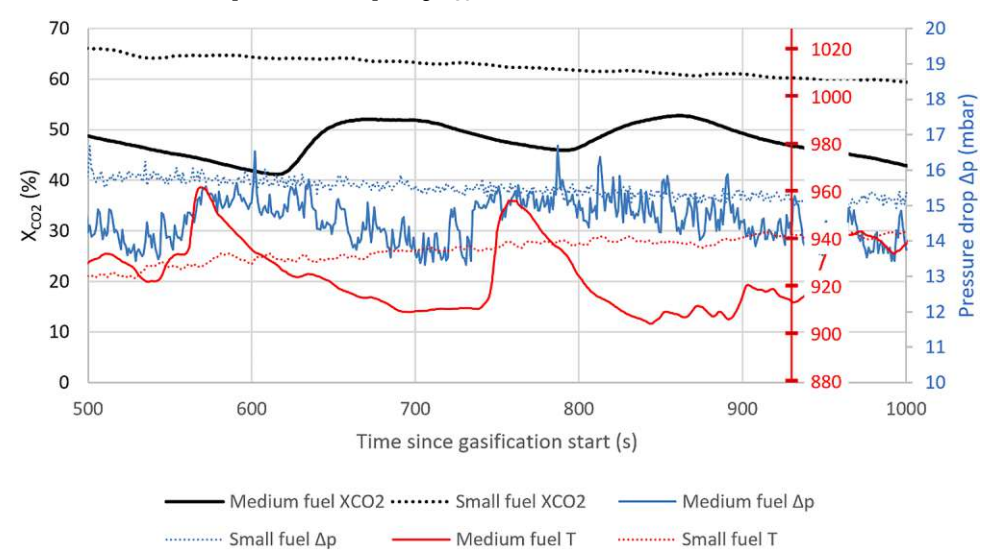
#### Appendix C. List of experiments

Exp. Nr	Fuel	Bed material		Target temperature	CO <sub>2</sub> feed	Number of new experiments
	_	height	height		Volume flow	

(continued on next page)

Table C-1 (continued)

			Bed material		Target temperature	CO <sub>2</sub> feed	Number of new experi
		<b>height</b> cm		<b>height</b> cm	°C	Volume flow NL/min	
		cm		cm	°C	NL/min	
1–5	Wood char	5	Silica sand sand	10	800   850 900   950 1000	7.2	5
6	Wood char	5	Silica sand sand	10	1000	5.1	1
7–11	Wood char	5	Limestone	10	800   850 900   950	7.2	5
12–16	Wood char	5	Olivine	10	1000 800   850 900   950	7.2	5
17–22	Wood char	5	Olivine	15 20	1000 900   950 1000	7.2	6
23–31	Wood char	5	Olivine	10 15	900   950 1000	5.1	9
32–35	Wood char	7.5 10	Olivine	20 10	900   1000	7.2	4
36–39	Wood char	7.5 10	Olivine	10	900   1000	5.1	4
40–43	Large wood char 5–8 mm	5 10	Olivine	10	1000	5.1 7.2	4
44_48	Medium wood char 2.5–5 mm	5 10 15	Olivine	10	1000	5.1 7.2	5
49–53	Small wood char 0.8–2.5 mm	5 10	Olivine	10	1000	5.1 7.2	5
Total variations	4	15 3	3	3	5	2	53
This section d	_	fferences ob-	served when in	nvestigating this work (	g fuel particles with d	ifferent sizes for a	longer duration than th
This section devaluation period CO <sub>2</sub> conversion of Data for exper	letails experimental di l, which is used to calc observed during the ev riments with an initial temperature and a CO	fferences ob- ulate and con valuation per fuel loading of 2 feed gas flo	served when in mpare $X_{CO2}$ in minor, see Section of 15 cm are given rate of 0.30.	nvestigating this work (and 3.1.3.) wen for med Nm <sup>3</sup> /h. Bo	g fuel particles with d Appendix B). For more dium and small fuel. Fi th investigations use 1	different sizes for a endormation about igure D-1 compares 0 cm olivine as bed	longer duration than th the effect of this param two experiments condu material and 15 cm init
This section devaluation period CO <sub>2</sub> conversion of Data for exper	letails experimental di l, which is used to calc observed during the ev riments with an initial temperature and a CO	fferences ob- ulate and con valuation per fuel loading of 2 feed gas flo	served when in mpare $X_{CO2}$ in minor, see Section of 15 cm are given rate of 0.30.	nvestigating this work (and 3.1.3.) wen for med Nm <sup>3</sup> /h. Bo	g fuel particles with d Appendix B). For more dium and small fuel. Fi th investigations use 1	different sizes for a endormation about igure D-1 compares 0 cm olivine as bed	longer duration than th the effect of this param two experiments condu material and 15 cm init
This section devaluation period CO <sub>2</sub> conversion of Data for exper	letails experimental di l, which is used to calc observed during the ev riments with an initial temperature and a CO	fferences ob- ulate and con valuation per fuel loading of 2 feed gas flo	served when in mpare $X_{CO2}$ in minor, see Section of 15 cm are given rate of 0.30.	nvestigating this work (and 3.1.3.) wen for med Nm <sup>3</sup> /h. Bo	g fuel particles with d Appendix B). For more dium and small fuel. Fi th investigations use 1	different sizes for a endormation about igure D-1 compares 0 cm olivine as bed	longer duration than the the effect of this parameter two experiments condumaterial and 15 cm initiates shown in Figure D
This section devaluation period CO <sub>2</sub> conversion of Data for exper	letails experimental di l, which is used to calcookserved during the evolution in initial interpretation and a CO eriments differ in initial initial interpretation and a column in the evalution in the evaluation in the evaluatio	fferences ob- ulate and con valuation per fuel loading of 2 feed gas flo	served when in mpare $X_{CO2}$ in minor, see Section of 15 cm are given rate of 0.30.	nvestigating this work (and 3.1.3.) wen for med Nm <sup>3</sup> /h. Bo	g fuel particles with d Appendix B). For more dium and small fuel. Fi th investigations use 1	different sizes for a see information about the information about the information about the information and small). The contraction is seen and small.	longer duration than the the effect of this parametric two experiments condumaterial and 15 cm initial data shown in Figure D
This section devaluation period CO <sub>2</sub> conversion of Data for exper	etails experimental di l, which is used to calcobserved during the eviments with an initial attemperature and a CO eriments differ in initiminutes after the eval	fferences ob- ulate and con valuation per fuel loading of 2 feed gas flo	served when in mpare $X_{CO2}$ in minor, see Section of 15 cm are given rate of 0.30.	nvestigating this work (and 3.1.3.) wen for med Nm <sup>3</sup> /h. Bo	g fuel particles with d Appendix B). For more dium and small fuel. Fi th investigations use 1	different sizes for a electric information about igure D-1 compares 0 cm olivine as bed in and small). The compares 1020	longer duration than the the effect of this parametric two experiments condumaterial and 15 cm initial data shown in Figure D
This section devaluation period CO <sub>2</sub> conversion of Data for exper	details experimental di l, which is used to calcobserved during the eviments with an initial temperature and a CO eriments differ in initiminutes after the eval	fferences ob- ulate and con valuation per fuel loading of 2 feed gas flo	served when in mpare $X_{CO2}$ in minor, see Section of 15 cm are given rate of 0.30.	nvestigating this work (and 3.1.3.) wen for med Nm <sup>3</sup> /h. Bo	g fuel particles with d Appendix B). For more dium and small fuel. Fi th investigations use 1	different sizes for a enformation about a enforcement a enforcem	longer duration than the the effect of this parametric two experiments condumaterial and 15 cm initial data shown in Figure D
This section devaluation period CO <sub>2</sub> conversion of Data for exper	details experimental di l, which is used to calcobserved during the eveniments with an initial attemperature and a CO eriments differ in initiminutes after the eval	fferences ob- ulate and con valuation per fuel loading of 2 feed gas flo	served when in mpare $X_{CO2}$ in minor, see Section of 15 cm are given rate of 0.30.	nvestigating this work (and 3.1.3.) wen for med Nm <sup>3</sup> /h. Bo	g fuel particles with d Appendix B). For more dium and small fuel. Fi th investigations use 1	different sizes for a enformation about igure D-1 compares 0 cm olivine as bed in and small). The compares 1000 1000 1000 1000 1000 1000 1000 10	longer duration than the the effect of this parametric two experiments condumaterial and 15 cm initial data shown in Figure D
This section devaluation period CO <sub>2</sub> conversion of Data for exper	details experimental di l, which is used to calcobserved during the every	fferences ob- ulate and con valuation per fuel loading of 2 feed gas flo	served when in mpare $X_{CO2}$ in minor, see Section of 15 cm are given rate of 0.30.	nvestigating this work (and 3.1.3.) wen for med Nm <sup>3</sup> /h. Bo	g fuel particles with d Appendix B). For more dium and small fuel. Fi th investigations use 1	different sizes for a se information about the information and small). The contract the information is a size of the information about the information abo	longer duration than the the effect of this parametric two experiments condumaterial and 15 cm initial data shown in Figure D
This section devaluation period CO <sub>2</sub> conversion of Data for exper	letails experimental di l, which is used to calcobserved during the eviments with an initial temperature and a CO eriments differ in initial minutes after the eval	fferences ob- ulate and con valuation per fuel loading of 2 feed gas flo	served when in mpare $X_{CO2}$ in minor, see Section of 15 cm are given rate of 0.30.	nvestigating this work (and 3.1.3.) wen for med Nm <sup>3</sup> /h. Bo	g fuel particles with d Appendix B). For more dium and small fuel. Fi th investigations use 1	different sizes for a enformation about igure D-1 compares 0 cm olivine as bed in and small). The olivine as bed in and small) and small igure D-1 compares 0 cm olivine as bed in and small). The olivine as bed in and small igure D-1 compares 0 cm olivine as bed in and small igure D-1 compares 0 cm olivine as bed in and small igure D-1 compares 0 cm olivine as bed in and small igure D-1 compares 0 cm olivine as bed in and small igure D-1 compares 0 cm olivine as bed in and small igure D-1 compares 0 cm olivine as bed in and small igure D-1 compares 0 cm olivine as bed in and small igure D-1 compares 0 cm olivine as bed in and small igure D-1 compares 0 cm olivine as bed in and small igure D-1 compares 0 cm olivine as bed in and small igure D-1 compares 0 cm olivine as bed in and small igure D-1 compares 0 cm olivine as bed in and small igure D-1 compares 0 cm olivine as bed in and small igure D-1 compares 0 cm olivine as bed in and small igure D-1 compares 0 cm olivine as bed in and small igure D-1 cm olivine as bed in and small igure D-1 cm olivine as bed in and small igure D-1 cm olivine as bed in and small igure D-1 cm olivine as bed in and small igure D-1 cm olivine as bed in an all igure D-1 cm olivine as bed in a bed in	longer duration than the the effect of this parametric two experiments condumaterial and 15 cm initiates shown in Figure December 19
This section devaluation period CO <sub>2</sub> conversion of Data for exper	letails experimental di l, which is used to calcobserved during the every during the every diments with an initial attemperature and a CO deriments differ in initial minutes after the evaluation of the evaluati	fferences ob- ulate and con valuation per fuel loading of 2 feed gas flo	served when ir mpare $X_{CO2}$ in iod, see Section of 15 cm are given rate of 0.30 rs only by choos for comparing	nvestigatin; this work (, n 3.1.3. ven for med Nm³/h. Bo oice of fuel g $X_{CO2}$ .	g fuel particles with dappendix B). For more dium and small fuel. Fith investigations use 1 particle size (medium	different sizes for a se information about the information about t	longer duration than the the effect of this parametric two experiments condumaterial and 15 cm initial data shown in Figure December 19
This section devaluation period CO <sub>2</sub> conversion of Data for exper	details experimental dial, which is used to calculate observed during the eviments with an initial attemperature and a CO deriments differ in initial minutes after the evaluation of the control of the	fferences ob- ulate and con- raluation per fuel loading of the loa	served when ir mpare $X_{CO2}$ in iod, see Sectio of 15 cm are given rate of 0.30 are only by choose for comparing the form of	nvestigating this work (an 3.1.3.) wen for med Nm³/h. Bo bice of fuel g $X_{CO2}$ .	g fuel particles with dappendix B). For more dium and small fuel. Fith investigations use 1 particle size (medium and small fuel of the investigations use 1 particle size (medium and small fuel of the investigations use 1 particle size (medium and small fuel of the investigations use 1 particle size (medium and small fuel of the investigations use 1 particle size (medium and small fuel of the investigations use 1 particle size (medium and small fuel of the investigations use 1 particle size (medium and small fuel of the investigations use 1 particle size (medium and small fuel of the investigations use 1 particle size (medium and small fuel of the investigations use 1 particle size (medium and small fuel of the investigations use 1 particle size (medium and small fuel of the investigations use 1 particle size (medium and small fuel of the investigations use 1 particle size (medium and small fuel of the investigations use 1 particle size (medium and small fuel of the investigations use 1 particle size (medium and small fuel of the investigations use 1 particle size (medium and small fuel of the investigations use 1 particle size (medium and small fuel of the investigations use 1 particle size (medium and small fuel of the investigations use 1 particle size (medium and small fuel of the investigations use 1 particle size (medium and small fuel of the investigations use 1 particle size (medium and small fuel of the investigations use 1 particle size (medium and small fuel of the investigations use 1 particle size (medium and small fuel of the investigations use 1 particle size (medium and small fuel of the investigations use 1 particle size (medium and small fuel of the investigations use 1 particle size (medium and small fuel of the investigations use 1 particle size (medium and small fuel of the investigations use 1 particle size (medium and small fuel of the investigations use 1 particle size (medium and small fuel of the investigations use 1 particle size (medium and small fuel of the investigations use 1 part	lifferent sizes for a e information about igure D-1 compares 0 cm olivine as bed in and small). The olivine as bed in and small) and small igure D-1 compares 0 cm olivine as bed in and small). The olivine as bed in and small) and small igure D-1 compares 0 cm olivine as bed in and small). The olivine igure D-1 compares 0 cm olivine as bed in and small igure D-1 compares 0 cm olivine as bed in and small igure D-1 compares 0 cm olivine as bed in and small igure D-1 compares 0 cm olivine as bed in and small igure D-1 compares 0 cm olivine as bed in and small igure D-1 compares 0 cm olivine as bed in and small igure D-1 compares 0 cm olivine as bed in and small igure D-1 compares 0 cm olivine as bed in and small igure D-1 compares 0 cm olivine as bed in and small igure D-1 compares 0 cm olivine as bed in and small igure D-1 compares 0 cm olivine as bed in and small igure D-1 compares 0 cm olivine as bed in and small igure D-1 compares 0 cm olivine as bed in and small igure D-1 compares 0 cm olivine as bed in and small igure D-1 compares 0 cm olivine as bed in and small igure D-1 compares 0 cm olivine as bed in and small igure D-1 compares 0 cm olivine as bed in and small igure D-1 cm olivine as bed in and small igure D-1 cm olivine as bed in and small igure D-1 cm olivine as bed in a cm olivi	longer duration than the the effect of this parametric two experiments condumaterial and 15 cm initial data shown in Figure December 19
This section devaluation period CO <sub>2</sub> conversion of Data for expersion of CO <sub>3</sub> conversion of Data for expersional conding. The expersecorded several condings of the CO <sub>3</sub> conversion of the CO <sub>3</sub> co	details experimental dial, which is used to calculate observed during the eviments with an initial attemperature and a CO deriments differ in initial minutes after the evaluation of the control of the	fferences ob- ulate and con- raluation per fuel loading of the loa	served when ir mpare X <sub>CO2</sub> in iod, see Section of 15 cm are given rate of 0.30 are only by choosed for comparing the form of the comparing t	nvestigating this work ( n 3.1.3. ven for med Nm³/h. Bo bice of fuel g $X_{CO2}$ .	g fuel particles with dappendix B). For more dium and small fuel. Fith investigations use 1 particle size (medium and small fuel of the investigations use 1 particle size (medium and small fuel of the investigations use 1 particle size (medium and small fuel of the investigations use 1 particle size (medium and small fuel of the investigations use 1 particle size (medium and small fuel of the investigations use 1 particle size (medium and small fuel of the investigations use 1 particle size (medium and small fuel of the investigations use 1 particle size (medium and small fuel of the investigations use 1 particle size (medium and small fuel of the investigations use 1 particle size (medium and small fuel of the investigations use 1 particle size (medium and small fuel of the investigations use 1 particle size (medium and small fuel of the investigations use 1 particle size (medium and small fuel of the investigations use 1 particle size (medium and small fuel of the investigations use 1 particle size (medium and small fuel of the investigations use 1 particle size (medium and small fuel of the investigations use 1 particle size (medium and small fuel of the investigations use 1 particle size (medium and small fuel of the investigations use 1 particle size (medium and small fuel of the investigations use 1 particle size (medium and small fuel of the investigations use 1 particle size (medium and small fuel of the investigations use 1 particle size (medium and small fuel of the investigations use 1 particle size (medium and small fuel of the investigations use 1 particle size (medium and small fuel of the investigations use 1 particle size (medium and small fuel of the investigations use 1 particle size (medium and small fuel of the investigations use 1 particle size (medium and small fuel of the investigations use 1 particle size (medium and small fuel of the investigations use 1 particle size (medium and small fuel of the investigations use 1 particle size (medium and small fuel of the investigations use 1 part	lifferent sizes for a e information about igure D-1 compares 0 cm olivine as bed in and small). The olivine as bed in and small) and small igure D-1 compares 0 cm olivine as bed in and small). The olivine as bed in and small) and small igure D-1 compares 0 cm olivine as bed in and small). The olivine igure D-1 compares 0 cm olivine as bed in and small igure D-1 compares 0 cm olivine as bed in and small igure D-1 compares 0 cm olivine as bed in and small igure D-1 compares 0 cm olivine as bed in and small igure D-1 compares 0 cm olivine as bed in and small igure D-1 compares 0 cm olivine as bed in and small igure D-1 compares 0 cm olivine as bed in and small igure D-1 compares 0 cm olivine as bed in and small igure D-1 compares 0 cm olivine as bed in and small igure D-1 compares 0 cm olivine as bed in and small igure D-1 compares 0 cm olivine as bed in and small igure D-1 compares 0 cm olivine as bed in and small igure D-1 compares 0 cm olivine as bed in and small igure D-1 compares 0 cm olivine as bed in and small igure D-1 compares 0 cm olivine as bed in and small igure D-1 compares 0 cm olivine as bed in and small igure D-1 cm olivine as bed in and small igure D-1 cm olivine as bed in and small igure D-1 cm olivine as bed in and small igure D-1 cm olivine as bed in a cm olivine as bed i	longer duration than the the effect of this parametric two experiments condumaterial and 15 cm initial data shown in Figure December 19



 $0.30 \text{ Nm}^3/\text{h}$  CO<sub>2</sub> feed flow rate is around 3.4 times  $u_{mf}$  for small wood char and 0.7 times  $u_{mf}$  for medium wood char. Therefore, one explanation could be that the bed for the experiment with medium-sized fuel deviates from bubbling bed behavior due to the fuel particles'  $u_{mf}$  value below 1. The temperature spikes shortly after the average pressure drop decreases. This temperature spike can be explained by insufficient mixing when considering the heat source is on the reactor walls while the temperature measurement is in the reactor's core. When mixing is insufficient for efficiently transporting heat from the hot walls to the reactor's core, this lowers the CO<sub>2</sub> conversion. As a result of the decreased heat transport, less energy is available for the endothermic gasification reactions in the reactor. The CO<sub>2</sub> conversion drops at a delay of around 60 seconds, which is explained by the time the gas needs to flow through the measurement line. These data indicate that smaller fuel might facilitate higher CO<sub>2</sub> conversion during continuous operation at high fuel loadings by improving fluidization.

#### References

- IPCC, Climate Change 2022 Mitigation of Climate Change, Cambridge, 2022, 10.1017/9781009157926.
- [2] 2017/2117 for the production of large volume organic chemicals, 2017. European Commission, Commission Implementing Decision (EU) .
- [3] IRENA and Methanol Institute, "Innovation Outlook: Renewable Methanol," Abu Dhabi, 2021.
- [4] M.F. Irfan, M.R. Usman, K. Kusakabe, Coal gasification in CO2 atmosphere and its kinetics since 1948: a brief review, Energy vol. 36 (1) (2011) 12–40, https://doi. org/10.1016/j.energy.2010.10.034.
- [5] R. Liu, Y. Zhang, Z. Ling, Y. Song, Some new insights into the synergy occurring during char gasification in CO2/H2O mixtures, Fuel vol. 268 (February) (2020) 1–8, https://doi.org/10.1016/j.fuel.2020.117307.
- [6] C. Guizani, O. Louisnard, F.J.E. Sanz, S. Salvador, Gasification of woody biomass under high heating rate conditions in pure CO2: experiments and modelling, Biomass. Bioenergy vol. 83 (2015) 169–182, https://doi.org/10.1016/j. biomass. 2015.00.17
- [7] V. Lenz, N. Szarka, M. Jordan, D. Thrän, Status and perspectives of biomass use for industrial process heat for industrialized countries, Chem. Eng. Technol. vol. 43 (8) (2020) 1469–1484, https://doi.org/10.1002/ceat.202000077.
- [8] S. De, A.K. Agarwal, V.S. Moholkar, B. Thallada, Coal and biomass gasification, Springer Singapore, 2018, https://doi.org/10.1007/978-981-10-7335-9.
- [9] Y.H. Chan, S.N.F. Syed Abdul Rahman, H.M. Lahuri, A. Khalid, Recent progress on CO-rich syngas production via CO2 gasification of various wastes: a critical review on efficiency, challenges and outlook, Environ. Pollut. vol. 278 (2021) 116843, https://doi.org/10.1016/j.envpol.2021.116843.
- [10] P. Lahijani, Z.A. Zainal, M. Mohammadi, A.R. Mohamed, Conversion of the greenhouse gas CO2 to the fuel gas CO via the Boudouard reaction: a review, Renew. Sustain. Energy Rev. vol. 41 (2015) 615–632, https://doi.org/10.1016/j. rser.2014.08.034.
- [11] X. Yao, Q. Yu, Z. Han, H. Xie, W. Duan, Q. Qin, Kinetics of CO2 gasification of biomass char in granulated blast furnace slag, Int. J. Hydrog. Energy vol. 43 (27) (2018) 12002–12012, https://doi.org/10.1016/j.ijhydene.2018.04.102.
- [12] N. Sadhwani, S. Adhikari, M.R. Eden, Biomass gasification using carbon dioxide: effect of temperature, CO2/C ratio, and the study of reactions influencing the process,", Ind. Eng. Chem. Res. vol. 55 (10) (2016) 2883–2891, https://doi.org/ 10.1021/acs.iecr.5b04000.
- [13] Z. Wang, et al., Towards enhanced catalytic reactivity in CO2-assisted gasification of polypropylene, Fuel vol. 284 (July 2020) (2021) 1–9, https://doi.org/10.1016/
- [14] P. Lahijani, M. Mohammadi, Z.A. Zainal, A.R. Mohamed, Advances in CO2 gasification reactivity of biomass char through utilization of radio frequency irradiation, Energy vol. 93 (2015) 976–983, https://doi.org/10.1016/j.energy.2015.09.092.
- [15] M. Pohořelý, M. Jeremiáš, K. Svoboda, P. Kameníková, S. Skoblia, Z. Beňo, CO2 as moderator for biomass gasification, Fuel vol. 117 (2014) 198–205, https://doi.org/ 10.1016/j.fuel.2013.09.068.
- [16] S. Tong, L. Li, L. Duan, C. Zhao, E.J. Anthony, A kinetic study on lignite char gasification with CO2 and H2O in a fluidized bed reactor, Appl. Therm. Eng. vol. 147 (June 2018) (2019) 602–609, https://doi.org/10.1016/j.applthermaleng.2018.10.113.
- -[17] L. Reyes, L. Abdelouahed, B. Campusano, J.C. Buvat, B. Taouk, Exergetic study of beech wood gasification in fluidized bed reactor using CO2 or steam as gasification agents, Fuel Process. Technol. vol. 213 (July 2020) (2021) 1–12, https://doi.org/ 10.1016/j.fuproc.2020.106664.
- [18] P. Stoesser, C. Schneider, T. Kreitzberg, R. Kneer, T. Kolb, On the influence of different experimental systems on measured heterogeneous gasification kinetics, Appl. Energy vol. 211 (October 2017) (2018) 582–589, https://doi.org/10.1016/j. apenergy.2017.11.037.
- [19] S. Gül, F. Akgün, E. Aydar, N. Ünlü, Pressurized gasification of lignite in a pilot scale bubbling fluidized bed reactor with air, oxygen, steam and CO2 agents, Appl. Therm. Eng. vol. 130 (2018) 203–210, https://doi.org/10.1016/j. applthermaleng.2017.11.021.
- [20] Z. Liu, F. Zhang, H. Liu, F. Ba, S. Yan, J. Hu, Pyrolysis/gasification of pine sawdust biomass briquettes under carbon dioxide atmosphere: Study on carbon dioxide reduction (utilization) and biochar briquettes physicochemical properties, Bioresour. Technol. vol. 249 (2018) 983–991, https://doi.org/10.1016/j. biortech.2017.11.012.
  - Y. Cheng, Z. Thow, C.H. Wang, Biomass gasification with CO2 in a fluidized bed, Powder Technol. vol. 296 (2016) 87–101, https://doi.org/10.1016/j. powtec.2014.12.041.

- [22] A.M. Mauerhofer, et al., Conversion of CO2 during the DFB biomass gasification process, Biomass. Convers. Biorefin. vol. 11 (1) (2021) 15–27, https://doi.org/ 10.1007/s13399-020-00822-x
- [23] S. Valin, L. Bedel, J. Guillaudeau, S. Thiery, S. Ravel, CO2 as a substitute of steam or inert transport gas in a fluidised bed for biomass gasification, Fuel vol. 177 (2016) 288–295, https://doi.org/10.1016/j.fuel.2016.03.020.
- [24] H.A. Kibret, Y.L. Kuo, T.Y. Ke, Y.H. Tseng, Gasification of spent coffee grounds in a semi-fluidized bed reactor using steam and CO2 gasification medium, J. Taiwan Inst. Chem. Eng. vol. 119 (2021) 115–127, https://doi.org/10.1016/j. itice.2021.01.029.
- [25] N. Spiegl, X. Long, C. Berrueco, N. Paterson, M. Millan, Oxy-fuel co-gasification of coal and biomass for negative CO2 emissions, Fuel vol. 306 (August) (2021) 1–8, https://doi.org/10.1016/j.fuel.2021.121671.
- [26] J. Fuchs, J.C. Schmid, S. Müller, H. Hofbauer, Dual fluidized bed gasification of biomass with selective carbon dioxide removal and limestone as bed material: A review, Renew. Sustain. Energy Rev. vol. 107 (June 2019) (2019) 212–231, https://doi.org/10.1016/j.rser.2019.03.013.
- [27] R.W. Missen, C.A. Mims, B.A. Saville, Introduction to Chemical Reaction Engineering and Kinetics, John Wiley & Sons, Inc, Toronto, 1999.
- [28] R. Liu, R. Tsiava, S. Xu, D. Chen, Experimental study of char gasification characteristics with high temperature flue gas, J. Energy Inst. vol. 97 (April) (2021) 187–193, https://doi.org/10.1016/j.joei.2021.04.015.
- [29] M. Baerns, et al., Technische Chemie, 1. Edition, WILEY-VCH, Weinheim, 2006.
- [30] C.E. Agu, C. Pfeifer, B.M.E. Moldestad, Prediction of void fraction and minimum fluidization velocity of a binary mixture of particles: bed material and fuel particles, Powder Technol. vol. 349 (2019) 99–107, https://doi.org/10.1016/j. powtec.2019.03.027.
- [31] C.E. Agu, L.A. Tokheim, C. Pfeifer, B.M.E. Moldestad, Behaviour of biomass particles in a bubbling fluidized bed: a comparison between wood pellets and wood chips, Chem. Eng. J. vol. 363 (November 2018) (2019) 84–98, https://doi.org/10.1016/j.cej.2019.01.120.
- [32] S. Gupta, S. Choudhary, S. Kumar, S. De, Large eddy simulation of biomass gasification in a bubbling fluidized bed based on the multiphase particle-in-cell method, Renew. Energy vol. 163 (2021) 1455–1466, https://doi.org/10.1016/j. reneps. 2020.07 127
- [33] J.J. Hernández, G. Aranda-Almansa, A. Bula, Gasification of biomass wastes in an entrained flow gasifier: effect of the particle size and the residence time, Fuel Process. Technol. vol. 91 (6) (2010) 681–692, https://doi.org/10.1016/j. fuproc.2010.01.018.
- [34] F.S. Char-co, G. Kinetics, I. Studies, Flax straw char-CO2 gasification kinetics and its inhibition studies with CO, Can. J. Chem. Eng. vol. 91 (May) (2013) 882–888, https://doi.org/10.1002/cjce.21696.
- [35] A. Gómez-Barea, P. Ollero, C. Fernández-Baco, Diffusional effects in CO2 gasification experiments with single biomass char particles. 1. experimental investigation, Energy Fuels vol. 20 (5) (. 2006) 2202–2210, https://doi.org/10.1001/cspresses
- [36] R. Bilbao, J. Lezaun, M. Menéndez, J.C. Abanades, Model of mixing-segregation for straw/sand mixtures in fluidized beds, Powder Technol. vol. 56 (3) (1988) 149–155, https://doi.org/10.1016/0032-5910(88)80026-3.
- [37] B. Cluet, G. Mauviel, Y. Rogaume, O. Authier, A. Delebarre, Segregation of wood particles in a bubbling fluidized bed, Fuel Process. Technol. vol. 133 (2015) 80–88, https://doi.org/10.1016/j.fuproc.2014.12.045.
- [38] L. Xiaodong, Y. Jianhua, N. Mingjiang, C. Kefa, Study on mixing performance of municipal solid waste (MSW) in differential density fluidized beds (FBs), Chem. Eng. J. vol. 84 (2) (2001) 161–166.
- [39] Q. Wang, et al., Application of CPFD method in the simulation of a circulating fluidized bed with a loop seal Part II-Investigation of solids circulation, Powder Technol. vol. 253 (2014) 822–828, https://doi.org/10.1016/j. powter 2013.11.040
- [40] X. Jing, et al., Evaluation of CO2 gasification reactivity of different coal rank chars by physicochemical properties, Energy Fuels vol. 27 (12) (2013) 7287–7293, https://doi.org/10.1021/ef401630v
- [41] X. Yao, Q. Yu, Z. Han, H. Xie, W. Duan, Q. Qin, Kinetics of CO2 gasification of biomass char in granulated blast furnace slag, Int. J. Hydrog. Energy vol. 43 (27) (2018) 12002–12012, https://doi.org/10.1016/j.ijhydene.2018.04.102.
- [42] P. Lahijani, Z.A. Zainal, A.R. Mohamed, M. Mohammadi, Microwave-enhanced CO2 gasification of oil palm shell char, Bioresour. Technol. vol. 158 (2014) 193–200, https://doi.org/10.1016/j.biortech.2014.02.015.
- [43] S. Pratschner, M. Hammerschmid, S. Müller, F. Winter, Evaluation of CO2 sources for power-to-liquid plants producing Fischer-Tropsch products, J. CO2 Util. vol. 72 (May) (2023) 102508, https://doi.org/10.1016/j.jcou.2023.102508.

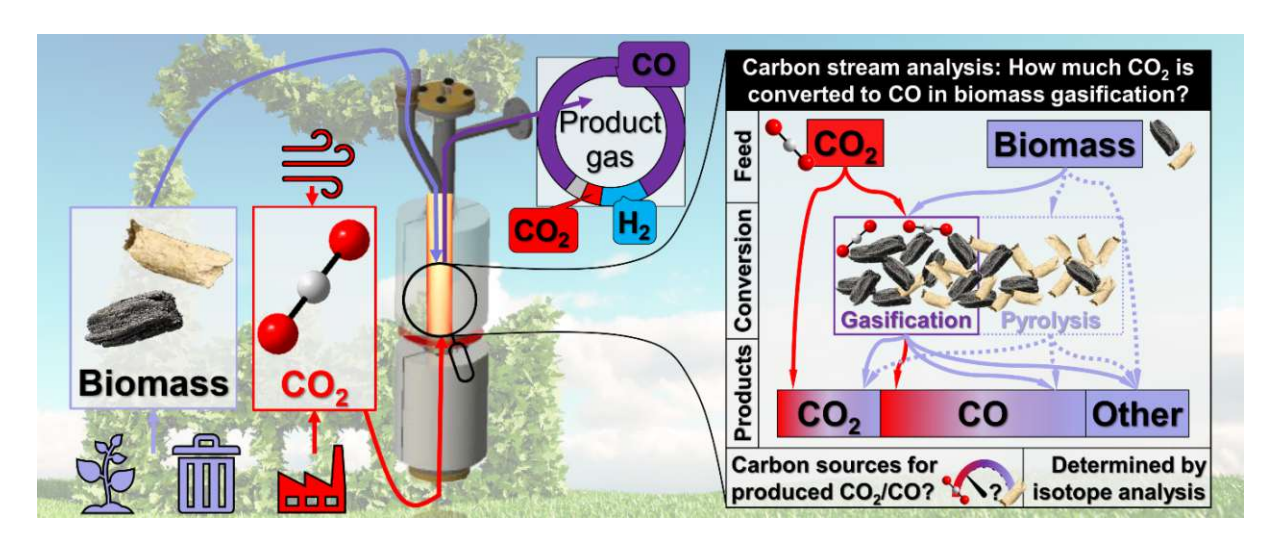
- [44] D. Kunii, O. Levenspiel, Fluidization Engineering, vol. 74, Butterworth-Heinemann, Bosten, London, singapore, Sydney, Toronto, Wellington, 1991, https://doi.org/
- [45] F. Scala, R. Chirone, P. Salatino, Combustion and attrition of biomass chars in a fluidized bed, Energy Fuels vol. 20 (1) (2006) 91-102, https://doi.org/10.1021/
- [46] P. Weerachanchai, M. Horio, C. Tangsathitkulchai, Effects of gasifying conditions and bed materials on fluidized bed steam gasification of wood biomass, Bioresour. Technol. vol. 100 (3) (2009) 1419-1427, https://doi.org/10.1016/j. biortech.2008.08.002.
- [47] A.M. Mauerhofer, J.C. Schmid, F. Benedikt, J. Fuchs, S. Müller, H. Hofbauer, Dual fluidized bed steam gasification: change of product gas quality along the reactor height, Energy vol. 173 (2019) 1256-1272, https://doi.org/10.1016/j
- [48] J.R. Grace, Contacting modes and behaviour classification of gas-solid and other two-phase suspensions, Can. J. Chem. Eng. vol. 64 (June) (1986) 353-363.
- [49] C.Y. Wen, Y.H. Yu, A generalized method for predicting the minimum fluidization velocity, Am. Inst. Chem. Eng. J. vol. 12 (3) (1966) 610-612, https://doi.org/
- [50] A. Fenghour, W.A. Wakeham, V. Vesovic, The viscosity of carbon dioxide, J. Phys. Chem. Ref. Data vol. 27 (1) (1998) 31-39, https://doi.org/10.1063/1.556013.

## Journal article II (JA II): CO<sub>2</sub> conversion to CO by fluidized bed biomass gasification: Measuring CO2 utilization via stable carbon isotope ratios

#### Bibliographical reference

F. J. Müller, J. Fuchs, S. Müller, and F. Winter, "CO2 conversion to CO by fluidized bed biomass gasification: Measuring CO2 utilization via stable carbon isotope ratios," Journal of CO2 Utilization, vol. 83, May 2024, doi: 10.1016/j.jcou.2024.102792.

#### Graphical abstract



#### Highlights

- Carbon from CO<sub>2</sub> and fuel were differentiated by stable carbon isotope analysis.
- Up to 93 % of feedstock CO<sub>2</sub> was converted to CO by gasification with biomass.
- The product gas is rich in carbon monoxide with a reduction potential of up to 14.
- Up to 50 % of carbon monoxide in product gas comes from CO<sub>2</sub> utilization.
- This method can be used for carbon accounting or process development.

Contents lists available at ScienceDirect

#### Journal of CO<sub>2</sub> Utilization

journal homepage: www.elsevier.com/locate/jcou



# CO<sub>2</sub> conversion to CO by fluidized bed biomass gasification: Measuring CO<sub>2</sub> utilization via stable carbon isotope ratios

Florian Johann Müller<sup>1,\*</sup>, Josef Fuchs<sup>2</sup>, Stefan Müller<sup>3</sup>, Franz Winter<sup>4</sup>

Technische Universität Wien, Faculty of Technical Chemistry, Institute of Chemical, Environmental and Bioscience Engineering, Getreidemarkt 9/166, Vienna 1060, Austria

#### ARTICLE INFO

# Keywords: CO<sub>2</sub> Conversion CCU Gasification Carbon Biomass

#### ABSTRACT

Thermochemical conversion of  $CO_2$  in biomass gasification is a promising technology for utilizing  $CO_2$  as a feedstock to produce a CO-rich gas. Simultaneous decomposition reactions of biomass and various gas-solid and gas-gas reactions form the product gas in this process. The overlap in sub-processes makes it challenging to assess the conversion of feedstock  $CO_2$  with common methods like mass balancing. This work introduces stable carbon isotope ratio analysis ( $\delta^{13}C$ ) to identify the sourcing of carbonaceous product gas components and determine the conversion of  $CO_2$ . This methodology is applied to evaluate experiments conducted for one hour of continuous operation in a lab-scale fluidized bed gasifier. Softwood pellets and wood char are used as fuel, with Olivine as a bed material, a target heating temperature of  $1000\,^{\circ}C$  and atmospheric pressure. Product gas with more than  $80\,vol^{\circ}C$  O was generated when wood char was used as fuel. Stable carbon isotope measurements show that  $CO_2$  is converted at 48–93% in this process, underpinning the position of biomass  $CO_2$  gasification as carbon capture and utilization technology. These results were up to 25% higher than suggested by mass balancing, with higher discrepancies at lower  $CO_2$  conversions when using softwood as fuel. Therefore, stable carbon isotope ratio measurement can be a valuable tool for improving the process understanding of biomass  $CO_2$  gasification. The results can be used for carbon accounting and the technical development of gasifiers with high  $CO_2$  utilization efficiency.

#### Nomenclature

,			
)	Symbol	Parameter description	Unit
)	A	Cross-section of the reactor	m <sup>2</sup>
)	Ar	Archimedes number	-
9	$c_A$	Volume concentration of species A in the product gas. The index <sub>db,N2-free</sub> describes that the volume concentration is expressed for dry-based gas(db) without nitrogen (N2-free)	%
5	$d_P$	Particle size (weighted average by sieving)	m
5	$d_{SV}$	Sauter diameter	m
,	$f_{umf}$	Factor from $\dot{V}_{mf}$ to applied feed gas flow rate	-
2	g LHV	Gravity of Earth (9.81 m/s <sup>2</sup> ) Lower heating value	$m/s^2$ $J/Nm^3$
)		(continued on	next column)

(continued)

Symbol	Parameter description	Unit
$\dot{m}_A$	Mass flow of species or sample A	kg/s
$\dot{m}_{CA}$	Mass flow of carbon in species or sample A	kg/s
$^{13}R_A$	<sup>13</sup> C/ <sup>12</sup> C ratio in the species or sample A	-
RP	Reduction potential	-
T	Temperature	°C
$u_{mf}$	Minimum fluidization velocity	m/s
$\dot{V}_{mf}$	Minimum fluidization flow rate (normal conditions)	Nm <sup>3</sup> /s
$\dot{V}_A$	Volume flow of species A (normal conditions)	Nm <sup>3</sup> /s
$X_{CO2}$	Feedstock CO <sub>2</sub> convertsion during gasification	%
stoichiometric	(calculated by product gas composition data)	
$X_{CO2,balance}$	Feedstock CO <sub>2</sub> conversion during gasification	%
	(calculated by mass balance)	

(continued on next page)

\* Corresponding author.

E-mail addresses: florian.johann.mueller@tuwien.ac.at (F.J. Müller), josef.fuchs@tuwien.ac.at (J. Fuchs), stefan.mueller@tuwien.ac.at (S. Müller), franz.winter@tuwien.ac.at (F. Winter).

- <sup>1</sup> https://orcid.org/0000-0002-8041-2317
- <sup>2</sup> https://orcid.org/0000-0002-4627-4475
- <sup>3</sup> https://orcid.org/0000-0001-8878-429X
- <sup>4</sup> https://orcid.org/0000-0001-9854-3836

https://doi.org/10.1016/j.jcou.2024.102792

Received 27 March 2024; Received in revised form 23 April 2024; Accepted 25 April 2024 Available online 2 May 2024

2212-9820/© 2024 The Authors. Published by Elsevier Ltd. This is an open access article under the CC BY license (http://creativecommons.org/licenses/by/4.0/).

#### (continued)

Symbol	Parameter description	Unit
$X_{CO2}$	Feedstock CO <sub>2</sub> conversion during gasification	%
	(calculated by stable carbon isotope analysis)	
X <sub>CO2 unconverted</sub>	Feedstock CO2 not converted during gasification	%
	(calculated by stable carbon isotope analysis)	
Y <sub>CO from CO2</sub>	Share of CO in product gas derived from feedstock	%
*	CO <sub>2</sub> (calculated by stable carbon isotope analysis)	
$Y_{CO\ from\ fuel}$	Share of CO in product gas derived from feedstock	%
	biomass (calculated by stable carbon isotope	
	analysis)	
$Y_{CO2\ from\ CO2}$	Share of CO2 in product gas derived from feedstock	%
	CO <sub>2</sub> (calculated by stable carbon isotope analysis)	
Y <sub>CO2</sub> from fuel	Share of CO <sub>2</sub> in product gas derived from feedstock	%
	biomass (calculated by stable carbon isotope	
40	analysis)	
$\delta^{13}C_A$	Carbon isotope abundance in the species A	‰
	compared to the VPDB standard	
$\varepsilon_A$	Isotope enrichment factor for component A (VPDB	‰
	standard)	
$\mu$	Dynamic viscosity (fluid)	N*s/m <sup>2</sup>
$\rho_F$	Density (fluid)	kg/m <sup>3</sup>
$\rho_P$	Density (particle)	kg/m <sup>3</sup>
Φ	Particle sphericity	-
Abbreviation	Term	
CCU	Carbon Capture and Utilization	
DRI	Direct reduced ironmaking	
EA-IRMS	Elemental Analyzer - Isotope-Ratio Mass	
	Spectrometer	
GC-C-IRMS	Gas Chromatography – Combustion - Isotope-Ratio	
D.C.	Mass Spectrometer	
PG	Product gas	
RED III	"Renewable Energy Directive III": Directive (EU)	
CIAI	2023/2413 [29]	
SW	Softwood pellets Vienna Peedee Belemnite	
VPDB	vienna Peedee beiennite	

#### 1. Introduction

#### 1.1. Biomass CO2 gasification

Humanity's use of fossil feedstocks undoubtedly contributes significantly to global warming [1]. Carbon Capture and Utilization (CCU) technologies are promising for defossilization because CO<sub>2</sub> emissions from using CCU-derived products can be offset by CO<sub>2</sub> being captured earlier in the process, e.g., by direct air capture [2,3]. Biomass gasification with CO<sub>2</sub> as an oxidizer is one such CCU process [4]. The product is a carbon monoxide-rich gas, which can be combined with low-emission hydrogen as feedstock to produce commodity chemicals like acrylic acid, formic acid, methanol, or dimethyl ether [5]. Alternatively, the generated gas could be used as an energy carrier or a preducing agent in heavy industry, e.g., ironmaking via the direct

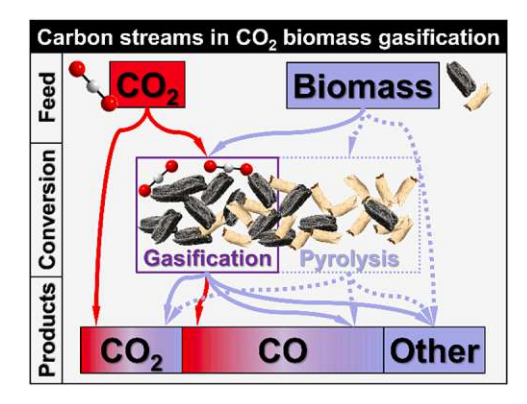


Fig. 1. Main carbon streams in biomass CO<sub>2</sub> gasification.

reduced ironmaking (DRI) route [6].

In this work, softwood, wood char, and  $CO_2$  are denoted as parental carbon sources of carbonaceous product gas species [7]. In biomass  $CO_2$  gasification,  $CO_2$  is reduced in endothermic reactions while biomass undergoes drying, devolatilization or pyrolysis, and gasification processes [8,9](Table 1). These overlapping sub-processes make it challenging to differentiate between  $CO_2$  and CO formed from the parental carbon sources  $CO_2$  and biomass in multiple pathways (Fig. 1). This challenge results in a knowledge gap in determining how much  $CO_2$  is utilized as a resource in this process. A new method capable of differentiating between devolatilization and  $CO_2$  utilization is presented in this study.

Gaining further insights into the carbon streams in biomass  $CO_2$  gasification is relevant for developing optimized biomass  $CO_2$  gasification processes.  $CO_2$  is mainly converted via the Boudouard-reaction (Eq. 1) [11–14], which produces CO as the primary product gas component. A high  $CO_2$  conversion increases CO yield per biomass by using  $CO_2$  as additional feedstock and can also improve product gas quality by lowering the  $CO_2$  concentration in the product gas [15]. Designing a process with high  $CO_2$  conversion based on literature is difficult because the reporting on  $CO_2$  conversion is underdeveloped. This study provides a new way of evaluating  $CO_2$  conversion, which should help stakeholders in this field overcome two issues with reporting in the current literature:

First, a substantial amount of literature on the topic does not investigate or discuss the role of  $\mathrm{CO}_2$  as a feedstock. Instead, these studies usually focus on the overall product gas composition, conversion of solid feedstock, or kinetic mechanisms and do not report  $\mathrm{CO}_2$  conversion results, e.g., [11,16–24]. This practice obscures how much these processes can be seen as Carbon Capture and Utilization because it remains unclear if and how much feedstock  $\mathrm{CO}_2$  is converted.

Table 1 Important reactions in  $CO_2$  gasification [5,10].

Reaction	$\Delta H_r^0$ (25 °C) in kJ/mol	Reaction name	
Heterogenous and homogenous reactions			
$C + CO_2 \leftrightarrow 2CO$	+173	Boudouard	Eq. 1
$C + H_2O \leftrightarrow CO + H_2$	+131	Steam-carbon (also water-gas)	Eq. 2
$C + 2H_2 \leftrightarrow CH_4$	-75	Methanation	Eq. 3
$CO + H_2O \leftrightarrow CO_2 + H_2$	-41	Water-gas shift	Eq. 4
Decomposition reactions of organic components			
$C_xH_yO_z \rightarrow Tar + Gas(CO, H_2, C_aH_b, CO_2) + Char(C)$	Endothermic	Pyrolysis (biomass)	Eq. 5
$C_xH_y \leftrightarrow (y/4)CH_4 + (x - y/4)C$	Endothermic	Pyrolysis (low O-content feedstocks)	Eq. 6
$C_xH_y \leftrightarrow C_{x-a}H_{y-z} + C_aH_b + ((z-b)/2)H_2$	Endothermic	Pyrolysis (low O-content feedstocks)	Eq. 7
$C_xH_y + xCO_2 \rightarrow 2xCO + (y/2)H_2$	Endothermic	Dry reforming	Eq. 8
$C_xH_y + xH_2O \rightarrow xCO + (y/2 + x)H_2$	Endothermic	Steam reforming	Eq. 9
$C_xH_y + (2x - y/2)H_2 \rightarrow xCH_4$	Exothermic	Hydrocracking	Eq. 10
$C_x H_y + CO_2 \rightarrow C_{x-1} H_{y-2} + 2CO + H_2$	Endothermic	Dry dealkylation	Eq. 11
$C_x H_y + H_2 O \rightarrow C_{x-1} H_{y-2} + CO + 2H_2$	Endothermic	Steam dealkylation	Eq. 12
$C_x H_y + H_2 \rightarrow C_{x-1} H_{y-2} + CH_4$	Exothermic	Hydrodealkylation	Eq. 13

Table 2
Properties of fuels used in this work.

		Eucalyptus globulus Pyrolyzed wood chips [15]	Softwood Pelletized [40]
Proximate and ultimate analysis			
Water content	wt%	7.1	7.2
Ash content	$\mathrm{wt}\%_{\mathrm{db}}$	6.28	0.2
Carbon content	wt% <sub>db</sub>	85.42	50.7
Hydrogen content	wt% <sub>db</sub>	1.98	5.9
Nitrogen content	wt% <sub>db</sub>	0.24	0.2
Sulfur content	wt% <sub>db</sub>	< 0.02	0.005
Chlorine content	wt% <sub>db</sub>	0.03	0.005
Volatile matter content	wt% <sub>db</sub>	15.06	85.4
Gross calorific value	kJ/kg	30,956	18,900
Net calorific value	kJ/kg	30,521	17,400
Analysis of ash melting behavior			
Deformation temperature	°C	1340	1335
Hemisphere temperature	°C	>1500	N.o.
Flow temperature	°C	>1500	1438
Ash composition			
CaO	wt%	53.0	55.2
K <sub>2</sub> O	wt%	14.0	13.4
SiO <sub>2</sub>	wt%	7.8	6.6
MgO	wt%	7.1	8.4
Fe <sub>2</sub> O <sub>3</sub>	wt%	3.8	0.9
$P_2O_5$	wt%	3.7	3.1
$Al_2O_3$	wt%	2.8	1.6
Na <sub>2</sub> O	wt%	2.5	1.1
MnO	wt%	1.7	5.4
$SO_3$	wt%	1.6	2.3
Rest	wt%	2.0	1.3

\*N.o... not occurred

Second, even for literature reporting on the conversion of CO<sub>2</sub>, the results are not measured but instead are based on different calculation schemes with varying assumptions, which lowers comparability. Most calculations are based on mass balancing the investigated reactor, e.g., [25,26], but other authors instead calculate CO<sub>2</sub> conversion from product gas composition only [15,27]. Since rapid devolatilization processes overlap with chemical reactions (Table 1) during gasification, some assumptions must be made when assessing CO<sub>2</sub> conversion via mass balancing. While some authors assume all CO2 leaving the reactor is leftover unconverted CO2 from the CO2 feedstock [28], other authors try to estimate the amount of CO2 produced from the solid feedstock and subtract this from the total CO2 in the product gas to calculate the unconverted CO<sub>2</sub> [25,26]. These studies further differ in the comparison case they use for this estimation. While [25] uses data from pyrolysis of the solid feedstock in a nitrogen atmosphere, [26] also proposed CO<sub>2</sub> formed during steam gasification for estimating CO2 released from biomass during CO<sub>2</sub> gasification. For these reasons, even review papers contain little to no information on the relative conversion of CO2 to CO in CO<sub>2</sub> gasification [8].

Knowing the parental carbon materials of carbonaceous gasification products is also imperative for carbon accounting. Much discussion and development of new legislation is ongoing regarding the sourcing of CO<sub>2</sub> for CCU processes, e.g., in the recently updated Renewable Energy Directive III (RED III). For example, RED III states that "Emission savings from carbon capture and replacement [...] shall be limited to emissions avoided through the capture of CO2 of which carbon originates from biomass [...]" [29]. Technically, CO<sub>2</sub> gasification is a feedstock-flexible process not limited to sustainably sourced biomass but has historically been used to process fossil fuels, e.g., coal to synthetic Diesel [30].  ${\rm CO}_2$  as an educt could practically also come from sources of varying sustainability: While direct air capture or biomass-based processes like bioenergy carbon capture and storage would provide CO<sub>2</sub> sourced from the atmosphere, other sources of CO2 could be fossil-sourced industrial off-gases from processes like blast furnaces or coal-fired power plants. A credible measurement of carbon sources per product that does not need the addition of expensive tracer materials could be helpful for carbon accounting schemes to differentiate between carbon sources of varying sustainability.

This new study introduces stable carbon isotope analysis to attribute product gas components to their parental carbon sources by measurement. This method is proposed to enable carbon accounting and further technical improvements in  $CO_2$  utilization for biomass  $CO_2$  gasification or similar processes.

#### 1.2. Stable carbon isotope analysis

Stable carbon isotope analysis has been used for decades in various scientific fields like medicine [31], biology [32], and chemistry [33]. Studies with closer relation to biomass  $CO_2$  gasification are, e.g., kinetic studies on the  $CO_2$ -carbon reaction [34,35] or the proposal to use the differences in isotopic fingerprints of  $CO_2$  designated for storage as markers to identify the origin of  $CO_2$  [36]. In 2014, one study by Bhagavatula et al. used stable carbon isotope analysis to attribute product gas components to the feedstock components of biomass-coal blends in steam gasification [7]. To the authors' knowledge, no study has been published yet attributing carbonaceous product gases to  $CO_2$  and solid feedstocks.

The stable carbon isotope  $^{13}\text{C}$  occurs naturally with relatively small deviations, so isotope chemists usually present its concentration as a relative value compared against a standard rather than an absolute value [37]. The most widespread standard is the Vienna Peedee Belemnite (VPDB) standard [38]. It is a virtual standard replicating and replacing the previously used physical standard Peedee Belemnite based on a calcium carbonate fossil from the Peedee formation in South Carolina [38]. A value of 0.011180 or 0.011180 $\pm$ 0.000028 based on measurements by Chang and Li is commonly used as a  $^{13}\text{C}/^{12}\text{C}$  ratio in VPDB [39]. New measurements and data are most often reported relative to this VPDB standard as isotopic abundance value  $\delta^{13}\text{C}_{\text{VPDB}}$  (Eq. 14).

$$\delta^{13}C_{VPDB} = \frac{^{13}R_{sample}}{^{13}R_{VPDB}} - 1 \tag{14}$$

The  $\delta^{13}C_{VPDB}$  measurements have natural abundance differences between different carbon sources. These natural abundance values of various resources are compared to values obtained in this work as part of

the results (Fig. 4). CO and CO<sub>2</sub> in the product gas contain a mixture of carbon that entered the gasification reactor either as CO2 or fuel (parental materials). The premise of this paper is that the different  $\delta^{13}C$ values of CO<sub>2</sub> and biomass can be used for fingerprinting to calculate the carbon sources of CO and CO<sub>2</sub> by some mixing equations [7]. The mixing equations used in this work are given and discussed in Section 2.3.

#### 2. Materials and methods

#### 2.1. Materials

The gases air (dry, compressed), CO<sub>2</sub> (99.995%), and N<sub>2</sub> (99.999%) were supplied to the feeding line with rotameters. Water was fed by a diaphragm pump and vaporized in the hot (300 °C) feed line before entering the reactor. Two types of solid fuel were used. The first fuel was wood char chips derived from Eucalyptus globulus and prepared by pyrolysis at 700 °C for 20 minutes. These char particles' length was between 0 and approximately 15 mm. The second fuel was softwood pellets produced based on the Austrian standard ÖNORM M 7135 with a diameter of 6 mm and a mean length of about 10 mm. Ultimate analysis of both fuels was performed using an Elementar Analyzer EA 1108 CHNS-O by Carlo Erba. An Axios advanced XRF device by Panalytical Analysis gave information on the ash content based on EN ISO 18122:2015-11. Water content was determined following DIN ⊇ 51718:2002–06 Method A, and volatile content following EN ISO 18123:2015-11. This information is summarized in Table 2. Wood char

and softwood were selected as feedstocks because of their difference in fixed carbon and volatile content. While softwood is assumed to undergo significant devolatilization during gasification, the wood char is expected to be mainly converted by gas-solid reactions.

The fluidized bed is formed by Olivine particles, which were observed to possibly catalyze the gasification process in a previous work [15]. The Olivine used in this study contains 48–50 wt% MgO, 39–42 wt  $\%~SiO_{2,}$  and 8.0--10.5 wt%  $Fe_{2}O_{3}.$  This bed material is fluidized at lower gas flow rates than the fuel because of its smaller particle size. Feed gas velocities are selected based on fluidization calculations with the goal of fluidized Olivine particles as a bubbling bed. Appendix A and a previous work give more information on the fluidization states for the used materials and the flow rate selection [15].

#### 2.2. Experimental setup

In continuous feeding operation, an electrically heated fluidized bed reactor with a maximum fuel input power of around 2 kWth using biochar and around 3 kW<sub>th</sub> using softwood pellets was used. Its schematic layout is presented in Fig. 2. This reactor is described in detail in a previous work [15]. Compared to that work, adaptations include adding a water feeding line and a sampling point for measuring stable carbon isotope ratios. Water was introduced into the gas feed line by a pump before preheating, evaporating, and heating it up to 400 °C.

The procedure described hereafter was followed to determine the  $\delta^{13}C_{VPDB}$  values of feedstock and product gas samples. Gas samples were

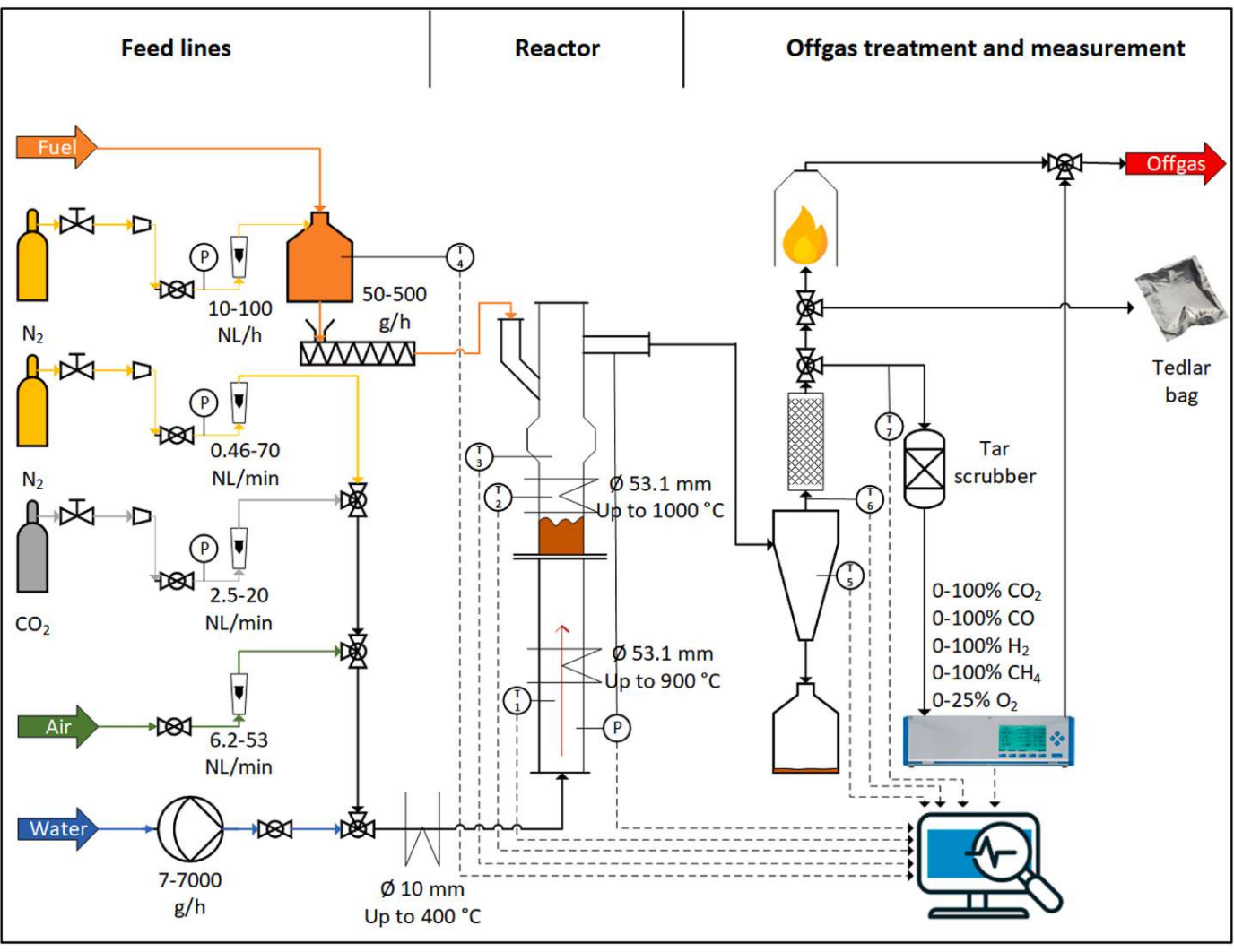


Fig. 2. Electrically heated fluidized bed reactor. Adjusted from [15].

approved original version of this doctoral thesis is available in print at TU Wien Bibliothek.

collected in Tedlar bags during stable operation. Filling a Tedlar bag took 1-3 minutes. Therefore, the sampled gas represents an average value from such duration. A gas-tight syringe was used to prepare the gas for transport by extracting around 10 mL per sample into gas chromatography vials. For each gas sample, three vials were used to compare the results against the accepted standard deviations and average the results. These vials were sent with solid samples of softwood and char to an external laboratory to measure the relative concentration of the isotope <sup>13</sup>C in carbon monoxide and carbon dioxide. The gas samples were separated by gas chromatography, combusted, and analyzed for isotope ratio using an isotope-ratio mass spectrometer (GC-C-IRMS). The solid samples were also combusted in an elemental analyzer before entering the isotope-ratio mass spectrometer (EA-IRMS). The EA-IRMS measurement was done with a Eurovector elemental analyzer (Pavia, Italy) and a NU Horizon 1 isotope ratio mass spectrometer (Wrexham, Great Britain). The equipment used for GC-C-IRMS was: Shimadzu AOC-5000 Autosampler – Shimadzu GC2010/ Shimadzu QP-2010 (Kyoto, Japan) coupled over a Hekatech combustion oven (Weinsberg, Germany) to the same NU Horizon 1 isotope ratio mass spectrometer. The measurement precision according to accreditation is  $\pm 0.63\%$  for EA-IRMS and  $\pm 1.10\%$  for GC-C-IRMS, given on the VPDB scale. These values include a hypothetical sampling error, which is unlikely to have happened in this work because the individual results from the triple analysis showed significantly lower standard deviations. An error estimate without this hypothetical sampling error is  $\pm 0.3\%$  for EA-IRMS and  $\pm 0.5\%$  for GC-C-IRMS.

#### 2.3. Calculation

#### 2.3.1. CO<sub>2</sub> conversion by stable carbon isotope analysis

This chapter describes how the  $CO_2$  conversion  $X_{CO2}$  is calculated from stable carbon isotope ratio data ( $\delta^{13}C$ ) and mass balancing. Balancing is performed using the process simulation software IPSEpro 8.0. IPSEpro is a steady-state, equation-oriented flowsheet simulation program. More information on the program and its use in gasification modeling is available in the literature, e.g., [41] and other publications by TUW. Appendix B has additional information on the modeling in this work.

Stable carbon isotope ratio data for the feedstocks CO2, softwood, and wood char can be combined with the data for CO and CO2 in product gas to calculate how much carbon of a feedstock is in which product (Eq. 15 - Eq. 18).  $Y_{A \text{ from } B}$  is introduced as a set of variables that describe parental carbon sourcing, or how much carbon in a product A is derived from a feedstock B. The basis of this calculation is a mixing equation, as proposed by [7]. Additionally, isotope enrichment factors  $\varepsilon_A$  are introduced in Eq. 15, Eq. 17, and Eq. 22 to account for isotopic fractionation effects. Isotopic fractionation is the change in the products' isotopic abundance that results from differences in reaction characteristics between isotopes. Differences in bond strength of <sup>12</sup>C and <sup>13</sup>C isotopes can lead to different reaction rates (kinetic isotope effect) and, therefore, to isotopic fractionation [36]. Introducing an isotope enrichment factor  $\varepsilon_A$ allows the mixing equations to account for the kinetic isotope effect and calculate the parental carbon materials' contributions to the product by removing this bias for isotopically lighter or heavier feedstocks. The sum of  $\varepsilon_A$  and the measured value  $\delta^{13}C_{A,out}$  for sample A can be interpreted as the isotope ratio the experiments would theoretically have yielded for product A if no such bias existed. To the authors' knowledge, no data on isotopic enrichment factors of different product gas components in CO<sub>2</sub> biomass gasification are available from the literature. For this reason, two assumptions are needed to determine the isotopic fractionation factors  $\varepsilon_{CO}$  and  $\varepsilon_{CO2}$  before closing isotopic balances and calculating  $Y_A$ from B values from measurement data.

$$Y_{\text{CO from CO}_2} = \frac{(\delta^{13}C_{\text{CO,out}} + \varepsilon_{\text{CO}}) - \delta^{13}C_{\text{fuel}}}{\delta^{13}C_{\text{CO}_2,\text{in}} - \delta^{13}C_{\text{fuel}}}$$
(15)

$$Y_{\text{CO from fuel}} = 1 - Y_{\text{CO from CO}_2} \tag{16}$$

$$Y_{\text{CO}_2 \text{ from CO}_2} = \frac{(\delta^{13}C_{\text{CO}_2,\text{out}} + \epsilon_{\text{CO}_2}) - \delta^{13}C_{\text{fuel}}}{\delta^{13}C_{\text{CO}_2,\text{in}} - \delta^{13}C_{\text{fuel}}}$$
(17)

$$Y_{\text{CO}_2 \text{ from fuel}} = 1 - Y_{\text{CO from CO}_2} \tag{18}$$

One study tried to assess  $^{13}\text{C}$  as a marker for  $\text{CO}_2$  from carbon capture and storage applications [36]. It concluded that isotopic fractionation of  $\text{CO}_2$  is likely averaging out in steam biomass gasification based on the following reason: The increased bond strength of the  $^{12}\text{C}_-^{13}\text{C}$  bond compared to  $^{12}\text{C}_-^{12}\text{C}$  suggests a  $^{13}\text{C}$  depletion in low molecular weight gases and an enrichment in heavy components such as tar [42]. The opposite result is achieved by the water-gas shift reaction (Eq. 4), which preferably produces  $^{12}\text{CO}_2$ , leading to a depletion of  $^{13}\text{CO}_2$  [36]. In summary, it was assumed that those effects roughly cancel each other out [36]. For this reason, the first assumption used in this work is that  $\epsilon_{\text{CO}2}$  is negligible and can be considered zero.

A second assumption is needed to close the isotope balances and calculate  $\varepsilon_{CO}$ , because the isotope ratio in products other than CO and CO<sub>2</sub> was not measured in this study. This study assumes that carbon from CO2 leaves the reactor as CO or CO2 but not as any other carbonaceous compound, such as tar or CH<sub>4</sub> (Eq. 20). This assumption is based on the primary reactions in CO<sub>2</sub> biomass gasification, which are given in Table 1. A result of this assumption is that all carbon in species other than CO and CO2 is derived from fuel, which means that Y<sub>rest from fuel</sub> in Eq. 22 has a value of 1. The subscript "rest" used for multiple variables refers to the sum of all gasification products other than CO and CO<sub>2</sub>. The isotopic enrichment factors  $\varepsilon_{CO}$  and  $\varepsilon_{rest}$  are calculated in this study based on mass and isotope balances. Eq. 19 describes the carbon isotope balance expressed in the VPDB scale. In this balance  $\dot{m}_{C.i.in}$  describes the carbon streams entering the reactor in the parental carbon materials i with the  $^{13}$ C abundance  $\delta^{13}C_{i.in}$ . These input streams are balanced by the outgoing carbon streams  $\dot{m}_{C.i.out}$  with the isotopic abundance  $\delta^{13}C_{i.out}$ , which describe all carbonaceous species leaving the reactor. The modeling of these outgoing streams also includes a stream of unconverted char, which likely was partially accumulated in the reactor during the experiments. This way of modeling ungasified char as an output stream is chosen because ungasified char is essential for closing balances, but the IPSEpro simulation is inherently steady state and does not include the option to model char accumulation dynamically. The mean isotope ratio of all carbonaceous gasification products other than CO and  $CO_2$  ( $\delta^{13}C_{rest,out}$ ) is calculated by Eq. 21. The variable  $\varepsilon_{rest}$  can be calculated from Eq. 22 and is briefly discussed as a plausibility check in Section 3.2.1.

A carbon exchange between CO and  $\mathrm{CO}_2$  during or after the gasification process could result in the products' isotopic abundance deviating from the mixture of parental carbon materials according to Eq. 15-Eq. 19. Such an isotope equilibrium as proposed by [43], shifting isotope ratios between CO and  $\mathrm{CO}_2$ , was investigated and ruled out in steam gasification experiments at temperatures similar to or even slightly higher than in this work [7]. The short residence time of the gas in the hot reactor also supports that such an equilibrium exchange did not significantly influence the stable carbon isotope ratio. Therefore, such an exchange is not considered in this study.

$$\sum \dot{m}_{C,i,in} \cdot \delta^{13} C_{i,in} = \sum \dot{m}_{C,j,out} \cdot \delta^{13} C_{j,out}$$
(19)

$$\dot{m}_{C,rest,out} = \dot{m}_{C,fuel,in} - \dot{m}_{C,CO,out} \cdot Y_{CO~from~fuel} - \dot{m}_{C,CO_2,out} \cdot Y_{CO_2~from~fuel} \tag{20}$$

$$\delta^{13}C_{\text{rest,out}} = \frac{\sum (\dot{m}_{\text{C,i,in}} \cdot \delta^{13}C_{\text{i,in}}) - \dot{m}_{\text{C,CO}_2,\text{out}} \cdot \delta^{13}C_{\text{CO}_2,\text{out}} - \dot{m}_{\text{C,CO,out}} \cdot \delta^{13}C_{\text{CO,out}}}{\dot{m}_{\text{C,rest,out}}}$$

Table 3
Experimental parameters investigated within this work. SW=softwood pellets. Char=pyrolyzed wood chips derived from Eucalyptus globulus.

Exp.	<b>Heating temp.</b> °C	Olivine height cm	CO <sub>2</sub> flow rate NL/min	Steam flow rate NL/min	Fuel type	Fuel feed g/min	$ \begin{aligned} & \textbf{Carbon ratio } C_{fuel} \\ & \textbf{C}_{CO2} \\ & \textbf{mol/mol} \end{aligned} $
#1	1000	10	2.8	0	SW	4.2	1.35
#2				0.23	SW	4.2	1.35
#3				0	SW	6.4	2
#4				0.23	SW	6.4	2
#5				0	Char	1.9	1
#6				0	Char	3.7	2
#7				0.36	Char	3.7	2

$$Y_{rest\ from\ fuel} = 1 = \frac{(\delta^{13}C_{rest,out} + \epsilon_{rest}) - \delta^{13}C_{CO_2,in}}{\delta^{13}C_{fuel} - \delta^{13}C_{CO_2,in}} \tag{22}$$

Mass flow data are necessary to relate the relative parameter  $Y_{CO2}$  from CO2 to the flow of  $CO_2$  going into the reactor ( $\dot{m}_{CO2,in}$ ) and determine  $X_{CO2}$ , the conversion of  $CO_2$  (Eq. 23 - Eq. 24). The outgoing mass flow of  $CO_2$  ( $\dot{m}_{CO2,out}$ ) is derived from mass balancing in IPSEpro.

$$X_{\text{CO2 unconverted}} = \frac{\dot{m}_{\text{CO2,out}}}{\dot{m}_{\text{CO2,in}}} Y_{\text{CO2 from CO2}}$$
 (23)

$$X_{\text{CO2}} = 1 - X_{\text{CO2 unconverted}} \tag{24}$$

#### 2.3.2. CO<sub>2</sub> conversion by other methods

Two calculation methods used in previous works are applied for comparison to demonstrate the variance in reported  $CO_2$  conversion caused by different calculation methods (Eq. 25 - Eq. 26). The first calculation was proposed by [44] and uses the dry-based volumetric product gas concentrations of CO,  $CO_2$  and  $H_2$  ( $c_A$ ). This calculation assumes all CO and CO and CO are produced by the Boudouard reaction (Eq. 1) or steam-carbon reaction (Eq. 2). It is denominated with the term *stoichiometric* in this work to differentiate between this calculation and the calculation by stable carbon isotope analysis.

$$\sum_{i=1}^{6} X_{\text{CO2,stoichiometric}} = \frac{c_{\text{CO}} - c_{\text{H2}}}{c_{\text{CO}} - c_{\text{H2}} + 2 \cdot c_{\text{CO2}}}$$
(25)

This equation allows the calculation of  $X_{CO2,stoichiometric}$  with the same time interval as available product gas composition data. The quick and continuous availability of data without mass balancing is a clear advantage of this method. However, this calculation also has some limitations [15]. An essential assumption this equation makes is the following:

CO or H<sub>2</sub> are products of the Boudouard and steam carbon reactions.
 This assumption is most valid for feedstocks like char and coal, which have relatively limited volatile content and do not contribute significantly to the gas composition via devolatilization. With increasing volatile content, the uncertainty of the calculation can increase.

The volatile content of around 85 wt% for softwood challenges the papplicability of this equation. For this reason, more significant differences between this simplified calculation and the calculation by isotopic tracing are expected when softwood as fuel is compared to wood char.

The second calculation performed for comparison is based on a mass balance of input and output streams in IPSEpro (Eq. 26). Following the calculation by [28], all CO<sub>2</sub> in the product gas is assumed as leftover feedstock CO<sub>2</sub>.

$$\mathbf{X}_{\text{CO2,balance}} = \frac{\dot{\mathbf{m}}_{\text{CO2,in}} - \dot{\mathbf{m}}_{\text{CO2,out}}}{\dot{\mathbf{m}}_{\text{CO2,in}}}$$
(26)

#### 2.3.3. Reduction potential

The reduction potential *RP* is introduced as a measure of product gas quality. This parameter describes the ratio of the reduced gases CO and

 $H_2$  to the fully oxidized compounds  $CO_2$  and  $H_2O$ . This parameter is used in direct reduced ironmaking as a descriptor of the gases' ability to reduce iron ore [6]. RP is calculated by Eq. 27, using  $c_A$ , which is the volume concentration of species A in the product gas.

$$RP = \frac{c_{CO} + c_{H2}}{c_{CO2} + c_{H2O}}$$
 (27)

#### 2.4. Conducted experiments

Previous works suggest high temperature, high gas-fuel contact times, and Olivine as bed material to achieve high CO<sub>2</sub> conversion [15]. Accordingly, the reactor's heating was set to the maximum temperature of 1000  $^{\circ}\text{C},$  a filling of 10 cm Olivine in the reactor was used as bed material, and a low CO2 flow rate was adopted while still forming a bubbling fluidized bed. The fuel height in the reactor is not available as a measurement from this experimental setup in continuous operation. Instead, different ratios of carbon fed in fuel and CO2 were used with the expectation that proportionally higher fuel feeding would also lead to a larger fuel reservoir in the reactor, thus increasing fuel-gas contact time. The Boudouard reaction demands a carbon ratio of 1 between solid carbon in fuel and CO<sub>2</sub>. The applied carbon ratios reach or exceed this stoichiometric ratio. Experiments were conducted with softwood pellets and biochar to investigate the influence of volatile content. Higher volatile content at similar total carbon ratios could lower the CO2 conversion because less fixed carbon is available for the Boudouard reaction after pyrolytic decomposition reactions. Some experiments were conducted with moisture in CO2 to compare a dry CO2 stream to a typical moist stream from a capture unit like an amine scrubber. The parameters chosen for the experiments are summarized in Table 3.

#### 3. Results and discussion

#### 3.1. Product gas

#### 3.1.1. Experimental data

Experiments were continued with continuous feeding for at least one hour. All values in Section 3.1 are averaged data from one hour of operation during which the measured product gas concentration remained largely stable. Supporting information on the experimental data and their interpretation is given in Appendix C. Dry-based product gas concentrations were combined with the water content data estimated by mass balancing to calculate the product gas composition for all conducted experiments, which is shown in Fig. 3. Fig. 3 also has data on the equilibrium product gas composition at the measured reaction zone temperature calculated by the minimization of free Gibbs energy in FactSage's equilibrium module. For most experiments, the experimental data show more CO2, H2O and CH4, and less CO and H2 than the equilibrium composition. The differences between thermodynamic equilibrium and observed concentrations are more significant for softwood experiments and experiment #5 with a lower char feeding rate than #6 and #7. Experimentally determined gas compositions for experiments #6 and #7 have high CO and low CO<sub>2</sub> content and are very similar to the calculated equilibrium gas composition, which suggests a high

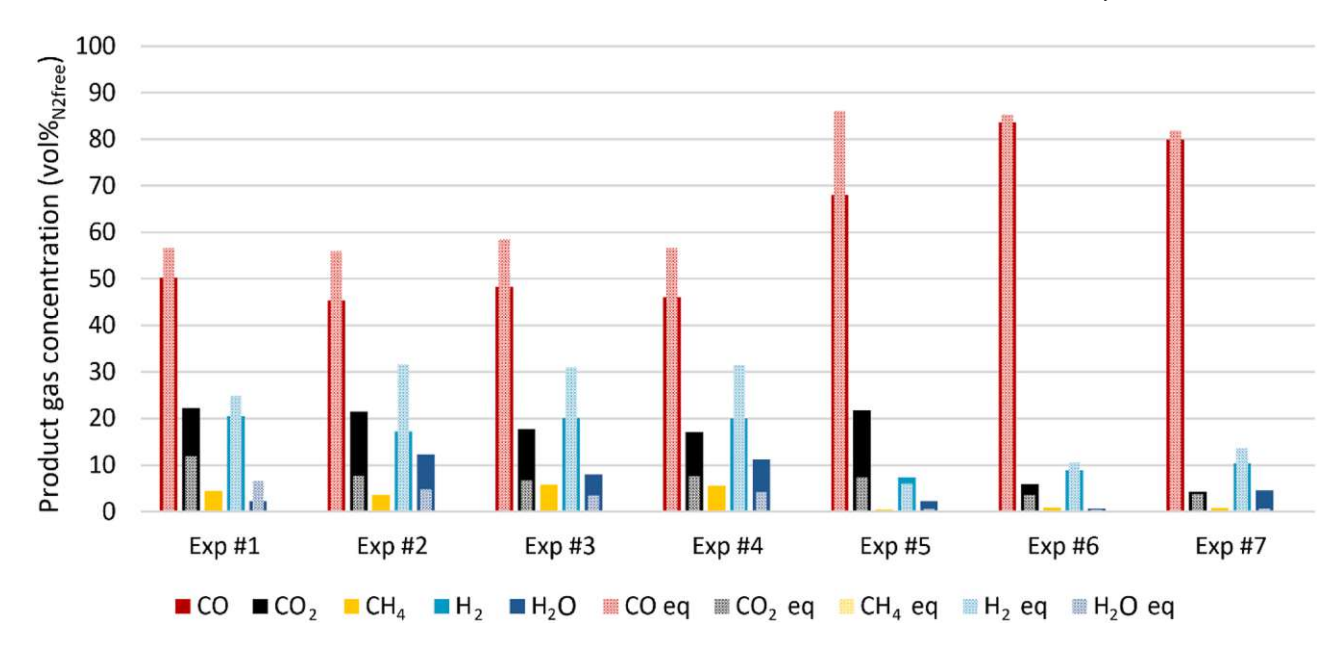


Fig. 3. Product gas composition: Measured concentrations (full bars) vs. thermodynamic equilibrium concentrations calculated in FactSage (checkered bars). H<sub>2</sub>O concentration was not measured but is a result of mass balancing.

Table 4

Key differences in operational parameters and performance indicators for all experiments. SW=softwood pellets. Char=pyrolyzed wood chips derived from Eucalyptus globulus.

Parameter	Unit	Data source	Exp. #1	Exp. #2	Exp. #3	Exp. #4	Exp. #5	Exp. #6	Exp. #7
Fuel type	-	Setting	SW	SW	SW	SW	Char	Char	Char
Carbon ratio C <sub>fuel</sub> :C <sub>CO2</sub>	-	Setting	1.35	1.35	2	2	1	2	2
ੁੱ H₂O added	-	Setting	No	Yes	No	Yes	No	No	Yes
Temperature	°C	Measurement	903	856	821	825	877	864	856
Unconverted fuel carbon	%	Mass balance	2	12	13	14	23	46	42
$\dot{V}_{total,out}$	NL/min	Mass balance	8.6	8.5	10.6	10.7	5.4	6.3	7.0
$\dot{V}_{CO,out}$	NL/min	Mass balance	4.2	3.9	5.0	5.0	3.9	5.3	5.6
$\dot{V}_{CO2,out}$	NL/min	Mass balance	1.8	1.8	1.9	1.8	1.0	0.4	0.3
$\dot{V}_{H2,out}$	NL/min	Mass balance	1.7	1.5	2.2	2.1	0.4	0.6	0.7
$\dot{V}_{CH4,out}$	NL/min	Mass balance	0.4	0.3	0.6	0.6	0.0	0.1	0.1
$\dot{V}_{H2O,out}$	NL/min	Mass balance	0.5	1.1	0.9	1.2	0.1	0.0	0.3
H <sub>2</sub> /CO ratio	-	Measurement	0.4	0.4	0.4	0.4	0.1	0.1	0.1
₹ RP	-	Mass balance	2.5	1.8	2.7	2.3	3.9	14.1	10.2
RP <sub>equilibrium</sub>	-	Gibbs energy minimization	4.4	7.1	8.8	7.5	11.6	23.2	21.3
LHV	$MJ/Nm^3$	Mass balance	9.8	8.8	10.3	10.0	10.0	11.8	11.5

conversion of the feedstock CO<sub>2</sub>.

Table 4 summarizes additional data measured or calculated by mass and energy balancing in IPSEpro for all experiments. Temperatures in Table 4 are taken from temperature measurement T2 (see Fig. 2), which is positioned in the reaction zone's center.

#### $\overline{\overline{\overline{\overline{\overline{\overline{\overline{\overline{\overline}}}}}}}}$ 3.1.2. Influence of fuel type

The product gas derived from the experiments with char is very rich in carbon monoxide, dry, and comparatively lean in hydrogen. These results fit well with the data from earlier works in semi-continuous operation, which had up to 83% CO content in the produced gas when high amounts of wood char were in this reactor [15]. In experiments with softwood as fuel, the main gas component, carbon monoxide, is produced at a similar rate, but water, hydrogen, and carbon dioxide have all increased. Softwood experiments also yield some methane in the resulting product gas, which is almost absent in the experiments with char.

The larger share of  $\rm H_2$ ,  $\rm H_2O$ , and  $\rm CH_4$  for experiments with softwood as fuel is caused by a higher hydrogen-to-carbon ratio in the fuel composition (Table 2). As a result, the  $\rm H_2$ -to-CO ratio is also higher in product gas from softwood experiments. For all experiments, the  $\rm H_2$ -to-

CO ratio is too low for direct conversion of the gas to methanol or in Fischer-Tropsch-synthesis, which need an  $H_2$ -to-CO ratio of around 2:1 [3,45]. For such applications, the gas would need  $H_2$  enrichment, e.g., by adding hydrogen from water electrolysis. In existing DRI plants, the reduction potential RP for the reducing gas usually has a value of around 9 or higher [6]. The gas produced in experiments #6 and #7 with char as fuel has sufficient reduction potential to fulfill this requirement without adjusting the gas composition by carbon capture or water condensation. Reduction potentials are lower when less char is fed (#5) and for all experiments conducted with softwood. The highest reduction potentials calculated for equilibrium gas compositions are achieved for experiments with high fuel feeding rate and dry  $CO_2$  feed. For softwood experiment #3 this maximum is 8.8; for wood char experiment #6 it is 23.2.

The changes in gas composition are minor when comparing experiments with dry and wet  $CO_2$  feed. A consistent trend is that steam flow rates in product gas increase when an  $H_2O/CO_2$  mixture is adopted as feedstock. This increase has a detrimental effect on the reduction power and lower heating value.

Since the methanation reaction (Eq. 3) proceeds at a very slow rate at these temperatures except at high pressures [7], the observed methane

for experiments with softwood is likely released by rapid pyrolysis, which proceeds the gasification of char in gasification [8,9]. The absence of CH4 in the calculated thermodynamic equilibrium compositions further confirms that it is a decomposition product rather than a product formed via the methanation reaction. H2, CO, and CO2 are other typical pyrolysis products from woody biomass, typically released during gasification at equal or higher amounts than methane [46]. The increased production of devolatilization products from softwood is apparent from proximate analysis and evident when comparing the total product gas flow rates and unconverted fuel carbon values. The Boudouard reaction demands a stoichiometric parental ratio of 1:1 (Eq. 1). In experiments #6 and #7, feeding wood char with low volatile content at a carbon ratio of 2:1, the mass balance suggests that nearly half of the fuel carbon was not converted in the process. On the contrary, the unconverted solid carbon was much lower in experiments #3 and #4, which supplied the same 2:1 parental carbon ratio via softwood. This difference is explained by considering that a sizeable amount of carbon from softwood was converted to gas by decomposition reactions. The increase in devolatilization in softwood experiments results in higher total syngas flow rates. At the same time, these overlapping processes make it harder to identify the CO<sub>2</sub> conversion by other methods than the proposed stable carbon isotope measurement scheme.

#### 3.1.3. Influence of fuel feeding rate

Increased fuel feeding was selected to achieve a larger fuel bed and increase the fuel-gas contact time, which was expected to increase CO2 conversion based on previous findings [15]. For softwood experiments, the changes in gas composition between experiments #1 and #2 with less fuel versus #3 and #4 with more fuel are relatively small. In these o experiments, the volume flows per component increase for all product gas components other than CO2, which remains stable. This trend is similar in wood char experiments, where the outgoing CO2 volume flow decreases at a higher fuel feeding rate. These changes in gas composition have little effect on the H2-to-CO ratio. The reduction potential is slightly increased for softwood experiments at higher fuel feeding rates. For wood char experiments, where the volume flow rate of CO2 in product gas decreases with higher fuel feeding rate, the reduction potential more than doubles when increasing the parental carbon ratio from 1:1-2:1. A drawback of this increase is calculated in the form of increased amounts of excess solid carbon.

Feeding softwood at a carbon ratio above 2 could increase the gases' reduction potential because too little fixed carbon might be available for the Boudouard reaction after devolatilization. However, this option is not feasible with the reactor used in this work because of limited heating capabilities. Temperatures on the reactor's outside wall are limited to 1000 °C for safety reasons. As a result, temperatures in the reaction zone are a complex result of heat transfer effects and energy demands of chemical reactions. The temperature differences for softwood experiments at carbon ratios of 1:1 versus experiments with a ratio of 2:1 in this work are likely a reason of increased energy demand for chemical reaction when a ratio of 2:1 was used. Increasing the carbon ratio even higher increases the energy demand from chemical reactions, possibly further lowering the temperature in the reaction zone. Since higher temperatures are beneficial for CO<sub>2</sub> conversion [15], this change might

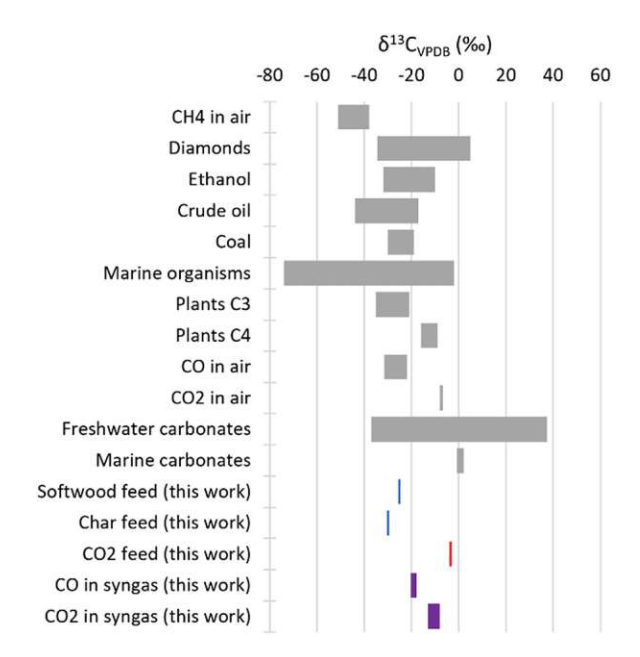


Fig. 4. Abundance of  $^{13}\text{C}$  given as  $\delta^{13}\text{C}_{VPDB}$  for various natural sources following [47] and all feeds and products in this work.

be detrimental to the reduction potential of the product gas. A dedicated experimental campaign using various gas and solid feed rates could clarify the optimum feed ratio for product gases with high reduction potential.

#### 3.2. Carbon stream analysis

The isotope ratios measured for carbonaceous feedstocks and product gas components are given in Table 5. Some of these data are depicted in Fig. 4 and compared to natural abundance values of various carbon sources. The label "Plants C3", showing  $\delta^{13}C$  values between -23 and -34% [36,47], describes almost 95% of plants on earth fixing carbon dioxide by the Calvin cycle [7]. Both biomass-derived feedstocks are in this stable isotope ratio range. The differences in stable carbon isotope ratio between softwood and char compared to the feedstock CO<sub>2</sub> are 21.8 and 26.4‰. These differences are multiple times the accredited standard deviation of  $\leq 0.63\%$  for bulk and  $\leq 1.10\%$  for gas measurements. Therefore, the differences in the natural abundance of  $^{13}C$  in feedstock CO<sub>2</sub> and fuel are significant enough to differentiate between parental carbon sources. The same is true for  $\delta^{13}C$  values for CO and CO<sub>2</sub> in the product gas, which are between the values measured for the parental carbon sources but still differ significantly from them.

#### 3.2.1. Isotopic fractionation

The  $\delta^{13}C$  data from measurements are expanded in Table 5 by information on the calculated isotope enrichment factors for carbon monoxide ( $\epsilon_{CO}$ ) and carbonaceous products other than CO or CO<sub>2</sub> ( $\epsilon_{rest}$ ). Additionally, the average stable carbon isotope ratio in products other than CO or CO<sub>2</sub> is calculated by isotope mass balances. More

**Table 5** Stable carbon isotope ratios  $\delta^{13}$ C for carbonaceous feedstocks and products in this work. PG = product gas.

0	CO <sub>2</sub> feed $\delta^{13}C_{CO2,in}$ % Measured	Bulk feed $\delta^{13}C_{fuel}$ % Measured	$CO_2$ in PG $\delta^{13}C_{CO2,out}$ % Measured	CO in PG $\delta^{13}C_{CO,out}$ % Measured	Enrichment factor (CO) $\varepsilon_{CO}$ %. Calculated	Other products $\delta^{13}C_{rest,out}$ % Calculated	Enrichment factor (rest) $\varepsilon_{rest}$ ‰ Calculated
Exp. #1	-3.4	-25.2	-8.0	-18.7	0.5	-21.6	-3.6
Exp. #2	-3.4	-25.2	-8.4	-19.3	1.9	-16.8	-8.4
Exp. #3	-3.4	-25.2	-11.0	-20.2	1.8	-19.0	-6.2
Exp. #4	-3.4	-25.2	-10.3	-19.7	1.2	-21.4	-3.8
Exp. #5	-3.4	-30.0	-7.8	-17.8	1.3	-23.0	-7.0
Exp. #6	-3.4	-30.0	-13.1	-18.6	1.5	-27.2	-2.8
Exp. #7	-3.4	-30.0	-11.4	-19.2	1.5	-26.6	-3.4



information on mass balancing is available in Appendix B.

The  $\delta^{13}C_{rest,out}$  data summarize the average  $^{13}$ C abundance in any carbonaceous product species other than CO and CO<sub>2</sub>. This summary includes CH<sub>4</sub>, higher hydrocarbons, tar, and ungasified char, of which the latter either leaves the reactor as fly char or is accumulated in the reactor during operation. The calculated values are closer to the isotope ratio of the solid parental carbon materials softwood and wood char than CO<sub>2</sub>. The value's proximity to the fuel value is explained by ungasified char being calculated as the prevalent compound in this mix.

The resulting  $\varepsilon_{rest}$  values show some  $^{13}\mathrm{C}$  enrichment for this group of compounds. Since various carbon side streams are summarized in the variables  $\delta^{13}C_{rest,out}$  and  $\varepsilon_{rest}$  the exact reason for this enrichment is challenging to pin down. The literature suggests that carbon from CO<sub>2</sub> could be substituted into the surface of ungasified char [34], potentially enriching it in <sup>13</sup>C because the feedstock CO<sub>2</sub> is isotopically heavier than the used biomass. However, because of the continuous nature of the experiment in this work, such an effect seems unlikely because the fuel is continuously replaced. Another explanation can be found in the increased bond strength of the 12C-13C bond compared to <sup>12</sup>C-<sup>12</sup>C. This bond strength difference suggests a <sup>13</sup>C depletion in low molecular weight gases and an enrichment in heavy components such as tar [42]. This explanation would also explain the positive values for the isotopic enrichment factor for CO ( $\varepsilon_{CO}$ ), calculated at 0.5–1.9‰. These values mean CO was produced with a slight preference for <sup>12</sup>C during gasification. Therefore, the measured  $\delta^{13}C_{CO,out}$  values are lower than they would be if no isotopic fractionation happened. The literature reports <sup>13</sup>CO enrichment after the water-gas shift reaction (Eq. 4) [36]. However, the experiments in this work were performed above 800 °C, where the reverse water-gas shift reaction becomes increasingly dominant over the water-gas shift reaction [26]. For this reason, the <sup>13</sup>CO depletion could be explained by the reverse water-gas shift u reaction, introducing the reverse trend to the trend reported in the literature for the water-gas shift reaction.

The trends calculated for isotopic fractionation can be reasonably explained based on the available literature. For this reason, the two main assumptions chosen for closing the balances and described in Section 2.3 are deemed acceptable:

- feedstock CO2 is only converted to CO in this process, and
- negligible isotopic fractionation for CO<sub>2</sub> occurred.

#### 3.2.2. Parental carbon sources of CO in product gas

The stable carbon isotope ratio data given in Table 5 are used to calculate how much carbon from the parental carbon sources  $\rm CO_2$ , softwood, and wood char is in the product gas components  $\rm CO$  and  $\rm CO_2$  (Eq 15 - Eq 18). These relative contributions are combined with the volume flow data for  $\rm CO$  and  $\rm CO_2$  (Table 4) to calculate  $\rm CO$  and  $\rm CO_2$  volume flows in product gas per parental carbon source. Both relative and absolute data are depicted in Fig. 5. Error ranges are calculated based on the precision of EA-IRMS and GC-C-IRMS measurements without the hypothetical sampling error.

The volume flow of CO in product gas is increased when more fuel is fed (exp. #3, #4, #6, and #7). CO with carbon from  $CO_2$  and from fuel is increased in these experiments (blue bars in Fig. 5). When more fuel is fed, CO with carbon from fuel is increased because more CO is released from pyrolysis. The increase of CO with carbon from  $CO_2$  at higher fuel feeding rates means that more  $CO_2$  was converted in these experiments (see Section 3.2.4). Previous works showed that an increase in fuel-gas contact time leads to higher  $CO_2$  conversion [15]. The most important reaction for converting  $CO_2$  in this system is the Boudouard reaction, which uses carbon from both parental sources to produce CO with an even split between both carbon sources.

The CO production from pyrolysis is more pronounced for softwood as fuel because the volatile content in wood char is low.  $Y_{CO\ from\ CO2}$  is around a third when softwood is used as fuel. This number is significantly higher at around 50% when using char. While the data show that feeding more fuel allows for the conversion of more CO<sub>2</sub> for both softwood and wood char as fuel,  $Y_{CO\ from\ CO2}$  slightly declines at higher fuel feeding rates. The reason for this is likely that increasing the fuel feeding rate increases the production of CO via pyrolysis of fuel faster than via the Boudouard reaction from CO<sub>2</sub>. These differences observed for the experiment pairings #1|3, #2|4, and #5|6 in this study are minor at 1–5% and more experiments are necessary to confirm that the relative

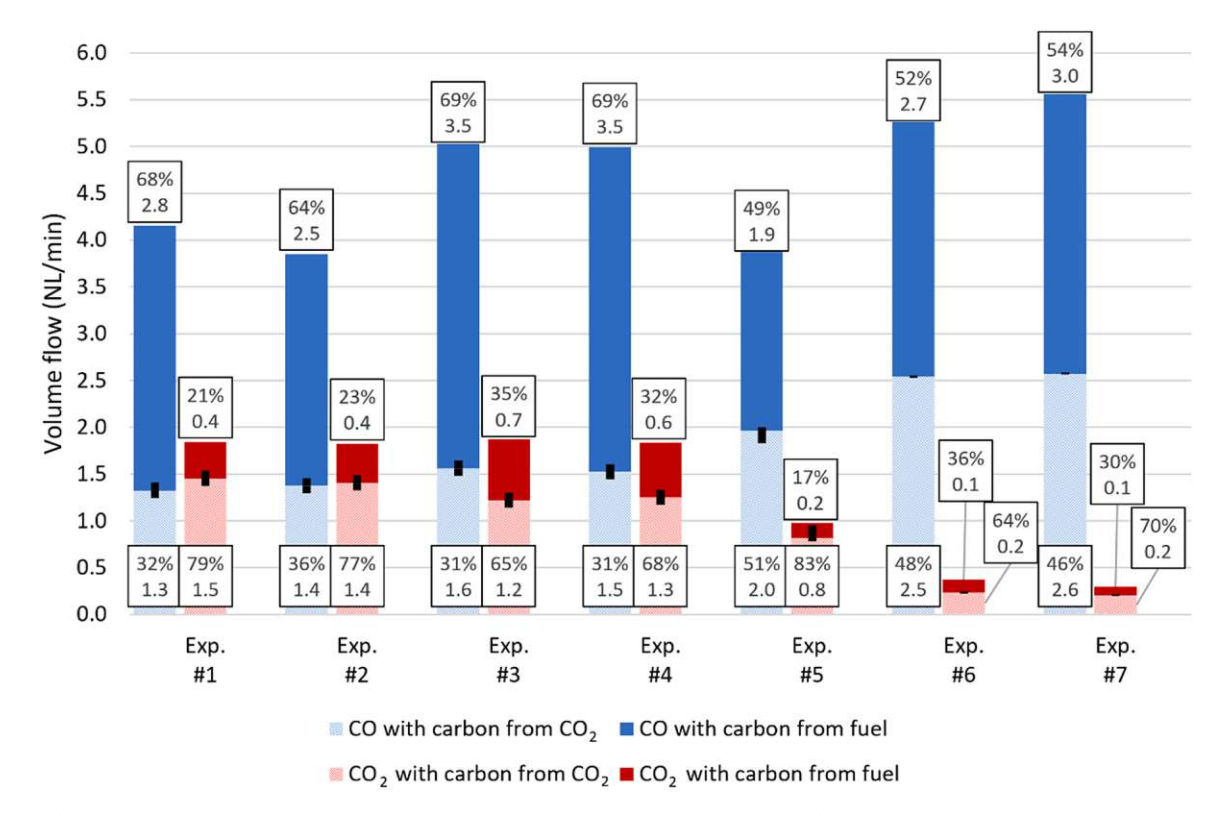


Fig. 5. Parental carbon sources of carbonaceous product gas components CO and CO<sub>2</sub>. Percentage values refer to the relative contribution of carbon sources, expressed as Y<sub>CO from CO2</sub>, Y<sub>CO from fuel</sub>, Y<sub>CO2 from CO2</sub>, and Y<sub>CO2 from fuel</sub>.

carbon contribution of CO<sub>2</sub> to CO declining at higher fuel feeding rates is a significant effect.

#### 3.2.3. Parental carbon sources of CO2 in product gas

The total volume flow of CO2 in product gas is similar for all softwood experiments (red bars in Fig. 5). Attributing carbon dioxide in the product gas to its parental carbon sources, fuel and CO2, shows that higher fuel:CO2 ratios decrease Y<sub>CO2 from CO2</sub> by lowering the amount of CO<sub>2</sub> with carbon from CO<sub>2</sub> and increasing the amount of CO2 with carbon from fuel. The decrease in CO2 with carbon from CO2 is explained by the increased conversion of CO2 at higher fuel-gas contact times [15]. This effect is much more pronounced in experiments with wood char than softwood. This difference could be caused by the high levels of unconverted char that were calculated (Table 4) for experiments #6 and #7, which likely resulted in a significant increase in fuel-gas contact time compared to experiment #5. Similarly, in all softwood experiments the values of unconverted fuel carbon were lower and CO2 with carbon from CO<sub>2</sub> was higher than in experiment #5. One conclusion from these data could be that for ideal CO2 conversion, an excess of char should be kept in the gasification reactor to reach higher fuel-gas contact times.

For softwood as fuel, increased CO<sub>2</sub> with carbon from fuel can be explained by increased pyrolysis activity when more fuel is present. For experiments with wood char as a fuel, CO<sub>2</sub> with carbon from fuel is not increased at higher fuel feeding rates. Instead, slightly less CO2 with carbon from fuel is observed in experiment #6 compared to #5. One explanation could be, that the CO2 released from pyrolysis reacts with fuel to CO, same as for CO<sub>2</sub> fed as fuel. The increased fuel-gas contact time in experiments with higher wood char feeding rates might have increased the conversion more than the addition of pyrolytic CO<sub>2</sub>, because of wood char's low volatile content. For high conversion of pyrolytic CO2, one option for process improvement could be the adoption of in-<u>□</u> bed feeding. Since in-bed feeding would move the point of CO<sub>2</sub> release away from the gas drain and towards the CO2 inlet, thereby increasing fuel-gas contact time, the pyrolytic CO2 might be converted to CO more efficiently.

#### 3.2.4. Conversion of feedstock CO2

While differences in CO2 conversion were already indirectly used to explain observed carbon conversion trends in Sections 3.2.2 and 3.2.3, this chapter explicitly calculates  $X_{CO2}$  according to Eq. 24. It compares the results in Fig. 6 to the calculation by other methods described in Section 2.3.2. Error ranges are calculated based on the precision of EA-IRMS and GC-C-IRMS measurements without the hypothetical sampling error.

 $X_{CO2}$  is significantly higher when using char as feedstock than when using softwood. Temperature differences are ruled out as an explanation because the highest (903  $^{\circ}\text{C})$  and lowest (821  $^{\circ}\text{C})$  average temperatures in the reaction zone are measured during experiments with softwood as fuel (Table 3). One reason might be found in softwood's lower fixed carbon content and calculated unconverted char, suggesting that the bed height during these experiments might also have been lower, decreasing the fuel-gas contact time and lowering CO<sub>2</sub> conversion. This hypothesis is also supported by higher observed CO<sub>2</sub> conversions when more fuel is fed. This effect is especially pronounced for char as fuel, where more than 90% of feedstock CO2 is converted. Another reason might be the difference in fuel characteristics. Surface area and porosity, active sites, mineral content, and particle size are suggested by comprehensive literature to affect char reactivity [5,8]. Char morphology is determined by reactive atmosphere, residence time, and temperature [8,48]. Higher pyrolysis temperatures are reported to reduce char reactivity [49]. This suggests that the higher temperatures for in-situ pyrolysis of softwood could lead to lower reactivity of the remaining char compared to the wood char previously prepared at 700 °C. Another reason might be the difference in mineral content between both fuels, which is regularly reported to catalyze gasification [5,8]. Related to their fixed carbon content, the softwood fuel has 1.37 wt%, while the wood char derived from Eucalyptus has 7.39% ash content. The higher amount of catalytically active ash elements in wood char, like Fe<sub>2</sub>O<sub>3</sub>, CaO, MgO, Na<sub>2</sub>O,

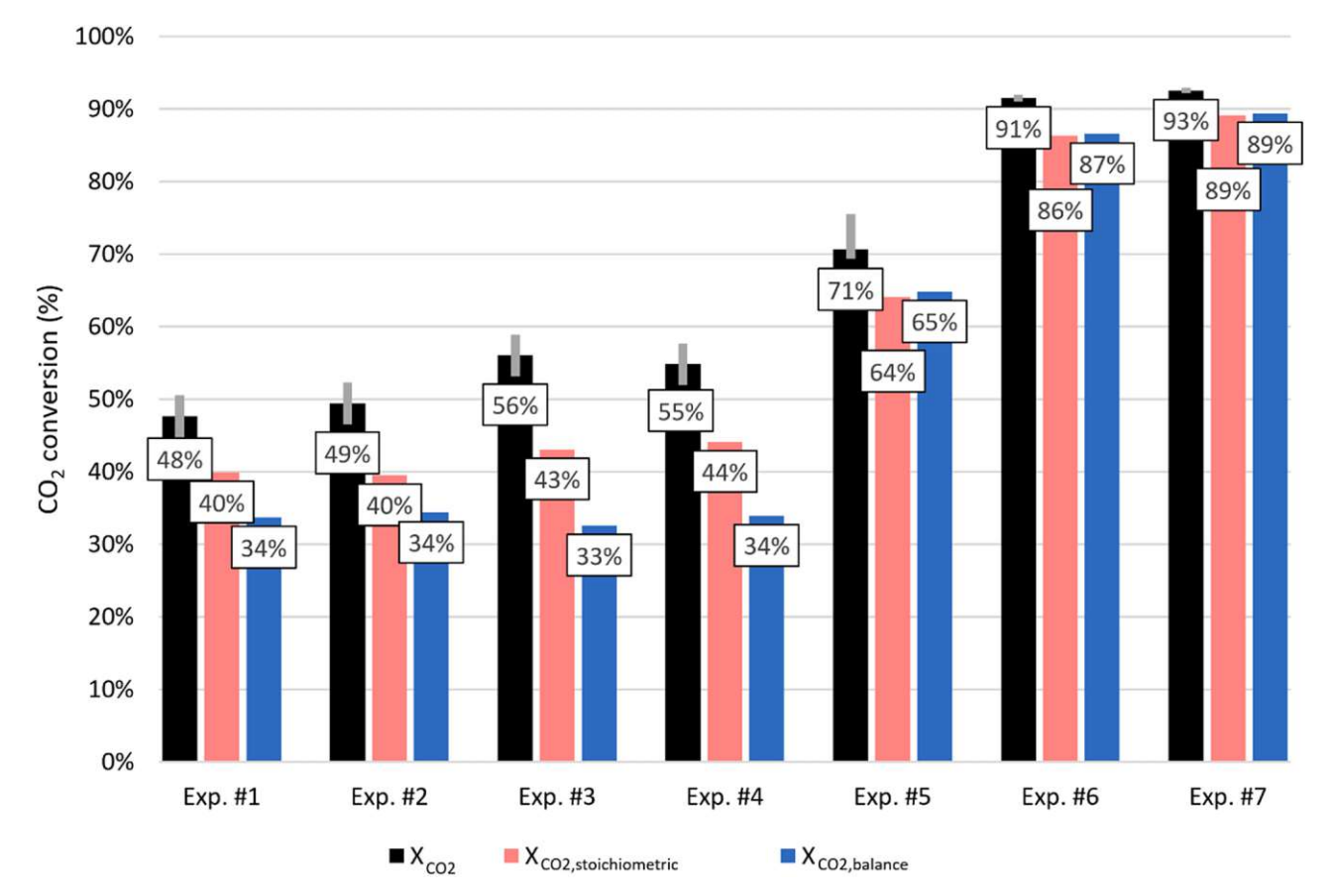


Fig. 6. Comparison of CO<sub>2</sub> conversion calculated by different methods.

and  $K_2O$  could have contributed to the observed increase in  $X_{CO2}$  upon using wood char as fuel.

Both simplified calculation results,  $X_{CO2,stoichiometric}$  and  $X_{CO2,balance}$  are lower than the  $X_{CO2}$  values, which are calculated based on stable carbon isotope analysis. The average gaps for  $X_{CO2.stoichiometric}$  are 10% for using softwood as a fuel (Exp #1 - #4) compared to 5% for char (Exp #5 - #7). For X<sub>CO2.balance</sub>, these numbers are 18% and 5% of average difference. This difference can be explained by the simplified calculation methods' inability to identify CO<sub>2</sub> produced from fuel; therefore, they underestimate how much feed CO2 has been converted. Because of its higher volatile content, more CO2 is produced from rapid devolatilization when using softwood, which leads to a sizeable error in determining the  $CO_2$  conversion by mass balancing ( $X_{CO2,balance}$ ). The differences in calculation results decrease when  $X_{CO2}$  approaches 100%, as all methods calculate the conversion as 100% if no CO2 is present in the product gas. Therefore, a conclusion could also be that stable carbon isotope analysis significantly improves process understanding when CO2 conversion is incomplete. These results prove why a reliable measurement method for these data is paramount.

#### 4. Conclusion

The central part of this work is the application of stable carbon isotope analysis to measure the conversion of CO2 in this system. A comparison with common calculation methods revealed that the new method yields CO<sub>2</sub> conversion results up to 23% points higher than calculated by mass balance. Other methods had considerable trouble identifying the CO2 conversion when additional CO2 was formed from the biomass by pyrolytic decomposition. The new method uses stable carbon isotope ratio analysis to differentiate between CO<sub>2</sub> formed from fuel and unconverted CO<sub>2</sub> fed as feedstock. This ability to differentiate can help to improve process understanding, facilitate technical development, and underpin biomass CO2 gasification's position as carbon capture and utilization technology. The presented analysis did not use a dedicated tracing substance, which could potentially incur significant costs. When char was used as fuel, around 50% of carbon monoxide was produced from CO2, proving that biomass CO2 gasification can utilize CO<sub>2</sub> as a resource very effectively. The new method can also help to answer legislative questions around carbon accounting.

This work contains experimental data from seven continuous feeding gasification experiments in a fluidized bed reactor. The product gas from these experiments had reduction potentials up to 14, significantly higher than typical values for reducing gas in existing direct reduction ironmaking plants, which are reported around 9. From a reduction potential standpoint, these gases could be directly used for direct reduction ironmaking without intermediate gas reforming or separation steps. Further investigation should be dedicated to clarifying if any and which technological steps are needed for direct connection of these processes, e.g., a tar separation step or removing other impurities. Still, When hydrogen is added from an external source like water electrolysis to adjust the H<sub>2</sub>-to-CO ratio, the CO-rich product gas could also be used as a feedstock for chemical synthesis.

A limitation of this study is that some assumptions were necessary for evaluation because of missing data, e.g., assuming the isotopic fractionation factor for CO<sub>2</sub> in the product gas as 0 based on the literature.

Measuring the stable carbon isotope ratio for products other than CO and CO<sub>2</sub> would also allow the calculation of this factor and improve the

Appendix A. Fluidization calculations

General information on the equations and assumptions for calculating of the softwood pellets have a diameter of 6 mm, which is assumed as the sphericity for softwood pellets is calculated as 0.85 using Eq. A-1, 750 kg. are reported around 9. From a reduction potential standpoint, these gases

results. If feedstocks with similar isotopic abundance are used, enriching or depleting feedstock CO<sub>2</sub> by adding <sup>13</sup>CO<sub>2</sub> or <sup>12</sup>CO<sub>2</sub> might be necessary to reduce the uncertainty. Additionally, this work only contains a small number of experiments and is focused on establishing stable carbon isotope analysis as a tool for carbon stream analysis in CO2 biomass gasification. A more extensive experimental campaign using this new method to look more closely into the effects of water/CO2 mixtures as feed, temperature, bed material variations, and other factors could improve process understanding further.

Nevertheless, these results provide critical insights into the CO2 gasification process and can be used for further technical development. The sharp increase in CO2 conversion when feeding more char as fuel confirms the importance of gas-solid contact time identified in previous works [15]. Based on this observation, a process improvement could be to optimize the contact time by leaving excess solid carbon in the gasification reactor, even if the system is operated as a circulating or bubbling fluidized bed. Another improvement could be to adjust the point of volatile release such that CO<sub>2</sub> released by rapid devolatilization of fuels is also in prolonged contact with the fuel bed. This adjustment could reduce CO2 generated from biomass in product gas by increased conversion to CO. This effect could be achieved by in-bed feeding of fuel instead of on-bed feeding. Another possibility would be to have a dedicated pyrolysis step before gasification, which could also lower the CO<sub>2</sub> content in produced gases based on the data in this work.

#### CRediT authorship contribution statement

Franz Winter: Writing – review & editing, Supervision, Resources, Project administration, Funding acquisition, Conceptualization. Stefan Müller: Supervision, Resources, Project administration, Funding acquisition, Conceptualization. Josef Fuchs: Writing – review & editing, Supervision, Resources, Project administration, Funding acquisition, Data curation, Conceptualization. Florian Johann Müller: Writing review & editing, Writing - original draft, Visualization, Validation, Software, Methodology, Investigation, Formal analysis, Data curation, Conceptualization.

#### **Declaration of Competing Interest**

The authors declare that they have no known competing financial interests or personal relationships that could have appeared to influence the work reported in this paper.

#### **Data Availability**

Data will be made available on request.

#### Acknowledgments

This study was carried out within the doctoral college CO<sub>2</sub>Refinery at TU Wien. The authors would like to thank Imprint Analytics GmbH (Neutal, Austria) for measuring stable carbon isotope ratios and providing advice for the sampling procedure. The authors acknowledge TU Wien Bibliothek for financial support through its Open Access Funding Programme.

General information on the equations and assumptions for calculating the fluidization state of particles was described in previous work; see Müller

The softwood pellets have a diameter of 6 mm, which is assumed as the particle size  $d_p$  for softwood pellets. At an average length of 10 mm, the sphericity for softwood pellets is calculated as 0.85 using Eq A-1. 750 kg/m $^3$  are used for the density of wood pellets.

$$d_{sv} = \Phi^* d_P$$
 (A-1)

The results of fluidization calculations summarized for Olivine, softwood pellets, and three size classes of wood char are given in Table A-1. Feed gas flow rates were selected at around 3 NL/min to form a bubbling fluidized bed from Olivine while keeping gas velocities low to increase fuel-gas contact time.

Table A-1 Fluidization properties of all used bed materials at 1200 K and atmospheric pressure [15].

		Olivine	Softwood pellets	Small char	Medium char	Large char
$d_P$	m	3.37E-04	6.00E-03	1.65E-03	3.75E-03	6.50E-03
$\Phi$	-	7.60E-01[50]	8.50E-01	6.60E-01[51]	6.60E-01[51]	6.60E-01[51]
$d_{SV}$	m	2.56E-04	5.10E-03	1.09E-03	2.48E-03	4.29E-03
$\rho_F$ (1200 K	kg/m <sup>3</sup>	4.34E-01	4.34E-01	4.34E-01	4.34E-01	4.34E-01
$\rho_P$	kg/m <sup>3</sup>	2.85E + 03[52]	7.50E+02	1.70E + 02[51]	1.70E + 02[51]	1.70E + 02[51]
μ (1200 K	$N*s/m^2$	4.68E-05[53]	4.68E-05	4.68E-05[53]	4.68E-05[53]	4.68E-05[53]
g	m/s <sup>2</sup>	9.81E+00	1.08E+01	9.81E+00	9.81E+00	9.81E+00
Ar	-	9.32E+01	2.13E+05	4.26E+02	5.00E+03	2.60E + 04
$u_{mf}$	m/s	2.37E-02	1.38E+00	2.54E-02	1.26E-01	3.31E-01
A	$m^2$	2.21E-03	2.21E-03	2.21E-03	2.21E-03	2.21E-03
$\dot{V}_{mf}$	Nm <sup>3</sup> /h	4.31E-02	2.51E+00	4.62E-02	2.29E-01	6.02E-01
$f_{umf}$ (2.8 NL/min)	-	3.90	0.07	3.64	0.73	0.28
$f_{umf}$ (3.0 NL/min)	-	4.18	0.07	3.90	0.79	0.30
f <sub>umf</sub> (3.2 NL/min)	-	4.45	0.08	4.16	0.84	0.32

#### Appendix B. Mass balancing in IPSEpro 8.0 in this work

General information on IPSEpro 8.0 and its use in gasification modeling is available in the literature, e.g., [54] and other publications by TUW. This work used a gasifier model typically used to simulate the gasification reactor of a dual-fluidized bed gasifier (Figure B-1)

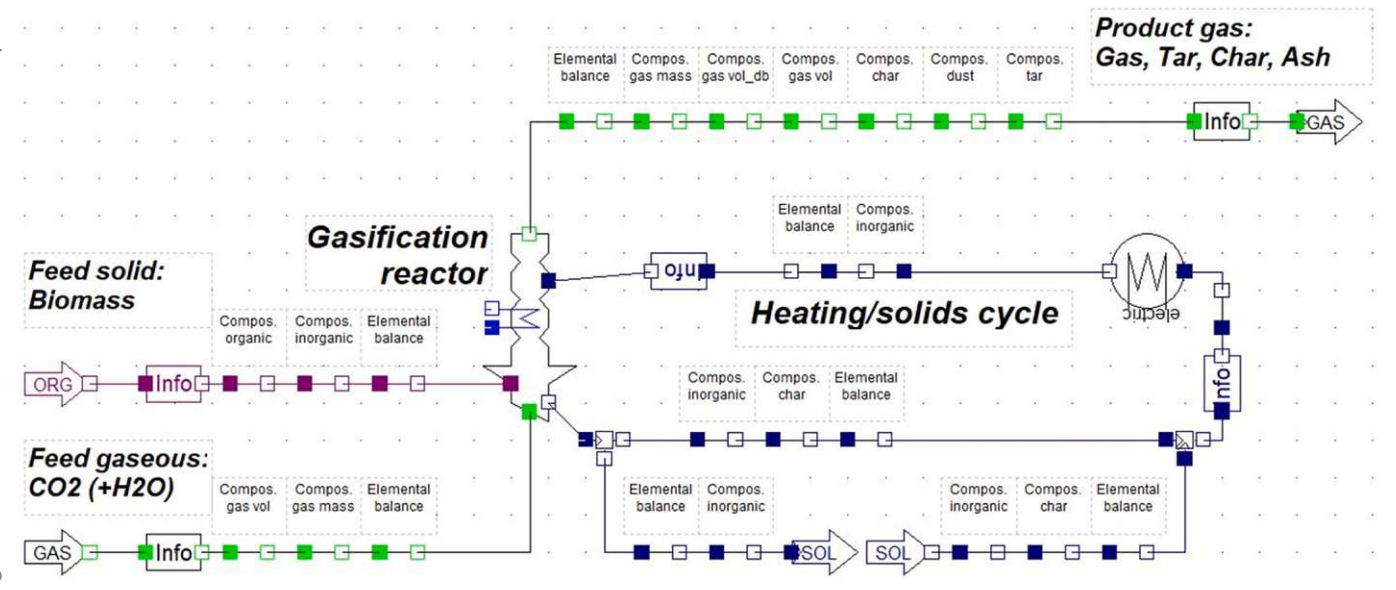


Figure B-1. Flowsheet model of gasifier used for mass balancing in IPSEpro 8.0.

The model has three inlets (fully colored connectors) and two outlets (empty connectors). Since IPSEpro is an equation-oriented tool, the number of equations must equal the number of variables. The model presented in Figure B-1 has nearly 1600 variables. Most input relevant to mass balancing is given as composition data. The biomass composition is known from proximate and ultimate analysis (Table 2). The feed gas composition is pure CO<sub>2</sub> or CO2 mixed with water, as given in the experimental matrix (Table 3). Dry-based composition data of CO, CO2, CH4, H2, and O2 is available from continuous analysis. The average data from one hour of stable operation are used for the product gas composition. Ash and bed material are simplified to singular substances with unchanging composition. The inlet and outlet in the solids cycle are necessary for model convergence. Nothing other than Olivine and ash is drained or added to the system in this cycle. The heating/solids cycle's primary function in the model is to close the energy balance, which is not the focus of this paper.

The only absolute values in the mass balance are for the flow rates of the feeding lines. The volume flow rate of CO<sub>2</sub> fed to the reactor ( $\dot{V}_{CO2,in}$ ), which was set using a rotameter and checked by a gas clock, is one of these two. The other absolute value is the biomass feed rate, set in the model relative to the gas inlet. The tar concentration in the product gas is assumed as 6.3 g/m3<sub>stp,db</sub> as given by literature for using CO<sub>2</sub> to gasify softwood pellets in a fluidized bed with Olivine as bed material [55]. The elemental tar composition was assumed to match the tar composition measured by M 🕏 GC/MS in CO2 gasification experiments with softwood pellets as fuel, e.g., [56], and is 92.8 wt% carbon, 7.0 wt% hydrogen, and 0.1 wt% oxygen. The share of fuel remaining in the reactor or entrained as ungasified char is not experimentally determined but can be calculated from the model. Ungasified char is assumed to match the elemental composition of wood char, which is used as fuel in this work (Table 2). Ungasified char is treated as an outgoing stream to allow for a steady state calculation in this black box model. With these data, the outgoing volume flows of CO ( $\dot{V}_{CO,out}$ ) and CO<sub>2</sub>  $(\dot{V}_{CO2,out})$ , which are needed for Eq. 23 - Eq. 24, can be derived from mass balancing. The global hydrogen balance allows for calculating the product gas's water content.

Stable carbon isotope ratios are used to build a  $^{12}$ C balance as an additional equation (Eq. 19). This means that not only must the global mass balance for carbon yield the same input and output to the process, but more specifically, the exact requirement is asked of  $^{12}$ C. When the global carbon balance and  $^{12}$ C balance are fulfilled, so is the  $^{13}$ C balance. The isotopic enrichment factor  $\varepsilon_{CO}$  and the mean isotope ratio of all carbonaceous outputs other than CO and CO<sub>2</sub> ( $\delta^{13}C_{rest,out}$ ) are calculated from these isotopic and global mass balances. Two more boundary conditions, which come from assumptions, are necessary for these calculations. The first assumption is that  $\varepsilon_{CO2}$  is assumed zero, and the second is that CO<sub>2</sub> is only converted to CO (see Section 2.3 for more information). The so-calculated  $\delta^{13}C_{rest,out}$  value is sensitive to error since minimal absolute changes lead to a sizeable deviation from zero in the VPDB scale (see Eq. 14). For this reason, it can be compared to the isotope ratio measurement of used biomass and used as a plausibility check for the whole balance.

#### Appendix C. Supporting information on experimental data

Experimental data are plotted in Figure C-1 for one experiment with each fuel type. Experiment #6 was conducted with wood char as fuel, while softwood pellets were used in experiment #3. The  $CO_2$  conversion  $X_{CO2,stoichiometric}$  is calculated using the simplified calculation as per Eq. 25. This equation estimates the  $CO_2$  conversion at the same time interval of product gas composition data, which is every 1 s. Temperature measurements are positioned as given in Fig. 2. Stream composition data is adjusted to remove  $N_2$ , which was used for purging the pressure measurement and fuel tank. Without adjustment, this  $N_2$  is under 5 vol% of the total gas stream going to the measurement. Both experiments were conducted with dry  $CO_2$  feed, and the parental carbon ratio of fuel to feedstock  $CO_2$  in both experiments was two.

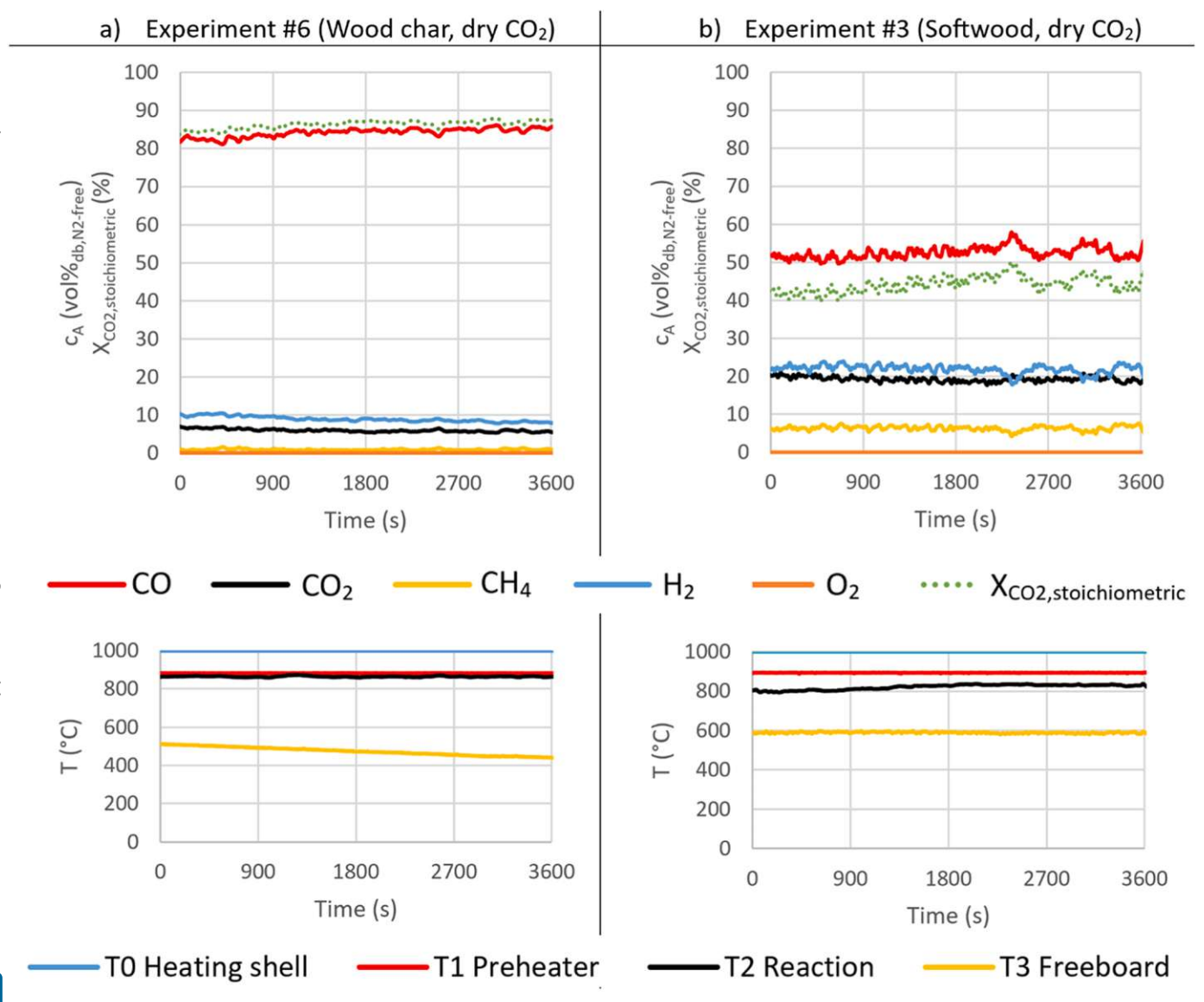


Figure C-1. Comparison of experimental data using different fuel types: a) wood char (left, experiment number #6), b) softwood pellets (right, experiment number #3). X<sub>CO2,stoichiometric</sub> is calculated by the simplified method given in Eq. 25.

The temperature TO Heating shell in this reactor is limited to 1000 °C, equal for both experiments. T2 Reaction is the measurement at the center of the fuel-filled zone. The temperature here is around 40 °C lower during experiment #3 using softwood compared to #6 using wood char. T3 Freeboard measures the temperature of the gas phase above the fluidized bed but inside the reactor. Contrary to T2 Reaction, T3 Freeboard averages around 100-200 °C higher when softwood is used as fuel. These observations cannot be explained with certainty because of a lack of information on the power supplied by the heating shells, heat losses, and heat transmission phenomena in and around the reactor. Interpretations for both differences are suggested by the mass and energy balance conducted in IPSEpro. The difference in freeboard temperature could be due to a significant amount of fuel surplus not converted during experiment #6 with wood char. According to the mass balance, around 46% of carbon fed via wood char was not converted, significantly higher than the 12% calculated for experiment #3 feeding softwood. While some of this surplus was leaving the reactor as fly char, in experiment #6, this surplus likely slowly built up in the reactor towards the freeboard. Char accumulation at some point before or during the experiments was also noticeable from ongoing CO production after the main investigation period had ended and no new fuel was added. CO was still produced when only CO<sub>2</sub> was fed after each experiment (except experiment #6). Due to uncertainties in volume flow after the investigated period, no values are estimated for the total char at the experiments' end. An explanation for the declining freeboard temperature could be that the rising bed transmits more energy to ambient through the reactor walls because the reactor is not as well insulated above the heating shell. The difference in reaction zone temperature can be explained by an increased cooling effect from endothermic pyrolysis reactions. The fluctuations in product gas concentration are consistently higher for softwood pellets than for char. The reason for this is the instability induced by the somewhat discontinuous feeding of fuel particles by the screw feeder, which is delivering discrete fuel particles. The larger softwood particles lead to small spikes in gas measurement because of rapid devolatilization [8]. This effect is expected to be absent in larger plants with higher feeding rates.

The equipment used in this study has the following error tolerances:

- Dry gas composition measurement: 1 vol% of calibrated maximum. The calibrated maxima were
  - o 100 vol% CO2
  - o 100 vol% CO
  - o 10.1 vol% CH<sub>4</sub>
  - o 20.9 vol% O2
  - o 100 vol% H<sub>2</sub>
- Temperature measurement by thermocouple type K: 4‰ of measured temperature
- EA-IRMS:  $\pm 0.63\%$  with and  $\pm 0.3\%$  without hypothetical sampling error
- GC-C-IRMS:  $\pm 1.10\%$  with and  $\pm 0.5\%$  without hypothetical sampling error
- The rotameter used for controlling the flow rate of CO<sub>2</sub> fed to the reactor has been compared to a gas clock with a precision of ±3% before experiments.

#### References

- [1] IPCC, Climate Change, The Physical Science Basis. Contribution of Working Group I to the Sixth Assessment Report on the Intergovernmental Panel on Climate Change, Cambridge University Press, Cambridge, 2021, p. 2021, https://doi.org/ 10.1017/9781009157896
- IPCC, Climate Change, Mitigation of Climate Change. Contribution of Working Group III to the Sixth Assessment Report of the Intergovernmental Panel on Climate Change, Cambridge University Press, Cambridge, 2022, p. 2022, https:// doi.org/10.1017/9781009157926
- IRENA and Methanol Institute, Innovation Outlook: Renewable Methanol, Abu Dhabi, 2021.
- S. De, A.K. Agarwal, V.S. Moholkar, B. Thallada. Coal and Biomass Gasification, 1st ed., Springer, Singapore, 2018. (https://doi.org/10.1007/978-981-10-7335-9).
- Y.H.Chan, S.N.F. Syed Abdul Rahman, H.M.Lahuri, A.Khalid, Recent progress on CO-rich syngas production via CO2 gasification of various wastes: A critical review on efficiency, challenges and outlookEnviron. Pollut.278202111610.1016/j. envpol.2021.116843.
- A. Nurdiawati, I.N. Zaini, W. Wei, R. Gyllenram, W. Yang, P. Samuelsson, Towards fossil-free steel: Life cycle assessment of biosyngas-based direct reduced iron (DRI) production process, J. Clean. Prod. 393 (2023) 136262, https://doi.org/10.1016/j.
- [7] A. Bhagavatula, G. Huffman, N. Shah, C. Romanek, R. Honaker, Source apportionment of carbon during gasification of coal-biomass blends using stable carbon isotope analysis, Fuel Process. Technol. 128 (2014) 83-93, https://
- [8] P. Lahijani, Z.A. Zainal, M. Mohammadi, A.R. Mohamed, Conversion of the greenhouse gas CO2 to the fuel gas CO via the Boudouard reaction: A review, Renew. Sustain. Energy Rev. 41 (2015) 615-632, https://doi.org/10.1016/j
- [9] S. Müller, Hydrogen from biomass for industry industrial application of hydrogen production based on dual fluid gasification, Dissertation, Technische Universität Wien, 2013. (https://resolver.obvsg.at/urn:nbn:at:at-ubtuw:1-96540
- M. Pohořelý, M. Jeremiáš, K. Svoboda, P. Kameníková, S. Skoblia, Z. Beňo, CO2 as moderator for biomass gasification, Fuel 117 (2014) 198-205, https://doi.org/ 10.1016/i.fuel.2013.09.068.
- X. Yao, Q. Yu, Z. Han, H. Xie, W. Duan, Q. Qin, Kinetics of CO2 gasification of biomass char in granulated blast furnace slag, Int J. Hydrog. Energy 43 (2018) 12002-12012, https://doi.org/10.1016/j.ijhydene.2018.04.102.
- N. Sadhwani, S. Adhikari, M.R. Eden, Biomass Gasification Using Carbon Dioxide: Effect of Temperature, CO2/C Ratio, and the Study of Reactions Influencing the

- Process, Ind. Eng. Chem. Res 55 (2016) 2883-2891, https://doi.org/10.1021/acs.
- [13] Z. Wang, X. Liu, K.G. Burra, J. Li, M. Zhang, T. Lei, A.K. Gupta, Towards enhanced catalytic reactivity in CO2-assisted gasification of polypropylene, Fuel 284 (2021) 1-9, https://doi.org/10.1016/j.fuel.2020.119076.
- [14] P. Lahijani, M. Mohammadi, Z.A. Zainal, A.R. Mohamed, Advances in CO2 gasification reactivity of biomass char through utilization of radio frequency irradiation, Energy 93 (2015) 976–983, https://doi.org/10.1016/j. energy.2015.09.092
- [15] F.J. Müller, J. Fuchs, M. Fanjul, A.O. Guti, S. Pratschner, S. Müller, F. Winter, CO2 conversion to CO by fluidized bed biomass gasification: Analysis of operational parameters, J. CO2 Util. 81 (2024), https://doi.org/10.1016/j.jcou.2024.102706.
- [16] M. Jeremiáš, M. Pohořelý, K. Svoboda, V. Manovic, E.J. Anthony, S. Skoblia, Z. Beňo, M. Šyc, Gasification of biomass with CO2 and H2O mixtures in a catalytic fluidised bed, Fuel 210 (2017) 605-610, https://doi.org/10.1016/i fuel.2017.09.006
- [17] S. Valin, L. Bedel, J. Guillaudeau, S. Thiery, S. Ravel, CO2 as a substitute of steam or inert transport gas in a fluidised bed for biomass gasification, Fuel 177 (2016) 288-295, https://doi.org/10.1016/j.fuel.2016.03.020.
- [18] S. Tong, L. Li, L. Duan, C. Zhao, E.J. Anthony, A kinetic study on lignite char gasification with CO2 and H2O in a fluidized bed reactor, Appl. Therm. Eng. 147 (2019) 602–609, https://doi.org/10.1016/j.applthermaleng.2018.10.113
- C. Liang, H. Zhang, Z. Zhu, Y. Na, Q. Lu, CO2-O2 gasification of a bituminous coal in circulating fluidized bed, Fuel 200 (2017) 81-88, https://doi.org/10.1016/j. fuel.2017.03.032.
- [20] K. Liu, Z. Yuan, C. Shi, H. Zhao, H. Wang, Effect of CaO-SiO2-FeO slag system on coal gasification reaction in CO2-Ar atmosphere and kinetic analysis, J. CO2 Util. 56 (2022) 101850, https://doi.org/10.1016/j.jcou.2021.101850.
- [21] A. Lampropoulos, N. Kaklidis, C. Athanasiou, M.A. Montes-Morán, A. Arenillas, J. A. Menéndez, V.D. Binas, M. Konsolakis, G.E. Marnellos, Effect of Olive Kernel thermal treatment (torrefaction vs. slow pyrolysis) on the physicochemical characteristics and the CO2 or H2O gasification performance of as-prepared biochars, Int J. Hydrog. Energy 46 (2021) 29126-29141, https://doi.org/10.1016/ iihvdene 2020 11 230.
- [22] L. Reyes, L. Abdelouahed, B. Campusano, J.C. Buvat, B. Taouk, Exergetic study of beech wood gasification in fluidized bed reactor using CO2 or steam as gasification agents, Fuel Process. Technol. 213 (2021) 1-12, https://doi.org/10.1016/j. fuproc.2020.106664.
- [23] N. Spiegl, X. Long, C. Berrueco, N. Paterson, M. Millan, Oxy-fuel co-gasification of coal and biomass for negative CO2 emissions, Fuel 306 (2021) 1-8, https://doi. org/10.1016/j.fuel.2021.121671.

- [24] R. Liu, Y. Zhang, Z. Ling, Y. Song, Some new insights into the synergy occurring during char gasification in CO2/H2O mixtures, Fuel 268 (2020) 1-8, https://doi. .1016/j.fuel.2020.117307
- [25] Z. Liu, F. Zhang, H. Liu, F. Ba, S. Yan, J. Hu, Pyrolysis/gasification of pine sawdust biomass briquettes under carbon dioxide atmosphere: Study on carbon dioxide reduction (utilization) and biochar briquettes physicochemical properties, Bioresour. Technol. 249 (2018) 983-991, https://doi.org/10.101 biortech.2017.11.012.
- [26] A.M. Mauerhofer, S. Müller, A. Bartik, F. Benedikt, J. Fuchs, M. Hammerschmid, H. Hofbauer, Conversion of CO2 during the DFB biomass gasification process, Biomass-.-. Convers. Biorefin 11 (2021) 15–27, https://doi.org/10.1007
- [27] R. Liu, R. Tsiava, S. Xu, D. Chen, Experimental study of char gasification characteristics with high temperature flue gas, J. Energy Inst. 97 (2021) 187-193, ioei.2021.04.015
- [28] Y. Cheng, Z. Thow, C.H. Wang, Biomass gasification with CO2 in a fluidized bed, Powder Technol. 296 (2016) 87-101, https://doi.org/10.1016/j. powtec, 2014, 12, 041.
- European Commission, Directive (EU) 2023/2413 of the European Parliament and of the Council of 18 October 2023 amending Directive (EU) 2018/2001, Regulation (EU) 2018/1999 and Directive 98/70/EC as regards the promotion of energy from renewable sources, Official Journal of the European Union 2413 (2023) 1–77. (https://eur-lex.europa.eu/legal-content/EN/TXT/?uri=CELEX 3A32023L2413&qid=1699364355105
- D. Leckel, Diesel production in coal-based high-temperature Fischer-Tropsch plants using fixed bed dry bottom gasification technology, Fuel Process. Technol. 92 (2011) 959-969, https://doi.org/10.1016/j.fuproc.2010.12.017.
- N.A. Matwiyoff, D.G. Ott, Stable isotope tracers in the life sciences and medicine, Science 181 (1979) (1973) 1125-1133, https://doi.org/10.1126/ science,181,4105,112
- L.Z. Gannes, C.M. Del Rio, P. Koch, Natural Abundance Variations in Stable Isotopes and their Potential Uses in Animal Physiological Ecology, Comp. Biochem Physiol. A Mol. Integr. Physiol. 119 (1998) 725-737, https://doi.org/10.1016/ S1095-6433(98)01016-2.
- I.S. Al-Aasm, B.E. Taylor, B. South, Stable isotope analysis of multiple carbonate samples using selective acid extraction, Chem. Geol.: Isot. Geosci. Sect. 80 (1990) 119-125, https://doi.org/10.1016/0168-9622(90)90020-D.
- F. Kapteijn, R. Meijer, J.A. Moulijn, D. Cazorla-Amóros, On why do different carbons show different gasification rates: A transient isotopic CO2 gasification study, Carbon N. Y 32 (1994) 1223-1231, https://doi.org/10.1016/0008-6223 (94)90106-6
- [35] D. Cazorla-Amorós, A. Linares-Solano, C.S.M. de Lecea, F. Kapteiin, Assessment of the CO2-carbon gasification catalyzed by calcium. A transient isotopic study, Carbon N. Y 32 (1994) 423-430, https://doi.org/10.1016/0008-6223(94)90162-7.
- S. Flude, G. Johnson, S.M.V. Gilfillan, R.S. Haszeldine, Inherent Tracers for Carbon Capture and Storage in Sedimentary Formations: Composition and Applications. Environ. Sci. Technol. 50 (2016) 7939–7955, https://doi.org/10.1021/acs st.6b01548
- D.W. Hoffman, C. Rasmussen, Absolute Carbon Stable Isotope Ratio in the Vienna Peedee Belemnite Isotope Reference Determined by <sup>1</sup>H NMR Spectroscopy, Anal. Chem. 94 (2022) 5240–5247, https://doi.org/10.1021/acs.analchem.1c04565.
- W.A. Brand, T.B. Coplen, J. Vogl, M. Rosner, T. Prohaska, Assessment of international reference materials for isotope-ratio analysis (IUPAC technical report), Pure Appl. Chem. 86 (2014) 425-467, https://doi.org/10.1515/pac-2013-
- IUPAC Commission on Atomic Weights and Isotopic Abundances, Atomic weights of the elements 1991, J. Phys. Chem. Ref. Data 22 (1993) 1571-1584. (https://doi. org/10.1063/1.555933\.

- [40] A.M. Mauerhofer, S. Müller, F. Benedikt, J. Fuchs, A. Bartik, H. Hofbauer, CO2 gasification of biogenic fuels in a dual fluidized bed reactor system, Biomass-.-. Convers. Biorefin 11 (2021) 1101–1116, https://doi.org/10.1007/s13399-019-
- [41] T. Pröll, H. Hofbauer, Development and application of a simulation tool for biomass gasification based processes, Int. J. Chem. React. Eng. 6 (2008), https://
- [42] Y. Bottinga, Calculated fractionation factors for carbon and hydrogen isotope exchange in the system calcite-carbon dioxide-graphite-methane-hydrogen-water vapor, Geochim Cosmochim. Acta 33 (1969) 49-64, https://doi.org/10.1016/
- [43] P. Richet, Y. Bottinga, M. Javoy, A Review of Hydrogen, Carbon, Nitrogen, Oxygen, Sulphur, and Chlorine Stable Isotope Fractionation Among Gaseous Molecules, Annu Rev. Earth Planet Sci. 5 (1977) 65-110, https://doi.org/10.1146/annurev.
- [44] R. Liu, R. Tsiava, S. Xu, D. Chen, Experimental study of char gasification characteristics with high temperature flue gas, J. Energy Inst. 97 (2021) 187-193, https://doi.org/10.1016/j.joei.2021.04.015.
- S. Pratschner, M. Hammerschmid, S. Müller, F. Winter, Evaluation of CO2 sources for Power-to-Liquid plants producing Fischer-Tropsch products, J. CO2 Util. 72 (2023) 102508, https://doi.org/10.1016/j.jcou.2023.102508.
- [46] J. Solar, I. de Marco, B.M. Caballero, A. Lopez-Urionabarrenechea, N. Rodriguez, I. Agirre, A. Adrados, Influence of temperature and residence time in the pyrolysis of woody biomass waste in a continuous screw reactor, Biomass-.-. Bioenergy 95 (2016) 416-423, https://doi.org/10.1016/j.biombioe.2016.07.004
- [47] A.J. Fleisher, H. Yi, A. Srivastava, O.L. Polyansky, N.F. Zobov, J.T. Hodges, Absolute 13C/12C isotope amount ratio for Vienna PeeDee Belemnite from infrared absorption spectroscopy, Nat. Phys. 17 (2021) 889-893, https://doi.org/ 10.1038/s41567-021-01226-
- [48] H.C. Butterman, M.J. Castaldi, CO2 as a carbon neutral fuel source via enhanced biomass gasification, Environ. Sci. Technol. 43 (2009) 9030-9037, https://doi. org/10.1021/es901509n.
- [49] F. Min, M. Zhang, Y. Zhang, Y. Cao, W.P. Pan, An experimental investigation into the gasification reactivity and structure of agricultural waste chars, J. Anal. Appl. Pyrolysis 92 (2011) 250-257, https://doi.org/10.1016/j.jaap.2011.06.005.
- D. Kunii, O. Levenspiel. Fluidization engineering, 2nd ed., Butterworth-Heinemann, Bosten, London, singapore, Sydney, Toronto, Wellington, 1991. (htt os://doi.org/10.1016/C2009-0-24190-0
- [51] F. Scala, R. Chirone, P. Salatino, Combustion and attrition of biomass chars in a fluidized bed, Energy Fuels 20 (2006) 91-102, https://doi.org/10.1021
- [52] A.M. Mauerhofer, J.C. Schmid, F. Benedikt, J. Fuchs, S. Müller, H. Hofbauer, Dual fluidized bed steam gasification: Change of product gas quality along the reactor height, Energy 173 (2019) 1256-1272, https://doi.org/10.1016/j energy, 2019, 02, 025
- [53] A. Fenghour, W.A. Wakeham, V. Vesovic, The viscosity of carbon dioxide, J. Phys. Chem. Ref. Data 27 (1998) 31-39, https://doi.org/10.1063/1.556013.
- T. Pröll, H. Hofbauer, Development and application of a simulation tool for biomass gasification based processes, Int. J. Chem. React. Eng. 6 (2008), https:// doi.org/10.2202/1542-6580.1769
- A.M. Mauerhofer, F. Benedikt, J.C. Schmid, J. Fuchs, S. Müller, H. Hofbauer, Influence of different bed material mixtures on dual fluidized bed steam gasification, Energy 157 (2018) 957-968, https://doi.org/10.1016/j. energy, 2018, 05, 158,
- [56] A.M. Mauerhofer, J. Fuchs, S. Müller, F. Benedikt, J.C. Schmid, H. Hofbauer, CO2 gasification in a dual fluidized bed reactor system: impact on the product gas composition, Fuel 253 (2019) 1605-1616, https://doi.org/10.1016/j. fuel 2019 04 168.

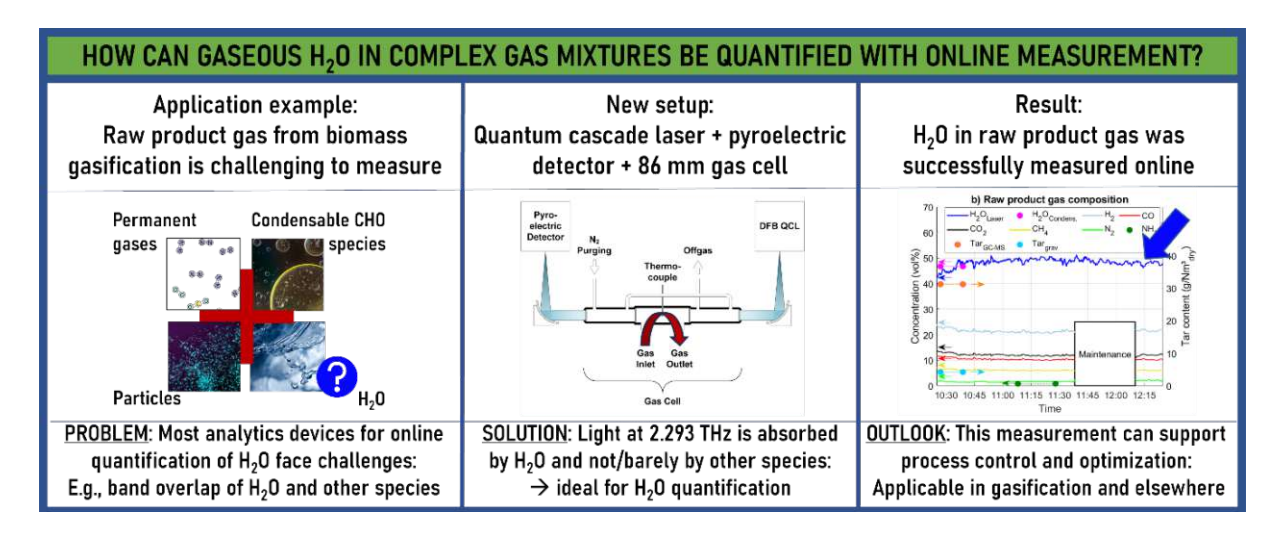


## Journal article III (JA III): Water vapor quantification in raw product gas by THz quantum cascade laser

#### Bibliographical reference

F. J. Müller, M. Jaidl, D. Theiner, J. Zeitlhofer, F. Benedikt, L. Steiner, A. Bartik, M.C. Ertl, A.M. Andrews, G. Strasser, S. Müller, F. Winter, K. Unterrainer, "Water vapor quantification in raw product gas by THz quantum cascade laser," Energy Conversion and Management: X, p. 100906, Feb. 2025, doi: 10.1016/J.ECMX.2025.100906.

#### Graphical abstract



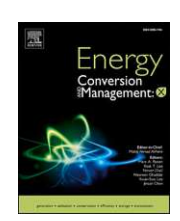
#### Highlights

- A novel spectroscopic setup was tested for online water vapor quantification.
- Measurements agreed well with discontinuous quantification by condensation.
- The setup used a quantum cascade laser, a hot gas cell and a pyroelectric detector.
- Measurements took place in hot and raw product gas from biomass steam gasification.
- H<sub>2</sub>, CO<sub>2</sub>, CO<sub>3</sub>, CH<sub>4</sub>, N<sub>2</sub>, NH<sub>3</sub>, H<sub>2</sub>S, and various tar compounds were present in the gas.

Contents lists available at ScienceDirect

### Energy Conversion and Management: X

journal homepage: www.sciencedirect.com/journal/energy-conversion-and-management-x





## Water vapor quantification in raw product gas by THz quantum cascade laser

Florian Johann Müller <sup>a,1,\*</sup>, Michael Jaidl <sup>b,1</sup>, Dominik Theiner <sup>b</sup>, Johann Zeitlhofer <sup>a</sup>, Florian Benedikt <sup>a,c</sup>, Lena Steiner <sup>a</sup>, Alexander Bartik <sup>a</sup>, Marie Christine Ertl <sup>b</sup>, Aaron Maxwell Andrews <sup>d</sup>, Gottfried Strasser <sup>d</sup>, Stefan Müller <sup>a</sup>, Franz Winter <sup>a</sup>, Karl Unterrainer b

a Technische Universität Wien, Faculty of Technical Chemistry, Institute of Chemical, Environmental and Bioscience Engineering, Getreidemarkt 9/166 1060 Vienna, Austria

b Technische Universität Wien, Faculty of Electrical Engineering and Information Technology, Photonics Institute, Gußhausstraße 25-29/387 1040 Vienna, Austria c BOKU University, Department of Material Sciences and Process Engineering, Institute of Chemical and Energy Engineering, Muthgasse 107/I 1190 Vienna, Austria d Technische Universität Wien, Faculty of Electrical Engineering and Information Technology, Institute of Solid State Electronics, Guβhausstraβe 25-25a 1040 Vienna,

#### ARTICLE INFO

Keywords: Online gas analysis QCL Gasification . <u>○</u> Spectroscopy Mater vapor of this doctoral thesis

#### ABSTRACT

Online quantification of water vapor in hot and complex gases, like raw product gas from biomass gasification, is essential for process understanding and control. The complex nature of these gases presents many challenges, e. g., band overlap or dust and tar deposits on equipment. Offline measurement by condensing water is laborintensive and does not provide continuous real-time data. This study introduces a spectroscopic setup consisting of a quantum cascade laser emitting in the far-infrared range, a gas cell heated to around 250 °C, and a pyroelectric detector to quantify water vapor content in real-time. A 1st-order distributed feedback grating ensures single-mode operation of the laser at the desired water absorption line (2.294 THz). This setup was successfully tested for online analysis of raw product gas from steam gasification of waste wood. The average result from the new spectroscopic setup was 45.8 vol-% water vapor content, compared to the condensation measurement, which showed 46.7 vol-% water vapor content. Uncertainty was determined as -0.7 to +1.1 vol-%H<sub>2</sub>O. New data from the QCL-based measurement were available every 1 to 5 s, allowing for a better understanding of the process while operating the gasifier. The permanent gas species detected in the raw gas included CO,  $H_2$ ,  $CO_2$ ,  $CH_4$ ,  $NH_3$ , and  $H_2S$ . Additionally,  $4.16\,\text{g/Nm}_{dry}^3$  of tar was detected gravimetrically and  $31.21\,\text{g/Nm}_{dry}^3$ Nm<sub>drv</sub> by gas chromatography-mass spectrometry. Measurement continued without issue in this raw, hot product gas from biomass steam gasification for two hours. This work showcases quantum cascade lasers' strong potential for spectroscopy applications in hot and complex gases.

#### 1. Introduction

1.1. Importance of water vapor quantification in hot gases

Climate change has led to greenhouse gas mitigation strategies aiming to limit the global average temperature increase and the

resulting severe consequences for the environment and humanity. In 2019, approximately 73 % of net global greenhouse gas emissions came from the sectors of energy (34 %), industry (22 %), and transport (15 %) [1]. Using biomass and waste as feedstock in thermochemical conversion processes, such as pyrolysis, gasification, and combustion, could occupy an essential role in the transition of the already mentioned sectors of energy, industry, and transport and is a critical enabling

\* Corresponding author.

E-mail addresses: florian.johann.mueller@tuwien.ac.at (F.J. Müller), michael.jaidl@tuwien.ac.at (M. Jaidl), dominik.theiner@tuwien.ac.at (D. Theiner), johann. zeitlhofer@tuwien.ac.at (J. Zeitlhofer), florian.benedikt@boku.ac.at (F. Benedikt), lena.steiner@tuwien.ac.at (L. Steiner), alexander.bartik@tuwien.ac.at (A. Bartik), marie.christine.ertl@tuwien.ac.at (M.C. Ertl), aaron.andrews@tuwien.ac.at (A.M. Andrews), gottfried.strasser@tuwien.ac.at (G. Strasser), stefan.mueller@tuwien. ac.at (S. Müller), franz.winter@tuwien.ac.at (F. Winter), karl.unterrainer@tuwien.ac.at (K. Unterrainer).

<sup>1</sup> These authors contributed equally to this paper.

f https://doi.org/10.1016/j.ecmx.2025.100906

Received 11 October 2024; Received in revised form 15 January 2025; Accepted 31 January 2025 Available online 3 February 2025

2590-1745/© 2025 The Author(s). Published by Elsevier Ltd. This is an open access article under the CC BY license (http://creativecommons.org/licenses/by/4.0/).

Nomenclature				
Paramete	er symbol Parameter description, unit			
$A_{CO}$	Absorbance of CO, –			
$c_{Beer}$	Concentration of H <sub>2</sub> O in the wet gas volume determined by			
	spectroscopy, mol/m <sup>3</sup>			
$c_{CO}$	Concentration of CO in the wet gas, mol/m <sup>3</sup>			
$c_{Condensatio}$	on Concentration of H <sub>2</sub> O in the wet gas determined by			
	condensation, mol/mol			
$c_{Laser}$	Concentration of H <sub>2</sub> O in the wet gas determined by			
	spectroscopy, mol/mol			
d	Optical path length through the measured medium, m			
I	Measured intensity of light at the lock-in amplifier during			
	experiment, V			
$I_{O}$	Baseline intensity of light at the lock-in amplifier without			
	H <sub>2</sub> O in cell, V			
$I_{0,N2}$	Baseline intensity of light at the lock-in amplifier with N <sub>2</sub>			
-,	in cell, V			
p	Pressure, Pa			
R	Ideal gas constant (8.3144), J/mol/K			
T	Temperature, K			
$\varepsilon$	Molar extinction coefficient, m <sup>2</sup> /mol			

Λ	Period length, m
$\nu$	Wave number, 1/cm
$\sigma$	Standard deviation of baseline signal, V
Abbrevia	tion Term
DA	Direct Absorption
DFB	Dual Fluidized Bed
FTIR	Fourier-Transform InfraRed
GATS	GATS, Inc.: Small aerospace company
GC-FID	Gas Chromatography – Flame Ionization Detector
GC-MS	Gas Chromatography – Mass Spectometry
IR-LAS	InfraRed Laser-Absorption Spectroscopy
NDIR	Non-Dispersive InfraRed
OF-CEAS	Optical Feedback Cavity-Enhanced Absorption
	Spectroscopy
QCL	Quantum Cascade Laser
SEM	Scanning Electron Microscopy
SNG	Synthetic Natural Gas
TCD	Thermal ConDuctivity
TDLAS	Tunable Diode Laser Absorption Spectrometry
VMR	Volume Mixing Ratio
WMS	Wavelength Modulation Spectroscopy

technology for various defossilization and negative emission technologies [2]. Switching the fuel from fossil to biomass and adapting the process by capturing CO<sub>2</sub> in situ, e.g., with chemical looping or in the flue gas, can lead to a so-called net-negative emission process [3]. In several industrial processes, e.g., thermochemical fuel conversion, energy generation, chemical production, and steel or concrete production, measuring the water vapor content in hot gases is crucial in process control. The variability of waste and biomass feedstocks, e.g., variations in moisture content resulting from changes in harvesting conditions [4], presents additional challenges for process control and optimization. The heterogeneity of these alternative feedstocks further increases the importance of accurate and real-time water vapor content measurement for assessing process efficiency, optimizing operational parameters, and ensuring safe operation.

## 1.2. Challenges for water vapor quantification on the application example of raw product gas

Biomass steam gasification is investigated in this new work as an d exemplary technology, notorious for presenting many challenges to water vapor measurement in raw and hot gas. A successful demonstration of water vapor quantification in this process would be promising for a future transfer of this technology into other industries, where gas compositions are often less challenging to measure. In gasification, the organic feedstock is not fully oxidized but converted with a gasifying agent such as steam, under-stoichiometric addition of air or oxygen, or CO2 into so-called raw product gas [5]. The main components of the raw product gas are hydrogen, carbon monoxide, carbon dioxide, methane, steam, and C2 and C3 permanent gases. Raw, in this context, refers to the gas before it is cleaned and still contains condensable species and possibly particles. The product gas can be further conditioned and prepared for the synthesis of various products; hence, the cleaned version is called synthesis gas or, in short, syngas. Syngas can be converted and refined to gaseous energy carriers, transportation fuels, and other chemical products such as Fischer-Tropsch products [6], synthetic natural gas (SNG) [7], hydrogen [8] and many more [9]. Biomass gasification using a dual-fluidized bed (DFB) reactor design with around 100 kWth biomass input has been a central research interest at TU Wien and is described in numerous publications, e.g., [7,8,10]. The DFB design consists of two interconnected reactors, where one generates the

raw product gas in an endothermic process. At the same time, the other provides heat for the endothermic gasification by combustion of additional feedstock. DFB reactors for biomass gasification are also relevant at larger scales, e.g., as shown by the GoBiGas plant that produced 20 MW of SNG until decommissioning in 2018 [11]. A good solution for measuring water vapor in the raw product gas from these reactors is missing, which is explained by the wide range of compounds in the gas.

The composition of raw product gas, especially its water vapor content, is heavily influenced by the amount and type of gasifying agent, the fuel water content, and the operating temperature [12]. The product gas's main gas composition, the so-called gas matrix, can vary significantly, complicating the analytics task. Common raw product gas impurities include particulate matter like dust and char particles, heavy organic compounds, and other species such as NH<sub>3</sub>, H<sub>2</sub>S, and HCl, which depend on the fuel used [13]. The formation of tar in the raw product gas is one of the significant challenges in the thermochemical conversion of biomass and waste through gasification. Several definitions for the term "tar" exist. The definitions for tar used in this work follow the prestandard CEN/TS 15439:2006, which defines tar as a "generic term for the totality of all organic compounds present in the product gas from gasification, with the exception of gaseous hydrocarbons (C1 to C6)" [14]. Tar can condense at temperatures around 200 °C and ambient pressure, which leads to significant issues regarding downstream equipment, e.g., particulate filters or heat exchangers [10]. For analytics in raw product gas, tar poses various problems for a wide range of gas analyzers, e.g., band overlap and fouling [15]. These other species complicate the water quantification task, and water vapor in raw product gas can also have detrimental effects on other analyses. Kleinhappl [16] discussed these problems, which include the dilution of solvents, phase separation, slip of non-polar fractions during sampling, ice formation, baseline instabilities in gas chromatography-flame ionization detectors (GC-FID), or discrimination during evaporation in GC injectors.

#### 1.3. Established water vapor quantification technologies

Measuring the main product gas components in the cold and waterfree state is sufficiently solved, e.g., after appropriate gas purification, combustion with subsequent cooling, or gas sampling equipped with condensation and filters. Measuring raw gas in the hot state is much more complicated, and no method has established itself as a standard for online water vapor quantification in raw and hot gases with complex compositions. Aranda Almansa et al. [15] report the state-of-the-art measuring procedures for water quantification in raw product gas and their shortcomings: Offline sampling methods like gravimetric quantification and solid phase adsorption are low-cost but suffer from manual procedure issues and often cannot accurately reflect dynamic system behavior. Online and semi-online sampling via chromatography face coadsorption and maintenance challenges. Real-time methods, including hygrometers, acoustic measurement, and spectrometry, are costly and often affected by dust, tar deposits, and band overlapping. Further challenges include the strong light attenuation of product gas, high temperatures, the significant number of different compounds, and especially the negative effect of particulate matter in the gas, lowering the possible optical path length if visible or near-infrared wavelengths are used [17].

The most widespread spectroscopic devices for combustion and gasification gas analysis are infrared laser-absorption spectrometers (IR-LAS), as described in several reviews [18,19]. IR-LAS instruments use the absorption and emission effects when the spacing between two discrete rotational-vibrational states equals the photon energy [18]. The density or concentration of the analyzed species can be derived from the total absorbed or emitted radiation. Most devices use light sources in the near- or mid-infrared domain [18]. Tunable laser diodes are widespread light sources, and tunable diode laser absorption spectroscopy (TDLAS) has been used extensively for quantitative online and in situ real-time combustion and gasification diagnostics [18,19]. Multiple signal evaluation strategies have been described and compared in the literature and can be summarized into two groups: direct absorption (DA) and wave-<u>value</u> length modulation spectroscopy (WMS) [18–20]. DA systems are generally simpler to build and calibrate but less sensitive and resistant to noise [21]. Sepman et al. have demonstrated in several studies the use of TDLAS for in situ H<sub>2</sub>O measurement in the reactor core of a biomass gasifier [22–25]. These studies showed reliable performance even under high-temperature and high-soot conditions. A TDLAS sensor near 4350 cm<sup>-1</sup> was developed for in situ CO, H<sub>2</sub>O, and soot concentration measurements in a pilot-scale gasifier's reactor core, achieving temperatureinsensitive species quantification from 1000 K to 1900 K [22]. H<sub>2</sub>O quantification uncertainties were reported as better than 10 % compared to calculations [24] and 20 % compared to micro-gas chromatograph data [22]. Sur et al. have shown that TDLAS can also be applied in pressurized gasifiers [26], [17,2717].

Other techniques for online or in situ determination of H<sub>2</sub>O content include Raman spectroscopy (RS) [28], acoustic measurements [29], humidity meters [30], soft sensors [31] and others, not all of which are explained in detail here. RS is highly flexible and can be used for various analysis tasks in the thermochemical processing of biomass, coal, and waste [28]. RS is based on inelastic scattering of light, where the frequency of photons is shifted due to interaction with molecular vibrations [32]. Raman spectroscopy has been demonstrated for H<sub>2</sub>O quantification in biogas [33] and biomass gasification [34] applications. However, Xu et al. [28] note in their review that Raman spectroscopy has rarely been used to analyze gas components. They suggest that this is caused by the low density and Raman cross-section of gases, making it challenging to obtain high-quality Raman spectra. Karellas and Karl also noted that high gas flows or tar contents lead to intense background signals, obscuring the Raman peaks of other gas compounds [34]. An online estimation method was recently proposed by TUW, consisting of a soft sensor that estimates raw product gas composition based on a Hammerstein model and two extended Karman filters [31]. However, this method requires training on historical data for the specific plant and relies on other measurements, such as gas chromatography, which presents challenges for new or dynamic systems.

#### 1.4. Water vapor measurement with a THz laser

The present work introduces a quantum cascade laser emitting light in the far-infrared domain at terahertz frequencies for continuous water vapor measurement in hot and raw product gas from gasification. As summarized in a recent review [35], lasers emitting in the THz spectral region (commonly defined as the frequency range 0.1 – 10 THz) have been tested for water detection in various applications [35]. Although the review describes a significant amount of research in this field, there is little information on high-temperature systems with complex gases from industrial applications. In general, water vapor has various absorption lines at sufficiently high temperatures to avoid tar condensation [30], with some even stronger at high-temperature than at room temperature [36]. Additionally, compared to other lasers used for spectroscopy in the visible, near- or mid-infrared spectral domains, THz lasers have longer wavelengths. These longer wavelengths make them more resistant to Mie scattering [37,38] from dust, which is typically present in off-gas flows from industrial applications [30,36]. Most organic compounds and inorganic ions absorb in the near- or midinfrared region between  $400-4000 \,\mathrm{cm}^{-1}$ , which is around 12 – 120 THz [17]. For these reasons, a THz laser in the far-infrared region is expected to be more robust against band overlapping with the various organic compounds in gasification processes.

Song et al. investigated THz lasers for their ability to measure water vapor content in N2/H2O mixtures at 773 K. They found three absorption peaks at 557 GHz, 658 GHz, and 752 GHz, where water vapor content could be quantified using a gas cell with a length of 1 m [36]. This work is promising; however, the tests were conducted in batches by feeding H<sub>2</sub>O with syringes into the cell, which otherwise only contained nitrogen from a gas bottle. Therefore, this test did not include the additional challenges posed by dust and various permanent and condensable gases mixed with water vapor in the raw product gas.

Bidgoli et al. investigated a spectroscopic setup for measuring water vapor from gasification [30]. They did screenings and statistical analysis with lasers between 300 and 500 GHz and a gas cell with a length of 1.6 m. They concluded that THz gas spectroscopy could efficiently provide real-time data on water vapor in complex gas mixtures containing dust particles and tar components. However, their publication had significant trouble correlating the measured signal to a volume mixing ratio (VMR) of water because of unclear temperatures in the gas cell. The extensive length of the cell worsened this problem.

This present work uses a similar spectroscopic setup as [30] with hot (~250 °C) gas flowing through the measurement cell to detect water vapor and measure its concentration by selective absorption of light emitted by a quantum cascade laser (QCL). A first experimental campaign was conducted with synthetically prepared gas mixtures. An advanced setup was used to measure raw product gas from biomass steam gasification. THz QCLs are electrically driven lasers with a semiconductor heterostructure [39]. Their advantages include a compact design, high output powers, and frequency tunability. The QCL in this new setup allows for a gas cell with a short beam path of only 86 mm, drastically reducing the cell temperature variations that [30] observed and making the setup more compact by reducing the gas cell length by over 90 %. This design is investigated in the present work for online analysis of water vapor. Raw and hot product gas from biomass steam gasification is measured and used as an example of a potential application scenario with significant challenges for online measurement.

#### 2. Theory and calculation

#### 2.1. Selection of laser frequency

Viveros Salazar et al. summarized the necessary steps and considerations to select a suitable laser frequency [20]. Computational prediction of absorption characteristics demands a line list including information such as wavelength, line strength, and collision-broadening effects for each chemical species. In this work, the Spectral Calculator developed by GATS, Inc. was used to calculate absorption and transmittance at specific wave numbers, temperatures, gas cell lengths, and volumetric mixing ratios [40]. This calculator uses the HITRAN2020 database [41] as a line list to perform line-by-line molecular absorption calculations based on the line-by-line model in the LinePak<sup>TM</sup> library [42]. The spectral calculator includes weighted air- and self-broadened halfwidths depending on pressure and temperature from the HITRAN2020 database to calculate the line shape. This method yields a combination of Doppler and Lorentz broadening, resulting in the more general Voigt profile.

The next step for laser frequency selection is estimating operating conditions [17,20]. Essential conditions to estimate include temperature, pressure, and other chemical components surrounding the measured species, which might contribute to absorption. Atmospheric pressure was selected for measurement since TUW usually does not pressurize their gasifiers. A temperature range of  $100-400\,^{\circ}\text{C}$  was considered appropriate to retain some flexibility in operation and avoid the condensation of water and tar in the cell. The concentration of gaseous main components and impurities in raw product gas heavily depends on fuel composition [43]. In addition, raw product gas can contain various tars, fly char, and dust, for which no information is available from the Spectral Calculator or in the HITRAN database. Bidgoli et al. [30] did not report a significant influence of these components in their work with laser frequencies between 300 and 500 GHz. A hot gas filter was used to reduce the particle density in the beam path in our work. Furthermore, the size of most particles after the gasification reactor's filter system in the present work is well below the laser wavelength of 130.69 µm. Therefore, particles are not assumed to impede the transmission of laser light significantly [37,38]. This work uses the simplification that no interaction between the laser light and any solid particles or molecules other than H2O or CO occurs.

Once absorption theory and operating conditions are established, the selection of a laser frequency needs to achieve sufficient selectivity over other components and absorption signal strength for detection [17,20]. Viveros Salazar et al. suggest a 10-90 % laser transmission for sensitive measurements [20]. The laser transmission depends on the beam path length (see Section 2.2). Our work also aimed to select a laser frequency at which the beam path could be relatively short while achieving the 10-90 % transmission criteria. A short beam path allows for a more compact setup, promising multiple benefits such as transportability and less temperature variation inside the measurement cell. Another important criterium for laser frequency selection is the availability of a

suitable laser.

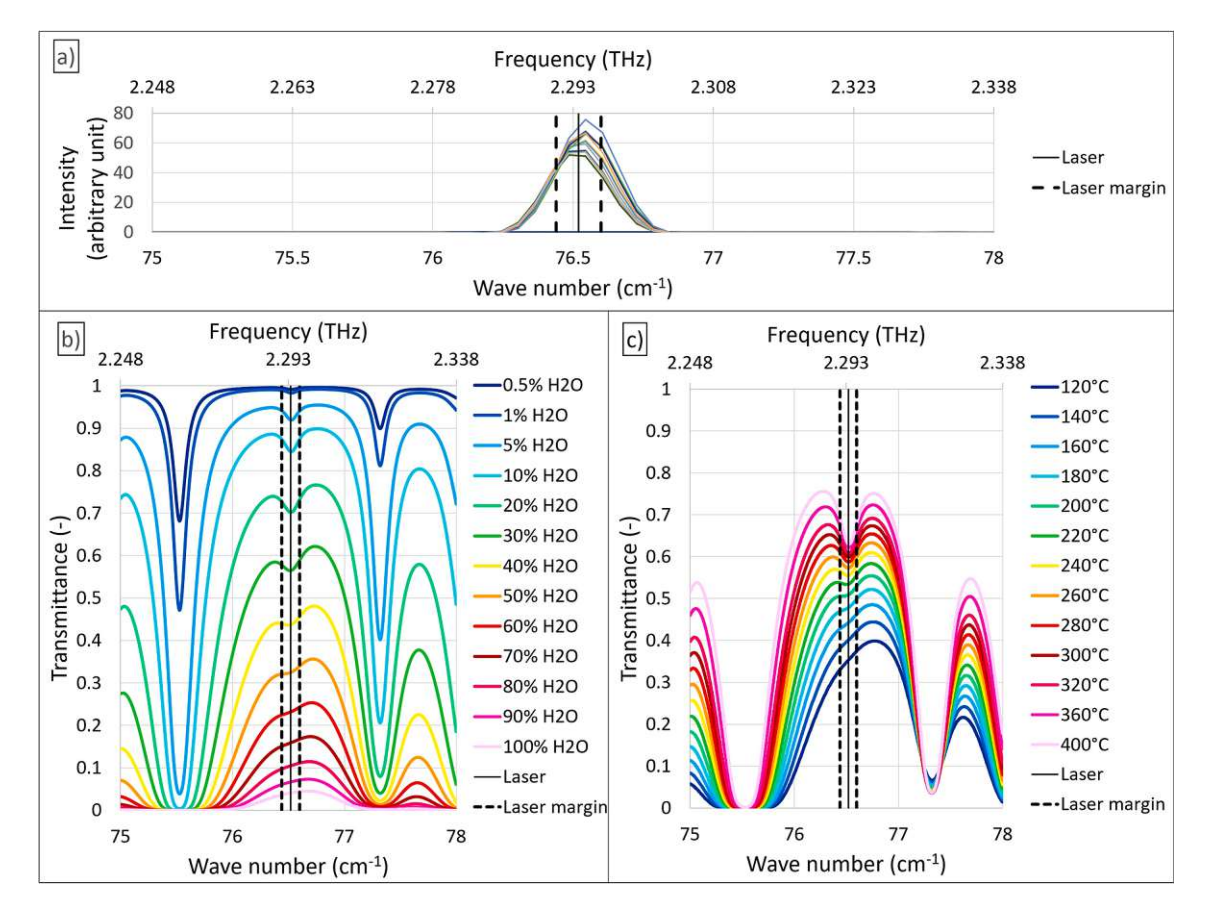
Data from the Spectral Calculator were used to identify 2.294 THz, respectively, a wave number of 76.52 cm<sup>-1</sup>, as a suitable water absorption frequency line for analysis of raw product gas from biomass gasification among available THz QCLs with sufficient power output. Other main components in typical product gas show comparably weak absorption at this frequency. Absorption values of the predominant product gas species from gasification are listed in Table 1. These values are calculated at 250  $^{\circ}\text{C}$  and 1.013 bar<sub>a</sub> for a cell with 86 mm optical path length, approximating the conditions used in this work. The absorption of water vapor at the chosen wave number is much stronger than the absorption of the following closest species, carbon monoxide, at a similar concentration. Other species absorb this light even weaker by multiple orders of magnitude. Among impurities, NH3 and HCN are calculated to show the highest absorption at typical gas concentrations from biomass gasification in a DFB reactor [44]. Their absorption at the highest typical concentrations is similar to the absorption of pure CO.

The absorption of  $\rm H_2O$  at 2.294 THz is calculated between 0.2 – 96%, corresponding to 0.1 – 100 vol-%  $\rm H_2O$  in the gas cell. The laser transmission is between 10 – 90 % when the  $\rm H_2O$  concentration is approximately 5 – 80 vol-% in the gas cell, suggesting that sensitive measurement is possible over a wide range of  $\rm H_2O$  concentrations (Fig. 1b). In contrast, even at their highest considered VMR, no other gas component in typical raw product gas from DFB gasification is estimated at more than 4% absorption, with average absorption being even lower by orders of magnitude. Furthermore, the absorption of CO can be dynamically excluded from the measurement using dry gas composition data from other measurements, e.g., non-dispersive infrared (NDIR) measurement. In summary, the frequency of 2.294 THz allows measurement with minimal cross-sensitivity for other gas components. This design allows the laser to quantify water vapor over a wide range of raw gas compositions.

Fig. 1a shows 16 Fourier-transform infrared spectrometer measurements, experimentally confirming that the laser emits light at the design frequency of 2.294 THz. The spectrometer's resolution of  $\pm 0.08~{\rm cm}^{-1}$  is defined by the path difference of the interferometer arms and leaves some margin of error, which is reflected in Fig. 1a. Spectra calculated for this laser frequency by the Spectral Calculator at various H<sub>2</sub>O concentrations (Fig. 1b) and temperatures (Fig. 1c) are examples of feasible operating conditions. Fig. 1b shows that H<sub>2</sub>O concentrations can be well differentiated over a wide range of water vapor concentrations at 250 °C. Fig. 1c demonstrates that H<sub>2</sub>O still absorbs at 400 °C, enabling the measurement in hot and raw gas to avoid extensive fouling from tar

Absorption of the typical raw product gas components and impurities from biomass gasification [45–47] as calculated by the Spectral Calculator [40] at  $\lambda = 2.294$  THz  $^{2}$  ( $\nu \approx 76.52$  cm $^{-1}$ ) for a gas cell with 8.6 cm length, 1013.25 mbar pressure, 523.15 K. The abbreviation "B.L." means "below limit", which was arbitrarily chosen at 1E-

2		Considered gas concentration	Absorption at the lowest considered concentration	Absorption at the highest considered concentration
5 <b>-</b>	Main component	vol-%	_	_
2	$H_2O$	0.1 - 100	1.7E-03	9.6E-01
)	$N_2$	0.1 - 100	B.L.	B.L.
	H <sub>2</sub>	0.1 - 100	B.L.	B.L.
	CH <sub>4</sub>	0.1 - 100	B.L.	3.9E-05
	$C_2H_4$	0.1 - 100	B.L.	B.L.
	CO	0.1 - 100	3.5E-05	3.7E-02
	$CO_2$	0.1 - 100	B.L.	B.L.
2	$O_2$	0.1 - 100	B.L.	1.2E-06
2	Impurity	ppm (vol.)	_	_
ng r	NH <sub>3</sub>	1,000 - 100,000	1.3E-04	1.8E-02
<u> </u>	HCN	10 – 1,000	3.3E-04	3.3E-02
2	H <sub>2</sub> S	10 – 1,000	2.5E-06	2.5E-04
2	COS	0.1 - 100	B.L.	B.L.
2	HCl	0.1 - 100	B.L.	2.7E-06
	NO	10 – 1,000	B.L.	5.6E-06
ú	$N_2O$	0.1 - 100	B.L.	B.L.
Ę	$NO_2$	0.01 - 1	B.L.	B.L.
	$SO_2$	0.1 - 100	B.L.	5.1E-04



 $\stackrel{>}{\approx}$  **Fig. 1.** A) Experimentally found laser spectra with margins of error resulting from discretized measurements. b-) and c): transmittance calculated with data from the  $_{\Omega}$  spectral calculator [40] for various volume mixing ratios of H<sub>2</sub>O at 250 °C (b), various temperatures at 30 vol-% H<sub>2</sub>O (c).

condensation. Transmittance at the example water vapor concentration of 30 vol-% is similar from 250 - 400 °C, showing robustness against temperature deviations in the measured gas in this range.

#### 2.2. Measurement of water vapor content

Fixed-wavelength direct absorption spectroscopy is used in this work to detect  $H_2O$ . The  $H_2O$  concentration  $c_{Laser}$  is calculated from Beer-Lambert's law (Eq. (1)), which describes the absorption as a function of line strength, line shape, gas pressure, the concentration of the gas in the light's path, and the optical path length [17]. Molar extinction coefficient data ( $\varepsilon$ ), which summarize several of these dependencies, are discussed for H<sub>2</sub>O and CO in Section 2.3. The absorption is calculated from the detected laser intensity during an experiment (I) and a baseline intensity with no  $H_2O$  in the cell ( $I_0$ ). Beer-Lambert's law typically expresses the concentration in  $mol/m^3$  (here termed  $c_{Beer}$  for differentiation). The ideal gas law accounts for the gas' thermal expansion. The  $H_2O$  concentration  $c_{Laser}$  in mol/mol or  $m^3/m^3$  is calculated by comparing  $c_{Beer}$  to the total gas per volume at the temperature T and pressure p (Eq. (2)). The temperature over the integration path is assumed as constant. This assumption is justified by preheating the gas in the sampling line and gas cell with the same heating coil and keeping the optical path length short at only 8.6 cm. The baseline intensity in N<sub>2</sub> atmosphere  $(I_{0,N2})$  is determined shortly before experiments. The absorption of gases other than N2, specifically CO, lowers the baseline intensity  $I_0$  during the experiment with gas mixtures compared to  $I_{0,N2}$ .  $I_0$  is not available as measurement during the experiments and is instead calculated from  $I_{0,N2}$  (Eq. (3)). The CO absorbance ( $A_{CO}$ ) is also calculated from Beer-Lambert's law using the wet CO gas concentration ( $c_{CO}$ ) (Eq. (4)). Dry gas composition data from non-dispersive infrared (NDIR) measurement (Section 3.3.2) are implemented in the solving algorithm (*Section 2.3*, Appendix A) to derive  $c_{CO}$ . The cell's inner optical path length through the measured gas has the length d.

$$c_{Beer} = \frac{log_{10}\left(\frac{l_0}{I}\right)}{\epsilon_{H2O} \cdot d} \tag{1}$$

$$c_{Laser} = \frac{R \cdot T \cdot log_{10} \left(\frac{l_0}{I}\right)}{\varepsilon_{H2O} \cdot d \cdot p} \tag{2}$$

$$I_0 = I_{0,N2} \cdot 10^{-A_{CO}} \tag{3}$$

$$A_{CO} = \frac{c_{CO} \cdot \varepsilon_{CO} \cdot d \cdot p}{R \cdot T} = log_{10} \left( \frac{I_{0,N2}}{I_0} \right) \tag{4}$$

#### 2.3. Molar extinction coefficient $\varepsilon$ and solving algorithm

The molar extinction coefficients of water vapor  $\varepsilon_{H2O}$  and CO  $\varepsilon_{CO}$  are determined from transmittance data given by the Spectral Calculator [48] for a cell with 86 mm optical path length at a pressure of 1013.25 mbar. Three wave numbers were considered: the design laser wave number and its experimentally found upper and lower margins of error:  $76.52\pm0.08~\text{cm}^{-1}$ . These data include VMR for H<sub>2</sub>O and CO between 0.1-100 vol-% and temperatures between 110-400~°C, representing the target operating conditions. Eq. (2) was rearranged to solve for  $\varepsilon_{H2O}$  and  $\varepsilon_{CO}$ . While  $\varepsilon_{CO}$  was found to be 1–2 orders of magnitude below  $\varepsilon_{H2O}$  and relatively constant at a higher wave number,  $\varepsilon_{H2O}$  depends on the temperature, water concentration, and wave number (Fig. 2).

At high temperatures and low water concentrations, the differences in  $\varepsilon_{H2O}$  for the investigated laser frequencies are sizeable, which is



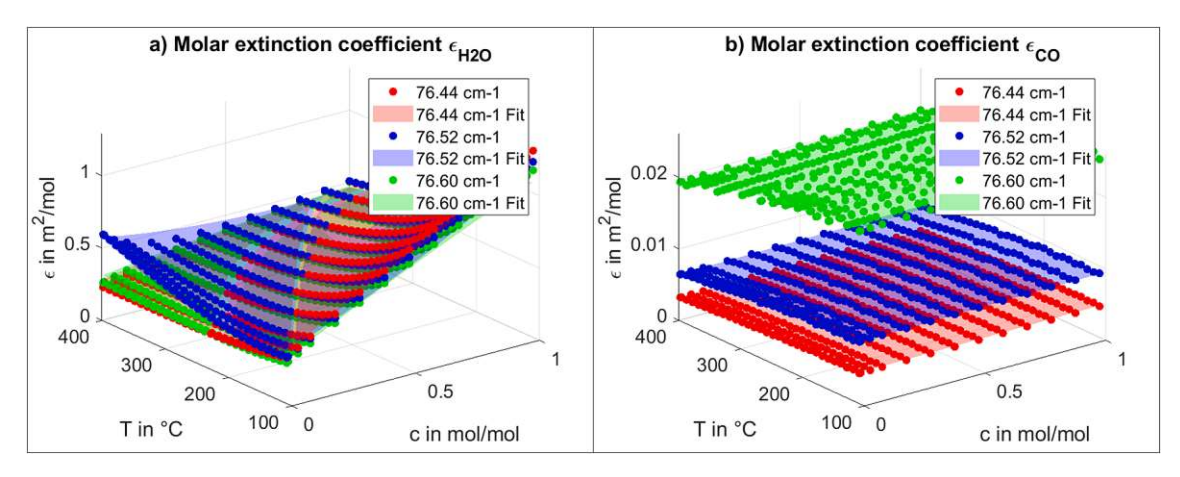


Fig. 2. Molar extinction coefficients fit (surface) based on data from Spectral Calculator (data points). A) H<sub>2</sub>O, b) CO.

reflected as uncertainty in the results of this work. The molar extinction coefficient's dependence on the temperature can be accounted for using temperature data from the measurement inside the cell. The molar extinction coefficient's dependence on the molar H2O concentration means that Eq. (2) needs to be solved iteratively. For this reason, a solving algorithm is adopted to determine  $c_{Laser}$  (Appendix A). Data are typically measured and evaluated internally at an interval of 1 s. Moving average data with a window size of 60 s are given as output to reduce noise. The NDIR measurement can be connected to the QCL setup's solving algorithm, adjusting the signal baseline for CO cross-absorption in real-time.

#### 3. Material and methods

#### 3.1. QCL-based H<sub>2</sub>O measurement

#### 3.1.1. THz QCL characteristics

The active region of the used laser consists of a bound-to-continuum design in the GaAs/AlGaAs-material system [49]. A picture taken by scanning electron microscopy (SEM) is included in Appendix B.

The center frequency of the gain bandwidth is at 2.3 THz. The heterostructure was processed into double-metal waveguides. A 1<sup>st</sup>-order distributed feedback grating [50] was employed on the 2.5 mm long ridge waveguide to ensure single-mode operation at the desired water absorption line (2.294 THz,  $130.69 \, \mu m$ ,  $76.52 \, cm^{-1}$ ). The emission wavelength can be tuned slightly by changing the operation temperature. Different gratings with varying periods were tested to determine the best fitting to the absorption line. In the first campaign, a laser with a period of  $\Lambda = 19.272$  µm was used, where the entire width of the ridge is 60 µm, and the setback is 10 µm. The second campaign used a device with an adjusted period of  $\Lambda = 19.22 \, \mu m$ . This adaptation was employed to reduce the required wavelength shift by temperature. This way, the operating temperature could be lowered, and the output power could be enhanced. A spectrometer with a resolution of  $\pm 0.08$  cm<sup>-1</sup> was used to check the wave number of the processed laser. The THz QCL is operated at a temperature of 90 K (resp. 70 K in the second campaign), enabled by a commercial Stirling cooler with a power of 70 W. A vacuum pump provides a pressure of 1.6•10<sup>-6</sup> mbar within the laser housing. The operating temperature is monitored by a PT100 sensor and is stabilized by a high-performance resistor used as a heater. Both are attached to the cold finger of the cryostat. Electrical pulses drive the QCL with a repetition rate of 100 kHz and a pulse length of 7 resp.  $9.5~\mu s$  (duty cycle: 70 resp. 95 %, voltage pulse generator: Agilent 8114A), which are again modulated with a gating frequency of 13 Hz (frequency generator: Agilent 33220A). This gating frequency enables signal detection at the pyroelectric detector, which is comparatively slow (bandwidth ~ 100

#### 3.1.2. Gas cell setup

The main components of the spectroscopy setup include the light source (THz QCL), the gas cell, the pyroelectric detector, and two parabolic mirrors. A sketch of these components' arrangement and the light's corresponding beam path is shown in Fig. 3a. The measurement cell is made from alumina (Fig. 3b). The cell is a hollow cylinder separated into three closed-off sections by quartz glass windows with a width of 1 mm each. The outer sections are flushed with nitrogen at 0.5 NL/ min to minimize the danger of the leakage of dangerous gas components like CO into the ambient. The flushing also lowers the outer quartz glass windows' temperature, protecting the pyroelectric detector from overload. A downside of this flushing is the increased risk of tar condensation in the central section caused by lower temperatures at the windows. The central section has an inner length of 86 mm and contains the measured gas sample. Trace heating was installed around the measurement cell to prevent condensation.

A prototype for the measurement cell without integrated temperature measurement was used during the first campaign with synthetically prepared gas mixtures from bottled gas. The temperature in the cell during these tests was measured with an infrared sensor by Beha-Amprobe on the cell's outside wall. An uncertainty of  $\pm 10$  °C compared to the temperature in the cell was assumed for these temperature measurements with the following reasoning: First, no water condensation inside the cell was observed at 110 °C outside wall temperature, suggesting that the maximum negative deviation could have been  $-10~^{\circ}$ C. Second, alumina's high heat conductivity and the small gas cell size suggest a relatively good heat distribution where even local hotspots are unlikely to exceed +10 °C. An advanced cell design, including a thermocouple type K and improved heating and insulation around the cell, was used for the second campaign measuring hot and raw product gas from a gasifier. Pictures of the advanced setup are available in Appendix B.

In the setup, the first parabolic mirror collects the laser beam emitted from the device, converts it to a parallel beam, and guides it to the measurement cell. The second parabolic mirror focuses the THz light from the measurement cell onto the pyroelectric detector. The detector measures the laser beam's intensity. To allow for the detection of the THz light by the pyroelectric detector and read out by a lock-in amplifier (Stanford Research SR830), the THz QCL is driven by a doublemodulated voltage signal (see Section 3.1.1).

#### 3.2. Gas production

This work describes two experimental campaigns. The setup prototype was used to investigate synthetically prepared gas mixtures and validate the basic functionality. The advanced setup was tested in a second campaign with raw product gas produced via steam gasification

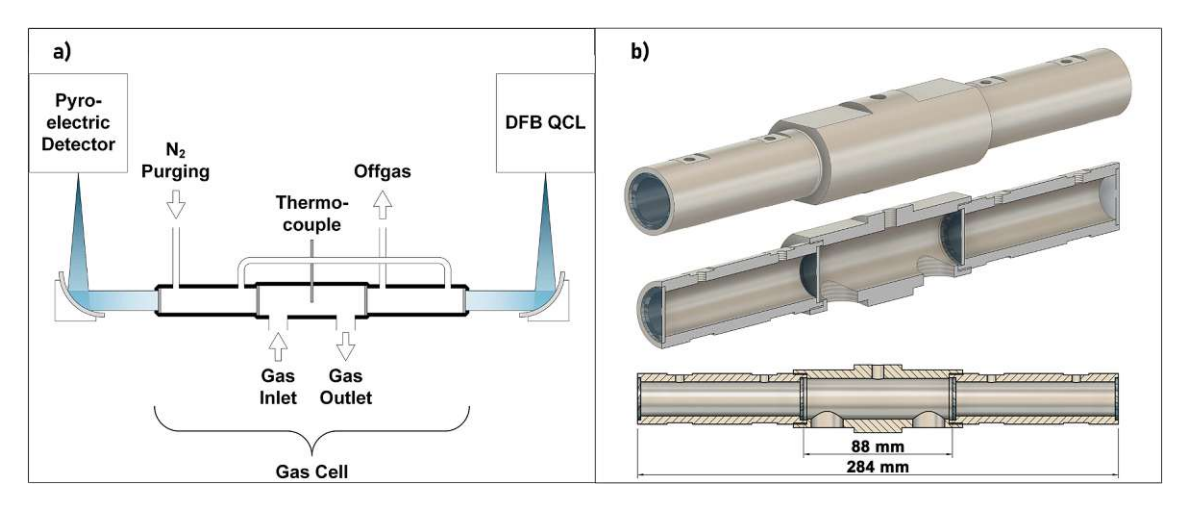


Fig. 3. Gas measurement cell. a) Sketch of gas and light pathways ("DFB OCL"=distributed feedback quantum cascade laser) and b) 3D design drawing,

of waste wood in a DFB gasifier. More detailed information on the gas sampling and measurements is given in Section 3.3.

#### 3.2.1. First campaign: Synthetically prepared gas mixtures

A gas preparation unit consisting of bottled gases, mass flow controllers (MFC), an electrically heated water evaporator, and a water pump was used to prepare the synthetic gas mixtures for the first campaign. Fig. 4 shows a basic flowsheet of the setup, with only one gas sampling point alternating between the H<sub>2</sub>O condensation or the H<sub>2</sub>O laser and dry product gas measurements. The pipes downstream of the evaporator were electrically heated to approximately 200 °C to prevent condensation.

Table 2 lists the target values of the dry gas composition for the permanent gases and the varying H2O content. The carrier gas for MIX 1-3 is nitrogen, while the carrier gas for MIX 4-6 resembles a typical product gas from fixed-bed air gasification [51]. The target water vapor content ranges between 10 and 50 vol-%. The liquid water flow to the evaporator was only controlled by the pump, and so the actual values might have differed.

#### 3.2.2. Second campaign: DFB gasification

A 100 kW<sub>th</sub> DFB gasification pilot plant at TU Wien was used to produce raw product gas. The DFB pilot plant and the SNG process chain have been described in various publications by TU Wien [7,44,46,52]. As the gasification process is not within the scope of this study, only a summary is given here.

A basic flowsheet of the setup is shown in Fig. 5, including the most

Table 2 Target gas compositions used for experiments with synthetically premixed gas.

Experiment	$N_2$	CO	$CO_2$	$H_2$	CH <sub>4</sub>	H <sub>2</sub> O
	vol- % <sub>dry</sub>	vol-%				
MIX 1	100	_	_	_	- '	25.0
MIX 2	100	_	_	_	_	10.0
MIX 3	100	_	_	_	_	50.0
MIX 4	45	20	13.3	19.25	2.45	42.5
MIX 5	45	20	13.3	19.25	2.45	50.0
MIX 6	45	20	13.3	19.25	2.45	35.0

relevant temperatures during the investigated gasification campaign's stationary operation. DFB gasification is built on the principle of two interconnected fluidized beds. In the gasification reactor, biomass is gasified with steam or other gasification agents like CO2 at approximately 800 °C, producing a raw product gas. Residual, ungasified char is transported to the combustion reactor with a circulating bed material. In the combustion reactor, char is combusted with air, and the hot bed material is transported back to the gasification reactor to drive the endothermic gasification reactions. The raw product gas leaves the gasifier via a cyclone and a radiation cooler where particles are reduced, and cooling occurs. A hot gas filter further reduces dust concentrations before the product gas is directed to a downstream synthetic natural gas process chain. For the investigated gasification campaign, 22.5 kg/h waste wood was gasified with steam at approximately 777 °C with an 80/20 wt-% mixture of olivine/limestone as bed material.

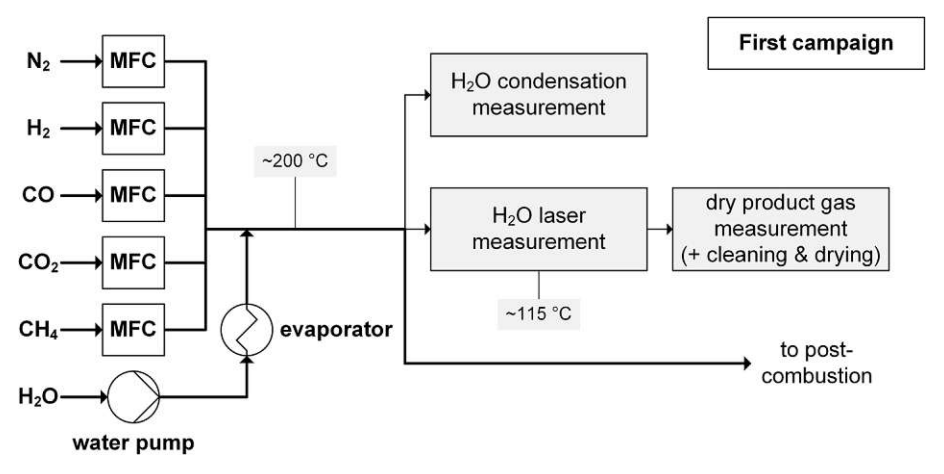


Fig. 4. Basic flowsheet of the gas preparation unit for synthetic mixtures.

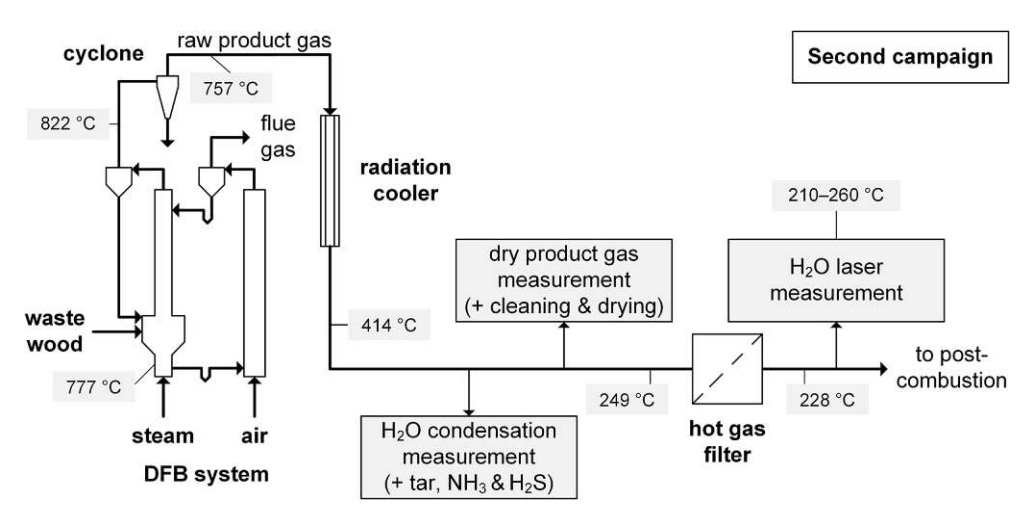


Fig. 5. Basic flowsheet of the raw product gas preparation from a 100 kW<sub>th</sub> DFB gasifier.

#### 3.3. Gas sampling and conditioning

This chapter describes the differences in sampling procedures for the various measurements conducted in this work.

#### 3.3.1. Condensation and dissolution measurements

Water vapor, tar, NH<sub>3</sub>, and H<sub>2</sub>S content can be measured discontinuously by condensing or dissolving them and relating the sampled amount to the dry carrier gas flow through the sampling line. This Φ methodology is well established and is the current standard used during

the measurement. Condensate was collected in chilled Impinger bottles filled with toluene in a cryostat filled with glycol at -8 °C. A diaphragm pump drew a sample gas stream through the cooled toluene in the Impinger bottles and a bellows gas meter measured the dry gas volume. The standard volume of sampled dry gas was calculated from the bellows gas meter's readout via the ideal gas law, using an integrated temperature measurement and ambient pressure data from a nearby weather station run by GeoSphere Austria [53]. The liquid mixture was transferred from the bottles into a separating funnel, where the denser water phase was collected at the bottom. This phase was separated into a measuring cylinder to determine the total volume of the liquid water collected. Depending on the estimated water content, sampling was done for 12 - 18 min.

Aqueous solvents replaced toluene to collect NH3 and H2S, for which the cryostat was tempered to +2 °C. NH<sub>3</sub> was captured in a 0.05 M H<sub>2</sub>SO<sub>4</sub> and H<sub>2</sub>S in 35 wt-% KOH. H<sub>2</sub>S was determined by titration and NH3 by ion chromatography from these aqueous samples. The exact procedure is further detailed in [54].

Gravimetric tar content is determined from the mass of solid residues after solvent distillation and evaporation of a sub-sample [14]. Another sub-sample of the tar-toluene mixture was further analyzed by coupled gas chromatography-mass spectrometry (GC-MS) to determine the tar concentration and composition. These data were used to derive the tar dew point. The dew point for these mixtures can be estimated from vapor/liquid equilibrium calculations for single components [56], followed by the application of Raoult's law [57].

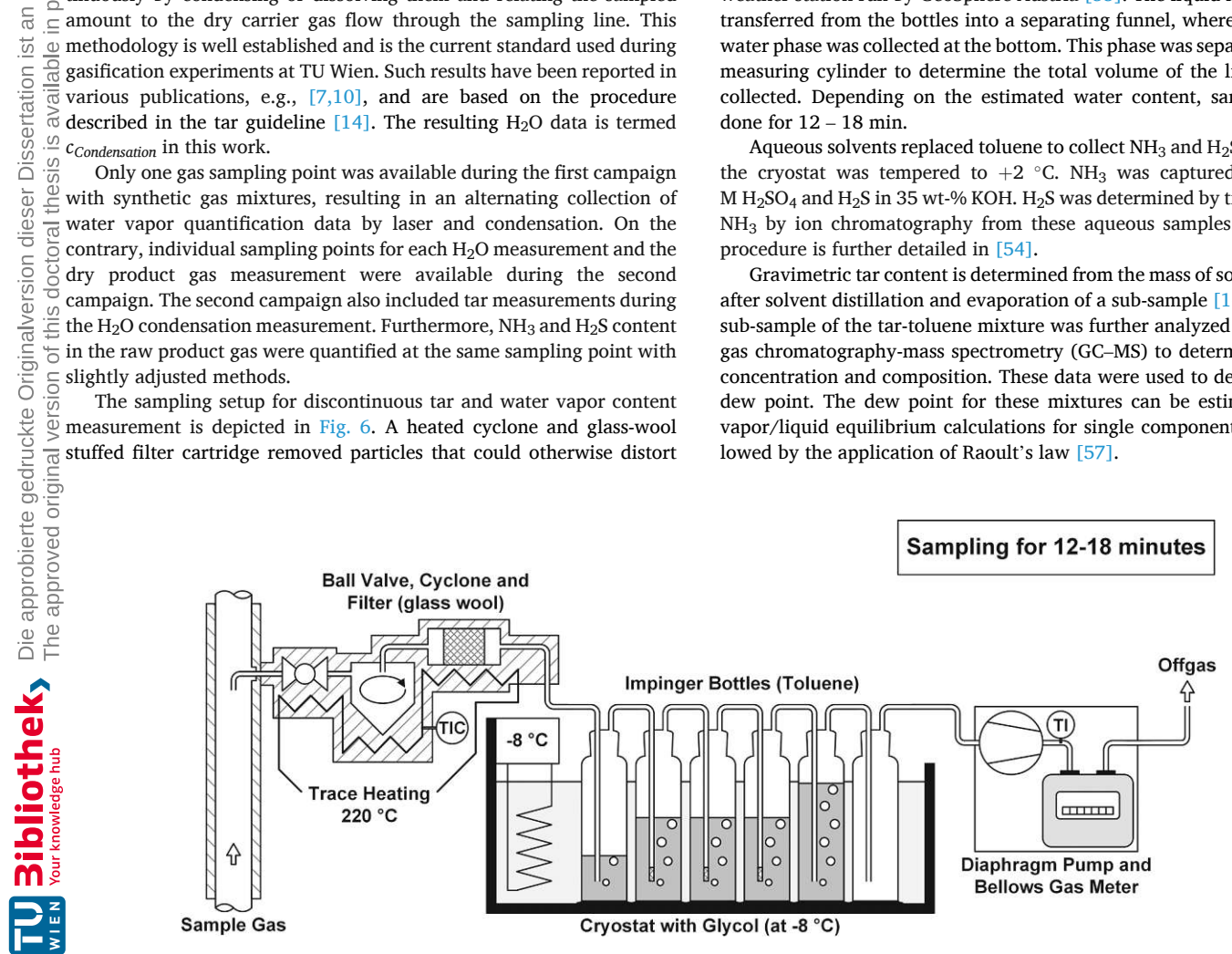


Fig. 6. Discontinuous tar and H<sub>2</sub>O condensation measurement via condensation in toluene, adjusted from [55].

#### 3.3.2. Spectroscopic measurements

The new QCL-based H<sub>2</sub>O measurement and Emerson's NGA2000 dry gas analyzer were used to collect data continuously. Gas was sampled from a single port, and both spectroscopic measurements were serialized during the first campaign (Fig. 7). The second campaign with raw product gas used two separate sampling lines: One without trace heating for the dry gas measurement and one without dry gas analyzer for the OCL-based H<sub>2</sub>O measurement. Fig. 7 shows the combined installation layout. The sampling point for the H<sub>2</sub>O laser measurement during the second campaign was placed after the inline hot gas filter to avoid high particle loads without installing another particle separation system.

The sampled gas was sucked through a section with trace heating, which covered the sampling line and the gas cell's central section. A temperature measurement located on the sampling line's outside wall was used for temperature control, which was set to 150 °C in the first campaign and 315 °C in the second campaign. Chilled impinger bottles filled with heating oil, followed by a glass-wool stuffed filter cartridge, were used to dry and clean the gas before the diaphragm pump. Finally, the gas stream was directed through the dry gas analyzer. This dry gas analyzer combines NDIR spectroscopy to measure CO, CO2, and CH4, paramagnetic O2 analysis, and a thermal conductivity (TCD) sensor to measure H2.

#### 4. Results

#### 4.1. First experimental campaign measuring synthetically prepared gas mixtures with setup prototype

Data for determining the water vapor content spectroscopically  $\underline{\underline{}}$  ( $c_{Laser}$ ) are given in Table 3. Each experiment's baseline signal ( $I_{0,N2}$ ) is the average signal measured over a few minutes of flowing only nitrogen through the cell. This procedure was performed before each experiment MIX 1-3 and once before experiments MIX 4-6. The extinction coefficient  $\varepsilon_{H2O}$  results from the iterative solving procedure described in **Section 2.3.** The uncertainties for  $\varepsilon_{H2O}$  and  $c_{Laser}$  include the spectrometer-related uncertainties in wave number determination and temperature measurement. A pressure of 1.013 bar in the cell is assumed for this measurement. Data used for determining  $c_{Condensation}$  are also presented in Table 3. There is no uncertainty provided for this measurement for two reasons: First, the uncertainties in this process are primarily related to manual labor steps and, therefore, are not easily 5 standardized. The uncertainties stem from handling and separation procedures, e.g., incomplete transfer of liquids between various equipment. Second, since there is a lack of established water vapor measuring procedures in gasification, this method has not been checked and

validated against other methods in any studies.

The results from the condensation and spectroscopic measurements are combined with dry gas data to calculate the full gas composition in Fig. 8. The rest of the gas mixtures was N2. The high uncertainties for  $c_{Laser}$  are rooted in the estimated temperature uncertainty inside the gas cell and the laser's wave number. These factors lead to uncertainty in calculating  $\varepsilon$  (Fig. 2) and, by extension,  $c_{Laser}$ . The data of both types of water vapor measurement fit well, especially considering the unknown accuracy of the condensation measurement. The average results for  $c_{Laser}$ are 4-18 % and for  $c_{Condensation}$  5-18 % below the target water vapor concentration. This negative deviation suggests that the pump likely delivered less than the target water flow rate. In conclusion, the spectroscopic setup provides results that agree with an established measurement over a wide range of H<sub>2</sub>O concentrations and typical gas mixtures from gasification.

#### 4.2. Second experimental campaign measuring raw and hot product gas from biomass steam gasification with advanced setup

The advanced spectroscopy setup was operated for around two hours during steam gasification of waste wood, and measurements were collected every 1 to 5 s. The baseline signal intensity in an N2 atmosphere  $(I_{0,N2})$  was measured as 5.71 mV at the lock-in amplifier before the experiment. The signal measured at the detector remained nearly constant during two hours of measuring hot and raw product gas from steady-state gasification. The average signal at the lock-in amplifier during the first hour of measurement was 2.03 mV, which is close to the average of 2.07 mV during the second hour. The baseline intensity  $I_{0.N2}$ was used as a constant factor for calculating  $c_{Laser}$  by **Eq.** (2) during the experiment in real-time. The results of these calculations are shown in Fig. 9.

Fig. 9a shows the measurement uncertainty resulting from the margin of error for experimentally determining the laser wave number. The average difference over the two hours of gasification between  $\nu=$ 76.44 cm<sup>-1</sup> and  $\nu = 76.52$  cm<sup>-1</sup> is rather small at 0.4 vol-%, while the difference between  $\nu = 76.52 \text{ cm}^{-1}$  and  $\nu = 76.60 \text{ cm}^{-1}$  is twice that at 0.8 vol-%. These results combine to a wavelength-uncertainty-related error of -0.4 to +0.8 vol-%  $H_2O$ . In the second campaign, the temperature was measured inside the cell by a Thermocouple type K with an error of  $\pm 1.5$  °C. This improvement drastically reduces the temperaturerelated uncertainty, which is further helped by the decreased temperature sensitivity of this water vapor absorption line at temperatures between 220 - 400 °C (Fig. 1b). The resulting temperature-uncertaintyrelated error is around  $\pm 0.3$  vol-%  $H_2O$ . The temperature and wavelength uncertainties combine to an estimated measuring error of

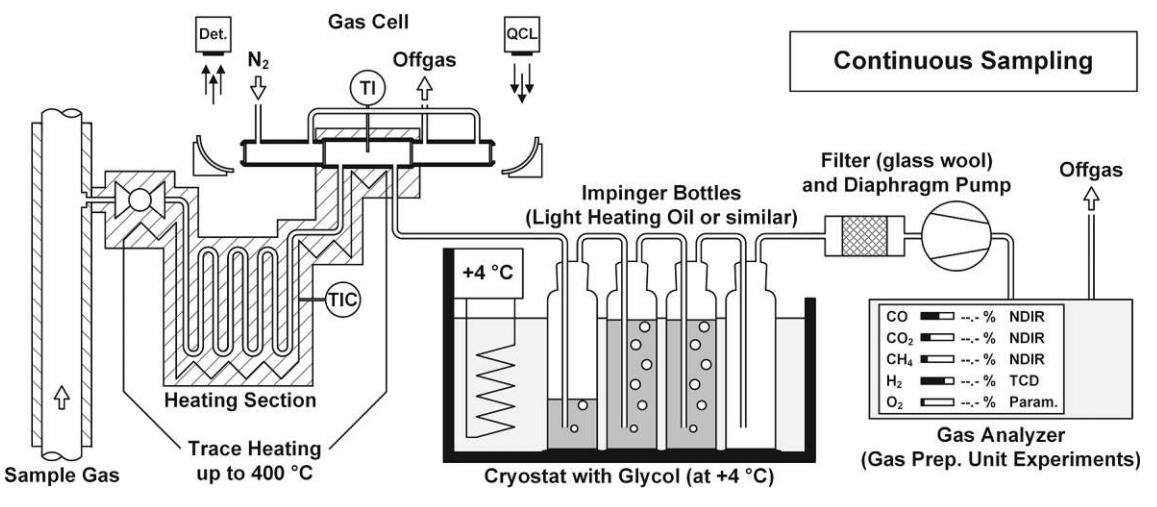


Fig. 7. Setup for the novel spectroscopic H<sub>2</sub>O measurements, adjusted from [55]. Det. = Pyroelectric detector, QCL = THz quantum cascade laser.

Table 3 Results for experiments with synthetically prepared gas mixtures.

	Wave number		Average baseline signal	Average experimental signal	Extinction coefficient	$H_2O$		$_{\mathrm{H_2O}}$
	ν	Temperature T	$I_{0,N2}$	I	$arepsilon_{H2O}$	target	$H_2O c_{Laser}$	$c_{Condens.}$
	cm <sup>-1</sup>	K	mV	mV	m <sup>2</sup> /mol	vol-%	vol-%	vol-%
MIX 1	$76.52\pm0.08$	$383\pm10$	9.57	4.66	0.485 - 0.555	25.0	$21.6\pm1.5$	22.8
MIX 2	$76.52\pm0.08$	$383\pm10$	10.62	8.30	0.378 - 0.445	10.0	$9.3\pm0.8$	8.2
MIX 3	$76.52\pm0.08$	$383\pm10$	9.66	1.61	0.647 - 0.723	50.0	$40.9 \pm 2.6$	46.5
MIX 4	$76.52\pm0.08$	$390\pm10$	5.73	1.38	0.593 - 0.663	42.5	$35.9 \pm 2.1$	37.5
MIX 5	$76.52\pm0.08$	$388\pm10$	5.73	0.82	0.662 - 0.736	50.0	$43.9 \pm 2.5$	47.6
MIX 6	$76.52\pm0.08$	$390\pm10$	5.73	1.57	0.576 – 0.644	35.0	$33.6 \pm 2.0$	32.1

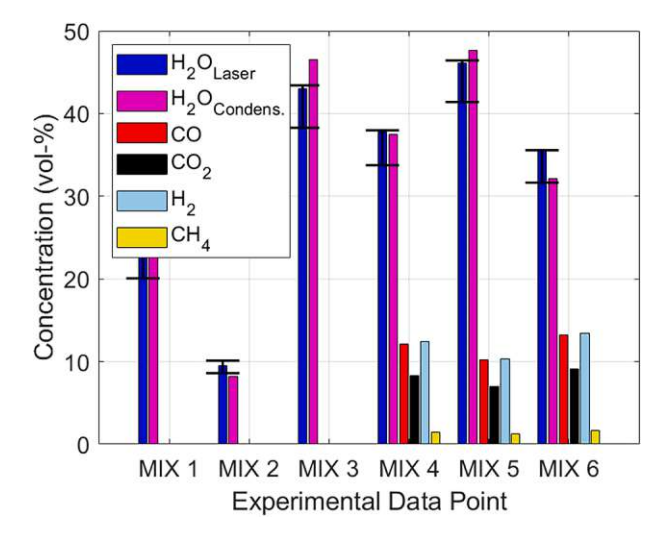


Fig. 8. Comparison of H<sub>2</sub>O concentrations measured by condensation (H2OCondens.) and spectroscopy (H2OLaser) in various experiments with synthetically prepared gas mixtures.

-0.7 to +1.1 vol-% H<sub>2</sub>O. This error margin substantially improved from the first campaign, which had higher uncertainties.

Fig. 9b shows the composition of the raw product gas over the experimental duration. The water vapor measurement results at the design wave number of  $\nu = 76.52 \text{ cm}^{-1}$  were combined with the dry gas composition to give this raw gas composition. The average H<sub>2</sub>O concentration for the condensation measurement, conducted from 10:27 to 10:39, was 46.7 vol-%. The spectroscopic measurement, on average, yielded 45.9 vol-%. Mass and energy balancing simultaneously

calculated in the process simulation software IPSEpro suggested 44.6 - 45.3 vol-%. Over two hours, the average  $c_{Laser}$  result was 48.2 vol-

These measurements were performed in a raw product gas with H<sub>2</sub>, CO2, CO, CH4, and N2 as the main dry gas components. Of these components, only CO was suggested by the Spectral Calculator to influence the H<sub>2</sub>O quantification in this QCL setup noticeably. Including CO measurement data from NDIR in the solving algorithm allowed for dynamically accounting for CO absorption. 15378 ppm NH<sub>3</sub> and 387 ppm H<sub>2</sub>S were also found in the dry gas. While these species' absorption was not dynamically considered, the spectral calculator estimates their influence was low. Absorption values of 2E-03 for NH3 and 9E-05 for H<sub>2</sub>S were calculated, corresponding to an H<sub>2</sub>O overestimation of 0.1 vol-%. This value can be used for calibration in post-processing, changing the spectroscopic measurement to 45.8 vol-% from 10:27 to 10:39 and 48.1 vol-% over the experimental duration. The total tar content in the raw product gas was determined as 31.21 g/Nm  $_{dry}^{3}$  by GC–MS, of which most were benzene and only 11.75 g/Nm<sub>drv</sub> were not benzene, toluene, ethylbenzene, or xylenes (Appendix C). Gravimetric tar was determined as 4.18 g/Nm<sub>dry</sub>. The tar dew point was calculated at 192 °C, suggesting that the temperature in the cell was sufficient to avoid tar condensation. This finding, the measurement's stability over two hours, and the comparison with the condensation measurement suggest that this novel device is well-equipped to handle tar-contaminated gases.

#### 5. Discussion

This section discusses some possible errors that might have influenced the H2O concentration results and how those errors could be reduced in future works.

Systematic errors are consistent and repeatable and occur due to flaws in the measurement system. This work used the simplification that the measurement signal at the lock-in amplifier is reduced from the

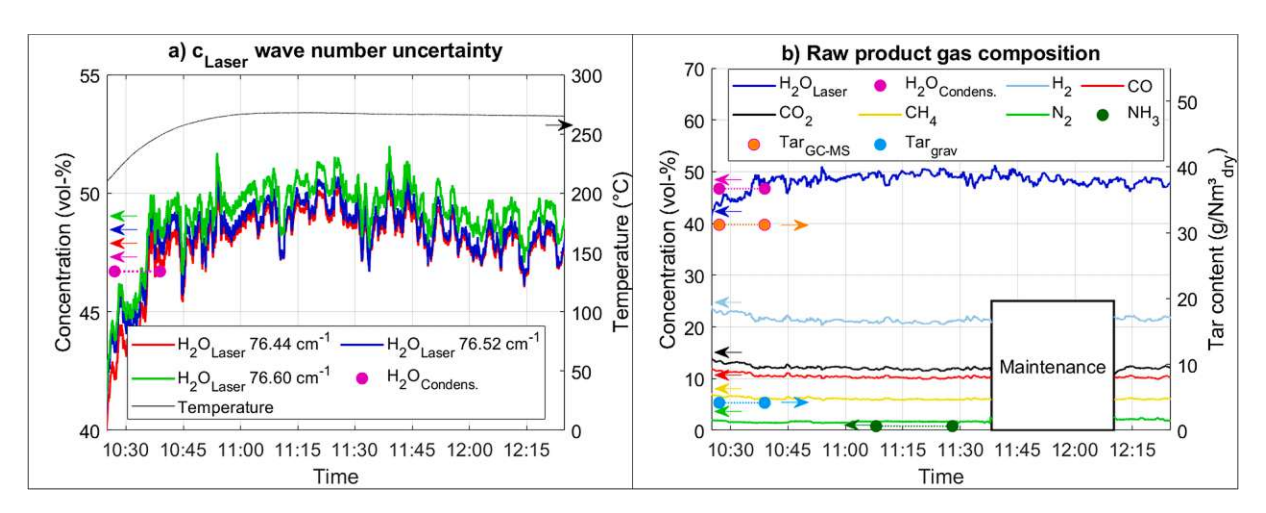


Fig. 9. H<sub>2</sub>O measurement data for hot and raw product gas from biomass steam gasification. a) Uncertainty was introduced into water vapor measurement due to uncertainty in laser wave number, and b) Raw product gas composition data.

baseline signal only by absorption from H<sub>2</sub>O and CO. Other effects that would reduce the baseline signal during measurement are neglected, which could lead to overestimating the H2O content in the gas. Measurement data in this work and HITRAN2020 data are available for NH<sub>3</sub>, H<sub>2</sub>S, H<sub>2</sub>, CO<sub>2</sub>, and CH<sub>4</sub>. H<sub>2</sub>, CO<sub>2</sub>, and CH<sub>4</sub> do not absorb significantly at 2.293 THz (see Section 2.1). Data on NH3 and H2S abundance were unavailable as online measurements, but post-processing revealed that these species led to overestimating the H<sub>2</sub>O concentration by 0.1 vol-%. If the setup was changed to allow for online measurement of NH3 and H<sub>2</sub>S, this error could be dynamically eliminated. The absorption from other components could not be considered since measurement or HITRAN2020 data were missing. An estimation for the maximum error during measurement can be given as the sum of errors induced by typical product gas impurities (see Table 1). If every impurity were present at its maximum considered concentration, this would result in a baseline decrease of around 5.1 %. At 250 °C, 1 atm, and  $\varepsilon_{H2O}$  of 0.5 m<sup>2</sup>/mol, this would correspond to a maximal H<sub>2</sub>O overestimation of 2.5 vol-%. This maximum error is primarily a result of absorption by 10 vol-% NH<sub>3</sub> and 0.1 vol-% HCN, which are very high numbers for biomass gasification. This estimation does not include the unknown absorption of any species for which data was unavailable in the HITRAN2020 database.

The baseline signal could also have been reduced through light scattering by particles or window fouling, possibly inducing another systematic error. The influence of these non-H<sub>2</sub>O-absorption-losses could be investigated in future work. This investigation could include dedicated experimental campaigns measuring the impact of various components. Alternatively, other measurement techniques could be adopted, such as normalized wavelength modulation spectroscopy, which has been reported to reduce these errors [18,20]. Another systematic error results from using simulated lineshape profiles to calculate the molecular absorption coefficients. Voigt profiles typically show residuals within 2 % of measured lineshape around standard temperature and pressure but can be less accurate under certain circumstances [18].

Random errors arise from unpredictable fluctuations in the process. The conditions in the laboratory with the gasifier were not as controlled as in an optical laboratory and were representative field tests of a realistic application environment. Various machines, heat sources, people, and dust were close to the gasifier and spectroscopic setup; furthermore, the windows were open, and the laboratory was not air-conditioned. Under these laboratory conditions and without encasing the setup, the baseline signal intensity in an  $N_2$  atmosphere  $(I_{0,N_2})$  was measured as 5.71 mV at the lock-in amplifier before the experiment. The signal-tonoise ratio was calculated as averaged signals versus the standard deviation  $\sigma$  of the transmitted signal. At  $\sigma = 0.24$  mV, the resulting signalto-noise ratio was 23.8 for the baseline signal. The signal-to-noise ratio was much lower at around 8 during actual measurement using the same standard deviation. Consequently, this means that very high H2O content and correspondingly low signals at the lock-in-amplifier would have very low signal-to-noise ratios, a drawback of the employed fixedfrequency approach. Encasing the setup could increase the signal-tonoise ratio since the baseline and signal-to-noise ratios were higher in the optical laboratory. Additionally, encasing the setup would be necessary for more extended tests to exclude any absorption from ambient moisture and ensure that ambient moisture variation between the time of baseline measurement and experiment does not alter the results. A laser with a higher power output could also increase signal-to-

Dynamic errors occur when the measurement system cannot respond quickly to the measured quantity. In the context of gasification analysis, the repetition rates of the used electronic equipment are fast enough to avoid such errors. The computation interval for new measurements was somewhat arbitrarily chosen as "every few seconds", sufficient for observing the product gas from a pilot-scale gasifier. One potential dynamic error occurs during temperature measurement in the cell by a thermocouple. The increase in  $c_{Laser}$  data near the start of the gasification experiment is not explained by a trend in the raw voltage signal at the

lock-in amplifier. Instead, this trend appears once the raw signal is combined with the gas cell temperature data. The temperature increase near the start is explained by a change in gas supply from nitrogen to hot and raw product gas less than three minutes before the condensation measurement. As a result, the gas temperature might have been underestimated before the setup's temperature was stabilized. One solution for future experiments is to avoid switching between gas supplies at varying temperature levels this close to the measurement. Another solution could be to implement spectroscopy-based temperature measurement with a faster response time, e.g., as Sepman et al. showed [23].

Instrumental errors are inherent to the measuring instruments and can be reduced by regular maintenance and calibration. Temperature measurements are one of the two primary sources of uncertainty discussed and presented in this work. Integrating the thermocouple directly into the cell helped to reduce this uncertainty considerably. The other prominently discussed uncertainty resulting from instrumental error is the laser frequency. The spectrometer's resolution is defined by the path difference of the interferometer arms as  $\pm~0.08~{\rm cm}^{-1}$  and leaves some uncertainty when measuring the laser wavelength. This uncertainty is mainly due to the laser's emitted frequency depending on the laser's temperature. Consequently, refined measuring and stabilizing procedures for the laser's temperature could reduce this uncertainty. These instrumental errors induced an error of  $-0.7~{\rm to}~+1.1~{\rm vol}-\%~{\rm H}_2{\rm O}$  in this work.

A total estimation of measurement error can be given as the sum of partial errors that could be quantified. These errors include misclassifying absorption by other gases as absorption by  $\rm H_2O$  and temperature- and wavelength-uncertainty-related errors. If all impurities listed in Table 1 were assumed to be unknown, the error would be increased to -3.2 to +1.1 vol-%  $\rm H_2O$ . Consequently, careful consideration should be given to the NH $_3$  and HCN content if nitrogen-rich feedstocks are combined with this measurement. The absorption by other components, including those not listed in the HITRAN2020 database, remains unknown. Future works should aim to investigate the baseline variability resulting from absorption and scattering.

The measured water vapor contents are plausible for biomass steam gasification [52], although higher than expected if the water–gas shift reaction were in equilibrium at these operating conditions. The high value is likely a result of TUW operating their DFB gasification process with excess steam to achieve the desired superficial gas velocity for fluidization. This measurement could be used to optimize the steam ratio in future campaigns. The results from the new laser measurements are within the uncertainty calculated for the new measurement in this section compared to the discontinuous concentration measurement and mass balance. The excellent agreement between these results highlights the potential of this technology as a reliable online measurement that can improve process understanding and control for processes with complex gas mixtures.

#### 6. Conclusion and outlook

This study introduced a novel spectroscopic device, including a quantum cascade laser emitting at 2.294 THz, a hot gas cell, and a pyroelectric detector to quantitatively measure  $H_2O$  in hot and raw product gas from biomass gasification. This design was chosen based on absorption data from the HITRAN2020 database calculated in the Spectral Calculator by GATS. Elevated temperatures of around 250 °C facilitated water vapor quantification without tar condensation impeding the measurement. The second campaign successfully adopted an advanced gas cell design at around 250 °C to avoid tar condensation and operate without interruption for two hours. The water vapor was embedded in a mixture that contained  $H_2$ ,  $CO_2$ , CO,  $CH_4$ ,  $N_2$ ,  $NH_3$ ,  $H_2S$ , and tar. Tar content in the raw product gas from steady-state gasification was determined as 31.21 g/Nm $_{dry}^3$  by GC–MS and 4.18 g/Nm $_{dry}^3$  gravimetrically. The average signal at the lock-in amplifier during the first hour of measurement was 2.03 mV, which is close to the average of

2.07 mV during the second hour of steady-state gasification. These results show that this technology can be used for hot and raw gases, including mixtures of permanent gases and uncondensed tar.

The measurements by QCL yielded results that were close to the results from offline analysis by condensation. When measuring raw product gas from biomass steam gasification, the condensation measurement showed 46.7 vol-%, while the spectroscopic measurement, on average, yielded 45.8 vol-%, and mass balancing suggested 44.6 – 45.3 vol-%. Both the condensation and the mass balancing results are within the uncertainty calculated for the spectroscopic measurement, which was -0.7 to +1.1 vol-%  $H_2O$ . The new laser method also provided preliminary results every 1 to 5 s in real-time, starkly contrasting the established condensation procedure, which produces average data for a given timespan and incurs a labor-related delay. Over two hours, the average  $c_{Laser}$  result was 48.1 vol-%. These points underscore that fixedwavelength direct absorption using a QCL emitting in the far-infrared range is a promising option for water vapor quantification in harsh environments.

Further temperature and gas composition screenings and validation campaigns could reinforce the findings of this study and help with potential applications outside of biomass gasification. A limitation of this work is the uncertainty in laser frequency, which was a primary source of water vapor content uncertainty in measurement and is increasingly problematic at low water vapor contents and high temperatures in the gas cell. This uncertainty is primarily due to the laser's emitted frequency depending on the laser's temperature. Consequently, refined measuring and stabilizing procedures for the laser's temperature could reduce this uncertainty. Furthermore, the baseline variability in various gas mixtures should be investigated in future work. Signal-to-noise ra-<u>v</u> u tios could likely be increased by encasing the setup. Wavelength modulation spectroscopy could be considered to improve sensitivity and resistance against noise. The heating and insulation setup could also be further improved to avoid a drop in cell temperature when switching from cold to hot gas feeds.

#### CRediT authorship contribution statement

Florian Johann Müller: Writing - review & editing, Writing original draft, Visualization, Software, Project administration, Methodology, Investigation, Formal analysis, Data curation, Conceptualization. Michael Jaidl: Writing - review & editing, Writing - original draft,

Visualization, Software, Project administration, Methodology, Investigation, Data curation, Conceptualization. Dominik Theiner: Writing review & editing, Software, Investigation, Data curation. Johann Zeitlhofer: Writing - review & editing, Writing - original draft, Visualization, Methodology, Investigation. Florian Benedikt: Writing - review & editing, Writing - original draft, Resources, Project administration, Investigation. Lena Steiner: Writing – review & editing, Writing – original draft, Investigation. Alexander Bartik: Writing – review & editing, Writing - original draft, Visualization, Resources, Project administration, Investigation, Funding acquisition. Marie Christine Ertl: Writing - review & editing. Aaron Maxwell Andrews: Writing – review & editing. Gottfried Strasser: Supervision, Resources, Funding acquisition. Stefan Müller: Writing - review & editing, Supervision, Resources, Funding acquisition. Franz Winter: Writing review & editing, Supervision, Resources, Funding acquisition. Karl Unterrainer: Writing - review & editing, Supervision, Resources, Funding acquisition.

#### **Declaration of competing interest**

The authors declare that they have no known competing financial interests or personal relationships that could have appeared to influence the work reported in this paper.

#### Acknowledgments

This study was carried out within the doctoral college CO<sub>2</sub> Refinery at TU Wien and is supported by the ERA-NET Bioenergy project Bio-HEAT (FO999889752), funded by the Austrian Climate and Energy Fund. The authors acknowledge TU Wien Bibliothek for financial support through its Open Access Funding Programme. The authors would also like to thank Fabian Dona and Thomas Pareihs for manufacturing the laser cell, the Test Laboratory for Combustion Systems at TU Wien for the analytical measurements and everyone who contributed to the preparation and operation of the gasifier experiment. The authors acknowledge financial support from the Austrian Science Fund FWF (TeraLearn P35932-N). A.M.A. acknowledges the support of the European Office of Aerospace Research and Development/Air Force Office of Scientific Research (EOARD/AFOSR No. FA8655-22-1-7170 and FA8655-23-1-7070), and the Austrian Research Promotion Agency (FFG) Project Green Sensing (No. 883941).

#### Appendix A. - Iterative solving algorithm

The molar extinction coefficient's dependence on the molar  $H_2O$  concentration means that Eq. (2) needs to be solved iteratively. For this reason, a solving algorithm is adopted to determine  $c_{Laser}$  by the following steps:

- a. Create parametrized, quadratic fits for  $\varepsilon_{H2O}$  and  $\varepsilon_{CO}$  that depend on the temperature and molar concentration and are based on data from the Spectral Calculator. (Fig. 2)
- b. Use 10 vol-% as a first guess for  $c_{Laser}$  and the dry gas measurement data from NDIR as a first guess for  $c_{CO}$ .
- c. Use the baseline intensity in nitrogen atmosphere as starting guess for  $I_0$ .

- a. Calculate new estimates for  $\varepsilon_{H2O}$  and  $\varepsilon_{CO}$  from the parametrized fits, using the measured gas temperature and the latest guess for  $\varepsilon_{LOSET}$  and  $\varepsilon_{CO}$  as
- b. Calculate a new  $c_{Laser}$  from Eq. (2) using constant values for R (8.3144 J•mol<sup>-1</sup>•K<sup>-1</sup>), p (101325 Pa), d (0.086 m), the latest estimate for the baseline intensity  $I_0$ , real-time measurement data for the temperature T and experimental intensity I, and the latest estimate for  $\varepsilon_{H20}$ .
- c. Calculate a new  $c_{CO}$  from the new  $c_{Laser}$  and dry gas composition data for CO from NDIR measurement.
- d. Calculate a new estimate for the baseline intensity  $I_0$  from the latest  $c_{CO}$  and  $I_{0,N2}$  data from Eq. (3) and Eq. (4), using the same constant values
- e. Compare the new calculation of  $c_{Laser}$  from step 2b to the previous estimate of  $c_{Laser}$ . If the difference between the two latest estimates for  $c_{Laser}$  is smaller than 0.01 vol-%, then accept the latest  $c_{Laser}$  as the measurement result. Otherwise, repeat the iteration loop.



#### Appendix B. - Pictures of the setup

Information on the used equipment is also available in Section 3.1.

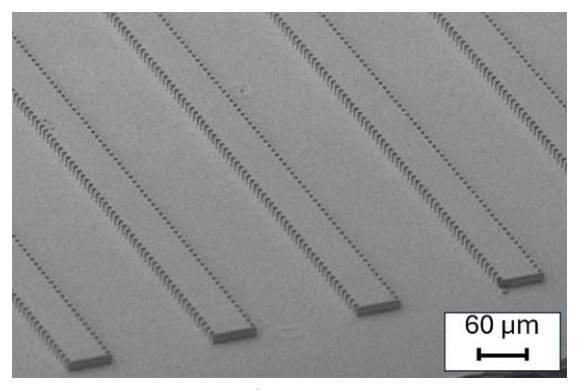


Fig. B1. Scanning electron microscope picture of ridge-type lasers with 1<sup>st</sup>-order distributed feedback grating for wavelength-selective single-mode emission

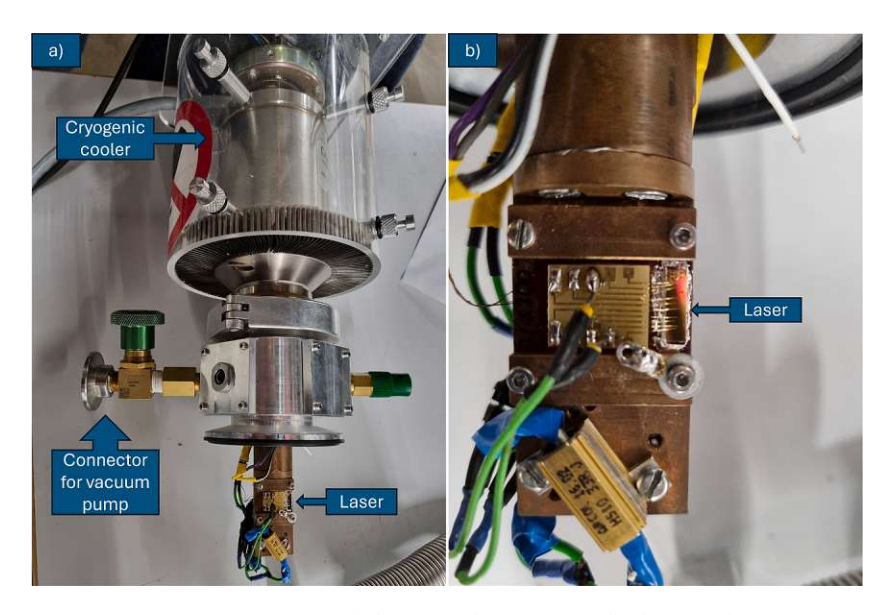


Fig. B2. Quantum cascade laser a) with cryogenic cooler, b) zoomed in

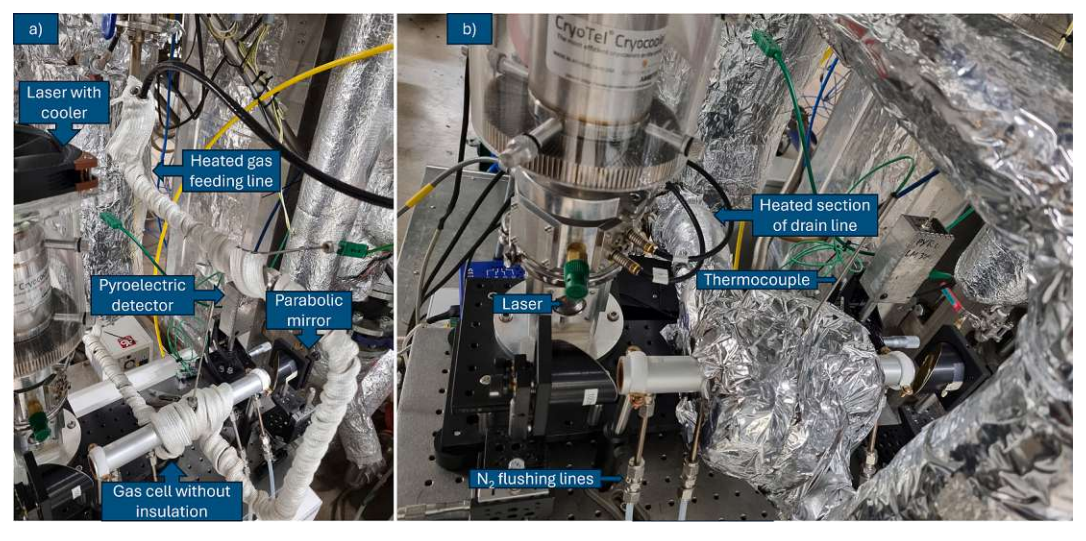


Fig. B3. Advanced gas cell setup: a) Without insulation, b) With insulation

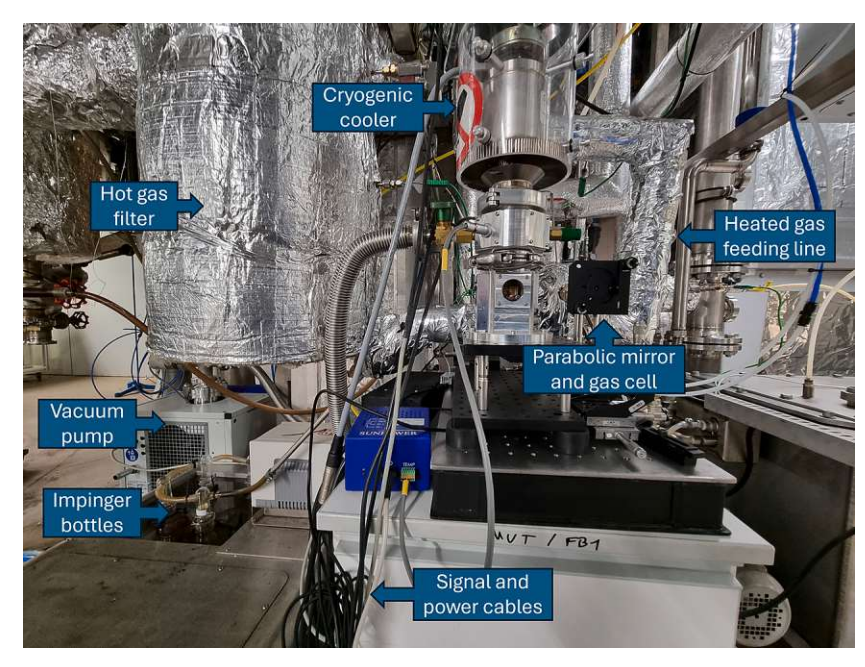


Fig. B4. Core gas cell setup including heated gas sampling line, quantum cascade laser, cryogenic cooler, parabolic mirror, gas drain line leading to Impinger bottles

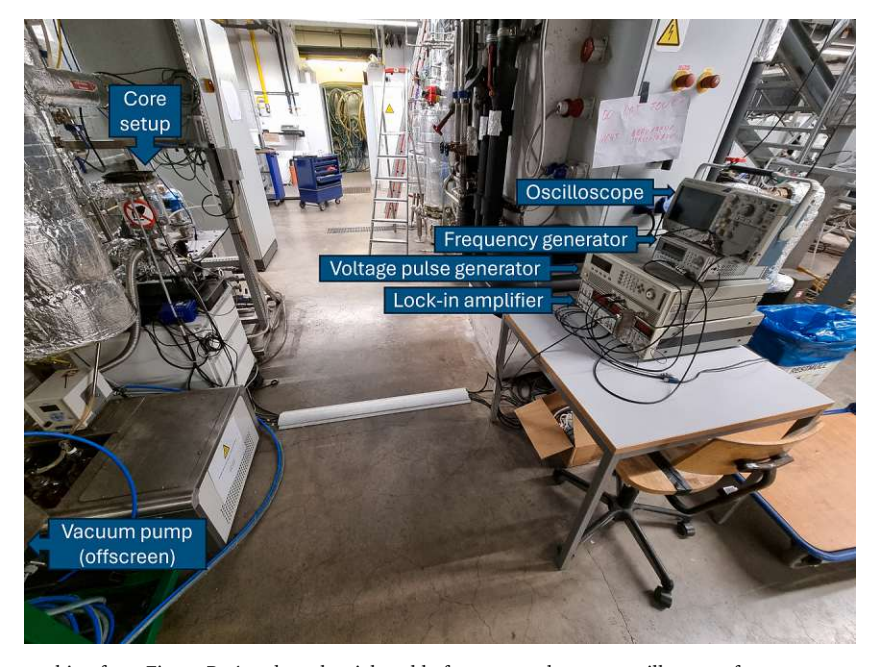


Fig. B5. Full setup including everything from Figure B- 4 and on the right table from top to bottom: oscilloscope, frequency generator (Agilent 33220A), voltage pulse generator (Agilent 8114A), lock-in amplifier (Stanford Research SR830)

#### Appendix C. - Detailed tar analysis

This tar analysis was conducted by GC-MS in the Testing Laboratory for Combustion Systems at Technische Universität Wien. The tar dew point for this mixture was estimated as 192 °C from vapor/liquid equilibrium calculations for single components [56], followed by the application of Raoult's

Table C1. Tar compound analysis via GC-MS. "n.m."=not measured.

Compound	Concentration	Compound	Concentration
	mg/Nm <sup>3</sup> <sub>dry</sub>		mg/Nm <sup>3</sup>
Benzene	19,459	Indole	•
Toluene	n.m.	Biphenyl	197
2-Methylpyridine	n.m.	1-Vinylnaphthalene	n,m.
			(continued on next page)



#### (continued)

Ethylbenzene         n.m.         2-Vinylnaphthalene         61           m- and p-Xylene         n.m.         Isoeugenol         n.m.           o-Xylene + Styrene         464         Acenaphthylene         1433           Phenylacetylene         n.m.         Acenaphthene         57           3- and 4-Methylpyridine         n.m.         Dibenzofuran         n.m.           Mesitylene         n.m.         Fluorene         415           Phenol         42         Dibenzofuran         n.m.           Benzofuran         n.m.         Anthracene         389           IH-Indene         1053         Phenanthrene         1365           2-Methylphenol         <19.93         4,5-Methylenephenanthrene         n.m.           3- and 4-Methylphenol         <19.93         4,5-Methylenephenanthrene         n.m.           2-Methylbenzofuran         n.m.         9-Methylanthracene         n.m.           2-Methylphenol         n.m.         Pluoranthene         585           2,5- and 2,4-Dimethylphenol         n.m.         Pyrene         375           3,5-Dimethylphenol         n.m.         Benzo [a]anthracene         120           2,3-Dimethylphenol         n.m.         Benzo [b]fluoranthene         95 <th>Compound</th> <th>Concentration</th> <th>Compound</th> <th>Concentration</th>	Compound	Concentration	Compound	Concentration
o-Xylene + Styrene         464         Acenaphthylene         1433           Phenylacetylene         n.m.         Acenaphthene         57           3- and 4-Methylpyridine         n.m.         Dibenzofuran         n.m.           Mesitylene         n.m.         Fluorene         415           Phenol         42         Dibenzothiophene         n.m.           Benzofuran         n.m.         Anthracene         389           1H-Indene         1053         Phenanthrene         1365           2-Methylphenol         <19.93	Ethylbenzene	n.m.	2-Vinylnaphthalene	61
Phenylacetylene         n.m.         Acenaphthene         57           3- and 4-Methylpyridine         n.m.         Dibenzofuran         n.m.           Mesitylene         n.m.         Fluorene         415           Phenol         42         Dibenzothiophene         n.m.           Benzofuran         n.m.         Anthracene         389           IH-Indene         1053         Phenanthrene         1365           2-Methylphenol         <19.93	m- and p-Xylene	n.m.	Isoeugenol	n.m.
3- and 4-Methylpyridine         n.m.         Dibenzofuran         n.m.           Mesitylene         n.m.         Fluorene         415           Phenol         42         Dibenzothiophene         n.m.           Benzofuran         n.m.         Anthracene         389           1H-Indene         1053         Phenanthrene         1365           2-Methylphenol         <19.93	o-Xylene + Styrene	464	Acenaphthylene	1433
Mesitylene         n.m.         Fluorene         415           Phenol         42         Dibenzothiophene         n.m.           Benzofuran         n.m.         Anthracene         389           1H-Indene         1053         Phenanthrene         1365           2-Methylphenol         <19.93	Phenylacetylene	n.m.	Acenaphthene	57
Phenol         42         Dibenzothiophene         n.m.           Benzofuran         n.m.         Anthracene         389           1H-Indene         1053         Phenanthrene         1365           2-Methylphenol         <19.93	3- and 4-Methylpyridine	n.m.	Dibenzofuran	n.m.
Benzofuran         n.m.         Anthracene         389           1H-Indene         1053         Phenanthrene         1365           2-Methylphenol         <19.93	Mesitylene	n.m.	Fluorene	415
IH-Indene         1053         Phenanthrene         1365           2-Methylphenol         <19.93	Phenol	42	Dibenzothiophene	n.m.
2-Methylphenol         <19.93	Benzofuran	n.m.	Anthracene	389
3- and 4-Methylphenol <19.93	1H-Indene	1053	Phenanthrene	1365
2-Methylbenzofuran         n.m.         9-Methylanthracene         n.m.           2,6-Dimethylphenol         n.m.         Fluoranthene         585           2,5- and 2,4-Dimethylphenol         n.m.         Pyrene         375           3,5-Dimethylphenol         n.m.         Benzo[a]anthracene         120           2,3-Dimethylphenol         n.m.         Chrysene         120           3,4-Dimethylphenol         n.m.         Benzo[b]fluoranthene         95           2-Methoxy-4-Methylphenol         n.m.         Benzo[k]fluoranthene         37           Naphthalene         4552         Benzo[a]pyrene         85           1-Benzothiophene         n.m.         Benzo[a]pyrene         n.m.           Quinoline         n.m.         Perylene         <19.93	2-Methylphenol	<19.93	Carbazole	n.m.
2,6-Dimethylphenol       n.m.       Fluoranthene       585         2,5- and 2,4-Dimethylphenol       n.m.       Pyrene       375         3,5-Dimethylphenol       n.m.       Benzo[a]anthracene       120         2,3-Dimethylphenol       n.m.       Chrysene       120         3,4-Dimethylphenol       n.m.       Benzo[b]fluoranthene       95         2-Methoxy-4-Methylphenol       n.m.       Benzo[k]fluoranthene       37         Naphthalene       4552       Benzo[e]pyrene       85         1-Benzothiophene       n.m.       Benzo[a]pyrene       n.m.         Quinoline       n.m.       Perylene       <19.93	3- and 4-Methylphenol	<19.93	4,5-Methylenephenanthrene	n.m.
2,5- and 2,4-Dimethylphenol       n.m.       Pyrene       375         3,5-Dimethylphenol       n.m.       Benzo[a]anthracene       120         2,3-Dimethylphenol       n.m.       Chrysene       120         3,4-Dimethylphenol       n.m.       Benzo[b]fluoranthene       95         2-Methoxy-4-Methylphenol       n.m.       Benzo[k]fluoranthene       37         Naphthalene       4552       Benzo[e]pyrene       85         1-Benzothiophene       n.m.       Benzo[a]pyrene       n.m.         Quinoline       n.m.       Perylene       <19.93	2-Methylbenzofuran	n.m.	9-Methylanthracene	n.m.
3,5-Dimethylphenol       n.m.       Benzo[a]anthracene       120         2,3-Dimethylphenol       n.m.       Chrysene       120         3,4-Dimethylphenol       n.m.       Benzo[b]fluoranthene       95         2-Methoxy-4-Methylphenol       n.m.       Benzo[k]fluoranthene       37         Naphthalene       4552       Benzo[e]pyrene       85         1-Benzothiophene       n.m.       Benzo[a]pyrene       n.m.         Quinoline       n.m.       Perylene       <19.93	2,6-Dimethylphenol	n.m.	Fluoranthene	585
2,3-Dimethylphenol       n.m.       Chrysene       120         3,4-Dimethylphenol       n.m.       Benzo[b]fluoranthene       95         2-Methoxy-4-Methylphenol       n.m.       Benzo[k]fluoranthene       37         Naphthalene       4552       Benzo[e]pyrene       85         1-Benzothiophene       n.m.       Benzo[a]pyrene       n.m.         Quinoline       n.m.       Perylene       <19.93	2,5- and 2,4-Dimethylphenol	n.m.	Pyrene	375
3,4-Dimethylphenol       n.m.       Benzo[b]fluoranthene       95         2-Methoxy-4-Methylphenol       n.m.       Benzo[k]fluoranthene       37         Naphthalene       4552       Benzo[e]pyrene       85         1-Benzothiophene       n.m.       Benzo[a]pyrene       n.m.         Quinoline       n.m.       Perylene       <19.93	3,5-Dimethylphenol	n.m.	Benzo[a]anthracene	120
2-Methoxy-4-Methylphenoln.m.Benzo[klfluoranthene37Naphthalene4552Benzo[e]pyrene851-Benzothiophenen.m.Benzo[a]pyrenen.m.Quinolinen.m.Perylene<19.93	2,3-Dimethylphenol	n.m.	Chrysene	120
Naphthalene         4552         Benzo[e]pyrene         85           1-Benzothiophene         n.m.         Benzo[a]pyrene         n.m.           Quinoline         n.m.         Perylene         <19.93	3,4-Dimethylphenol	n.m.	Benzo[b]fluoranthene	95
1-Benzothiophenen.m.Benzo[a]pyrenen.m.Quinolinen.m.Perylene<19.93	2-Methoxy-4-Methylphenol	n.m.	Benzo[k]fluoranthene	37
Quinolinen.m.Perylene<19.932-Methylnaphthalene172Dibenz[a,h]anthracene<19.93	Naphthalene	4552	Benzo[e]pyrene	85
2-Methylnaphthalene 172 Diberz[a,h]anthracene <19.93 Isoquinoline n.m. Benzo[g,h,i]perylene 23 1-Methylnaphthalene 75 Indeno[1,2,3-cd]pyrene 35	1-Benzothiophene	n.m.	Benzo[a]pyrene	n.m.
Isoquinolinen.m.Benzo[s,h,i]perylene231-Methylnaphthalene75Indeno[1,2,3-cd]pyrene35	Quinoline	n.m.	Perylene	<19.93
1-Methylnaphthalene 75 Indeno[1,2,3-cd]pyrene 35	2-Methylnaphthalene	172	Dibenz[a,h]anthracene	<19.93
	Isoquinoline	n.m.	Benzo[g,h,i]perylene	23
1-Indanone n.m. Anthanthrene n.m.	1-Methylnaphthalene	75	Indeno[1,2,3-cd]pyrene	35
	1-Indanone	n.m.	Anthanthrene	n.m.
Eugenol n.m. Coronene <19.93	Eugenol	n.m.	Coronene	<19.93

## Data availability

Data will be made available on request.

#### References

- [1] Lee H, Calvin K, Dasgupta D, Krinner G, Mukherji A, Thorne PW, et al. Climate Change 2023: Synthesis Report. Contribution of Working Groups I, II and III to the Sixth Assessment Report of the Intergovernmental Panel on Climate Change. Geneva, Switzerland: 2023. https://doi.org/10.59327/IPCC/AR6-978929169
- Fawzy S, Osman AI, Doran J, Rooney DW. Strategies for mitigation of climate change: a review. Environ Chem Lett 2020;18:2069-94. https://doi.org/10.1007/
- Pröll T, Zerobin F. Biomass-based negative emission technology options with combined heat and power generation. Mitig Adapt Strateg Glob Chang 2019;24: 1307-24. https://doi.org/10.1007/s11027-019-9841-4.
- Williams CL, Westover TL, Emerson RM, Tumuluru JS, Li C. Sources of biomass feedstock variability and the potential impact on biofuels production. Bioenergy Res 2016;9:1-14. https://doi.org/10.1007/s12155-015-96
- Molino A, Chianese S, Musmarra D. Biomass gasification technology: the state of the art overview. J Energy Chem 2016;25:10-25. https://doi.org/10.1016/j. jechem.2015.11.005.
- Gruber H, Groß P, Rauch R, Reichhold A, Zweiler R, Aichernig C, et al. Fischer-Tropsch products from biomass-derived syngas and renewable hydrogen. Biomass Convers Biorefin 2021;11:2281–92. https://doi.org/10.1007/s13399-019-00459-
- [7] Bartik A, Benedikt F, Fuchs J, Hofbauer H, Müller S. Experimental investigation of hydrogen-intensified synthetic natural gas production via biomass gasification: a technical comparison of different production pathways. Biomass Convers Biorefin 2023. https://doi.org/10.1007/s13399-023-04341-3.
- Gubin V, Benedikt F, Thelen F, Hammerschmid M, Popov T, Hofbauer H, et al. Hydrogen production from woody biomass gasification: a techno-economic analysis. Biofuels Bioprod Biorefin 2024;1:1-19. https://doi.org/10.1002/
- Rauch R, Hrbek J, Hofbauer H. Biomass gasification for synthesis gas production and applications of the syngas. Adv Bioenergy: Sustainab Challenge 2015:73-91. https://doi.org/10.1002/9781118957844.CH7
- [10] Benedikt F, Kuba M, Schmid JC, Müller S, Hofbauer H. Assessment of correlations between tar and product gas composition in dual fluidized bed steam gasification for online tar prediction. Appl Energy 2019;238:1138-49. https://doi.org/ 10.1016/j.apenergy.2019.01.181.
- Thunman H, Seemann M. The gobigas plant. substitute natural gas from waste: technical assessment and industrial applications of biochemical and thermochemical processes. Elsevier 2019:455-74. https://doi.org/10.1016/B978-0-12-815554-7.00017-9.
  - Hofbauer H. Rauch R. Stoichiometric Water Consumption of Steam Gasification by the FICFB-Gasification Process. Progress in Thermochemical Biomass Conversion (Vol.1), Blackwell Science Ltd; 2001, p. 199-208.

- [13] Veress M. Optimization of a process concept for the industrial production of Bio-SNG from low-grade fuels. Master Thesis Technische Universität Wien 2020. https://doi.org/10.34726/hss.2020.63703.
- [14] DIN Deutsches Institut für Normung e.V. Biomass gasification tar and particles in product gas - sampling and analysis: DIN CEN/TS 15439 2006.
- IEA Bioenergy. Gas analysis in gasification of biomass and waste Guideline Report Document 1, 2018.
- [16] Kleinhappl M. Water measurement; an introduction. Webinar Presentation 2014.
- [17] IEA. Gas analysis in gasification of biomass and waste Guideline Report Document 2 - Factsheets on gas analysis techniques. 2018.
- [18] Goldenstein CS, Spearrin RM, Jeffries JB, Hanson RK. Infrared laser-absorption sensing for combustion gases. Prog Energy Combust Sci 2017;60:132-76. https:// doi.org/10.1016/j.pecs.2016.12.002.
- Bolshov MA, Kuritsyn YA, Romanovskii YV. Tunable diode laser spectroscopy as a technique for combustion diagnostics. Spectrochim Acta Part B at Spectrosc 2015; 106:45-66. https://doi.org/10.1016/j.sab.2015.01.010.
- [20] Salazar DV, Goldenstein CS, Jeffries JB, Seiser R, Cattolica RJ, Hanson RK. Design and implementation of a laser-based absorption spectroscopy sensor for in situ monitoring of biomass gasification. Meas Sci Technol 2017;28. https://doi.org/ 10.1088/1361-6501/aa8cf6.
- [21] Lu F, Cao Z, Chang L, Zhao K, Xue X, Lin Y, et al. Precise velocity measurement by using even-symmetric 2f/1f harmonics extracted from up- and down-scanning WMS signal. IEEE Trans Instrum Meas 2024;73:1-11. https://doi.org/10.1109/
- [22] Sepman A, Ögren Y, Gullberg M, Wiinikka H. Development of TDLAS sensor for diagnostics of CO, H2O and soot concentrations in reactor core of pilot-scale gasifier. Appl Phys B 2016;122:1-12. https://doi.org/10.1007/s00340-016-6319-
- [23] Sepman A, Ögren Y, Qu Z, Wiinikka H, Schmidt FM. Real-time in situ multiparameter TDLAS sensing in the reactor core of an entrained-flow biomass gasifier. Proc Combust Inst 2017;36:4541–8. https://doi.org/10.1016/j.proci.2016.07.011.
- [24] Sepman A, Fredriksson C, Ögren Y, Wiinikka H. Laser-based, optical, and traditional diagnostics of no and temperature in 400 kw pilot-scale furnace. Appl Sci (switzerland) 2021;11. https://doi.org/10.3390/app11157048.
- Sepman A, Wennebro J, Fernberg J, Wiinikka H. Following fuel conversion during biomass gasification using tunable diode laser absorption spectroscopy diagnostics. Fuel 2024:374:132374, https://doi.org/10.1016/j.fuel.2024.132374
- Sur R. Sun K. Jeffries JB. Hanson RK. Pummill RJ. Waind T. et al. TDLAS-based sensors for in situ measurement of syngas composition in a pressurized, oxygenblown, entrained flow coal gasifier. Appl Phys B 2014;116:33–42. https://doi.org/ 10.1007/s00340-013-5644-6.
- De JW, Hein KRG. Nitrogen compounds in pressurised fluidised bed gasification of biomass and fossil fuels. Technical University Delft: 2005, PhD thesis.
- [28] Xu J, He Q, Xiong Z, Yu Y, Zhang S, Hu X, et al. Raman spectroscopy as a versatile tool for investigating thermochemical processing of coal, biomass, and wastes: Recent advances and future perspectives. Energy Fuel 2021;35:2870-913. https:// doi.org/10.1021/acs.energyfuels.0c03298.
- [29] Wu J, Deng K-L, Guida R, Lee BK. Fiber-optic photo-acoustic spectroscopy sensor for harsh environment gas detection. Proc.SPIE, vol. 6698, 2007, p. 66980E. http s://doi.org/10.1117/12.734092.

- [30] Bidgoli H, Cherednichenko S, Nordmark J, Thunman H, Seemann M. Terahertz spectroscopy for real-time monitoring of water vapor and CO levels in the producer gas from an industrial biomass gasifier. IEEE Trans Terahertz Sci Technol 2014;4: 722–33. https://doi.org/10.1109/TTHZ.2014.2357344.
- [31] Vogler J, Stanger L, Bartik A, Schirrer A, Kozek M. Soft Sensor Design for Product Gas Composition Monitoring Including Fault Isolation in a Dual Fluidized Bed Biomass Gasifier. 2024 International Conference on Control, Automation and Diagnosis (ICCAD), IEEE; 2024, p. 1-6. https://doi.org/10.1109/ICCAD60883.
- [32] Suzuki EM, Buzzing P. Applications of Raman spectroscopy in forensic science. I: Principles, comparison to infrared spectroscopy, and instrumentation. Forensic Sci Rev 2018;30:111–35.
- [33] Eichmann SC, Kiefer J, Benz J, Kempf T, Leipertz A, Seeger T. Determination of gas composition in a biogas plant using a Raman-based sensorsystem. Meas Sci Technol //doi.org/10.1088/0957-0233/25
- [34] Karellas S, Karl J. Analysis of the product gas from biomass gasification by means of laser spectroscopy. Opt Lasers Eng 2007;45:935-46. https://doi.org/10.1016/j. optlaseng.2007.03.006.
- Ge H, Sun Z, Jiang Y, Wu X, Jia Z, Cui G, et al. Recent Advances in THz Detection of Water. Int J Mol Sci 2023;24. https://doi.org/10.3390/ijms241310936.
- Song Y, Wang Z, Loh J, Thomson MJ. High-Temperature H2O Vapor Measurement Using Terahertz Spectroscopy for Industrial Furnace Applications. IEEE Trans Terahertz Sci Technol 2016;6:26-31. https://doi.org/10.1109/
- Sudiarta IW, Chýlek P. Mie scattering by a spherical particle in an absorbing medium. Appl Opt 2002;41:3545. https://doi.org/10.1364/ao.41.003545.
- Wang Y, Zhao P, Gao W, Chen X. Optimization of forward-scattered light energy and de-coherence of Mie scattering for speckle suppression. Opt Quantum Electron 2015;47:235-46. https://doi.org/10.1007/s11082-014-9907-1
- Köhler R, Tredicucci A, Beltram F, Beere HE, Linfield EH, Davies AG, et al. Terahertz semiconductor-heterostructure laser. Nature 2002;417:6885. 2002;417: 156-9. https://doi.org/10.1038/417156a.
- GATS. Calculation of molecular spectra with the Spectral Calculator 1994:1-15. Gordon IE, Rothman LS, Hargreaves RJ, Hashemi R, Karlovets EV, Skinner FM,
- et al. The HITRAN2020 molecular spectroscopic database. J Quant Spectrosc Radiat Transf 2022;277:107949. https://doi.org/10.1016/j.jqsrt.2021.107949. Gordley LL, Marshall BT, Allen CuD. Linepak: Algorithms for modeling spectral transmittance and radiance. J Quant Spectrosc Radiat Transf 1994;52:563-80.

https://doi.org/10.1016/0022-4073(94)90025-6.

De S, Agarwal AK, Moholkar VS, Thallada B. Coal and Biomass Gasification. 1st ed. Singapore: Springer; 2018. https://doi.org/10.1007/978-981-10-7335-9.

- [44] Benedikt F. Fuel flexible advanced dual fluidized bed steam gasification. Dissertation Technische Universität Wien 2020. https://doi.org/10.34726/
- [45] Karl J, Pröll T. Steam gasification of biomass in dual fluidized bed gasifiers: a review. Renew Sustain Energy Rev 2018;98:64-78. https://doi.org/10.1016/j. rser.2018.09.010.
- [46] Mauerhofer AM, Müller S, Bartik A, Benedikt F, Fuchs J, Hammerschmid M, et al. Conversion of CO2 during the DFB biomass gasification process. Biomass Convers Biorefin 2021;11:15-27. https://doi.org/10.1007/s13399-020-00822-
- Müller FJ, Fuchs J, Müller S, Winter F. CO2 conversion to CO by fluidized bed biomass gasification: Measuring CO2 utilization via stable carbon isotope ratios. J CO2 Util 2024;83. https://doi.org/10.1016/j.jcou.2024.102792.
- [48] GATS. Spectral Calculator-Hi-resolution gas spectra 2023. https://www.spectralca lc.com/calc/spectralcalc.php (accessed August 17, 2023).
- Amanti MI, Scalari G, Terazzi R, Fischer M, Beck M, Faist J, et al. Bound-tocontinuum terahertz quantum cascade laser with a single-quantum-well phonon extraction/injection stage. New J Phys 2009;11. https://doi.org/10.1088/1367-2630/11/12/125022.
- [50] Williams BS, Kumar S, Hu Q, Reno JL. Distributed-feedback terahertz quantumcascade lasers with laterally corrugated metal waveguides. Opt Lett 2005;30:2909. https://doi.org/10.1364/OL.30.002909.
- [51] Kaltschmitt M, Hofbauer H, Lenz V. Energie aus Biomasse. 4th ed. Wiesbaden: Springer Fachmedien Wiesbaden; 2024. https://doi.org/10.1007/978-3-65
- [52] Schmid JC, Benedikt F, Fuchs J, Mauerhofer AM, Müller S, Hofbauer H. Syngas for biorefineries from thermochemical gasification of lignocellulosic fuels and residues—5 years' experience with an advanced dual fluidized bed gasifier design. Biomass Convers Biorefin 2021;11:2405-42. https://doi.org/10.1007/s13399 019-00486-2
- [53] GeoSphere Austria. Messstationen Stundendaten v2 2024. https://doi.org/ 10.60669/9bdm-yq93
- Wilk V. Extending the range of feedstock of the dual fluidized bed gasification process towards residues and waste. Dissertation Technische Universität Wien 2013
- [55] Kern S, Pfeifer C, Hofbauer H. Gasification of wood in a dual fluidized bed gasifier: influence of fuel feeding on process performance. Chem Eng Sci 2013;90:284-98. https://doi.org/10.1016/j.ces.2012.12.044.
- [56] Rabou LPLM, Zwart RWR, Vreugdenhil BJ, Bos L. Tar in biomass producer gas, the Energy research Centre of The Netherlands (ECN) experience: An enduring challenge. Energy Fuel 2009;23:6189-98. https://doi.org/10.1021/ef9007032.
- Thersites: Tar dew point n.d. https://www.thersites.nl/tardewpoint.aspx (accessed September 4, 2024).

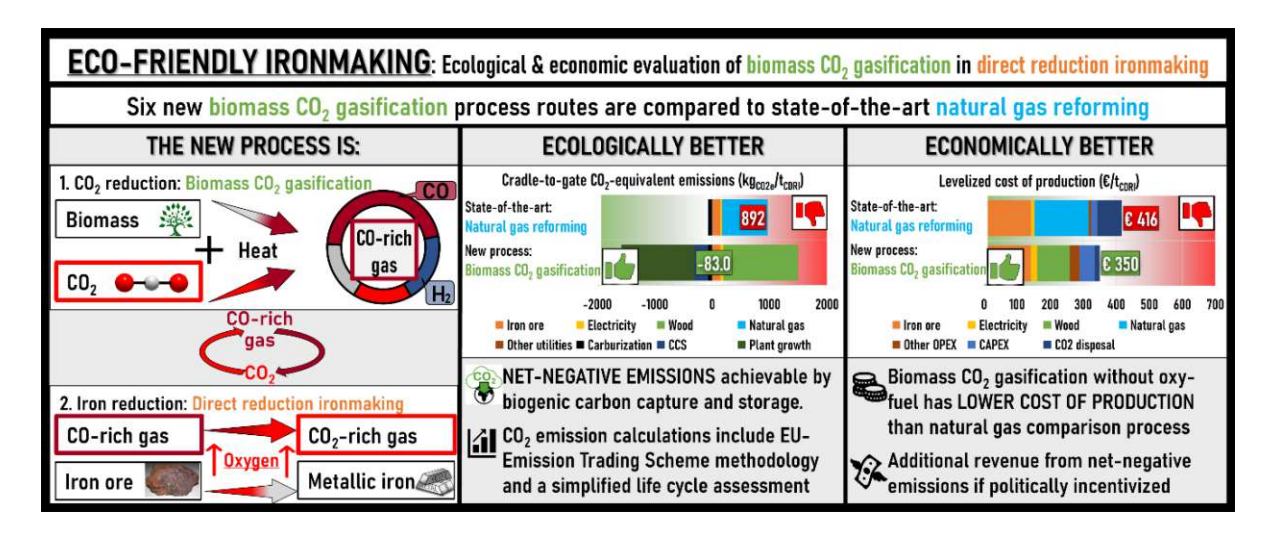
# Journal article IV (JA IV): Eco-friendly ironmaking by biomass CO<sub>2</sub> gasification: Process simulations for ecological and economic evaluation of CO2 recycling in direct reduction ironmaking

#### Bibliographical reference

F. J. Müller, S. Jankovic, J. Fuchs, D. Dimande, S. Müller, and F. Winter, "Eco-friendly ironmaking by biomass CO2 gasification: Process simulations for ecological and economic evaluation of CO2 recycling in direct reduction ironmaking," Energy Conversion and Management, under review at the time of thesis submission.

Please note: The formatting of this article was aligned with the rest of the thesis, and some typos were corrected; otherwise, this pre-print is equivalent to the most recently submitted version.

#### Graphical abstract



#### Highlights

- Biomass CO<sub>2</sub> gasification can supply reducing gas for direct reduction ironmaking.
- Energy demand is 12.4-18.0 GJ/t<sub>CDRI</sub> at 39-56 % energy efficiency of ironmaking.
- Net-negative CO<sub>2</sub> emissions are possible using biogenic carbon capture and storage.
- The cost of producing 1 t of CDRI by CO<sub>2</sub> gasification is calculated at 350–554 €.
- Higher CO<sub>2</sub> conversion in the gasifier increases process efficiency and profit.

biomass **Eco-friendly ironmaking by**  $CO_2$ gasification: Process simulations for ecological and economic evaluation of CO<sub>2</sub> recycling in direct reduction ironmaking

#### Authors:

Florian Johann Müller<sup>a</sup> (florian.johann.mueller@tuwien.ac.at; https://orcid.org/0000-0002-8041-2317)

Stefan Jankovic<sup>a</sup> (stefan.jankovic@tuwien.ac.at; https://orcid.org/0000-0001-5334-6660),

Josef Fuchs<sup>a,\*</sup> (josef.fuchs@tuwien.ac.at; https://orcid.org/0000-0002-4627-4475),

Diana Dimande<sup>a</sup> (diana.dimande@tuwien.ac.at, https://orcid.org/0009-0007-8342-5897),

Stefan Müller<sup>a</sup> (stefan.mueller@tuwien.ac.at; https://orcid.org/0000-0001-8878-429X),

Franz Winter<sup>a</sup> (<u>franz.winter@tuwien.ac.at</u>; <u>https://orcid.org/0000-0001-9854-3836</u>)

<sup>a</sup>Technische Universität Wien, Faculty of Technical Chemistry, Institute of Chemical, Environmental and Bioscience Engineering, Getreidemarkt 9/166, 1060 Vienna, Austria

\*Correspondence to Josef Fuchs (josef.fuchs@tuwien.ac.at)

Keywords: CO<sub>2</sub> reduction, CO<sub>2</sub> capture and utilization, Heavy emission industry, Gasification, Biomass, Renewable energy

### **Abstract**

This concept study provides the first description of a process where the reducing gas for direct reduction ironmaking (DRI) is produced from renewable feedstocks by biomass gasification with CO2 as the gasifying agent. The combined process recycles CO2 from the DRI process as a reactant to the gasifier and converts it in reactions with biomass to CO. Using CO<sub>2</sub> instead of steam as a gasification agent brings unique advantages to the DRI process, such as lower H<sub>2</sub>:CO ratios and higher reduction potential. This study includes process simulations of six novel biomass CO<sub>2</sub> gasification-direct reduction ironmaking (BCG-DRI) routes and two simulations using established natural gas reforming technology (NGR-DRI). The BCG-DRI routes produce reducing gas with higher reduction potential (13 - 29) and lower  $H_2$ :CO ratio (0.5 – 0.7) compared to NGR-DRI (9 and 1.8). Energy efficiency is higher for the NGR-DRI configurations (63 – 64 % versus 39 – 56 %). All BCG-DRI routes show significantly lower CO<sub>2</sub>-equivalent emissions, reaching net-negative emissions up to -1,227 kg<sub>CO2e</sub>/t<sub>CDRI</sub>. At current wood and natural gas prices in Austria, BCG-DRI routes have levelized cost of production (LCOP) down to 350 €/t<sub>CDRI</sub>. LCOP is calculated at 416 €/t<sub>CDRI</sub> for the NGR-DRI process. Based on this work's results, a new plant should strive to reach a high conversion of CO<sub>2</sub> in the gasifier, as this brings advantages in key areas like process efficiency and production costs. The combination of economic and ecological advantages identified for biomass CO<sub>2</sub> gasification is crucial because it can help the industry to defossilize while remaining competitive.

## 1. Introduction

# 1.1. The importance of direct reduction ironmaking for decarbonization

The Intergovernmental Panel on Climate Change (IPCC) details in its sixth assessment report that the average carbon intensity of steelmaking in 2020 was 2.3 t<sub>CO2</sub>/t<sub>Steel</sub> [1], while global steel demand was around 1.81 Gt in 2023 [2]. As a result, the steelmaking sector was responsible for 4.1 Gt<sub>CO2-eq.</sub> or 6.9 % of all global emissions, making it imperative to adjust existing and develop new low-emission processes for iron- and steelmaking [1]. Around 70 % of global production is currently covered by the blast furnace-basic oxygen furnace (BF-BOF) process, with the rest mostly coming from electric arc furnaces (EAF) [3]. Global steel production capacity is estimated at 2.43 Gt, which exceeds the current demand by around 600 Mt/y [4]. Another 68 Mt/y of capacity additions are underway until 2026, and 89 Mt/y are in the planning phase [4]. Since the average lifetime of BOF is reported at 100 years and EAF at 67 years [5], it is imperative to find options for deep decarbonization that can include existing facilities.

Today's production via the EAF route is typically less emission-intensive and offers more straightforward options for further emission reduction. The EAF process can either produce secondary steel from up to 100 % recycled steel scrap [6], or be coupled with a direct reduction ironmaking (DRI) step, which reduces iron ore and prepares it for use in the EAF [4]. DRI processes reduce iron ore by reacting it with a reducing gas that contains hydrogen and carbon monoxide [7]. The market-leading DRI production technology is the MIDREX process, a shaft furnace process that uses natural gas (NG) as feedstock and produced 57.8 % of all DRI in 2022 [8]. In this process, natural gas is used as both energy and chemical feedstock to produce  $H_2$  and CO-rich reducing gas by natural gas reforming (NGR). While the NGR-DRI-EAF process' global warming potential is estimated to be around 40 % lower than the coal-driven BF-BOF process [9,10], this unabated use of fossil gas is still in conflict with net-zero emission strategies. Further reductions are possible when secondary steel is produced from scrap metal instead of iron ore in the EAF. This configuration is estimated at 37-71 % less emissions and 58-60% less energy per ton of steel compared to the BF-BOF route [11]. However, the limited availability of

scrap is and will continue to be a challenge for the widespread adoption of this technology. Forecasts by the World Steel Association project scrap availability at 600 Mt/y by 2030 and 900 Mt/y by 2050 [6], which is significantly lower than global steel demand. Consequently, developing net-zero and belowzero emission processes for DRI production is vital for decreasing the iron- and steelmaking sector's emissions.

## 1.2. Low-emission technologies for direct reduced iron

The most common suggestions for lowering emissions in the DRI process are the inclusion of carbon capture and storage (CCS) into existing DRI processes and replacing natural gas as feedstock with hydrogen [12]. The integration of CCS into the NGR-DRI-EAF route has been described in scientific literature to decrease the global warming potential of crude steel production by 62 % [10] while increasing costs by only 7% [12]. However, just one such facility is currently operated commercially [13]. After eight years of operation, this facility captures only 45 % of the produced CO<sub>2</sub> and uses it for enhanced oil recovery [14].

Replacing the reducing gas formed from natural gas with hydrogen for direct reduction ironmaking (H<sub>2</sub>-DRI) is discussed as a vital part of decreasing the steelmaking sector's emissions by various institutions, such as the International Energy Agency (IEA) [3,13] and the Organization for Economic Co-operation and Development (OECD) [4]. In Sweden, construction of the first two commercial H<sub>2</sub>-DRI projects is underway [13]. The reduction in global warming potential for H<sub>2</sub>-DRI-EAF compared to NGR-DRI-EAF has been estimated at -64 % for using green H<sub>2</sub> produced with Sweden's electricity mix [10]. However, these savings could be much lower in countries with significant electricity production from fossil feedstocks. For example, India produces over half its electricity from coal and another 30 % from oil [15]. India's emission intensity of steel production is higher than the global average, although EAF is overrepresented at 45 % of the country's production capacity [4]. Furthermore, economic operation remains challenging for H<sub>2</sub>-DRI [12,16]. Benavides et al. estimated the costs of H<sub>2</sub>-DRI-EAF to increase by 18 % for using blue hydrogen and 79 % for using green hydrogen when compared to the NGR-DRI-EAF route [12]. Technical challenges for H<sub>2</sub>-DRI include heat distribution due to the endothermic reduction process and balancing the carbon content in the produced steel [16].

The production of reducing gas for DRI could also be achieved by biomass gasification. Some authors have suggested steam or steam/oxygen-blown biomass gasification as a low-emission alternative to produce a reducing gas that contains both CO and H<sub>2</sub> [17–20], similar to the reducing gas produced from natural gas. Their economic performance was described as competitive with NGR-DRI, although this was partially based on favorable assumptions, such as the option to generate profit from biogenic carbon capture and storage (BCCS) [20] and oxygen available on site from existing installations [19]. It has been reported that if biomass is sustainably sourced and CCS is included in the process, these processes offer the possibility to achieve net-negative CO<sub>2</sub> emissions [18–20]. The exothermic iron reduction



process with CO could help with the heat distribution challenges observed for the H<sub>2</sub>-DRI route. Furthermore, solid carbon can be introduced into the DRI product by various carburization reactions [20], decreasing the risk of iron re-oxidation by contact with air and helping the EAF process in multiple ways, e.g., by reducing energy demand [21].

# 1.3. A novel concept - Biomass CO<sub>2</sub> gasification for direct reduction ironmaking

This study is the first investigation of biomass gasification with CO<sub>2</sub> as a gasification agent for direct reduction ironmaking. While previous studies have investigated the more established biomass steam gasification processes, our new study proposes using CO2 as a gasification agent instead. CO2 is not sourced externally but is available by capture from the DRI process. CO2 can be recycled back to the gasifier as a reactant, where it is converted by reaction with biomass to CO [22–26]. The generated CO is reused in the DRI process, creating a compact carbon capture and utilization loop. Using CO<sub>2</sub> as a gasification agent provides unique advantages over previously proposed biomass steam gasification processes and direct reduction with hydrogen.

First, the experimentally found product gas from biomass CO<sub>2</sub> gasification is sufficiently rich in CO and H<sub>2</sub> to be directly suitable for DRI, while the product gas from steam gasification generally has too much H<sub>2</sub>O and CO<sub>2</sub>. The molar ratio of (H<sub>2</sub>+CO)/(H<sub>2</sub>O+CO<sub>2</sub>) is referred to as reduction potential (RP) in ironmaking [19,27]. RP of around 9 can be considered sufficient for DRI [27]. The gas produced by steam gasification processes considered by Zaini et al. [18] and Hammerschmid et al. [19] had RP below 1 due to its high H<sub>2</sub>O content. In contrast, our earlier work experimentally demonstrated that it is possible in biomass CO<sub>2</sub> gasification to produce a reducing gas with very low H<sub>2</sub>O and CO<sub>2</sub> content [22], suitable for the DRI process at reduction potentials of up to 14. This difference could help process efficiency because it reduces the need for adjustments.

Second, a potential appeal of such a gasifier could be found in lower H<sub>2</sub>:CO ratios in the reducing gas. Reducing gas mixtures with H<sub>2</sub>:CO ratios around 1:3 to 1:1 have been reported to bind the most carbon in the solid DRI product as Fe<sub>3</sub>C [28] and could be achieved by biomass CO<sub>2</sub> gasification. These lower H<sub>2</sub>:CO ratios might be favorable for carburization [28] and heat management in the direct reduction reactor compared to gas from other gasification types. These advantages would be heightened when compared to pure H<sub>2</sub> from H<sub>2</sub>-DRI.

The present work aims to provide a holistic assessment of biomass CO<sub>2</sub> gasification's potential in ironmaking. The influence of gasification data on overall process performance is investigated by using three biomass CO<sub>2</sub> gasification datasets. These three datasets span a wide range of CO<sub>2</sub> conversion effectiveness in the gasifier, which allows for investigating if there are ecological and economic benefits from designing a process with high conversion of CO<sub>2</sub> in the gasifier. Each dataset is investigated with

air and oxy-fuel combustion, leading to six process simulations that describe how biomass CO2 gasification can be integrated into direct reduction ironmaking (BCG-DRI). The results are compared to conventional natural gas reforming technology (NGR-DRI), which is included in this work as a benchmark. The core questions answered in this study are:

- How should a BCG-DRI process look like that captures CO<sub>2</sub> from the DRI exhaust and recycles it to the gasifier for conversion?
- How high is the energy efficiency of the new BCG-DRI processes compared to established natural gas reforming technology?
- How high are the CO2 emissions of the new BCG-DRI processes compared to established natural gas reforming technology?
- How high are the costs of producing DRI using the new BCG-DRI processes compared to established natural gas reforming technology?

### 2. Methods

The process simulations in this work are built on previously published experimental data on CO2 gasification [22,29]. These data are combined with other literature sources to create multiple flowsheet models producing cold direct reduced iron (CDRI), the most common product from today's MIDREX plants [30]. Similar simulations for the established NGR-DRI process are added to enable comparisons using the same methods and assumptions. The derived mass and energy balance data are the basis for the techno-economic and CO<sub>2</sub> emission assessments.

## 2.1. Process modeling

### 2.1.1. System overview

Process modeling in this work was performed in IPSEpro 8.0. IPSEpro is a steady-state, equationoriented flowsheet simulation program for mass and energy balancing [31]. Model libraries for this program have been developed for gasification and are commonly used at TU Wien for mass and energy balancing, e.g., [32]. The program can use external libraries for the thermodynamic properties of species but, generally, does not assess or include kinetic or equilibrium behavior. Mass and energy data for individual simulation units are taken from experiments, literature, or other simulation tools. Sufficient data input allows the user to calculate missing values by closing mass and energy balances. The validity of the overall simulation is ensured by careful selection of input data, which are presented in Sections *2.1.2-2.1.8*.

Figure 1 provides an overview of all simulated routes and their key differences, while more detailed settings for each part of the simulation are discussed the following sections. This work includes eight



simulated process routes producing cold direct reduced iron (CDRI) in a shaft furnace similar to the one used in the MIDREX process [8]. The two simulations using natural gas reforming for reducing gas production are referred to as NGR-DRI throughout this work. The other six simulations use biomass CO<sub>2</sub> gasification and are collectively called BCG-DRI. Further differences are reflected in the simulation's name in parentheses and concern:

- the inclusion of carbon capture and storage for the NGR-DRI simulations (no CCS or CCS),
- type of combustion technology for the BCG-DRI simulations (AIR or OXY) and,
- and conversion of CO<sub>2</sub> in the underlying gasification experiment for the BCG-DRI simulations (low (LC), medium (MC), high (HC) conversion).

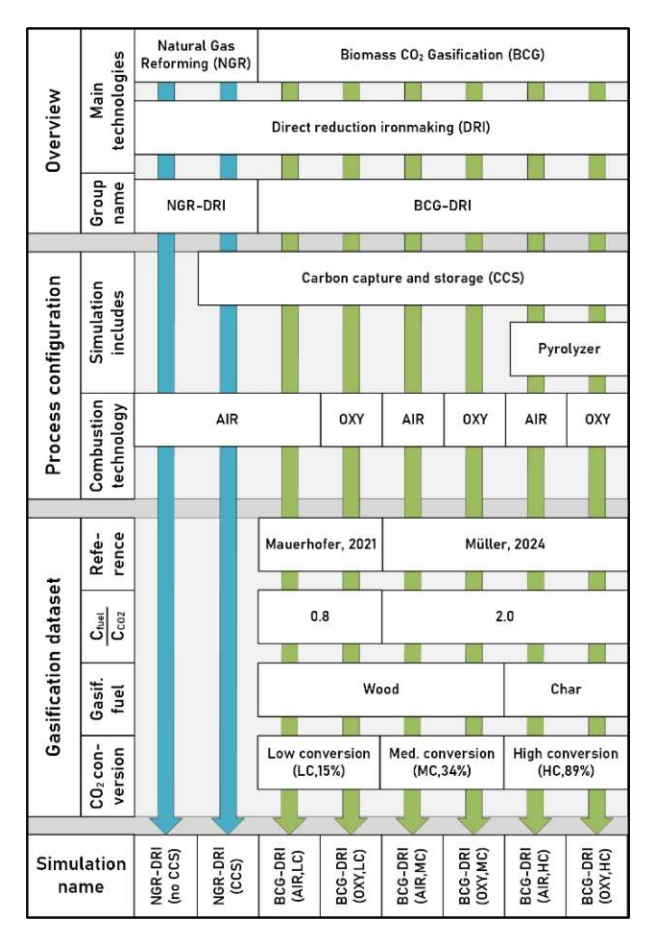


Figure 1: Overview of process routes simulated within this work. Gasification datasets are taken from these sources: "Mauerhofer, 2021"=[29], "Müller, 2024"=[22]

This NGR-DRI process consists of a reformer, shaft furnace, and a heat recovery system and mostly follows data published on the Gilmore plant in Portland, Oregon [27]. Natural gas is mixed with dried process gas from the DRI shaft to form so-called feed gas, which is preheated and fed to a reformer. The reformer converts feed gas in an endothermic process to reducing gas with H<sub>2</sub> and CO as the main components. The reducing gas and a gas stream called carburization gas enter the shaft furnace. In the NGR-DRI cases, the carburization gas is natural gas. Iron ore is reduced in the shaft furnace by transferring oxygen to the reducing gas, forming CO<sub>2</sub> and H<sub>2</sub>O. The used reducing gas, the so-called top gas, still contains some H2 and CO and is dried before a part stream is used as combustion fuel in the

reformer to provide the energy needed to create reducing gas. The flue gas from top gas combustion in the reformer is used for heat exchange before being released to the ambient. The rest of the top gas is merged with additional natural gas to create new feed gas for the reformer. In addition to this base case, one simulation also considers including a mono-ethanolamine (MEA) based carbon capture system that captures CO<sub>2</sub> from the reformer's flue gas and prepares it for transport and storage. This simulation is named NGR-DRI(CCS).

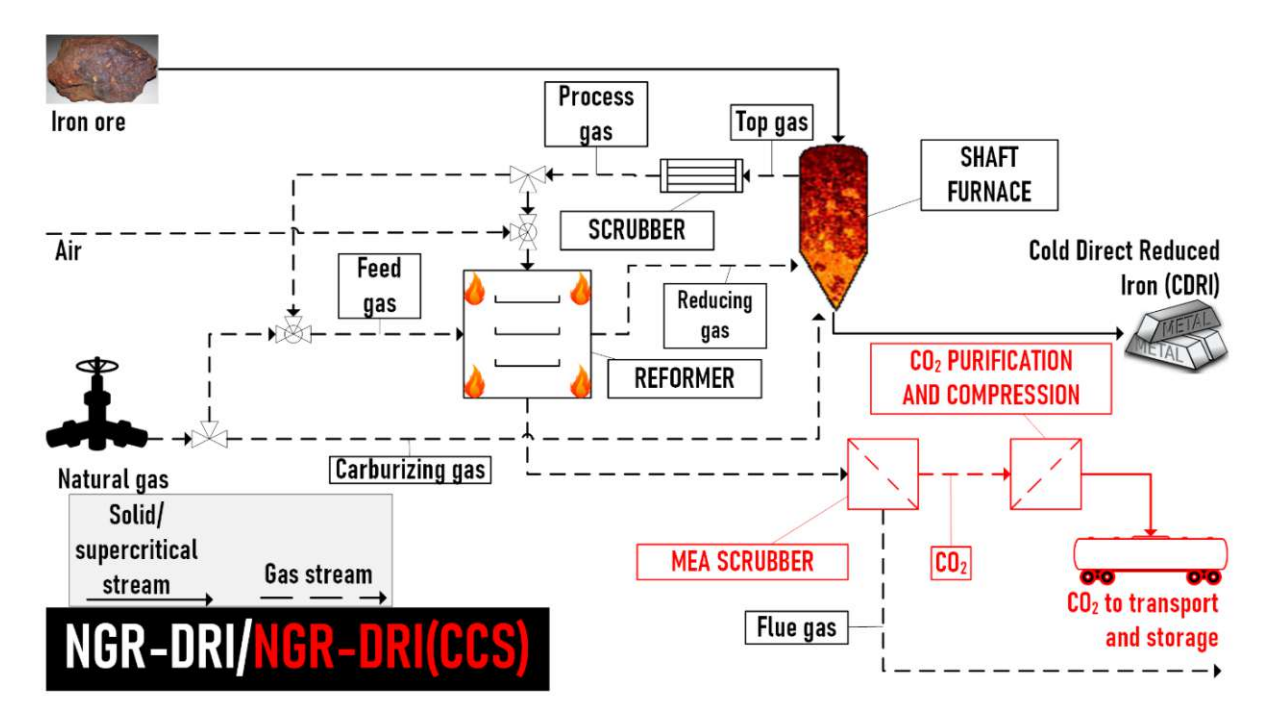


Figure 2: Simplified overview of the Natural Gas-Direct Reduction Ironmaking (NGR-DRI) process route. Process units in red are only included in the adapted NGR-DRI(CCS) simulation, including Carbon Capture and Storage.

The other six process configurations keep the DRI shaft but replace the natural gas reformer with biomass CO<sub>2</sub> gasification in a dual fluidized bed (DFB) gasifier to create the reducing and carburizing gas (*Figure 3*). In the gasifier section of the DFB gasifier, biomass and CO<sub>2</sub> endothermally react to form the product gas. This hot product gas is used for heat exchange, cleaned in a scrubber filled with rapeseed methyl-ester (RME), and mixed with top gas from the DRI shaft. The mixture is fed to the MEA scrubber for carbon capture. Part of the captured CO<sub>2</sub> is fed back as a gasification agent to the gasifier, while the rest is prepared for transport and storage. The uncaptured gas that passes through the MEA scrubber constitutes the reducing and carburizing gas in this process. The reducing gas is preheated and fed to the shaft furnace, where iron ore is reduced. Part of the top gas is recycled into the MEA scrubber, and the rest is used as combustion fuel in the DFB gasifier, pyrolyzer, and secondary combustion chamber. The pyrolyzer is only included in the process for the (HC) configurations and provides wood char as gasification feedstock. The gaseous side-products from pyrolysis are termed pyrolysis gas and, in this simulation, merged with raw product gas before it undergoes gas conditioning.

The three simulations with the added suffix (OXY) use an air separation unit (ASU), and a wet flue gas recycle loop for oxy-fuel combustion. These configurations were added because the MEA scrubber is

at a different position than for the NGR-DRI(CCS) simulation, and the scrubber does not capture CO<sub>2</sub> from combustion. Oxy-fuel combustion was selected to capture CO2 from combustion because it potentially incurs a lower energy penalty than post-combustion capture [33,34]. There could also be synergy effects with air separation units in existing iron- and steelmaking facilities, but this is not an assumption in this work. The oxy-fuel configurations allow for sending all produced CO<sub>2</sub> to transport and storage.

Three experimental gasification datasets with varying conversion of CO<sub>2</sub> in the gasifier are used. CO<sub>2</sub> conversion was determined by differing methods in the underlying works [22,29]; therefore, a mass balance estimation of CO<sub>2</sub> conversion (Eq. 1) is applied here ensure data consistency and enable a discussion on equal footing. CO2 conversion is determined for the three datasets as 15 % (low conversion, "LC"), 34 % (medium conversion, "MC"), and 89 % (high conversion, "HC").

$$X_{CO2,balance} = \frac{\dot{m}_{CO2,in} - \dot{m}_{CO2,out}}{\dot{m}_{CO2,in}}$$
 Eq. 1

Each dataset is used in two simulations: one with air combustion and one with oxy-fuel combustion. (LC) and (MC) used softwood pellets as gasification feedstock [22,29]. (HC) used Eucalyptus globulusderived char as gasification feedstock [22]. For the (HC) configurations, a pyrolyzer converts wood into char before gasification. The low-conversion data were taken from an experiment in the 100 kW<sub>th</sub> dual fluidized bed (DFB) gasifier at TU Wien, as reported by Mauerhofer et al. [29]. Medium- and highconversion data from the 100 kWth DFB gasifier were unavailable. They were instead taken from our earlier work [22] with an electrically heated, single fluidized bed gasifier with 3 kW<sub>th</sub> fuel power. All six BCG-DRI simulations use the DFB gasifier concept, which provides energy to the gasification reactor by external combustion in the combustion reactor.

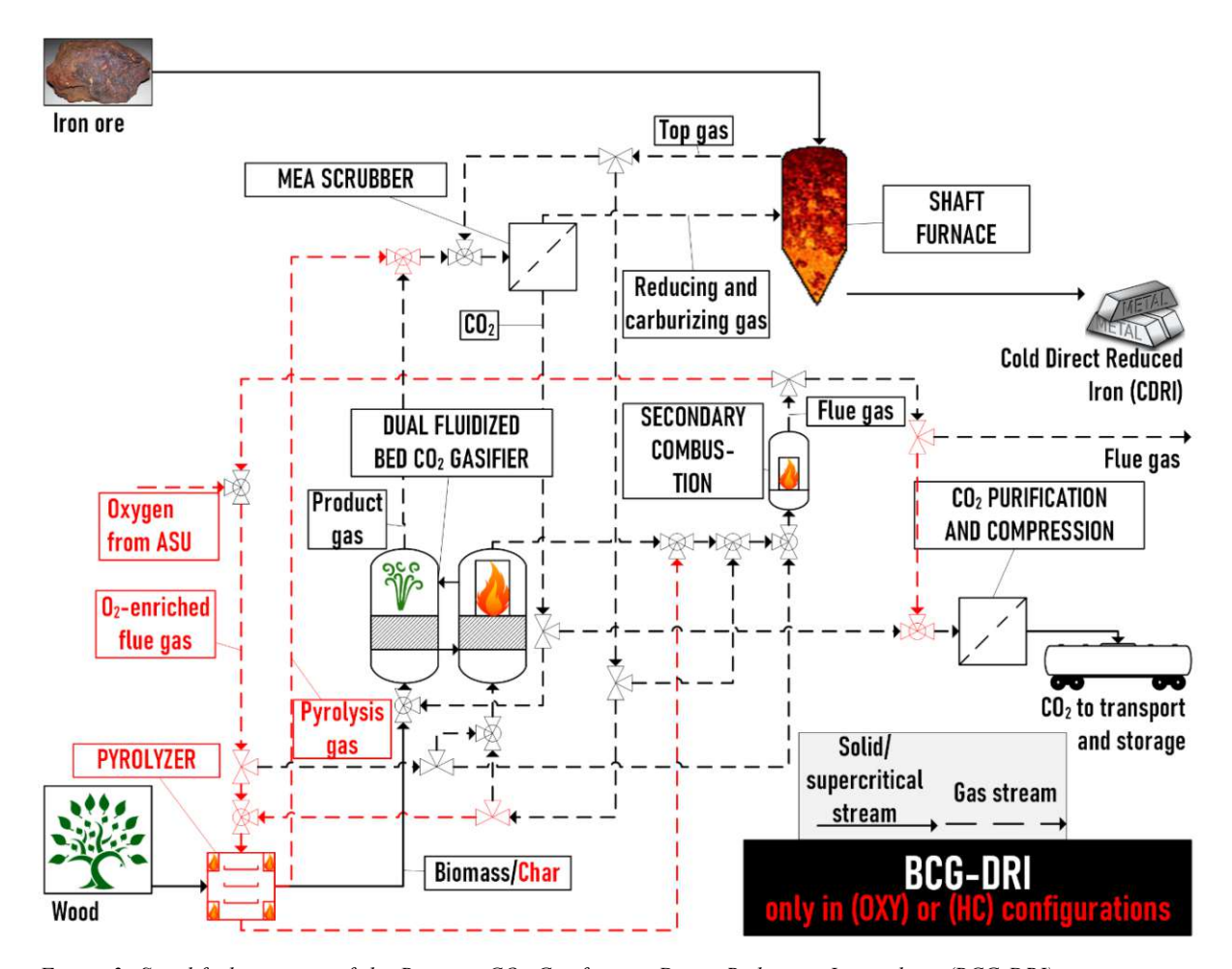


Figure 3: Simplified overview of the Biomass CO<sub>2</sub> Gasification-Direct Reduction Ironmaking (BCG-DRI) process routes. Process units in red are only included in the (OXY) and (HC) configurations, including oxy-fuel combustion or pyrolysis.

### 2.1.2. Feedstocks

All feed streams, other than water for district heating, are assumed to enter the process at ambient temperature and pressure. Ambient air conditions are supposed to be 10 °C, 1 atm pressure, and 80 % relative humidity. CDRI is produced from DR-grade iron ore pellets. Iron ore pellet and gangue composition follow supplementary data from Nurdiawati et al. [35] without moisture. These authors noted that the composition with low SiO<sub>2</sub> and high MgO is typical for pellets from the LKAB Swedish mining company. The natural gas composition follows the typical values provided by Enbridge Gas [36]. Dry softwood composition is assumed to be the same as for the underlying CO<sub>2</sub> gasification experiments [22,29]. A moisture content of 35 wt.-% before drying is chosen for the softwood to fit available market data for the techno-economic analysis [37]. Make-up streams of triethylene glycol (TEG), monoethanolamine (MEA), and rapeseed methyl ester (RME) are assumed as pure species. Olivine is treated as pure and inert in the model. A representative olivine composition used in gasification experiments at TU Wien is 48-50 wt.-% MgO, 39-42 wt.-% SiO<sub>2</sub>, and 8.0-10.5 wt.-% Fe<sub>2</sub>O<sub>3</sub> [23]. Additional information on feedstock compositions is given in *Appendix A*.

Oxygen for oxy-fuel combustion is assumed to be produced by a cryogenic air separation unit (ASU). The ASU is not simulated in detail in this work but is included in the energy demand and technoeconomy calculations. Following Habib et al., oxygen purity of 95 %, nitrogen as the rest, and an electrical demand of 0.24 kWh/kg<sub>02</sub> are assumed for oxygen production [33].

Excess heat is available from the flue gas in the NGR-DRI simulations. For these simulations, a district heating feed-in option is included as a low-temperature excess heat utilization option. District heating water is assumed to return to the facility at 60 °C and be fed to the district heating at 100 °C, resembling Vienna's primary district heating network [38,39]. A return pressure of 5 bara and a feed pressure of 15 bar<sub>a</sub> is assumed based on the technical specifications of the primary district heating network, which generally lists minimum and maximum difference pressures of 1 and 15 bar<sub>a</sub> [39]. Demand for district heating is assumed to be 5800 h/a [40,41].

#### 2.1.3. Shaft furnace

The shaft furnace simulation is based on the NGR-DRI data published on the Gilmore Steel Corporation reactor in Portland, U.S.A. [42,43]. The main assumptions used in the simulation are presented in *Table* 1. The shaft furnace fulfills two main functions for CDRI production: Iron ore reduction to metallic iron and carburization of metallic iron to Fe<sub>3</sub>C. The simulation has been split into a reducing and a carburization/cooling section to better reflect the temperature levels in both sections, mirroring the modeling approach taken by [10,20,43], and others.

Table 1: Key settings used in the simulation of the shaft furnace

Parameter	Unit	Value	Data source
Reducing gas temperature	°C	930	[43]
Reducing gas pressure	bar <sub>a</sub>	2.4	[42,43]
Carburizing gas pressure	bara	2.5	Assumption
Top gas pressure	bar <sub>a</sub>	1.53	[43]
Top gas $RP$ =molar ratio (H <sub>2</sub> +CO)/(H <sub>2</sub> O+CO <sub>2</sub> )	-	1.6	[27]
CDRI drain temperature	°C	58	[43]
Metallization degree (by weight, rest is FeO)	$Fe_{met}/Fe_{tot}$	0.93	[42,43]
Carburization	wt% C	2	[43]
Heat loss relative to energy for iron reduction	%	2.5	[18,20]

Iron ore and gases flow through the shaft in a counter-current configuration, with the iron ore being fed at the shaft's top and drained at its bottom. Iron ore first enters the reducing section, where it is contacted with a mixture of hot reducing gas and transition gas, which is the outlet gas of the carburization/cooling section. In this reducing section, iron ore is reduced to metallic iron by reactions with CO and H<sub>2</sub>. Nonferrous components in the iron ore, termed gangue, are treated as inert species in the shaft furnace. The thermodynamic stability of elemental iron is checked at the reducing gas temperature and composition by comparison with Baur-Glässner plots in mixed H<sub>2</sub>-H<sub>2</sub>O and CO-CO<sub>2</sub> atmospheres [44]. Phase transition lines in mixed hydrous and carbonaceous atmospheres were derived from linear interpolation according to the molar composition of the top gas. This work uses the assumption that CDRI composition is the same for all process routes irrespective of reducing gas composition and follows [42,43] for metallization and carburization degrees.

10



In the carburization section, the hot and reduced iron ore is contacted by carburizing gas. The carburizing gas reacts with elemental iron to form Fe<sub>3</sub>C. Carburization is beneficial for ironmaking for several reasons: It stabilizes iron ore against re-oxidation and helps in the EAF process by reducing its energy consumption and supporting the foaming of the slag and removal of nitrogen [20]. Carburization is modeled to occur via Eq. 2 with methane (27 kJ/mol<sub>Fe</sub>) in the NGR-DRI case and via Eq. 3 with CO (-56 kJ/mol<sub>Fe</sub>) in all biomass configurations [20]. The carburizing gas, which is not preheated, also cools the iron ore to the outlet temperature [43].

$$Fe + \frac{1}{3}CH_y \rightarrow \frac{1}{3}Fe_3C + \frac{y}{6}H_2$$
 Eq. 2

$$Fe + \frac{2}{3}CO \rightarrow \frac{1}{3}Fe_3C + \frac{1}{3}CO_2$$
 Eq. 3

The reducing gas' fitness for iron ore reduction in DRI is often described by the so-called reduction potential (RP) [19,27]. RP is the molar ratio of H<sub>2</sub> and CO to H<sub>2</sub>O and CO<sub>2</sub>. It is formally introduced as a key performance indicator in Section 2.2.1 in Eq. 4. RP values of 8.7 - 11.5 for reducing gas and 1.55 – 1.65 for top gas can be calculated from data reported on the Siderca and Gilmore NGR-DRI MIDREX plants [27]. As part of this simulation, RP in the top gas is defined as 1.6 for all cases, while RP for the reducing gas varies based on the process route. The reformer delivers hot reducing gas for the NGR-DRI case. Although some authors have described that adding oxygen to the reducing gas or shaft furnace can support heat distribution and reduce gas flow [45,46], no oxygen addition was considered in this work to match the data provided on the Gilmore plant [42,43]. For all BCG-DRI cases, the reducing gas from the MEA scrubber is compressed before a condenser removes water and increases RP. After the condenser, reducing gas is preheated by heat exchange with the off-gas from combustion in the DFB reactor. Iron reduction with CO is globally exothermic, while it is endothermic with H<sub>2</sub> [47]. Carburizing gas is assumed to be compressed natural gas in the NGR-DRI case and additional reducing gas in the BCG-DRI cases. In both cases, carburizing gas is not preheated outside the shaft furnace and cools down the CDRI in the carburizing section.

Complete conversion of all hydrocarbons larger than methane is assumed in the shaft reactor. Top gas composition for NGR-DRI results from mass and energy balances. Pissot et al. proposed to use the water-gas shift reaction's quotient to predict the relative conversion of H<sub>2</sub> and CO [20]. Experimental data from the Gilmore NGR-DRI plant [27] showed a molar ratio of around 1.3 for (CO<sub>2</sub>+H<sub>2</sub>)/(H<sub>2</sub>O+CO), which is also used to calculate this study's top gas compositions in the biomass gasification simulations.

### 2.1.4. Natural Gas Reformer

In the MIDREX process, the top gas leaving the shaft furnace is cooled in a scrubber [8]. The remaining gas is called process gas and split into two parts: Around two-thirds of process gas is mixed with natural



gas and fed to the reformer as feed gas to produce fresh reducing gas [8,20]. The rest of the process gas is fed to the reformer and combusted with air to satisfy the energy demand of the endothermic reforming reactions [8,48]. The reformer in the MIDREX process is a furnace with up-fired boilers and vertical reactor tubes, typically operated at 2-3 bar<sub>a</sub> [48]. The flue gas from combustion is used for heat exchange and preheats the combustion air and feed gas [8,48]. The reducing gas is produced at high temperatures, which is suitable for ironmaking. Key simulation settings derived from the literature are given in Table 2.

Table 2: Key settings used in the simulation of the MIDREX reformer

Parameter	Unit	Value	Data source
Feed gas temperature	°C	400	[48]
Feed gas pressure drop	bara	0.34	Calculated from [48]
Combustion air pressure	bara	1.1	Assumption
Oxygen ratio	O <sub>2,fed</sub> /O <sub>2,stoich</sub>	1.18	Calculated from [48]
Flue gas temperature	°C	1120	[48]
Reducing gas H <sub>2</sub>	vol%	52.58	[43]
Reducing gas CO	vol%	29.97	[43]
Reducing gas H <sub>2</sub> O	vol%	4.65	[43]
Reducing gas CO <sub>2</sub>	vol%	4.80	[43]
Reducing gas rest=(CH <sub>4</sub> +N <sub>2</sub> )	vol%	8.1	[43]
Reducing gas RP	-	8.7	Calculated from [43]
Heat loss relative to fuel power	%	2.5	Assumption

### 2.1.5. Carbon capture, drying, and compression

Carbon capture is included in all simulated cases besides NGR-DRI(no CCS). MIDREX suggests including carbon capture by MEA scrubber either in the top gas line from the shaft furnace or the flue gas line from the reformer [49]. In this work, the MEA scrubber is included in the flue gas line since the CO<sub>2</sub> emission savings potential is higher and estimated by MIDREX at ~0.5 t<sub>CO2</sub>/t<sub>DRI</sub> [49]. Product gas, pyrolysis gas and top gas are combined and fed to the MEA scrubber for all BCG-DRI cases. Including the MEA scrubber in this position increases the reduction potential for the recycled top gas by separating CO<sub>2</sub>. The disadvantage is that this configuration does not capture CO<sub>2</sub> emissions from combustion in the flue gas. Pissot et al. [20] proposed a second amine scrubber to reduce these flue gas emissions. Our work does not include a second MEA scrubber; instead, it considers oxy-fuel combustion for its lower energy demand per captured CO<sub>2</sub> [33,34] in the three simulations with the suffix (OXY) and no additional carbon capture in the three simulations with the suffix (AIR).

The simulation for the MEA scrubber largely follows the design specifications described by Madeddu et al. [50]. CO<sub>2</sub> is captured in this simulation by an aqueous MEA solution in an absorber, and the rich MEA is transferred via a counter-current heat exchanger to the stripper, where CO<sub>2</sub> is removed. Heat is supplied to the stripper's reboiler by heat exchange with hot process streams. For the NGR-DRI(CCS) case, the flue gas stream is cooled in the stripper's reboiler before the flue gas enters the absorber. For the biomass gasification cases, an ambient air stream is preheated in a multi-component heat exchanger by contact with the hot top gas, flue gas, and product gas streams. This hot air stream is then partially

cooled in the MEA reboiler before being mixed with ambient air and used for drying biomass. Lean MEA is removed from the stripper and cooled by heat exchange with the rich MEA flowing from the absorber to the stripper. A small make-up stream of fresh MEA is constantly fed, and a similar stream of lean MEA is removed and sent to combustion to avoid solvent degradation and impurity accumulation over time. MEA loss by entrainment in outgoing gas is neglected in this work.

The wet CO<sub>2</sub> stream exiting the stripper is cooled and dried to a moisture content that fits the experimental gasification data. Part of this stream is used as a gasification agent for CO<sub>2</sub> biomass gasification in the DFB gasifier. The rest of the CO<sub>2</sub> stream is merged with flue gas for the simulation cases with oxy-fuel combustion. In all biomass gasification cases, this stream is then compressed to 100 bar<sub>a</sub> in six compressors with intermittent cooling in condensers and a TEG scrubber, as described by Bielka et al. [51]. The outlet pressure of 100 bar<sub>a</sub> is suitable for ensuring CO<sub>2</sub> is in a supercritical state for transport, which is more efficient [51]. Transport and storage of CO2 are only included in the techno-economic assessment and not in this simulation's mass and energy balances.

For the simulations that include oxy-fuel combustion, a wet flue gas recycle stream is enriched with 30 vol.-% O<sub>2</sub> from an ASU and replaces the air for combustion in the DFB combustor, pyrolyzer, and secondary combustion chamber. The selection of oxygen enrichment results from balancing the continuity of adiabatic flame temperature and superficial gas velocity [52], and 30 vol.-% has been proposed for the combustion reactor of DFB gasifiers [53]. A further gas purification step is needed to remove oxygen and nitrogen impurities from the CO<sub>2</sub> stream for the oxy-fuel cases. Several authors have suggested around 0.1 vol.-% O2 or even lower as a limit to avoid threatening the storage integrity by dissolving caprock [54,55], pipeline corrosion [56], overheating injections points from reaction with residual hydrocarbons [57] and other issues. Furthermore, an upper limit of 4 vol.-% for the sum of gases other than CO2 was proposed, mainly for economic reasons [51,58]. These limits can be achieved by cryogenic CO<sub>2</sub> purification, which can provide more than 99.9 vol.-% pure CO<sub>2</sub>[34]. This work does not include a detailed simulation of this process. Still, a simplified purification procedure is modeled after the TEG scrubber and before the final compressor, where the gas already has more than 30 bara and is dry. The simplified model only considers electrical energy demand for the separation and uses an energy penalty derived from Xu et al. [34] for a CO<sub>2</sub> stream that starts at around 80 – 90 vol.-% purity and 15 bara. This unit is called the CO<sub>2</sub> separation unit (CSU) in this work, keeping the name similar to an ASU.

Table 3: Key settings used in the simulation of the carbon capture, drying, and compression section

Parameter	Unit	Value	Data source	
MEA concentration in solution	wt%	30	[50]	
Heat of absorption for ~30 wt% MEA solution at	kJ/mol <sub>CO2</sub>	-84.3	[59]	
<0.4 mol <sub>CO2</sub> /mol <sub>MEA</sub> and 40 °C				
MEA make-up stream	$kg_{MEA}/t_{CO2,capt.}$	0.3	[60]	
Heat loss in each absorber and stripper (relative to	%	2.5	Assumption	
sensible heat of gas stream)				
Temperature approach in lean/rich-MEA heat exchanger	°C	10	[50]	
Absorber temperature	°C	40	[50]	
Absorber pressure	bar <sub>a</sub>	1	[50]	
CO <sub>2</sub> separation efficiency	%	90	[50]	
Rich MEA loading	kg <sub>CO2</sub> /kg <sub>MEA</sub>	0.37	[61]	
Lean MEA loading	$kg_{\rm CO2}/kg_{\rm MEA}$	0.22	Calculated	from
			[50]	
Reboiler temperature	°C	120	[18]	
Stripper pressure	bara	1.8	[50]	
H <sub>2</sub> O evaporated per CO <sub>2</sub> in stripped gas	mol/mol	1.02	Calculated	from
			[50] p.82	
Maximum gas temperature after compressors 1-5	°C	95	[51]	
Temperature after condensers	°C	15	Assumption	
TEG scrubber temperature	°C	15	[51]	
Rich TEG water content	wt%	18.6	Calculated	from
			[51]	
Final pressure of CO <sub>2</sub> for transport and storage	bar <sub>a</sub>	100	[51]	
Electrical energy demand for air separation unit	$MJ/kg_{CO2}$	0.864	[33]	
Oxygen enrichment of flue gas for oxy-fuel combustion	vol% O <sub>2</sub>	30	[53]	
Electrical energy demand for CO <sub>2</sub> purification in oxy- fuel simulation routes	MJ/kg <sub>CO2</sub>	0.3	[34]	

### 2.1.6. Biomass pretreatment

All biomass gasification simulations assume that biomass is delivered with a high moisture content and dried in a continuously operated biomass dryer to the moisture content used in the gasification experiments [22,29]. Ambient air is mixed with hot air from the MEA reboiler and fed to the biomass dryer. Biomass is dried by direct contact with the hot air, which could, for example, be realized in a rotary drum dryer to achieve the desired moisture content [62]. The air is enriched with H<sub>2</sub>O from the biomass, cooled, and vented to the ambient air. The dried wood is transferred to the DFB gasifier for the low- and medium-conversion simulations and to the pyrolyzer for the high-conversion simulations.

Hot wood char as feedstock for the gasifier is produced in the BCG-DRI(HC) simulations by a pyrolyzer with continuous feed, e.g., an auger screw reactor [63-65]. Biomass pyrolysis yields solid biochar and a mixture of permanent and condensable gases [65], called pyrolysis gas in this work. Data on the split of products are derived from experiment L8 reported by Solar et al. [65], who pyrolyzed *Pinus pinaster* in a laboratory-scale auger reactor similar to industrial plants. The dataset by Solar et al. includes various simulation data in one place, e.g., solid/liquid/gas product split or liquid analysis. For this reason, these data are chosen over general data on pyrolysis [66] or auger screw reactors [67]. Their feedstock composition was roughly similar to the Eucalyptus composition reported by Bagatini et al. [68], but had

a higher oxygen content. This difference is considered by fixing the ratio of product gas components instead of their concentration, allowing for more oxygen in the pyrolysis gas. Top gas combustion with air or oxygen-enriched flue gas provides heat to the pyrolyzer by external heating [67], similar to the natural gas reformer described in Section 2.1.4. The pyrolysis gas is merged with the product gas stream from gasification. Critical assumptions for simulating the biomass pretreatment are summarized in Table 4.

Table 4: Key settings used in the simulation of the biomass dryer and pyrolyzer

Parameter	Unit	Value	Data source
Biomass moisture before dryer	wt%	35	[37]
Biomass moisture after dryer	wt%	7.2	[22,29,62]
Air feed temperature	°C	80	[53]
Air drain relative humidity	<b>%</b>	80	[53]
Heat loss in dryer (sensible heat)	<b>%</b>	2.5	Assumption
Pyrolysis solids yield	wt%	30.8	[65] exp. L8
Pyrolysis permanent gas yield	wt%	47.1	[65] exp. L8
Pyrolysis gas CO:H <sub>2</sub> ratio	mol/mol	0.64	[65] exp. L8
Pyrolysis gas CO:CO <sub>2</sub> ratio	mol/mol	1.24	[65] exp. L8
Oxygen ratio pyrolyzer combustion	O <sub>2,fed</sub> /O <sub>2,stoich</sub>	1.18	Assumed to match the natural gas reformer
Pyrolysis temperature	°C	800	[65] exp. L8
Heat loss in pyrolyzer relative to combustion fuel power	%	2.5	Assumption

### 2.1.7. Dual fluidized bed gasification

Gasification is simulated in a DFB gasifier model, similar to the 100 kWth fuel power DFB gasifier studied for biomass CO<sub>2</sub> gasification by Mauerhofer et al. at TU Wien [24]. The DFB system consists of a gasification and a combustion reactor interconnected by loop seals. Inorganic solids, called bed material, and unconverted char are cycled between the two reactors, while gases cannot pass from one reactor to another. Olivine was used as bed material in the underlying gasification experiments [22,29] because it is also used in industrial-sized biomass gasification [69,70] and shows catalytically active behavior [23,71,72]. The gasification reactor's upper part is operated as a counter-current column, while the lower part is a bubbling bed. In the bubbling bed, biomass fuel reacts with CO<sub>2</sub> in globally endothermic reactions to form a product gas. The Boudouard reaction is the most essential reaction for converting CO<sub>2</sub> in this process and significantly contributes to the formation of a CO-rich product gas [22,23,73-76].

The separation of gasification and combustion into two reactors allows for the use of air in the combustion reactor without diluting the product gas with nitrogen [24]. Furthermore, recycling waste streams for combustion creates the opportunity for process integration. This work assumes that waste streams equal to their respective make-up streams of the used scrubbing agents MEA, TEG, and RME are co-fed as fuel to the DFB gasifier to avoid the accumulation of impurities. Most of the thermal power for combustion is provided by transferring unconverted char from the gasification reactor to the combustion reactor or by recirculating top gas back to the combustor. Recirculation of top gas, which

15



has higher CO<sub>2</sub> content than the reducing gas, saves energy for carbon capture. For the BCG-DRI(LC) process, feeding additional dry biomass directly to the combustion reactor is more efficient, and less top gas is recirculated. The flue gas from the DFB combustor is mixed with flue gas from the pyrolyzer for the BCG-DRI(HC) simulations and further transported to a secondary combustion chamber, where sufficiently high air ratios ensure complete combustion. A top gas part stream is fed to the secondary combustion chamber to cover internal heat demands. After heat exchange and particle separation, the flue gas is exhausted to ambient for the non-oxy-fuel simulations or sent to CO<sub>2</sub> compression and purification for the oxy-fuel simulations.

Table 5: Key settings used in the simulation of the dual fluidized bed gasifier for all biomass gasification routes

Parameter	Unit	Value	Data source
Tar in product gas	g/Nm³	6.2	[29] Exp.5
Dust in product gas	$g/Nm^3$	0.6	[29] Exp.5
Fly char in product gas	g/Nm³	0.5	[29] Exp.5
Bed material make-up	$kg_{bed}/(h\cdot MW_{th,gasifier})$	1.5	[77]
Temperature difference bubbling bed/combustion flue	°C	127	[29] Exp.5
gas			
Air ratio in combustion reactor	$O_{2,fed}/O_{2,stoich}$	1.25*	[41]
CO slip from combustion reactor	mol <sub>CO</sub> /mol <sub>CO2</sub>	0.05	[77]
Heat loss relative to fuel power in gasification reactor	%	1.0	[41]
Heat loss relative to fuel power in combustion reactor	%	1.6	[41]

<sup>\*</sup>The air ratio was allowed to be higher for the BCG-DRI(HC) configurations to avoid combustion temperatures over 1000 °C from combusting high amounts of char transported from the gasification to the combustion reactor.

Experimental data from the 100 kWth DFB gasifier at TU Wien are used to simulate the DFB system. Data from experiment #5 by Mauerhofer et al. [29] with low CO<sub>2</sub> conversion are used for the BCG-DRI(LC) cases. Data for the medium-conversion (MC) and high-conversion (HC) simulations were described in our earlier work as experiments #4 and #7 [22], which used an electrically heated single bubbling bed reactor at a laboratory scale. Both works used similar temperatures in the bubbling bed, olivine of the same composition as bed material, and CO<sub>2</sub> as a gasification agent. Experiment #4 (MC simulations) in our earlier work also used the same pelletized softwood fuel as Mauerhofer et al. [29] (LC simulations). A critical difference between these experiments is the ratio of fuel to gasification agent supplied to the gasification reactor. While Mauerhofer et al. used excess CO2, more carbon was fed via biomass in our earlier work.

The abundance of tar, dust, and fly char [29] and the elemental composition of tar [78] and fly char in the product gas were assumed to be equal for all simulated biomass CO<sub>2</sub> gasification cases. The elemental composition of fly char is supposed to match the composition of ungasified char transported from the gasification to the combustion reactor. It follows data reported for Eucalyptus char produced at 900 °C [68]. The amount of char transported from the gasification reactor to the combustion reactor results from mass and energy balancing. For the (HC) simulations feeding char as feedstock to the gasifier, char transport is significantly higher. The air ratio in the combustion reactor is increased for



these simulations to keep flue gas temperatures below 1000 °C. The data in Table 6 is used for both oxy-fuel and non-oxy-fuel simulations.

Table 6: Key settings used to simulate the dual fluidized bed gasifier for individual process routes.

Parameter		Unit	BCG-	BCG-	BCG-
			DRI(AIR,LC)	DRI(AIR,MC)	DRI(AIR,HC)
			BCG-	BCG-	BCG-
			DRI(OXY,LC)	DRI(OXY,MC)	DRI(OXY,HC)
Data source			[29] Exp.5	[22] Exp.4	[22] Exp.7
Fuel type gasifier			Softwood	Softwood	Wood char
CO <sub>2</sub> conversion	in	%	15	34	89
gasifier by Eq. 1					
Feed ratio Cfuel: CCO2		mol/mol	0.8	2	2
Feed	ratio	mol/mol	0.04	0.10	0.08
$H_2O/(C_{fuel}+C_{CO2})$					
Bubbling	bed	°C	837	825	856
temperature					
CO in product gas		vol%	37.6	46.0	80.0
CO <sub>2</sub> in product gas		vol%	38.2	17.1	4.2
CH <sub>4</sub> in product gas vol%		vol%	5.6	5.6	0.8
H <sub>2</sub> in product gas		vol%	11.6	20.0	10.4
H <sub>2</sub> O in product gas		vol%	7.0	11.2	4.6

### 2.1.8. Auxiliary equipment

The hot gases from biomass gasification and pyrolysis contain impurities such as dust and tar particles and condensable organic compounds [24], often referred to as tar [79]. These impurities are typically removed or reduced by combining gas-cleaning steps [77]. Some tar compounds can condense at ambient pressure and around 200 °C, possibly leading to problems in heat exchangers and filters [69]. For this reason, many processes include a tar removal step, either by reforming the tars to permanent gases and water [17,18], or by condensing or absorbing them in a scrubber [19,20]. A scrubber is selected for this work because it allows for simultaneous water removal, thereby increasing the reducing gas' reduction potential.

The gas cleaning steps in this work follow the course gas cleaning procedure described for product gas from a DFB gasifier by Hammerschmid et al. [77]. After heat exchange and cooling, a baghouse gas filter removes particles. Hammerschmid et al. proposed a product gas temperature of 180 °C before the baghouse filter [77]. Our work assumes a higher inlet gas temperature of 200 °C for the filter to prevent tar condensation at the cost of some waste heat that could be additionally recovered at 180 °C. In the second step, tar and water are removed in a scrubber using RME as solvent. The scrubber includes a phase separator, allowing for the recirculation of RME to the scrubber. Water is removed from the phase separator and disposed of, while an emulsion phase, including RME and tars, is recirculated to the DFB combustor and used as fuel.

Furthermore, Hammerschmid et al. propose an activated carbon filter and a ZnO guard bed when utilizing the product gas for synthetic natural gas production. These steps are omitted in this work because the ironmaking process is reported to be more resistant to the presence of various organic and sulfur compounds [17]. In reducing gas, acceptable levels of sulfur contamination are reported as 100 – 3000 ppm [17] to achieve satisfactory DRI quality. Based on the fuel used in this simulation, the sulfur content in the reducing gas is calculated at only 20-40 ppm.

Heat integration is included to reduce total fuel consumption and increase process efficiency. The simulation includes three gas-gas heat exchangers, which heat the reducing gas, gasification agent, and air for MEA stripping and biomass drying. While the former two are straightforward in design and include only one hot and one cold gas stream each, air is heated in the third heat exchanger by contact with three hot gas streams. All heat exchangers are operated in counter-current mode.

Several condensers are included in this work for gas cooling and water removal. Water at ambient temperature is assumed to be available for cooling. Condensate from CO<sub>2</sub> drying is recirculated to the MEA scrubber, and other condensates are disposed of as wastewater.

The pressure levels for the gases and liquids in this simulation range between 1-100 bara and are based on literature data where possible, e.g., for the shaft furnace [43] and the carbon capture section [50,51]. Determining the configuration and individual pressure drop for auxiliary equipment like heat exchangers, particle separators, and condensers is beyond the scope of this study; instead, standard values are assumed for these types of equipment. If gas streams are merged, the resulting pressure is considered equal to the feed stream with the lowest pressure. Pumps and compressors not mentioned in Section 2.1.5 are simulated as single-stage pressurization.

Table 7: Key settings used in the simulation for auxiliary equipment.

Parameter	Unit	Value	Data source
Dust in product gas after filter	g/Nm³	0.025	[19]
Char in product gas after filter	$g/Nm^3$	0	Assumption
Tar in product gas after scrubber	g/Nm³	0.025	[19]
Product gas temperature before RME scrubber	°C	200	Assumption
RME make-up stream	$kg_{RME}/(h\cdot MW_{th,gasifier})$	1.1	[77]
Minimum temperature difference in heat exchangers	°C	10	[18]
Cooling water temperature in	°C	10	Assumption
Cooling water temperature out	°C	20	Assumption
Flue gas exhaust temperature	°C	140	Assumption
Sensible heat loss in filters, scrubbers and heat	%	2.5	Assumption
exchangers			
Pressure drop in condensers	mbar	100	Assumption
Pressure drop in filters, scrubbers and heat	mbar	25	Assumption
exchangers			
Isentropic efficiency product gas blower	%	50	[53]
Isentropic efficiency CO <sub>2</sub> compressors	%	84 - 74	[51]
Isentropic efficiency other blowers	%	65	[53]
Isentropic efficiency pumps	%	50	[53]
Mechanical efficiency blowers, compressors, pumps	%	98	[53]
Electrical efficiency drive systems	%	90	[53]
Mechanical efficiency drive systems	%	100	[53]

### 2.2. Performance indicators

### 2.2.1. Technical assessment

The quality of reducing gas is often compared using the reduction potential (RP: Eq. 4). RP expresses the molar ratio of H<sub>2</sub> and CO compared to H<sub>2</sub>O and CO<sub>2</sub>. Higher RP values in the reducing gas mean the gas can take up more oxygen from the iron ore until the thermodynamic equilibrium is reached at similar operating conditions, hydrogen content, and carbon content in the overall gas. The H<sub>2</sub>:CO ratio is also important because it influences carburization and sensible heat demand in the shaft furnace.

The specific energy demand for carbon capture  $(e_{CO2,CAP}: Eq. 5)$  includes the reboiler heat duty  $(\dot{Q}_{RB})$ , the electrical power demand of auxiliary equipment like pumps and compressors in the MEA scrubber and  $CO_2$  compression/drying section ( $P_{CCS-AUX}$ ), the chemical energy of the MEA and TEG make-up streams, and, in the case of oxy-fuel combustion, the electrical demand for air  $(P_{ASU})$  and  $CO_2$   $(P_{CSU})$ separation units. These energy demands are related to the mass flows of CO2 fed back to the gasifier  $(\dot{m}_{CO2,DFB,in})$  or prepared for storage  $(\dot{m}_{CO2,CCS})$ . This value is mainly helpful for validating the simulations. Simulations without oxy-fuel combustion can be compared to the existing literature on carbon capture in an MEA scrubber. Furthermore, it can be checked if the inclusion of oxy-fuel lowers the specific energy demand for carbon capture or if another MEA scrubber should be installed instead.

Chemical energy for the MEA make-up stream and other organic and gaseous fuel streams is calculated in this work from their respective lower heating values (LHV) and mass flows ( $\dot{m}$ ). The energy efficiency of ironmaking ( $\eta_{IRON}$ : Eq. 6) relates the enthalpy change from iron ore to CDRI ( $\Delta \dot{H}_{IRON}$ ) to

the overall energy demand, which is the sum of electrical and thermal input power. Thermal input power is calculated from lower heating values (LHV) and mass flows (m) of each feed stream. Some authors instead report the specific energy demand for reduction per mass unit of CDRI (e<sub>IRON</sub>: Eq. 7), although this representation loses information about iron ore quality and CDRI carburization. The NGR-DRI route also includes the utilization of waste heat for district heating  $(\Delta \dot{H}_{DH})$ , which is included in the overall energy efficiency of the process ( $\eta_{TOT}$ : **Eq. 8**).

Table 8: Technical key performance indicators

Table 8. Technical key perjormance indicators	
Reducing gas quality	
$RP = \frac{n_{H_2} + n_{CO}}{n_{H_2O} + n_{CO_2}}$	Eq. 4
Process energy efficiency	
$e_{CO2,CAP} = \frac{\dot{Q}_{RB} + P_{CCS-AUX} + P_{ASU} + P_{CSU} + \sum_{TEG,MEA} (LHV \cdot \dot{m})}{\dot{m}_{CO2,DFB,in} + \dot{m}_{CO2,CCS}}$	Eq. 5
$\eta_{IRON} = rac{\Delta \dot{H}_{IRON}}{P_{EL,TOT} + \sum_{BM,NG,TEG,MEA,RME}(LHV \cdot \dot{m})}$	Eq. 6
$e_{IRON} = rac{P_{EL,TOT} + \sum_{BM,NG,TEG,MEA,RME}(LHV \cdot \dot{m})}{\dot{m}_{CDRI}}$	<b>Eq.</b> 7
$\eta_{TOT} = rac{\Delta \dot{H}_{IRON} + \Delta \dot{H}_{DH}}{P_{EL,TOT} + \sum_{BM,NG,TEG,MEA,RME}(LHV \cdot \dot{m})}$	Eq. 8

### 2.2.2. CO<sub>2</sub> emission calculation

Three strategies of emission calculation are included in this work to serve different purposes. 1 t<sub>CDRI</sub> is the functional unit for all three calculations; all results are presented in kgco2/tcpRI or kgco2e/tcpRI.

- The first calculation method follows the rules of the European Union Emission Trading Scheme (EU-ETS). It is used to calculate the cost of CO2 allowances in the techno-economic section of this work.
- The second strategy proposes a hypothetical change to the EU-ETS methodology that would allow net-negative emission processes to profit from creating and selling carbon reduction credits within the EU-ETS. This scenario is also included as the basis for techno-economic calculations. It is used to estimate how a change of political regulation with more focus on BCCS could impact profitability.
- Third, a simplified life-cycle assessment is included as an ecological key performance indicator, which sums direct and indirect CO<sub>2</sub>-equivalent emissions. This calculation encompasses a cradle-to-gate scope to compare the radiative forcing impact between the investigated processes.

The techno-economic assessment uses an emission calculation ( $CF_{EU-ETS}$ : Eq. 9) following the current legal framework of the EU-ETS. Annex I of the EU-ETS Directive 2003/87/EC stipulates that processes in which pig iron or steel is produced and which have a capacity exceeding 2.5 tons per hour (approx.



20 kt/a) are subject to the EU-ETS for their carbon dioxide emissions [80]. Article 25 of the Commission Implementing Regulation 2018/2066 in its amended form [81] states: "Under the mass balance methodology, the operator shall calculate the quantity of CO<sub>2</sub> corresponding to each source stream [...] with the fuel's or material's carbon content multiplied by 3.664 t<sub>CO2</sub>/t<sub>C</sub> [..]". The number 3.664 is used in this context because it is the molar mass ratio of CO<sub>2</sub> and carbon. In Paragraph 2 of Article 38, the emission factor of biomass is set to zero, provided Paragraph 5 is considered, rendering the relevant emissions of the entire stream zero. Paragraph 5 refers to "the sustainability and greenhouse gas emissions saving criteria in paragraphs 2 to 7 and 10 of Article 29 of Directive (EU) 2018/2001" that must be fulfilled if biomass is used for combustion and should not be counted as fossil carbon. This work assumes that the wood used for gasification fulfills those sustainability criteria as described in Article 29 of Directive (EU) 2018/2001 ("Renewable Energy Directive") [82]. For simplicity and to have a conservative estimation, all other carbon input streams are assumed to be fossil in origin, and the emission calculation follows Article 25 of 2018/2066 [81].

The transfer of inherent and formed CO<sub>2</sub> from a facility is regulated in Articles 48 and 49 of Regulation 2018/2066 [81]. The transport of inherent CO<sub>2</sub>, such as the carbon content of CDRI after carburization, is not counted as emission if the transfer is to another installation covered by Directive 2003/87/EC. Carbon dioxide, transferred from a plant to a capture installation, a transport network, or a storage site for long-term geological storage, is subtracted from the facility's emissions. However, if the input streams of the facility were already rated zero (as would be in the case that only biomass is used), the transferred inherent and formed CO<sub>2</sub> would also be rated zero. Therefore, the generation of emission certificates through "negative emissions" stemming from BCCS (bioenergy, carbon capture, and storage) is currently not possible within the framework of the EU-ETS [83-85]. The first calculation strategy ( $CF_{EU-ETS}$ ) assumes that all transferred inherent and formed  $CO_2$  in the biomass gasification routes is biogenic and does not reduce the need for emission allowances from using other utilities.

Various authors have discussed the importance and challenges of implementing an option to create CO<sub>2</sub> removal credits into the EU-ETS to create economic benefits [83] while ensuring that permanence and liability questions are addressed [84]. While the "how" is yet unsolved, there seems to be an agreement that carbon dioxide removal, including BCCS, needs to be incentivized to match the IPCC's [1] and EU's [86] proposed decarbonization targets and offset emissions in hard-to-abate sectors. Our work assumes that the regulations would be changed to allow the subtraction of biogenic CO2 and create netnegative emissions within the EU-ETS. This change would reward the plant operator with CO<sub>2</sub> removal credits that could be traded at the same price as emissions allowances within the EU-ETS. The technoeconomic calculations include this case as a second, hypothetical scenario ( $CF_{EU\text{-}ETS,BCCS}$ : **Eq. 10**).

Both calculation methods based on the EU-ETS neglect the indirect upstream emissions of materials and energy entering the process. For this reason, a third  $CO_2$ e footprint calculation is included ( $CF_{LCA}$ : Eq. 11). It is a simplified life cycle assessment with only one impact category that uses mass balance

data and  $CO_2$ -equivalent emission factors ( $f_{CO2e}$ ), similar to the methodology described by the Federal Environmental Agency of Austria (Umweltbundesamt) [87,88]. A cradle-to-gate system boundary was selected, including the upstream emissions of utilities but not the further use of CDRI. This selection allows for the relative comparison of all investigated process routes, assuming that downstream use of CDRI would be equal regardless of ironmaking process choice.

Table 9: Carbon footprint calculation strategie.

$$CF_{EU-ETS} = \frac{\sum_{NG,TEG,MEA,RME} (\dot{m}_{C} \cdot 3.664) - \dot{m}_{C \ in \ CDRI} \cdot 3.664 - \dot{m}_{CO2,CCS,fossil}}{\dot{m}_{CDRI}}$$

$$CF_{EU-ETS,BCCS} = \frac{\sum_{NG,TEG,MEA,RME} (\dot{m}_{C} \cdot 3.664) - \dot{m}_{C \ in \ CDRI} \cdot 3.664 - \dot{m}_{CO2,CCS}}{\dot{m}_{CDRI}}$$

$$CF_{LCA} = \frac{\sum_{all \ streams} (reference \ unit \ flow \cdot f_{CO2e})}{\dot{m}_{CDRI}}$$

$$Eq. \ 10$$

The  $f_{CO2e}$  factors for each stream are calculated as the sum of indirect CO<sub>2</sub>e emissions listed in the ecoinvent database (version 3.10.1) [89] plus the direct CO<sub>2</sub> emissions that would originate from combustion. Additionally, mass balance data are used to calculate negative factors for streams that reduce or offset the sum of the feed-related emissions. These negative factors include the amount of CO2 that is not emitted but captured in the process and sent to transport and storage or is inherently contained in CDRI after carburization. Additionally, the carbon contained in biomass is assumed to originate from the atmosphere and offset the direct biomass emissions. The carbon content of the fuel used in the (LC) and (MC) simulations is slightly different than in the (HC) simulations (Appendix A), which leads to different  $f_{CO2e}$  values.

*Table 10: CO₂e emission factors used for CF<sub>LCA</sub> carbon footprint calculation.* 

Stream	Unit	fc02e	Direct CO <sub>2</sub> emissions by mass balance	Indirect CO <sub>2</sub> e emissions (upstream)	Source
Iron ore pellets	kg <sub>CO2e</sub> /kg <sub>iron ore</sub>	0.103		0.1033	[90]
Triethylene glycol	$ m kg_{CO2e}/kg_{TEG}$	3.968	1.758	2.21	[91]
Monoethanolamine	kg <sub>CO2e</sub> /kg <sub>MEA</sub>	5.827	1.847	3.98	[92]
Rapeseed methyl ester	kg <sub>CO2e</sub> /kg <sub>RME</sub>	5.340	2.840	2.5*	[93]
Olivine	kg <sub>CO2e</sub> /kg <sub>olivine</sub>	0.043		0.0432**	[94]
Biomass (LC/MC)-	kg <sub>CO2e</sub> /kg <sub>dry</sub> wood	1.906	1.861	0.045	[95]
simulations	(LC/MC)				
Biomass (HC)-	kg <sub>CO2e</sub> /kg <sub>dry</sub> wood	1.793	1.748	0.045	[95]
simulations	(HC)				
Electricity	kg <sub>CO2e</sub> /kWh <sub>grid elect.</sub>	0.260		0.26	[96]
Natural gas	kg <sub>CO2e</sub> /m <sup>3</sup> <sub>natural gas</sub>	2.646	2.046	0.6	[97]
CO <sub>2</sub> to storage	kg <sub>CO2e</sub> /kg <sub>CO2 to CCS</sub>	-1.000	-1.000		
Carburization	kg <sub>CO2e</sub> /kg <sub>CDRI</sub>	-0.073	-0.073		
Plant growth	kg <sub>CO2e</sub> /kg <sub>dry</sub> wood	-1.861		-1.861	Mass
(LC/MC)-simulations	(LC/MC)				balance
Plant growth (HC)-	kgco2e/kgdry wood	-1.748		-1.748	Mass
simulations	(HC)				balance

<sup>\*</sup>Data for fatty acid methyl ester.

<sup>\*\*</sup>Data for silica sand.



#### 2.2.3. Economic assessment

The techno-economic assessment (TEA) in this work uses the net present value method to determine the levelized cost of DRI production (LCOP: Eq. 12), which is the cost of producing one unit of product in a new plant [98-100]. This method assesses an investment by introducing a cumulative discount factor (CDF: Eq. 13) to relate the value of future cash flows to the present. LCOP includes the estimated investment costs  $(I_0)$ , expenses (E), and revenues from secondary products (R). Various authors have used this method for cost estimation of biomass-fed gasifier systems [19,41,77].

The process scale is assumed as 1 Mt<sub>CDRI</sub>/a, comparable to the assumption of 1 Mt<sub>steel</sub>/a proposed by Pissot et al. for a similar system [20]. The LCOP calculation includes the investment costs ( $I_0$ : Eq. 14), also referred to as capital expenditure (CAPEX) in this work. The installed costs of equipment at the design size ( $C_{eq,design}$ : Eq. 15) can typically be estimated for a first-of-a-kind plant at this stage with an accuracy of -30 to +50 % using the capacity method [99], for which reference costs are given in Appendix B. The CAPEX estimation for the whole system is calculated as the sum of estimations for each of the main sub-systems described in Sections 2.1.3-2.1.7.

Additionally, this work calculates the emission allowance break-even price (EABEP: Eq. 16) as an additional economic indicator. EABEP is a comparative indicator and describes the emission allowance price for a process to reach cost parity with the NGR-DRI(no CCS) case. If an emission allowance price  $(p_{EA,0})$  other than  $0 \notin t_{CO2}$  was already assumed in the LCOP calculation, this price must be added to calculate EABEP. EABEP<sub>BCCS</sub> is a variation of this indicator that uses  $CF_{EU-ETS,BCCS}$  instead of  $CF_{EU-ETS}$ for the hypothetical scenario where it is possible to generate profit from CO2 removal credits within the EU-ETS.

Table 11: Economic equations and key performance indicators

table 11: Economic equations and key performance indicators	
$LCOP = \frac{I_0 + (E - R) \cdot CDF}{m_{CDRI} \cdot CDF}$	Eq. 12
$CDF = \frac{(1+i)^n - 1}{i \cdot (1+i)^n}$	Eq. 13
$I_0 = \sum_i C_{eq,design,i}$	Eq. 14
$C_{eq,design} = C_{eq,base} \cdot \left(\frac{S_{design}}{S_{base}}\right)^{r} \cdot Z \cdot \frac{CEPCI_{base\ year}}{CEPCI_{2024}}$	Eq. 15
$EABEP = \frac{LCOP_{process} - LCOP_{NG-DRI}}{CF_{EU-ETS,NG-DRI} - CF_{EU-ETS,process}} + p_{EA,0}$	Eq. 16

Operational expenditures (OPEX) that arise during the operation of the plant are distinguished into fixed OPEX and variable OPEX in this work, for which assumptions are given in Table 12. Fixed OPEX is associated with investment costs and depends on the equipment size. Variable OPEX arises from the input and output streams necessary to produce one CDRI unit. The energy prices are based on average data from Austria and Germany from November 2023 to October 2024. Other cost factors were



preferably used from other works on biomass gasification in Austria or Germany and adjusted for Austrian inflation using the consumer price index [101].

The CO<sub>2</sub> transport and storage costs are based on European CCS potentials and a pessimistic transportation range of around 500 km to a suitable storage site [102]. While the average price of CO<sub>2</sub> emission certificates via the European Union Emission Trading System (EU-ETS) was only 67.44 €/t [103] from November 2023 to October 2024, this price is forecast to increase significantly in the coming years [104]. The predicted value for 2030 is 146 €/t<sub>CO2</sub>, which is around halfway between the forecasts for 2025 (80 €/ $t_{CO2}$ ) and 2035 (194 €/ $t_{CO2}$ ) [104]. The forecasted value of 146 €/ $t_{CO2}$  for 2030 is used as  $p_{EA,0}$  over the proposed plant lifetime of 20 years.  $CF_{EU-ETS}$  (Eq. 9) is used to calculate emission allowance costs per ton of produced CDRI. The calculation is instead also performed using  $CF_{EU-ETS,BCCS}$ (Eq. 10) to calculate  $LCOP_{BCCS}$  if a plant operator could economically profit from BCCS by selling  $CO_2$ removal credits within the EU-ETS.

Table 12: Parameters assumed for techno-economic calculations

Net present value calculation	Unit	Value	Source
Nameplate capacity	Mt <sub>CDRI</sub> /a	1000	Assumption based on [20]
Plant lifetime	a	20	[105]
Interest rate	%	6	[106]
Fixed OPEX	Unit	Value	Source
calculation			
Maintenance cost per year	% of CAPEX/a	2.00	[107]
Insurance, administration, and tax per year	% of CAPEX/a	1.50	[19]
Cost of one employee per year	€/a	88000	[19] i.a.*
Operating hours	h/a	8000	[19]
Number of employees	-	25	Assumption based on [19,105]
Variable OPEX	Unit	Cost in €/unit	Source
calculation: expenses			
Wood (35 wt% H <sub>2</sub> O)	$MWh_{LHV}$	28.8**	[37] 1 year average
Natural gas	$MWh_{LHV}$	56.5	[108] 1 year average
Electricity	MWh	74.8	[109] 1 year average
Iron ore pellets	t	104	[110] 1 year average
Rapeseed Methyl Ester	t	1300	[105] i.a.*
Process water	t	2.4	[107] i.a.*
Olivine	t	260	[53] i.a.*
Triethylene glycol	t	1000	Online markets
Monoethanolamine	t	850	Online markets
Cooling water	t	0.06	[111] 1 year average
Ash/olivine landfilling	t	125	[53] i.a.*
Wastewater disposal	t	4	[105] i.a.*
CO <sub>2</sub> transport and storage	t	60	[102]

CO <sub>2</sub> emission price (fossil)	t	146	[104] 2030 forecast
Side revenues	Unit	Cost in €/unit	Source
CO <sub>2</sub> removal credit	t	146	[104] 2030 forecast
District heating	MWh	15	[105] i.a.*

<sup>\*</sup>i.a.=inflation-adjusted (and rounded) from year of cost data to October 2024 based on Austria's consumer price index \*\*Recalculated from a net price of 89.6 €/t using a calculated lower heating value (LHV) of 3.17 MWh/t

### 3. Results and discussion

## 3.1. Mass and energy balancing

#### 3.1.1. Process flows

The central mass and energy streams for the novel biomass CO<sub>2</sub> gasification routes derived from modeling in IPSEpro are presented as Sankey diagrams. All streams are scaled to the base of 1 t of CDRI. Streams under 5 kg or 5 MJ per ton of CDRI, the cooling water, the water recirculated between the CO<sub>2</sub> capture and CO<sub>2</sub> compression sections, and the heat loss streams are omitted from the figures to improve readability. The mass flow of drying air is depicted at a 1:10 scale because it is much larger than the other streams. Figure 4 and Figure 5 compare the main streams between two different BCG-DRI process configurations to highlight some significant differences for illustration. The following chapters, which discuss the results by topic, include data for all BCG-DRI routes (given in Appendix C). These process data are the basis for all technical (3.1), environmental (3.2), and economic (3.3) discussions.

BCG-DRI(AIR,LC) uses air as the combustion agent and has low (15 %) CO<sub>2</sub> conversion during gasification with wood. In contrast, BCG-DRI(OXY,HC) uses an oxygen-enriched flue gas recycle as the combustion agent and has high (89 %) of CO<sub>2</sub> conversion during gasification by reactions with wood char, produced in an intermediate pyrolysis step. This pyrolyzer also produces pyrolysis gas, which is merged with the product gas from gasification. The amount of product gas is significantly higher for the BCG-DRI(AIR,LC) simulation without a pyrolyzer (Figure 4). This difference has multiple reasons: First, more product gas is needed without pyrolysis gas. Second, the product gas from the lowconversion process has a higher CO<sub>2</sub> content so the total gas flow is higher to have a similar CO and H<sub>2</sub> flow. Third, due to higher internal heat demand, more top is fed to combustion for the low-conversion process, and less top gas is available to form new reducing gas. The increased amount of CO<sub>2</sub> flowing to the capture unit also incurs a significantly higher energy demand. The amount of sensible heat needed for the MEA reboiler is around twice as high for the low-conversion process, which also needs to feed a significant amount of top gas to the secondary combustion chamber to cover the sensible heat demand (Figure 5). This energy demand creates a negative feedback cycle, where more top gas is combusted for energy and replaced with more product gas with a high CO<sub>2</sub> content, leading to higher energy demand for carbon capture.



The high demand for internal CO<sub>2</sub> recirculation for the low-conversion process also comes at the cost of available CO2 for transport and storage. No excess CO2 is available for sequestration in the lowconversion process with air as the combustion agent, so there is no CO<sub>2</sub> compression and purification section. Instead, most biogenic CO<sub>2</sub> from this process is vented to ambient air after combustion in the DFB gasifier or the secondary combustion chamber. On the contrary, the high-conversion process with oxy-fuel combustion has two CO<sub>2</sub>-rich streams sent to the compression and purification unit: One stream of excess CO2 from the MEA scrubber (CO2 capture) and, in addition, the flue gas from oxy-fuel combustion, which is mostly CO2 and H2O. Of these two streams, the amount of biogenic CO2 for sequestration from oxy-fuel combustion is higher. Oxy-fuel combustion also makes it possible to send some biogenic CO<sub>2</sub> for sequestration in the low- and medium-conversion processes. This fact is shown in the data in *Appendix C* and further discussed in *Section 3.2*, which discusses process CO<sub>2</sub> emissions.

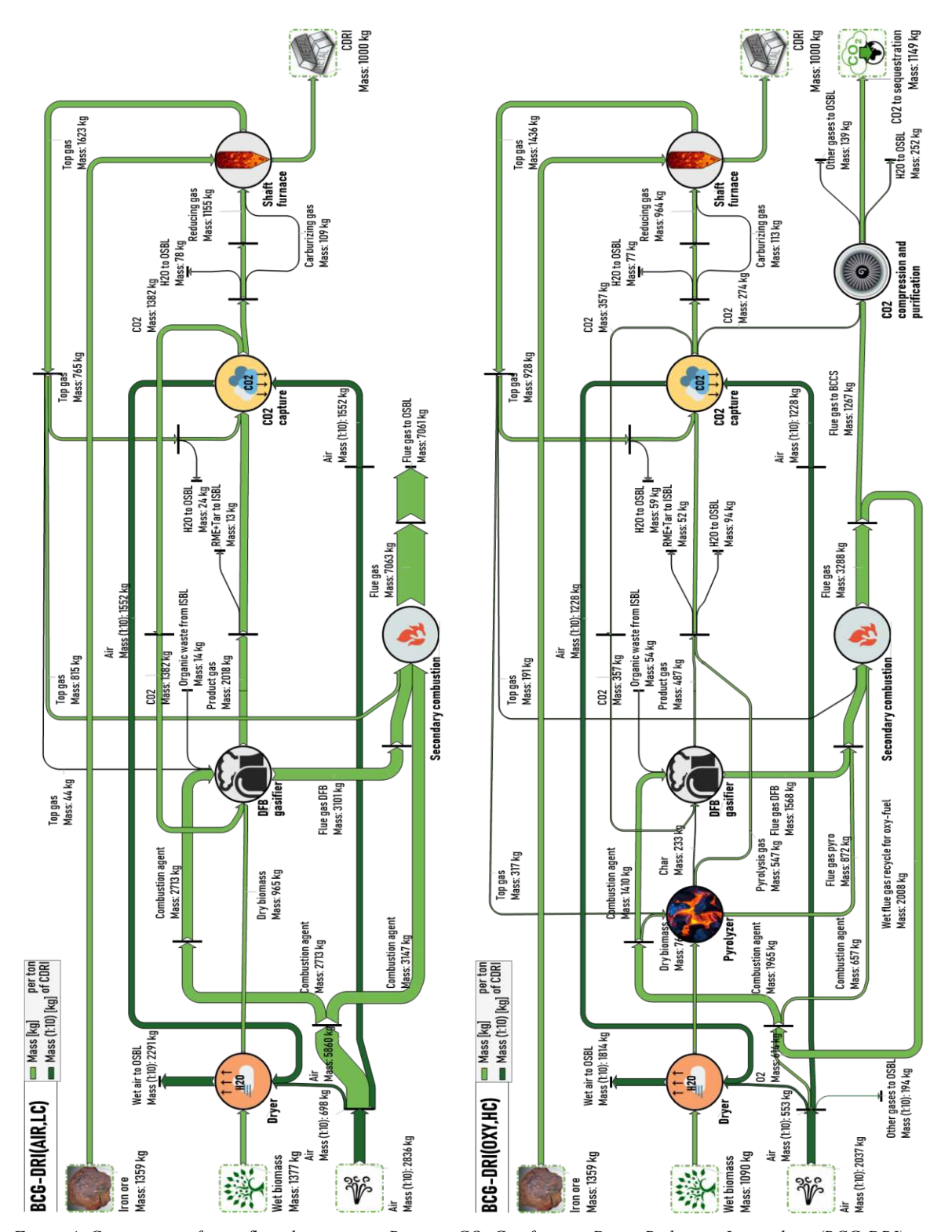


Figure 4: Comparison of mass flows between two Biomass CO2 Gasification-Direct Reduction Ironmaking (BCG-DRI) routes. The processes use air (AIR) or oxygen-enriched flue gas (OXY) for combustion. (LC) and (HC) stand for Low or High Conversion of CO<sub>2</sub> during gasification. SH=Sensible Heat, LHV=Lower Heating Value, ISBL/OSBL=Inside/Outside Battery Limit

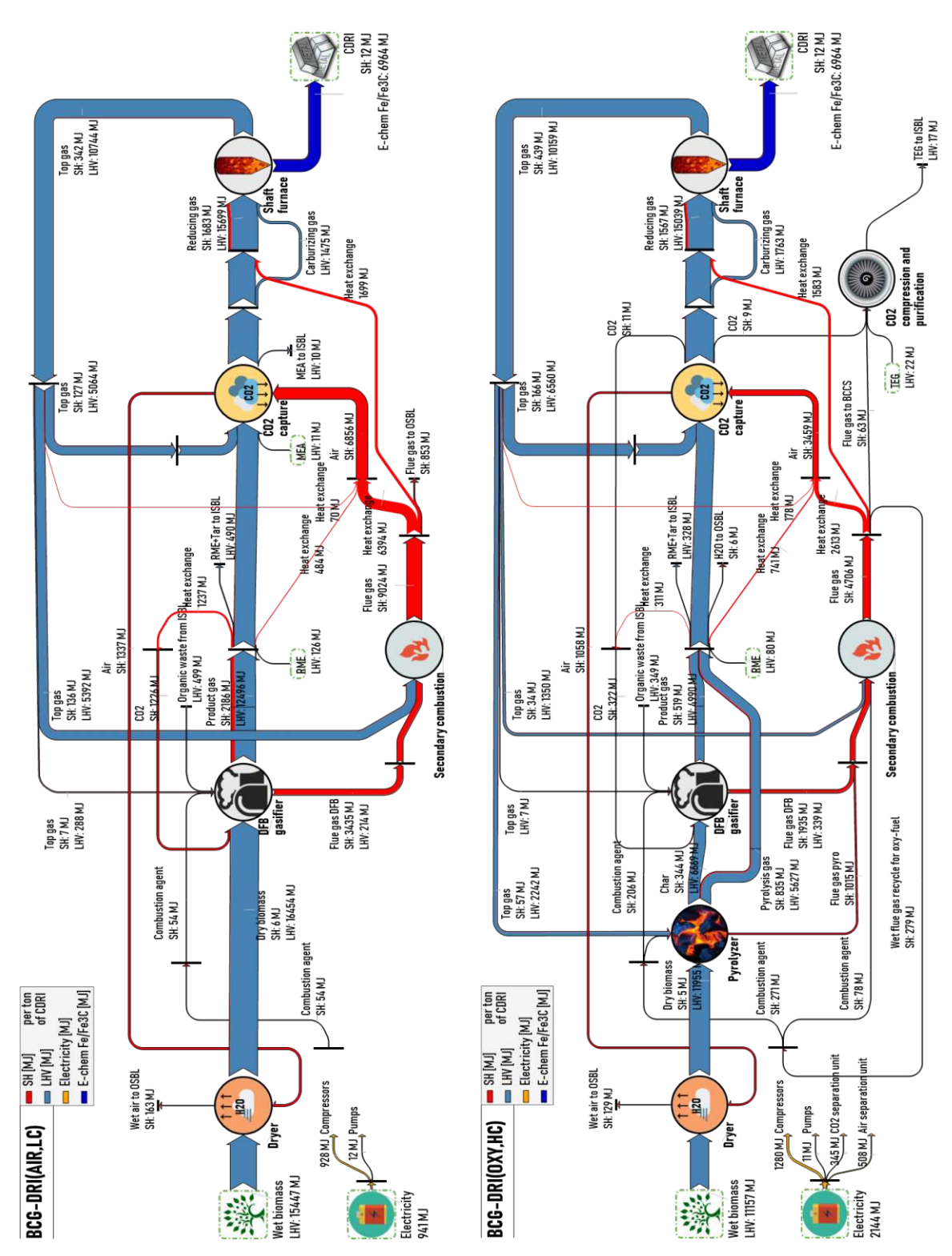


Figure 5: Comparison of energy flows between two Biomass CO2 Gasification-Direct Reduction Ironmaking (BCG-DRI) routes. The processes use air (AIR) or oxygen-enriched flue gas (OXY) for combustion. (LC) and (HC) stand for Low or High Conversion of CO2 during gasification. SH=Sensible Heat, LHV=Lower Heating Value, ISBL/OSBL=Inside/Outside Battery Limit

### 3.1.2. Material and energy efficiency

Technical key performance indicators are summarized for all investigated processes in Table 13. The table also includes the necessary gasifier input power and wood demand per year for the 1 Mt<sub>CDRI</sub>/a design scale to compare with existing DFB gasifiers and biomass potentials. The order of energy

efficiencies of ironmaking  $\eta_{IRON}$  for the biomass gasification routes is (HC)>(MC)>>(LC) with and without oxy-fuel combustion. The difference between (MC) and (LC) is more than 10 %-points despite sharing the same process configuration. This significant difference indicates that high process efficiency is highly correlated with high conversion of CO<sub>2</sub> in the gasifier. The even higher efficiency of the (HC) over (MC) routes suggests the same trend. However, this comparison is less clear-cut as the (HC) routes use a different configuration and include a pyrolyzer.

Including oxy-fuel combustion slightly lowers the biomass demand, but electricity demand for ASU, CSU, and compressors increases significantly. The specific energy demand for carbon capture  $e_{CO2,CAP}$ is lower once oxy-fuel combustion is included, which agrees with the literature [33,34]. Despite these energy savings per unit, the oxy-fuel processes are overall less energy efficient. The decrease in process efficiency is because the total amount of captured CO<sub>2</sub> is significantly higher for the oxy-fuel processes, and, therefore, so is the total energy demand for carbon capture.

Waste heat is internally and wholly used for the biomass gasification routes, and it is almost entirely used for the NGR-DRI(CCS) route. As a result, there is no and respectively little difference between the energy efficiency of ironmaking and the overall process efficiency for these processes. The high overall process efficiency of nearly 80 % for the NGR-DRI(no CCS) case in this study results from assuming waste heat can be utilized for district heating.

Table 13: Energy demand and efficiency for all investigated process routes. PJ/a is equivalent to GJ/tcdrl at the simulated 1 Mtcdri/a plant capacity.

міськуй рійн сара		NGR- DRI	NGR- DRI	BCG- DRI	BCG- DRI	BCG- DRI	BCG- DRI	BCG- DRI	BCG- DRI
		(no CCS)	(CCS)	(AIR, LC)	(OXY, LC)	(AIR, MC)	(OXY, MC)	(AIR, HC)	(OXY, HC)
Total energy efficiency									
$e_{CO2,CAP}$	$MJ/kg_{CO2}$	0.0	4.3	3.9	2.6	3.9	2.3	4.1	2.5
<i>e</i> <sub>IRON</sub>	MJ/kg <sub>CDRI</sub>	11.0	11.1	16.5	18.0	12.6	13.7	12.4	13.4
$\eta_{IRON}$	%	63.5	62.6	42.3	38.7	55.2	50.9	56.3	52.1
$\eta_{TOT}$	%	79.1	63.5	42.3	38.7	55.2	50.9	56.3	52.1
Process size 1 Mt <sub>CDRI</sub> /a									
Wood/NG	$GJ_{LHV}/t_{CDRI}$ = $PJ_{LHV}/a$	10.4	10.4	15.4	14.8	11.7	11.4	11.4	11.1
Electricity	GJ/t <sub>CDRI</sub> =PJ/a	0.5	0.7	0.9	3.1	0.8	2.1	0.9	2.1
DFB product gas output (LHV)	MW			434	434	449	437	177	173

The results can be validated by comparison with other authors' results. Hammerschmid et al. have summarized the energy demands of various iron- and steelmaking routes [19]. Based on their summary, the energy demand for the reducing agent is around 10 GJ/t of crude steel for MIDREX process configurations using natural gas. This number is close to the 10.4 GJ/t<sub>CDRI</sub> calculated in our study. Typically, 3 – 4 MJ/kg<sub>CO2</sub> are reported as the specific energy demand for carbon capture in literature



[112], of which the reboiler duty is the most significant factor needing a minimum of  $1.7 - 4.1 \text{ MJ/kg}_{\text{CO}2}$ for different configurations and assumptions [50]. This work finds 3.9 – 4.3 MJ/kg<sub>CO2</sub> for non-oxy-fuel routes. The numbers in this work include the energy demand for compression and purification to prepare the CO<sub>2</sub> for CCS, which explains why the numbers are towards the higher end of the 3-4 MJ/kg<sub>CO2</sub> range. A significant reduction by several hundred kJ/kg<sub>CO2</sub> would be possible by assuming a 5 °C pinch temperature instead of the more conservative 10 °C proposed by Madeddu et al. [50] in the heat exchanger connecting lean and rich MEA. A 5 °C temperature approach in the heat exchanger would mean that more sensible heat stored in hot lean MEA flowing from the stripper to the absorber would be used to preheat rich MEA. This change would decrease the reboiler duty and put e<sub>CO2,CAP</sub> firmly into the 3-4 MJ/kg<sub>CO2</sub> range for the simulations without oxy-fuel combustion.

The DFB gasifier scale of 173 – 449 MW<sub>LHV</sub> calculated for the production of 1 Mt<sub>CDRI</sub>/a is more extensive than any realized biomass DFB gasifiers to date, of which the GoBiGas plant was the largest at 32 MW biomass power input until its decommissioning in 2018 [113]. In techno-economic studies published by the research groups connected to the GoBiGas plant [114] and gasifier development at TU Wien [77], DFB gasifiers with 100-200 MW have been discussed as target commercial scales. This scale would match the calculation results of the BCG-DRI(HC) plants. It has to be noted that the biomass demand for these routes is similar to the biomass demand for the BCG-DRI(MC) routes because of the additional biomass demand for the pyrolyzer.

Various studies have reported on the reduced technical biomass potential in 2050 in Austria [77,115– 117], which can be understood as the amount that does not endanger sustainable agriculture and forestry practices and can be made available by societal and political measures [77]. For 2050, these studies have reported the reduced technical potential for biomass gasification feedstocks at 50 – 126 PJ/a of woody biomass, 80 - 200 PJ/a of agricultural raw materials and residues, and 10 - 67 PJ/a of other organic residues and waste. These estimates can be combined with the biomass demand identified in this work for the investigated biomass gasification routes to calculate how much CDRI could theoretically be produced. At 11.1 – 15.4 PJ<sub>wood</sub>/(a·Mt<sub>CDRI</sub>) and the given reduced technical biomass potentials,  $3.2-11.3~\mathrm{Mt_{CDRI}/a}$  could be produced from woody biomass and  $9.1-35.3~\mathrm{Mt_{CDRI}/a}$  from all biomass sources. The World Steel Association reported Austria's pig iron production and apparent consumption in 2023 as 5.5 Mt [118]. Transport limitations and biomass competition from other technologies will likely reduce biomass availability for ironmaking from the high-end of the calculated availabilities. Nevertheless, these results indicate that reduced technical biomass potentials in Austria in 2050 are large enough to replace a significant share of Austria's pig iron production by the investigated biomass CO<sub>2</sub> routes.

#### 3.1.3. Reducing gas composition

The composition of reducing streams to the DRI shaft is summarized for all process routes in Table 14. Additional data for carburizing gas and top gas compositions are available in Appendix D. The optional inclusion of oxy-fuel combustion in the biomass CO<sub>2</sub> gasification routes and a MEA scrubber in the natural gas comparison process have nearly no consequences on these streams.

All biomass gasification processes show higher RP values than NGR-DRI, meaning iron reduction is thermodynamically feasible with all investigated processes. The reducing gas from biomass gasification has a much lower H<sub>2</sub>O content than in the NGR-DRI case. While the reducing gas is not cooled between the reformer and the DRI shaft in the NGR-DRI case, most water is removed in a condenser between the MEA scrubber and the DRI shaft for the biomass gasification routes. The MEA scrubber's position in the BCG-DRI cases also results in the removal of most CO<sub>2</sub> from the gas, increasing RP. The CO<sub>2</sub> content in the reducing gas is lower for the (MC) and (HC) and higher for the (LC) routes compared to NGR-DRI. This discrepancy is caused by the low CO<sub>2</sub> conversion and high product gas flow rates for the (LC) simulations, coupled with a CO<sub>2</sub> capture efficiency of only 90 %. The higher conversion and lower product gas flow rates result in reduced CO<sub>2</sub> contents in the reducing gas for the (MC) and (HC) routes. This reduction in CO<sub>2</sub> content results in RP values of 25 and more for BCG-DRI(MC) and BCG-DRI(HC), clearly surpassing the BCG-DRI(LC) and NGR-DRI cases.

The reducing gas flow and H<sub>2</sub>:CO ratios are significantly lower in all biomass gasification processes. The endothermic iron reduction with hydrogen demands a larger sensible heat supply in the DRI shaft, which increases the demand for hot reducing gas at higher H2:CO ratios. Lowering the reducing gas flow rate lowers the compression energy and can help decrease equipment size. The H<sub>2</sub>:CO ratios between 0.46 and 0.68 for the biomass gasification processes are in the range reported as ideal for carburization [28]. This result suggests that it is valid to use these reducing gases as carburization gas. Furthermore, the low H<sub>2</sub>:CO ratios from biomass gasification and exothermic iron ore reduction reaction with CO suggest that these processes should face fewer heat distribution problems than H<sub>2</sub>-DRI pathways [16]. These values are also much lower than the 1.31 [18] to 4.0 [20] reported for processes with steam gasification, demonstrating that CO<sub>2</sub> gasification could be uniquely advantageous compared to other biomass gasification technologies for ironmaking due to the lower sensible heat demand in the shaft furnace and higher potential for carburization.

Table 14: Reducing gas compositions used as feed for the DRI shaft furnace

Process		NGR-	NGR-	BCG-	BCG-	BCG-	BCG-	BCG-	BCG-
route		DRI							
		(no	(CCS)	(AIR,	(OXY,	(AIR,	(OXY,	(AIR,	(OXY,
		CCS)		LC)	LC)	MC)	MC)	HC)	HC)
Flow rate	Nm³/	1720	1717	1232	1232	1177	1187	1180	1187
	$(h \cdot t_{CDRI})$								
CO	vol%	30.0%	30.0%	59.8%	59.8%	58.6%	58.2%	55.1%	54.8%
$CO_2$	vol%	4.8%	4.8%	5.8%	5.8%	2.8%	2.9%	2.5%	2.6%
$H_2$	vol%	52.6%	52.6%	27.3%	27.3%	32.2%	32.8%	37.2%	37.5%
$H_2O$	vol%	4.7%	4.7%	0.7%	0.7%	0.7%	0.7%	0.7%	0.7%
$CH_4$	vol%	7.8%	7.8%	6.3%	6.3%	5.5%	5.3%	3.4%	3.3%
Rest	vol%	0.2%	0.2%	0.2%	0.2%	0.2%	0.2%	1.1%	1.1%
H <sub>2</sub> :CO	mol/mol	1.75	1.75	0.46	0.46	0.55	0.56	0.67	0.68
RP	mol/mol	8.74	8.74	13.47	13.47	25.76	25.49	28.80	28.53

# 3.2. CO<sub>2</sub> and CO<sub>2</sub>-equivalent process emissions

Process CO<sub>2</sub> and CO<sub>2</sub>e emissions are summarized in *Figure 6*, as calculated by the three strategies discussed in Section 2.2.2. Regardless of the calculation strategy, all biomass CO<sub>2</sub> gasification processes show lower emissions than the NGR-DRI(no CCS) case. The same is true for comparing BCG-DRI with the NGR-DRI(CCS) case, which reduces the emissions from the NGR-DRI case by installing a carbon capture system with 90 % separation efficiency. For the techno-economy, the relevant calculations are  $CF_{EU-ETS}$  and  $CF_{EU-ETS,BCCS}$ , while  $CF_{LCA}$  aims to compare the climate change contribution of the processes.

 $CF_{EU\text{-}ETS}$ , which does not allow the creation of CO<sub>2</sub> removal credits from BCCS, is positive for all routes. Consequently, all investigated process routes must pay for CO<sub>2</sub> emission allowances under current EU-ETS rules. However, the BCG-DRI routes need around 80 % less emission allowances than the NGR-DRI(CCS) case and around 98 % less than the NG-DRI(no CCS) case.

CF<sub>EU-ETS,BCCS</sub> assumes that creating CO<sub>2</sub> removal credits from BCCS would be possible. This would not change anything for the NGR-DRI cases, which do not use a biogenic carbon feedstock. In contrast, all BCG-DRI routes would be eligible for generating CO<sub>2</sub> removal credits and need no more CO<sub>2</sub> emission allowances. Creating CO<sub>2</sub> removal credits would offer an alternative revenue stream for the BCG-DRI processes. Without oxy-fuel combustion, the BCG-DRI(HC) process is the only route that could generate more than 100 kg<sub>CO2</sub>/t<sub>CDRI</sub> in removal credits. Including oxy-fuel combustion in the three investigated (OXY) routes allows for capturing CO<sub>2</sub> from combustion and generating more than 1,000 kg<sub>CO2</sub>/t<sub>CDRI</sub> in removal credits each.

The  $CF_{LCA}$  calculation includes direct  $CO_2$  emissions and indirect upstream emissions of  $CO_2$  and other substances contributing to radiative forcing, e.g., methane leaks from pipelines and fossil fuel consumption during iron ore pellet preparation. The data reveal that the consumption of natural gas, electricity, and iron ore contributes the most to global warming. The direct emissions from biomass use are even higher but nearly offset by biomass capturing CO<sub>2</sub> from the atmosphere during growth. CO<sub>2</sub>

sequestration lowers emissions for all processes that include CCS, and carburization stores some carbon in the CDRI product. The results show that all three (OXY) processes and the BCG-DRI(AIR,HC) route reach net-negative emissions due to the permanent sequestration of biogenic CO<sub>2</sub>. Including biogenic carbon capture and storage in the flue gas allows the (OXY) routes to reach significant net-negative emissions of -910 to -1,227 kg<sub>CO2e</sub>/t<sub>CDRI</sub>. These net-negative emissions could make such an ironmaking process an asset in the global struggle to meet net-zero emissions goals because it can be used to offset hard-to-abate emissions elsewhere.

The results also show that the proposed change to the EU-ETS, which aims at strengthening BCCS processes economically ( $CF_{EU-ETS,BCCS}$ ), would bring the results closer to the  $CF_{LCA}$  calculation for the processes with significant net-negative emissions. However, the actual CO<sub>2</sub>e emissions would be systematically underestimated. The reason for this is not BCCS-specific but is rooted in the different accounting scope. The scope 1 accounting approach of the EU-ETS also leads to an underestimation of the actual radiative forcing for the NGR-DRI cases because indirect emissions from electricity and material supply are neglected.

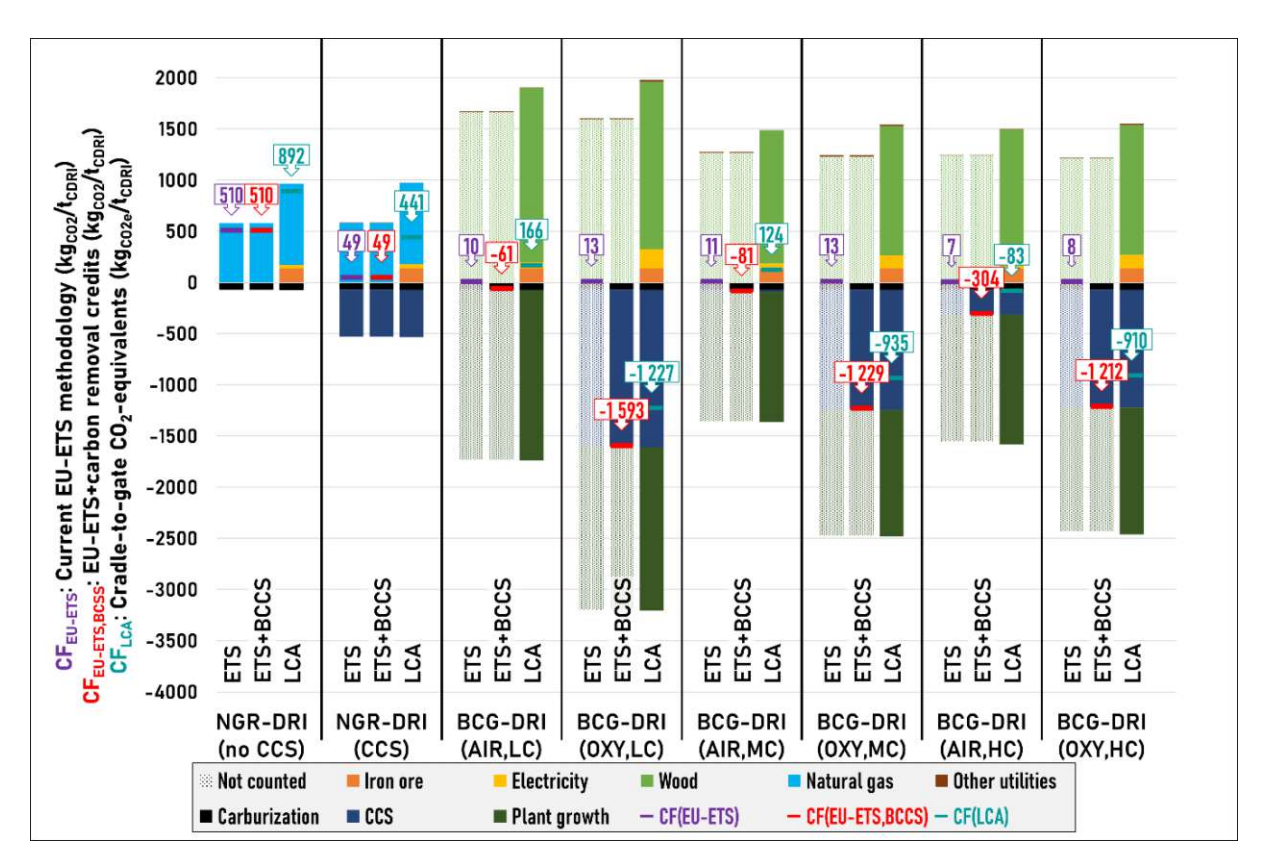


Figure 6: Comparison of emissions for each process by different calculation schemes: CF<sub>EU-ETS</sub> (first column for each process route, purple) follows current EU-ETS emission accounting, CF<sub>EU-ETS,BCCS</sub> (second column, red) extends EU-ETS accounting by the option to generate CO<sub>2</sub> removal credits from biogenic carbon capture and storage, CF<sub>LCA</sub> (third column, turquoise) includes direct CO2 emissions and cradle-to-gate CO2-equivalent emissions based on data from the ecoinvent database. The data labels refer to the total net values, which include both the (counted) positive and negative contributions.



### 3.3. Economics

#### 3.3.1. CAPEX estimation

The CAPEX estimations for the proposed process scale of 1 Mt<sub>CDR1</sub>/a are summarized in *Table 15*. The presented estimations include installation and auxiliary equipment, and each is the average of multiple estimations using data from different sources. The total CAPEX of the NGR-DRI(no CCS) process is lowest at 204 M€. The biomass gasification routes were calculated to 520 – 988 M€, a 155 – 385 % increase over the NGR-DRI(no CCS) case. The increase also means that CAPEX-related costs constitute a larger share of the levelized cost of production for biomass gasification than for the natural gas routes (Figure 7). The numbers agree in order of magnitude with the CAPEX estimations by Pissot et al., who reported 760 – 1000 M€ for similar biomass gasification-direct reduced ironmaking concepts in 2021 [20]. Their simulations were for a 1 Mt<sub>steel</sub>/a plant with steam gasification including an EAF but no oxyfuel combustion or pyrolyzer.

Adding carbon capture as in an MEA scrubber in the NGR-DRI(CCS) case constitutes an increase of around 50 % for a total of 315 M€. Costs for the MEA scrubber are similar for the BCG-DRI(MC) and BCG-DRI(HC) cases, which have low CO<sub>2</sub> content in the product gas. The BCG-DRI(LC) process has significantly higher flow rates and, therefore, higher CAPEX for the MEA scrubber. This high CAPEX results from the low CO<sub>2</sub> conversion in the gasifier, which results in a high CO<sub>2</sub> pump-around.

The DFB system, which includes the two reactors, the biomass dryer, coarse gas cleaning, secondary combustion chamber, and other auxiliary equipment, is the most expensive part of every simulated biomass gasification process. The BCG-DRI(HC) routes show cost advantages in the DFB gasifier since part of the biomass is processed in the pyrolyzer instead. Processing some biomass in the pyrolyzer appears advantageous to minimize CAPEX, as the combined CAPEX of the pyrolyzer and the DFB system for the (HC) configurations is lower than the DFB CAPEX alone for the alternative process configurations.

The air separation and cryogenic CO<sub>2</sub> purification units included in the oxy-fuel cases increase CAPEX by another 173 – 215 M€. This increase could also be considered an optimistic estimation since no structural changes required for the use of oxy-fuel combustion in the DFB system were included in the CAPEX estimation.

Table 15: CAPEX estimations for a plant producing 1 Mtcdri/a.

All data in M€	NGR-	NGR-	BCG-	BCG-	BCG-	BCG-	BCG-	BCG-
	DRI (no	DRI (CCS)	DRI (AIR,	DRI (OXY,	DRI (AIR,	DRI (OXY,	DRI (AIR,	DRI (OXY,
	CCS)	(CCS)	LC)	LC)	MC)	MC)	HC)	HC)
Shaft furnace	66.7	66.7	66.7	66.7	66.7	66.7	66.7	66.7
NG reformer	137.6	137.7						
MEA scrubber		111.1	214.3	214.3	125.9	129.4	124.2	126.5
ASU				95.4		150.9		149.3
CO <sub>2</sub> purification				77.9		64.5		63.6
Pyrolyzer							49.8	49.0
DFB system			523.3	523.3	536.3	525.7	279.7	275.3
SUM	204.3	315.4	804.4	977.7	728.9	937.3	520.3	730.4

## 3.3.2. Levelized cost of production

The most impactful LCOP drivers under base scenario assumptions are shown in Figure 7 for all simulated routes. The investigated biomass CO<sub>2</sub> gasification routes without oxy-fuel combustion show an LCOP reduction of -5 % to -16 % compared to the NGR-DRI(no CCS) process, even if not considering the option to profit from BCCS. In the hypothetical "BCCS profit"-scenario, the oxy-fuel processes are even more profitable at LCOP reductions of -23 % to -33 % compared to NGR-DRI(no CCS).

Iron ore and fuel (wood or natural gas) are the most expensive categories of LCOP drivers at these assumptions. Iron ore costs the same for each process. Fuel costs are correlated with process efficiency and price per energy unit, where wood is cheaper than natural gas. CAPEX, electricity, and other OPEX per ton of CDRI are higher for the BCG-DRI routes because the processes involve more unit operations than the NGR-DRI simulations.

The CO<sub>2</sub> disposal cost shown in Figure 7 summarizes the cost of emission allowances within the EU-ETS and the cost of transport and storage for captured CO<sub>2</sub> sent to storage. At 90 % CO<sub>2</sub> capture rate in the MEA scrubber, 146 €/t<sub>CO2</sub> for emission allowances and 60 €/t<sub>CO2</sub> for transport and storage, this reduces the CO<sub>2</sub> disposal costs for the NGR-DRI(CCS) case by around 50 % compared to NGR-DRI(no CCS). However, adding more carbon capture increases the CAPEX, electricity demand, and other OPEX, e.g., the cost of fresh MEA. Based on our calculations, including carbon capture and storage in a NGR-DRI process with these assumptions would still be economically profitable, although not by much (-3 % LCOP).

Since emissions from biomass use are considered exempt from buying CO<sub>2</sub> allowances based on the legislation in the EU-ETS (explained in Section 2.2.2), the depicted CO<sub>2</sub> disposal costs for the biomass routes only result from the costs of transport and storage for BCCS. The cases without oxy-fuel combustion emit most of the produced CO2 and only store a small fraction, leading to low CO2 disposal costs. These costs are much higher for the simulated oxy-fuel cases since they also capture and store CO<sub>2</sub> from the flue gas. Other OPEX, CAPEX, and especially electricity costs per ton of CDRI are also much higher for the oxy-fuel cases since they need additional energy for air and CO<sub>2</sub> separation, as well

as CO<sub>2</sub> compression. Therefore, in the current EU-ETS scenario, where no opportunity to profit from BCCS exists, including oxy-fuel combustion to generate net-negative emissions only increases the cost of production. In fact, under current legislation, every BCG-DRI route would be able to reduce costs further by releasing any captured CO<sub>2</sub> into the air instead of paying for transport and storage. However, if BCCS could be monetized, these process routes would be 8 -17 % cheaper than the comparable routes without oxy-fuel combustion. CO<sub>2</sub> emission allowance pricing is further discussed in **Section 3.3.3**.

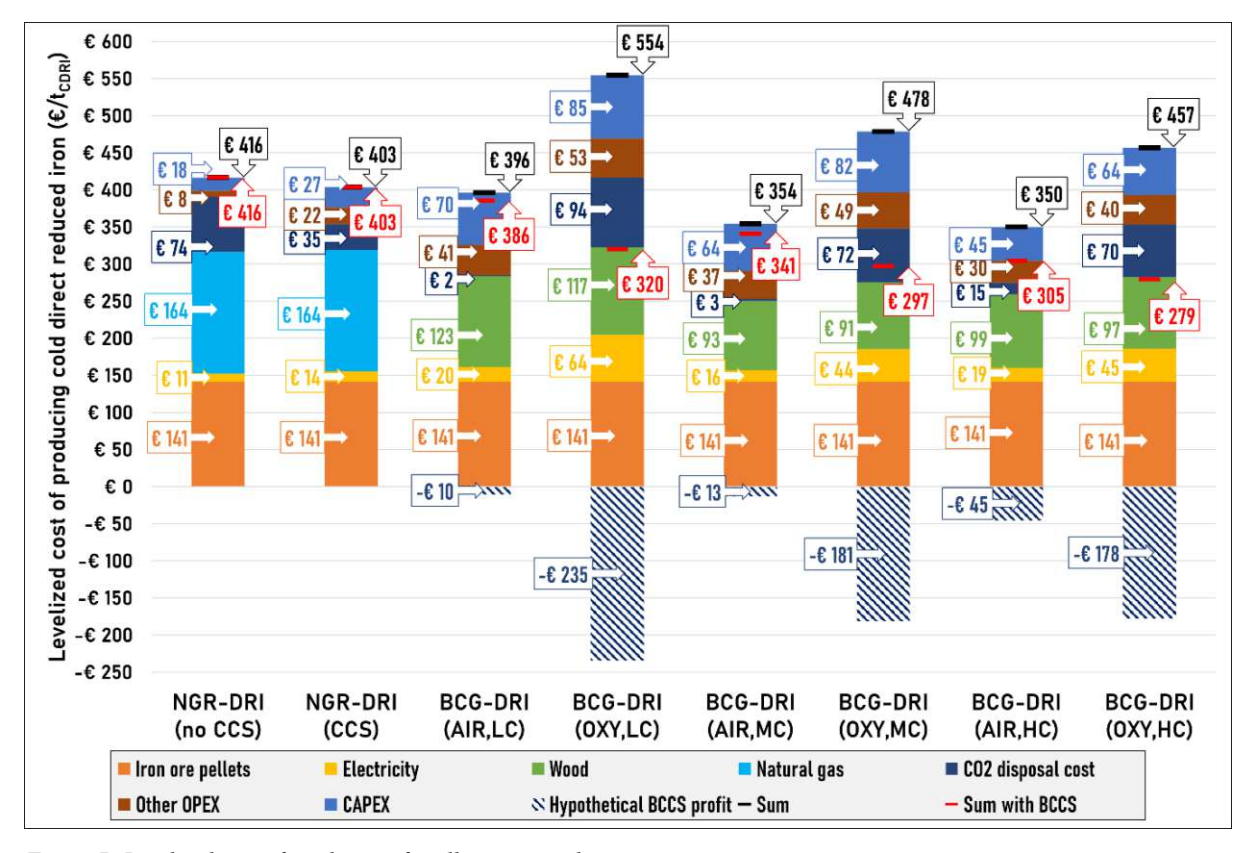


Figure 7: Levelized cost of production for all investigated process routes

The effects of changing the cost assumptions for various parameters are shown in sensitivity analysis plots. Sensitivity analysis plots for the NGR-DRI(no CCS) and the BCG-DRI(AIR,HC) case are compared in Figure 8 and discussed here. Plots for all process routes are available in Appendix E. Figure 8 confirms the high significance of iron ore pellets, natural gas, and wood pricing for LCOP. The pricing of emission allowances is significant for the NGR-DRI(no CCS) process, which emits fossil CO<sub>2</sub>. In contrast, LCOP is sensitive to fluctuations in CAPEX cost and operating hours for the BCG-DRI processes, which have much higher investment costs.

Iron ore pellet demand and pricing are the same for each route, and fluctuations affect all processes equally. The natural gas costs in Austria have increased significantly since 2021 and were around double the average from 2018-2020 in the first half of 2024 [108]. This work uses the price average of the last year, which is around 30 % lower than the historic maximum reported in the second half of 2022 following Russia's invasion of Ukraine. This example shows that geopolitical factors strongly influence natural gas prices. Since natural gas price deviation shows the highest effect on LCOP for the NGR-DRI

process, the total cost for the NGR-DRI processes can vary heavily by region and over time. Comparatively, wood prices have been more stable in middle Europe recently [37], likely because biomass is typically supplied via more diversified and local supply chains, which are less prone to external geopolitical factors. However, the local supply chains can also lead to significant regional price differences [119]. The net biomass price used in this work is around 30 % higher than the price average between 2018-2020. This more modest increase compared to natural gas is very noticeable in the LCOP calculation, as wood costs per ton of CDRI are lower than natural gas costs for all investigated biomass gasification routes despite the higher process efficiency for the NGR-DRI routes.

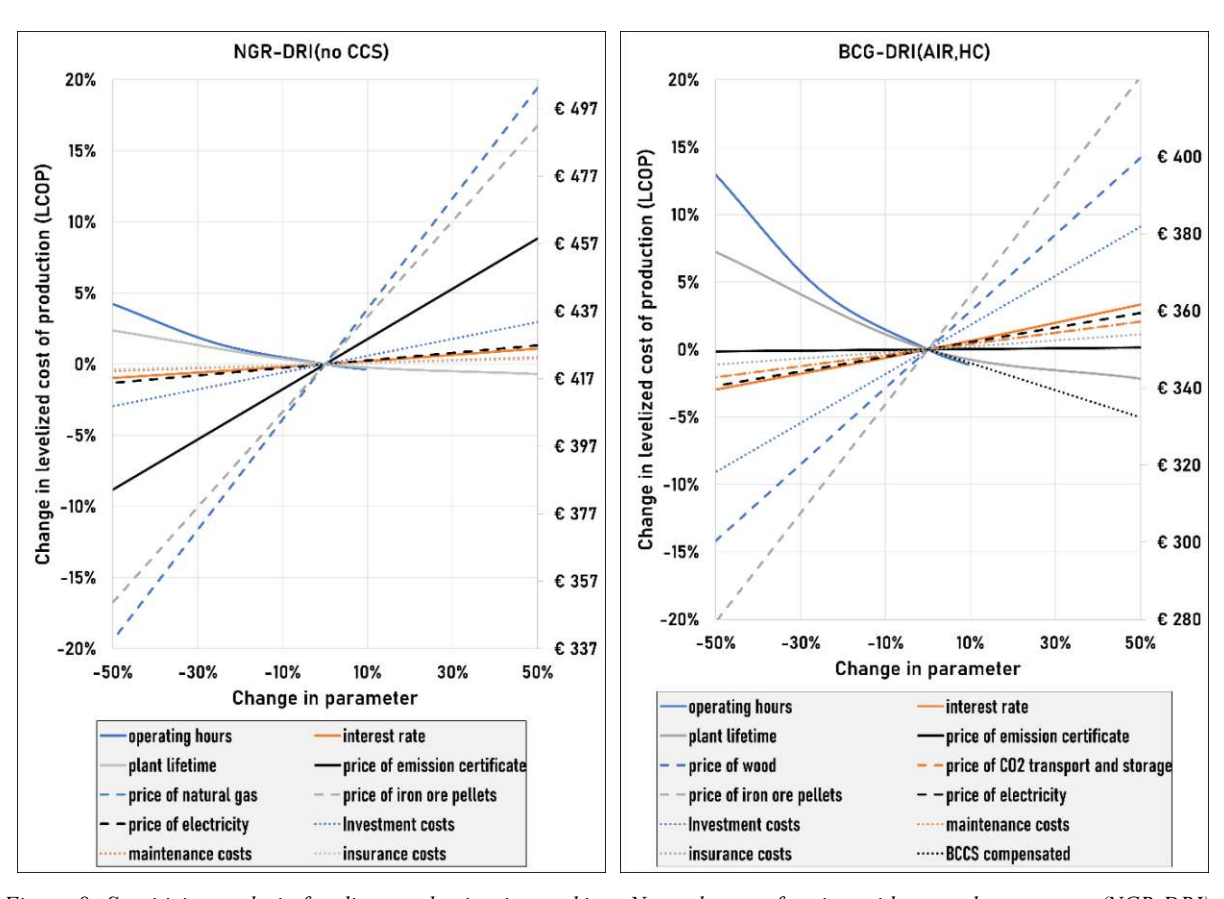


Figure 8: Sensitivity analysis for direct reduction ironmaking: Natural gas reforming without carbon capture (NGR-DRI) versus biomass CO2 gasification with air as combustion agent and high CO2 conversion "BCG-DRI(AIR,HC)"

### 3.3.3. CO<sub>2</sub> emission allowance pricing

The emission allowance break-even price (EABEP, Figure 9) is the CO<sub>2</sub> certificate price at which a process can be profitable in the EU-ETS framework. In principle, the EABEP expresses how much economic incentive in the EU-ETS is necessary to make it profitable to reduce one ton of CO<sub>2</sub> emissions by replacing the high-emission NGR-DRI(no CCS) process with one of the lower-emission processes. For the NGR-DRI(CCS) route, these costs are around 118 €/t<sub>CO2</sub>, which is between the price forecasts for 2025 and 2030 [104]. EABEP<sub>BCCS</sub>, which contains a hypothetical economic profit from creating and



selling CO<sub>2</sub> removal credits, is the same as EABEP for the NGR-DRI(CCS) route since no biogenic CO<sub>2</sub> is created or stored.

EABEP and EABEP<sub>BCCS</sub> differ significantly between biomass gasification routes. All BCG-DRI processes have negative  $CF_{EU-ETS,BCCS}$  and can profit from selling  $CO_2$  removal credits, which is why EABEP<sub>BCCS</sub> is lower than EABEP for all biomass gasification routes. This relative difference is more pronounced if the amount of CO<sub>2</sub> stored per ton of CDRI is higher, which affects the (OXY) routes the most.

In the current EU-ETS scenario, BCCS creates costs for capture, transport, and storage, but brings no economic benefit. As a result, EABEP for the oxy-fuel routes, which also store CO<sub>2</sub> from flue gas, is very high at 227 – 424 €/t<sub>CO2</sub>. These numbers are even higher than the 2035 forecast [104]. The results would change if the oxy-fuel processes would profit from creating net-negative emissions, putting EABEP<sub>BCCS</sub> for these routes between the emission allowance price in 2024 and the 2030 forecast [104]. The increased amount of CO<sub>2</sub> stored via BCCS in the oxy-fuel routes helps these processes profit more substantially once the actual emission price clears EABEP<sub>BCCS</sub>. This higher deployment leads to lower LCOP values for the oxy-fuel routes than the (AIR) routes in the BCCS-profit scenario based on the given assumptions (Figure 7). A downside of the more substantial BCCS deployment of the oxy-fuel routes is their need to cover more CO<sub>2</sub> transport and storage costs. In contrast, the biomass gasification routes without oxy-fuel combustion utilize BCCS less and, therefore, show less reliance on emission allowance pricing and the profitability of BCCS. The process efficiency of the BCG-DRI(MC) and BCG-DRI(HC) scenarios and the economic advantages of using wood instead of natural gas make these routes already economically favorable compared to the NGR-DRI(no CCS) route at 2024's emission allowance price.

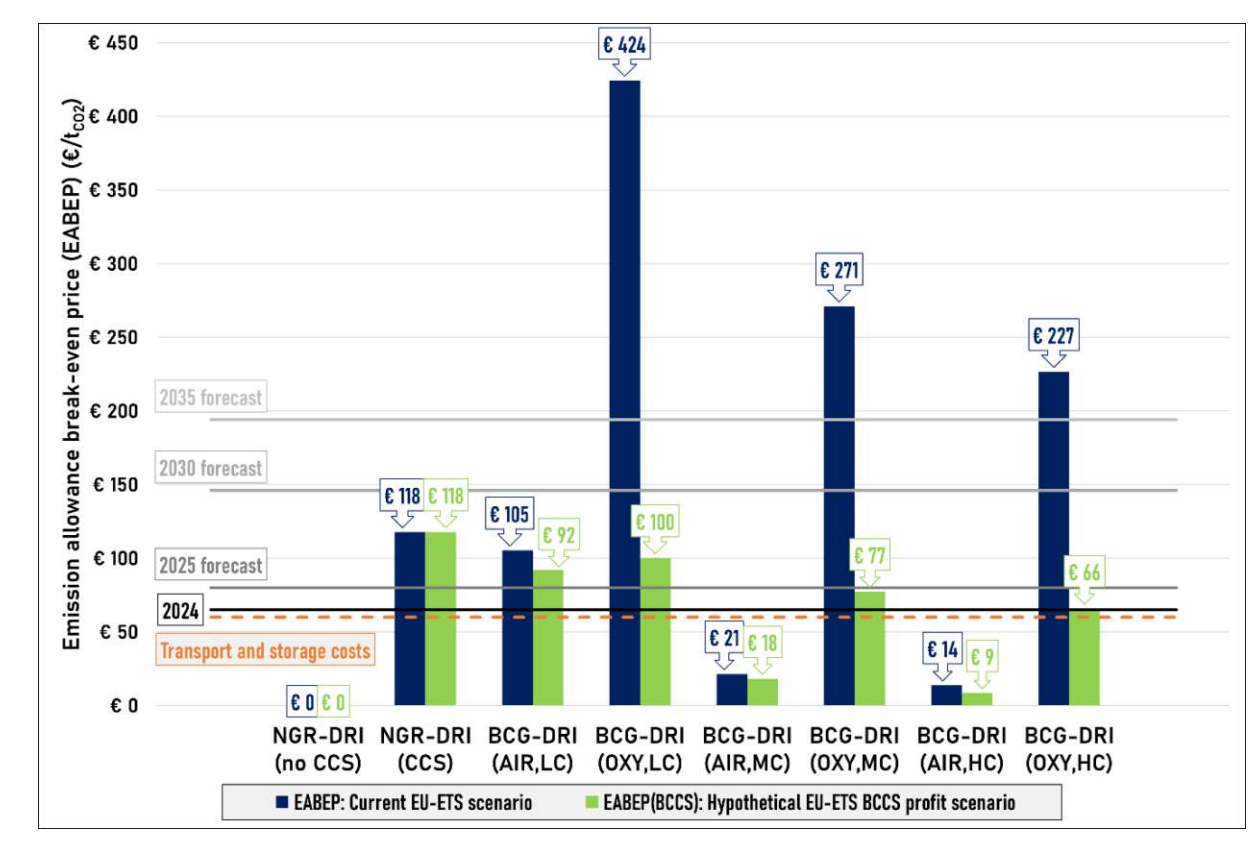


Figure 9: Emission allowance break-even price for all process routes with the base scenario NGR-DRI. Emission allowance cost forecasts are based on a BloombergNEF survey [104]. Transport and storage costs assume around 500 km transportation

# 4. Comparison of the investigated biomass CO<sub>2</sub> gasification routes

The main economic (LCOP, LCOP<sub>BCCS</sub>) and ecological ( $CF_{LCA}$ ) KPIs investigated in this work are combined in Figure 10 for the six investigated BCG-DRI process routes to identify overall trends regarding the main differentiating features: a) CO<sub>2</sub> conversion in the gasifier and b) choice of combustion technology.

Higher CO<sub>2</sub> conversions in the gasifier are found to improve five of the six depicted KPIs, including economic KPIs and, for the cases using air as a combustion agent, also the CO2-equivalent process emissions. The only value negatively impacted (it increases) is  $CF_{LCA}$  in the case of oxy-fuel combustion. These trends are correlated with process efficiency, which was discussed in Section 3.1.2. The decrease in CO<sub>2</sub> concentration in the gasification product gas at higher CO<sub>2</sub> conversion values means that less CO<sub>2</sub> needs to be captured in the MEA scrubber, which reduces the reboiler duty. Overall, this effect reduces energy and material demand, which benefits the techno-economy. This decrease in material demand is also the reason for the increase in CO<sub>2</sub>e emissions from processes with oxy-fuel combustion at higher CO<sub>2</sub> conversion: The decreased demand for biomass at more efficient operation means less biogenic CO<sub>2</sub> is formed, which can be stored for net-negative emissions.

The efficiency increase, and therefore the improvement of five KPIs, is more pronounced for the first increase in CO<sub>2</sub> conversion from (LC) to (MC), which uses the same unit operations. While including the pyrolyzer in the (HC) simulations further lowers the CO<sub>2</sub> concentration in the product gas, it also induces additional CO<sub>2</sub> to be captured from the pyrolysis gas. Overall, the total capture demand is slightly lowered, and the (HC) configuration is a slight overall process efficiency increase, positively influencing the economic and emission KPIs. Based on these trends, it seems clear that process design should aim for efficient CO<sub>2</sub> conversion in the gasifier, likely even if this necessitates the inclusion of a pyrolyzer as an additional unit operation for biomass pretreatment.

The inclusion of oxy-fuel combustion is more complicated to assess overall. A clear advantage is that these routes offer the option for significant net-negative CO<sub>2</sub>e emissions. If carbon removal credits economically incentivized these net-negative emissions, this would also bring economic advantages making the choice to include oxy-fuel combustion clear. However, there is no such incentive under current EU-ETS rules, and the oxy-fuel routes are much more expensive than the routes with air as a combustion agent. For this reason, a sensible strategy could be to target a plant with air as a combustion agent first and prepare for plant design adjustments enabling oxy-fuel combustion later if the political/economic framework changes.

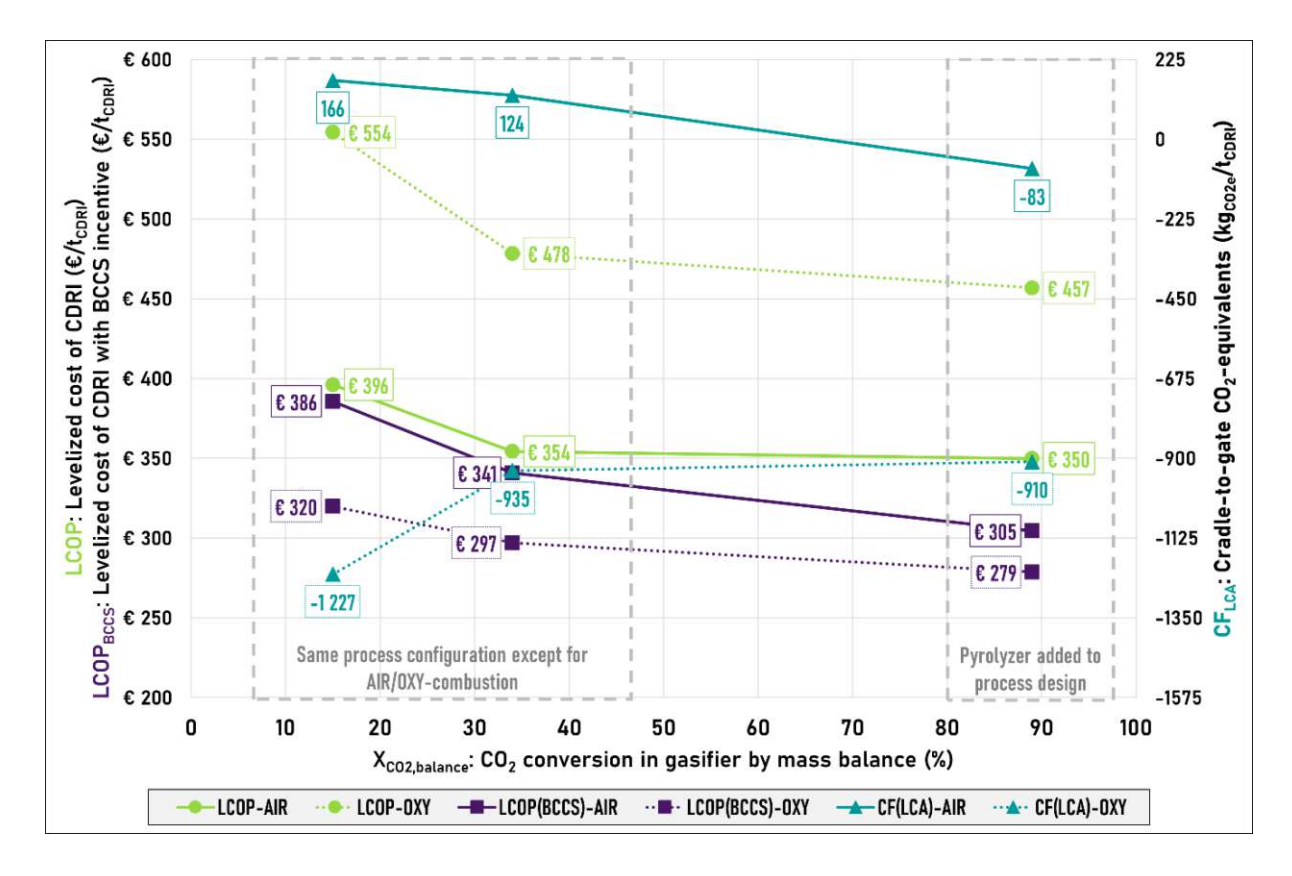


Figure 10: Economic and ecological trends observed for the six investigated biomass CO2 gasification - direct reduction ironmaking process routes.

## 5. Conclusion

Previous studies have investigated biomass gasification as an option to produce reducing gas for the direct reduction ironmaking process. These studies showed that biomass gasification has the technical potential to fulfill DRI process requirements while potentially creating below-zero CO<sub>2</sub> emissions. However, none of these previous studies have investigated biomass gasification with CO<sub>2</sub> as a gasification agent. This new work provides a first holistic description of biomass CO2 gasification's integration into ironmaking.

The study contains mass and energy balance data calculated in the process simulation software IPSEpro 8.0. Six biomass CO<sub>2</sub> gasification process routes for ironmaking were proposed and compared with two routes using natural gas reforming. All biomass CO<sub>2</sub> gasification processes and one variant of the natural gas case include carbon capture. These cases assume the captured CO2 would be compressed and transported to permanent sequestration. The main findings of this study are:

- Reducing gas quality: All proposed biomass CO<sub>2</sub> gasification processes provide reducing gas at a higher reduction potential (13-28) than in the comparison process with natural gas (9). Furthermore, the reducing gas has a higher CO content. This high CO content could prove beneficial for temperature control and carburization in the DRI reactor, especially if compared to H<sub>2</sub>-DRI with pure hydrogen.
- Energy efficiency: The process efficiency of ironmaking, relating the chemical change in the ferrous phase to the total process input power, was found to be 38.7 - 56.3 % for the biomass CO<sub>2</sub> gasification routes. The natural gas process was calculated at 63.5 % without carbon capture and 62.6 % with carbon capture. Higher CO<sub>2</sub> conversion in the gasifier correlated with higher process efficiency. This correlation was stark when comparing the low-conversion and medium-conversion simulations, which had the same process configuration but more than 10 % points difference in efficiency. Oxy-fuel combustion lowered process efficiency by around 4 % points due to additional electrical demand for air and CO<sub>2</sub> separation and compressors.
- CO<sub>2</sub>-equivalent emissions: Calculations resulted in significantly lower emissions for the biomass-based processes than the natural gas process, and could even result in net-negative emissions. The natural case with and without carbon capture had CO2 emissions of 441 – 892 kg<sub>CO2e</sub>/t<sub>CDRI</sub>. The biomass CO<sub>2</sub> gasification routes without oxy-fuel combustion sharply reduced CO<sub>2</sub>e emissions to 166 kg<sub>CO2e</sub>/t<sub>CDRI</sub> at low CO<sub>2</sub> conversion and further down to -83 kg<sub>CO2e</sub>/t<sub>CDRI</sub> at high conversion. Oxy-fuel combustion, capturing CO<sub>2</sub> in the flue gas that originated from biomass, further decreased these emissions and resulted in net-negative emissions of -910 to -1,227 kg<sub>CO2e</sub>/t<sub>CDRI</sub>.
- Levelized cost of production: The reduction in emissions by EU-ETS calculation is also one of the main factors for pushing the levelized cost of producing (LCOP) cold DRI via biomass CO<sub>2</sub>



gasification below the cost of the natural gas process. The other main factor for biomass CO<sub>2</sub> gasification's low LCOP is the low price of wood compared to natural gas in Austria. LCOP was found to decrease at higher CO<sub>2</sub> conversion. When using carbon emission price allowance predictions for 2030, 350 €/t<sub>CDRI</sub> were found for the biomass CO<sub>2</sub> gasification process with high conversion, compared to 416 €/t<sub>CDRI</sub> for the natural gas case without carbon capture. Emission allowance break-even calculations showed that biomass CO<sub>2</sub> gasification processes are already cheaper than the natural gas process at 2024's emission allowance price.

- Biomass availability: A comparison with Austria's reduced technical biomass potential forecast in 2050 revealed that biomass CO<sub>2</sub> gasification could replace a sizeable part of Austria's ironmaking production from woody biomass alone.
- Incentives for net-negative emission technologies: Capturing, transporting, and storing biogenic CO<sub>2</sub> brings additional costs and is not compensated under current EU-ETS legislation. Based on this work, the EU-ETS would need to allow for the creation and trading of CO2 removal credits to make sequestrating captured biogenic CO<sub>2</sub> profitable. If it were possible to generate CO<sub>2</sub> removal credits and sell them at the emission allowance price, this work would find the oxy-fuel processes to be the most profitable due to their significant net-negative emissions.

A limitation of this study is that it had to use process data from various sources and scales. For many variables, e.g., heat loss of specific units, no data were available, and the estimations introduce uncertainty. Consequently, the promising results of this study should be grounds for future research that tries to combine the proposed processes experimentally and increase the technological readiness level of the overall process. A key aspect is the experimental validation of a combined pyrolysis-biomass CO<sub>2</sub> gasification process, as simulated in the BCG-DRI(HC) route based on various literature sources. Another aspect that was simplified in this study and warrants experimental investigation is the dependence of CDRI characteristics based on product gas composition and temperature. If experimental validations are promising, biomass CO<sub>2</sub> gasification could be a key technology in future ironmaking.

These results suggest that biomass CO<sub>2</sub> gasification has vast potential for application in ironmaking. It offers the chance to create net-negative emissions and is cheaper than the natural gas comparison process. This combination of economic and ecological advantages is crucial because it can help the industry to decarbonize while remaining competitive. Based on this work's results, a new plant should strive to reach a high conversion of CO<sub>2</sub> in the gasifier, as this brings advantages in key areas like process efficiency and production costs.

# Nomenclature

m 11	1/	m ·	7
Inhlo	10.	Termi	$n \cap l \cap m$
1 uoic	10.	10111111	ioiozv

Abbreviation	Term
ASU	Air Separation Unit
BCCS	Biogenic Carbon Capture and Storage
BCG	Biomass CO2 Gasification
BF	Blast Furnace
BOF	Basic Oxygen Furnace
CAPEX	CAPital EXpenditure
CCS	Carbon Capture and Storage
CDRI	Cold Direct Reduced Iron
CSU	CO <sub>2</sub> Separation Unit
DFB	Dual Fluidized Bed
DRI	Direct Reduction Ironmaking, Direct Reduced Iron
EAF	Electric Arc Furnace
EU-ETS	European Union Emission Trading Scheme
НС	High conversion of CO <sub>2</sub> in gasifier
IEA	International Energy Agency
IPCC	Intergovernmental Panel on Climate Change
ISBL	InSide Battery Limit
LC	Low Conversion of CO <sub>2</sub> in gasifier
LHV	Lower Heating Value
MC	Medium Conversion of CO <sub>2</sub> in gasifier
MEA	Mono-EthanolAmine
NGR	Natural Gas Reforming
OECD	Organization for Economic Co-operation and Development
OPEX	OPerational EXpenditure
OSBL	OutSide Battery Limit
OXY	OXY-fuel combustion
RME	Rapeseed Methyl-Ester
TEG	TriEthylene Glycol

#### Table 17: Math

10000 17.1110000		
Symbol	Parameter description	Unit
CDF	Cumulative discount factor	-
CEPCI	Chemical engineering plant cost index	-
$C_{eq,design}$	Installed equipment cost at the design size	€
$CF_{EU ext{-}ETS}$	Carbon footprint following current EU-ETS methodology	kg <sub>CO2</sub> /t <sub>CDRI</sub>
$CF_{EU}$	Carbon footprint following EU-ETS methodology with	
ETS,BCCS	opportunity to create CO <sub>2</sub> removal credits from BCCS	$kg_{CO2}/t_{CDRI}$
$CF_{LCA}$	Carbon footprint by simplified life cycle assessment	$kg_{CO2e}/t_{CDRI}$
E	Expenses	€
<i>EABEP</i>	Emission allowance break-even price	€/t <sub>CO2</sub>
$e_{CO2,CAP}$	Specific energy demand for carbon capture	J/kg <sub>CO2</sub>
$e_{IRON}$	specific energy demand for reduction per mass unit of CDRI	$J/kg_{CDRI}$
$f_{CO2e}$	CO <sub>2</sub> -equivalent emission factor	kg <sub>CO2e</sub> /kg <sub>reference unit</sub>
i	Interest rate	%
$I_0$	Investment costs, also referred to as CAPEX	€
LCOP	Levelized cost of production	€/t <sub>CDRI</sub>
ṁ	Mass flow	kg/s
n	Amount of substance	mol
$P_{ASU}$	Electrical demand for air separation unit	W



Ş	
ē	
문	hub
Ö	agpa
픙	owle
☵	urk
m	۶
	z

	Electrical demand for auxiliary equipment related to carbon	
$P_{CCS ext{-}AUX}$	capture	W
$P_{CSU}$	Electrical demand for CO <sub>2</sub> separation unit	W
$p_{EA,0}$	Base scenario price of CO <sub>2</sub> allowances	€/t <sub>CO2</sub>
$P_{EL,TOT}$	Total electrical power demand	W
$\dot{Q}_{RB}$	Reboiler heat duty	W
R	Revenue for secondary products	€
r	Scale factor	-
RP	Reduction Potential	mol/mol
S	Equipment size	-
Z	Overall installation factor	-
$\Delta \dot{H}_{DH}$	Enthalpy change between district heating feed and drain	W
$\Delta \dot{H}_{IRON}$	Enthalpy change from iron ore to CDRI	W

# CRediT authorship contribution statement

Florian Johann Müller: Conceptualization, data curation, formal analysis, investigation, methodology, project administration, software, supervision, validation, visualization, writing – original draft, writing – review & editing

Stefan Jankovic: Formal analysis, methodology, software, visualization, writing – review & editing

Josef Fuchs: Conceptualization, funding acquisition, project administration, resources, supervision, writing – review & editing

Diana Dimande: Methodology, writing - review & editing

Stefan Müller: Funding acquisition, resources, supervision, writing – review & editing

Franz Winter: Funding acquisition, resources, supervision, writing – review & editing

# **Declaration of competing interest**

The authors declare no conflict of interest.

# Data availability

Data were shared with reviewers and will be made public upon manuscript acceptance.

# **Acknowledgments**

This study was carried out within the doctoral college  $CO_2Refinery$  at TU Wien. The authors acknowledge TU Wien Bibliothek for financial support through its Open Access Funding Programme.

## Literature

- [1] IPCC. Climate Change 2022: Mitigation of Climate Change. Contribution of Working Group III to the Sixth Assessment Report of the Intergovernmental Panel on Climate Change. Cambridge: Cambridge University Press; 2022. https://doi.org/10.1017/9781009157926.
- World Steel Association (worldsteel). "worldsteel Short Range Outlook October 2023" 2023. [2]
- IEA, IRENA, UN Climate Change High-Level Champions. Breakthrough Agenda Report 2023. [3] Paris: 2023.
- Nakamizu M. Latest developments in steelmaking capacity and outlook until 2026. 2024. [4]
- [5] Worrell E, Biermans G. Move over! Stock turnover, retrofit and industrial energy efficiency. Energy Policy 2005;33:949–62. https://doi.org/10.1016/j.enpol.2003.10.017.
- [6] World Steel Association (worldsteel). Scrap use in the steel industry - Fact sheet 2021.
- [7] Direct Reduced Iron (DRI) International Iron Metallics Association n.d. https://www.metallics.org/dri.html (accessed October 15, 2024).
- [8] Midrex Technologies Inc. MIDREX® Process - Midrex Technologies, https://www.midrex.com/technology/midrex-process/ (accessed October 15, 2024).
- [9] Trinca A, Patrizi D, Verdone N, Bassano C, Vilardi G. Toward green steel: Modeling and environmental economic analysis of iron direct reduction with different reducing gases. J Clean Prod 2023;427. https://doi.org/10.1016/j.jclepro.2023.139081.
- [10] Nurdiawati A, Zaini IN, Wei W, Gyllenram R, Yang W, Samuelsson P. Towards fossil-free steel: Life cycle assessment of biosyngas-based direct reduced iron (DRI) production process. J Clean Prod 2023;393:136262. https://doi.org/10.1016/j.jclepro.2023.136262.
- [11] Yu B, Dai Y, Fu J, Qi J, Li X. Industrial risks assessment for the large-scale development of electric arc furnace steelmaking technology. Appl Energy 2025;377. https://doi.org/10.1016/j.apenergy.2024.124611.
- Benavides K, Gurgel A, Morris J, Mignone B, Chapman B, Kheshgi H, et al. Mitigating [12] emissions in the global steel industry: Representing CCS and hydrogen technologies in integrated assessment modeling. International Journal of Greenhouse Gas Control 2024;131. https://doi.org/10.1016/j.ijggc.2023.103963.
- Iron & steel IEA n.d. https://www.iea.org/energy-system/industry/steel#tracking (accessed [13] October 16, 2024).

- Emirates Steel Arkan -Investor Presentation 2023. [14]
- India's Energy Mix & Power Sector Overview n.d. https://iced.niti.gov.in/energy (accessed [15] October 16, 2024).
- [16] Shahabuddin M, Brooks G, Rhamdhani MA. Decarbonisation and hydrogen integration of steel industries: Recent development, challenges and technoeconomic analysis. J Clean Prod 2023;395:136391. https://doi.org/10.1016/j.jclepro.2023.136391.
- Bürgler T, Di Donato A. Biomass gasification for DRI production. La Revue de Métallurgie [17] 2009. https://doi.org/10.1051/metal/2009075.
- [18] Zaini IN, Nurdiawati A, Gustavsson J, Wei W, Thunman H, Gyllenram R, et al. Decarbonising the iron and steel industries: Production of carbon-negative direct reduced iron by using biosyngas. Energy Convers Manag 2023;281:116806. https://doi.org/10.1016/j.enconman.2023.116806.
- Hammerschmid M, Müller S, Fuchs J, Hofbauer H. Evaluation of biomass-based production of [19] below zero emission reducing gas for the iron and steel industry. Biomass Convers Biorefin 2021;11:169–87. https://doi.org/10.1007/s13399-020-00939-z.
- [20] Pissot S, Thunman H, Samuelsson P, Seemann M. Production of negative-emissions steel using gasification. dfb Energies reducing gas derived from (Basel) 2021;14. https://doi.org/10.3390/en14164835.
- Kieush L, Lesiak S, Rieger J, Leitner M, Schmidt L, Daghagheleh O. Reoxidation Behavior of [21] the Direct Reduced Iron and Hot Briquetted Iron during Handling and Their Integration into Steelmaking: A Review. Metals Electric Arc Furnace (Basel) 2024;14. https://doi.org/10.3390/met14080873.
- Müller FJ, Fuchs J, Müller S, Winter F. CO2 conversion to CO by fluidized bed biomass [22] gasification: Measuring CO2 utilization via stable carbon isotope ratios. Journal of CO2 Utilization 2024;83. https://doi.org/10.1016/j.jcou.2024.102792.
- Müller FJ, Fuchs J, Fanjul Cuesta M, Oblanca Gutiérrez A, Pratschner S, Müller S, et al. CO2 [23] conversion to CO by fluidized bed biomass gasification: Analysis of operational parameters. Journal of CO2 Utilization 2024;81. https://doi.org/10.1016/j.jcou.2024.102706.
- [24] Mauerhofer AM. Carbon Utilization by Application of CO2 Gasification. Dissertation. Technische Universität Wien, 2020.
- Chan YH, Syed Abdul Rahman SNF, Lahuri HM, Khalid A. Recent progress on CO-rich syngas [25] production via CO2 gasification of various wastes: A critical review on efficiency, challenges

- **Pollution** and outlook. Environmental 2021;278:1-16. https://doi.org/10.1016/j.envpol.2021.116843.
- Lahijani P, Zainal ZA, Mohammadi M, Mohamed AR. Conversion of the greenhouse gas CO2 [26] to the fuel gas CO via the Boudouard reaction: A review. Renewable and Sustainable Energy Reviews 2015;41:615–32. https://doi.org/10.1016/j.rser.2014.08.034.
- [27] Béchara R, Hamadeh H, Mirgaux O, Patisson F. Optimization of the iron ore direct reduction through multiscale modeling. Materials 2018;11:1-18. process process https://doi.org/10.3390/ma11071094.
- [28] Ali ML, Fradet Q, Riedel U. Kinetic Mechanism Development for the Direct Reduction of Single Hematite **Pellets** H2/CO Atmospheres. Steel Res 2022;93. Int https://doi.org/10.1002/srin.202200043.
- Mauerhofer AM, Müller S, Bartik A, Benedikt F, Fuchs J, Hammerschmid M, et al. Conversion [29] of CO2 during the DFB biomass gasification process. Biomass Convers Biorefin 2021;11:15-27. https://doi.org/10.1007/s13399-020-00822-x.
- [30] Forms of DRI - Midrex Technologies, Inc. n.d. https://www.midrex.com/technology/directreduced-iron/forms-of-dri/ (accessed December 13, 2024).
- Perz E. A computer method for thermal power cycle calculation. Proceedings of the ASME [31] Turbo Expo 1990;4. https://doi.org/10.1115/90-GT-351.
- [32] Pröll T, Hofbauer H. Development and application of a simulation tool for biomass gasification processes. International Journal of Chemical Reactor Engineering https://doi.org/10.2202/1542-6580.1769.
- [33] Habib MA, Nemitallah M, Ben-Mansour R. Recent development in oxy-combustion technology and its applications to gas turbine combustors and ITM reactors. Energy and Fuels 2013;27:2-19. https://doi.org/10.1021/ef301266j.
- [34] Xu G, Liang F, Yang Y, Hu Y, Zhang K, Liu W. An improved CO2 separation and purification system based on cryogenic separation and distillation theory. Energies (Basel) 2014;7:3484-502. https://doi.org/10.3390/en7053484.
- [35] Supplementary Material Towards fossil-free steel: Life cycle assessment of biosyngas-based direct reduced iron (DRI) production process Anissa Nurdiawati 2018.
- Learn About Natural Gas | Enbridge Gas n.d. https://www.enbridgegas.com/about-enbridge-[36] gas/learn-about-natural-gas (accessed October 5, 2023).



- C.A.R.M.E.N. n.d. [37] Marktpreise Hackschnitzel e.V. https://www.carmenev.de/service/marktueberblick/marktpreise-energieholz/marktpreise-hackschnitzel/ (accessed November 12, 2024).
- [38] Primär- und Sekundärnetze - e-genius n.d. https://www.e-genius.at/mooc/smart-cities-teil-2/woche-7-waerme-und-kaeltenetze-1/714-beispiel-fernwaerme-wien/primaer-undsekundaernetze (accessed October 29, 2024).
- Wien Energie. TR 2013 Technische Auslegungsbedingungen | Wien Energie 2013. [39]
- [40] Zeymer M, Herrmann A, Oehmichen K, Schmersah R, Schneider R, Heidecke P, et al. Kleintechnische Biomassevergasung - Option für eine nachhaltige und dezentrale Energieversorgung. 2013.
- [41] Gubin V, Benedikt F, Thelen F, Hammerschmid M, Popov T, Hofbauer H, et al. Hydrogen production from woody biomass gasification: a techno-economic analysis. Biofuels, Bioproducts and Biorefining 2024;18:818–36. https://doi.org/10.1002/bbb.2647.
- [42] Parisi DR, Laborde MA. Modeling of counter current moving bed gas-solid reactor used in direct reduction of iron ore. Chemical Engineering Journal 2004;104:35-43. https://doi.org/10.1016/j.cej.2004.08.001.
- Shams A, Moazeni F. Modeling and Simulation of the MIDREX Shaft Furnace: Reduction, [43] Transition and Cooling Zones. Jom 2015;67:2681–9. https://doi.org/10.1007/s11837-015-1588-0.
- [44] Skorianz M. Classification of iron ores regarding their reduction behaviour in fluidized bed technologies. Dissertation. Montanuniversität Leoben, 2012.
- [45] Da Rocha EP, De Castro JA, Silva L, De Souza Caldas R. Computational analysis of the performance of shaft furnaces with partial replacement of the burden with self-reducing pellets containing biomass. Materials Research 2020;22. https://doi.org/10.1590/1980-5373-MR-2019-0533.
- Liu BN, Li Q, Zou ZS, Yu AB. Discussion on chemical energy utilisation of reducing gas in [46] Steelmaking 2014;41:568-74. reduction shaft furnace. Ironmaking and https://doi.org/10.1179/1743281213Y.0000000168.
- Patisson F, Mirgaux O, Birat JP. Hydrogen steelmaking. Part 1: Physical chemistry and process [47] metallurgy. Materiaux et Techniques 2021;109:1-10. https://doi.org/10.1051/mattech/2021025.

- Farhadi F, Motamed Hashemi MY, Bahrami Babaheidari M. Modelling and simulation of syngas [48] unit in large scale direct reduction plant. Ironmaking and Steelmaking 2003;30:18-24. https://doi.org/10.1179/030192303225009515.
- [49] Carbon Capture & Use - Midrex Technologies, Inc. n.d. https://www.midrex.com/carboncapture-use/ (accessed October 30, 2024).
- [50] Madeddu C, Errico M, Baratti R. CO2 Capture by Reactive Absorption-Stripping. Modeling, Analysis and Design. 1st ed. Cham: SpringerBriefs in Energy; 2019. https://doi.org/10.1007/978-3-030-04579-1 2.
- Bielka P, Kuczyński S, Nagy S. CO2 Compression and Dehydration for Transport and [51] Geological Storage. Energies (Basel) 2023;16. https://doi.org/10.3390/en16041804.
- [52] Hrdlicka J, Vodička M, Skopec P, Hrdlička F, Dlouhý T. CO2 Separation, Purification and Conversion to Chemicals and Fuels - Chapter 5: CO2 Capture by Oxyfuel Combustion. Singapore: Springer; 2019.
- [53] Müller S. Hydrogen from biomass for industry - industrial application of hydrogen production based on dual fluid gasification. Dissertation. Technische Universität Wien, 2013.
- [54] Pearce JK, Dawson GKW, Law ACK, Biddle D, Golding SD. Reactivity of micas and cap-rock in wet supercritical CO2 with SO2 and O2 at CO2 storage conditions. Applied Geochemistry 2016;72:59–76. https://doi.org/10.1016/j.apgeochem.2016.06.010.
- [55] Ahmad AA, M. Saaid I, Muhammad MA, Husein N, Zaidin MF, Mohamad Sabil K. Physical and chemical effect of impurities in carbon capture, utilisation and storage. J Pet Explor Prod Technol 2023;13:1235–46. https://doi.org/10.1007/s13202-023-01616-3.
- [56] Hua Y, Jonnalagadda R, Zhang L, Neville A, Barker R. Assessment of general and localized corrosion behavior of X65 and 13Cr steels in water-saturated supercritical CO2 environments with SO2/O2. International Journal of Greenhouse Gas Control 2017;64:126-36. https://doi.org/10.1016/j.ijggc.2017.07.012.
- Zheng Q, Zhou S, Lail M, Amato K. Oxygen Removal from Oxy-Combustion Flue Gas for CO2 [57] Purification via Catalytic Methane Oxidation. Ind Eng Chem Res 2018;57:1954-60. https://doi.org/10.1021/acs.iecr.7b04577.
- Walspurger S, Dijk H a. J Van. EDGAR CO2 purity: type and quantities of impurities related to [58] CO2 point source and capture technology: a Literature study 2012:48.

- [59] Kim I, Hoff KA, Mejdell T. Heat of absorption of CO2 with aqueous solutions of mea: New experimental data. Energy Procedia https://doi.org/10.1016/j.egypro.2014.11.154. [60]
- Moser P, Schmidt S, Sieder G, Garcia H, Stoffregen T. Performance of MEA in a long-term test at the post-combustion capture pilot plant in Niederaussem. International Journal of Greenhouse Gas Control 2011;5:620–7. https://doi.org/10.1016/j.ijggc.2011.05.011.

2014;63:1446-55.

- Gonzalez-Garza D, Rivera-Tinoco R, Bouallou C. Comparison of ammonia, monoethanolamine, [61] diethanolamine and methyldiethanolamine solvents to reduce CO2 greenhouse gas emissions. Chem Eng Trans 2009;18:279–84. https://doi.org/10.3303/CET0918044.
- [62] Hamelinck CN. Outlook for advanced Biofuels. Dissertation. Universiteit Utrecht, 2004.
- [63] Sahoo K, Upadhyay A, Runge T, Bergman R, Puettmann M, Bilek E. Life-cycle assessment and techno-economic analysis of biochar produced from forest residues using portable systems. International Life Cycle Journal Assessment 2021;26:189–213. https://doi.org/10.1007/s11367-020-01830-9.
- Zimmer T, Rudi A, Glöser-Chahoud S, Schultmann F. Techno-Economic Analysis of [64] Intermediate Pyrolysis with Solar Drying: A Chilean Case Study. Energies (Basel) 2022;15. https://doi.org/10.3390/en15062272.
- [65] Solar J, de Marco I, Caballero BM, Lopez-Urionabarrenechea A, Rodriguez N, Agirre I, et al. Influence of temperature and residence time in the pyrolysis of woody biomass waste in a continuous screw reactor. **Biomass** Bioenergy 2016;95:416–23. https://doi.org/10.1016/j.biombioe.2016.07.004.
- [66] Neves D, Thunman H, Matos A, Tarelho L, Gómez-Barea A. Characterization and prediction of pyrolysis Combust Sci 2011;37:611-30. biomass products. Prog Energy https://doi.org/10.1016/j.pecs.2011.01.001.
- [67] Campuzano F, Brown RC, Martínez JD. Auger reactors for pyrolysis of biomass and wastes. Renewable Sustainable Reviews 2019;102:372-409. and Energy https://doi.org/10.1016/j.rser.2018.12.014.
- Bagatini MC, Kan T, Evans TJ, Strezov V. Iron Ore Reduction by Biomass Volatiles. Journal of [68] Sustainable Metallurgy 2021;7:215–26. https://doi.org/10.1007/s40831-021-00337-3.
- [69] Benedikt F, Kuba M, Schmid JC, Müller S, Hofbauer H. Assessment of correlations between tar and product gas composition in dual fluidized bed steam gasification for online tar prediction. Appl Energy 2019;238:1138–49. https://doi.org/10.1016/j.apenergy.2019.01.181.



- Kirnbauer F, Hofbauer H. The mechanism of bed material coating in dual fluidized bed biomass [70] steam gasification plants and its impact on plant optimization. Powder Technol 2013;245:94-104. https://doi.org/10.1016/j.powtec.2013.04.022.
- Koppatz S, Pfeifer C, Hofbauer H. Comparison of the performance behaviour of silica sand and [71] olivine in a dual fluidised bed reactor system for steam gasification of biomass at pilot plant Chemical 2011:175:468-83. scale. Engineering Journal https://doi.org/10.1016/j.cej.2011.09.071.
- Mauerhofer AM, Benedikt F, Schmid JC, Fuchs J, Müller S, Hofbauer H. Influence of different [72] bed material mixtures on dual fluidized bed steam gasification. Energy 2018;157:957-68. https://doi.org/10.1016/j.energy.2018.05.158.
- Yao X, Yu Q, Han Z, Xie H, Duan W, Qin Q. Kinetics of CO2 gasification of biomass char in [73] J Hydrogen 2018;43:12002-12. granulated blast furnace slag. Int Energy https://doi.org/10.1016/j.ijhydene.2018.04.102.
- Sadhwani N, Adhikari S, Eden MR. Biomass Gasification Using Carbon Dioxide: Effect of [74] Temperature, CO2/C Ratio, and the Study of Reactions Influencing the Process. Ind Eng Chem Res 2016;55:2883–91. https://doi.org/10.1021/acs.iecr.5b04000.
- Wang Z, Liu X, Burra KG, Li J, Zhang M, Lei T, et al. Towards enhanced catalytic reactivity in [75] CO2-assisted gasification polypropylene. Fuel 2021;284:1-9. of https://doi.org/10.1016/j.fuel.2020.119076.
- [76] Lahijani P, Mohammadi M, Zainal ZA, Mohamed AR. Advances in CO2 gasification reactivity of biomass char through utilization of radio frequency irradiation. Energy 2015;93:976-83. https://doi.org/10.1016/j.energy.2015.09.092.
- [77] Hammerschmid M, Bartik A, Benedikt F, Veress M, Pratschner S, Müller S, et al. Economic and Ecological Impacts on the Integration of Biomass-Based SNG and FT Diesel in the Austrian Energy System. Energies (Basel) 2023;16. https://doi.org/10.3390/en16166097.
- Mauerhofer AM, Fuchs J, Müller S, Benedikt F, Schmid JC, Hofbauer H. CO2 gasification in a [78] dual fluidized bed reactor system: Impact on the product gas composition. Fuel 2019;253:1605-16. https://doi.org/10.1016/j.fuel.2019.04.168.
- DIN Deutsches Institut für Normung e.V. DIN CEN/TS 15439: Biomass gasification tar and [79] particles in product gas - sampling and analysis 2006.

- European Commission. DIRECTIVE 2003/87/EC OF THE EUROPEAN PARLIAMENT AND [80] OF THE COUNCIL establishing a scheme for greenhouse gas emission allowance trading within the Community. vol. 275. 2003.
- [81] European Commission. COMMISSION IMPLEMENTING REGULATION (EU) 2018/2066 of 19 December 2018 on the monitoring and reporting of greenhouse gas emissions pursuant to Directive 2003/87/EC of the European Parliament and of the Council and amending Commission Regulation (EU) No 601/2012 (Text with EEA relevance). 2024.
- European Commission. DIRECTIVE (EU) 2018/2001 OF THE EUROPEAN PARLIAMENT [82] AND OF THE COUNCIL of 11 December 2018 on the promotion of the use of energy from renewable sources (recast) (Text with EEA relevance). 2024.
- Rickels W, Proelß A, Geden O, Burhenne J, Fridahl M. Integrating Carbon Dioxide Removal [83] Into European **Emissions** Trading. Frontiers in Climate 2021;3:1–10. https://doi.org/10.3389/fclim.2021.690023.
- [84] Schuett L. Permanence and Liability: Legal Considerations on the Integration of Carbon Dioxide Removal into the EU Emissions Trading System. Transnational Environmental Law 2024;13:87–110. https://doi.org/10.1017/S2047102524000013.
- Directorate-General for Climate Action. Carbon Removals and Carbon Farming European [85] Commission n.d. https://climate.ec.europa.eu/eu-action/carbon-removals-and-carbonfarming en (accessed December 4, 2024).
- [86] European Commission. Commission presents a recommendation for 2040 emissions reduction target to set the path to climate neutrality in 2050 2024:1–3.
- Fritz D, Gössl M, Hatzl E, Poupa S, Pölz W, Schreiber H. Harmonisierte österreichische direkte [87] ud indirekte THG-Emissionsfaktoren für relevante Energieträger & Technologien. Wien: 2023.
- [88] Federal Environmental Agency Austria (Umweltbundesamt). Berechnung von Treibhausgas (THG)-Emissionen verschiedener Energieträger. HARMONISIERTE ÖSTERREICHISCHE DIREKTE UND INDIREKTE THG-EMISSIONSFAKTOREN FÜR RELEVANTE ENERGIETRÄGER & **TECHNOLOGIEN** 2022. https://secure.umweltbundesamt.at/co2mon/co2mon.html (accessed November 26, 2024).
- Wernet G, Bauer C, Steubing B, Reinhard J, Moreno-Ruiz E, Weidema B. The ecoinvent [89] database version 3 (part I): overview and methodology. International Journal of Life Cycle Assessment 2016;21:1218–30. https://doi.org/10.1007/s11367-016-1087-8.

- [90] [dataset] system/ecoinvent. Market for iron pellet, GLO, Allocation, APOS, ecoinvent 3.10.1 2023.
- [91] [dataset] D. FitzGerald/ecoinvent. Market for triethylene glycol, RER, Allocation, APOS, ecoinvent 3.10.1 2023.
- [92] [dataset] system/ecoinvent. Market for monoethanolamine, GLO, Allocation, APOS, ecoinvent 3.10.1. 2023.
- [93] [dataset] system/ecoinvent. Market for fatty acid methyl ester, RoW, Allocation, APOS, ecoinvent 3.10.1 2023.
- [94] [dataset] system/ecoinvent. Market for silica sand, GLO, Allocation, APOS, ecoinvent 3.10.1 2023.
- [95] [dataset] F. Werner/ecoinvent. Market for wood chips, wet, measured as dry mass, Europe without Switzerland, Allocation, APOS, ecoinvent database version 3.10.1. 2023.
- [96] [dataset] K. Treyer/ecoinvent. Market for electricity high voltage, AT, Allocation, APOS, ecoinvent database version 3.10.1. 2023.
- [97] [dataset] M. Faist Emmenegger/ecoinvent. Market for natural gas, high pressure, AT, Allocation, APOS, ecoinvent database version 3.10.1. 2023.
- [98] Sinnott R, Towler G. Chemical Engineering Design. 6th ed. Oxford: Butterworth-Heinemann (Coulson & Richardson's chemical engineering series); 2019.
- [99] Green DW, Southard MZ. Perry's Chemical Engineers' Handbook. McGraw-Hill Education; 2019.
- [100] Kunysz DO. Kostenschätzung im chemischen Anlagenbau. Leverkusen: Springer Fachmedien Wiesbaden GmbH; 2020. https://doi.org/10.1007/978-3-658-29251-5.
- [101] Consumer price index (CPI/HICP) STATISTICS AUSTRIA The Information Manager n.d. https://www.statistik.at/en/statistics/national-economy-and-public-finance/prices-and-priceindices/consumer-price-index-cpi/-hicp (accessed November 12, 2024).
- [102] Moen V. The Economics of Carbon Capture and Storage. Master thesis. University of Stavanger, 2023.
- [103] EU-ETS price 2022-2024 | Statista n.d. https://www.statista.com/statistics/1322214/carbonprices-european-union-emission-trading-scheme/ (accessed November 12, 2024).

- [104] BloombergNEF. Forecast European Union Emissions Trading System (EU-ETS) average carbon allowance prices from 2024 to 2035 (in euros per metric ton of CO2 equivalent) 2024. https://www.statista.com/statistics/1401657/forecast-average-carbon-price-eu-emissionstrading-system/ (accessed November 12, 2024).
- [105] DBFZ Deutsches Biomasseforschungszentrum gemeinnützige GmbH/Helmholtz-Zentrum für Umweltforschung **GmbH** UFZ/Universität Leipzig, DBFZ Deutsches Biomasseforschungszentrum, GreenDeltaTC GmbH, Hochschule Zittau/Görlitz, International Institute for Sustainability Analysis and Strategy - IINAS, Öko-Institut e.V., et al. Methodenhandbuch Stoffstromorientierte Bilanzierung der Klimagaseffekte - Methoden zur Bestimmung von Technologiekennwerten, Gestehungskosten und Klimagaseffekten von Vorhaben im Rahmen der energetischen Biomassenutzung. 5th ed. DBFZ Deutsches Biomasseforschungszentrum gemeinnützige GmbH; 2021. https://doi.org/10.48480/ddpt-ys74.
- [106] Hofbauer H, Mauerhofer AM, Benedikt F, Martin H, Bartik A, Veress M. Reallabor zur Herstellung von Holzdiesel und Holzgas aus Biomasse und biogenen Reststoffen für die Landund Forstwirtschaft 2020:218.
- [107] Hofbauer H, Bolhar-Nordenkampf M, Kaltschmitt M, Vogel A. Analyse und Evaluierung der thermo-chemischen Vergasung von Biomasse - in Schriftenreihe "Nachwachsende Rohstoffe" Band 29. Landwirtschaftsverlag GmbH; 2006.
- [108] Österreich 2024 Gaspreis Statista n.d. Industrie https://de.statista.com/statistik/daten/studie/323647/umfrage/gaspreise-fuer-industriekunden-inoesterreich/ (accessed November 12, 2024).
- [109] Austria: electricity prices 2024 Statista monthly n.d. https://www.statista.com/statistics/1271527/austria-monthly-wholesale-electricity-price/ (accessed November 12, 2024).
- [110] Iron Ore PRICE Today | Iron Ore Spot Price Chart | Live Price of Iron Ore per Ounce | Markets https://markets.businessinsider.com/commodities/iron-ore-price (accessed November 12, 2024).
- [111] Cooling Water Costs Current and Forecast Intratec.us n.d. https://www.intratec.us/products/water-utility-costs/commodity/cooling-water-cost October 6, 2023).
- [112] Abu Zahra MRM. Carbon Dioxide Capture from Flue Gas Development and Evaluation of Existing and Novel Process Concepts. Doctoral thesis. TU Delft, 2009.

- [113] Thunman H, Seemann M. The gobigas plant. Substitute Natural Gas from Waste: Technical Assessment and Industrial Applications of Biochemical and Thermochemical Processes, Elsevier; 2019, p. 455–74. https://doi.org/10.1016/B978-0-12-815554-7.00017-9.
- [114] Thunman H, Gustavsson C, Larsson A, Gunnarsson I, Tengberg F. Economic assessment of advanced biofuel production via gasification using cost data from the GoBiGas plant. Energy Sci Eng 2019;7:217–29. https://doi.org/10.1002/ese3.271.
- [115] Dißauer C, Rehling B, Strasser C. Machbarkeitsuntersuchung Methan aus Biomasse. 2019.
- [116] Österreichischer Biomasseverband. Basisdaten 2019 Bioenergie. 2019.
- [117] Kranzl L, Haas R, Kalt G, Diesenreiter F, Eltrop L, König A, et al. Strategien zur optimalen Erschließung der Biomassepotenziale in Österreich bis zum Jahr 2050 mit dem Ziel einer maximalen Reduktion an Treibhausgasemissionen. Vienna: 2008.
- [118] 2024 World Steel in Figures. Beijing: 2024.
- [119] Karras T, Brosowski A, Thrän D. A Review on Supply Costs and Prices of Residual Biomass in Techno-Economic Models Sustainability (Switzerland) 2022;14. for Europe. https://doi.org/10.3390/su14127473.
- [120] Alamia A, Larsson A, Breitholtz C, Thunman H. Performance of large-scale biomass gasifiers in a biorefinery, a state-of-the-art reference. Int J Energy Res 2017;41:2001–19. https://doi.org/10.1002/er.3758.
- [121] Toan Vu T, Seo J, Kim E, Ryoo SG, Park BC, Song D. Techno-economic analysis of integrated MIDREX process with CO2 capture and storage: Evaluating sustainability and viability for iron 2024;189:1314-22. production. **Process** Safety and Environmental Protection https://doi.org/10.1016/j.psep.2024.07.005.
- [122] Arvidsson M, Morandin M, Harvey S. Biomass gasification-based syngas production for a conventional oxo synthesis plant - Greenhouse gas emission balances and economic evaluation. J Clean Prod 2015;99:192–205. https://doi.org/10.1016/j.jclepro.2015.03.005.
- [123] Heyne S, Harvey S. Impact of choice of CO2 separation technology on thermo-economic performance of Bio-SNG production processes. Int J Energy Res 2014;38:299-318. https://doi.org/10.1002/ER.3038.
- [124] Li K, Leigh W, Feron P, Yu H, Tade M. Systematic study of aqueous monoethanolamine (MEA)based CO2 capture process: Techno-economic assessment of the MEA process and its improvements. Appl Energy 2016;165:648–59. https://doi.org/10.1016/j.apenergy.2015.12.109.

- [125] Batidzirai B, Mignot APR, Schakel WB, Junginger HM, Faaij APC. Biomass torrefaction technology: Techno-economic status and future prospects. Energy 2013;62:196-214. https://doi.org/10.1016/j.energy.2013.09.035.
- [126] Veress M. Optimization of a process concept for the industrial production of Bio-SNG from lowfuels. thesis. Technische Universität 2020. grade Master Wien, https://doi.org/10.34726/hss.2020.63703.
- [127] Poudel T, Bhandari S, Thapa Y, Nepal S. Design of Major Components of Green Urea Production Plant. International Journal on Engineering Technology 2024;1:132-48. https://doi.org/10.3126/injet.v1i2.66724.
- [128] Rosner F, Papadias D, Brooks K, Yoro K, Ahluwalia R, Autrey T, et al. Green steel: design and cost analysis of hydrogen-based direct iron reduction. Energy Environ Sci 2023;16:4121-34. https://doi.org/10.1039/d3ee01077e.
- [129] Zhou C, Shah K, Moghtaderi B. Techno-economic assessment of integrated chemical looping air separation for oxy-fuel combustion: An Australian case study. Energy and Fuels 2015;29:2074-88. https://doi.org/10.1021/ef5022076.

# **Appendix A: Feedstock compositions**

This section provides additional data on the feedstock compositions used in this work's flowsheet simulations.

All simulations use identical iron ore compositions.

Table A-1: Iron ore composition follows supplemental material data provided by Nurdiawati et al. without moisture [10]

Component	Wt%
FeO	0.00
Fe <sub>3</sub> O <sub>4</sub>	0.97
$Fe_2O_3$	96.30
Fe <sub>3</sub> C	0.00
Fe	0.00
Total gangue	2.73
$Al_2O_3$	0.17
CaO	0.89
CaSO <sub>4</sub>	0.01
$K_2O$	0.03
MgO	0.65
$Na_2O$	0.04
$SiO_2$	0.80
$TiO_2$	0.14

Dry wood compositions for the BCG-DRI routes are the same as experimentally used for CO<sub>2</sub> gasification at TU Wien [22,29]. The Eucalyptus globulus char used for gasification in our earlier work [22,23] and included in the BCG-DRI(HC) simulations was delivered by an external supplier who did not provide much data on the pyrolysis process or raw Eucalyptus globulus composition. Therefore, the Eucalyptus globulus raw composition is taken from Bagatini et al. [68], who pyrolyzed Eucalyptus and reported char compositions similar to the feedstock composition in our earlier work.

Table A- 2: Woody biomass feedstock composition.

Parameter	BCG-DRI(LC) BCG-DRI(MC)	BCG-DRI(HC)	Unit
_		F. 607	
Data source	[22,29]	[68]	
$H_2O$	35	35	wt%
Ash	0.2	2.0	wt% dry basis
Carbon	50.7	46.8	wt% dry basis
Hydrogen	5.9	6.0	wt% dry basis
Oxygen	43.0	45.0	wt% dry basis
Nitrogen	0.2	0.2	wt% dry basis
Sulfur	0.005	0.005	wt% dry basis
Chlorine	0.005	0.005	wt% dry basis
Lower Heating Value	11,215	10,233	kJ/kg

Natural gas composition resembles the typical natural gas composition provided by Enbridge Gas [36].



Table A- 3: Typical natural gas composition provided by Enbridge Gas [36] and recalculated to mass fractions.

Parameter	Value	Unit
$C_2H_6$	7.51	
C <sub>3</sub> H <sub>8</sub>	0.52	
CH <sub>4</sub>	90.51	
$CO_2$	0.79	
$N_2$	0.67	
Lower Heating Value	49,074	kJ/kg
Lower Heating Value	36,822	kJ/Nm³

## **Appendix B: Investment cost estimation**

The CAPEX reported for the sub-systems in literature are scaled to the design scale ( $S_{design}$ ) by employing a scale factor r, multiplied by an overall installation factor Z if the reported costs did not include installation, and recalculated to present-day values by using historic and May 2024 chemical engineering plant cost index (CEPCI) data (Eq. 15). If data had been reported in \$ or SEK, it was recalculated to  $\in$  by using 0.91  $\in$ /\$ and 11.56  $\in$ /SEK as conversion factors. A scale factor r of 0.7 and an overall installation factor Z of 5 were assumed, where no values were given. Some authors also proposed other CAPEX estimation equations, as shown in *Table B-1*. The calculation results from all sources were averaged for each sub-system to improve data credibility by not relying on singular references.

Table B-1: Cost basis for CAPEX estimation

<b>Sub-system</b>	Source	Year	$C_{eq,base}$	$S_{base}$	r	$\boldsymbol{Z}$
Shaft furnace	[121]	2024	56,735,000 €*	423.5 t <sub>iron ore</sub> /h	0.7	1
Natural gas reformer	[121]	2024	228,032,000 €**	$423.5 t_{iron ore}/h$	0.7	1
CO <sub>2</sub> capture	[122]	2012	6,700,000 €	8,640 Nm³ <sub>CO2</sub> /h (calculated)	0.7	5.5
CO <sub>2</sub> capture	[123]	2010	5,190,000 €	6,557 Nm³ <sub>CO2</sub> /h (calculated)	0.6	4.8
CO <sub>2</sub> capture	[124]	2016	138,777,000 €	$1,000,000 t_{\rm CO2}/a$	0.7	1
Pyrolyzer	[63]	2019	618,800 €	$1 t_{Wood}/h$	0.6	5
Pyrolyzer	[125]	2013	4,004,000€	5 t <sub>Wood</sub> /h	0.72	1
Pyrolyzer	[64]	2022	2,030,668 €	3577 t <sub>Char</sub> /a	0.7	1
DFB+dryer	[53,126]	2013	25,500,000 €	15 MW <sub>product gas</sub>	0.7	1
DFB+dryer	[114]	2014	68,257,000 €***	28.3 MW <sub>product gas</sub> ****	0.7	1
Air separation unit	[127]	2024	12,476,000 €	7.11 t <sub>air</sub> /h	0.7	1
Cryogenic CO <sub>2</sub> purification	[34]	2014	30,527,000 €	274.25 t <sub>CO2</sub> /h	0.7	1
Other correlati	ons					
Shaft furnace	[128]	2022	$C_{eq,design}$ (\$	$(5) = 49,080 \left(\frac{\$ \cdot h}{kg}\right) \cdot \dot{m}_{CDRI}$	$(\frac{kg}{h})$	
Natural gas reformer	[128]	2022	$C_{eq,design}$ (\$)	$=4,903,889(\frac{\$}{MW})\cdot Q_{trans}$	$_{\rm s}(MW)$	
CO <sub>2</sub> capture	[124]	2016	$C_{eq,design}$ (\$) = 4,5	$903,889(\frac{\$}{MW}) \cdot Q_{trans,ref}$	ormer (MV	V)
Air separation unit	[129]	2014	$C_{eq,design}$ (\$)	$\begin{array}{l} (3) = 49,080(\frac{\$ \cdot h}{kg}) \cdot \dot{m}_{CDRI} \\ = 4,903,889(\frac{\$}{MW}) \cdot Q_{trans} \\ 903,889(\frac{\$}{MW}) \cdot Q_{trans,refo} \\ = 4,417,2000(\frac{\$}{MW}) \cdot P_{ASU} \end{array}$	(MW)	

<sup>\*</sup>Includes shaft furnace, warehouse, site development, piping

<sup>\*\*</sup>Includes oxygen supply, reformer, recycle compressor, cooling tower

<sup>\*\*\*</sup>The value reported by Thunmann et al. was reduced by 33 %, because it includes various sections dedicated to synthesizing synthetic natural gas. The 33 % reduction for an ironmaking process was previously estimated by [20]. \*\*\*\*28.3 MW<sub>product</sub> gas was calculated from 20 MW<sub>biomethane</sub> at a biomethane production efficiency of 61.8 % and a raw product gas efficiency of 87.3 % as reported by Alamia et al. [120]

# Appendix C: Main mass and energy streams of all investigated BCG-DRI routes

The flow data calculated in IPSEpro 8.0 were used to prepare Sankey diagrams showing the central mass and energy flows in e!Sankey 4 (Figure C-1-Figure C-6). All streams are scaled to the base of 1 t<sub>CDRI</sub>. Streams under 5 kg or 5 MJ per ton of CDRI, the cooling water, the water recirculated between the CO<sub>2</sub> capture and CO<sub>2</sub> compression sections, and the heat loss streams are omitted from the figures to improve readability. The mass flow of drying air is depicted at a 1:10 scale because it is much larger than the other streams.

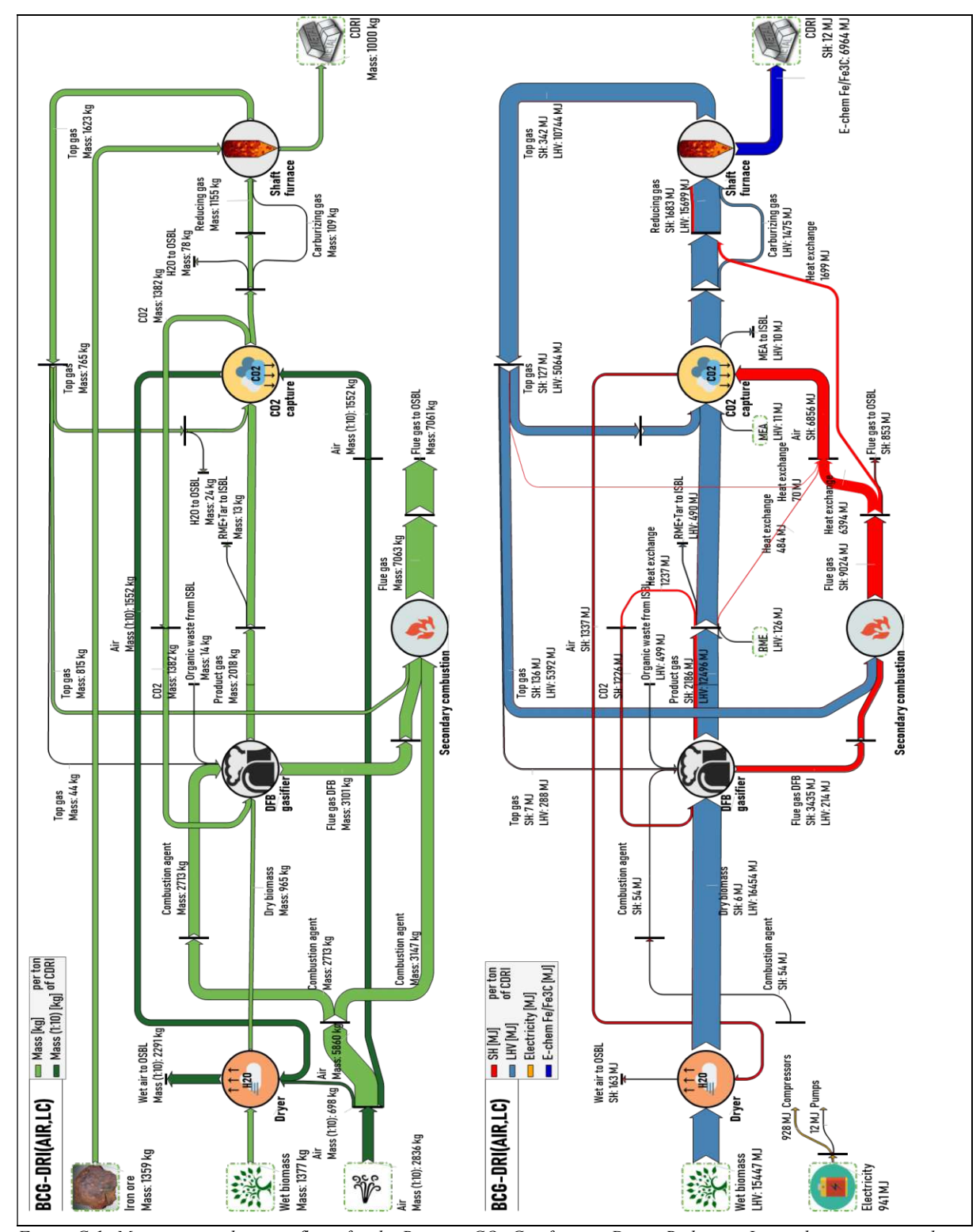


Figure C-1: Main mass and energy flows for the Biomass CO<sub>2</sub> Gasification-Direct Reduction Ironmaking process with aircombustion and low conversion of CO<sub>2</sub> in the gasifier: "BCG-DRI(AIR,LC)". SH=Sensible Heat, LHV=Lower Heating Value, ISBL/OSBL=Inside/Outside Battery Limit

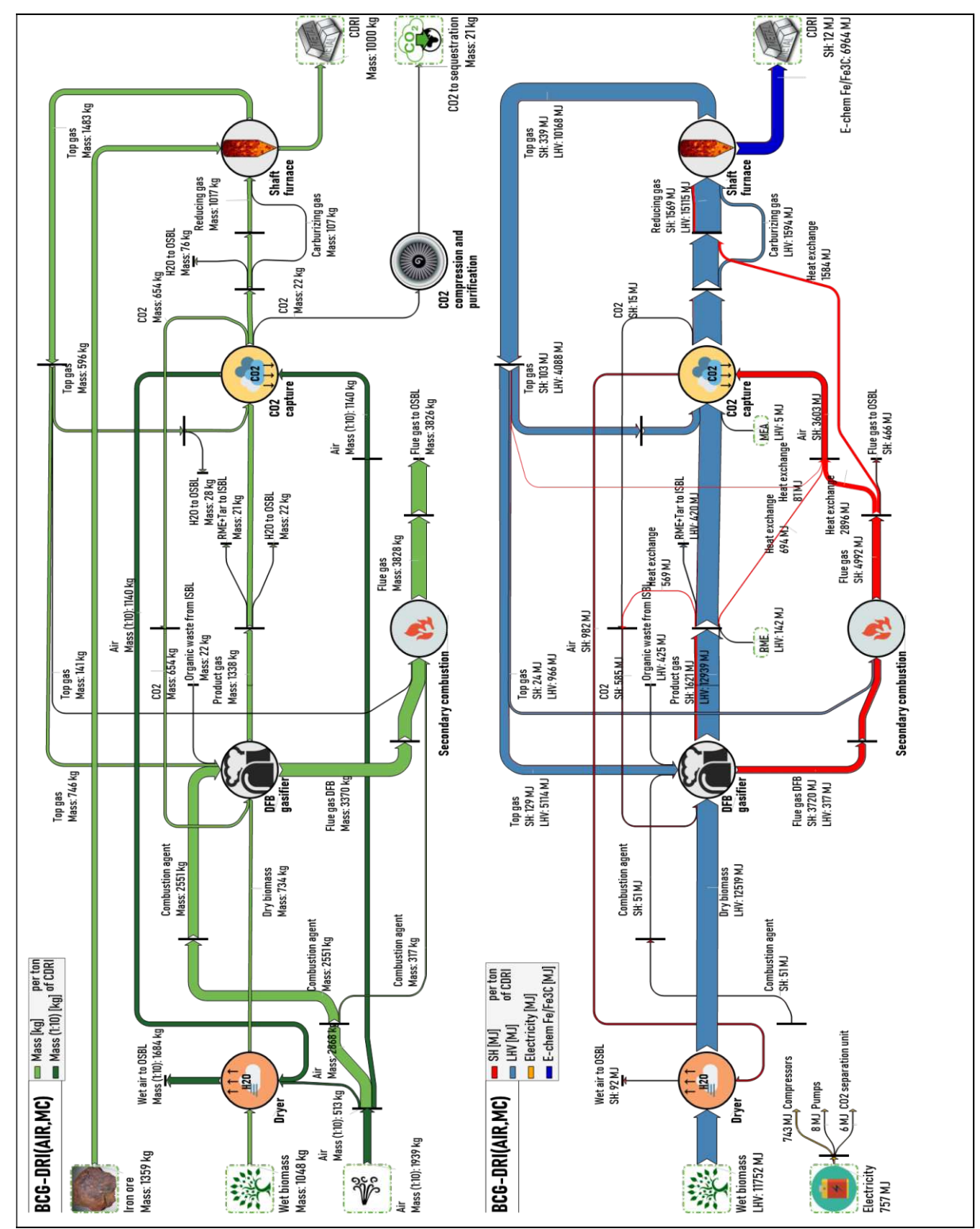


Figure C-2: Main mass and energy flows for the Biomass CO2 Gasification-Direct Reduction Ironmaking process with aircombustion and medium conversion of CO<sub>2</sub> in the gasifier: "BCG-DRI(AIR,MC)". SH=Sensible Heat, LHV=Lower Heating Value, ISBL/OSBL=Inside/Outside Battery Limit

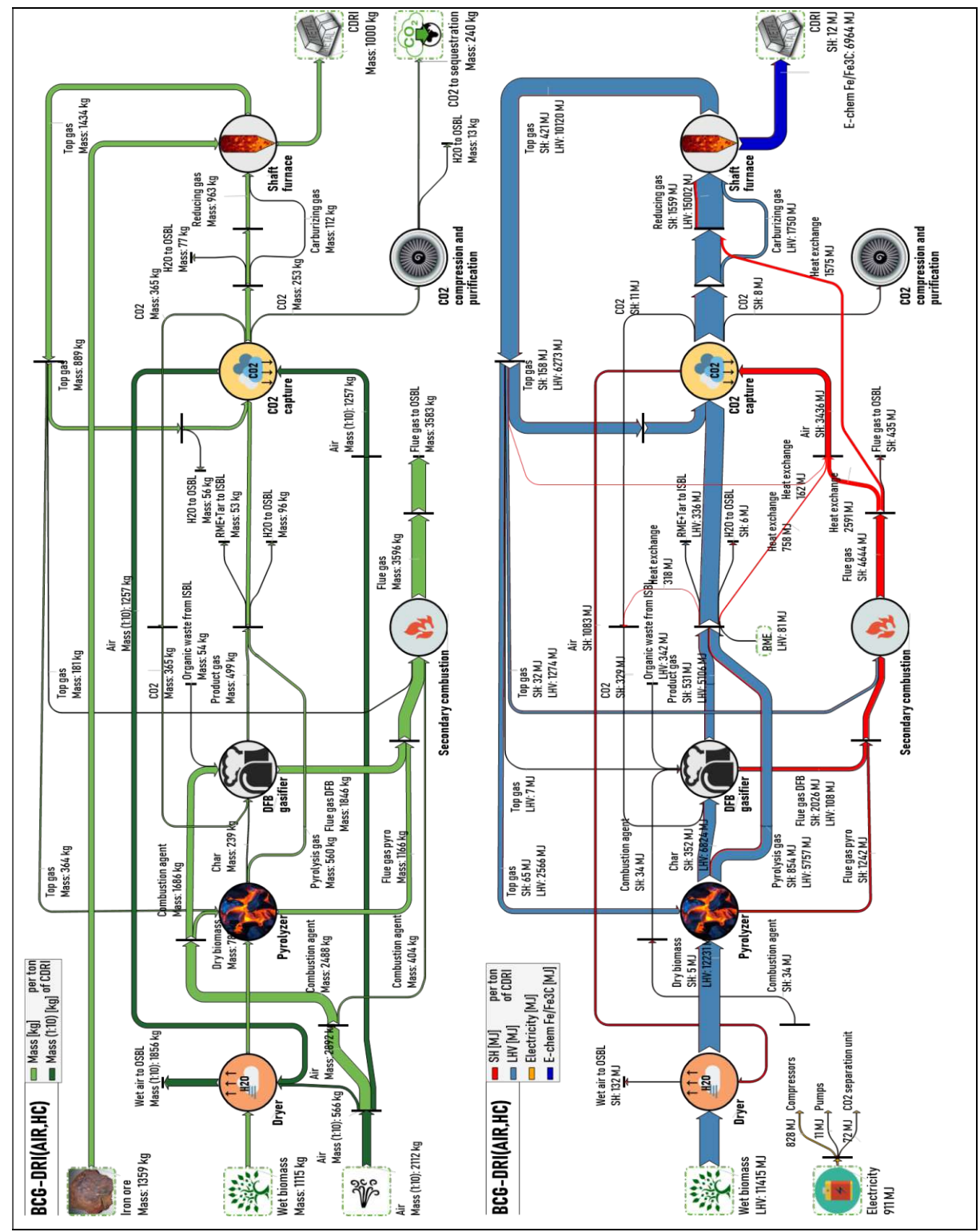


Figure C-3: Main mass and energy flows for the Biomass CO<sub>2</sub> Gasification-Direct Reduction Ironmaking process with aircombustion and high conversion of CO<sub>2</sub> in the gasifier: "BCG-DRI(AIR,HC)". SH=Sensible Heat, LHV=Lower Heating Value, ISBL/OSBL=Inside/Outside Battery Limit

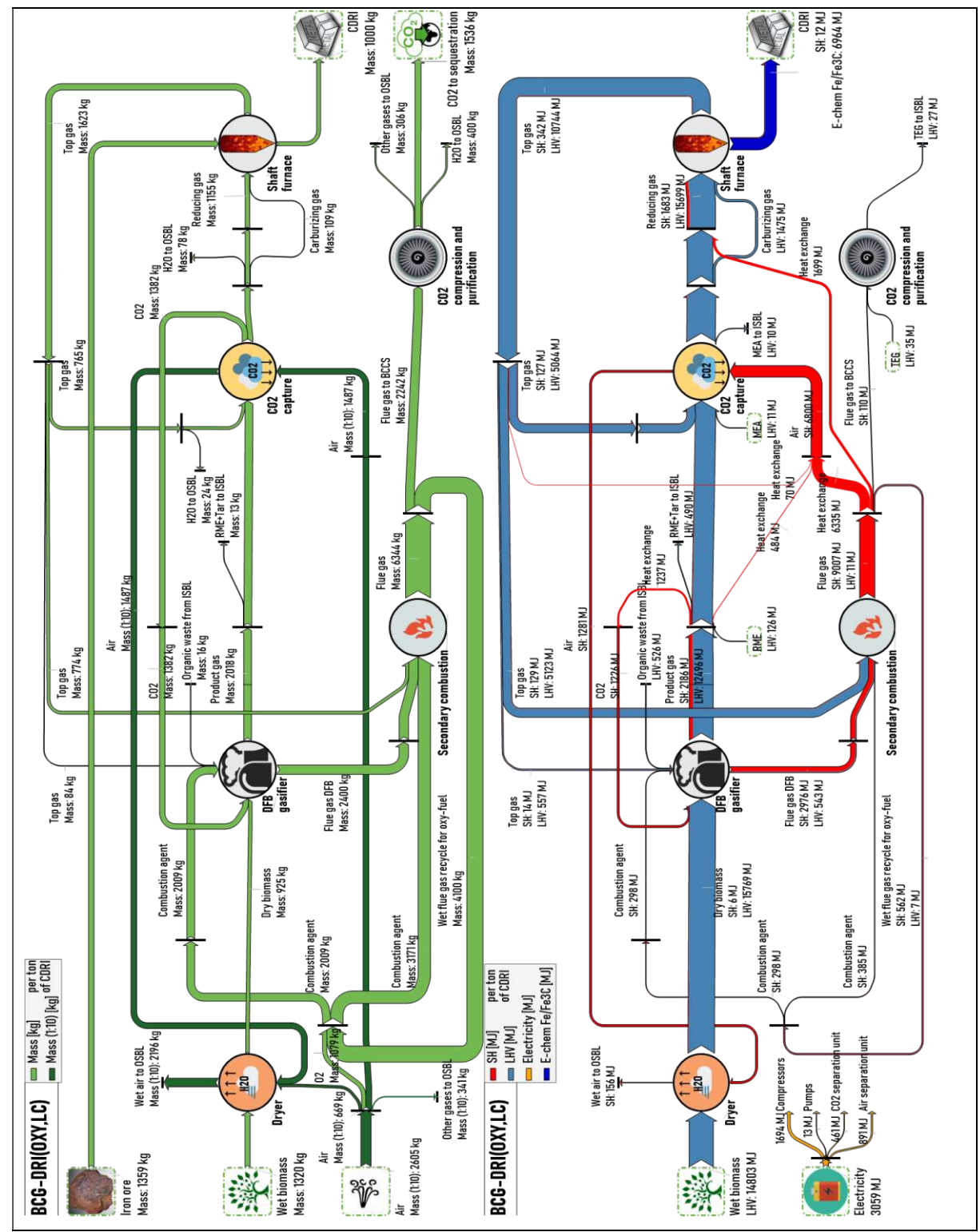


Figure C-4: Main mass and energy flows for the Biomass CO<sub>2</sub> Gasification-Direct Reduction Ironmaking process with oxyfuel combustion and low conversion of CO<sub>2</sub> in the gasifier: "BCG-DRI(OXY,LC)". SH=Sensible Heat, LHV=Lower Heating Value, ISBL/OSBL=Inside/Outside Battery Limit

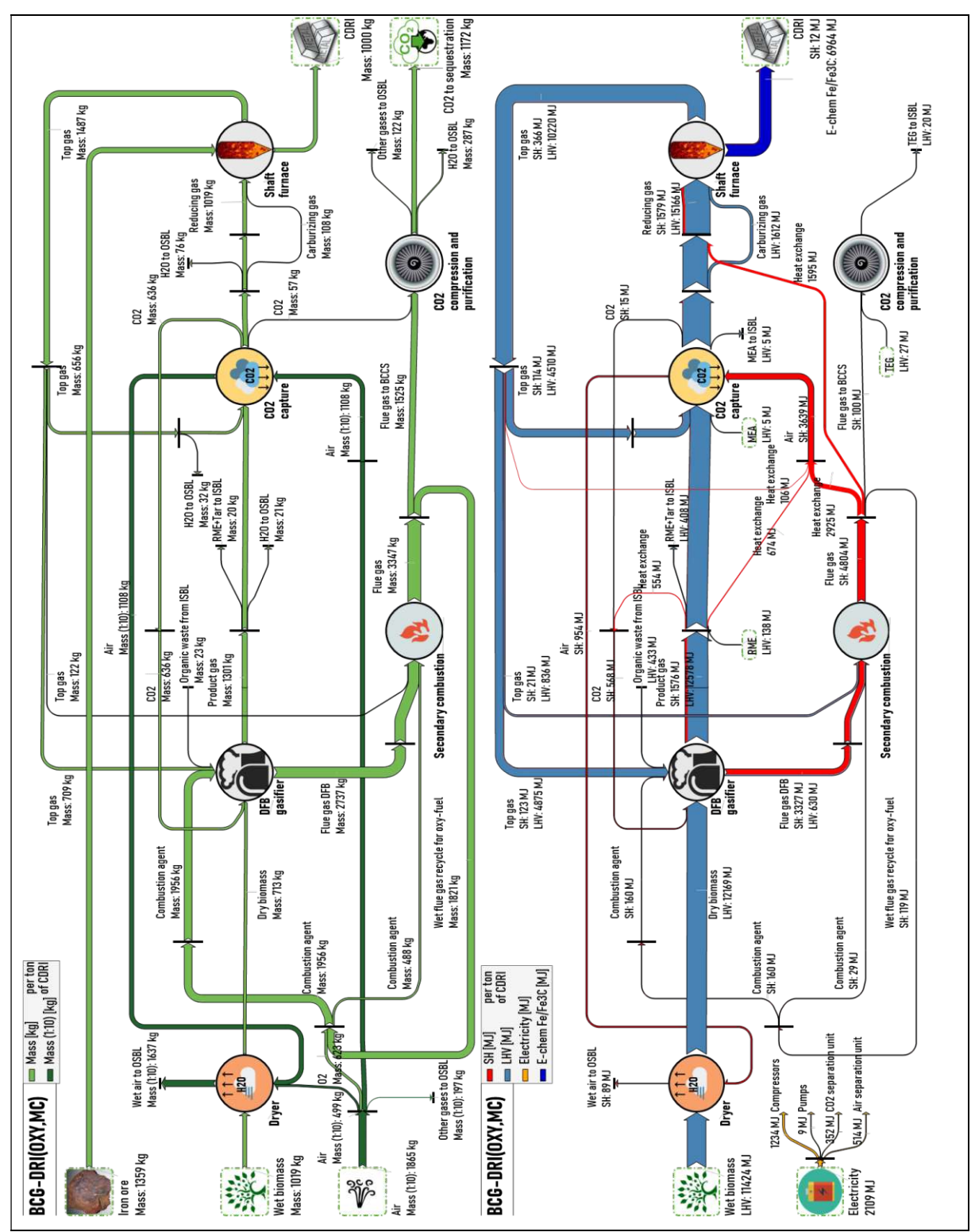


Figure C-5: Main mass and energy flows for the Biomass CO2 Gasification-Direct Reduction Ironmaking process with oxyfuel combustion and medium conversion of CO2 in the gasifier: "BCG-DRI(OXY,MC)". SH=Sensible Heat, LHV=Lower Heating Value, ISBL/OSBL=Inside/Outside Battery Limit

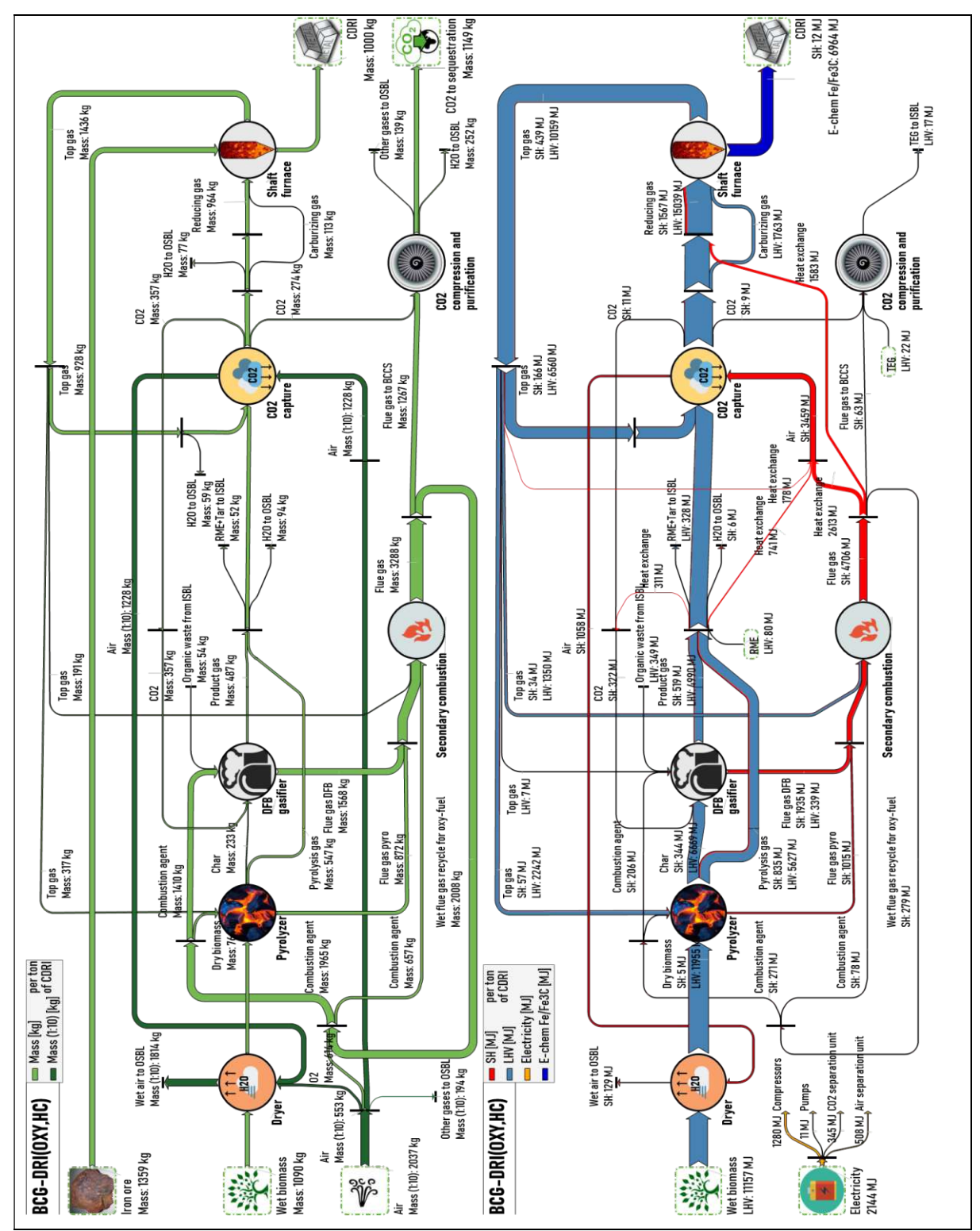


Figure C-6: Main mass and energy flows for the Biomass CO2 Gasification-Direct Reduction Ironmaking process with oxyfuel combustion and high conversion of CO<sub>2</sub> in the gasifier: "BCG-DRI(OXY,HC)". SH=Sensible Heat, LHV=Lower Heating Value, ISBL/OSBL=Inside/Outside Battery Limit

# Appendix D: Reducing gas, carburizing gas, and top gas compositions

This Appendix extends the information provided in Section 3.1.3 on the gas composition and flows to and from the shaft furnace. These compositions were calculated based on mass and energy balances that use the data presented in the methodology section.

Table D-1: Gas composition to and from the DRI shaft furnace

		NGR-	NGR-	BCG-	BCG-	BCG-	BCG-	BCG-	BCG-
		DRI	DRI	DRI	DRI	DRI	DRI	DRI	DRI
			(CCS)	(AIR,	(OXY,	(AIR,	(OXY,	(AIR,	(OXY,
				LC)	LC)	MC)	MC)	HC)	HC)
Reducing									
gas									
Flow rate	Nm³/	1720	1717	1232	1232	1177	1187	1180	1187
	(h·t <sub>CDRI</sub> )				/		/		
CO	vol%	30.0%	30.0%	59.8%	59.8%	58.6%	58.2%	55.1%	54.8%
$CO_2$	vol%	4.8%	4.8%	5.8%	5.8%	2.8%	2.9%	2.5%	2.6%
$H_2$	vol%	52.6%	52.6%	27.3%	27.3%	32.2%	32.8%	37.2%	37.5%
H <sub>2</sub> O	vol%	4.7%	4.7%	0.7%	0.7%	0.7%	0.7%	0.7%	0.7%
CH <sub>4</sub>	vol%	7.8%	7.8%	6.3%	6.3%	5.5%	5.3%	3.4%	3.3%
Rest	vol%	0.2%	0.2%	0.2%	0.2%	0.2%	0.2%	1.1%	1.1%
H <sub>2</sub> :CO	mol/mol	1.75	1.75	0.46	0.46	0.55	0.56	0.67	0.68
RP	mol/mol	8.74	8.74	13.47	13.47	25.76	25.49	28.80	28.53
Carburizing									
gas									
Flow rate	Nm³/	85	85	116	116	124	126	138	139
	$(h \cdot t_{CDRI})$								
CO	vol%	0.0%	0.0%	Carburi	zation gas	compos	ition is th	e same as	s reducing
CO <sub>2</sub>	vol%	0.3%	0.3%		position 1				E
$H_2$	vol%	0.0%	0.0%	Ü	1				
H <sub>2</sub> O	vol%	0.0%	0.0%						
CH <sub>4</sub>	vol%	94.9%	94.9%						
Rest	vol%	4.8%	4.8%						
H <sub>2</sub> :CO	mol/mol	∞	∞						
RP	mol/mol	0.03	0.03						
Top gas									
Flow rate	Nm³/	1895	1893	1481	1481	1408	1416	1408	1414
	(h·t <sub>CDRI</sub> )	-0,0	-0,0						
CO	vol%	19.1%	18.9%	34.0%	34.0%	32.2%	32.0%	30.6%	30.5%
$CO_2$	vol%	13.9%	14.1%	29.0%	29.0%	27.2%	27.0%	25.6%	25.5%
H <sub>2</sub>	vol%	37.1%	37.3%	27.5%	27.5%	29.3%	29.4%	30.8%	30.9%
H <sub>2</sub> O	vol%	21.3%	21.1%	9.4%	9.4%	11.3%	11.4%	12.8%	12.9%
CH <sub>4</sub>	vol%	8.4%	8.4%	0.0%	0.0%	0.0%	0.0%	0.0%	0.0%
Rest	vol%	0.2%	0.2%	0.076	0.0%	0.1%	0.0%	0.0%	0.2%
H <sub>2</sub> :CO	mol/mol	1.94	1.97	0.170	0.170	0.170	0.170	1.01	1.01
RP	mol/mol	1.60	1.60	1.60	1.60	1.60	1.60	1.60	1.60
M	11101/11101	1.00	1.00	1.00	1.00	1.00	1.00	1.00	1.00

## Appendix E: Sensitivity analysis for all process routes

The sensitivity analysis plots for all routes are shown in this Appendix in Figure E-1-Figure E-4. The levelized costs of product (LCOP) results are discussed in Section 3.3. The basis for each sensitivity analysis is the current EU-ETS scenario without a profit option from BCCS.

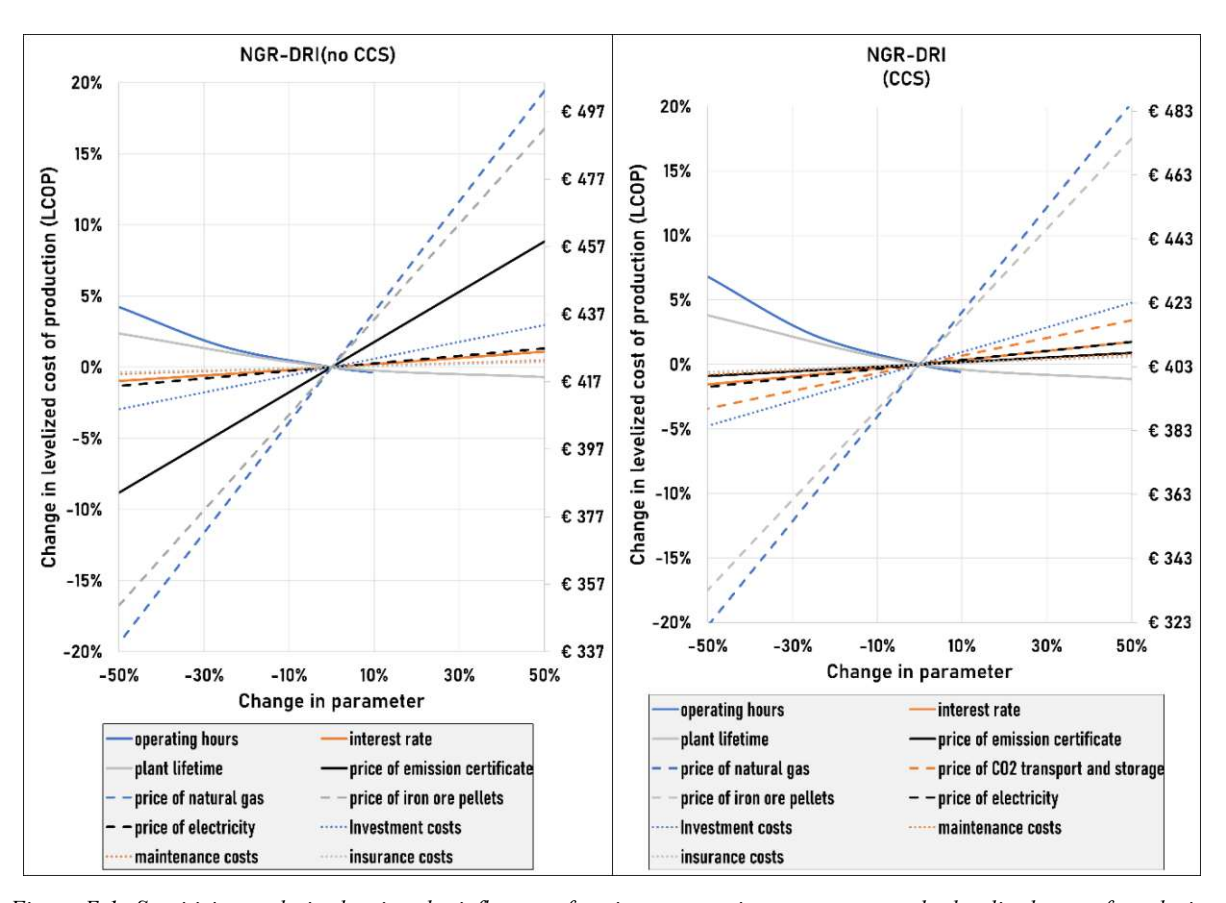


Figure E-1: Sensitivity analysis showing the influence of various economic parameters on the levelized cost of producing (LCOP) one ton of cold direct reduced iron. The process acronyms "NGR-DRI(no CCS)" and "NGR-DRI(CCS)" stand for Natural Gas Reforming – Direct Reduction Ironmaking with and without Carbon Capture and Storage.

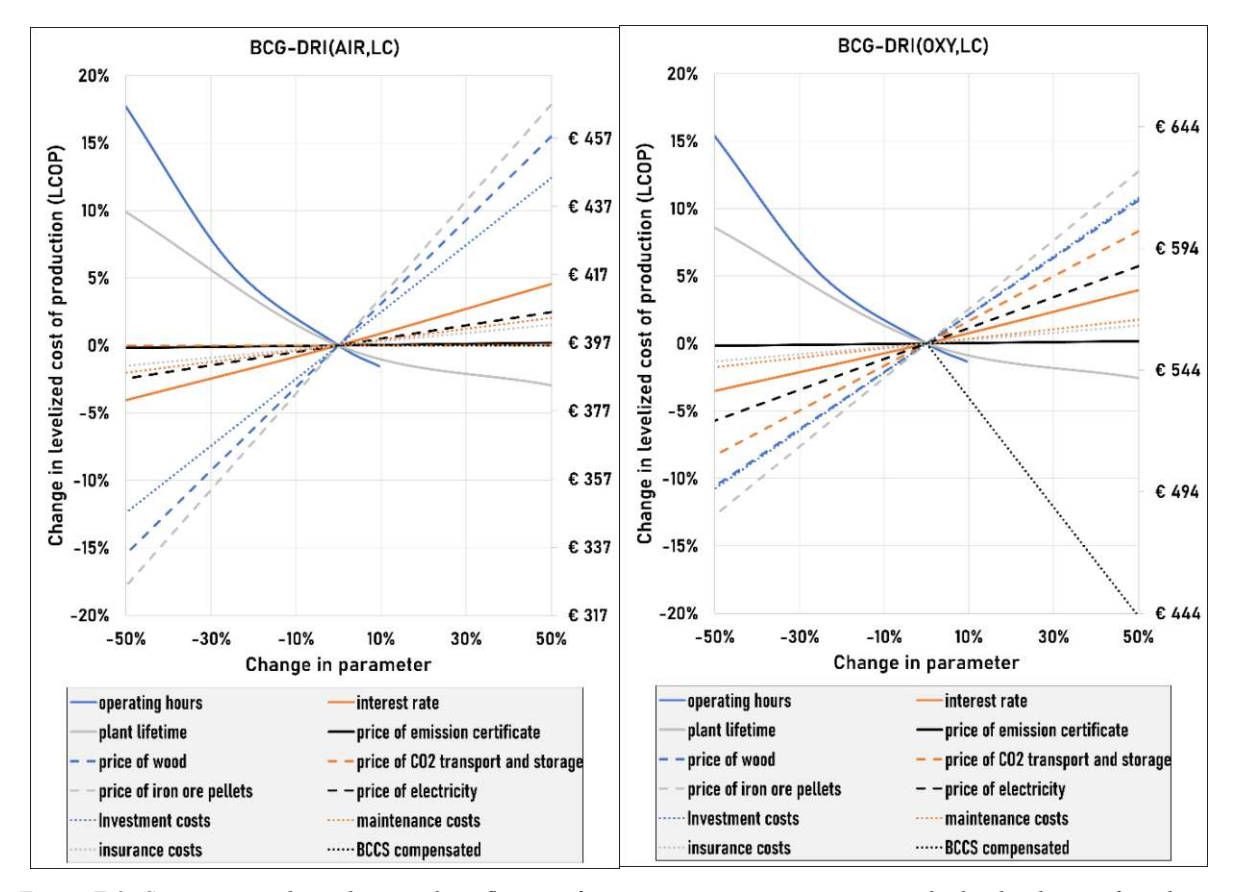


Figure E-2: Sensitivity analysis showing the influence of various economic parameters on the levelized cost of producing (LCOP) one ton of cold direct reduced iron. The process acronyms "BCG-DRI(AIR,LC)" and "BCG-DRI(OXY,LC)" stand for Biomass CO<sub>2</sub> Gasification – Direct Reduction Ironmaking with air or oxygen-enriched flue gas as combustion agent and low conversion of CO2 in the gasifier.



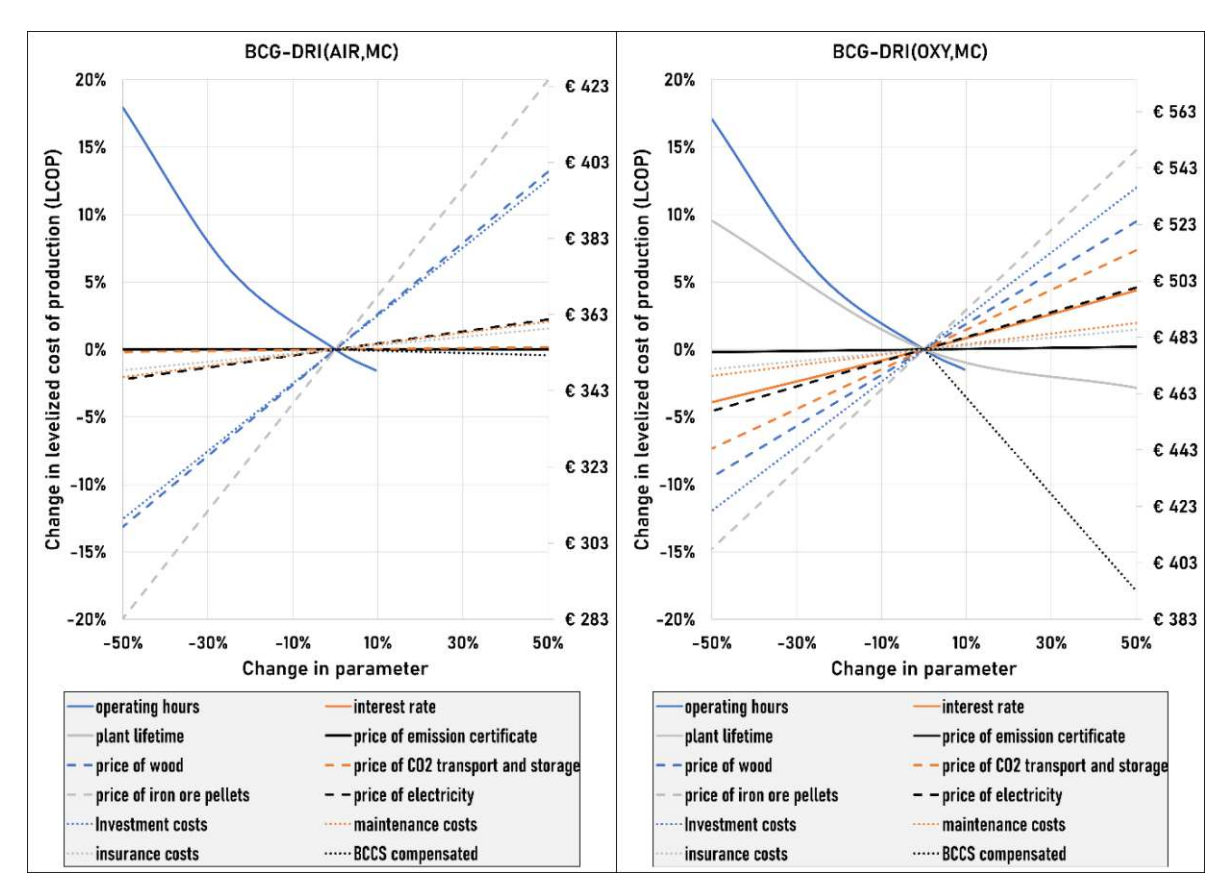


Figure E-3: Sensitivity analysis showing the influence of various economic parameters on the levelized cost of producing (LCOP) one ton of cold direct reduced iron. The process acronyms "BCG-DRI(AIR,MC)" and "BCG-DRI(OXY,MC)" stand for Biomass CO2 Gasification - Direct Reduction Ironmaking with air or oxygen-enriched flue gas as combustion agent and medium conversion of CO2 in the gasifier.

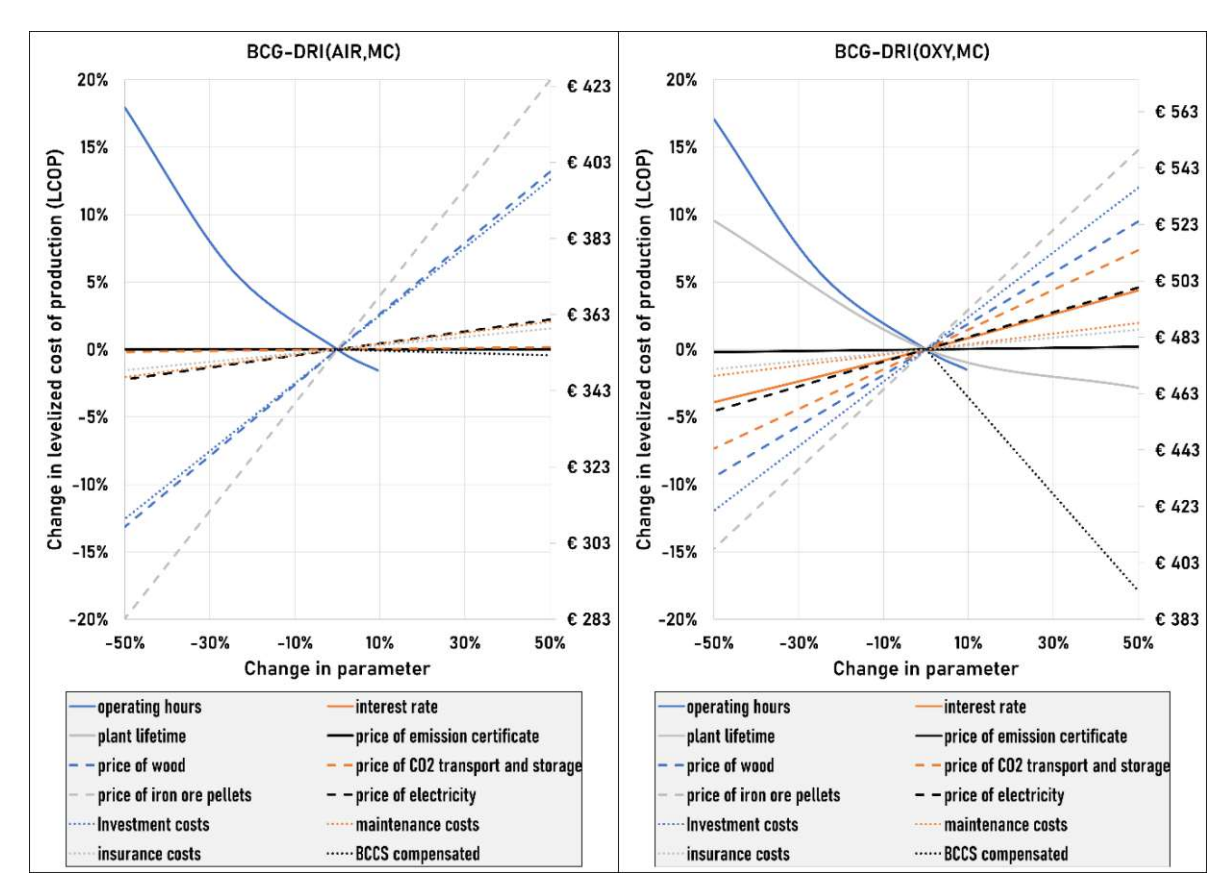


Figure E-4: Sensitivity analysis showing the influence of various economic parameters on the levelized cost of producing (LCOP) one ton of cold direct reduced iron. The process acronyms "BCG-DRI(AIR,HC)" and "BCG-DRI(OXY,HC)" stand for Biomass CO2 Gasification - Direct Reduction Ironmaking with air or oxygen-enriched flue gas as combustion agent and high conversion of CO2 in the gasifier.

# Conference article I (CA I): Surface adjustment of biochar by CO2 gasification under fixed and fluidized bed conditions

#### Bibliographical reference

F. J. Müller, C. Rodríguez M., E. Schöfbänker, and F. Winter, "Surface adjustment of biochar by CO2 gasification under fixed and fluidized bed conditions," in Proceedings of the 14th International Conference on Fluidized Bed Technology, G. Yue, H. Yang, T. Zhou, and S. Ma, Eds., Taiyuan, China, 2024. doi: 10.34726/9639.

## SURFACE ADJUSTMENT OF BIOCHAR BY CO<sub>2</sub> GASIFICATION UNDER FIXED AND FLUIDIZED BED CONDITIONS

Florian J. Müller<sup>1\*</sup>, Camila Rodríguez M.<sup>1</sup>, Eugen Schöfbänker<sup>1</sup>, Franz Winter<sup>1</sup>

Technische Universität Wien, Institute of Chemical, Environmental and Bioscience Engineering, Getreidemarkt 9/166, 1060 Wien, Austria

\*E-mail: florian.johann.mueller@tuwien.ac.at

#### Abstract

This paper explores how torrefaction and CO<sub>2</sub> gasification can be combined to create biochar with a high surface area from Pinus sylvestris wood pellets. Raw pellets were pretreated in a torrefaction process at 300 °C before conducting biomass CO<sub>2</sub> gasification experiments under various operating conditions. Gasification was performed under fixed and fluidized bed conditions at temperatures between 800 to 900 °C and biomass residence times of 15 or 25 minutes. Biomass burn-off and BET surface areas were analyzed individually and combined to determine the surface yield per raw Pinus sylvestris feedstock. Higher temperatures, higher biomass residence times, and fixed bed conditions increased burn-off and BET surface areas up to 798 m<sup>2</sup>/g. Surface yield per raw biomass was instead found to be the highest from fluidized bed experiments, which yielded around 100 m<sup>2</sup>/g<sub>feedstock</sub> after gasification at 850 to 900 °C.

#### 1. Introduction

Biomass CO<sub>2</sub> gasification is a carbon capture and utilization technology producing CO-rich gas [1]. Potential applications of such gas are for iron ore reduction in a direct reduced ironmaking shaft furnace [2] or, if sustainable hydrogen is added, as a synthesis gas for producing renewable chemicals and energy carriers [3]. If no oxygen is fed to the gasification reaction, biomass is often not fully converted, and the residual char is frequently used for energy generation [5]. The specific surface areas of typical biochars (from 0.1 to 500 m<sup>2</sup>/g) make them suited for applications like soil amendment [7] and to restore degraded sites [8]. Activated biochars with high specific surface areas of 200 to 2500 m<sup>2</sup>/g can be produced from various biomass feedstocks by thermochemical treatment and can be used for higher-value applications like catalysis, electrochemistry, or energy storage [9]. An ongoing research project on phytoremediation at TU Wien investigates the encapsulation of heavy metals in biochar. In this project, one investigated process route is a multi-stage process consisting of a torrefaction process at mild temperatures as pretreatment and a CO2 gasification step for surface activation at high temperatures. This paper investigates the influence of CO2 gasification operating conditions on the surface characteristics of biochar.

#### 1.1. State of the art on surface adjustment by gasification

The manufacturing process of activated biochar generally consists of a carbonization step, creating a biochar structure with pores that are often blocked by tar compounds, and an activation step, during which these blockages are removed and the pores are widened [10]. This activation step can be realized by adding chemicals before thermal or physical activation through gasification, where oxidizing gases penetrate the structure at temperatures between 700 and 1000 °C [11]. The characteristics of the final product depend mainly on feedstock composition and process conditions such as heating rate, temperature, and residence time

CO<sub>2</sub> and H<sub>2</sub>O are the most common gasification agents for producing high surface area biochars because their endothermic reactions can be controlled well [13]. Chang et al. reported on the gasification of corn cob agro-waste that at 900 °C higher Brunauer-Emmett-Teller (BET) surface areas and total pore volumes were found with CO<sub>2</sub> as gasification agent compared to steam (1705 vs. 1063 m<sup>2</sup>/g; 0.884 vs. 0.536 cm<sup>3</sup>/g) [14]. The opposite trend was reported at 800 °C (670 vs. 998 m²/g; 0.342 vs. 0.511 cm³/g), which can be attributed to the higher reaction rate for the steam-carbon reaction with H<sub>2</sub>O compared to the Boudouard reaction with CO<sub>2</sub> [13]. Pallarés et al. reported a similar trend reversion when they studied the activation of barley straw after carbonization via pyrolysis at 500 °C [11]. BET surface area and pore volume were higher from CO<sub>2</sub> gasification at 800 °C (789 vs. 534 m<sup>2</sup>/g; 0.3495 vs. 0.2576 cm³/g), but higher surface area was found for steam gasification at 700 °C (211 vs. 552 m<sup>2</sup>/g). Additionally, Ngernyen et al. reported a linear increase in burn-off values and BET surface area with increasing activation time between 60 and 300 minutes for the CO2 activation of Eucalyptus and Wattle wood [15].

Based on the presented literature, activation time and temperature were selected to investigate *Pinus sylvestris* pellets' surface evolution during CO<sub>2</sub> gasification. Additionally, the experiments were performed under fixed and fluidized bed conditions to examine if this would lead to different results, e.g., from differences in heat transfer.

### 2. Materials and methods

#### 2.1. Experimental design

Pellets with a diameter of approximately 4 mm and varying lengths between 5 to 20 mm were produced from a mixture of *Pinus sylvestris* needles and branches (Table 1). The pellets were subjected to a pre-treatment phase by torrefaction and further activation by gasification. The torrefaction process was performed under an N2 atmosphere and fixed bed conditions in a separate reactor with an inner diameter of 53 mm. This larger reactor was used because it enabled the production of torrefied intermediate products for all gasification experiments in a single batch. The pellets were kept at 300 °C for 45 minutes under a nitrogen flow of 0.8 Nm<sup>3</sup>/h. Quartz sand with a density of 2650 kg/m<sup>3</sup> and a particle mean diameter determined by sieving analysis at 370 µm was used as bed material during fluidized bed experiments. CO<sub>2</sub> and N<sub>2</sub> from gas bottles were used as gaseous feed.

Table 1: Elemental analysis of raw Pinus sylvestris pellets

	Water content	С	Н	N	S	0
wt%	4.6	50.0	6.9	1.1	0.7	41.3

Torrefied biochar was activated by gasification with CO<sub>2</sub> in a stainless-steel batch reactor with an inner diameter of 38 mm (Figure 1a). Two external half-shells electrically heated the reactor (Figure 1b). Temperatures were measured by thermocouples type K. A gas mixture of 1.6 NL/min N<sub>2</sub> and 0.4 NL/min CO<sub>2</sub> was supplied to the reactor and controlled by mass flow controllers for all experiments. Gas entered the reactor through an empty preheating section before a Quartz glass frit distributed the gas evenly into the upper section, where the activation process was carried out (reaction zone). Fuel was inserted into the reaction zone batch-wise. It was placed into a metal cage with a mesh size of approximately 500 µm, which was used for extracting the activated biochar after the experiment. Fuel was added after the reactor had reached its desired temperature.

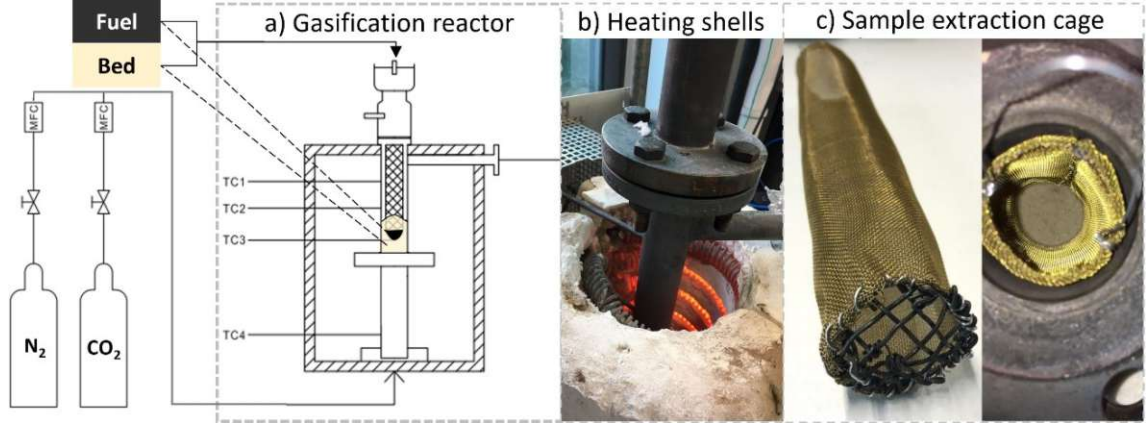


Figure 1:a) Gasification reactor schematic layout, b) Reactor with heating, c) Sample extraction cage



For fluidized bed experiments, fuel was submerged in Quartz sand. Fluidization equations proposed by Grace [16], Wen, and Yu [17] were used to calculate that the selected feed gas flow rate of 2.0 NL/min resulted in around 5 times the minimum fluidization velocity. Therefore, the fluidized bed conditions were achieved by forming a bubbling fluidized bed from Quartz sand particles around the fuel in the sample extraction cage (Figure 1c).

A four-step procedure was followed after the activation time to stop reactions and freeze the surface state of biochar: 1. The electrical heating was turned off, 2. CO<sub>2</sub> was no longer fed to the reactor (only N<sub>2</sub>), 3. 50 mL of Quartz sand at room temperature was fed through the ball valve lock to lower the temperature in the reactor, and 4. A part of the insulation was removed to cool down the biochar faster. After the reactor had cooled down, the activated biochar samples were removed by carefully lifting the cage.

A list of the selected experimental conditions for activation is given in Table 2.

Table 2: Investigated gasification conditions

Name	ne Fluidization		7	emperatur	Activation time		
	Fluidized bed	Fixed bed	800°C	850°C	900°C	15 min	25 min
E1		Х	Χ			Х	
E2		Х		Χ		Х	
E3		Х			Χ	Х	
E4		Х	Χ				Χ
E5		Χ		Χ			Χ
E6		X			Χ		Χ
E7	X		Χ			Х	
E8	X			Χ		Х	
E9	X				Χ	Х	
E10	Х		Х				Х
E11	Х			Х			Х
E12	Х				Х		Х

#### 2.2. Sample characterization

The weight loss of the solid samples during processing is described by the burn-off value (b), which is formed from the weight before the conversion step ( $w_0$ ) and the weight of the final product  $(w_f)$ ; see Eq. 1.

$$b = \frac{w_0 - w_f}{w_0}$$
 Eq. 1

Nitrogen adsorption isotherms for surface characterization were measured using an ASAP 2020 Plus adsorption analyzer by Micromeritics for the torrefied biochar and a Belsorp Max G by Microtrac Retsch for samples after activation. These measurements were also used to determine the total pore volume. Before measurement, the activated samples were degassed under vacuum in a Belprep Vac degassing station for 24 hours at 150°C, which is suggested as degassing temperature in the European Biochar Certification [18]. The torrefied sample was degassed at 200 °C for 4 hours. Isotherm data were used to calculate a specific surface area a<sub>BET</sub> following the proposed method by Brunauer-Emmett-Teller (BET) [19]. Guidelines for applying this method to microporous materials, as given in Annex C of DIN ISO 9277:2014-01, were followed for activated samples. These guidelines were proposed by Rouquerol et al. [20] and are as follows:

- C must be positive
- Application of the BET equation must be limited to the range where the term V(1-P/P<sub>0</sub>) continuously increases with P/P<sub>0</sub>
- The P/P<sub>0</sub> value corresponding to the monolayer volume should be within the selected BET range.

Two further criteria were followed to select the appropriate range for multi-point BET in this analyzer:

The first point of the fit must be at least 1.10<sup>-3</sup> Pa following pressure measurement sensitivity.

The last point of the fit is chosen to achieve the highest correlation coefficient between data and fit.

Furthermore, light microscopy using a Keyence VHX-S650E and a VH-ZST dual zoom objective and scanning electron microscopy (SEM) were used to evaluate surface adjustments. Samples were sputtered with gold before analysis in a COXEM EM-30 Plus microscope. Increasing the surface area further and further might not bring additional benefits for some applications, which might, for example, only need 500 m<sup>2</sup>/g to reach process demands. In such cases, optimal operating conditions to produce biochar could be identified by considering both a<sub>BET</sub> and b. A surface yield parameter (y) is proposed that relates the final biochar surface area a<sub>BET</sub> to the mass of *Pinus sylvestris* feedstock used for producing this biochar (Eq. 2). Higher v values indicate that higher total surface area is produced per mass of raw feedstock.

$$y = a_{BET} \cdot (1 - b_{torrefaction}) \cdot (1 - b_{gasification})$$
 Eq. 2

### 3. Results and discussion

#### 3.1. Biomass conversion

A burn-off value (b) of 32.64 % was recorded during torrefaction. The torrefied pellets were dark brown and softer in texture compared to the raw pellets, suggesting a slight surface degradation and the presence of tar in the pore structures. Investigations by SEM at various magnifications from x50 to x2000 confirmed that the pore structure remained relatively closed after torrefaction (Figure 2). Small hollows and irregularities were visible in the raw and torrefied samples due to the pelletization process mixing needles and branches. At the process temperature of 300 °C and under constant nitrogen flow, this weight loss was likely caused by drying and the decomposition of hemicellulose [13].

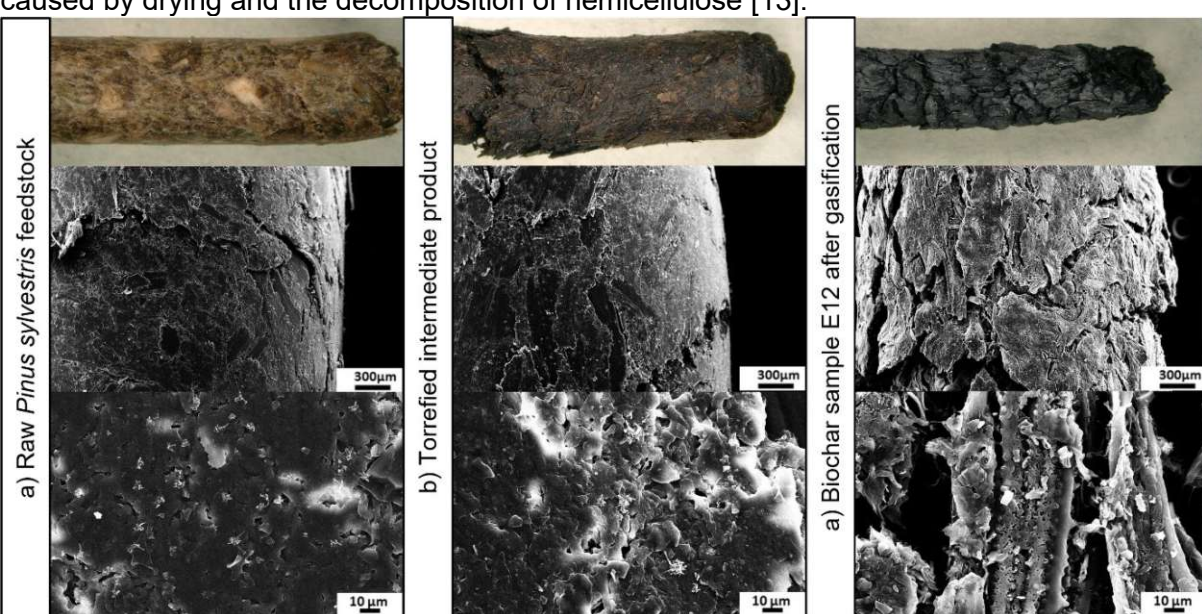


Figure 2: Evolution of Pinus sylvestris pellets during thermal processing investigated by light and scanning electron microscopy (x50, x1000 magnifications).

Significant further weight losses were recorded during gasification with CO<sub>2</sub> (Figure 3). Burnoff was calculated relative to the torrefied intermediate product. Biochar pellets were black and brittle after gasification, and their diameter had decreased by 25 % on average. Morphological examination under light microscopy and SEM revealed a surge in fragmentations and the development of both, narrow and larger pore structures that were not there before gasification. The inner structure showed the presence of channels and hollow areas next to each other, which might be related to solid-gas reactions with CO<sub>2</sub>.





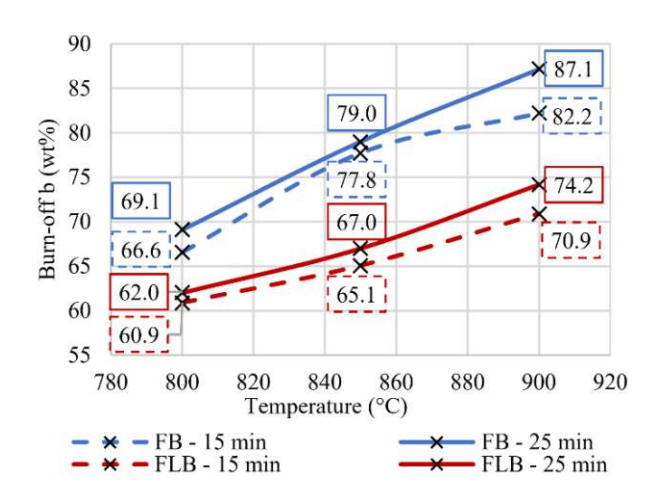


Figure 3: Burn-off during CO<sub>2</sub> gasification under various conditions. FB=Fixed bed; FLB=Fluidized bed.

The increase in biochar residence time from 15 to 25 minutes increased burn-off for fluidized bed and fixed beds experiments. Burn-off was also increased at higher temperatures. Devolatilization at high temperatures is a fast process [6], suggesting that the burn-off increase at longer residence times was a result of ongoing gas-solid reactions. Temperatures exceeding 800 °C lead to the pyrolytic decomposition of more stable biomass components [22] and also favor fixed carbon conversion by gas-solid reactions, mainly the Boudouard reaction [1]. Therefore, the increase in burn-off at higher temperatures can be attributed to a mixture of pyrolytic decomposition and reactions with the gasification agent CO<sub>2</sub>.

Burn-off values across all temperatures and residence times were higher under fixed bed than under fluidized bed conditions. Various factors could influence this result, e.g., an inhibition effect of silicon in the bed material could have lowered the biomass conversion under fluidized bed conditions [1][21]. Another reason could be lower fuel-gas contact times under fluidized bed conditions, due to inconsistent fluidization and effects like gas channeling around the sample cage. Differences in heat transfer from the external heating shell to the thermocouples outside the sample extraction cage and biomass inside the cage could also lead to this result because the cage could have decreased heat transfer from the heating to the sample by hindering radial mixing. As a result, the samples' actual temperature could have been higher under fixed bed than under fluidized bed conditions.

#### 3.2. BET surface

Multi-point fitting data, calculated BET surface areas, and total pore volumes are given in Table 3. Correlation coefficients between isotherm measurement data and selected multi-point fits were at least 0.9981.

Table 3: Surface characterization data from BET surface measurement by N₂ adsorption

Name	p/p <sub>0</sub>		С	Isotherm data points	BET surface	Total pore
	Low point	High point		in the fitting range	area (m²/g)	volume (cm³/g)
Torref.	1.01E-02	0.07	46	4	0.65	9E-04
E1	1.16E-03	0.23	261	16	201	0.09
E2	1.12E-03	0.20	812	30	387	0.17
E3	1.76E-03	0.05	2902	8	608	0.25
E4	1.07E-03	0.14	1177	9	193	0.09
E5	2.13E-03	0.04	3702	6	498	0.20
E6	1.39E-03	0.05	1913	12	798	0.34
E7	3.28E-03	0.10	645	6	55	0.03
E8	1.10E-03	0.20	796	24	340	0.15
E9	1.03E-03	0.04	3811	8	482	0.20
E10	4.76E-03	0.14	655	9	240	0.11
E11	1.76E-03	0.03	4088	5	451	0.18
E12	1.44E-03	0.04	3472	7	560	0.23

Surface areas and total pore volume are orders of magnitude higher for biochar samples after CO<sub>2</sub> gasification. BET surface area and total pore volume increased with higher burn-off values. Samples prepared under fixed bed conditions generally showed higher surface areas and pore volumes than samples prepared under fluidized bed conditions. Both values were increased for samples prepared at higher gasification temperatures and solid residence times. The surface area measured after 25 minutes of fixed bed operation was around 4 times as much as the surface area after treatment at 800 °C under otherwise equivalent conditions, showing that temperature had a high impact.

This indicates two things: First, heat transfer problems under fluidized bed conditions might also explain the differences observed in surface area and pore volume compared to fixed bed conditions. Second, since the difference between 800 and 900 °C significantly impacts the thermodynamic equilibrium and reaction kinetics of the Boudouard reaction in biomass CO<sub>2</sub> gasification [1], these results suggest that surface area growth is largely caused by the Boudouard reaction.

While these results suggest fixed bed conditions, long solid residence times, and high temperatures for producing biochar with a high BET surface area, fixed bed conditions did not yield the highest surface area per mass of raw feedstock. Figure 4 compares the BET surface area results side-by-side with the surface yield. The second metric suggests that the yield of surface area per mass of feedstock was higher from gasification under fluidized bed conditions. Around 100 m<sup>2</sup>/g<sub>feedstock</sub> are found for gasification under fluidized bed conditions and at 850 °C or 900 °C. Since the BET surface area measured for these samples was also near or above 500 m<sup>2</sup>/g, fluidized bed operation seems to have an edge in yield for applications that do not need BET surface areas over 500 m<sup>2</sup>/g.

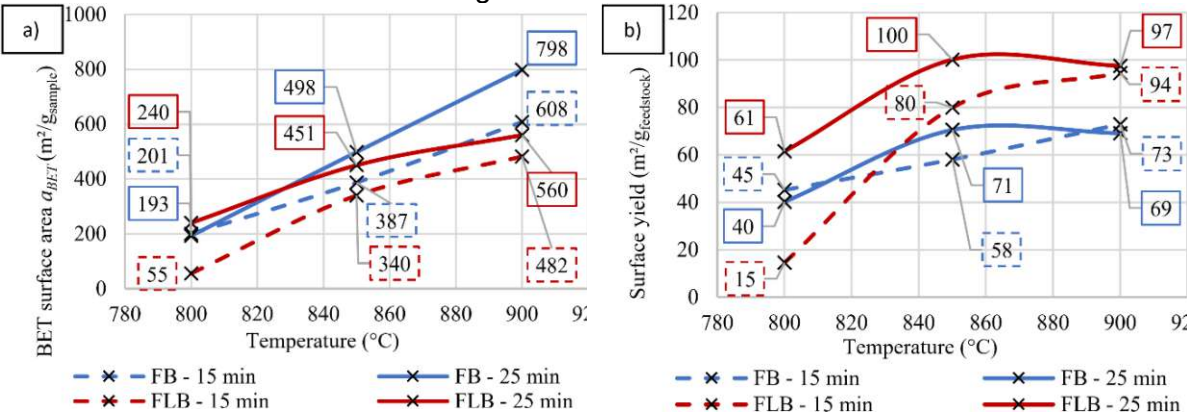


Figure 4: a) BET surface area of biochar, b) Surface yield from raw biomass to biochar.

#### 4. Conclusion

The combination of torrefaction pretreatment and biomass CO<sub>2</sub> gasification produced biochar with a high surface area. CO<sub>2</sub> gasification increased BET surface areas by two to three orders of magnitude compared to the torrefied intermediate product. Higher temperatures and solid residence times lead to higher BET surface areas, burn-off, and surface yields. While fixed bed conditions were used to produce the highest BET surface areas and pore volumes in this work, fluidized bed conditions yielded more total surface area per raw feedstock due to lower burn-off values during gasification. Therefore, fluidized bed gasification should be considered if the biochar meets the application's demands. Further research could help to determine if the observed differences in burn-off are a system-specific result of this experimental setup. Since high temperatures and solid residence times are also favorable for utilizing CO<sub>2</sub> in this process, using biomass CO<sub>2</sub> gasification as a CCU process and for producing high-quality biochar is promising.

## **Acknowledgment**

This study was carried out within the doctoral college CO₂Refinery at TU Wien and was part of the research project Processes for metal-to-char encapsulation (I 5404) funded under the grant-DOI 10.55776/I5404. N. Steinacher and J. Piotrowska of TU Wien, and A. Korus of Silesian University of Technology are acknowledged for their help with surface analysis.



### References

- F. J. Müller et al., "CO2 conversion to CO by fluidized bed biomass gasification: [1] Analysis of operational parameters," Journal of CO2 Utilization, vol. 81, no. March 2024, 2024, doi: 10.1016/j.jcou.2024.102706.
- A. Nurdiawati, I. N. Zaini, W. Wei, R. Gyllenram, W. Yang, and P. Samuelsson, [2] "Towards fossil-free steel: Life cycle assessment of biosyngas-based direct reduced iron (DRI) production process," J Clean Prod, vol. 393, no. January, p. 136262, 2023, doi: 10.1016/j.jclepro.2023.136262.
- [3] Y. H. Chan, S. N. F. Syed Abdul Rahman, H. M. Lahuri, and A. Khalid, "Recent progress on CO-rich syngas production via CO2 gasification of various wastes: A critical review on efficiency, challenges and outlook," Environmental Pollution, vol. 278, pp. 1-16, 2021, doi: 10.1016/j.envpol.2021.116843.
- A. Lampropoulos et al., "Effect of Olive Kernel thermal treatment (torrefaction vs. slow [4] pyrolysis) on the physicochemical characteristics and the CO2 or H2O gasification performance of as-prepared biochars," International Journal of Hydrogen Energy, vol. 46, no. 57. pp. 29126–29141, 2021. doi: 10.1016/j.ijhydene.2020.11.230.
- A. M. Mauerhofer et al., "Conversion of CO2 during the DFB biomass gasification [5] process," Biomass Convers Biorefin, vol. 11, no. 1, pp. 15-27, 2021, doi: 10.1007/s13399-020-00822-x.
- P. Lahijani, Z. A. Zainal, M. Mohammadi, and A. R. Mohamed, "Conversion of the [6] greenhouse gas CO2 to the fuel gas CO via the Boudouard reaction: A review," Renewable and Sustainable Energy Reviews, vol. 41, pp. 615-632, 2015, doi: 10.1016/j.rser.2014.08.034.
- [7] B. M. Ohsowski, K. Dunfield, J. N. Klironomos, and M. M. Hart, "Plant response to biochar, compost, and mycorrhizal fungal amendments in post-mine sandpits," Restor Ecol, vol. 26, no. 1, pp. 63-72, Jan. 2018, doi: 10.1111/rec.12528.
- M. Ahmad, S. S. Lee, S. E. Lee, M. I. Al-Wabel, D. C. W. Tsang, and Y. S. Ok, "Biochar-[8] induced changes in soil properties affected immobilization/mobilization of metals/metalloids in contaminated soils," J Soils Sediments, vol. 17, no. 3, pp. 717-730, Mar. 2017, doi: 10.1007/s11368-015-1339-4.
- [9] F. L. Braghiroli, H. Bouafif, C. M. Neculita, and A. Koubaa, "Influence of Pyro-Gasification and Activation Conditions on the Porosity of Activated Biochars: A Literature Review," Waste and Biomass Valorization, vol. 11, no. 9. Springer, pp. 5079-5098, Sep. 01, 2020. doi: 10.1007/s12649-019-00797-5.
- V. Benedetti, F. Patuzzi, and M. Baratieri, "Gasification Char as a Potential Substitute [10] of Activated Carbon in Adsorption Applications," in Energy Procedia, Elsevier Ltd, 2017, pp. 712-717. doi: 10.1016/j.egypro.2017.03.380.
- J. Pallarés, A. González-Cencerrado, and I. Arauzo, "Production and characterization [11] of activated carbon from barley straw by physical activation with carbon dioxide and steam," Biomass Bioenergy, vol. 115, pp. 64–73, Aug. 2018, 10.1016/j.biombioe.2018.04.015.
- A. Korus, "Investigation of Tar Conversion Over Biomass Char," University of Lincoln, [12] 2019. doi: https://doi.org/10.24385/lincoln.24326497.v1.
- P. Basu and P. Kaushal, "Biomass Gasification, Pyrolysis, and Torrefaction: Practical [13] Design, Theory, and Climate Change Mitigation, Fourth Edition," Biomass Gasification, Pyrolysis, and Torrefaction: Practical Design, Theory, and Climate Change Mitigation, Fourth Edition, pp. 1–681, Jan. 2023, doi: 10.1016/C2022-0-02464-8.
- C. F. Chang, C. Y. Chang, and W. T. Tsai, "Effects of burn-off and activation [14] temperature on preparation of activated carbon from corn cob agrowaste by CO2 and steam," J Colloid Interface Sci, vol. 232, no. 1, pp. 45-49, Dec. 2000, doi: 10.1006/jcis.2000.7171.
- Y. Ngernyen, C. Tangsathitkulchai, and M. Tangsathitkulchai, "Porous properties of activated carbon produced from Eucalyptus and Wattle wood by carbon dioxide activation," Korean Journal of Chemical Engineering, vol. 23, no. 6, pp. 1046-1054, Nov. 2006, doi: 10.1007/S11814-006-0028-9/METRICS.
- J. R. Grace, "Contacting Modes and Behaviour Classification of Gas-Solid and Other [16] Two-Phase Suspensions," Can J Chem Eng, vol. 64, no. June, pp. 353-363, 1986.



- [17] C. Y. Wen and Y. H. Yu, "A generalized method for predicting the minimum fluidization velocity," American Institute of Chemical Engineers Journal, vol. 12, no. 3, pp. 610-612, 1966, doi: 10.1002/aic.690120343.
- "Analytical Methods." Accessed: Mar. 14, 2024. [Online]. [18] Available: https://www.european-biochar.org/en/ct/8
- S. Brunauer, P. H. Emmett, and E. Teller, "Adsorption of Gases in Multimolecular [19] Layers," 1938. Accessed: Mar. 14, 2024. [Online]. Available: https://pubs.acs.org/sharingguidelines
- J. Rouquerol, P. Llewellyn, and F. Rouquerol, "Is the bet equation applicable to [20] microporous adsorbents?," Stud Surf Sci Catal, vol. 160, pp. 49–56, Jan. 2007, doi: 10.1016/S0167-2991(07)80008-5.
- D. Neves, H. Thunman, A. Matos, L. Tarelho, and A. Gómez-Barea, "Characterization [21] and prediction of biomass pyrolysis products," Prog Energy Combust Sci, vol. 37, no. 5, pp. 611-630, Sep. 2011, doi: 10.1016/J.PECS.2011.01.001.
- X. Jing et al., "Evaluation of CO2 gasification reactivity of different coal rank chars by [22] physicochemical properties," Energy and Fuels, vol. 27, no. 12, pp. 7287-7293, 2013, doi: 10.1021/ef401639v.